భీమన్న 'త్రిపద'లు – హేతువాద గుళికలు

– డా॥. పి. జయచంద్రుడు, తెలుగు అధ్యాపకులు, ఎస్.వి.సి.ఆర్. ప్రభుత్వ డిగ్రీ కళాశాల, పలమనేరు.

భాష మానవజాతిని ఏకం చేస్తే సాహిత్యం మానవజాతి మనసులను రంజింపజేసింది. ఆలోచింపచేసింది. చైతన్యవంతం చేసింది. ఏ భాషాసాహిత్యమైనా ఆ జాతి సమకాలీన సమాజాన్ని ఆవిష్కరిస్తుంది. తెలుగు ప్రాచీన సాహిత్యం సమాజ సమస్యలకంటే పురాణాలకు, ఇతిహాసాలకు ప్రాధాన్యమిచ్చింది. ప్రాచీన సాహిత్యం పరిధి చాలా చిన్నది. ఆధునిక సాహిత్యం విశ్వమంత విశాలంగా తన పరిధిని విస్తరింపజేసింది. ఏదో ఒక వర్గానికి మాత్రం పరిమితమైన ప్రాచీన సాహిత్యం కుల, మత, వర్ణ, వర్గ, వివక్షత లేకుండా ఆధునిక సాహిత్యం సాగింది. ఆధునిక సాహిత్యం వాస్తవిక సాహిత్యప్రయోజనాల్ని చేకూర్చాయి. ప్రజల సమస్యల్ని సమాజమంతా తెలిసేలా ఆవిష్కరించాయి. ప్రాచీన సాహిత్యం ప్రక్రియలు పరిమితమైనది. ఆధునిక సాహిత్యం ప్రక్రియ బాహుళ్యం కలది. ఆధునిక సాహిత్యం సమాజంలోని ప్రతి సమస్యను గుర్తించి విశ్లేషించింది. ధనికవర్గానికో, పాలితవర్గానికో పరిమితమై ఆకాశంలో విహరిస్తున్న సాహిత్యాన్ని అణగారిన జీవితాలను ఆవిష్కరించడానికి ఆధునిక సాహిత్యం నేలపై పయనించింది. కందుకూరి వీరేశలింగం సమాజంలోని రుగ్మతలను ప్రశ్నించి సంఘసంస్కరణలకు పూనుకున్నాడు. గురజాడ అప్పారావు తన భాషాసంస్కరణతో సమాజంలో ప్రతి వర్గంలోని లోసుగులను బయటకు తీసాడు. ముఖ్యంగా బాల్యవివాహాలు, కన్యాశుల్కం మునుగుల్లో స్త్రీలు అనుభవిస్తున్న దుర్భరమైన జీవితాలను ఆవిష్కరించి స్త్రీ జాతిని చైతన్యవంతం చేయడానికి ప్రయత్నించాడు. అలాగే వర్ణప్రధాన సమాజమైన మన భారతసమాజంలో పంచమజాతి అనుభవిస్తున్న హేయమైన జీవితాలను ఆవిష్కరించడానికి ఎందరో కవులు పుట్టుకొచ్చారు. దళితుల

గురించి మొట్టమొదటి సారిగా శ్రీకృష్ణదేవరాయలు ప్రస్తావించినా దళితుల బాగోగులను ఎవరూ పెద్దగా పట్టించుకోలేదు. దళితజాతి సమస్యలను దళిత జాతే పరిష్కరిస్తుందని దళితకవులు ముందుకొచ్చారు. అలాంటి దళితకవుల శ్రేష్ఠులలో బోయి భీమన్న ఒకరు. బోయి భీమన్న తన కవితాఖడ్గంతో దళితసమస్యల్ని ఖండించ ప్రయత్నించాడు. భీమన్నగారి పాలేరు నాటకం దళిత సమస్యల చిత్రీకరణకు, దళిత అభ్యుదయానికి ఒక కరదీపిక. బోయి భీమన్న దళిత సమస్యలనే కాకుండా సమాజంలోని రుగ్మతలను, మానవజీవితంలో సంభవించు నిత్యసత్యాలను ఆవిష్కరించడానికి 'త్రిపద' అనే నూతన ప్రక్రియకు నాంది పలికాడు.

తెలుగు సాహిత్యంలో ద్విపద ప్రక్రియ సుపరిచితమే. కానీ ద్విపద ప్రక్రియవలె త్రిపదలను సృష్టించిన ఘనత భీమన్నది. కన్నడ సాహిత్యంలో త్రిపదలున్నట్లు పెద్దలభిప్రాయం. వాటికి వీటికి ఎలాంటి సంబంధం లేదు. చిన్నిచిన్ని పాదాలతో స్పష్టమైన భావాలతో పాఠకుల హృదయంలో మెరుపులాంటి ఆనందాన్ని కల్గిస్తుంది. మేధస్సుకు పదునుపెడుతుంది ఈ త్రిపదలు. నేటి అత్యాధునిక కవిత్వంలోని హైకూలు వలె, మిని కవితలవలె భీమన్న త్రిపదలు భాసిస్తాయి. ఈ త్రిపదులలో భీమన్న తన అనుభవాలతో సమాజాన్ని ఎలా ఆవిష్కరించాడో చూడవచ్చు. ఇందులో ప్రతిది హేతువాదబద్ధమైంది. ప్రతిదీ నిత్యసత్యమైంది. అన్ని కాలాలకు వర్తించే అంశాలు ఈ త్రిపదుల్లో చూడవచ్చు. సమాజంలో తనకెదురైన, తాను అనుభవించిన, తాను తెలుసుకున్న నిత్యసత్యాలను త్రిపదుల్లో ఎలా ఆవిష్కరించాడో పరిశీలించడం నా పత్రోద్దేశం.

భారతదేశం వేదభూమి, కర్మభూమి. అలాంటి దేశంలో వర్ణవ్యవస్థ మానవజాతిని విభజించింది. అది

మానవజాతి అభివృద్ధికి మొదటి ఆటంకం. తర్వాత కాలానికి పంచమకులాన్ని సృష్టించారు. దేశానికి తమ శ్రమతో రక్తం ధారపోసి దళితులు అణగారిన వర్గంగా జీవించడం జరిగింది. సమాజంలో అనేక అవమానాలకు గురికావాల్సి వచ్చింది. దేశానికి తిండిపెడుతున్నా ఆకలిమంటలతో అల్లాడవలసివచ్చింది. దేశప్రజలకు చెప్పులా తోడ్పడినా చెప్పులు లేని నడకతో జీవించింది పంచమకులం. మనుషులతో మనిషిగా జీవించలేని స్థితి. మనశ్శాంతికి దైవదర్శనానికి నోచుకోని అభాగ్యులు. ఇలా సమాజంలో అన్నివిధాలుగా దుర్భరజీవితాల్ని అనుభవించాల్సి వచ్చింది. దళితులు, పంచమకులం, అణగారిన వర్గమని చులకనకు గురై అజ్ఞానంలో జీవించారు. అలాంటి పంచమకులంలో పుట్టి, పంచమజాతి ఉద్ధరణకు కలమెత్తిన, గళమెత్తిన కవిసైనికుడు. భారత దేశంలోని ప్రజలంతా అన్నదమ్ములవలె జీవించాలని, సమైక్యత భారతదేశమని, లౌకికరాజ్యమని చెప్పుకోవడమే గానీ ఆచరణలో వివక్షత ఎప్పటికీ ఉన్నదని అధిక వర్గం అణగారినవర్గాన్ని వేరుగానే చూస్తుందని తన అనుభవాలను క్రిందివిధంగా కవిత్వీకరించాడు.

"అందరి శరీరాలు దేవాలయాలే అయితే
అందరి ఆత్మలు పరంజ్యోతులే అయితే
ఫలాని వ్యక్తిని ప్రేమించానంటాడేం మనిషి?"

"చూడగా చూడగా నాకనిపిస్తున్నది -
శరీరమే సత్యం, తక్కినదంతా అసత్యమని!
అందుకే నీవూ, నేనూ ఒక్కరం కాదని"

"ప్రేమించాను, ప్రేమించబడ్డాను
ఆనందబ్రహ్మలో ఐక్యం కూడా అయ్యాను
అయినా ఎందుకో శరీరం కోసం ఈ తపన!"

బోయిభీమన్న ప్రబోధించిన నిత్యసత్యాల్లో ఒకటి మానవుడు ఇంతవరకు తాను పొందాల్సిన ఆనందం, చేరాల్సిన లక్ష్యం ఇంకా చేరలేదనేది. మానవుడు ఆటవిక జీవితం నుంచి నాగరికత జీవితానికి ఎదిగినా ఆనంద దాయకమైన, శాంతియుత జీవితాన్ని పొందలేదని భీమన్న

పేర్కొన్నాడు. సకలసృష్టిలో మానవుడు ఒక అద్భుతమైన జీవి. ఆలోచనాశక్తి కల్గిన విచక్షణాజీవి. కానీ ఇప్పటికీ మానవుడు విచక్షణ కోల్పోయి తాను పొందాల్సిన ఆనందాన్ని, తాను సాధించాల్సిన లక్ష్యాన్ని ఇప్పటికీ పొందలేదని, చేరుకోలేదని ఇంకా మానవుని మేధస్సు శాంతియుత, అహింసామార్గంలో నడిచి సమైక్యతవైపు, సమసమాజం వైపు నడవాలని ఆశిస్తున్నాడు.

"సౌందర్యం నగ్నం, దాన్ని చూడలేదు మనిషి!
సత్యం నగ్నం దాన్ని ధరించలేదు మనిషి!
పరబ్రహ్మం నగ్నం దాన్ని పొందలేదు మనిషి!"

"ప్రవక్తలు పుట్టని భగవంతుడవతరించని,
సత్యం సత్యమే లోకంలో -
స్వార్ధం ముందు పరమార్ధం వెనక మనిషికి!"

మానవజీవితం సమస్తం స్వార్ధపూరితమని, స్వార్ధం కోసం సత్యాన్ని దాచగలరని, స్వార్ధమే పరమార్ధమని నేటి సమాజం ప్రవర్తిస్తున్నదని, ఈ స్వార్ధంవల్ల బడుగు, బలహీనవర్గాలు అభివృద్ధికి, ఆనందానికి నోచుకోలేదని, స్వార్ధమే సకల సమస్యలకు కారణమని హేతువాద దృక్పథంతో తన అభిప్రాయాల్ని వెలిబుచ్చాడు. స్వార్ధం కోసం శత్రువులు మిత్రులుగా, మిత్రులు శత్రువులుగా తయారవుతున్నారని క్రింది విధంగా కవిత్వీకరించాడు.

"శత్రువు శత్రువూ కాదు, మిత్రుడు మిత్రుడూ కాదు
ఎవ్వరికీ, ఎల్లప్పుడూ ప్రపంచంలో
ఎల్లప్పుడూ ఉండేది ఒక్కటే - అది స్వార్ధం!"

"స్వార్ధం లేకుండా వ్యక్తి లేదు
వ్యక్తి లేకుండా సమాజం లేదు
సమాజం లేకుండా భగవంతుడే లేడు!"

మానవుడు తన ఆధిక్యత కోసం, తన స్వార్ధపరతకోసం ఎదుటివారిని అణగత్రొక్కి అందలమెక్కుతాడు. తన స్వార్ధంకోసం ఇతరులను పీడించడం, హింసించడం చేయడం మానవస్వభావం. పశువు ఆకలేస్తే గడ్డి తింటుంది. క్రూరమృగం ఆకలేస్తే మాంసం తింటుంది.

భావవీణ

కానీ మానవుడు ఆకలేయకపోయినా అడ్డమైన గడ్డికోసం సమాజాన్ని మాంసముద్దలా మింగేసే స్వార్థపరుడని, ఆ స్వార్థంవల్లే సమాజంలో వర్గభేదాలు, వర్ణభేదాలు పుట్టుకొచ్చాయని వాపోయాడు. మానవుడు తాను స్వార్థ పరుడైన ఎదుటివారిని నిందిస్తూ లౌక్యంగా ప్రవర్తిస్తున్నా డని, మానవుడు గోముఖ వ్యాఘ్రమని అభివర్ణించాడు.

"తనకు లేదని, ఎదుటివాడికున్నదని ఏడుస్తూ
పైకి అరుస్తాడు "అతినీతి" అంటూ లౌక్కుడు!
వ్యాఘ్రం కంటె గోముఖవ్యాఘ్రం ప్రమాదకరం"

"గోవు గడ్డి తింటుంది, వ్యాఘ్రం మాంసం తింటుంది
ప్రతి జీవికి ఒక విశిష్ట స్వభావం ఉంది
మనిషి ఒక్కడే గోముఖ వ్యాఘ్రం"

లోకంలో నీతివర్తనులు నేతిబీరకాయ వలె ప్రవర్తిస్తున్నారని, సమాజంలో నీతి శూన్యమని ప్రబోధిం చాడు. నీతి రత్నాలకంటే గొప్పదని పలికే మానవుడు రత్నాలకిచ్చే విలువ నీతికివ్వడం లేదు. నీతికి విలువిచ్చే మానవుడే నిజమైన ధనవంతుడని భీమన్న అభిప్రాయ పడ్డాడు. రత్నాలు ఆకలి తీర్చవని, నీతిమార్గం పాటిస్తే ఆకలికేకలు ఉండవని భీమన్న భావన. ఈ విషయాన్ని భీమన్న ఈ క్రింది త్రిపదలలో సూత్రీకరించాడు.

"తిండి కొనగలవు రత్నాలు
తినడానికి మాత్రం పనికిరావవి!
అలాంటివే నీతులు, లోకంలో!"

"రత్నాలకంటే నీతులు ప్రాచీనం
రత్నాలకంటే నీతులు సురక్షితం
రత్నవర్తకుల కంటే నీతివర్తకులే ధనికులు!"

మానవుడు ఎంత బుద్ధిమంతుడైనా అంతే అజ్ఞాని, ఎంత పరాక్రమవంతుడైనా అంతటి భయస్థుడు. మానవుడు నిరంతరం ప్రతి విషయానికి భయపడుతూ జీవిస్తాడు. భయం మరణంతో సమానం. ధైర్యం జీవించడంతో సమానం. భయపడుతూ బ్రతకడం కన్నా మరణం మేలని, మరణానికి మించిన నష్టం మనిషికి

మరొకటి లేదని, మనిషి జీవితంలో దేనికి భయపడాల్సిన అవసరంలేదని ప్రబోధించాడు.

"మృత్యువును మించి జరిగే హాని లేదు
మృత్యువుకు జడిసి లాభమూ లేదు జీవికి!
ఇంకెందుకో మరొకరికి భయపడటం!"

"ఒక రథం పోతే మరొక రథం విజయప్రతుడికి
సంసారసాగరంలో కూడా అంతే!
శరీరం సాధనమే, ఫలితార్థం కాదు!"

"తన మాటను తానే నమ్ముని జీవి -
తన పని తనకే నచ్చని జీవి -
తన వూహకు తానే బెదిరే జీవి - మనిషి!"

మానవసేవే మాధవసేవ. మానవుడే మాధవుడని పెద్దలు సెలవిచ్చారు. అంటే దానర్థం మాధవుడు మానవ రూపంలోనే ఉంటాడని, మానవుని గౌరవిస్తే మాధవుని ఆరాధించినట్లేనని ఈ మాటలకు తాత్పర్యాలు. మనిషిని మనిషిగా చూడని తత్త్వం మంచిదికాదని, భగవత్ప్రార్థన కంటే మానవుని అభిమానించడం గొప్పదని భీమన్న వాదం. భక్తిమానవుని అహంకారవ్యాధికి ఔషధమని భీమన్న వేదం. భగవంతుడు తనకు మానవుడి నుండి కోరుకునేది ఆరాధన కాదని, సహ మానవులపట్ల ప్రేమాభి మానాలు చూపించడం భగవంతుని పట్ల చూపే నిజమైన కర్తవ్యమని భీమన్న అభిప్రాయం. ప్రజలంతా వివక్ష లేకుండా అన్నదమ్ములవలె జీవించాలన్నది భగవంతుని అభిప్రాయమని భీమన్న తన త్రిపదలో కవిత్వీకరించారు.

"భగవత్ప్రార్థన అవసరమే మనిషికి
అయితే అది భగవంతుడి బాగుకోసమా?
తన అహంకార వ్యాధికే ఔషధం అది!"

"భగవంతుడు కోరేది వట్టి భజన కాదు
తానిచ్చిన పనిని చక్కగా నిర్వహించడం
తండ్రి కోరేది బిడ్డల ప్రయోజకత్వం మాత్రం!"

ఆధునికయుగం శాస్త్రసాంకేతిక యుగం. కాలం వేగంగా తిరుగుతున్నది. మనిషి కాలంతో పాటు

తిరుగుతూ కాలాన్ని జయించే ప్రయత్నం చేస్తున్నాడు. ఆ ప్రయత్నంలో మనిషికి విశ్రాంతి దొరకడం లేదు. విశ్రాంతి లేని మనిషికి సుఖం మాయమయ్యింది. సుఖం లేక మనిషికి చివరికి దుఃఖమే మిగిలిందని భీమన్న వాపోయాడు. పూర్వకాలంలో మనిషి ప్రశాంతంగా తినేవాడు. నేటికాలంలో మనిషి నిలబడితింటున్నాడని, రాబోయే రాకెట్కాలంలో పరిగెడుతూ తింటాడేమోనని తన త్రిపదుల్లో చమత్కరించాడు.

"కూర్చుని తినేవాడు పూర్వం మనిషి
నిలబడి తింటున్నాడీ మెషీనుకాలంలో
పరిగెడుతూ తింటాడిక రాకెట్ యుగంలో!"

"మనిషి వేగం పెరిగి విశ్రాంతి తరిగింది
విశ్రాంతి తరిగి సుఖం విరిగింది
సుఖం విరిగి దుఃఖం వెల్లివిరిసింది!"

ఇలా బోయి భీమన్న తన త్రిపదలలో నిత్యసత్యాలను హేతువాద దృక్పథంతో కవిత్వీకరించాడు. నిజాన్ని నిర్భయంగా చెప్పేవాళ్ళను సమాజంలోని రాక్షస స్వభావం గల వాళ్ళు బాధిస్తారని, అణిచివేస్తారని హెచ్చరించాడు. స్వార్థపరుడైన మానవుడు అల్పుడై ఆనందంకోసం వెంపర్లాడుతాడు. నీతిశతకాలు ఎన్ని నీతులు ప్రబోధించినా మానవుడు ఆచరణలో పెట్టడని, తన స్వార్థం కోసమే పాటుపడతాడని భావించాడు. మానవుడు స్వార్థాన్ని విడిచి నిస్వార్థంగా జీవిస్తే మహా పురుషు డౌతాడని భీమన్నగారి అభిప్రాయం. జీవితం అందమైన పుస్తకమని, ఆ పుస్తకంలో ఉన్న తప్పుల్ని దిద్దుకుంటే జీవితం పరమానందభరితమని, మంచిని పెంచమని, మంచిని పంచమని, తాను ఆనందిస్తూ, ఇతరులు ఆనందంగా ఉండేటట్లు చూడటంలో మానవ జీవిత పరమార్థం దాగివుందని భీమన్న గారి జీవితానుభవం.

"జీవితం ఒక అకౌంటు పుస్తకం
ఒకటి రెండు తప్పుల్ని దిద్దుకోవచ్చు అందులోనే,
అన్నీ తప్పులే అయితే పుస్తకాన్నే మార్చకతప్పదు!"

"పది గ్రంథాలను ఒక్కసారి చదివే కంటే
ఒక్క మంచి గ్రంథాన్ని పదిసార్లు చదువు!
ఒక్క జీవమంత్రాన్ని వందసార్లు పఠించు!"

పరిశీలనా గ్రంథాలు :

1. త్రిపదలు - భీమన్న బోయి

2. తెలుగు సాహిత్యచరిత్ర - శాస్త్రి. ద్వా.నా

3. గబ్బిలము - జాషువా గుర్రం

4. పాలేరు నాటకం - భీమన్న బోయి

✿ ✿ ✿

INTERNATIONAL JOURNAL OF INNOVATIVE RESEARCH

IN COMPUTER & COMMUNICATION ENGINEERING

INTERNATIONAL STANDARD SERIAL NUMBER INDIA

Impact Factor: 8.165

A Review on Recent Medical Applications of Image Processing

M. Kiran Babu[1], K.CH.V. Subbaiah Naidu[2]

Department of Mathematics, SVCR Govt. Degree College, Palamaner, India[1,2]

ABSTRACT: In sciences and technology, image processing is becoming more widely recognized as a critical component of scientific study and development. It is no exaggeration to say that image processing has countless applications in almost every field known to mankind. Image processing has various applications in remote sensing, medical imaging, non-destructive evaluation, forensic studies, textile industry, material science, military, film industry, document processing, and printing industry, just to name a few. In the present work, we sketch some of the recent medical applications of image processing.

KEYWORDS: Image Processing, medical, imaging, applications

I. INTRODUCTION

In the sciences and technology, image processing is becoming more widely recognized as a critical component of scientific study and development.A digital image is an image function f(x,y) that has been discretised both in spatial coordinates and brightness. It is represented by a series of 2D arrays. Each element of this array is called "pixel" [14]. Image processing allows for the improvement of information available in these images for human interpretation and for autonomous machine perception [8]. It is no exaggeration to say that image processing has countless applications in almost every field known to mankind. Image processing has various applications in remote sensing, medical imaging, non-destructive evaluation, forensic studies, textile industry, material science, military, film industry, document processing, and printing industry, just to name a few [4]. Researchers are continuously striving to improve the image processing techniques and further expand the impact of image processing in this computer era.

Medical image processing comprises of techniques and processes that are used to create images of human body for clinical purposes and medical procedures [19]. The use of image processing techniques in medical field strengthens the quantitative analysis. Generally, human observers analyse the medical images.This type of analysis has limitations caused by interobserver variations and errors due to fatigue and limited experience. But by the use of image processing techniques and computer analysis, it is possible to highly improve the diagnostic accuracy and confidence of medical personnel [7].

A very interesting review of the medical applications of image processing can be found in [12]. Another research found on image processing systems for medical applications is [16]. Trends and analysis of medical images using image processing techniques can be found in [6]. In the present work, we sketch some of the recent medical applications of image processing.

II. IMAGE PROCESSING

The complete image processing system consists of both hardware and software. This system is capable of acquiring the image, storing the image, processing the image according to the user's requirement and then finally displays the image on suitable medium such as television or monitor. Image processing is not a single-step process. Generally many operations are performed sequentially to gain the desired output. The image processing operations which are used to manipulate the acquired image can be grouped into five categories [7]:

1. Image enhancement: It helps to make the image better by adjusting the brightness or contrast, smoothing the image or sharpening it.
2. Image restoration: It is used to reverse the degradation caused by uneven illumination, distortion, unwanted noise, movement of the abject etc.
3. Image analysis: It is mainly used for classifying images into groups by recognizing patterns.
4. Image compression: It is used to reduce the size of the image by eliminating the redundant information used to store the image.
5. Image synthesis: This technique helps in creating new images from other images and non-image data.

These image processing operations and techniques when combined with the knowledge of the application area, solutions to many problems can be obtained.

III. RECENT MEDICAL APPLICATIONS OF IMAGE PROCESSING

A. *EUS - FNAB Specimen Evaluation:*

Endoscopic ultrasound (EUS) is used for detecting pancreatobiliary diseases, for visualizing lesions etc. Endoscopic ultrasound-guided fine needle aspiration biopsy (EUS-FNAB) gives extra pathological information. Thisenhances the diagnostic capabilities of EUS [21]. Using a needle, a EUS-FNAB sample is collected from the patient and then studied. In [13], Okuwaki et al., used automated multiband imaging system (AMUS) to study the sample. The multiband image data is obtained using automated multiband imaging device provided by Olympus Corporation as shown in Fig 1. Then whitish core quantity is calculated using image segmentation techniques. The quantity calculated using AMUS strongly correlates with manual assessments.Since this method is cost-effective, this type of evaluation can be introduced at any facility to obtain objective assessments.
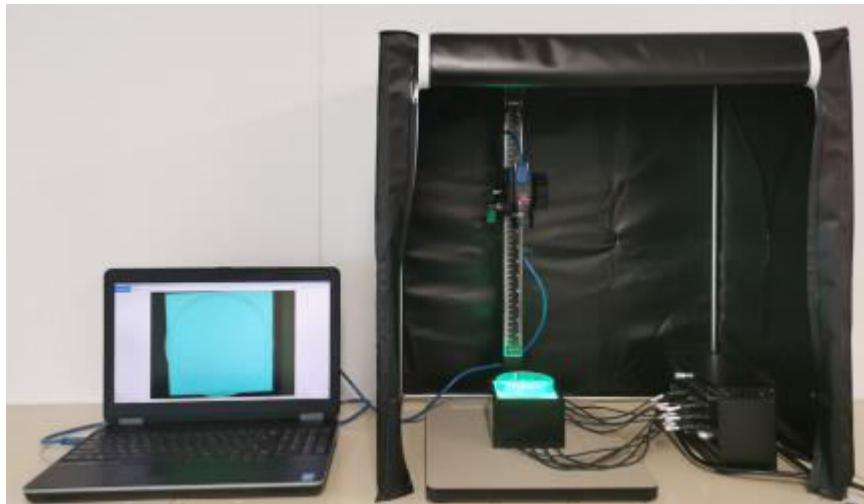
Fig.1: Set-up of automated multiband imaging device [13]

B. *Detection of Tuberculosis Disease*

Tuberculosis (TB), commonly known as consumption, is a long-term infection caused by the Mycobacterium tuberculosis bacteria. The bacteria are most commonly found in the lungs, but they can potentially harm other organs in the human body. It is preventable and curable if identified early; else, it may result in the patient's death.To determine if a person has TB disease, tests such as a chest X-ray or a sputum sample culture can be performed. [15] Mohammad Alsaffar et al., proposed a method to detect the presence of TB in medical X-ray imaging (see Fig.2) using image processing techniques.KERAS, an open source neural networks library is used to extract the picture properties from the medical images that are used as classification attributes. Support Vector Machines (SVMs), Logistic Regression (LR) and KNN, K-Neighbors Classifier are the three classification methods used. Their proposed CNN architecture could automatically categorize the medical images by visual modality and anatomic location. An excellent overall classification accuracy (> 99.5%) is achieved using this method.

C. *Glaucoma Diagnosis*

Glaucoma is a common eye disease that, if left untreated, can result in irreversible blindness. Glaucoma is one of the most common causes of blindness [10].To examine the pattern of rim loss, estimate quantitative parameters, and discover morphological symptoms of glaucoma in the eyeball, an efficient and correct segmentation of the OD and optic cup is required [18].Recent studies show that the CAD system can improve diagnostic accuracy while also reducing fatigue, reducing the number of diseases missed owing to exhaustion or disregarded data, and increasing

reader variability.In [18] Shubham Joshi et al., proposed a computer-aided design (CAD) system to help in the early identification of glaucoma as well as the screening and treatment of the disease using fundus camera. The proposed CAD system would help ophthalmologists diagnose ocular disorders by offering a second opinion in the form of a verdict made by human professionals in a controlled setting. It uses three pretrained CNNs for the categorization of glaucoma viz., residual network (ResNet), visual geometry group network (VGGNet) and GoogLeNet.
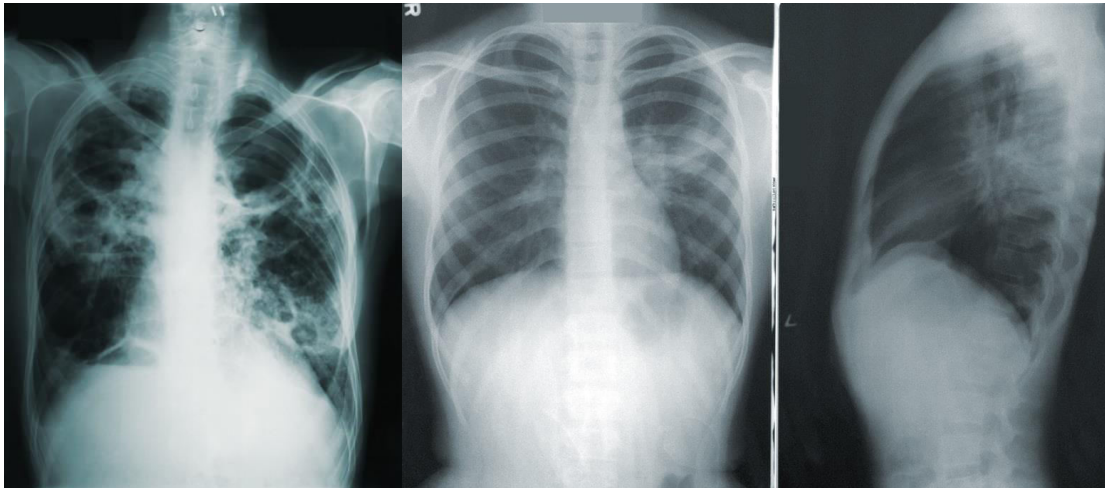
Fig.2: Chest X-ray images

D. *Analysis of Blood Cancer*

Blood cancer, often known as leukaemia, is a type of cancer in which the blood marrow produces abnormal white blood cells in the bloodstream [9]. Blood cancers affect the blood cells, bone marrow, lymph nodes, as well as other parts of the lymphatic system [17].In [9] Harisudha K et al., developed a method to identify all types of blood cancer using image processing techniques like segmentation and feature extraction. Microscopic photographs of blood are taken and lymphocytes are extracted. Different classification techniques like SVM, LDA are used to detect healthy or cancerous cells and KNN algorithm is used to detect the type of cancer. This method is accurate, fast and cheap.
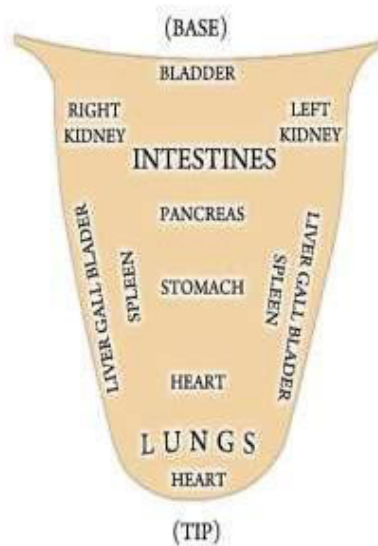

Fig.3: Reflex zones of tongue [1]

E. *Tongue Diagnosis*

The tongue is an organ that is a reflection of the body's physiological and clinicopathological state. Tongue inspection makes use of visual information. The major criteria to evaluate for diagnosis are the colour, form, motility, substance, and coating of the tongue. The geometric shape of the tongue also aids in the diagnosis of one's health. [3] By describing differences in tongue features, a system for analyzing and classifying tongue images for disease diagnosis was developed by Shreya Devkar et al., in [5]. Images of the tongue captured by a good resolution smartphone camera can be used. Using an algorithm, required part of the tongue from the image is identified and features are extracted. They used four techniques employing Gabor filter, energy, color histogram and geometrical figures. Energy method has an accurate rate of 95% and gives good results for normal and diabetes images.

F. *Breast Cancer Prediction and Trail*

Other than nonmelanoma skin cancer, breast cancer is the most frequent cancer among women [2]. It is one of the most prevalent cancers in women in India. It can strike at any age, but it is most common in the early thirties and peaks between the ages of 50 and 64.Patients' survival rates are improved when this condition is detected early. Y Venugeetha et al., developed a method to identify the cancer using Machine learning and image processing techniques in [20]. Mammogram images are used in this method. Using Fuzzy C-Means (FCM) technique, image segmentation is carried out and features are extracted using Gray-Level Co-occurrence Matrix (GLCM), Multi-level Discrete Wavelet Transform and Principal Component Analysis (PCA). KNN algorithm is employed for classification of images. Finally, the tumor affected areas are marked and can be shown to the doctor.

IV. CONCLUSION

In this paper we have tried to discuss the recent medical applications of image processing techniques. The findings can be formulated as follows:

Application	Techniques Used	Database Used	Accuracy
EUS-FNAB specimen evaluation [13]	AMUS	Images obtained using automated multiband imaging device	When the cutoff value was more than 8 mm^2, the AMUS had a high diagnostic sensitivity.
Detection of TB disease [11]	KERAS, SVM, LR, KNN, RESNET50 neural network	Montgomery database	99.5% classification accuracy
Glaucoma diagnosis [18]	Contrast limited histogram equalization (CLAHE), VGGNet-16, ResNet-50, GoogLeNet, MATLAB	PSGIMSR, DRIONS-DB, HRF, DRISHTI-GS	88.96% accuracy, 93.95% precision
Analysis of blood cancer [9]	SVM, LR, LDA, KNN, DT, GB and PCA.	ALLDB-1 dataset, images from Kaggle.	KNN algorithm detects the type of cancer with 97% accuracy.
Tongue diagnosis [5]	MATLAB, Gabor filter, color histogram, Fourier transform to find pixel density	Private database	Energy method has 95% accuracy on normal and diabetes images.

The use of image processing techniques in medical field strengthens the quantitative analysis. EUS-FNAB specimen evaluation for pancreatic diseases, detection of TB disease, Glaucoma diagnosis, Analysis of blood cancer, tongue diagnosis and breast cancer prediction are the applications discussed. In future, image processing techniques can be used to identify and diagnose many other diseases.

REFERENCES

1. Bagaria, Rinisha&Wadhwani, Sulochana. 'Tongue Diagnosis by Image Segmentation', International Journal of Advanced and Innovative Research, Vol. 6, Issue 4, 132-136, 2017.
2. Bray F, Ferlay J, Soerjomataram I, Siegel RL, Torre LA, Jemal A. Global cancer statistics 2018: GLOBOCAN estimates of incidence and mortality worldwide for 36 cancers in 185 countries. CA Cancer J Clin. 2018;68(6):394-424
3. Chang Jin Jung, Young JuJeon, Jong Yeol Kim, Keun Ho Kim, 'Review on the current trends in tongue diagnosis systems', Integrative Medicine Research, Volume 1, Issue 1, pp. 13-20, 2012.
4. Chitradevi, B., and P. Srimathi, 'An overview on image processing techniques', International Journal of Innovative Research in Computer and Communication Engineering 2.11, 6466-6472, 2014.
5. Devkar, S., Mhatre, A., Pawaskar, S., Dodani, S.,'Tongue Diagnosis Using Image Processing.' In: Reddy, V.S., Prasad, V.K., Wang, J., Reddy, K.T.V. (eds) Soft Computing and Signal Processing. Advances in Intelligent Systems and Computing, vol 1340, 2022.
6. Dinesh, B., Rishi, 'Trends and Analysis of medical images using image processing Techniques, Applications, challenges', International Journal of Computer Science Trends and Technology (IJCST), Vol. 6, Issue 5, 39-50, 2018.
7. Dougherty, Geoff, 'Digital Image Processing for Medical Applications', N.p., Cambridge University Press, 2009.
8. Gonzalez, Rafael C., and Woods, Richard Eugene, 'Digital image processing', Italy, Pearson/Prentice Hall, 2008.
9. Kuresan, H., Sabastian Satish, J., &Shanmugam, N., 'Analysis of Blood Cancer Using Microscopic Image Processing', In Soft Computing and Signal Processing, pp. 403-415, 2022.
10. Lee, David A., and Eve J. Higginbotham, "Glaucoma and its treatment: a review", American journal of health-system pharmacy 62, no. 7, 691-699, 2005.
11. Mohammad Alsaffar, GharbiAlshammari, Abdullah Alshammari, Saud Aljaloud, Tariq S. Almurayziq, Abdulsattar Abdullah Hamad, Vishal Kumar, Assaye Belay, "Detection of Tuberculosis Disease Using Image Processing Technique", Mobile Information Systems, vol. 2021, Article ID 7424836, 7 pages, 2021.
12. Naseera, Shaik&Rajini, G.K. &Venkateswarlu, B. &pemeenapriyadarsini, Jasmine,'A Review on Image Processing Applications in Medical Field', Research Journal of Pharmacy and Technology, 10, 3456-3460, 2017.
13. Okuwaki, K., Imaizumi, H., Kida, M., Masutani, H., Watanabe, M., et al., 'New image-processing technology for endoscopic ultrasound-guided fine-needle aspiration biopsy specimen evaluation in patients with pancreatic cancer', DEN Open, 2(1), e21, 2022.
14. Petrou, Costas, and Petrou, Maria M. P., 'Image Processing: The Fundamentals', United Kingdom, Wiley, pp. 1, 2010.
15. R. S. Radhwan and F. S. Al-Nasiri, "Detection of infection with hydatid cysts in abattoirs animals at Kirkuk governorate, Iraq," Tikrit Journal of Pure Science, vol. 26, no. 4, pp. 24–32, 2021.
16. Rama Devi, O., M. SaiChitraMeghana, K. JeevanaShruti, 'Medical Image Processing-An Overview', International Journal of Innovations in Engineering and Technology (IJIET), Vol.7, Issue 3, 362-365, 2016.
17. Rupapara, V., Rustam, F., Aljedaani, W. et al.,'Blood cancer prediction using leukemia microarray gene data and hybrid logistic vector trees model.',Sci Rep 12, 1000, 2022.
18. Shubham Joshi, B. Partibane, WesamAtefHatamleh, HussamTarazi, Chandra ShekharYadav, Daniel Krah, "Glaucoma Detection Using Image Processing and Supervised Learning for Classification", Journal of Healthcare Engineering, vol. 2022, Article ID 2988262, 12 pages, 2022.
19. Sinha, G.R., and Patel, BhagwatiCharan, 'Medical Image Processing', India, Phi Learning, 2014.
20. Venugeetha, Y., Harshitha, B.M., Charitha, K.P., Shwetha, K., Keerthana, V.,'Breast Cancer Prediction and Trail Using Machine Learning and Image Processing' In: Kumar, A., Senatore, S., Gunjan, V.K. (eds) ICDSMLA 2020. Lecture Notes in Electrical Engineering, vol 783, 2022.
21. Yamao, K., Sawaki, A., Mizuno, N. et al. 'Endoscopic ultrasound-guided fine-needle aspiration biopsy (EUS-FNAB): past, present, and future', J Gastroenterol 40, 1013, 2005.

INTERNATIONAL JOURNAL OF INNOVATIVE RESEARCH

IN COMPUTER & COMMUNICATION ENGINEERING

📱 **9940 572 462** 🟢 **6381 907 438** ✉️ **ijircce@gmail.com**

Scan to save the contact details

Effect of temperature, nature of anion and alkyl chain length on the volumetric and acoustic properties of ionic liquid [C₄C₁im][MeSO₄] with alkyl nitriles

P. Bhanuprakash [a,b], R. Prathibha [a], Ramesh L. Gardas [c], K. Sivakumar [d,*], N.V.V. Jyothi [a,*]

[a] Department of Chemistry, S.V. University, Tirupati 517502, A.P., India
[b] Department of Chemistry, S.V.C.R. Govt. Degree College, Palamaner 517408, A.P., India
[c] Department of Chemistry, Indian Institute of Technology Madras, Chennai 600036, T.N., India
[d] Department of Chemistry, S.V. Arts Degree & P.G. College (T.T.D'S), Tirupati 517502, A.P., India

ARTICLE INFO

ABSTRACT

Densities (ρ) and speeds of sound (u) of 1-butyl-3-methylimidazolium methyl sulphate, [C₄C₁im][MeSO₄] with acetonitrile (ACN), propionitrile (PCN) and n-butyronitrile (n-BCN) in the complete composition range at temperatures between 298.15 K and 313.15 K with 5 K intervals and atmospheric pressure is reported. Solute-solvent interactions have been evaluated in the mixtures of [C₄C₁im][MeSO₄] with alkyl nitriles by calculating excess volumes (V^E) and excess isentropic compressibilities (κ_s^E). The V^E and κ_s^E values as a function of mole fraction are correlated using a Redlich-Kister type expression. The excess functions (V^E and κ_s^E) are found to be negative over the complete range of mole fraction for the investigated binary solutions. The studied excess properties are found to increase with the increase in the alkyl chain length of alkyl nitriles. The excess thermodynamic properties of the mixed solvents are discussed in relation to intermolecular interactions and structural effects existing between the component molecules. In addition, the effect of the nature of anion of ionic liquid and temperature on the excess thermodynamic properties has been investigated.

© 2020 Elsevier B.V. All rights reserved.

1. Introduction

Ionic liquids (ILs) are a new class of complex molecules with very low melting temperatures, composed solely of organic/inorganic ions. They are known as "designer solvents" as their physicochemical properties can be fine-tuned at ease for a specific task by modifying the ion substituents and choosing the proper combination of ions [1]. Replacing the traditional solvents with non-volatile, and non-flammable ILs may reduce the negative foot-print of these solvents on the environment. Hence, they are also termed as "green solvents". The distinctive properties of ILs include good ionic conductivity, excellent thermal stability, high heat capacity, wide liquid range, high polarity, potential recoverability and favourable solvation capacity [1,2]. Strong coulombic forces (ion-ion, ion-dipole attractions), moderate hydrogen bonds and weak van der Waals attraction forces are the intermolecular interactions existing in the ILs, which determine their miscibility with polar solvents.

The favourable and typical properties of ILs make them ubiquitous in the industrial applications ranging from organic synthesis to electrochemistry and analytics to advanced materials. A wide range of ILs has been used as the environmentally benign catalysts and solvents in organic synthesis [2–4]. They have been potentially employed as electrolyte materials in different electrochemical applications such as rechargeable batteries, electrochemical capacitors, fuel cells, dye-sensitized solar cells, etc. [2,5–7]. They have also been used as media in separation and extraction technologies [8]. The ILs have been explored as functional and advanced materials like heat storage-thermal fluids, hydraulic fluids, liquid crystals, fuel additives, surfactants and lubricants [9,10]. They are finding their way in the area of analytics as matrix materials for mass spectrometry, gas chromatography columns and as mobile phase in liquid chromatography [2,4]. Further, they find application in biomedicine, drug delivery, biomass processing and embalming [2,11].

Ionic Liquids (ILs) based on 1-alkyl-3-methylimidazolium cation, and anions like [X]⁻, [BF₄]⁻, [PF₆]⁻, [NTf₂]⁻, [CF₃SO₃]⁻, [CF₃COO]⁻, alkyl sulphates, alkyl sulphonates, etc., are one of the most investigated ILs because of their remarkable properties. Alkylimadazolium based ILs find applications as a green solvent and eco-friendly catalyst in organic synthesis [4]. On hydrolysis, the ILs with fluorinated anions such as [BF₄]⁻, [PF₆]⁻, [NTf₂]⁻, lead to the emission of corrosive and toxic volatile gases like hydrogen fluoride (HF) and phosphorus oxytrifluoride (POF₃). An interest in halide-free, alkyl sulphate-based imidazolium ILs is increasing because of their favourable properties such as ease of

* Corresponding authors.
E-mail addresses: sivakumarkasi64@gmail.com (K. Sivakumar), nvvjyothi73@gmail.com (N.V.V. Jyothi).

synthesis in an atom-efficient way from cost-effective and easily available alkylating agents, excellent purity, hydrolysis-stable, water-soluble, non-corrosive, tunable polarity, non-toxic, low glass transition temperature and low viscosity [12–14]. Imidazolium based ILs can be potentially applied as electrolytes in electrochemical devices [2]. In the petrochemical field, imidazolium based alkyl sulphate ILs finds application as extracting solvents in the separation of azeotropic mixtures. $[C_4C_1im]^+$ based alkyl sulphate ILs are used in the extraction of nitrogen and sulphur compounds from diesel and gasoline [15], purification of hexane from its mixture with ethanol [16] and toluene from its mixtures with heptane [17]. Moreover, imidazolium based ILs finds applications as media for CO_2 capture and in the separation of the acidic flue gases CO_2 and SO_2 [18]. The applications of alkyl sulphate-based imidazolium ILs in organic synthesis, separation technologies, and electrochemical applications have become the motivation for choosing $[C_4C_1im]$ $[MeSO_4]$ for the present study.

Alkyl nitriles self-associate through dipole-dipole interactions (Fig. S1) in their pure liquid state [19] as indicated by their high dipole moments (μ) and high dielectric constants (ε) [20]. The cyano group ($-C \equiv N$) of nitriles also acts as hydrogen bond acceptors [21]. Alkyl nitriles find application as a solvent in petroleum refining, and synthesis of pharmaceuticals [22,23]. Owing to its transparency towards UV light and low viscosity, ACN is widely used as a mobile phase in Liquid Chromatography [24]. Due to high dielectric constant, good electrochemical window, and the ability to dissolve more CO_2 than water, ACN is often used in the electrochemical reduction of CO_2 using different capable metal electrodes [25]. It is also used as a promising electrolyte in capacitors, super capacitors and dye-sensitized solar cell [2].

The high viscosities and hydrophobic nature of ILs might restrict their diverse applications in certain fields. Mixing of an IL with suitable organic solvents to form binary systems could be an alternative method to decrease the viscosity as well as to fine-tune their unique properties and thereby their complete exploitation in novel applications [26]. In order to explore new applications for ILs and also to have a proper understanding of the chemical structure and nature of intermolecular interactions in the IL-based mixtures, it is necessary to have a detailed knowledge on their thermo-physical and thermodynamic properties. Further, the sound knowledge of these properties of the IL-based mixtures is crucial in the design of task-specific ILs and also in the development of reliable theoretical simulations in solution theories [27]. The investigation on thermo-physical properties of binary solutions containing ILs is essential to contribute huge data to thermodynamic data bank [28]. Hence, a clear understanding of intermolecular interactions prevailing in the IL+ alkyl nitrile mixtures are prerequisite for their applications in electrochemical devices as an electrolyte, petrochemical field as extracting solvents, as media for CO_2 capture and electrochemical reduction of CO_2. Moreover, excess thermodynamic properties of mixed systems containing ILs are essential not only in understanding the solute-solvent behaviour but also in designing efficient separation processes, transport equipment and in many design engineering calculations involving heat transfer, fluid flow, mass transfer, electrochemical application, etc. [29].

Many researchers have reported density, speed of sound, viscosity and refractive index for the binary mixtures of $[C_4C_1im][MeSO_4]$ with water [1,30], methanol [31–34], ethanol [32,34–37], 1-propanol [32,33], 2-propanol [33], 1-butanol [33,34], 1-hexanol, 1-octanol, 1-decanol [34], nitromethane [35], 1,3-dichloropropane [35], diethylene glycol monoethyl ether [35], propane-1,2-diol [38] and ethylene glycol [39] at different temperatures. The excess volumes (V^E) for $[C_4C_1im]$ $[BF_4]$ + acetonitrile [40], $[C_4C_1im][PF_6]$ + acetonitrile [40,41], $[C_4C_1im]$ $[NTf_2]$ + acetonitrile [42] and $[C_4C_1im][SCN]$ + acetonitrile [43] have been reported previously. A review of the literature reveals that there is no published data on volumetric and acoustic studies on the binary solutions of $[C_4C_1im][MeSO_4]$ with alkyl nitriles. In this context to understand the non-ideal mixing behaviour, excess volumes (V^E) and excess isentropic compressibilities (κ_s^E) for the binary systems have been

evaluated from the experimental density and speed of sound data at temperatures between 298.15 K and 313.15 K and atmospheric pressure. The excess properties are correlated with Redlich–Kister (R-K) polynomial [44] and the fitting coefficients are derived. The results on the excess thermodynamic properties of the mixed solvents are discussed in relation to ion-dipole interactions and structural effects existing between the component molecules. Similarly, the effect of the nature of anion of ionic liquid and temperature on the excess functions has been discussed.

2. Experimental

2.1. Materials

1-Butyl-3-methylimidazolium methyl sulphate ($[C_4C_1im][MeSO_4]$, $M_w = 250.32$ g·mol^{-1}), is acquired from Sigma-Aldrich, India with mass fraction purity higher than 0.980. The IL is subjected to vacuum drying at 343.15 K for 48 h before its use. The content of water in the dried IL sample is estimated by Karl–Fischer Titrator and the average value was found to be <400 ppm. The chemicals: acetonitrile (ACN, Thermo Fisher Scientific, purity ≥0.998), propionitrile (PCN, Sigma-Aldrich, purity ≥0.995), n-butyronitrile (n-BCN, Avra, purity ≥0.990) are procured and are used as received from the supplier without further purification. The molecular structure of the investigated IL is depicted in Fig. S2. The detailed information on all the materials used in this work is listed in Table 1. The purity of the chemicals and quality of measurements is further ensured by the comparison of the measured densities (ρ) and speeds of sound (u) of pure liquids with the reported values [30,33,36,37,40,45–62] as a function of temperature between 298.15 K and 313.15 K and are given in Table S1 in the Supplementary Information. The density and speed of sound data for pure solvents are in accordance with the literature values.

2.2. Methods

The binary mixtures of IL with alkyl nitriles were prepared gravimetrically by syringing known amounts of the pure liquids into ultra-clean, airtight vials using an analytical balance (Sartorius CPA225D) with a precision of ± 0.01 mg, covering the entire range of mole fraction. Each binary mixture was stirred for 10–15 min at room temperature to ensure the complete homogeneity of the two components. The prepared samples were found to be clear and the colour of the solution varies from colourless to pale yellow. Each sample was prepared immediately prior to performing density (ρ) and speed of sound (u) measurements to minimize variations in composition due to evaporation of solvent or absorption of moisture by the hygroscopic IL. The uncertainties for mole fraction $u(x_1)$ of binary solutions is estimated to be u $(x_1) = \pm 5 \times 10^{-5}$.

The density (ρ) and speed of sound (u) of pure $[C_4C_1im][MeSO_4]$ and its mixtures with alkyl nitriles were simultaneously measured at temperatures between 298.15 K and 313.15 K with 5 K intervals and at 0.1 MPa pressure using Anton-Paar (DSA 5000 M) vibrating U-tube digital density and speed of sound analyzer. It measures the period of oscillation of a vibrating U-tube filled with a liquid sample, which is directly related to the sample density. The speed of sound (u) was determined by using a time propagation technique, in which one transducer emits sound waves at a frequency of 3 MHz and a second transducer receives those waves. The speed of sound value was obtained by dividing the known distance between the transmitter and receiver with the propagation time of sound waves. Before carrying out the ρ and u measurements, the instrument was calibrated with dry air, Millipore quality water at atmospheric pressure. The temperature of the sample in the cells of the apparatus is maintained by a built-in Peltier thermostat within $u(T) = \pm 0.01$ K. The experimental uncertainty in density (ρ) and speeds of sound (u) measurements are found to be $\pm 5 \times 10^{-5}$ g. cm^{-3} and ± 0.5 m.s^{-1} respectively.

Table 1
Characteristics of chemicals used in this research work.

Name of the component	Acronym	CAS Number	Molar mass/g·mol^{-1}	Source	Mass fraction purity[a]	Water content by KF (%)
1-Butyl-3-methylimidazolium methyl sulphate	[C$_4$C$_1$im][MeSO$_4$]	401788-98-5	250.32	Sigma-Aldrich, India	0.980	0.04
Acetonitrile	ACN	75-05-8	41.05	Thermo Fisher Scientific, India	0.999	0.01
Propionitrile	PCN	107-12-0	55.08	Sigma-Aldrich, India	0.995	0.02
n-Butyronitrile	n-BCN	109-74-0	69.11	Avra, India	0.990	0.05

[a] Mass fraction purity as specified by supplier.

3. Results and discussion

3.1. Densities (ρ) and excess volumes (V^E)

The experimental densities (ρ) for the [C$_4$C$_1$im][MeSO$_4$] (1) + alkyl nitriles (2) mixtures, as a function of mole fraction of IL (x_1) in the temperature range from 298.15 K to 313.15 K, with a step of 5 K are incorporated in Table 2. The measured densities (ρ) as a function of mole fraction of [C$_4$C$_1$im][MeSO$_4$] (x_1) for the investigated mixtures at 298.15 K ≤ T ≤ 313.15 K are shown in Figs. S3–S5. At constant temperatures, the densities (ρ) of the mixed solutions increase with an increase in x_1 because [C$_4$C$_1$im][MeSO$_4$] is much denser compared with alkyl nitriles. It is also found that at fixed x_1, ρ of the binary solutions follow a decreasing trend with an increase in temperature. This might be attributed to an increase in the kinetic energy of the

molecules with temperature, which enhances the molecular agitations in binary solutions, resulting in low density values. At constant T and x_1, densities of studied mixed systems fall in the order: [C$_4$C$_1$im][MeSO$_4$] + ACN > [C$_4$C$_1$im][MeSO$_4$] + PCN > [C$_4$C$_1$im][MeSO$_4$] + n-BCN. Higher densities observed for [C$_4$C$_1$im][MeSO$_4$] + ACN is ascribed to the relatively stronger specific interactions between [C$_4$C$_1$im][MeSO$_4$] and ACN molecules.

To understand the volumetric behaviour of [C$_4$C$_1$im][MeSO$_4$] upon mixing with alkyl nitriles through the competition effects between ions and polar molecular solvents, the excess volumes (V^E) of the mixtures are calculated through the known equation:

$$V^E = \frac{x_1 M_1 + x_2 M_2}{\rho} - \left[\frac{x_1 M_1}{\rho_1} + \frac{x_2 M_2}{\rho_2}\right] \quad (1)$$

where ρ is the density of the binary mixture, p_1 and p_2 represent the densities of pure components, x_1 and x_2 represent the mole fractions, M_2 and M_2 represent the molar masses of [C$_4$C$_1$im][MeSO$_4$] as component-1 and alkyl nitriles as component-2 respectively.

The experimental data on excess volumes is one of the significant ways to measure the degree of non-ideality of a liquid mixture. The V^E values of the mixed solutions are the resultant of the balance between the following volume expansion and contraction factors [8,10,63]:

(a) Volume contraction factors: Ion-dipole, dipole-dipole, hydrogen bonding, donor-acceptor (D-A) complexes, n-π & π-π interactions among the dissimilar components of the mixture, geometrical fitting of smaller molecules into others interstices possibly results in the contraction of volume in mixtures.

(b) Volume expansion factors: The weak London dispersion forces, disruption of stronger and specific interactions between the dissimilar components of the mixture, unfavorable packing effect between the mixed components will mainly contribute in expansion of volume in the mixed systems.

Table 2
Experimental values of densities (ρ/g·cm^{-3}) as a function of mole fraction of [C$_4$C$_1$im][MeSO$_4$] (x_1),for the binary solutions of [C$_4$C$_1$im][MeSO$_4$] with ACN, PCN and n-BCN from T/K = 298.15–313.15 and 0.1 MPa pressure.

x_1	ρ/g·cm^{-3}			
	T/K = 298.15	303.15	308.15	313.15
[C$_4$C$_1$im][MeSO$_4$] (1) + ACN (2)				
0.0000	0.77663	0.77122	0.76575	0.76028
0.1070	0.92697	0.92227	0.91756	0.91285
0.2018	1.00749	1.00317	0.99883	0.99450
0.3135	1.06963	1.06560	1.06154	1.05749
0.4127	1.10779	1.10395	1.10010	1.09626
0.5049	1.13437	1.13069	1.12699	1.12330
0.6053	1.15683	1.15325	1.14966	1.14608
0.7116	1.17566	1.17217	1.16865	1.16514
0.8165	1.19093	1.18748	1.18402	1.18056
0.9056	1.20201	1.19860	1.19518	1.19177
1.0000	1.21209	1.20874	1.20538	1.20204
[C$_4$C$_1$im][MeSO$_4$] (1) + PCN (2)				
0.0000	0.77689	0.77186	0.76681	0.76173
0.1032	0.89253	0.88799	0.88343	0.87885
0.2030	0.97158	0.96722	0.96282	0.95843
0.3610	1.05745	1.05342	1.04934	1.04526
0.4129	1.07877	1.07480	1.07082	1.06684
0.5141	1.11339	1.10960	1.10580	1.10202
0.6347	1.14588	1.14227	1.13864	1.13503
0.7157	1.16389	1.16035	1.15679	1.15324
0.8202	1.18387	1.18039	1.17690	1.17342
0.9070	1.19835	1.19493	1.19151	1.18810
1.0000	1.21209	1.20874	1.20538	1.20204
[C$_4$C$_1$im][MeSO$_4$] (1) + n-BCN (2)				
0.0000	0.78626	0.78163	0.77701	0.77234
0.1117	0.89225	0.88804	0.88382	0.87957
0.2128	0.96386	0.95984	0.95581	0.95175
0.3714	1.04605	1.04225	1.03843	1.03460
0.4263	1.06855	1.06480	1.06103	1.05725
0.5115	1.09909	1.09540	1.09170	1.08798
0.6345	1.13581	1.13219	1.12857	1.12496
0.7161	1.15644	1.15290	1.14934	1.14579
0.8065	1.17648	1.17303	1.16956	1.16611
0.9072	1.19602	1.19266	1.18929	1.18593
1.0000	1.21209	1.20874	1.20538	1.20204

The standard uncertainties are $u(x) = 5 \times 10^{-5}$, $u(\rho) = 5 \times 10^{-5}$ g·cm^{-3}, $u(T) = 0.01$ K, $u(P) = 1$ kPa, $u(V^E) = 0.005$ cm^3·mol^{-1}.

The V^E values for [C$_4$C$_1$im][MeSO$_4$] + alkyl nitriles against x_1 in the temperature range of 298.15 to 313.15 K are given in Table S2 in the Supplementary Information and also depicted in Figs. 1-3. It is clear that V^E values are negative over the complete composition range (x_1) at all investigated temperatures, which indicates a stronger interaction between IL and alkyl nitrile molecules compared to the respective substances in their pure state. The excess volumes versus composition curves of the binary systems are found to be asymmetric with their minima in V^E skewed towards alkyl nitriles-rich compositions (i.e., at x_1 between 0.3 and 0.4). Similar type of behaviour was observed in the binary systems of acetonitrile with different ILs like [C$_4$C$_1$im][PF$_6$] [40], [C$_4$C$_1$im][BF$_4$] [40] and [C$_4$C$_1$im][SCN] [50]. This type of trend is generally observed because of a large difference in molar mass and molar volume of the components in the binary systems.

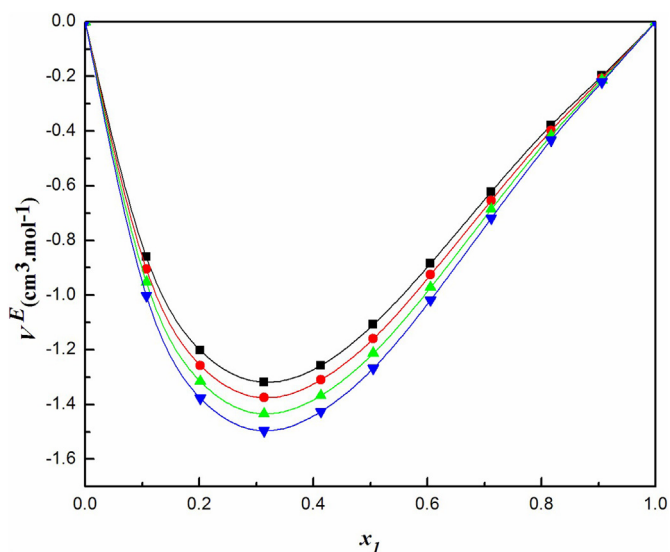The absolute values of excess volume (V^E) at a fixed temperature and mole fraction increases in the order:

[C$_4$C$_1$im][MeSO$_4$] + n−BCN<[C$_4$C$_1$im][MeSO$_4$] + PCN<[C$_4$C$_1$im][MeSO4] + ACN
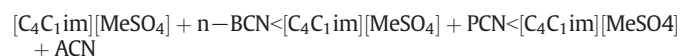
Fig. 1. Excess volumes (V^E) of the system {[C$_4$C$_1$im][MeSO$_4$] (1) + ACN (2)} as a function of mole fraction (x_1) at T = 298.15 K (■), 303.15 K (●), 308.15 K (▲) and 313.15 K (▼).

The maximum negative values of V^E at T = 298.15 K are (−1.318, −1.119, and −0.954) cm^3·mol^{-1} with x_1 = (0.3135, 0.3610, and 0.3714) for [C$_4$C$_1$im][MeSO$_4$] + ACN, [C$_4$C$_1$im][MeSO$_4$] + PCN, and [C$_4$C$_1$im][MeSO$_4$] + n-BCN mixtures respectively. In the pure state, the self-association in [C$_4$C$_1$im][MeSO$_4$] is mainly due to the coulombic ion-ion attractions between the polar C−H groups of [C$_4$C$_1$im]$^+$ cation and the oxygen atom of [MeSO$_4$]$^-$ anion and also π-π interactions between [C$_4$C$_1$im]$^+$ cations. Upon mixing, the complex IL molecules are capable of interacting with a molecular solvent like alkyl nitriles through ionic, hydrogen bonding, or dipolar interactions [64]. The values of V^E for the investigated systems is a consequence of the relative strength of the following volume expansion and contraction effects that occur due to mixing of [C$_4$C$_1$im][MeSO$_4$] with alkyl nitriles: (i) expansion in volume of self-associated, ordered structures of alkyl nitriles due to breaking of dipole-dipole interactions [19], (ii) expansion in strongly associated [C$_4$C$_1$im][MeSO$_4$] due to the disruption of π-π interactions and weakening of ion-ion interactions, (iii) contraction in volume due to formation of ion-dipole interaction between [C$_4$C$_1$im]$^+$ cation and polar cyano group (−C≡N) of alkyl nitriles and also between [CH$_3$SO$_4$]$^-$ anion and −C≡N group of molecular solvents, and (iv) the
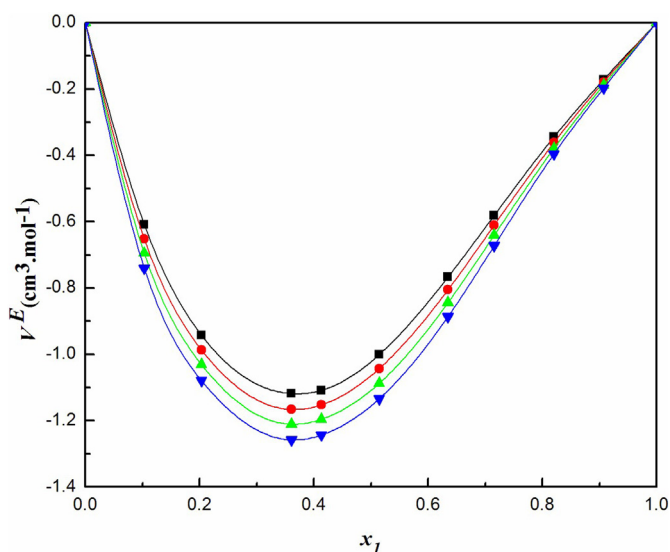
Fig. 2. Excess volumes (V^E) of the system {[C$_4$C$_1$im][MeSO$_4$] (1) + PCN (2)} as a function of mole fraction (x_1) at T = 298.15 K (■), 303.15 K (●), 308.15 K (▲) and 313.15 K (▼).
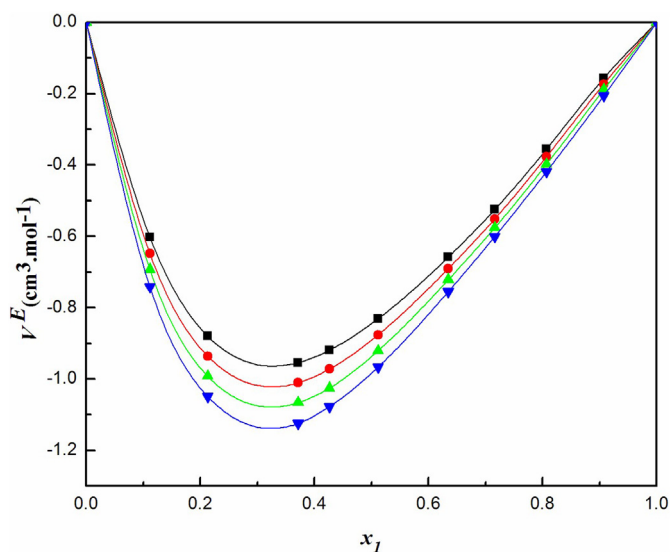
Fig. 3. Excess volumes (V^E) of the system {[C$_4$C$_1$im][MeSO$_4$] (1) + n-BCN (2)} as a function of mole fraction (x_1) at T = 298.15 K (■), 303.15 K (●), 308.15 K (▲) and 313.15 K (▼).

geometrical fitting of smaller alkyl nitriles into the interstices of [C$_4$C$_1$im][MeSO$_4$] due to differences in their molar and free volumes lead to volume contraction. The negative excess volumes (V^E) suggest that the volume contraction factors (iii) and (iv) predominates over the volume expansion factors (i) and (ii) in the mixed solutions. All minima in V^E found in the molecular solvent-rich region can be interpreted as the suitable combination of strong and specific attractive interactions like ion-dipole interactions between components of the mixture and also the packing effect of alkyl nitriles into the interstices of IL network [1].

The polarity of a solvent is generally expressed by its dielectric constant (ε). The polar molecular solvents of high ε value show good solubility and exhibit stronger interactions with ILs [26]. The V^E values for [C$_4$C$_1$im][MeSO$_4$] + ACN mixture are more negative than the [C$_4$C$_1$im][MeSO$_4$] + BCN mixture, suggesting comparatively stronger ion-dipole interactions between [C$_4$C$_1$im]$^+$ or [MeSO$_4$]$^-$ and −C≡N group of ACN. The stronger interactions in ACN mixtures resulting in more negative V^E could be attributed to the higher dielectric constant and relative permittivity for ACN (ε = 36.64, at T = 293.15 K) [19] compared to PCN (ε = 29.70 at T = 293.15 K) and n-BCN (ε = 24.83 at T/K = 293.15) [55]. The higher dielectric constant and relative permittivity for ACN results in effective breakdown of the IL ion-pairs in [C$_4$C$_1$im][MeSO$_4$] + ACN solution, resulting in stronger ion-dipole interactions between the ions and ACN molecule.

Longer the alkyl group of the alkyl nitrile, higher the strength of the positive inductive effect (+I-effect). The +I-effect which is also known as electron releasing effect, operates in an alkyl nitrile molecule through which the sigma bonded electrons between the carbon of the alkyl group and carbon of the nitrile group will slightly displace towards nitrile group resulting in weakening the partial positive charge on the carbon of the nitrile group as shown in Fig. S6. Due to the greater +I-effect of the larger -C$_3$H$_7$ alkyl group in n-BCN, the nitrile carbon becomes less electron deficient, and consequently, the polarity of the −C≡N group decreases [65]. ACN with smaller –CH$_3$ alkyl group (lesser +I-effect) and highly polar −C≡N group facilitates relatively stronger ion-dipole interaction with [C$_4$C$_1$im][MeSO$_4$] than BCN resulting in the more negative V^E for [C$_4$C$_1$im][MeSO$_4$] + ACN solutions.

Further, it is noteworthy to consider the factors like the size and shape of molecules as well to correlate the negative excess volumes of the investigated systems. The molar volumes of [C$_4$C$_1$im][MeSO$_4$], ACN, PCN, n-BCN calculated from the measured densities are 206.52, 52.86, 70.90, and 84.08 cm^3·mol^{-1} respectively at T = 298.15 K. The negative V^E results from the geometrical fitting of smaller alkyl nitrile

molecules into the voids created by the network of bigger IL molecules [50]. The larger negative V^E values of $[C_4C_1im][MeSO_4]$ + ACN than $[C_4C_1im][MeSO_4]$ + n-BCN indicate that packing effects are relatively stronger in ACN solutions than n-BCN solutions. The simple structure and smaller size of ACN result in most favourable interstitial accommodation with IL compared to n-BCN achieving more negative V^E. A similar kind of trend in excess volumes is reported by Rajgopal et al. [55] in their investigation on the impact of carbon chain length of alkyl nitriles in the binary systems containing toluene. Singh et al. [33] reported similar behaviour for the effect of alkyl chain length of molecular solvents in $[C_4C_1im][MeSO_4]$ + alcohol systems.

To study the influence of nature of the anion of IL on the excess volumes of the binary mixtures, the minimum excess volumes (V^E_{min}) of $[C_4C_1im][MeSO_4]$ + ACN and similar $[C_4C_1im]^+$ based ILs with ACN [40–43] at $T = 298.15$ K are compared in Table 3. The minimum excess volumes for IL mixtures shown in Table 3 reveal that V^E_{min} values increases in the following order: $[C_4C_1im][SCN]$ + ACN < $[C_4C_1im]$ $[BF_4]$ + ACN < $[C_4C_1im][MeSO_4]$ + ACN < $[C_4C_1im]$ $[PF_6]$ + ACN < $[C_4C_1im][NTf_2]$ + ACN. This clearly indicates that excess volumes of these mixtures are sensitive to the change in anion structure of the IL. The more negative V^E for $[C_4C_1im][SCN]$ + ACN suggests a more efficient packing and stronger ion-dipole interactions between the components due to the linear geometry, a stronger localized charge of $[SCN]^-$ anion and the linear C—C≡N skeleton of polar ACN. The V^E values for the above systems may be attributed to the relative size or molar volumes of anions of ILs which follow the order: $[BF_4]^- < [MeSO_4]^- < [PF_6]^- < [NTf_2]^-$ [47,66,67]. The $[BF_4]^-$ anion is relatively smaller and hence has high charge density than $[MeSO_4]^-$, $[PF_6]^-$ and $[NTf_2]^-$. Consequently, $[C_4C_1im][BF_4]$ interacts strongly with ACN and also leads to efficient interstitial accommodation between the components resulting in more negative V^E values than $[C_4C_1im]^+$ based ILs with $[MeSO_4]^-$, $[PF_6]^-$ and $[NTf_2]^-$ anions.

A comparison of the minimum excess volumes (V^E_{min}) of $[C_4C_1im]$ $[MeSO_4]$ + alkyl nitriles obtained in this work with the reported values of $[C_4C_1im][MeSO_4]$ in different molecular solvents [30–36,38,39] at $T = 298.15$ K are given in Table 4. From these data, it is clear that V^E is affected by the nature of intermolecular forces between the components of the mixtures, and by the packing effect due to the differences in size and shape of molecules. It shows that V^E_{min} is more negative for $[C_4C_1im][MeSO_4]$ + ACN or PCN than $[C_4C_1im]$ $[MeSO_4]$ + methanol system [31–34]. Previously reported V^E values for the binary solutions of $[C_4C_1im][PF_6]$ with ACN or methanol [41] also adhere to this trend. This may be ascribed due to the fact that the hydrogen bonding interactions in methanol is stronger than dipole-dipole interactions in alkyl nitrile. On mixing with IL, the self-associated alkyl nitrile are easily disrupted than methanol and results in an easy hetero-association of alkyl nitrile having linear dipoles with IL and favourable geometrical fitting resulting in more negative V^E values in IL + alkyl nitrile solutions. The negative V^E_{min} for the IL

Table 3
The comparison of minimum excess volumes (V^E_{min}/cm³·mol⁻¹) obtained in this work with the literature values of similar $[C_4C_1im]^+$ based ILs with ACN at T = 298.15 K.

Binary system	V^E_{min}
	(cm³·mol⁻¹)
$[C_4C_1im][MeSO_4]$ + ACN[a]	−1.318
$[C_4C_1im][BF_4]$ + ACN[b]	−1.397
$[C_4C_1im][PF_6]$ + ACN[c]	−1.296
$[C_4C_1im][NTf_2]$ + ACN[d]	−0.712
$[C_4C_1im][SCN]$ + ACN[e]	−1.420

[a] Present work.
[b] Ref. [40].
[c] Ref. [40,41].
[d] Ref. [42].
[e] Ref. [43].

mixtures with (C_1–C_4) alcohols [31–36] suggests the favourable packing effect of smaller alcohol molecules into IL interstices and the existence of stronger hydrogen bonding and ion-dipole interactions between the unlike molecules than in the pure components. With an increase in the alkyl chain length of the alcohols, V^E_{min} is found to be less negative for (C_1–C_4) alcohols and more positive for higher alcohols [34]. This suggests the dominance of disruption of self-associated molecular entities than the hetero-association between the components and the less effective packing of alcohols into voids created by IL network due to a decrease in the difference between free volumes of the components with an increase in chain length of alcohols. The V^E_{min} value of $[C_4C_1im][MeSO_4]$ + 2-propanol [33] is more negative than $[C_4C_1im]$ $[MeSO_4]$ + 1-propanol [33] which indicates that change in the position of hydroxyl group leads to the variation in the interaction between the alcohol and IL. The more negative V^E_{min} in IL + 2-propanol system could be attributed to the closer approach between dissimilar component molecules. The positive minimum excess volumes of $[C_4C_1im]$ $[MeSO_4]$ + 1,2-diols [38,39] is ascribed to the fact that 1,2-diols with two hydroxyl (-OH) groups are strongly self-associated by intra-molecular and inter-molecular hydrogen bonding. On mixing IL with 1,2-diols, the volume expansion factors i.e., the disruption of self-association between like molecules dominates the specific interactions between the unlike molecules of the mixture resulting in positive V^E value. Thus, the alkyl group chain length, position of hydroxyl group and number of hydroxyl groups in alcohols play a significant role in the volumetric properties of $[C_4C_1im][MeSO_4]$ + alcohols.

As can be seen in Table 4, V^E_{min} values are found to be negative for $[C_4C_1im][MeSO_4]$ + water [30], + nitromethane [35], + 1,3-dichloropropane [35], and + diethylene glycol monoethyl ether (DEGEE) [35] which suggests the dominance of specific intermolecular forces between the unlike components of the mixtures and also the interstitial accommodation of molecular solvents into the voids of IL. A weak mixing effect as indicated by least negative V^E_{min} has been observed for $[C_4C_1im][MeSO_4]$ + water system, despite of the smallest molecule size of water than all molecular solvents studied. The protic water molecules are strongly self-associated through hydrogen bonds and this could prevent dense packing of smaller water molecules into the interstices of IL. The magnitude of V^E_{min} for the other three polar solvents in IL suggests the extent of ion-dipole and/or cross hydrogen bonding interactions which follow the order: nitromethane <1,3-dichloropropane < DEGEE. The more negative V^E_{min} for IL + DEGEE system is attributed to the presence of a hydroxyl (–O-H) group and two ether oxygen atoms in DEGEE for favourable ion-dipole and hydrogen bonding interactions with IL.

A comparison of V^E_{min} between $[C_4C_1im][MeSO_4]$ + ACN and similar systems in ACN reported in the literature [43,68] at $T = 298.15$ K fall in the following order: $[C_2C_1im][EtSO_4]$ (−1.508 cm³·mol⁻¹) < $[C_4C_1im]$ $[MeSO_4]$ (−1.318 cm³·mol⁻¹) < $[C_2C_1im][CF_3SO_3]$ (−1.142 cm³· mol⁻¹). This shows that the excess volumes are influenced by the alkyl chain of cation and anion of the IL. The more negative V^E_{min} for $[C_2C_1im][EtSO_4]$ + ACN could be attributed to the stronger ion-dipole interaction between the relatively smaller structure of $[C_2C_1im]^+$ in ACN than larger structure of $[C_4C_1im]^+$ in ACN. The less negative V^E_{min} for $[C_2C_1im][CF_3SO_3]$ + ACN than the other two alkylsulphate based IL is due to extra stabilization of trifluoromethanesulphonate anion by the electron-withdrawing nature of –CF₃ group.

The V^E_{min} for the similar IL mixtures with ACN, reported in the literature [69], increases in the following order: $[C_2C_1im][BF_4]$ + ACN < $[C_4C_1im]$ $[BF_4]$ + ACN < $[C_4C_1im][MeSO_4]$ + ACN < $[C_6C_1im][BF_4]$ + ACN. This signifies that excess volumes are sensitive to the change in alkyl chain length of the cation of IL. This could be due to the fact that with an increase in the alkyl chain length in the cation, the specific interaction between unlike molecules decreases and the packing effect becomes less effective. Similarly, V^E_{min} is observed to be less negative for $[C_6C_1im][NTf_2]$ + ACN [70] than $[C_2C_1im][NTf_2]$ + ACN [42] because the bulkier cation does not interact much with ACN.

Table 4
The comparison of minimum excess volumes ($V_{min}^E/cm^3 \cdot mol^{-1}$) obtained in this work with the literature values of [C$_4$C$_1$im][MeSO$_4$] in different molecular solvents at $T = 298.15$ K.

Binary system	V_{min}^E $(cm^3 \cdot mol^{-1})$	Binary system	V_{min}^E $(cm^3 \cdot mol^{-1})$
[C$_4$C$_1$im][MeSO$_4$] + ACN	−1.318[a]	[C$_4$C$_1$im][MeSO$_4$] + 1-octanol	+0.476[d]
[C$_4$C$_1$im][MeSO$_4$] + PCN	−1.119[a]	[C$_4$C$_1$im][MeSO$_4$] + 1-decanol	+0.646[d]
[C$_4$C$_1$im][MeSO$_4$] + n-BCN	−0.954[a]	[C$_4$C$_1$im][MeSO$_4$] + ethane−1,2-diol	+0.555[h]
[C$_4$C$_1$im][MeSO$_4$] + methanol	-1.100[b], −1.093[c], −1.134[d], −0.90[e],	[C$_4$C$_1$im][MeSO$_4$] + propane-1,2-diol	+0.517[i]
[C$_4$C$_1$im][MeSO$_4$] + ethanol	−0.647[b], −0.663[d], −0.707[f], −0.706[g]	[C$_4$C$_1$im][MeSO$_4$] + water	−0.346[j]
[C$_4$C$_1$im][MeSO$_4$] + 1-propanol	−0.449[c]	[C$_4$C$_1$im][MeSO$_4$] + nitromethane	−0.572[f]
[C$_4$C$_1$im][MeSO$_4$] + 2-propanol	−0.717[c]	[C$_4$C$_1$im][MeSO$_4$] + 1,3-dichloropropane	−0.707[f]
[C$_4$C$_1$im][MeSO$_4$] + 1-butanol	−0.172[c], −0.154[d]	[C$_4$C$_1$im][MeSO$_4$] + diethylene glycol monoethyl ether	−0.850[f]
[C$_4$C$_1$im][MeSO$_4$] + 1-hexanol	+0.271[d]		

[a] Present work.
[b] Ref. [32].
[c] Ref. [33].
[d] Ref. [34].
[e] Ref. [31].
[f] Ref. [35].
[g] Ref. [36].
[h] Ref. [39].
[i] Ref. [38].
[j] Ref. [30].

The $\frac{\partial V^E}{\partial T}$ is found to be negative for all the investigated systems. V^E increases in absolute value over the entire range of composition as the temperature increases. The dependence of V^E on temperature suggests that the temperature has a great influence on intermolecular interactions in the studied mixtures. A similar effect of temperature on V^E was reported by Zafarani-Moattar et al. [41] and Singh et al. [43] for [BMIM][PF$_6$] + acetonitrile and [BMIM][SCN] + acetonitrile systems, respectively. The more negative V^E values with increasing temperature indicate that strong interaction occurs between solute and solvent molecules at a higher temperature. As temperature increases, the interactions between pure alkyl nitrile molecules are predominantly weakened and the coulombic ion-dipole interactions between IL and alkyl nitrile might become stronger in the mixture resulting in more negative V^E values. Another dominating factor for the decrease in V^E with an increase in temperature can be understood as a greater packing efficiency [27] between [C$_4$C$_1$im][MeSO$_4$] and alkyl nitriles due to enlargement of interstices of IL network with temperature.

3.2. Speed of sound (u) and excess isentropic compressibilities (κ_s^E)

The measurement of the speed of sound (u) enables the accurate determination of isentropic compressibility (κ_s) and excess isentropic compressibility (κ_s^E) which can be used to evaluate the information about the intermolecular interactions occurring in the liquid mixtures. The experimental speeds of sound (u) for [C$_4$C$_1$im][MeSO$_4$] + alkyl nitriles at 298.15 K ≤ T ≤ 313.15 K, at 5 K interval are collected in Table 5. Figs. S7–S9 illustrates the variations of speed of sound (u) versus mole fraction of [C$_4$C$_1$im][MeSO$_4$] (x_1) for the three investigated binary solutions at $T = 298.15$ K to 313.15 K. At a fixed temperature, speeds of sound increase with an increase in x_1, which could be attributed to the packing effect between [C$_4$C$_1$im][MeSO$_4$] and alkyl nitriles due to the significant difference in their molar volumes. For a fixed composition (x_1), u values of the studied mixtures follow a decreasing trend with an increase in temperature, which could be attributed to the increase in the availability of free spaces for the geometrical accommodation of smaller alkyl nitriles into the interstices of IL.

In order to evaluate molecular compactness, Laplace-Newton's equation is used to calculate the isentropic compressibilities (κ_s) of (IL + alkyl nitriles) system:

$$\kappa_s = \frac{1}{u^2 \rho} \tag{2}$$

The excess isentropic compressibility (κ_s^E) which signifies the difference in compressibilities of the pure components and the mixture is obtained from the ideal isentropic compressibilities (κ_s^{id}) according to the standard relation:

$$\kappa_s^E = \kappa_s - \kappa_s^{id} \tag{3}$$

The ideal isentropic compressibility (κ_s^{id}) can be obtained from the well-known relation [71]:

$$\kappa_s^{id} = \sum_{i=1}^{2} \varnothing_i \left[\kappa_{s,i} + \frac{TV_i(\alpha_i^2)}{C_{p,i}} \right] - \left\{ T \left(\sum_{i=1}^{2} x_i V_i \right) \left(\sum_{i=1}^{2} \varnothing_i \alpha_i \right)^2 / \sum_{i=1}^{2} x_i C_{p,i} \right\} \tag{4}$$

where V_i is the molar volume, ϕ_i is the volume fraction, T is the absolute temperature, $\kappa_{s,i}$ is the isentropic compressibility, $C_{p,i}$ is molar heat capacity and α_i represents thermal expansivity of ith component in the binary solution. The $C_{p,i}$ values for the pure liquids used in the work are obtained from the literature [37,40,60,61]. $C_{p,i}$ values for PCN and n-BCN at few temperatures are calculated by using group contribution method and all the values are incorporated in Table S1. The isobaric thermal expansion coefficients (α_i) for the pure liquids at required temperatures are calculated based on their density (ρ) data with the help of the relation,

$$\alpha_i = \left(\frac{1}{V} \right) \left(\frac{\partial V}{\partial T} \right)_P = -\left(\frac{1}{\rho} \right) \left(\frac{\partial \rho}{\partial T} \right)_P = -\left(\frac{\partial \ln \rho}{\partial T} \right)_P \tag{5}$$

Experimental values of κ_s and κ_s^E against x_1 for the binary systems of [C$_4$C$_1$im][MeSO$_4$] with alkyl nitriles at T = (298.15–313.15) K are included in Tables 5 and S3 respectively. The visual presentation of κ_s^E as a function of x_1 for the three systems are shown in Figs. 4–6 which reveals that κ_s^E values are negative over the entire range of mole fraction at four studied temperatures. The negative κ_s^E values of binary mixtures suggest the higher structural order and lesser compressibility than the corresponding ideal mixtures. The representative plots of κ_s^E vs. x_1 are asymmetric with its minima in κ_s^E skewed towards alkyl nitriles-rich mole fractions, which are generally seen in the binary solutions with a large difference in the molar volumes of the component molecules.

Analysis of κ_s^E data reveals that its behaviour is similar to the previously discussed V^E data at all the investigated temperatures. The contributions to κ_s^E values for the mixtures are the result of chemical effect and

Table 5

Mole fraction of [C$_4$C$_1$im][MeSO$_4$] (x_1), Speeds of sound (u/m·s^{-1}), isentropic compressibilities (κ_S/T·Pa^{-1}) for [C$_4$C$_1$im][MeSO$_4$] + ACN/PCN/n-BCN mixtures at 298.15 ≤ T/K ≤ 313.15 and 101.3 kPa pressure.

x_1	u/m·s^{-1}	κ_S/T·Pa^{-1}	u/m·s^{-1}	κ_S/T·Pa^{-1}
[C$_4$C$_1$im][MeSO$_4$] (1) + ACN (2)				
T/K = 298.15			T/K = 303.15	
0.0000	1278.8	787.3	1258.7	818.4
0.1070	1371.8	573.2	1353.6	591.7
0.2018	1450.9	471.5	1433.7	485.0
0.3135	1520.1	404.6	1504.1	414.8
0.4127	1566.0	368.1	1550.2	377.0
0.5049	1597.9	345.3	1582.6	353.1
0.6053	1620.8	329.1	1606.2	336.1
0.7116	1634.2	318.5	1620.1	325.0
0.8165	1642.7	311.2	1628.9	317.4
0.9056	1649.3	305.8	1636.2	311.6
1.0000	1654.9	301.2	1642.5	306.7
T/K = 308.15			T/K = 313.15	
0.0000	1238.6	851.2	1218.5	885.9
0.1070	1335.4	611.1	1317.2	631.4
0.2018	1416.6	498.9	1399.5	513.4
0.3135	1487.7	425.6	1471.3	436.8
0.4127	1534.3	386.1	1518.4	395.6
0.5049	1567.3	361.2	1552.0	369.6
0.6053	1591.8	343.3	1577.5	350.6
0.7116	1606.1	331.7	1592.1	338.6
0.8165	1615.0	323.8	1601.0	330.5
0.9056	1623.0	317.6	1609.9	323.7
1.0000	1630.2	312.2	1618.2	317.7
[C$_4$C$_1$im][MeSO$_4$] (1) + PCN (2)				
T/K = 298.15			T/K = 303.15	
0.0000	1262.9	807.1	1242.7	838.9
0.1032	1321.1	642.0	1302.5	663.8
0.2030	1383.9	537.4	1366.9	553.4
0.3610	1468.2	438.7	1452.3	450.1
0.4129	1490.9	417.0	1475.3	427.5
0.5141	1529.7	383.8	1514.4	393.0
0.6347	1566.6	355.6	1552.1	363.4
0.7157	1587.3	341.0	1573.4	348.1
0.8202	1611.2	325.4	1598.0	331.8
0.9070	1632.1	313.3	1619.3	319.1
1.0000	1654.9	301.2	1642.5	306.7
T/K = 308.15			T/K = 313.15	
0.0000	1222.4	872.7	1201.9	908.8
0.1032	1284.0	686.6	1265.5	710.5
0.2030	1349.9	570.0	1332.8	587.3
0.3610	1436.4	461.9	1420.5	474.1
0.4129	1459.7	438.3	1444.1	449.5
0.5141	1499.1	402.4	1483.8	412.1
0.6347	1537.6	371.5	1523.1	379.8
0.7157	1559.5	355.5	1545.5	363.0
0.8202	1584.9	338.3	1571.7	345.0
0.9070	1606.5	325.2	1593.7	331.4
1.0000	1630.2	312.2	1618.2	317.7
[C$_4$C$_1$im][MeSO$_4$] (1) + n-BCN (2)				
T/K = 298.15			T/K = 303.15	
0.0000	1279.9	776.3	1260.6	805.0
0.1117	1341.8	622.5	1323.5	642.9
0.2128	1395.9	532.4	1378.9	547.9
0.3714	1468.7	443.2	1452.9	454.5
0.4263	1490.6	421.2	1475.5	431.4
0.5115	1521.4	393.1	1506.8	402.1
0.6345	1559.7	361.9	1545.8	369.6
0.7161	1582.5	345.3	1568.8	352.4
0.8065	1605.3	329.8	1592.2	336.3
0.9072	1630.9	314.3	1618.2	320.2
1.0000	1654.9	301.2	1642.5	306.7
T/K = 308.15			T/K = 313.15	
0.0000	1241.0	835.6	1221.2	868.2
0.1117	1305.2	664.2	1286.9	686.5
0.2128	1361.8	564.2	1344.7	581.1
0.3714	1437.1	466.3	1421.4	478.4
0.4263	1460.3	442.0	1444.9	453.0
0.5115	1492.0	411.5	1477.3	421.0
0.6345	1531.9	377.6	1517.9	385.8
0.7161	1555.1	359.8	1541.4	367.3

Table 5 (*continued*)

x_1	u/m·s^{-1}	κ_S/T·Pa^{-1}	u/m·s^{-1}	κ_S/T·Pa^{-1}
0.8065	1579.1	342.9	1566.0	349.7
0.9072	1605.5	326.2	1592.8	332.4
1.0000	1630.2	312.2	1618.2	317.7

The standard uncertainties are $u(x) = 5 \times 10^{-5}$, $u(u) = 0.5$ m·s^{-1}, u(T) = 0.01 K, u(P) = 1 kPa.

more relevant structural effects between IL and alkyl nitriles. The chemical effects comprising of strong hetero-molecular association in the liquid mixtures through dipole-dipole, ion-dipole, charge transfer, and hydrogen bonding interactions between unlike molecules leads to negative κ_s^E data [72]. The weakening of self-association of IL (ion-ion interactions) or alkyl nitriles (dipole-dipole attractions) on mixing and subsequent hetero-association between IL and polar alkyl nitriles through ion-dipole interactions decreases the compressibility, which might produce negative κ_s^E values for the mixtures. The negative κ_s^E data is also an indication of a strong structural effect comprising of packing of smaller alkyl nitriles into the voids created by the network of [C$_4$C$_1$im][MeSO$_4$] molecules.

The absolute values of κ_s^E of the liquid mixtures increase in the order:

[C$_4$C$_1$im][MeSO$_4$] + n−BCN < [C$_4$C$_1$im][MeSO$_4$] + PCN < [C$_4$C$_1$im][MeSO4] + ACN
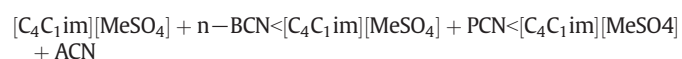
As the chain length of alkyl nitriles increases, the excess isentropic compressibility (κ_s^E) values become more negative at four investigated temperatures. The dielectric constant (ε) value of the alkyl nitriles follows this order: ACN > PCN > n-BCN, which implies that the IL can interact relatively stronger with ACN through the ion-dipole interaction in the mixtures making a more negative contribution to κ_s^E. Further, the difference in molar volumes of [C$_4$C$_1$im][MeSO$_4$] and alkyl nitriles decreases in the order: ACN > PCN > n-BCN. The reduction in the difference between free volumes of components indicates a relatively less effective accommodation of longer alkyl nitrile into the interstices between ions of IL, causing less negative κ_s^E values. In conclusion, the better geometrical fitting and stronger intermolecular interactions between [C$_4$C$_1$im][MeSO$_4$] and ACN molecules might lessen the intermolecular space available between components, which in turn leads to a decrease in intermolecular free length and compressibility creating more compact structures leading to more negative κ_s^E values.

Figs. 4–6 illustrate that the values of κ_s^E become more negative with an increase in temperature for the mixture of IL with alkyl nitrile. This could be due to the fact that the strength of interactions between similar molecules (IL…IL or nitrile…nitrile) decreases more with temperature compared to the interactions between dissimilar molecules (IL…nitrile) [73]. Moreover, in the binary systems formed by IL and alkyl nitriles, an increase in the temperature causes the enlargement of interstices, leading to better packing efficiency between the participating [C$_4$C$_1$im][MeSO$_4$] and alkyl nitrile molecules. This makes the binary solutions more rigid and compact causing more negative κ_s^E values with temperature [43].

3.3. Correlation of derived properties

The studied excess properties (V^E and κ_s^E) of [C$_4$C$_1$im][MeSO$_4$] + alkyl nitrile systems at each composition and temperatures from 298.15 to 313.15 K are further correlated by a fourth-degree Redlich–Kister polynomial (Eq. (6)): [74].

$$Q^E = x_1 x_2 \sum_{i=0}^{4} A_i (2x_1 - 1)^i \tag{6}$$

where $Q^E = V^E$ (cm^3·mol^{-1}) and κ_s^E (T.Pa^{-1}); x_1 and x_2 represent the mole fraction of [C$_4$C$_1$im][MeSO$_4$] and alkyl nitrile respectively, and A_i
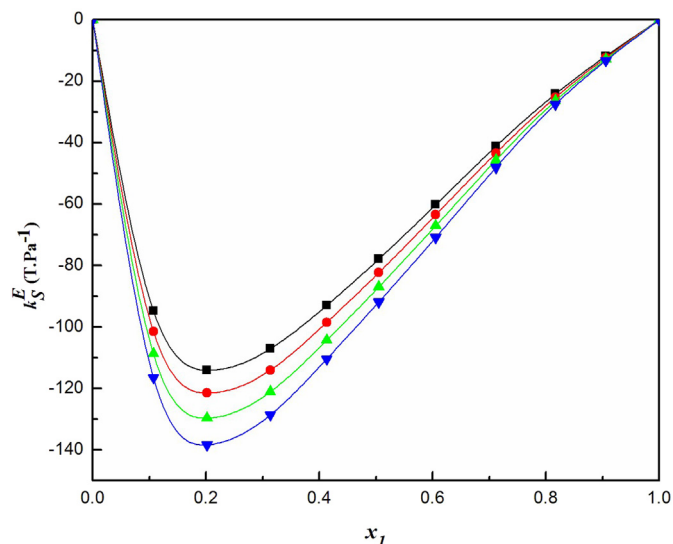
Fig. 4. Plot of excess isentropic compressibilities (κ_s^E) obtained for {[C$_4$C$_1$im][MeSO$_4$] (1) + ACN (2)} against mole fraction (x_1) at different temperatures: 298.15 K (■), 303.15 K (●), 308.15 K (▲) and 313.15 K (▼).

represents the adjustable fitting parameters of R-K equation which has a close relationship with the nature of the binary solutions.

The standard deviation $\sigma\left(Q^E\right)$ between experimental and correlated data is computed as follows [75]:

$$\sigma\left(Q^E\right) = \left[\frac{\sum\left(Q_{exp}^E - Q_{cal}^E\right)^2}{(m-n)}\right]^{\frac{1}{2}} \tag{7}$$

where m is the number of experimental measurements and n is the adjustable parameters.

The Redlich−Kister coefficients ($A_0 − A_4$) for all the investigated binary systems are obtained by fitting the V^E and κ_s^E values with a least-squares fitting method. The calculated smoothing coefficients of R-K polynomial and the corresponding standard deviations (σ) are given in Table 6. The correlating ability of the R-K polynomial is found to be good as indicated by the lower values of standard deviation obtained
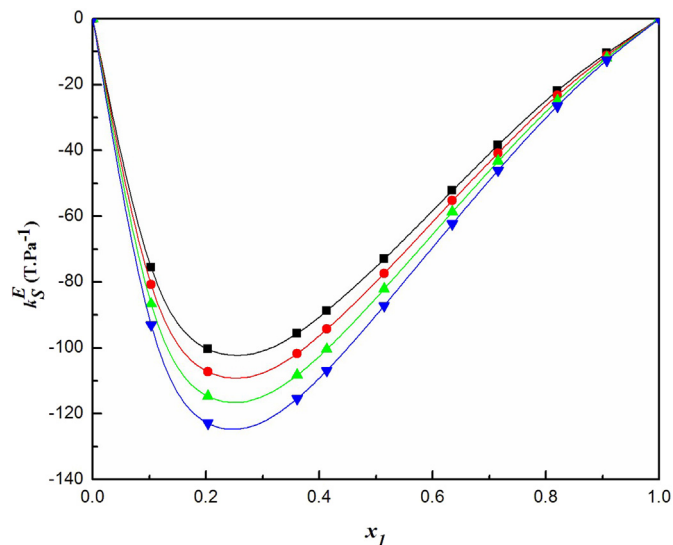
Fig. 5. Plot of excess isentropic compressibilities (κ_s^E) obtained for {[C$_4$C$_1$im][MeSO$_4$] (1) + n-PCN (2)} against mole fraction (x_1) at different temperatures: 298.15 K (■), 303.15 K (●), 308.15 K (▲) and 313.15 K (▼).
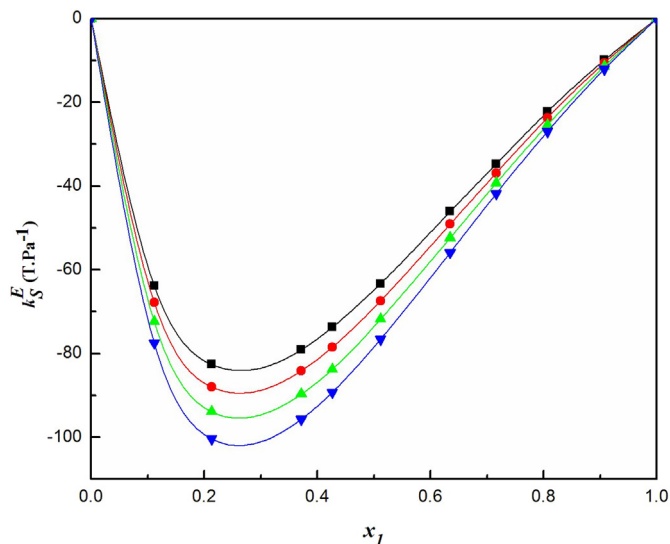
Fig. 6. Plot of excess isentropic compressibilities (κ_s^E) obtained for {[C$_4$C$_1$im][MeSO$_4$] (1) + n-BCN (2)} against mole fraction (x_1) at different temperatures: 298.15 K (■), 303.15 K (●), 308.15 K (▲) and 313.15 K (▼).

for [C$_4$C$_1$im][MeSO$_4$] + alkyl nitrile systems at the four investigated temperatures.

4. Conclusion

The effect of composition and temperature on densities (ρ) and speeds of sound (u) for the solutions based on the 1-butyl-3-methylimidazolium methyl sulphate, [C$_4$C$_1$im][MeSO$_4$] and alkyl

Table 6
Fitting parameters ($A_0 - A_4$) of the Redlich–Kister equation and the standard deviations σ (Q^E) for excess functions obtained for [C$_4$C$_1$im][MeSO$_4$] + alkyl nitriles at four investigated temperatures.

Temperature	A_0	A_1	A_2	A_3	A_4	σ (Y^E)
[C$_4$C$_1$im][MeSO$_4$] (1) + ACN (2) V^E/cm$^3\cdot$mol^{-1}						
298.15	−4.470	3.857	−1.087	0.636	−1.382	0.0010
303.15	−4.673	3.964	−1.142	0.832	−1.482	0.0013
308.15	−4.888	4.080	−1.176	1.059	−1.658	0.0011
313.15	−5.105	4.203	−1.227	1.312	−1.795	0.0011
[C$_4$C$_1$im][MeSO$_4$] (1) + ACN (2) κ_s^E/T$\cdot$Pa^{-1}						
298.15	−314.3	336.4	−263.5	331.0	−231.5	0.1896
303.15	−332.4	358.6	−282.3	360.7	−254.2	0.1693
308.15	−351.5	381.9	−302.9	395.1	−278.6	0.1266
313.15	−371.6	406.8	−323.1	433.4	−307.1	0.1228
[C$_4$C$_1$im][MeSO$_4$] (1) + PCN (2) V^E/cm$^3\cdot$mol^{-1}						
298.15	−4.080	2.824	0.163	0.046	−0.863	0.0016
303.15	−4.257	2.854	0.219	0.354	−1.208	0.0009
308.15	−4.440	2.863	0.302	0.703	−1.603	0.0020
313.15	−4.631	2.882	0.378	1.059	−1.987	0.0026
[C$_4$C$_1$im][MeSO$_4$] (1) + PCN (2) κ_s^E/T$\cdot$Pa^{-1}						
298.15	−301.3	331.3	−215.0	164.9	−88.39	0.0966
303.15	−319.5	354.3	−238.6	175.8	−86.84	0.1016
308.15	−339.2	379.2	−264.4	189.7	−86.30	0.0801
313.15	−360.2	406.3	−292.1	207.6	−86.92	0.0774
[C$_4$C$_1$im][MeSO$_4$] (1) + n-BCN (2) V^E/cm$^3\cdot$mol^{-1}						
298.15	−3.376	2.360	−1.555	0.480	0.833	0.0011
303.15	−3.560	2.550	−1.613	0.466	0.570	0.0011
308.15	−3.746	2.738	−1.663	0.455	0.296	0.0012
313.15	−3.932	2.924	−1.724	0.465	0.003	0.0012
[C$_4$C$_1$im][MeSO$_4$] (1) + n-BCN (2) κ_s^E/T$\cdot$Pa^{-1}						
298.15	−258.9	257.9	−164.6	129.0	−65.94	0.0932
303.15	−275.6	275.4	−177.8	133.2	−65.50	0.1090
308.15	−293.8	293.9	−190.4	142.1	−70.47	0.1145
313.15	−313.3	314.4	−205.8	154.0	−74.28	0.1239

nitriles (ACN, PCN and n-BCN) at 298.15 K ≤ T ≤ 313.15 K, at 5 K interval has been investigated. The excess volumes (V^E) and excess isentropic compressibilities (κ_S^E) evaluated from ρ and u data are negative for the binary systems of $[C_4C_1im][MeSO_4]$ with alkyl nitriles. It is observed that the non-ideality of the studied mixtures decreases with an increase in the alkyl chain length of alkyl nitriles in the order of ACN > PCN > n-BCN. The thermodynamic behaviour (V^E and κ_S^E) of the liquid mixtures have been discussed in terms of non-covalent interactions and geometrical effects between $[C_4C_1im][MeSO_4]$ and alkyl nitriles. Moreover, an increase in temperature leads to an increase in the non-ideality of binary solutions.

CRediT authorship contribution statement

P. Bhanuprakash: Conceptualization, Methodology, Investigation, Writing - original draft. **R. Prathibha:** Investigation. **Ramesh L. Gardas:** Resources, Formal analysis, Validation. **K. Sivakumar:** Conceptualization, Methodology, Writing - review & editing. **N.V.V. Jyothi:** Resources, Supervision, Writing - review & editing.

Declaration of competing interest

The authors declare that they have no known competing financial interests or personal relati03onships that could have appeared to influence the work reported in this paper.

Appendix A. Supplementary data

Supplementary data to this article can be found online at https://doi.org/10.1016/j.molliq.2020.112507.

References

[1] A. Bhattacharjee, C. Varanda, M.G. Freire, S. Matted, L.M.N.B.F. Santos, I.M. Marrucho, J.A.P. Coutinho, J. Chem. Eng. Data 57 (2012) 3473–3482.
[2] T.L. Greaves, C.J. Drummond, Chem. Rev. 115 (2015) 11379–11448.
[3] R.L. Vekariya, J. Mol. Liq. 227 (2017) 44–60.
[4] T.L. Greaves, C.J. Drummond, Chem. Rev. 108 (2008) 206–237.
[5] S. Seki, Y. Ohno, Y. Kobayashi, H. Miyashiro, A. Usami, Y. Mita, H. Tokuda, M. Watanabe, K. Hayamizu, M. Tsuzuki, M. Hattori, N. Terada, J. Electrochem. Soc. 154 (2007) A173–A177.
[6] A. Noda, M.A.B.H. Susan, K. Kudo, S. Mitsushima, K. Hayamizu, M. Watanabe, J. Phys. Chem. B 107 (2003) 4024–4033.
[7] D. Kuang, P. Wang, S. Ito, S.M. Zakeeruddin, M. Gratzel, J. Am. Chem. Soc. 128 (2006) 7732–7733.
[8] P. Bhanuprakash, N.V.V. Jyothi, C. Narasimharao, M. Raveendra, K. Sivakumar, J. Chem. Thermodyn. 122 (2018) 113–124.
[9] S.S. Bittencourt, H.E. Hoga, R.B. Torres, J.V. Hallak dAngelo, J. Therm. Anal. Calorim. 135 (2019) 2519–2539.
[10] P. Bhanuprakash, C. Narasimha Rao, K. Sivakumar, J. Mol. Liq. 219 (2016) 79–87.
[11] G. Liu, R. Zhong, R. Hu, F. Zhang, Biophys. Rev. Lett. 07 (2012) 121–134.
[12] S. Himmler, S. Hormann, R. Hal, P.S. Schulz, P. Wasserscheid, Green Chem. 8 (2006) 887–894.
[13] J. Jacquemin, P. Husson, V. Majer, A.A.H. Padua, M.F.C. Gomes, Green Chem. 10 (2008) 944–950.
[14] A. Romero, A. Santos, J. Tojo, A. Rodriguez, J. Hazard. Mater. 151 (2008) 268–273.
[15] J. Esser, P. Wasserscheid, A. Jess, Green Chem. 6 (2004) 316–322.
[16] A.B. Pereiro, A. Rodriguez, Green Chem. 11 (2009) 346–350.
[17] G.W. Meindersma, A.J.G. Podt, A.B.S. De Haan, Fluid Phase Equilib. 247 (2006) 158–168.
[18] M.B. Shiflett, A. Yokozeki, Energy Fuel 24 (2010) 1001–1008.
[19] D. Patterson, J. Solut. Chem. 23 (1994) 105–109.
[20] W. Dannhauser, A.F. Flueckinger, J. Phys. Chem. 68 (1964) 1814–1819.
[21] J.Y. Le Questel, M. Berthelot, C. Laurence, J. Phys. Org. Chem. 13 (2000) 347–358.
[22] R.J. Lewis, Sax's Dangerous Properties of Industrial Materials, ninth ed. Van Nostrand Reinhold, New York, 1996 2799.
[23] P. Pollak, G. Romeder, F. Hagedorn, H.-P. Gelbke, Ullmann's Encyclopedia of Industrial Chemistry, Wiley-VCH, Weinheim, 2002.
[24] L. Peng, S. Jayapalan, B. Chankvetadze, T. Farkas, J. Chromatogr. A 1217 (2010) 6942–6955.
[25] M.A.R. Khan, M. Mehedi Hasan Rocky, F. Islam Chowdhury, M. Shamsuddin Ahmed, S. Akhtar, J. Mol. Liq. 277 (2019) 681–691.
[26] S. Hina, X. Zhu, Y. Chen, Y. Zhang, Chin. J. Chem. Eng. 23 (2015) 804–811.
[27] X. Yang, Y. Fang, J. Chem. Eng. Data 64 (2019) 722–735.
[28] R.L. Gardas, M.G. Freire, P.J. Carvalho, I.M. Marrucho, I.M.A. Fonseca, A.G.M. Ferreira, J.A.P. Coutinho, J. Chem. Eng. Data 52 (2007) 80–88.
[29] S. Brahma, R.L. Gardas, J. Mol. Liq. 256 (2018) 22–28.
[30] G. García-Miaja, J. Troncoso, L. Romaní, J. Chem. Thermodyn. 41 (2009) 161–166.
[31] D. Matkowska, T. Hofman, J. Solut. Chem. 42 (2013) 979–990.
[32] P.N. Sibiya, N. Deenadayalu, S. Afr. J. Chem. 62 (2009) 20–25.
[33] S. Singh, M. Aznar, N. Deenadayalu, J. Chem. Thermodyn. 57 (2013) 238–247.
[34] U. Domanska, A. Pobudkowska, A. Wisniewska, J. Solut. Chem. 35 (2006) 311–334.
[35] M.A. Iglesias-Otero, J. Troncoso, E. Carballo, L. Romani, J. Chem. Thermodyn. 40 (2008) 949–956.
[36] A.B. Pereiro, A. Rodriguez, J. Chem. Thermodyn. 39 (2007) 978–989.
[37] G. García-Miaja, J. Troncoso, L. Romaní, Fluid Phase Equilib. 274 (2008) 59–67.
[38] A. Paul, M. Saini, B. Kumar, Fluid Phase Equilib. 411 (2016) 66–73.
[39] B. Kumar, T. Singh, K. Srinivasa Rao, A. Pal, A. Kumar, J. Chem. Thermodyn. 44 (2012) 121–127.
[40] M.T. Zafarani-Moattar, H. Shekaari, J. Chem. Thermodyn. 38 (2006) 1377–1384.
[41] M.T. Zafarani-Moattar, H. Shekaari, J. Chem. Eng. Data 50 (2005) 1694–1699.
[42] M. Geppert-Rybczynska, A. Heintz, J.K. Lehmann, A. Golus, J. Chem. Eng. Data 55 (2010) 4114–4120.
[43] S. Singh, I. Bahadur, G.G. Redhi, D. Ramjugernath, E.E. Ebenso, J. Mol. Liq. 200 (2014) 160–167.
[44] O. Redlich, A.T. Kister, Ind. Eng. Chem. 40 (1948) 345–348.
[45] A.B. Pereiro, P. Verdía, E. Tojo, A. Rodríguez, J. Chem. Eng. Data 52 (2007) 377–380.
[46] J.S. Torrecilla, J. Palomar, J. García, F. Rodríguez, J. Chem. Eng. Data 54 (2009) 1297–1301.
[47] M. Tariq, P.A.S. Forte, M.F. Costa Gomes, J.N. Canongia Lopes, L.P.N. Rebelo, J. Chem. Thermodyn. 41 (2009) 790–798.
[48] A. Fernandez, J. Garcia, J.S. Torrecilla, M. Oliet, F. Rodríguez, J. Chem. Eng. Data 53 (2008) 1518–1522.
[49] T. Singh, A. Kumar, J. Solut. Chem. 38 (2009) 1043–1053.
[50] S. Singh, I. Bahadur, G.G. Redhi, D. Ramjugernath, E.E. Ebenso, J. Mol. Liq. 200 (2014) 160–167.
[51] M. Geppert-Rybczynska, M. Sitarek, J. Chem. Eng. Data 59 (2014) 1213–1224.
[52] P. Droliya, A.K. Nain, J. Chem. Thermodyn. 123 (2018) 146–157.
[53] H.H. Ghazoyan, Z.L. Grigoryan, L.S. Gabrielyan, S.A. Markarian, J. Mol. Liq. 284 (2019) 147–156.
[54] J.A. Riddick, W.B. Bunger, T.K. Sakano, Organic Solvents. Physical Properties and Methods of Purification, John Wiley and Sons, New York, 1986.
[55] K. Rajagopal, S. Chenthilnath, A.K. Nain, J. Mol. Liq. 151 (2010) 23–29.
[56] S.K. Mehta, A.K. Sharma, Fluid Phase Equilib. 205 (2003) 37–51.
[57] S.L. Oswal, N.B. Patel, J. Chem. Eng. Data 40 (1995) 845–849.
[58] K. Govindarajulu, K.S.V. Krishna Rao, R. Bharathi, A.B.V. Kiran Kumar, M.C.S. Subha, G.N. Swamy, J. Pure Appl. Ultrason. 29 (2007) 54–59.
[59] A.A. Mirzaliev, Sh.G. Shakhuradov, S.O. Guseinov, Izv. Vyssh. Ucheb. Zaved., Neft i Gaz 30 (1987) 55–58(in Russian).
[60] S.O. Guseinov, A.A. Mirzaliev, Izv. Vyssh. Ucheb. Zaved., Neft i Gaz 28 (1985) 58–62 (in Russian).
[61] J.S. Lopez-Lazaro, G.A. Iglesias-Silva, A. Estrada-Baltazar, J. Barajas-Fernandez, J. Chem. Eng. Data 60 (2015) 1823–1834.
[62] S. Martínez, R. Garriga, P. Perez, M. Gracia, J. Chem. Eng. Data 45 (2000) 1182–1188.
[63] M. Musiał, E. Zorebski, M. Geppert-Rybczynska, J. Chem. Thermodyn. 87 (2015) 147–161.
[64] N. Deenadayalu, P. Bhujrajh, J. Chem. Thermodyn. 38 (2006) 278–282.
[65] J.A. Gonzalez, I.G. de la Fuente, J.C. Cobos, C.A. Tristan, L.F. Sanz, Ind. Eng. Chem. Res. 54 (2015) 550–559.
[66] Y.H. Yu, A.N. Soriano, M.H. Li, Thermochim. Acta 482 (2009) 42–48.
[67] H. Jin, B. O'Hare, J. Dong, S. Arzhantsev, G.A. Baker, J.F. Wishart, A.J. Benesi, M. Maroncelli, J. Phys. Chem. B 112 (2008) 81–92.
[68] N. Anwar, Riyazuddeen, J. Chem. Eng. Data 63 (2018) 269–289.
[69] A. Stoppa, J. Hunger, G. Hefter, R. Buchner, J. Phys. Chem. B 116 (2012) 7509–7521.
[70] E.J. González, Á. Domínguez, E.A. Macedo, J. Chem. Thermodyn. 47 (2012) 300–311.
[71] G.C. Benson, O. Kiyohara, J. Chem. Thermodyn. 11 (1979) 1061–1064.
[72] R.J. Fort, W.R. Moore, Trans. Faraday Soc. 61 (1965) 2102–2111.
[73] Y. Zhong, H. Wang, K. Diao, J. Chem. Thermodyn. 39 (2007) 291–296.
[74] O. Redlich, A.T. Kister, Ind. Eng. Chem. 40 (1948) 345–348.
[75] M. Behroozi, H. Zarei, J. Chem. Thermodyn. 47 (2012) 276–287.

Data Article

Excess volume, speed of sound and isentropic compressibility data of ternary mixtures containing N-methylcyclohexylamine, p-xylene and (C$_3$-C$_5$) 1-alkanols

Ch. Bharath Kumar [a], P. Bhanuprakash [b], C. Narasimha Rao [c], R.L. Gardas [d], K. Sivakumar [a],*

[a] *Department of Chemistry, S.V. Arts Degree & P.G. College (T.T.D'S), Tirupati-517502, A.P., India*
[b] *Department of Chemistry, S.V.C.R. Govt. Degree College, Palamaner-517408, A.P., India*
[c] *Department of Chemistry, Sri Venkateswara University, Tirupati-517502, A.P., India*
[d] *Department of Chemistry, Indian Institute of Technology Madras, Chennai-600036,T.N., India*

ARTICLE INFO

ABSTRACT

Excess volume (V^E_{123}) and speed of sound (u_{123}) data of three ternary mixtures of N-methylcyclohexylamine (NMC) (1) + p-xylene (2) + 1-alkanols (C$_3$-C$_5$) were determined as a function of composition at 303.15 K and atmospheric pressure. From the measured data, isentropic compressibility (k_{s123}), deviation in isentropic compressibility ($k_s'_{123}$) and the quantity Δk_{s123}, the difference between measured value and that of computed from the constituent binary data were derived. The V^E_{123} data of all the mixtures were analyzed in terms of different theoretical models. The experimental and predicted results indicate that the theoretical expressions give good estimation of the derived functions for the studied ternary systems. The excess and deviation properties were discussed in terms of intermolecular interactions prevailing between component molecules in the liquid mixtures.

© 2020 Elsevier B.V. All rights reserved.

Specifications Table

Subject area	Physical Chemistry, Chemical Engineering, Chemical Thermodynamics
Compounds	N-methylcyclohexylamine, p-xylene and 1-alkanols
Data category	Physicochemical properties, Density, ultrasound velocity
Data acquisition format	Chemical data analysis
Data type	Calculated, analyzed
Procedure	Density measurements are made by using single-stem bicapillary pycnometer of bulb capacity 12 cm³, and speeds of sound are estimated with single crystal ultrasonic interferometer (model F-82) from Mittal Enterprises, New Delhi, India
Data accessibility	Data is with this article

1. Rationale

Thermodynamic investigation of liquid mixtures is of great interest because of their extensive utilization in process designing, petrochemical industry, textile industry, pharmaceutical industry and in many other chemical engineering appli-

---

* Corresponding author.
E-mail address: sivakumarkasi64@gmail.com (K. Sivakumar).

cations. When two or more solvent molecules are associated with one another it results in significant differences in their intermolecular interactions. In recent years, measurement of excess volumes and isentropic compressibilities has been adequately employed in understanding molecular interactions in pure liquids and in liquid mixtures [1–4]. Keeping both the industrial and scientific interest in mind, many studies pertaining to thermophysical properties of binary mixtures have been reported in the literature, whereas the same for the ternary systems in particular are scarce. Hence in the present work, we report here new excess volume and deviation in isentropic compressibility data of ternary mixtures containing NMC and p-xylene with 1-alkanols (C_3-C_5) at T = 303.15 K and atmospheric pressure.

NMC has wide application in the production of pharmaceuticals, insecticides and pesticides [5]. Xylenes are used in printing, rubber and leather industries. Alkanols are extensively utilized in the manufacture of fuel, perfumes, cosmetics, paints, varnishes, drugs, explosives, fats, waxes, resins, etc., [6]. Because of their extensive industrial applications, knowledge of their thermophysical properties is of great importance from a practical point of view. Therefore, these systems have been selected in order to study the molecular interactions between NMC, p-xylene and 1-alkanols (C_3-C_5). In addition, the ternary V^E_{123} data of all the mixtures were analyzed in terms of predictive expressions [7–9]. The experimental data were discussed in terms of molecular interactions between component molecules.

2. Procedure

2.1. Reagents

All chemicals used were of analytical grade. N-methylcyclohexylamine (NMC) (>99.5% of purity) and 1-propanol (>99.7% of purity) were obtained from Sigma Aldrich. m-Xylene (>99.5% of purity), 1-butanol (>99.5% of purity) and 1-pentanol (>99.5% of purity) were purchased from Merck. All the chemicals were purified by the standard methods described in the literature [10–11]. The chemical names, acronyms, CAS numbers, molar mass, supplier, and molecular purities of the liquids used were reported in Table 1. The purities of the samples were checked by comparing the measured densities (ρ) and speed of sound (u) of the components with those reported in the literature [12-14] and these values were presented in Table 2.

2.2. Apparatus and procedures (Measurements)

A single-stem bicapillary pycnometer (made of borosil glass) of bulb capacity 12 cm^3 was utilized for density measurements. Excess volume (V^E_{123}) data for the ternary mixtures were measured using dilatometer [15]. The mixing cell contained three bulbs of different capacities that were connected by a W-tube. Mercury was used to separate three component liquids. One of the three bulbs was fitted with a capillary and the other two were fitted with ground-glass stoppers. Each bulb of the dilatometer was filled with a component whose mass was determined directly by weighing. The entire dilatometer was placed in a thermostat that could be maintained to 303.15 ± 0.01 K. All the measurements were made at constant temperature employing a thermostat. The measured ternary excess volume data (V^E_{123}) were accurate to ± 0.003 cm^3 mol^{-1}.

The speeds of sound data (u123) were measured [3] by a single crystal ultrasonic interferometer (model F-82) from Mittal Enterprises, New Delhi, India. A thermostatically controlled, well-stirred circulated water bath with a temperature controlled to ±0.01 K was used to maintain temperature stability. The uncertainty in sound speed measurement was is ± 0.3%.

Table 1
Characteristics of liquids used in the present work.

Material	Provenance	Molar mass (g.mol^{-1})	CAS number	Mass fraction purity
N-methylcyclohexylamine (NMC)	Sigma-Aldrich, India.	113.2	100-60-7	99.5%
1-propanol	Sigma-Aldrich, India.	60.1	71-23-8	99.7%
1-butanol	Merck, India.	74.1	71-36-3	99.5%
1-pentanol	Merck, India.	88.1	71-41-0	99.5%

Table 2
Density (ρ) and speed of sound (u) of pure components at 303.15 K and atmospheric pressure.

Compound	ρ (g.cm^{-3}) Experimental	Literature	u (m.s^{-1}) Experimental	Literature
N-methyl cyclohexylamine	0.84683	0.84686 [12]	1356	1354 [12]
p-xylene	0.85229	0.85230 [13]	1289	1290 [13]
1-propanol	0.79566	0.79602 [14]	1189	1192 [14]
1-butanol	0.80205	0.80203 [14]	1229	1227 [14]
1-pentanol	0.80764	0.80764 [14]	1256	1258 [14]

Table 3

Mole fractions of N-methylcyclohexylamine (x_1), p-xylene (x_2), experimental and predicted excess volumes for the ternary mixtures of N-methylcyclohexylamine (NMC) (1) + p-xylene (2) + 1-alkanols (3) at 303.15 K and atmospheric pressure.

x_1	x_2	V^E (cm^3. mol^{-1}) Experimental	(Redlich-Kister)	Kohler	Tsao-Smith	Hwang	$\Delta V^E{}_{123}$*
N-methylcyclohexylamine (NMC) (1) + p-xylene (2) + 1-propanol (3)							
0.1010	0.0741	-0.522	-0.525	-0.507	-0.537	-0.550	0.003
0.1113	0.1021	-0.564	-0.567	-0.546	-0.597	-0.595	0.003
0.2224	0.1341	-0.968	-0.974	-0.962	-1.056	-1.014	0.006
0.2092	0.2847	-0.720	-0.732	-0.739	-0.925	-0.801	0.012
0.1729	0.3429	-0.577	-0.590	-0.598	-0.798	-0.649	0.013
0.0564	0.4634	-0.197	-0.210	-0.201	-0.308	-0.229	0.013
0.1373	0.5423	-0.292	-0.306	-0.322	-0.517	-0.359	0.014
0.1658	0.6216	-0.223	-0.238	-0.248	-0.379	-0.301	0.015
0.1275	0.6712	-0.161	-0.172	-0.182	-0.322	-0.219	0.011
0.1626	0.7631	-0.110	-0.117	-0.100	-0.061	-0.166	0.007
0.1056	0.8323	-0.070	-0.074	-0.068	-0.052	-0.107	0.004
0.0801	0.8616	-0.049	-0.052	-0.049	-0.052	-0.078	0.003
N-methylcyclohexylamine (NMC) (1) + p-xylene (2) + 1-butanol (3)							
0.0800	0.049	-0.330	-0.331	-0.324	-0.332	-0.343	0.001
0.1034	0.1026	-0.407	-0.409	0.397	-0.434	-0.426	0.002
0.1204	0.159	-0.198	-0.202	-0.203	-0.384	-0.468	0.004
0.0807	0.2251	-0.284	-0.293	-0.283	-0.351	-0.310	0.009
0.0937	0.3429	-0.265	-0.277	-0.273	-0.377	-0.297	0.012
0.0992	0.4126	-0.236	-0.249	-0.249	-0.369	-0.271	0.013
0.1115	0.5012	-0.196	-0.211	-0.217	-0.354	-0.239	0.015
0.1124	0.5624	-0.156	-0.170	-0.177	-0.312	-0.198	0.014
0.0918	0.6209	-0.095	-0.106	-0.112	-0.232	-0.130	0.011
0.0823	0.6714	-0.062	-0.069	-0.073	-0.183	-0.090	0.007
0.1108	0.7326	-0.072	-0.077	-0.080	-0.154	-0.104	0.005
0.0878	0.8409	-0.041	-0.044	-0.044	-0.049	-0.067	0.003
N-methylcyclohexylamine (NMC) (1) + p-xylene (2) + 1-pentanol (3)							
0.0510	0.081	-0.265	-0.267	-0.270	-0.293	-0.246	0.002
0.1057	0.1534	-0.455	-0.457	-0.466	-0.539	-0.451	0.002
0.0930	0.201	-0.382	-0.385	-0.398	-0.483	-0.377	0.003
0.0648	0.2709	-0.25	-0.255	-0.269	-0.349	-0.247	0.005
0.0966	0.3392	-0.303	-0.309	-0.330	-0.455	-0.300	0.006
0.1081	0.4298	-0.264	-0.273	-0.296	-0.446	-0.267	0.009
0.0654	0.5436	-0.114	-0.126	-0.143	-0.265	-0.123	0.012
0.1818	0.6121	-0.197	-0.211	-0.223	-0.310	-0.228	0.014
0.0678	0.6762	-0.068	-0.079	-0.093	-0.214	-0.081	0.011
0.0992	0.7126	-0.094	-0.104	-0.117	-0.222	-0.112	0.010
0.0477	0.7562	-0.024	-0.032	-0.040	-0.137	-0.035	0.008
0.0676	0.8532	-0.044	-0.049	-0.053	-0.087	-0.062	0.005

$\Delta V^E{}_{123}$ = $V^E{}_{123}$(Exp) - $V^E{}_{123}$(bc)
Where $V^E{}_{123}$(bc) is computed from constituent binary data using Redlich-Kister equation.

3. Data, value and validation

3.1. Excess volume

The measured excess volume data ($V^E{}_{123}$) of three ternary liquid mixtures containing NMC and p-xylene with 1-propanol, 1-butanol and 1-pentanol at 303.15 K and atmospheric pressure were reported in Table 3 along with those values calculated from predictive expressions namely Redlich-Kister, Kohler, Tsao-Smith and Hwang et al. equations. These data were also graphically depicted in Figs. 1–3.

Redlich-Kister equation [7,8] can be expressed as:

$$V^E_{123} = \sum_{i<j} V^E_{ij}(x_i, x_j) \tag{1}$$

where $V^E_{ij} = x_i x_j \sum_{s=0}^{n} (A_s)_{ij}(x_i - x_j)^s$ and x_i, x_j are the mole fractions of the components in a ternary mixture.

Kohler Expression [7]:

$$V^E_{123} = (x_1 + x_2)^2 V^E_{12} + (x_1 + x_3)^2 V^E_{13} + (x_2 + x_3)^2 V^E_{23} \tag{2}$$

where $V^E_{ij} = x'_i x'_j \sum_{s=0}^{n} (A_s)_{ij}(x'_i - x'_j)^s$ at composition (x'_i, x'_j), such that $x'_i = 1 - x'_j = \frac{x_i}{x_i + x_j}$ where x_i and x_j are the ternary mole fractions.
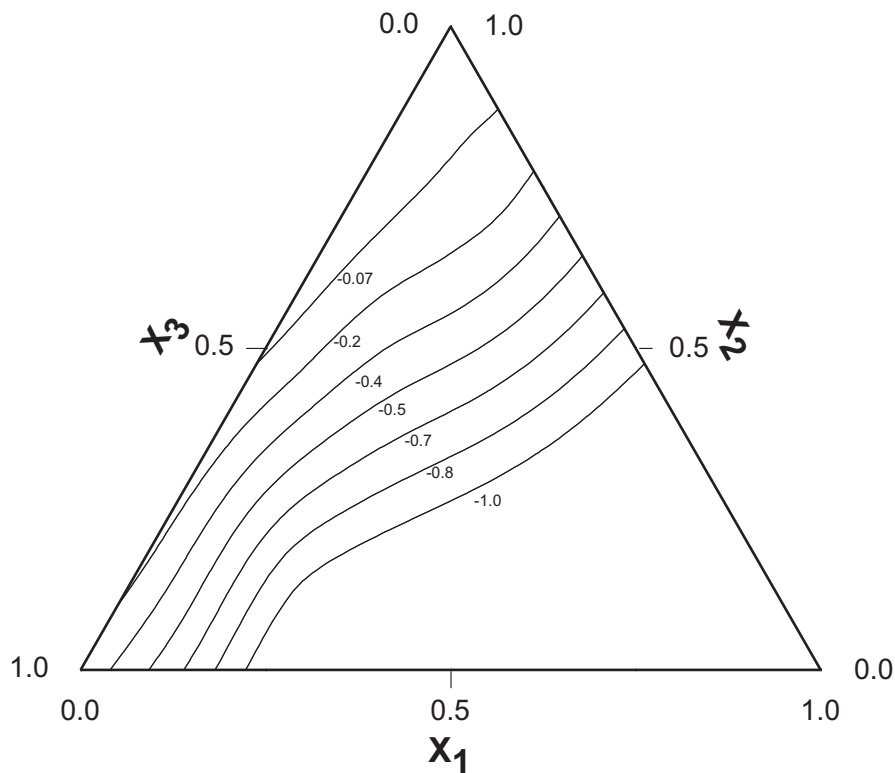
Fig. 1. Excess volumes (V^E_{123}) data for N-methylcyclohexylamine (NMC) (1) + *p*-xylene (2) + 1-propanol (3) at 303.15 K.
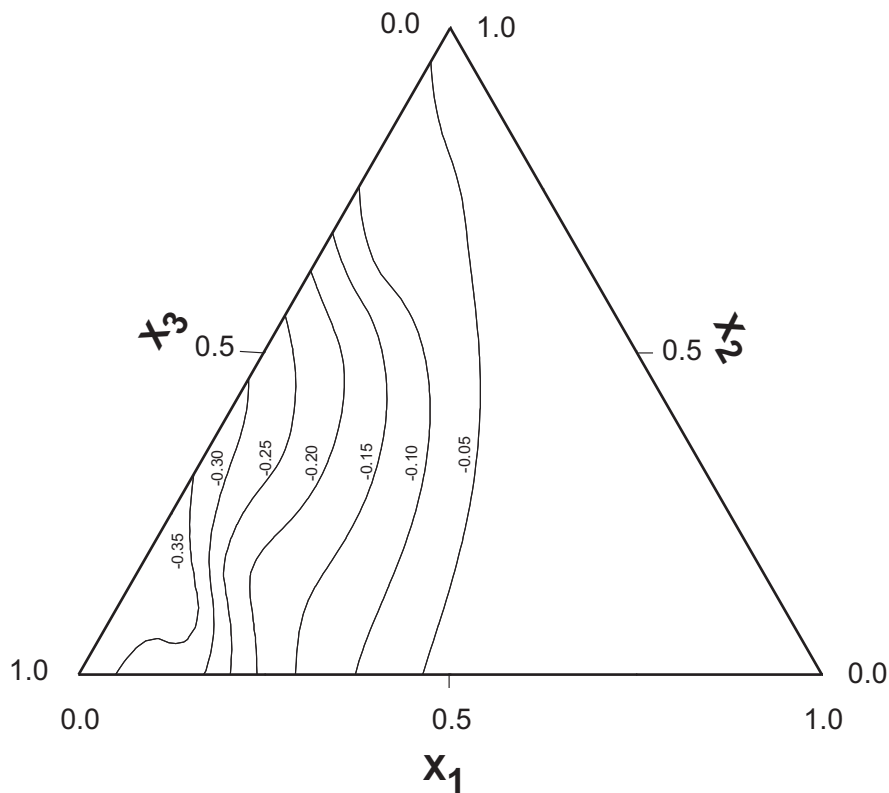
Fig. 2. Excess volumes (V^E_{123}) data for N-methylcyclohexylamine (NMC) (1) + *p*-xylene (2) + 1-butanol (3) at 303.15 K.
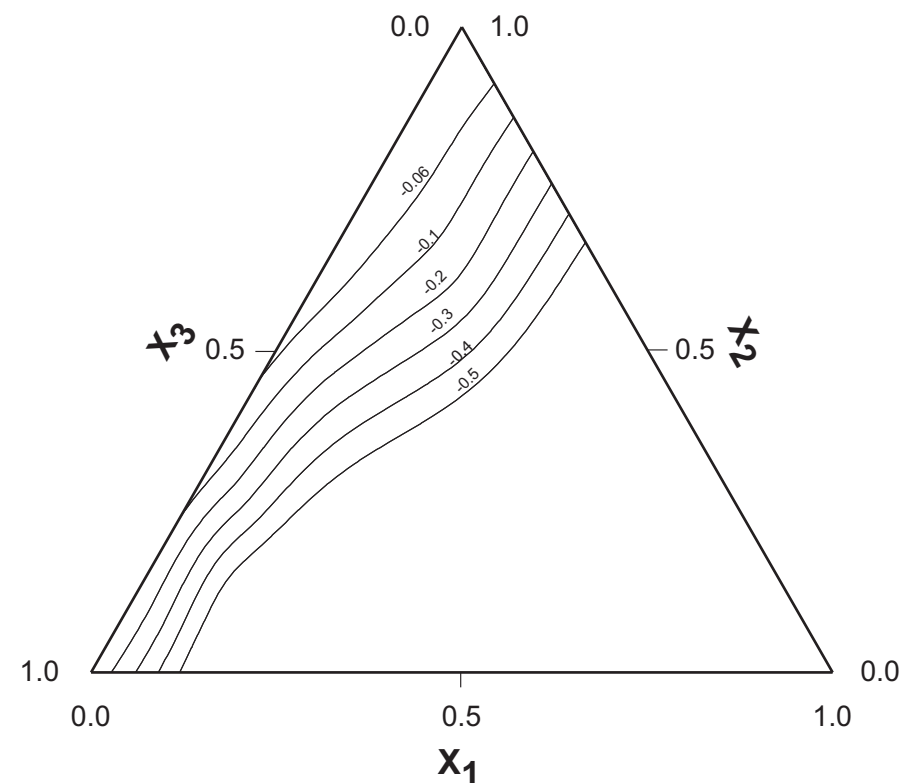
Fig. 3. Excess volumes (V^E_{123}) data for N-methylcyclohexylamine (NMC) (1) + p-xylene (2) + 1-pentanol (3) at 303.15 K.

Table 4
The standard deviation values (Redlich-Kister and Hwang eqns) of binary systems of $\sigma(V^E)$ at 303.15 K.

System	Redlich-Kister				Hwang			
	a_0 cm^3mol^{-1}	a_1	a_2	$\sigma(V^E)$	b_0	b_1	b_2	$\sigma(V^E)$
N-methyl cyclohexylamine (1)+ p-xylene (2)	-0.122	1.220	0.009	0.002	-0.125	1.464	-1.440	0.008
p-xylene (2)+ 1-propanol (3)	-0.076	0.560	0.463	0.000	-0.230	1.285	-0.050	0.006
p-xylene (2) + 1-butanol (3)	0.125	0.576	0.359	0.000	0.005	1.164	-0.207	0.000
p-xylene (2) + 1-pentanol (3)	0.090	0.371	0.027	0.002	0.081	0.477	-0.406	0.007
N-methyl cyclohexylamine (1) +1-propanol (3)	-6.237	2.703	3.925	0.002	-7.545	8.449	2.015	0.002
N-methyl cyclohexylamine (1) +1-butanol (3)	-5.219	0.847	1.908	0.001	-5.852	3.461	1.531	0.002
N-methyl cyclohexylamine (1) +1-pentanol (3)	-5.243	0.955	0.417	0.002	-5.382	1.695	-0.580	0.003

Tsao–Smith expression [7] is of the form:

$$V^E_{123} = x_2(1+x_1)^{-1}V^E_{12} + x_3(1-x_1)^{-1}V^E_{13} + (1-x_1)V^E_{23} \tag{3}$$

where V^E_{12}, V^E_{13} and V^E_{23} are the binary excess volumes at composition (x'_i, x'_j), such that $x'_i = x_1$ for 1,2 and 1,3 binary systems and $x'_2 = \frac{x_2}{x_2+x_3}$ for 2,3 binary system.

Hwang et al. equation [9]:

$$V^{E(123)}/cm^3mol^{-1} = x_1x_2\left(b_0^{(12)} + b_1^{(12)}x_1^3 + +b_2^{(12)}x_2^3\right) + x_1x_3\left(b_0^{(13)} + b_1^{(13)}x_1^3 + +b_3^{(13)}x_3^3\right)$$
$$+x_2x_3\left(b_0^{(23)} + b_2^{(23)}x_2^3 + +b_3^{(23)}x_3^3\right) \tag{4}$$

The quantity ΔV^E_{123}, difference between measured ternary data and computed from the constituent binary data through the Redlich-Kister relation were given in last column of Table 3. The binary data which was used to compute ternary excess volume data for the mixtures NMC+m-xylene [12], NMC+1-alkanols [16] and p-xylene +1-alkanols [17] were collected from the literature and these data were included in Table 4 along with standard deviation values $\sigma(V^E)$.

The sign and magnitude of V^E_{123} data depends upon the resultant of the following factors [18]:

i dissociation of associated alkanols in solution systems

ii donor-acceptor interaction between π-electrons of the aromatic ring and the alkanols

iii a possible inclusion of p-xylene into the structural network of alkanols.

The first factor contributes to expansion in volume and the second and third factors lead to contraction in volume. The experimental V^E_{123} data in Table 2 suggest that the combined effects for volume contraction i.e., donor-acceptor interactions and inclusion of p-xylene into the structural network of alkanols exceed the factors responsible for volume expansion.

The molecular interaction between NMC and 1-alkanols in the studied ternary mixtures can be explained as follows [19]. Negative contributions in the mixtures containing NMC and 1-alkanol arise from two factors: a) changes in free volumes in the real mixtures and b) the presence of electron donor-acceptor interactions between NMC and 1-alkanol. The negative V^E_{123} values in the present ternary system emphasis that the breaking of the three-dimensional associated network of the alkanol is incomplete and that the aromatic hydrocarbon molecules are more or less fitted into the alkanol networks.

In addition, specific interactions due to the formation of N––H•••π type hydrogen bond between NMC and electrons in aromatic ring of p-xylene also contribute significantly to negative V^E_{123} data of the studied ternary mixtures [12].

A perusal of Table 3 clearly indicates that V^E_{123} data is more negative for the ternary mixtures containing 1-propanol and the negative value decreases with increase in chain length from 1-propanol to 1-pentanol. The effect of increasing chain length of 1-alkanol on the V^E_{123} data can be considered using the effective dipole moment. The negative V^E_{123} values decrease with decreasing effective dipole moment of 1-alkanol in the systems of cyclic amine with alcohols [6] which can be explained as follows. The dipole moment of 1-alkanols decreases with increase in chain length. Polarity of hydroxyl group also decreases with increase in chain length of 1-alkanol. These two factors result in the rupture of alkanol-alkanol hydrogen bonds. Moreover, in higher alkanols, hydroxyl group proton will be shielded by the adjacent methyl groups, thus availability of such protons will be diminished for the formation heteroassociates which ultimately results in decrease in negative V^E_{123} data in higher 1-alkanols [4] in the following order:1-propanol > 1-butanol >1-pentanol.

An examination of ternary data in Table 3 reveal that the predictive expressions proposed by Redlich-Kister, Kohler, Tsao-Smith and Hwang et al. gives satisfactory estimation in terms of ternary excess volumes in all the mixtures.

3.2. Isentropic compressibility

The isentropic compressibility of ternary mixtures (κ_{s123}) was calculated from the expression

$$\kappa_{s123} = u^{-2}_{123}\rho^{-1}_{mix123} \tag{5}$$

where u_{123} and ρ_{mix123} indicate speed of sound and density of ternary mixtures respectively.

The density of a ternary liquid mixture (ρ_{mix123}) was computed using the expression

$$\rho_{mix123} = x_1 M_1 + x_2 M_2 + x_3 M_3/V + V^E_{123} \tag{6}$$

where x_1, x_2 and x_3 represent mole fractions and M_1, M_2 and M_3 are the molecular weights of NMC, p-xylene and 1-alkanols respectively; V is the molar volume of the mixture and V^E_{123} is ternary excess volume.

The deviation in isentropic compressibility (κ'_{s123}) was estimated using the relation

$$\kappa'_{s123} = k_{s123} - \o_1 k_{s1} - \o_2 k_{s2} - \o_3 k_{s3} \tag{7}$$

where $\o_1$, $\o_2$, $\o_3$, κ_{s1}, κ_{s2} and κ_{s3} are the volume fractions and isentropic compressibilities of the pure components 1, 2 and 3 respectively. The quantity $\Delta\kappa_{s123}$, the difference between measured value of $\kappa_{s}'_{123}$ and that of computed from binary data $\kappa'_{s123\,(b)}$ has been calculated using the relation

$$\Delta\kappa_{s\,123} = \kappa'_{s\,123} - \kappa'_{s\,123\,(b)} \tag{8}$$

The latter quantity, $\kappa_{s}'_{123(b)}$ was computed using Redlich-Kister relation [8]

$$\kappa'_{s123\,(b)} = \kappa_{s12} + \kappa_{s13} + \kappa_{s23} \tag{9}$$

where κ_{s12}, κ_{s13} and κ_{s23} denote the deviation in isentropic compressibilities for the three binary mixtures and these are estimated using the smoothing equation

$$\kappa_{sij} = \o_1 \o_2 \left[a_0 + a_1(\o_1 - \o_2) + a_2(\o_1 - \o_2)^2 \right] \tag{10}$$

where a_0, a_1 and a_2 are the constants obtained by the method of least squares. Further, the binary parameters that were required to compute $k_s'_{123(b)}$ for the mixtures of NMC with p-xylene [20], NMC with 1-alkanols [21] and p-xylene with 1-alkanols [17] were collected from the literature and these were given in Table 5 along with standard deviation $\sigma(\Delta\kappa_s)$.

The speed of sound (u), density of the mixture (ρ_{mix123}), isentropic compressibility (κ_{s123}), deviation in isentropic compressibility (κ'_{s123}) and the quantity $\Delta\kappa_{s123}$, the difference between measured data of $\kappa_{s}'_{123}$ and that of computed from the constituent binary data $\kappa'_{s123\,(b)}$ were presented in Table 6. Moreover, the deviation in isentropic compressibility $(\Delta\kappa_{s123})$ for the three ternary mixtures was also graphically represented in Figs. 4–6.

An examination of $\Delta\kappa_{s123}$ values in Table 6 suggest that the values were positive over the entire composition range in all the binary mixtures of NMC and p-xyleme with 1-alkanols and these were 3 to 4 times to the experimental error.
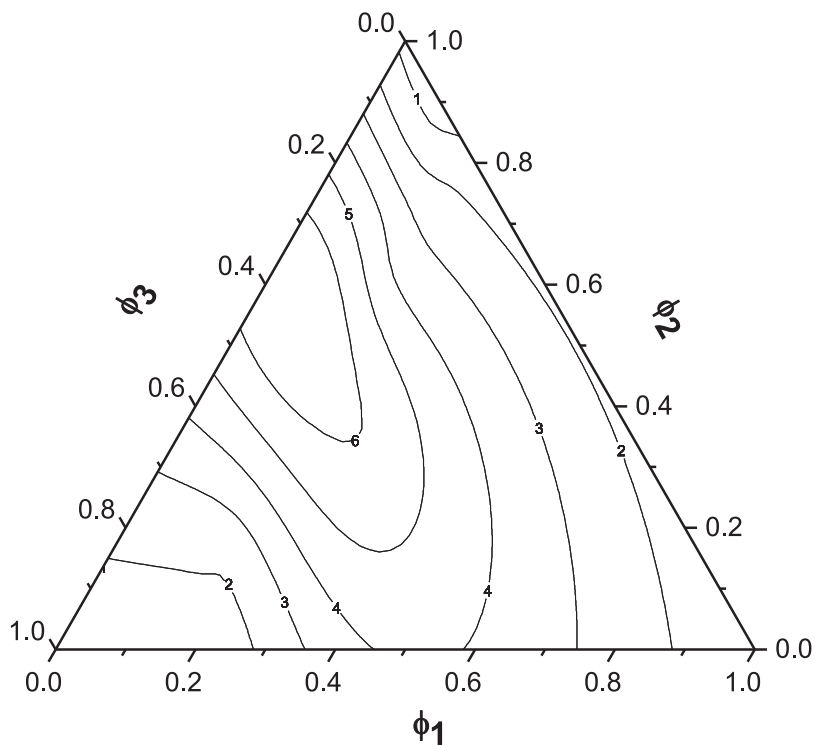
Fig. 4. Deviation in isentropic compressibility ($\Delta\kappa_{s123}$) data for N-methylcyclohexylamine (NMC) (1) + p-xylene (2) + 1-propanol (3) at 303.15 K.
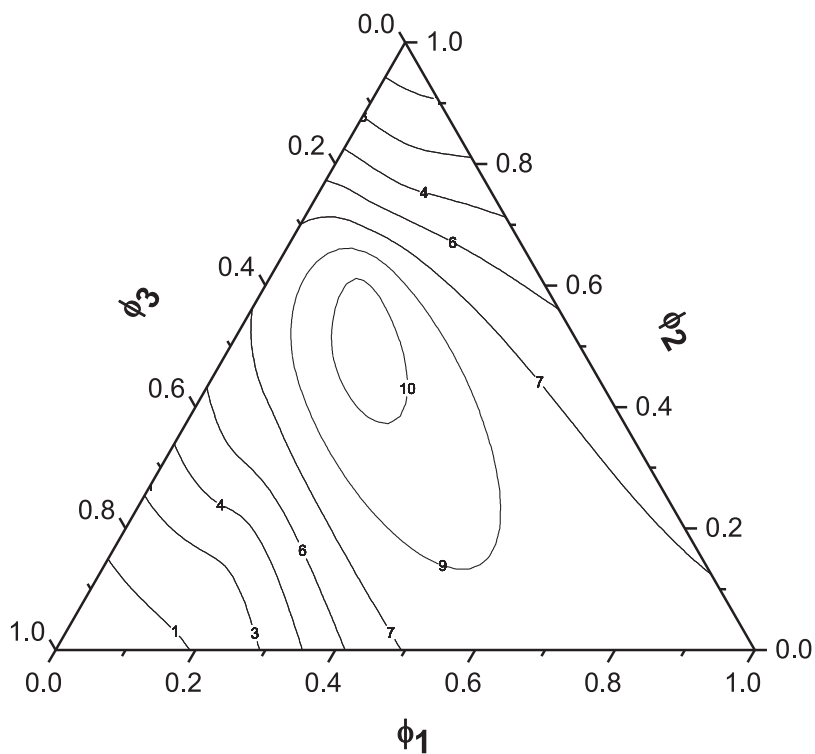

Fig. 5. Deviation in isentropic compressibility ($\Delta\kappa_{s123}$) data for N-methylcyclohexylamine (NMC) (1) + p-xylene (2) + 1-butanol (3) at 303.15 K.

Table 5

The standard deviation $\sigma(k_s)$ values of all the binary systems computed from Redlich-Kister equation at 303.15 K.

System	a_0 TPa-1	a_1	a_2	$\sigma(k_s)$
N-methyl cyclohexylamine (1)+ p-xylene (2)	-21.80	33.60	24.01	2
p-xylene (2)+1-propanol (3)	35.13	106.01	40.15	2
p-xylene (2)+ 1-butanol (3)	62.49	112.94	7.07	0
p-xylene (2)+ 1-pentanol (3)	80.95	138.16	32.51	0
N-methyl cyclohexylamine (1)+1-propanol (3)	-219.00	35.40	-68.30	2
N-methyl cyclohexylamine (1)+1-butanol (3)	-166.50	21.84	89.70	2
N-methyl cyclohexylamine (1)+1-pentanol (3)	-147.50	3.05	61.40	3

Table 6

Volume fractions of N-methylcyclohexylamine (ϕ_1), p-xylene (ϕ_2), density (ρ), speed of sound (u_{123}), isentropic compressibility (k_{s123}), deviation in isentropic compressibility (κ_{s123}), deviation in isentropic compressibility computed from constituent binary data $(\kappa_{s123(b)})$ and $\Delta\kappa_{s123}$ values for ternary systems N-methylcyclohexylamine (NMC) (1) + p-xylene (2) +1-alkanols (3).

$\Phi 1$	$\Phi 2$	P (g.cm^3)	U (m.s^{-1})	κ_{s123}	κ_{s123} TPa-1	$\kappa_{s123(b)}$	$\Delta\kappa_{s123}$
N-methylcyclohexylamine (NMC) (1) p-xylene (2) + 1-propanol (3)							
0.1587	0.1085	0.81490	1238	800	-29	-31	2
0.1709	0.1461	0.81796	1244	790	-29	-31	2
0.1127	0.7157	0.83005	1254	766	-33	-37	4
0.275	0.3488	0.83539	1271	741	-16	-22	6
0.2257	0.4171	0.83551	1267	745	-11	-17	6
0.0742	0.5685	0.83323	1248	771	6	-1	7
0.1667	0.6135	0.84110	1274	732	-2	-6	4
0.1916	0.6695	0.84498	1286	715	-3	-6	3
0.1471	0.7216	0.84520	1283	719	0	-3	3
0.1775	0.7766	0.84946	1298	699	-2	-4	2
0.1152	0.8466	0.84995	1295	702	-1	-2	1
0.0874	0.8766	0.85008	1292	705	0	-1	1
N-methylcyclohexylamine (NMC) (1) + p-xylene (2) + 1-butanol (3)							
0.1099	0.0629	0.81287	1250	787	-12	-13	1
0.1382	0.1278	0.81799	1258	772	-14	-16	2
0.157	0.1932	0.82036	1265	762	-12	-15	3
0.1047	0.2723	0.82267	1255	772	-2	-7	5
0.1167	0.3961	0.82930	1257	763	7	0	7
0.1208	0.4682	0.83275	1258	759	12	3	9
0.1317	0.5519	0.83710	1261	751	16	6	10
0.1305	0.6085	0.83958	1263	747	19	8	11
0.1056	0.6658	0.84089	1264	744	19	11	8
0.0937	0.7124	0.84245	1266	740	18	12	6
0.1229	0.7571	0.84606	1279	722	11	7	4
0.0953	0.8511	0.84933	1288	710	6	4	2
N-methylcyclohexylamine (NMC) (1) + p-xylene (2) + 1-pentanol (3)							
0.0611	0.0904	0.81599	1269	761	-5	-6	1
0.1238	0.1675	0.82324	1277	745	-7	-10	3
0.1086	0.2187	0.82439	1273	748	-2	-6	4
0.0754	0.2937	0.82548	1269	752	4	0	4
0.1106	0.362	0.83027	1271	746	8	2	6
0.122	0.4522	0.83374	1270	744	14	7	7
0.0734	0.5685	0.83667	1263	749	22	18	4
0.1975	0.6197	0.84438	1286	716	10	7	3
0.0747	0.6948	0.84204	1266	740	23	20	3
0.1082	0.7243	0.84484	1275	728	18	15	3
0.0523	0.7723	0.84430	1268	737	23	21	2
0.0729	0.8574	0.84905	1283	715	11	10	1

This suggests that Redlich-Kister equation is capable of giving good estimation of deviation in isentropic compressibility of ternary mixtures from that of constituent binaries [17,20,21].

The deviation in isentropic compressibility ($\Delta\kappa_{s123}$) data in the studied ternary mixtures is influenced by three factors: i) structure-breaking effects ii) structure making effects and iii) change in geometrical factors [2]. Structure breaking effects contribute to an increase in free spaces [22] between the molecules leading to positive deviation in compressibility. On the other hand, structure making effect and geometrical effect cause decrease in free spaces of the component molecules on mixing there by leading to negative deviation in isentropic compressibility. The actual deviation would depend up on
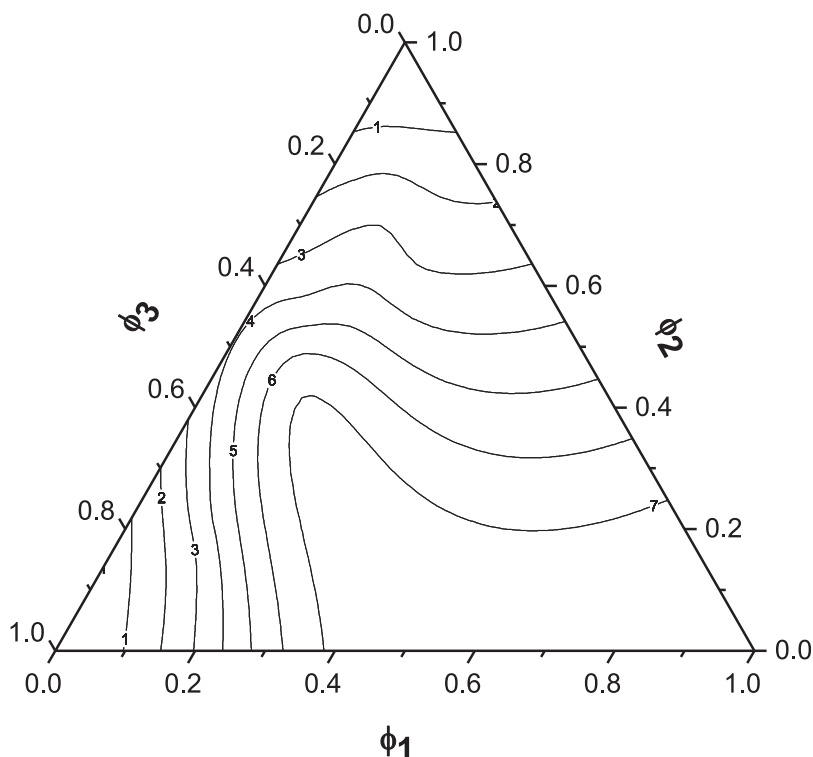
Fig. 6. Deviation in isentropic compressibility ($\Delta \kappa_{s123}$) data for N-methylcyclohexylamine (NMC) (1) + p-xylene (2) + 1-Pentanol (3) at 303.15 K.

Table 7
The standard deviation values $\sigma(\Delta V^E{}_{123})$ and $\sigma(\Delta \kappa_{s123})$ for ternary systems of N- methylcyclohexylamine (NMC) (1) + p-xylene (2)+1-alkanols (3).

system	A $cm^3\,mol^{-1}$	B	C	$\sigma(\Delta V^E{}_{123})$	A TPa^{-1}	B	C	$\sigma(\Delta \kappa_{s13})$
NMC (1) + p-xylene (2)+ 1-propanol(3)	0.639	2.026	-11.054	0.003	243.51	609.37	-4292.23	3
NMC (1) + p-xylene (2) + 1-butanol(3)	0.617	-11.177	-92.757	0.005	389.68	1843.89	-13821.03	1
NMC (1) + p-xylene (2) + 1-pentanol(3)	691.209	-1.737	-64.668	0.006	298.12	29.10	-20220.44	0

the balance between these two opposing effects. The experimental $\Delta \kappa_{s123}$ values indicate that structure breaking effect is dominant in all the three ternary mixtures.

The experimental $\Delta V^E{}_{123}$ and $\Delta \kappa_{s123}$ data were fitted to the following equation proposed by Redlich-Kister [8]:

$$\Delta V^E{}_{123}/cm^3 mol^{-1} = x_1 x_2 x_3 \left[A + B x_1 (x_2 - x_3) + C\, x_1^2 (x_2 - x_3)^2 \right] \tag{11}$$

$$\Delta \kappa_{s123}/TPa^{-1} = \o_1 \o_2 \o_3 \left[A + B\, \o_1 (\o_2 - \o_3) + C\, \o_1^2 (\o_2 - \o_3)^2 \right] \tag{12}$$

where A, B and C are the ternary constants which were calculated by least square method. The values of coefficients were inturn used to compute standard deviation $\sigma(Y^E{}_{123})$.

$$\sigma \left(Y^E{}_{123} \right) = \left[\Sigma \left(Y^E{}_{123\ exp} - Y^E{}_{123\ cal} \right)^2 / (m - n) \right]^{1/2} \tag{13}$$

where $\sigma(Y^E{}_{123}) = \Delta V^E{}_{123}$ (or) Δk_{s123}

'm' is the total number of experimental points and 'n' is the number of coefficients in Equation (11) and (12) and the values of ternary constants A, B and C along with their standard deviation values were given in Table 7.

4. Conclusions

In the present investigation, excess volume, sound speed and deviation in isentropic compressibility data were reported for three ternary mixtures of N-methylcyclohexylamine (NMC) + p-xylene + 1-propanol or + 1-butanol + 1-pentanol at

303.15 K and atmospheric pressure. Experimental excess volume data were found to be negative as a function of composition. The negative V^E_{123} data for the studied systems follow the order: 1-propanol > 1-butanol >1-pentanol. Whereas $(\triangle k_{s123})$ data were found to be positive for all the ternary mixtures. The experimental ternary (V^E_{123}) data were compared with theoretical models proposed by Redlich-Kister, Kohler, Tsao-Smith and Hwang et al. and found in good agreement between the predicted and experimental data. The V^E_{123} $\triangle \kappa_{s123}$ parameters were analyzed interms of intermolecular interactions between component molecules.

Declaration of Competing Interest

The authors declare that they have no known competing financial interests or personal relationships that could have appeared to influence the work reported in this paper.

Acknowledgements

References

[1] L. Venkatramana, K. Sreenivasulu, K. Sivakumar, K.Dayananda Reddy, Thermodynamic properties of binary mixtures containing 1-alkanols, J. Therm. Anal. Calorim. 115 (2014) 1829–1834.
[2] L. Venkatramana, K. Sivakumar, V. Govinda, K.Dayananda Reddy, Study on solution properties of some industrially important solvents with an aromatic alcohol, J. Mol. Liq. 186 (2013) 163–170.
[3] K. Sreenivasulu, V. Govinda, P. Venkateswarlu, K. Sivakumar, Thermodynamic properties of non-electrolyte solutions, J. Therm. Anal. Calorim. 115 (2014) 1805–1811.
[4] P. Venkatesu, G. Chandra Sekhar, M.V. Prabhakara Rao, T. Hofman, Excess molar volumes of N, N-dimethylformamide+ 2-pentanone+ alkan-1-ols mixed solvent systems at 303.15 K, Thermochim. Acta 443 (2006) 62–71.
[5] P.S. Slobodan, L.K. Mirjana, R.R. Ivona, D.D. Bojan, Effect of temperature on the excess molar volumes of some alcohol + aromatic mixtures and modelling by cubic EOS mixing rules, Fluid Phase Equilib 239 (2006) 69–82.
[6] P.S. Slobodan, L.K. Mirjana, R.R. Ivona, D.D. Bojan, Densities and excess molar volumes of alcohol+ cyclohexylamine mixtures, J. Serb. Chem. Soc. 74 (2009) 1303–1318.
[7] W.E. Acree, in: Thermodynamics of non-electrolyte solutions, Academic Press, Orlando, 1984, p. 64.
[8] O. Redlich, A.T. Kister, Algebraic representation of thermodynamic properties and the classification of solutions, Ind. Eng. Chem. 40 (1948) 345–348.
[9] C.A. Hwang, J. Holste, K.R. Hall, G.A. Mansoori, A simple relation to predict or to correlate the excess functions of multi component mixtures, Fluid Phase Equilib 62 (1991) 173–189.
[10] J.A. Riddick, W.B. Bunger, T.K. Sakano, Techniques of Chemistry, 4th edition, Willey Inter Science, New York, 1986.
[11] A.I. Vogel, A text book of practical organic chemistry, 5th edition, John Willey, New York, 1989.
[12] C. Chennarayappa, K. Rambabu, P. Venkateswarlu, G.K. Raman, Acoust. Lett. 15 (1991) 83–86.
[13] J.A. Al-Kandary, A.S. Al-Jimaz, A.H.M. Abdul-Latif, Viscosities, densities, and speeds of sound of binary mixtures of Benzene, Toluene, o-Xylene, m-Xylene, p-Xylene, and Mesitylene with Anisole at (288.15, 293.15, 298.15, and 303.15) K, J. Chem. Eng. Data 51 (2006) 2074–2082.
[14] J. Rajasekhar, P.R. Naidu, Speed of sound of 1,3 dichlorobenzene + methyl ethyl ketone + 1-alkanols at 303.15 K, J. Chem. Eng. Data 41 (1996) 373–375.
[15] V. Syamala, K. Sivakumar, P. Venkateswarlu, Volumetric behaviour of ternary organic liquid mixtures containing dimethylsulphoxide, 1, 2-dichlorobenzene and 1-alkanols at 303.15 K, J. Mol. Liq. 136 (2007) 29–34.
[16] C. Chennarayappa, K. Rambabu, P. Venkateswarlu, G.K. Raman, Excess volumes of binary liquid mixtures of N-methylcyclohexylamine, Indian J. Chem. Sci. 5 (1991) 73–76.
[17] L. Venkatramana, C. Narasimha Rao, R.L. Gardas, K.S. Kumar, FT-IR study of excess thermodynamic properties of binary liquid mixtures of p-xylene with 1-alkanols at 303.15 K, J. Mol. Liq. 207 (2015) 171–176.
[18] M.A. Saleh, M. Habibullah, M. Shamsuddin Ahmed, M. Ashraf Uddin, S.M.H. Uddin, M. Afsar Uddin, F.M. Khan, Excess molar volumes of the systems m-xylene+ 1-propanol, +2-propanol, +1-butanol, +2-methyl-2-propanol, Phys. Chem. Liq. 43 (2005) 139–148.
[19] B.L. Yadav, S. Maken, K.C. Karla, K.C. Singh, Excess volumes of (an alkanol+ an aromatic hydrocarbon) at the temperature 308.15 K, J. Chem. Thermodyn. 25 (1993) 1345–1350.
[20] C.L. Prabhavathi, K. Sivakumar, P. Venkateswarlu, G.K. Raman, Speed of Sound and Isentropic Compressibilities of N-Methylcyclohexylamine with Benzene and Substituted Benzenes at 303.15 K, Phys. Chem. Liq. 38 (2000) 705–712.
[21] C. Chennarayappa, K. Rambabu, P. Venkateswarlu, G.K. Raman, Ultrasonic studies in binary mixtures of n-methyl cyclohexylamine with alcohols at 303.15 K, Accoust. Lett. 15 (1999) 83–86.
[22] B. Jacobson, Ultrasonic velocity in liquids and liquid mixtures, J. Chem. Phys. 20 (1952) 9271–9928.
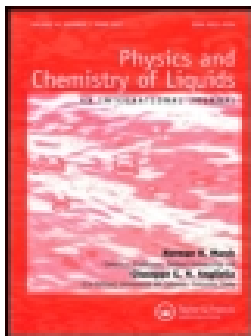
Insights into non-ideal behaviour of benzyl alcohol with (C$_2$-C$_4$) carboxylic acids through volumetric, ultrasonic and ATR-FTIR spectroscopic studies

P. Bhanuprakash , Ramesh L. Gardas , R. Prathibha , K. Sivakumar & N.V.V. Jyothi

Taylor & Francis
Taylor & Francis Group

ARTICLE

Check for updates

Insights into non-ideal behaviour of benzyl alcohol with (C$_2$-C$_4$) carboxylic acids through volumetric, ultrasonic and ATR-FTIR spectroscopic studies

P. Bhanuprakash [ID][a,b], Ramesh L. Gardas [ID][c], R. Prathibha[a], K. Sivakumar[d] and N.V.V. Jyothi[a]

[a]Department of Chemistry, S.V. University, Tirupati, India; [b]Department of Chemistry, S.V.C.R. Govt. Degree College, Palamaner, India; [c]Department of Chemistry, Indian Institute of Technology Madras, Chennai, India; [d]Department of Chemistry, S.V. Arts Degree & P.G. College (T.T.D'S), Tirupati, India

ABSTRACT

In the present work, experimental density (ρ) and speed of sound (u) data for the binary mixtures of benzyl alcohol with acetic acid, propionic acid, and n-butyric acid have been reported over the complete range of mole fraction at 298.15 K ≤ T ≤ 313.15 K. Excess volumes (V^E), excess isentropic compressibilities (κ_s^E), excess partial molar volumes ($\overline{V_i}^E$), and excess partial molar volumes at infinite dilution ($\overline{V_i}^{E,\infty}$) have been computed from the experimental data. The excess thermodynamic properties are found to be negative over the entire range of composition at the investigated temperatures. The temperature dependence of the excess thermodynamic properties has been investigated. All the excess functions are correlated with the Redlich-Kister equation. Further, attenuated total reflection Fourier transform infrared (ATR-FTIR) spectra for the studied binary solutions have been recorded at the equimolar composition to evaluate the extent of cross-association between component molecules through intermolecular hydrogen bonding.

1. Introduction

The sound knowledge on structure-property relationships of binary liquid mixtures through accurate density (ρ) and speed of sound (u) measurements as a function of composition has relevance in industrial, chemical engineering and technological processes not only in development of efficient separation processes, transport equipment but also in the design of engineering calculations involving chemical purification, heat transfer, mass transfer, fluid flow, etc. [1–3]. The study on excess thermodynamic properties of mixed solvents is one of the excellent methods to understand the intermolecular forces qualitatively and quantitatively and also the geometrical effects existing between the components with different molecular sizes, shapes and chemical nature [4,5]. Further, the understanding of thermo-physical (ρ and u) and thermodynamic properties (V^E and κ_s^E) is indispensable in the development of thermodynamic models, namely, group contribution methods, reliable correlations and to test the existing solution theories [6,7]. The investigation on excess thermodynamic properties of binary solutions also contributes a huge data to thermodynamic data bank [8].

The carboxylic acids (CA) are considered to be highly polar protic solvents as indicated by their high dipole moments. The strongly polarised hydroxyl group (-O-H) and carbonyl group

---
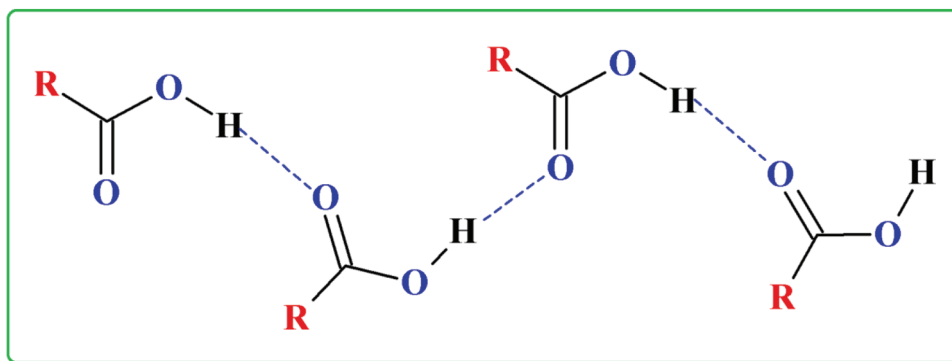
Figure 1. Self-association of carboxylic acids through hydrogen bonding.

(>C = O) of carboxylic acid functions as hydrogen-bond donors and hydrogen-bond acceptors respectively. In their pure state, they show a high degree of self-association through hydrogen bonding and predominantly exist as a chain structure [9] as depicted in Figure 1. The hydrogen bonding interactions appear to play a more dominant role in strong self-association of carboxylic acids and hydrophobic interactions also have increasing roles in self-association with longer alkyl chain carboxylic acids [10]. Carboxylic acids are one of the versatile classes of raw materials used in a wide range of industrial applications such as manufacture of rubber, pharmaceuticals, biodegradable plastics, and in separation processes. They find applications as natural colourants, acidulants, food preservatives, flavouring agents, fungicides, insecticides, cleaning agents, buffers, etc. [11–13]. Likewise, they serve as catalysts in the synthesis of biodiesel. Acetic and propionic acids are used in the feed industry to control mould growth. Due to the unpleasant odour, butyric acid is found to use as a fishing bait additive.

Benzyl alcohol (Bn-OH) is a polar protic primary alcohol in which the hydroxyl group (-O-H) serves as both hydrogen-bond donor and acceptor. In the native state, it is strongly self-associated through intermolecular hydrogen bonding [14,15]. Bn-OH is widely used as a solvent due to its favourable properties like low toxicity, good polarity, and low vapour pressure. It is primarily used as a solvent for paints, inks, gelatin, epoxy resin coatings, lacquers, shellac, cellulose acetate [15,16]. It serves as an embedding material in microscopy, as a preservative in cosmetics and medications, as an antimicrobial agent in the pharmaceutical industry [17,18]. It is a well-known precursor to several esters, used in the manufacture of soaps, skin lotions, perfumes, topical creams, shampoos, and flavour industries. It is also utilised as a local anaesthetic, insect repellent, degreaser and as flavour enhancer in e-cigarettes.

The favourable properties and diversified applications of the carboxylic acids (CA) and benzyl alcohol (Bn-OH) in several industries have motivated to elucidate the nature and extent of intermolecular interactions through volumetric, acoustic studies in the binary mixtures of Bn-OH with (C_2-C_4) carboxylic acids at different temperatures. For the effective utilisation and also to explore new industrial applications of the investigated solvents, it is essential to have sound knowledge of their physicochemical and thermodynamic properties. The proper understanding of the information about chemical structures and molecular inter-action changes occurring on mixing the molecular solvents is necessary as it provides an opportunity for the design and development of new processes and equipment [19]. Moreover, the excess property measurements in highly non-ideal binary systems containing carboxylic acids assist in understanding the hydrophobic and hydrogen bonding interactions between the components of the mixtures. Further, the present study aims at investigating the influence of alkyl chain length of carboxylic acids, temperature and composition on excess thermodynamic

properties (V^E, $\kappa_s^{\,E}$, $\overline{V}_i^{\,E}$ and $\overline{V}_i^{\,E,\infty}$) of binary solutions to establish the relationship between thermodynamic properties and the molecular structures of components.

Many researchers have reported the thermodynamic properties for the binary mixtures of benzyl alcohol with (C_1–C_4) 1-alkanols [20], (C_5–C_{10}) 1-alkanols [21,22], 2-propanol [23], isomeric butanols [7], alkoxyalkanols [24], isomeric cresols [25], poly(propylene glycol) [26], chloroalkanes [27], isomeric chlorobenzenes [28], monocyclic aromatics [14], isomeric chloro and nitrotoluenes [29], N,N-dimethylacetamide [30], N,N-dimethylformamide [31], dimethylsulfoxide [32], (C_2-C_4) alkylacetates [15], ethylchloroacetate [33], vinyl acetate [34], t-butyl acetate [34], benzyl acetate [16], and 1,2-butanediol [35]. A comprehensive survey of the literature shows that no systematic data is currently available on the thermo-physical and excess thermodynamic properties for the binary solutions studied.

In the present study, experimental measurements on densities (ρ) and speeds of sound (u), excess volumes (V^E), excess isentropic compressibilities ($\kappa_s^{\,E}$), excess partial molar volumes ($\overline{V}_i^{\,E}$) and excess partial molar volumes at infinite dilution ($\overline{V}_i^{\,E,\infty}$) over the whole range of concentration for the binary solutions of Bn-OH and (C_2-C_4) homologous series of carboxylic acids at 298.15 K ≤ T ≤ 313.15 K, every 5 K, and atmospheric pressure have been reported. Further, attenuated total reflection-Fourier transform infrared (ATR-FTIR) spectra for the studied pure liquids and their equimolar binary mixtures have been recorded at room temperature to interpret the strength of the hydrogen bonding interactions between Bn-OH and CA molecules in the mixed systems. The experimental results emanating from this work have been discussed in terms of cross-association through hydrogen bonding and packing effects between Bn-OH and carboxylic acids.

2. Experimental

2.1. Materials

Benzyl alcohol (Bn-OH, Merck, purity ≥ 99.5%), acetic acid (AA, Merck, purity ≥ 99.8%), propionic acid (PA, Sigma-Aldrich, purity ≥ 99.5%) and n-butyric acid (n-BA, SRL, purity ≥ 99.5%) of analytical reagent grade were purchased and used in the sample preparation without further purification. The description of the chemicals used in this work including the percentage of water content was presented in Table 1. Before the experimental measurements, the chemicals were degassed ultrasonically and dried over freshly activated 4A° molecular sieves for about 48 h. To assess the purity of the liquid components, their experimental densities (ρ) and speeds of sound (u) were compared with the corresponding literature values [7,13,16,34–40] at 298.15 K ≤ T ≤ 313.15 K and are shown in Table 2. The experimental ρ and u values for pure chemicals are found to be in the best accordance with the published values.

Table 1. Description of chemicals used in the study.

Name of the chemical	CAS No	Molar mass (g·mol^{-1})	Source	Mass fraction purity by GC*	Water content by KF (%)
Benzyl alcohol	100–51–6	108.14	Merck, India	≥ 0.995	≤ 0.1
Acetic acid	64–19-7	60.05	Merck, India	≥ 0.998	≤ 0.2
Propionic acid	79–09-4	74.08	Sigma-Aldrich, India	≥ 0.995	≤ 0.2
n-Butyric acid	107–92–6	88.11	SRL, India	≥ 0.995	≤ 0.1

*The purity is reported by supplier.

Table 2. Experimental density (ρ) and speed of sound (u) values of the pure liquid compounds and their corresponding literature values from T/K = 298.15 to 313.15 at 0.1 MPa pressure.

Liquid	T (K)	ρ(g.cm^{-3})		u (m.s^{-1})	
		Exp.	Lit	Exp.	Lit
Benzyl alcohol (Bn-OH)	298.15	1.041271	1.041216[a] 1.04138[b] 1.04134 [c]	1525.21	1525.17[a]
	303.15	1.037374	1.037352[a] 1.03750[b] 1.03745 [c]	1509.59	1509.34[a]
	308.15	1.033481	1.033474[a] 1.03363[b]	1493.71	1493.62[a]
	313.15	1.029586	1.029583[a] 1.02961[b] 1.02971 [c]	1478.09	1478.03[a]
Acetic acid (AA)	298.15	1.043931	1.04413[d] 1.0427[e]	1134.19	1135.7[d]
	303.15	1.038262	1.03848[d] 1.0371[e] 1.03844 [f]	1117.41	1118.4[d] 1117.5 [f]
	308.15	1.032623	1.03283[d] 1.0314[e] 1.03261 [f]	1100.62	1101.2[d] 1102.4 [f]
	313.15	1.026981	1.02718[d] 1.0258[e] 1.02704 [f]	1083.43	1084.0[d] 1084.4 [f]
Propanoic acid (PA)	298.15	0.988111	0.98794[d] 0.9882[e] 0.98848 [g]	1146.51	1146.0[d] 1146.7 [g]
	303.15	0.982809	0.98254[d] 0.9829[e] 0.98307 [g]	1127.39	1127.1[d] 1127.7 [g]
	308.15	0.977468	0.97714[d] 0.9774[e] 0.97767 [g]	1108.61	1108.3[d] 1108.9 [g]
	313.15	0.972122	0.97175[d] 0.9721[e] 0.97227 [g]	1089.78	1089.6[d] 1090.2 [g]
n-Butyric acid (n-BA)	298.15	0.952791	0.95281 [h] 0.95282[i]	1176.68	1176.9 [h]
	303.15	0.947892	0.94794 [h] 0.94784[i] 0.94789 [f]	1158.09	1158.2 [h] 1159.0 [f]
	308.15	0.942904	0.94292 [h] 0.94288[i] 0.94319 [f]	1139.41	1139.7 [h] 1140.1 [f]
	313.15	0.937966	0.93805 [h] 0.93791[i] 0.93856 [f]	1121.08	1121.3 [h] 1122.0 [f]

[a]Ref [7,35]. [b]Ref [34]. [c]Ref [16]. [d]Ref [36]. [e]Ref 37. [f]Ref [38]. [g]Ref [39].[h]Ref [40]. [i]Ref [13].
Standard uncertainties are $u(\rho)$ = 5x10^{-5} g.cm^{-3}, $u(u)$ = 0.5 m.s^{-1},and u (T) = 0.01 K.

2.2. Methods

2.2.1. Sample preparation

The homogeneous binary mixtures of Bn-OH with (C$_2$-C$_4$) carboxylic acids were prepared gravimetrically covering the complete range of mole fraction from 0.1 to 0.9 in a clean, airtight screw-capped glass vial. The mass of liquids is measured by using a digital electronic balance (Sartorius CPA225D) with an accuracy of $\pm 1 \times 10^{-5}$ g. Density and speed of sound measurements were carried immediately on the same day of sample preparation to avoid loss due to evaporation. Considering the mass of each component, the uncertainty in the mole fraction $u(x_1)$ of mixtures was estimated to be less than $\pm 5 \times 10^{-5}$.

2.2.2. Density and speed of sound measurements

The densities (ρ) and speeds of sound (u) of pure Bn-OH and its mixtures with (C_2-C_4) carboxylic acids were automatically measured at T = (298.15–313.15) K with a temperature step of 5 K and at 0.1 MPa pressure using vibrating U-tube digital density and sound velocity metre (Anton-Paar DSA 5000 M). The temperature of the sample in the density and sound velocity cells of the apparatus is controlled by a built-in Peltier thermostat with stability of ± 0.01 K. It measures the period of oscillation of a vibrating U-shaped tube filled with a sample, which is directly related to density (ρ) of the sample. The speed of sound (u) of a liquid sample is determined using a time propagation technique, in which the sample is sandwiched between two piezoelectric ultrasound transducers. One transducer emits sound waves through the sample at a frequency of 3 MHz and a second transducer receives those waves. The ratio of the known distance between the transmitter and receiver with the measured propagation time of the sound wave results in the speed of sound [41]. Prior to carrying out the measurements, the calibration of the instrument was done with dry air, Millipore quality water as standards at atmospheric pressure. The uncertainty in the measurement of density (ρ) and speed of sound (u) values is found to be ± 5 × 10^{-5} g.cm^{-3} and ± 0.5 m.s^{-1} respectively.

2.2.3. Infrared measurements

Fourier-transform infrared (FTIR) spectra of the pure components and the equimolar binary mixtures of benzyl alcohol with (C_2-C_4) carboxylic acids were recorded using Alpha-ATR-FTIR spectrometer (Bruker, Germany). ATR-FTIR interferometer containing a single-point reflection sampling module was equipped with ZnSe crystal onto which a drop of the homogeneous sample has been placed to record the spectra at room temperature in the region 4000 − 600 cm^{-1} with 4.0 cm^{-1} spectral resolution.

3. Results and discussion

3.1. Densities and excess volumes (V^E)

Densities (ρ) are measured for the binary mixtures Bn-OH with (C_2-C_4) carboxylic acids over the entire concentration range at T = (298.15 to 313.15) K, with a temperature step of 5 K to understand the extent of intermolecular interactions. The experimental ρ values are listed in Table 3. At a fixed temperature, the densities (ρ) of the investigated binary systems increase with an increase in the concentration of Bn-OH (x_1) except for the (Bn-OH + AA) system as Bn-OH is much denser than carboxylic acids. The increase in ρ values with an increase in x_1 is due to the strengthening of Bn-OH and carboxylic acid interactions. From Table 3, it is observed that the ρ values of (Bn-OH + AA) increases, reaches a maximum at x_1 = 0.3750 and then decreases continuously. This suggests that the specific interactions between Bn-OH and AA are relatively stronger between $0.25 \leq x_1 \leq 0.45$ than that in acetic acid-rich and benzyl alcohol-rich regions. A similar type of behaviour has been observed in the binary solutions of acetic acid with water [42–44] and 1-butyl-3-methylimidazolium thiocyanate ionic liquid [45]. Further, at constant x_1, ρ values of the investigated systems decrease with an increase in the temperature. This might be due to an increase in the translational energy of the molecules with temperature, which increases the molecular agitations, leading to a decrease in intermolecular interactions in the mixed solutions.

The excess volumes (V^E) were evaluated for the three investigated mixtures containing Bn-OH and (C_2-C_4) carboxylic acids according to the equation:

$$V^E = \frac{x_1 M_1 + x_2 M_2}{\rho} - \left[\frac{x_1 M_1}{\rho_1} + \frac{x_2 M_2}{\rho_2} \right] \tag{1}$$

where M_1 and M_2, x_1 and x_2, ρ_1 and ρ_2 represent the molar mass, mole fraction, and density of Bn-OH and (C_2-C_4) carboxylic acids respectively, ρ_m represents the density of the binary mixture.

Table 3. Experimental values of densities (ρ/g.cm^{-3}) and excess volumes (V^E/cm^3.mol^{-1}) as a function of mole fraction of Bn-OH (x_1), for the binary solutions of Bn-OH with AA, PA and n-BA from T/K = 298.15 to 313.15 and 101.3kPa pressure.

x_1	ρ/gcm^{-3}				V^E/cm^3.mol^{-1}			
	T/K = 298.15	303.15	308.15	313.15	T/K = 298.15	303.15	308.15	313.15
0.0000	1.04393	1.03826	1.03262	1.02698	0.000	0.000	0.000	0.000
0.1283	1.04558	1.04034	1.03512	1.02989	−0.134	−0.139	−0.143	−0.148
0.2455	1.04623	1.04130	1.03638	1.03146	−0.216	−0.224	−0.231	−0.239
0.3750	1.04625	1.04159	1.03694	1.03228	−0.265	−0.273	−0.282	−0.290
0.4435	1.04602	1.04149	1.03696	1.03243	−0.273	−0.282	−0.291	−0.300
0.5293	1.04552	1.04113	1.03675	1.03236	−0.265	−0.274	−0.283	−0.293
0.6243	1.04485	1.04058	1.03632	1.03206	−0.241	−0.249	−0.257	−0.266
0.7300	1.04393	1.03978	1.03565	1.03152	−0.193	−0.199	−0.206	−0.213
0.8329	1.04294	1.03890	1.03487	1.03084	−0.129	−0.133	−0.138	−0.143
0.9132	1.04213	1.03817	1.03422	1.03026	−0.069	−0.073	−0.076	−0.079
1.0000	1.04127	1.03737	1.03348	1.02959	0.000	0.000	0.000	0.000
0.0000	0.98811	0.98281	0.97747	0.97212	0.000	0.000	0.000	0.000
0.1052	0.99909	0.99401	0.98890	0.98377	−0.276	−0.282	−0.288	−0.293
0.2023	1.00776	1.00283	0.99791	0.99297	−0.467	−0.474	−0.484	−0.493
0.3067	1.01559	1.01087	1.00612	1.00137	−0.601	−0.612	−0.623	−0.636
0.3999	1.02136	1.01685	1.01227	1.00769	−0.655	−0.673	−0.687	−0.701
0.4587	1.02453	1.02010	1.01561	1.01112	−0.664	−0.682	−0.696	−0.711
0.5620	1.02921	1.02492	1.02062	1.01629	−0.627	−0.645	−0.662	−0.678
0.6612	1.03286	1.02868	1.02449	1.02030	−0.541	−0.556	−0.571	−0.587
0.7790	1.03633	1.03227	1.02821	1.02414	−0.385	−0.396	−0.408	−0.420
0.9056	1.03933	1.03537	1.03142	1.02747	−0.173	−0.179	−0.185	−0.191
1.0000	1.04127	1.03737	1.03348	1.02959	0.000	0.000	0.000	0.000
0.0000	0.95279	0.94789	0.94290	0.93797	0.000	0.000	0.000	0.000
0.1083	0.96552	0.96077	0.95594	0.95115	−0.204	−0.211	−0.217	−0.223
0.2101	0.97698	0.97236	0.96766	0.96301	−0.373	−0.383	−0.393	−0.404
0.3145	0.98795	0.98347	0.97895	0.97447	−0.494	−0.509	−0.526	−0.544
0.4116	0.99742	0.99311	0.98875	0.98441	−0.555	−0.578	−0.601	−0.623
0.5010	1.00551	1.00132	0.99708	0.99286	−0.568	−0.594	−0.620	−0.645
0.6128	1.01475	1.01070	1.00659	1.00249	−0.523	−0.550	−0.575	−0.601
0.7171	1.02258	1.01860	1.01459	1.01059	−0.424	−0.448	−0.471	−0.495
0.8238	1.02991	1.02600	1.02208	1.01816	−0.277	−0.295	−0.314	−0.333
0.9110	1.03561	1.03172	1.02783	1.02393	−0.141	−0.152	−0.163	−0.173
1.0000	1.04127	1.03737	1.03348	1.02959	0.000	0.000	0.000	0.000

The standard uncertainties are $u(x) = 5\times10^{-5}$, $u(\rho) = 5\times10^{-5}$ g.cm^{-3}, $u(T) = 0.01$ K, and u (V^E) = 0.005 cm^3.mol^{-1}

The excess thermodynamic properties could provide useful insights into the degree of non-ideality of a binary solution. Generally, the sign and magnitude of excess volumes of the mixed solutions depend on the relative strength of the following volume contraction and expansion factors [12,15,43]:

The factors that lead to volume contraction on mixing the components are:

(i) The predominance of strong specific interactions like charge-dipole, hydrogen bonds, dipole-dipole, dipole-induced dipole interactions, etc. between unlike components (chemical contribution).

(ii) Favourable geometrical fitting among the component molecules or accommodation of one component into others interstices (structural contribution).

The factors that lead to volume expansion on mixing the components are:

(i) Disruption of the molecular associates (chemical contribution).

(ii) Weak London dispersion forces between the components (physical contribution).

(iii) Steric hindrance caused by the structure of the component molecules.

(iv) Unfavourable geometrical fitting between the mixed components (structural contribution).

The excess volumes (V^E) against the mole fraction of Bn-OH (x_1) for the binary systems at T = (298.15 to 313.15) K, are plotted in Figure 2–4 and these values are listed in Table 3. A perusal of V^E data reveals that the property was negative for all the systems studied over the complete range of composition at the investigated temperatures. The magnitude of excess volumes (V^E) at a fixed temperature and composition varies in the following order:

$$Bn-OH + PA > Bn-OH + n-BA > Bn-OH + AA$$
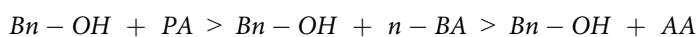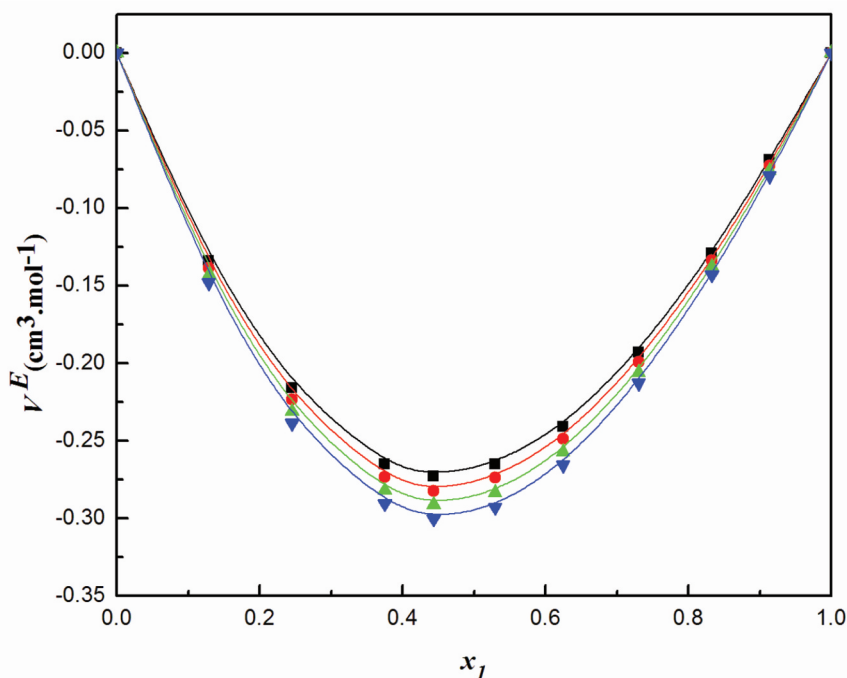
Figure 2. Plot of Excess volumes (V^E) vs. mole fraction (x_1) for Bn-OH (1) + AA (2) binary system at T = 298.15 K (■), 303.15 K (●), 308.15 K (▲) and 313.15 K (▼).

The negative V^E reveals that the specific interactions between Bn-OH and CA are stronger than between similar component molecules in their pure state. During mixing of Bn-OH with CA, the following volume contraction and expansion factors occur simultaneously: (a) disruption of associated structure of the pure benzyl alcohol through the breaking of hydrogen bonds, (b) rupture of hydrogen bonding interactions in self-associates of carboxylic acids, (c) formation of a cross hydrogen bond and new −H····π interaction between Bn-OH and carboxylic acids [20] and (d) interstitial accommodation (packing effect) of carboxylic acids in π····π and hydrogen-bonded and benzyl alcohol aggregates. The volume expansion factors (a) and (b) provide a positive contribution to V^E and the volume contraction factors (c) and (d) make a negative contribution to V^E. The actual V^E values for the studied systems are a consequence of the balance between the two volume expansion and contraction factors that occur due to mixing. The obtained negative excess volume (V^E) data points to the fact that the volume contraction factors (c) and (d) dominate over the volume expansion factors (a) and (b) in these systems at the investigated temperatures. Hence, the cross-association through H-bonding between -O-H group of Bn-OH and -O-H or >C = O group of carboxylic acids and the favourable packing effects due to significant differences in the free volume size, and molar volume between the components are the two factors that govern the molecular structures of studied systems.

The V^E data is found to be more negative for Bn-OH + PA system than Bn-OH + AA and Bn-OH + BA systems. The magnitude of V^E for the mixtures follows the same order as pK_a values of carboxylic acids which are 4.76, 4.87, and 4.82 for AA, PA, and n-BA respectively [46]. A similar trend in V^E values has been reported for the mixed solutions of carboxylic acids with methanol [47], acetonitrile [48] and acetophenone [49]. The dimerisation constant (K_d) of carboxylic acids tends to increase with an increase in the alkyl chain length of carboxylic acids. According to Lark et al. [50], the increased dimerisation constant of PA (K_d = 2.301 at T = 298.15 K) than that of AA (K_d = 1.982 at T = 298.15 K) could reduce the positive contribution to V^E, resulting in more negative V^E for Bn-
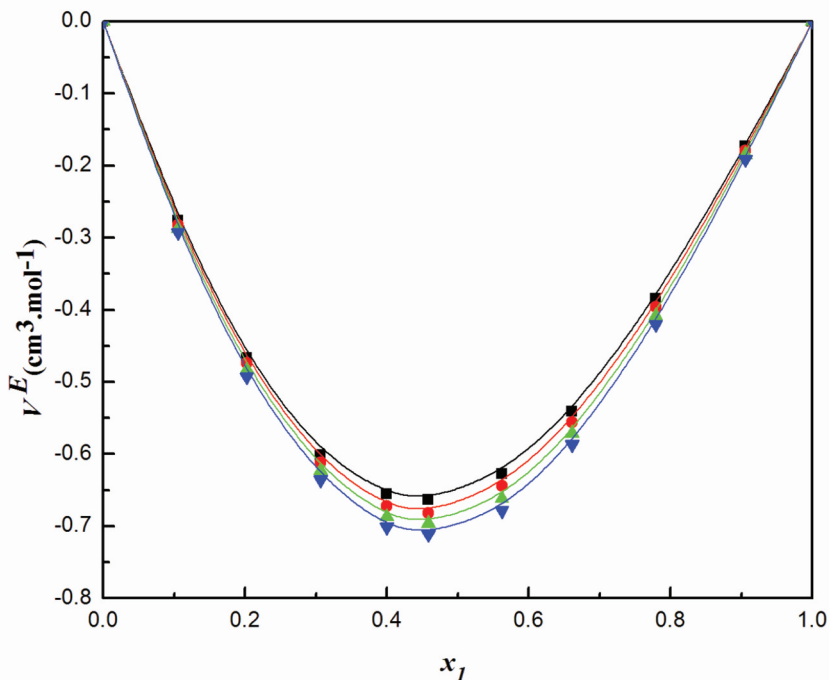
Figure 3. Plot of Excess volumes (V^E) *vs*. mole fraction (x_1) for Bn-OH (1) + PA (2) binary system at T = 298.15 K (■), 303.15 K (●), 308.15 K (▲) and 313.15 K (▼).

OH + PA. The more negative V^E for Bn-OH + PA than Bn-OH + AA is attributed to more positive inductive effect (+I) of the larger – C_2H_5 alkyl group in PA, which increases electron density on the oxygen atoms and consequently resulting in the formation of an energetically more favoured cross H-bonding between Bn-OH and PA. The stronger cross H-bonding in Bn-OH + PA is also evidenced by its FT-IR data. Similarly, one would expect the large negative V^E for Bn-OH + BA due to the larger +I-effect of its – C_3H_7 group. But, the V^E values for Bn-OH + BA system are found to be less negative than for the mixtures of BnOH + PA. In addition to the +I-effect of CA, their molecular geometry should be considered as well to correlate less negative V^E values for Bn-OH + n-BA. The larger – C_3H_7 group in BA makes it less planar and restricts the closer approach of Bn-OH [51], which sterically hinders the interaction of its – COOH group with O-H of Bn-OH and results in less negative V^E values than BnOH + PA. Hence, the observed trend in V^E for the studied systems suggests that the contribution to volume change from cross-association through H-bonding, geometrical effect and steric factor between components of the mixture are equally important.

As can be observed in Figure 2–4, the values of the V^E are more negative with the increase in temperature for all binary mixtures studied. With an increase in the temperature, kinetic energy increases and the interactions between the like molecules of the pure components might be decreased more than that of between unlike component molecules. Consequently, volume contraction increases leading to more negative V^E values. The more negative V^E data with an increase in temperature could also be understood as the enlargement of interstices and thereby more favourable interstitial accommodation between carboxylic acid and benzyl alcohol molecules. This leads to an increased contraction in volume resulting in more negative V^E values.
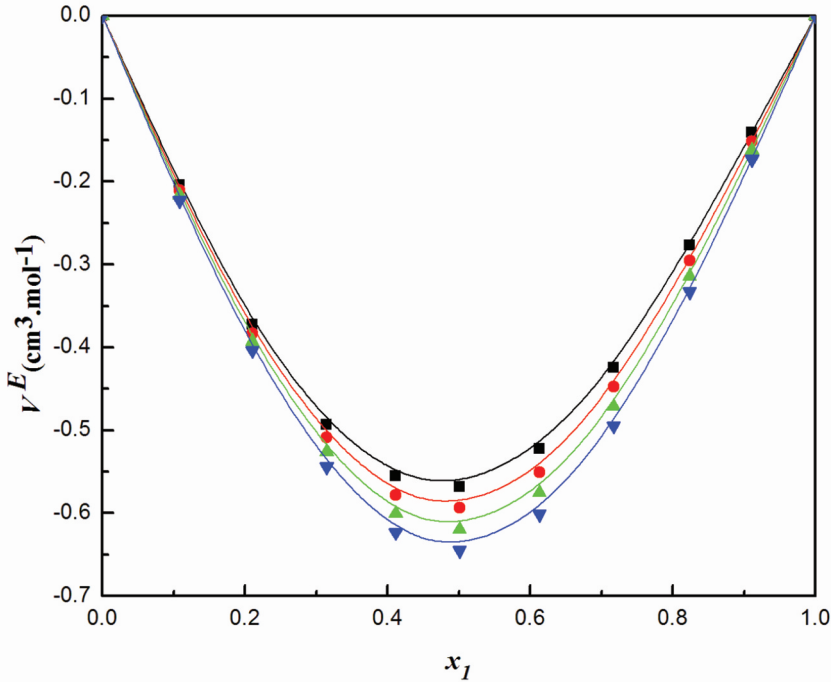
Figure 4. Plot of Excess volumes (V^E) *vs.* mole fraction (x_1) for Bn-OH (1) + n-BA (2) binary system at T = 298.15 K (■), 303.15 K (●), 308.15 K (▲) and 313.15 K (▼).

3.2. Excess isentropic compressibilities (κ_s^E)

The speeds of sound (u) measurements and evaluation of excess isentropic compressibilities (κ_s^E) provide useful insights into the molecular compactness and intermolecular interactions between the components of the mixed solutions. The sign and magnitude of excess isentropic compressibilities (κ_s^E) are reliant on the nature and extent of the intermolecular forces which in turn depend on the size and molecular geometry of the component molecules of the binary solutions. The speeds of sound (u) for the binary systems of Bn-OH with (C_2-C_4) carboxylic acids over the entire range of concentration at T = (298.15 to 313.15) K are incorporated in Table 4. It is clear that values of u increase with an increase in mole fraction of Bn-OH and decrease with an increase in temperature from 298.15 to 313.15 K.

The isentropic compressibilities (κ_s) are calculated from density (ρ) and speed of sound (u) data by using the Laplace-Newton's equation:

$$\kappa_s = \frac{1}{u^2\rho} \quad (2)$$

The excess isentropic compressibilities (κ_s^E) are computed for the mixtures containing Bn-OH and (C_2-C_4) carboxylic acids by using the relation:

$$\kappa_s^E = \kappa_s - \kappa_s^i d \quad (3)$$

where, κ_s^{id} represents the ideal isentropic compressibility.

The ideal isentropic compressibilities (κ_s^{id}) were evaluated from the expression suggested by Benson and Kiyohara [52]:

Table 4. Mole fraction of Bn-OH (x_1), speeds of sound ($u/m.s^{-1}$), isentropic compressibilities ($\kappa_S/T.Pa^{-1}$) for Bn-OH + AA/PA/n-BA mixtures at 298.15 ≤ T/K ≤ 313.15 and 0.1 MPa pressure.

x_1	$u/m.s^{-1}$	$\kappa_S/T.Pa^{-1}$	$\kappa_S^E/T.Pa^{-1}$	x_1	$u/m.s^{-1}$	$\kappa_S/T.Pa^{-1}$	$\kappa_S^E/T.Pa^{-1}$
Bn-OH (1) + AA (2)							
T/K = 298.15				T/K = 303.15			
0.0000	1134.2	744.7	0.0	0.0000	1117.4	771.4	0.0
0.1283	1204.5	659.2	−18.4	0.1283	1188.5	680.5	−20.5
0.2455	1265.6	596.7	−28.8	0.2455	1249.4	615.2	−31.2
0.3750	1327.9	542.0	−34.0	0.3750	1311.3	558.4	−36.0
0.4435	1357.2	519.0	−33.6	0.4435	1340.6	534.2	−35.7
0.5293	1391.8	493.8	−32.0	0.5293	1375.1	507.9	−33.7
0.6243	1425.5	471.0	−27.7	0.6243	1408.9	484.2	−29.1
0.7300	1458.1	450.6	−20.9	0.7300	1441.7	462.7	−21.9
0.8329	1485.6	434.5	−13.0	0.8329	1469.5	445.7	−13.6
0.9132	1505.1	423.6	−6.5	0.9132	1489.3	434.3	−6.9
1.0000	1525.2	412.8	0.0	1.0000	1509.6	423.0	0.0
T/K = 308.15				T/K = 313.15			
0.0000	1100.6	799.4	0.0	0.0000	1083.4	829.5	0.0
0.1283	1172.4	702.8	−22.6	0.1283	1156.2	726.4	−25.2
0.2455	1233.3	634.4	−33.7	0.2455	1217.3	654.2	−37.0
0.3750	1294.6	575.4	−38.1	0.3750	1277.9	593.2	−40.6
0.4435	1324.1	550.1	−37.7	0.4435	1307.6	566.5	−40.2
0.5293	1358.4	522.8	−35.4	0.5293	1341.1	538.6	−37.0
0.6243	1391.9	498.1	−30.3	0.6243	1374.8	512.6	−31.5
0.7300	1425.2	475.4	−22.9	0.7300	1408.5	488.6	−23.9
0.8329	1453.4	457.4	−14.4	0.8329	1437.4	469.5	−15.2
0.9132	1473.6	445.3	−7.5	0.9132	1457.9	456.7	−8.0
1.0000	1493.7	433.7	0.0	1.0000	1478.1	444.6	0.0
Bn-OH (1) + PA (2)							
T/K = 298.15				T/K = 303.15			
0.0000	1146.5	769.9	0.0	0.0000	1127.4	800.5	0.0
0.1052	1199.6	695.5	−26.8	0.1052	1181.5	720.7	−29.5
0.2023	1244.6	640.6	−40.3	0.2023	1227.2	662.1	−44.3
0.3067	1289.6	592.1	−46.8	0.3067	1272.4	611.0	−50.9
0.3999	1326.9	556.1	−47.3	0.3999	1310.1	573.0	−51.5
0.4587	1349.4	536.1	−45.9	0.4587	1332.6	552.0	−49.8
0.5620	1387.8	504.5	−41.4	0.5620	1371.1	519.0	−44.6
0.6612	1422.8	478.3	−34.8	0.6612	1406.5	491.4	−37.6
0.7790	1462.8	451.0	−25.3	0.7790	1446.8	462.8	−27.3
0.9056	1501.6	426.7	−12.4	0.9056	1485.9	437.4	−13.3
1.0000	1525.2	412.8	0.0	1.0000	1509.6	423.0	0.0
T/K = 308.15				T/K = 313.15			

(Continued)

Table 4. (Continued).

x1				x1			
0.0000	1108.6	832.4	0.0	0.0000	1089.8	866.2	0.0
0.1052	1163.4	747.1	-32.1	0.1052	1145.3	775.0	-34.9
0.2023	1209.8	684.7	-48.3	0.2023	1192.3	708.4	-52.6
0.3067	1255.2	630.8	-55.2	0.3067	1238.1	651.5	-59.9
0.3999	1293.2	590.7	-55.7	0.3999	1276.4	609.1	-60.5
0.4587	1315.8	568.7	-53.8	0.4587	1299.0	586.1	-58.2
0.5620	1354.4	534.2	-48.1	0.5620	1337.7	549.9	-51.7
0.6612	1390.2	505.1	-40.5	0.6612	1373.7	519.4	-43.5
0.7790	1430.7	475.1	-29.4	0.7790	1414.7	487.9	-31.6
0.9056	1470.2	448.5	-14.5	0.9056	1454.5	460.0	-15.5
1.0000	1493.7	433.7	0.0	1.0000	1478.1	444.6	0.0

Bn-OH (1) + n-BA (2)

T/K = 298.15				T/K = 303.15			
0.0000	1176.7	758.0	0.0	0.0000	1158.1	786.6	0.0
0.1083	1215.6	700.9	-18.2	0.1083	1197.8	725.5	-20.0
0.2101	1252.3	652.7	-30.0	0.2101	1234.9	674.4	-32.7
0.3145	1289.8	608.4	-37.2	0.3145	1272.4	628.0	-40.1
0.4116	1324.4	571.6	-40.0	0.4116	1307.0	589.4	-42.9
0.5010	1355.5	541.3	-39.2	0.5010	1338.5	557.4	-42.1
0.6128	1394.4	506.8	-35.2	0.6128	1377.2	521.7	-37.4
0.7171	1430.2	478.1	-28.6	0.7171	1413.1	491.7	-30.2
0.8238	1466.4	451.6	-19.4	0.8238	1449.8	463.7	-20.4
0.9110	1495.3	431.9	-10.1	0.9110	1479.2	443.0	-10.7
1.0000	1525.2	412.8	0.0	1.0000	1509.6	423.0	0.0

T/K = 308.15				T/K = 313.15			
0.0000	1139.4	816.9	0.0	0.0000	1121.1	848.3	0.0
0.1083	1179.9	751.4	-22.1	0.1083	1162.0	778.6	-24.0
0.2101	1217.4	697.3	-35.8	0.2101	1199.7	721.5	-38.4
0.3145	1254.8	648.8	-43.3	0.3145	1237.4	670.2	-46.5
0.4116	1289.5	608.2	-46.0	0.4116	1272.1	627.8	-49.1
0.5010	1321.2	574.5	-45.2	0.5010	1304.0	592.3	-48.2
0.6128	1360.0	537.1	-39.9	0.6128	1342.9	553.2	-42.4
0.7171	1396.1	505.7	-32.1	0.7171	1379.3	520.2	-34.1
0.8238	1433.2	476.4	-21.7	0.8238	1416.6	489.4	-23.0
0.9110	1463.3	454.4	-11.6	0.9110	1447.2	466.3	-12.3
1.0000	1493.7	433.7	0.0	1.0000	1478.1	444.6	0.0

The standard uncertainties are $u(x) = 5 \times 10^{-5}$, $u(u) = 0.5$ m.s^{-1}, and $u(T) = 0.01$ K

$$\kappa_s^{id} = \sum_{i=1}^{2} \emptyset_i \left[\kappa_{s.i} + \frac{TV_i(\alpha_i^2)}{C_{p.i}} \right] - \left\{ T \left(\sum_{i=1}^{2} x_i V_i \right) \left(\sum_{i=1}^{2} \emptyset_i \alpha_i \right)^2 \Big/ \sum_{i=1}^{2} x_i C_{p.i} \right\} \qquad (4)$$

The φ_i, V_i, x_i, $\kappa_{s,i}$, α_i and $C_{p,i}$ represents the volume fraction, molar volume, mole fraction, isentropic compressibility, thermal expansion coefficient, and molar heat capacity of ith component respectively. The $C_{p,i}$ values for the pure liquids are collected from the literature [12,15,40] and α_i values for the pure components are calculated from the experimental density (ρ) data according to the relation:

$$\alpha_i = \left(\frac{1}{V} \right) \left(\frac{\partial V}{\partial T} \right)_P = - \left(\frac{1}{\rho} \right) \left(\frac{\partial \rho}{\partial T} \right)_P = - \left(\frac{\partial \ln \rho}{\partial T} \right)_P \qquad (5)$$

The experimental κ_s and κ_s^E values for the binary systems over the complete range of concentration at T = (298.15 to 313.15) K are included in Table 4. The variation of κ_s^E as a function of x_1 for the investigated binary series is plotted in Figure 5–7. An examination of curves in Figure 5–7 reveals that κ_s^E data are negative from $x_1 = 0.1$ to 0.9 at 298.15 K $\leq$ T $\leq$ 313.15 K for the solutions of Bn-OH with (C$_2$-C$_4$) carboxylic acids. The trend in κ_s^E correlates with that of V^E for the investigated systems at four different temperatures. The negative κ_s^E data suggests that the studied binary mixtures might be less compressible than the corresponding ideal mixtures. This could be attributed to a favourable closer approach and stronger intermolecular interaction between the unlike components present in the mixed-species leading to a more compact structure. The negative κ_s^E values at a fixed temperature for the binary solutions fall in the following order:

$$Bn - OH + PA > Bn - OH + n - BA > Bn - OH + AA$$
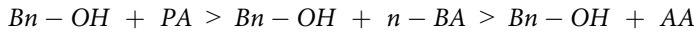
The negative κ_s^E values could be attributed to two factors namely (i) formation of cross H-bonding interactions between Bn-OH and (C$_2$-C$_4$) carboxylic acids and (ii) interstitial accommodation of carboxylic acids in hydrogen-bonded benzyl alcohol aggregates due to the considerable difference in their molecular sizes and molar volumes. The above order of κ_s^E data for the studied binary mixtures is a consequence of the balance between the factors (i) and (ii) that occurs due to the mixing of pure liquids. Hence, the trend in κ_s^E could be interpreted as the suitable combination of cross H-bond interactions and geometrical effect between unlike component molecules of the mixture. One would expect more negative κ_s^E for Bn-OH + AA mixture due to the largest differences in molar volumes between Bn-OH and AA but the strength of the specific interactions between the unlike components of the mixture are considered to be equally important. The cross H-bonding interactions are relatively weaker between Bn-OH and AA due to the lesser +I-effect of the smaller – CH$_3$ group in AA, resulting in less negative κ_s^E values for Bn-OH + AA.

The negative κ_s^E values increase with an increase in temperature because the decrease in intermolecular interactions between like molecules is more compared to those between dissimilar molecules [53]. In addition, an increase in temperature results in the enlargement of interstices, which in turn leads to more efficient packing between Bn-OH and (C$_2$-C$_4$) carboxylic acids. Hence, the binary solutions become more rigid and difficult to compress leading to more negative κ_s^E values.

3.3. Correlation of derived properties

The experimental V^E and κ_s^E of Bn-OH + (C$_2$-C$_4$) carboxylic acids at 298.15 K $\leq$ T $\leq$ 313.15 K, are correlated with mole fraction, using the Redlich-Kister (R-K) polynomial equation [54]:

$$Y^E = x_1 x_2 \sum_{i=0}^{n} A_i (2x_1 - 1)^i \qquad (6)$$

where $Y^E = V^E or \kappa_s^E$; x_1 is the mole fraction of pure benzyl alcohol.

The adjustable parameters A_0, A_1, and A_2 of each excess function are computed by the procedure of least-squares. The correlation parameters are included in Table 5 along with the standard deviations $\sigma(Y^E)$. These deviations for the investigated excess properties are determined by using the expression:

$$\sigma\left(Y^E\right) = \left[\frac{\sum\left(Y_{exp}^E - Y_{cal}^E\right)^2}{(m-n)}\right]^{\frac{1}{2}} \quad (7)$$

where m is the number of experimental measurements and n is the number of correlation parameters; Y_{cal}^E and Y_{exp}^E are the calculated and experimental values of excess functions respectively.

The low $\sigma(Y^E)$ values between the calculated and experimental values of excess parameters obtained at 298.15 K ≤ T ≤ 313.15 K for Bn-OH + CA indicate that the experimental V^E and κ_s^E data is consistent.

3.4. Excess partial molar volumes

The partial molar properties have often been used to get insights into the solute-solvent interactions that govern the binary mixture behaviour over the entire range of composition. The partial molar volumes of Bn-OH $(\overline{V_1})$ and (C₂-C₄) carboxylic acids $(\overline{V_2})$, in these mixtures over the complete range of composition were computed by using the following Equation [15, 55]:

$$\overline{V_1} = V^E + V_1^0 - x_2\left(\frac{\partial V^E}{\partial x_2}\right)_{T,P} \quad (8)$$

$$\overline{V_2} = V^E + V_2^0 + x_1\left(\frac{\partial V^E}{\partial x_2}\right)_{T,P} \quad (9)$$

where x_1, V_1^0 and x_2, V_2^0 represent the mole fractions and molar volumes of Bn-OH and (C₂-C₄) carboxylic acids respectively.
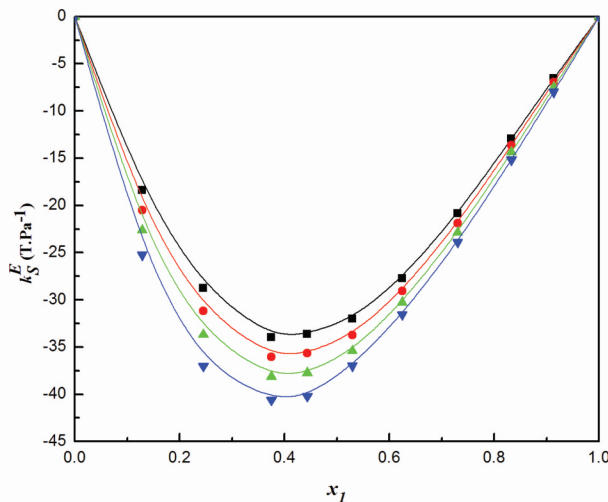
Figure 5. Excess isentropic compressibilities (κ_s^E) for Bn-OH (1) + AA (2) mixture against composition (x_1) at investigated temperatures: 298.15 K (■), 303.15 K (●), 308.15 K (▲) and 313.15 K (▼).
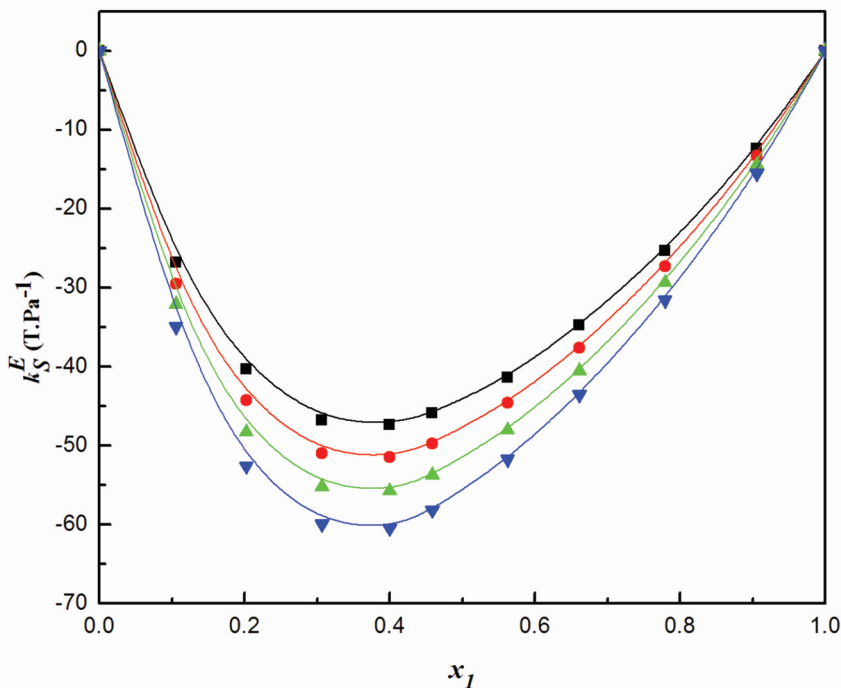
Figure 6. Excess isentropic compressibilities (κ_s^E) for Bn-OH (1) + PA (2) mixture against composition (x_1) at investigated temperatures: 298.15 K (■), 303.15 K (●), 308.15 K (▲) and 313.15 K (▼).

The $\left(\frac{\partial V^E}{\partial x_2}\right)$ term in Equation 8 and 9 is calculated by differentiating Equation 6, which leads to the following expressions for $\overline{V_1}$ and $\overline{V_2}$ respectively:

$$\overline{V_1} = V_1^0 + x_2^2 \sum_{i=0}^{n} A_i(1 - 2x_2)^i + 2(1 - x_2)x_2^2 \sum_{i=0}^{n} A_i(i)(1 - 2x_2)^{i-1} \tag{10}$$

$$\overline{V_2} = V_2^0 + (1 - x_2)^2 \sum_{i=0}^{n} A_i(1 - 2x_2)^i - 2(1 - x_2)x_2^2 \sum_{i=0}^{n} A_i(i)(1 - 2x_2)^{i-1} \tag{11}$$

To study the changes in the association patterns between components of the binary mixture, the excess partial molar volumes of Bn-OH ($\overline{V_1}^E$) and (C_2-C_4) carboxylic acids ($\overline{V_2}^E$), have been computed using the following Equation [56].:

$$\overline{V_1}^E = \overline{V_1} - V_1^0 \tag{12}$$

$$\overline{V_2}^E = \overline{V_2} - V_2^0 \tag{13}$$

The partial molar volumes at infinite dilution give some information about the solvent effect on the structure of the solute in the mixed solutions. The partial molar volumes of Bn-OH at infinite dilution in (C_2-C_4) carboxylic acids ($\overline{V_1}^\infty$) and C_2-C_4) carboxylic acids in Bn-OH ($\overline{V_2}^\infty$) have been evaluated with the help of the R-K coefficients by using the following expressions [56,57]:

$$\overline{V_1}^\infty = V_1^0 + \sum_{i=0}^{n} A_i(-1)^i \tag{14}$$
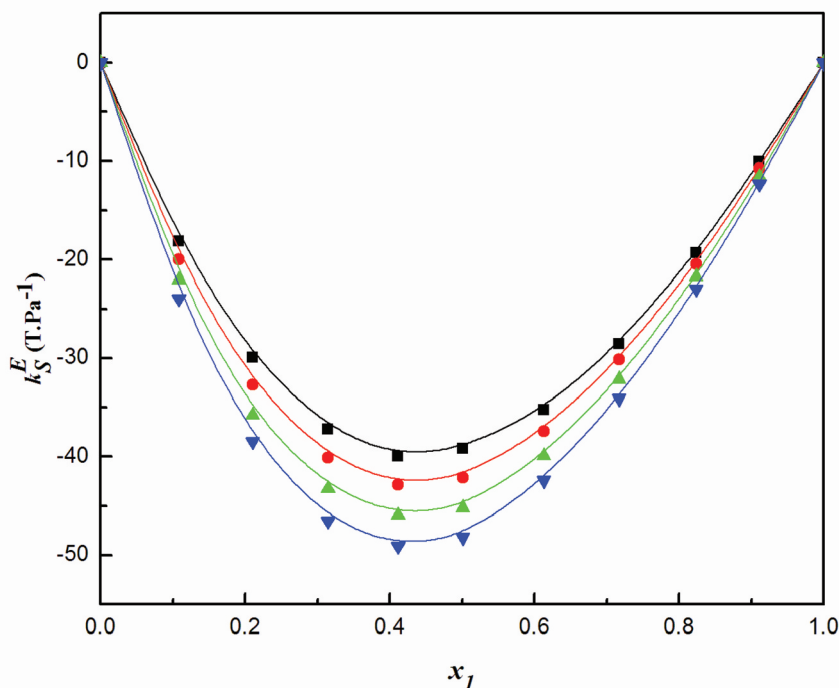
Figure 7. Excess isentropic compressibilities (κ_s^E) for Bn-OH (1) + n-BA (2) mixture against composition (x_1) at investigated temperatures: 298.15 K (■), 303.15 K (●), 308.15 K (▲) and 313.15 K (▼).

$$\bar{V}_2^\infty = V_2^0 + \sum_{i=0}^{n} A_i \tag{15}$$

In addition, the excess partial molar volumes of Bn-OH ($\bar{V}_1^{E,\infty}$) and (C$_2$-C$_4$) carboxylic acids ($\bar{V}_2^{E,\infty}$) at infinite dilution are evaluated with the following Eq

$$\bar{V}_1^{E,\infty} = \bar{V}_1^\infty - V_1^0 = \sum_{i=0}^{n} A_i(-1)^i \tag{16}$$

$$\bar{V}_2^{E,\infty} = \bar{V}_2^\infty - V_2^0 = \sum_{i=0}^{n} A_i \tag{17}$$

The values of $\bar{V}_1, \bar{V}_2$, $\bar{V}_1^E$ and $\bar{V}_2^E$ of Bn-OH+AA/PA/n-BA are collected in Table S1 in the supplementary material. The variation of $\bar{V}_1^E$ and $\bar{V}_2^E$ values with mole fraction (x_1) for the investigated systems at T = (298.15, 303.15, 308.15 and 313.15) K are presented in Figure 8–10. A kind perusal of Figure 8–10 indicates that $\bar{V}_1^E$ and $\bar{V}_2^E$ values are negative over complete concentration range for Bn-OH+AA/PA/n-BA systems at four investigated temperatures. This suggests that the partial molar volumes ($\bar{V}_i$) of each component in the binary solution were less than their corresponding pure molar volume (V_i^0).

The overall negative magnitude of $\bar{V}_i^E$ follows the order:
$$\bar{V}_i^E(\text{Bn-OH + PA}) > \bar{V}_i^E(\text{Bn-OH + n-BA}) > \bar{V}_i^E(\text{Bn-OH + AA})$$

The negative $\bar{V}_i^E$ values of each component in the mixture suggest that there is a contraction in volume on mixing Bn-OH + AA/PA/n-BA due to the presence of solute-solvent interactions

Table 5. The Redlich–Kister fitting parameters (A_0– A_2) and standard deviations $\sigma(Y^E_F)$ for excess functions obtained for Bn-OH (1) + carboxylic acids (2) at T/K = 298.15 to 313.15 and 0.1 MPa.

T(K)	Excess function	Redlich–Kister				Excess function	Redlich–Kister			
		A_0	A_1	A_2	$\sigma(Q^E_F)$		A_0	A_1	A_2	$\sigma(Q^E_F)$
Bn-OH (1) + acetic acid (2)										
298.15	V^E (cm^3.mol^{-1})	−1.081	0.200	0.057	0.0008	κ_S^E (TPa^{-1})	−131.5	51.41	9.540	0.1521
303.15		−1.116	0.204	0.048	0.0008		−138.5	60.41	1.101	0.1341
308.15		−1.152	0.207	0.039	0.0007		−145.4	68.79	−9.059	0.1315
313.15		−1.187	0.210	0.032	0.0009		−153.0	80.72	−21.85	0.1507
Bn-OH (1) + propionic acid (2)										
298.15	V^E (cm^3.mol^{-1})	−2.626	0.573	0.219	0.0012	κ_S^E (TPa^{-1})	−177.3	88.07	−59.49	0.1178
303.15		−2.693	0.562	0.227	0.0015		−192.0	99.15	−68.27	0.1447
308.15		−2.755	0.552	0.221	0.0014		−207.3	108.6	−76.43	0.1287
313.15		−2.818	0.540	0.222	0.0013		−223.9	120.0	−84.32	0.1237
Bn-OH (1) + n-butyric acid (2)										
298.15	V^E (cm^3.mol^{-1})	−2.279	0.222	0.530	0.0018	κ_S^E (TPa^{-1})	−157.7	39.18	0.134	0.1286
303.15		−2.378	0.173	0.537	0.0015		−168.5	46.54	−3.521	0.0939
308.15		−2.476	0.126	0.541	0.0010		−180.0	53.78	−10.97	0.1289
313.15		−2.576	0.080	0.547	0.0010		−191.7	60.57	−14.25	0.1291

between dissimilar molecules. The increase in $\overline{V_1^E}$ data at lower x_1 and decrease in $\overline{V_2^E}$ values at higher x_1 is clear evidence of disruption of the hydrogen-bonded Bn-OH and CA self associates respectively. The observed negative $\overline{V_i^E}$ data indicates of the dominance of cross H-bonding formation between Bn-OH and CA over the structure breaking effect between like molecules. The negative $\overline{V_1^E}$ and $\overline{V_2^E}$ are also equally attributed to the significant geometrical fitting between the component molecules in Bn-OH + AA/PA/n-BA. The reasons for the above observed trend in $\overline{V_i^E}$ and its variation with temperature were similar to those of V^E.

From Table S2 in supplementary material, it is evident that the partial properties at infinite dilution ($\overline{V_1^\infty}$ and $\overline{V_2^\infty}$) are lower than the respective pure molar volumes (V_1^0 and V_2^0) for all the investigated binary systems at each temperature. This emphasises that there is a contraction in volume due to better packing effect on mixing Bn-OH with AA/PA/n-BA. An examination of values in Table S2 also reveals that $\overline{V_1^{E,\infty}}$ and $\overline{V_2^{E,\infty}}$ for Bn-OH and CA respectively are negative at all investigated temperatures. This indicates that at infinite dilution, the intermolecular interactions between dissimilar molecules exceed the structure breaking effect between similar molecules i.e., the cross hydrogen bonding between Bn-OH and CA is not broken in dilute regions. In addition, the negative $\overline{V_1^E}$ and $\overline{V_2^E}$ are also equally attributed to the packing effect in Bn-OH + CA. The more negative $\overline{V_1^{E,\infty}}$ and $\overline{V_2^{E,\infty}}$ values for Bn-OH + PA is attributed to energetically more favoured solute-solvent interactions at infinite dilution. The values of $\overline{V_1^E}$ and $\overline{V_2^E}$ become more negative with the increase in temperature for each system investigated, which indicates a more favourable interstitial accommodation between component molecules due to the enlargement of interstices. These results further support the trends observed in V^E and κ_s^E data for the investigated binary systems.
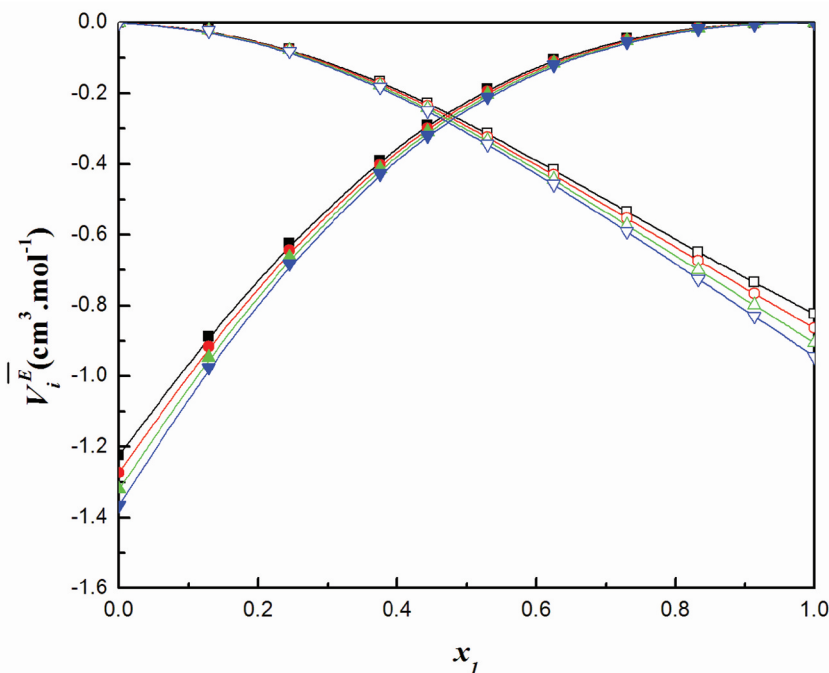
Figure 8. Plot of excess partial molar volumes of Bn-OH in AA ($\overline{V_1^E}$) and AA in Bn-OH ($\overline{V_2^E}$) at T = 298.15 K (■ and □), 303.15 K (● and ○), 308.15 K. (▲ and △), and 313.15 K (▼ and ▽) respectively.
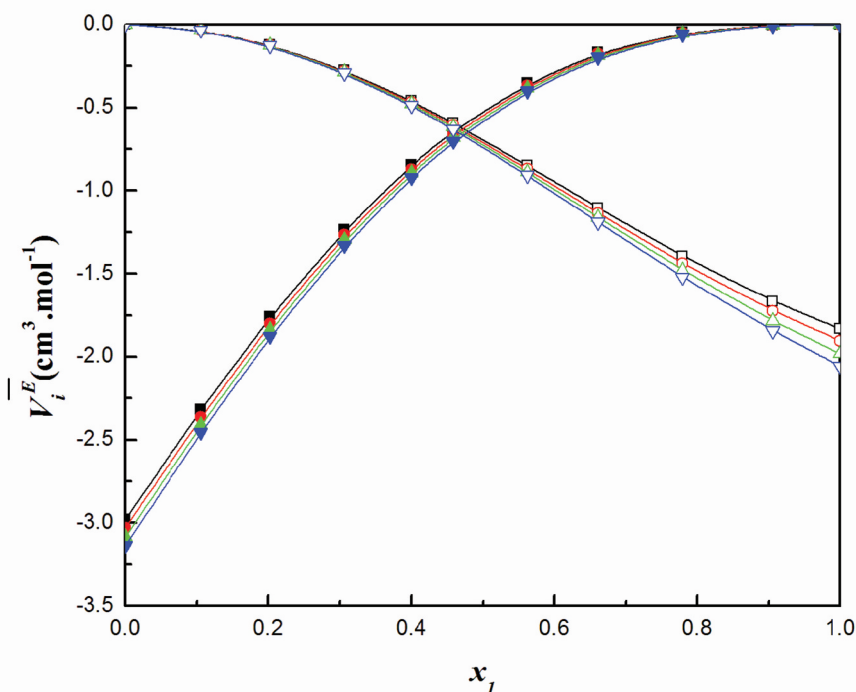
Figure 9. Plot of excess partial molar volumes of Bn-OH in PA ($\overline{V_1}^E$) and PA in Bn-OH ($\overline{V_2}^E$) at T = 298.15 K (■ and □), 303.15 K (● and ○), 308.15 K. (▲ and △), and 313.15 K (▼ and ▽) respectively.

3.5. ATR-FTIR investigations

Attenuated total reflection Fourier transform infrared (ATR-FTIR) spectroscopic technique is one of the powerful tools used to investigate the nature and extent of intermolecular interactions like hydrogen bonding between components in the mixtures by analysing the position, shape and, shifts of the FT-IR band [58]. In general, the H-bonding results in broadening and shifting of the X-H stretching band (X is highly electronegative than H) to lower frequencies (red shift). The existence of cross H-bonding and its strength in Bn-OH + AA/PA/n-BA could be identified by comparison of shift in the absorption band of hydroxyl group v(-O-H) of Bn-OH with the respective bands in their pure states.

In alcohols, the characteristic stretching frequency of free O–H group is observed around 3700–3650 cm^{-1} and H-bonded v(-O-H) shows a broad band around 3550–32,000 cm^{-1} [59]. The partial ATR-FTIR spectra of pure benzyl alcohol recorded at T = 298.15 K is shown in Figure 11, which shows that v(-O-H) absorption band appears at 3317.8 cm^{-1}.This broad -O-H band clearly indicates Bn-OH was self associated through intermolecular H-bonding. The -O-H stretching frequencies of pure AA, PA, and n-BA are in the order of 3018.6 cm^{-1}, 2983.9 cm^{-1}, and 2968.5 cm^{-1} respectively. ATR-FTIR spectra of equimolar binary solutions of Bn-OH with AA/PA/n-BA are recorded and the corresponding v(O-H) absorption bands of Bn-OH at x_1 = 0.5 are presented in Table 6 and Figure 11. The v(O-H) bands for the equimolar mixtures of Bn-OH + AA, Bn-OH + PA and Bn-OH + n-BA are found to be 3292.5 cm^{-1}, 3232.7 cm^{-1} and 3273.2 cm^{-1} respectively. The red shift (Δv) of -O-H stretching frequency of Bn-OH in AA/PA/n-BA is calculated and incorporated in Table 6. The red shift (Δv) of v(O-H) peak position of Bn-OH in equimolar mixtures of carboxylic acids fall in the order:
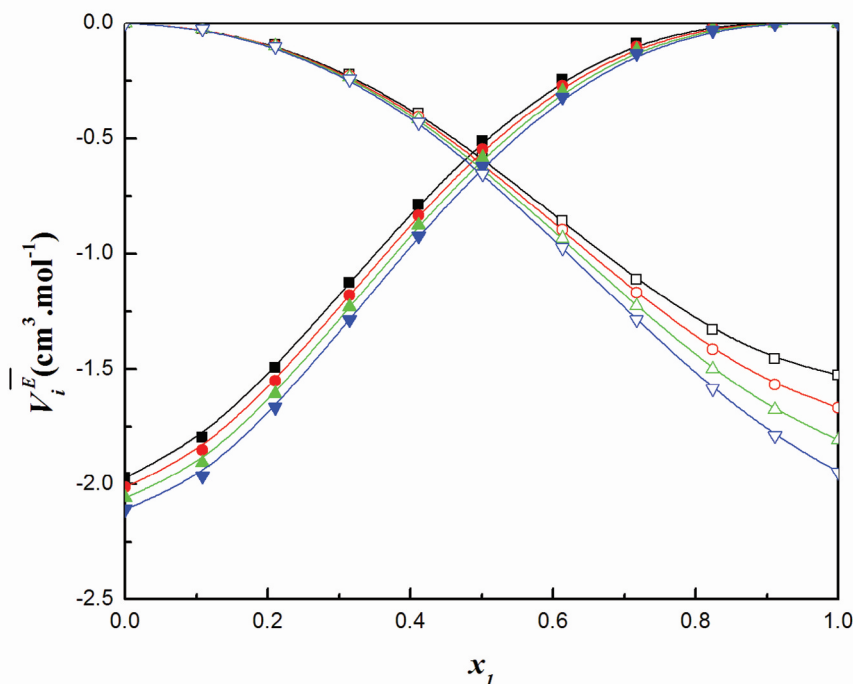
Figure 10. Plot of excess partial molar volumes of Bn-OH in n-BA ($\overline{V_1}^E$) and n-BA in Bn-OH ($\overline{V_2}^E$) at T = 298.15 K (■ and □), 303.15 K (● and ○), 308.15 K. (▲ and △), and 313.15 K (▼ and ▽) respectively.

Bn-OH + PA (-79.1 cm^{-1}) > Bn-OH + n-BA (-38.6 cm^{-1}) > Bn-OH + AA(-19.3 cm^{-1})

The red shift of v(O-H) absorption band appeared in the range of $3292.5 - 3273.2$ cm^{-1} for the three binary mixtures studied shows the existence of cross H-bonding between the hydroxyl group of Bn-OH and (C$_2$-C$_4$) carboxylic acids. It is well-known that the degree of red shift of v(O-H) band is a direct measure of the strength of intermolecular H-bond [58,59]. The larger red shift of v(O-H) absorption peak in Bn-OH + PA suggests that a stronger cross H-bonding exists between Bn-OH and PA system compared to those of Bn-OH + n-BA and Bn-OH + AA systems. Thus, the excess thermodynamic properties studied in the present investigation are supported by ATR-FTIR spectral analysis through the elucidation of cross H-bonding between Bn-OH and AA/PA/n-BA systems.

4. Conclusion

In this study, densities (ρ) and speeds of sound (u) have been measured for binary solutions of Bn-OH with (C$_2$-C$_4$) carboxylic acids for the whole concentration range at 298.15 K ≤ T ≤ 313.15 K under atmospheric pressure. The various excess properties (V^E, κ_s^E, $\overline{V_i}^E$, and $\overline{V_i}^{E,\infty}$) are evaluated from the experimental ρ and u results. The sign of the studied excess functions was found to be negative for the binary mixtures over the complete range of mole fraction. It is observed that (i) formation of cross hydrogen bonding between Bn-OH and (C$_2$-C$_4$) carboxylic acids (ii) packing effects between components of the mixture, and (iii) steric hindrance effect equally contributes to the magnitude of the evaluated excess parameters. At a fixed composition, the non-ideality of Bn-OH + AA/PA/n-BA systems increases with an increase in the temperature. In addition, the experimental excess volumes
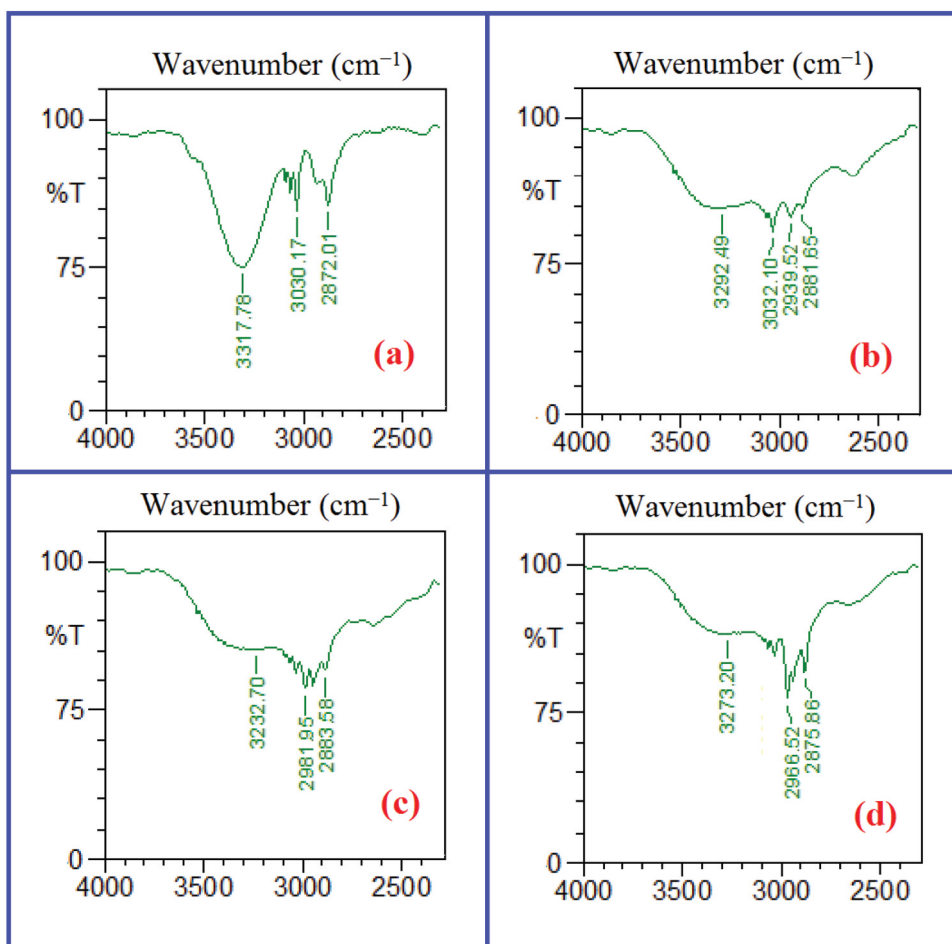
Figure 11. The partial ATR-FTIR spectra of (a) pure Bn-OH in the v(O-H) region; -O-H stretching frequencies of Bn-OH at $x_1 = 0.5$ in the binary systems of (b) Bn-OH + AA; (c) Bn-OH + PA; and (d) Bn-OH + n-BA.

(V^E), excess isentropic compressibilities (κ_s^E) have been correlated with Redlich-Kister equation. The thermodynamic conclusions are found to be in good agreement with the ATR-FTIR spectral studies of the binary systems.

Table 6. Experimental ATR-FTIR vibrational frequencies, v_{max} (cm^{-1}) of the pure and equimolar binary mixtures of Bn-OH with (C$_2$-C$_4$) carboxylic acids at ambient temperature.

System	Vibrational band	Experimental vibrational frequencies v_{max} (cm^{-1})	Shift of vibrational frequencies Δv_{max} (cm^{-1})
Pure Bn-OH	-O-H (a)	3317.8	-
Pure EA	-O-H (b)	3018.6	-
Pure PA	-O-H (c)	2983.9	-
Pure n-BA	-O-H (d)	2968.5	-
Bn-OH + AA	-O-H⋯O-H (e)	3292.5	−25.3 (e-a)
Bn-OH + PA	-O-H⋯O-H (f)	3232.7	−85.1 (f-a)
Bn-OH + n-BA	-O-H⋯O-H (g)	3273.2	−44.6 (g-a)

Acknowledgements

Disclosure statement

ORCID

P. Bhanuprakash 🆔 http://orcid.org/0000-0002-8885-4689
Ramesh L. Gardas 🆔 http://orcid.org/0000-0002-6185-5825

References

[1] Malek NI, Ijardar SP, Master ZR, et al. Temperature dependence of densities, speeds of sound, and derived properties of cyclohexylamine + cyclohexane or benzene in the temperature range 293.15–323.15 K. Thermochim Acta. 2012;547:106–119.

[2] Peralta RD, Infente R, Cortze G, et al. Densities and excess volumes of benzene with ethyl acrylate, butyl acrylate, methyl methacrylate, and styrene at 298.15 K. Thermochim Acta. 2003;398:39–46.

[3] Reddy PM, Sivakumar K, Venkatesu P. Densities and ultrasonic studies for binary mixtures of tetrahydrofuran with chlorobenzenes, chlorotoluenes and nitrotoluenes at 298.15. Fluid Phase Equilib. 2011;310:74–81.

[4] Marianoa A, Mussari L, Orozc M, et al. Volumetric and transport properties of the ternary mixtures of toluene (1) + benzene (2) + butyl acetate (3) at different temperatures. Phys Chem Liq. 2015;53:587–598.

[5] Parveen S, Singh S, Shukla D, et al. Study of molecular interactions in binary mixtures of aniline with carboxylic acids at 293.15 K, 303.15 K and 313.15 K. J Solution Chem. 2012;41:156–172.

[6] Letcher TM, Redhi GG. Thermodynamic excess properties for binary mixtures of (benzonitrile + a carboxylic acid) at T = 298.15 K. Fluid Phase Equilib. 2002;198:257–266.

[7] Alavianmehr MM, Hemmati N, Ghodrati H. Excess molar volumes, excess thermal expansion coefficients and isentropic compressibility deviations for binary mixtures of benzyl alcohol + (1-butanol, 2-butanol, 2-methyl-1-butanol and *tert*-butanol) at T = (298.15-328.15) K and ambient pressure. Phys Chem Liq. 2017;55:85–99.

[8] Gardas RL, Freire MG, Carvalho PJ, et al. High-pressure densities and derived thermodynamic properties of imidazolium-based ionic liquids. J Chem Eng Data. 2007;52:80–88.

[9] Takamuku T, Kyoshoin Y, Noguchi H, et al. Liquid structure of acetic acid–water and trifluoroacetic acid –water mixtures studied by large-angle x-ray scattering and NMR. J Phys Chem B. 2007;111:9270–9280.

[10] Chen J, Brooks CL, Scheraga HA. Revisiting the carboxylic acid dimers in aqueous solution: interplay of hydrogen bonding, hydrophobic interactions, and entropy. J Phys Chem B. 2008;112:242–249.

[11] Clifford SL, Ramjugernath D, Raal JD. Subatmospheric vapor pressure curves for propionic acid, butyric acid, isobutyric acid, valeric acid, isovaleric acid, hexanoic acid, and heptanoic acid. J Chem Eng Data. 2004;49:1189–1192.

[12] Bhanuprakash P, Narasimha Rao C, Sivakumar K. Evaluation of molecular interactions by volumetric and acoustic studies in binary mixtures of the ionic liquid [EMIM][MeSO4] with ethanoic and propanoic acid at different temperatures. J Mol Liq. 2016;219:79–87.

[13] Bahadur I, Deenadayalu N, Naidoo P, et al. Density, speed of sound, and refractive index measurements for the binary systems (butanoic acid + propanoic acid, or 2-methyl-propanoic acid) at T = (293.15 to 313.15) K. J Chem Thermodyn. 2013;57:203–211.

[14] Ali A, Tariq M. Thermodynamic and transport behaviour of binary liquid mixtures of benzyl alcohol with monocyclic aromatics at 303.15 K. J Mol Liq. 2006;128:50–55.

[15] Bhanuprakash P, Jyothi NVV, Narasimharao C, et al. Elucidation of molecular interactions in the mixtures of benzylalcohol with (C_2–C_4) alkylacetates through volumetric, ultrasonic, theoretical and ATR-FTIR spectroscopic studies at T = (298.15, 303.15, 308.15 and 313.15) K. J Mol Liq. 2017;234:49–63.

[16] Chen KD, Lin YF, Tu CH. Densities, viscosities, refractive indexes, and surface tensions for mixtures of ethanol, benzyl acetate, and benzyl alcohol. J Chem Eng Data. 2012;57:1118–1127.

[17] Martindale W. The Extra Pharmacopoeia. 33rd ed. London: Pharmaceutical Press; 2002.

[18] O'Neil MJ, ed. The merck index-an encyclopedia of chemicals, drugs and biologicals. 13th ed. Whitehouse Station. NJ: Merck and Co., Inc; 2001.

[19] Hong YK, Hong WH, Han DH. Application of reactive extraction to recovery of carboxylic acids. Biotechnol Bioprocess Eng. 2001;6:386–394.

[20] Neyband RS, Yousefi A, Zarei H. Experimental and computational thermodynamic properties of (benzyl alcohol+ alkanols) mixtures. J Chem Eng Data. 2015;60:2291–2300.

[21] Venkatramana L, Sreenivasulu K, Sivakumar K, et al. Thermodynamic properties of binary mixtures containing 1-alkanols. J Therm Anal Calorim. 2014;115:1829–1834.

[22] Venkatramana L, Sivakumar K, Gardas RL, et al. Effect of chain length of alcohol on thermodynamic properties of their binary mixtures with benzylalcohol. Thermochim Acta. 2014;581:123–132.

[23] Yeh CT, Tu CH. Densities, viscosities, refractive indexes, and surface tensions for binary mixtures of 2-propanol+ benzyl alcohol,+ 2-phenylethanol and benzyl alcohol + 2-Phenylethanol at T = (298.15, 308.15, and 318.15) K. J Chem Eng Data. 2007;52:1760–1767.

[24] Raveendra M, Narasimharao C, Venkatramana L, et al. Effect of chain length of alcohol on thermodynamic properties of their binary mixtures with benzylalcohol. J Chem Thermodyn. 2016;92:97–107.

[25] Raveendra M, Chandrasekhar M, Narasimharao C, et al. Elucidation of hydrogen bonding formation by a computational, FT-IR spectroscopic and theoretical study between benzyl alcohol and isomeric cresols. RSC Adv. 2016;6:27335–27348.

[26] Comelli F, Ottani S. Excess enthalpies of binary mixtures containing poly (propylene glycols) + benzyl alcohol, or + m-cresol, or + anisole at 308.15 K and at atmospheric pressure. Thermochim Acta. 2005;430:123–128.

[27] Kumar RV, Rao AA, Rao MV, et al. Excess molar enthalpies of chloroalkanes or chloroalkenes+ benzyl alcohol at 298.15 K. J Chem Eng Data. 1995;40:99–101.

[28] Venkatramana L, Sivakumar K, Govinda V, et al. Study on solution properties of some industrially important solvents with an aromatic alcohol. J Mol Liq. 2013;186:163–170.

[29] Venkatramana L, Gardas RL, Sivakumar K, et al. Thermodynamics of binary mixtures: the effect of substituents in aromatics on their excess properties with benzylalcohol. Fluid Phase Equilib. 2014;367:7–21.

[30] Ali A, Nain AK, Chand D, et al. Volumetric and viscometric studies of molecular interactions in binary N, N-dimethylacetamide + benzyl alcohol mixtures at different temperatures. S Afr J Chem. 2005;58:98–104.

[31] Nikam PS, Kharat SJ. Densities and viscosities of binary mixtures of N, N-dimethylformamide with benzyl alcohol and acetophenone at (298.15, 303.15, 308.15, and 313.15) K. J Chem Eng Data. 2003;48:1291–1295.

[32] Francesconi R, Bigi A, Rubini K, et al. Excess enthalpies, heat capacities, densities, viscosities and refractive indices of dimethyl sulfoxide + three aryl alcohols at 308.15 K and atmospheric pressure. J Chem Eng Data. 2005;50:1932–1937.

[33] Nayak JN, Aralaguppi MI, Aminabhavi TM. Density, viscosity, refractive index, and speed of sound in the binary mixtures of ethyl chloroacetate + cyclohexanone, + chlorobenzene, + bromobenzene, or + benzyl Alcohol at (298.15, 303.15, and 308.15) K. J Chem Eng Data. 2003;48:628–631.

[34] Rafiee HR, Sadeghi S. The study of excess molar volumes and related properties for binary mixtures containing benzyl alcohol and 1,3-dichloro-2-propanol with vinyl acetate, ethyl acetate and t-butyl acetate at T = 293.15 to 313.15 K and P = 0.087 MPa. Thermochim Acta. 2016;633:149–160.

[35] Alavianmehr MM, Shahsavar S, Ghodrati H, et al. Measurement and modeling of volumetric properties and speeds of sound of several mixtures of alcohol liquids containing butanediol. J Chem Eng Data. 2015;60:1956–1967.

[36] Singh S, Bahadur I, Redhi GG, et al. Density and speed of sound of 1-ethyl-3-methylimidazolium ethyl sulphate with acetic or propionic acid at different temperatures. J Mol Liq. 2014;199:518–523.

[37] Vong WT, Tsai FN. Densities, molar volumes, thermal expansion coefficients, and isothermal compressibilities of organic acids from 293.15 K to 323.15 K and at pressures up to 25 MPa. J Chem Eng Data. 1997;42:1116–1120.

[38] Mukesh B, Gowrisankar M, Krishna TS, et al. Studies on the importance of thermodynamic and transport properties of liquid mixtures at various temperatures. J Therm Anal Calorim. 2018;132:1167–1181.

[39] Bahadur I, Naidoo P, Singh S, et al. Effect of temperature on density, sound velocity, refractive index and their derived properties for the binary systems (heptanoic acid + propanoic or butanoic acids). J Chem Thermodyn. 2014;78:7–15.

[40] Bahadur I, Singh S, Deenadayalu N, et al. Influence of alkyl group and temperature on thermophysical properties of carboxylic acid and their binary mixtures. Thermochim Acta. 2014;590:151–159.

[41] Fortin TJ, Laesecke A, Freund M, et al. Advanced calibration, adjustment, and operation of a density and sound speed analyzer. J Chem Thermodyn. 2013;57:276–285.

[42] Motin MA, Kabir MH, Huque EM. Densities and excess molar volumes of formic acid, acetic acid and propionic acid in pure water and in water + Surf Excel solutions at different temperatures. Phys Chem Liq. 2005;43:277–288.

[43] Kumari A, Sandeepa K, Kumar TP, et al. Solubility, thermodynamic properties, and derived excess properties of benzoic acid in (acetic acid + water) and (acetic acid + toluene) binary mixtures. J Chem Eng Data. 2016;61:67–77.

[44] Gonzalez B, Dominguez A, Tojo J. Dynamic viscosities, densities, and speed of sound and derived properties of the binary systems acetic acid with water, methanol, ethanol, ethyl acetate and methyl Acetate at T = (293.15, 298.15, and 303.15) K at atmospheric pressure. J Chem Eng Data. 2004;49:1590–1596.

[45] Singh S, Bahadur I, Redhi GG, et al. Influence of the alkyl group on thermophysical properties of carboxylic acids in 1-butyl-3-methylimidazolium thiocyanate ionic liquid at various temperatures. J Chem Thermodyn. 2015;89:104–111.

[46] Tummanapelli AK, Vasudevan S. Dissociation constants of weak acids from ab initio molecular dynamics using metadynamics: influence of the inductive effect and hydrogen bonding on pK_a Values. J Phys Chem B. 2014;118(47):13651–13657.

[47] Lark BS, Singh S, Aggarwal SK, et al. volumes of n-butyric acid + various polar and nonpolar solvents. J Chem Eng Data. 1985;30:467–469.

[48] Letcher TM, Redhi GG. Excess enthalpies and volumes for mixtures of (acetonitrile + a carboxylic acid) at 298.15 K. J Chem Eng Data. 2000;45:57–60.

[49] Ahluwalia R, Gupta R, Vashisht JL, et al. Thermophysical properties of binary liquid systems of ethanoic acid, propanoic acid, and butanoic acid with benzene or acetophenone. ISRN Phys Chem. 2013;2013:1–13. ArticleID 612837.

[50] Lark BS, Banipal TS. Excess volumes and excess enthalpies of acetic and its methyl-substituted acids + acetonitrile. Can J Chem. 1985;63:3269–3275.

[51] Dalai B, Dash SK, Singh SK. Viscometric, volumetric and acoustic properties of binary mixtures of a nuclear extractant with monocarboxylic acids (C$_1$-C$_3$) at 303.15 K. Indian J Pure Appl Phys. 2014;52:24–29.

[52] Benson GC, Kiyohara O. Evaluation of excess isentropic compressibilities and isochoric heat capacities. J Chem Thermodyn. 1979;11:1061–1064.

[53] Zhong Y, Wang H, Diao K. Densities and excess volumes of binary mixtures of the ionic liquid 1-butyl-3-methylimidazolium hexafluorophosphate with aromatic compound at T=(298.15 to 313.15) K. J Chem Thermodyn. 2007;39:291–296.

[54] Redlich O, Kister AT. Algebraic representation of thermodynamic properties and the classification of solutions. Ind Eng Chem. 1948;40:345–348.

[55] Wood SE, Battino R. Thermodynamics of chemical systems. Cambridge: Cambridge University Press; 1990.

[56] Iloukhani H, Zarei HA. Volumetric properties of dimethyl sulfoxide with some alcohols at 298.15 K. Phys Chem Liq. 2008;46:154–161.

[57] Pal A, Kumar A, Kumar H. Volumetric properties of binary mixtures of some n-alkoxyethanols with 2-pyrrolidinone and N-methyl-2-pyrrolidinone at 298.15 K. Indian J Chem. 2002;41:2017–2024.

[58] Wei Q, Guo X, Wang Y, et al. Temperature-dependent FTIR study on three kinds of hydrogen-bonded benzoic acid dimers in their melt states. J Mol Liq. 2013;177:225–228.

[59] Silverstein RM, Webster FX. Spectrometric Identification of Organic Compounds. 6th ed. New Delhi: Wiley-India; 2007.

Data Article

Investigation on thermodynamic properties and spectroscopic studies of binary mixtures of 1, 2, 4-trichlorobenzene with alkyl acetates (C1-C5) at $T = (303.15$ to $318.15)$ K

R. Raju [a], S. Ravikumar [a], K. Sivakumar [b], P. Bhanuprakash [c], V. Pandiyan [a] ✉

Show more ∨

☰ Outline | ⤳ Share �" Cite

Get rights and content

Abstract

The measurements of experimental densities (ρ) and speeds of sound (u) of binary mixtures of 1, 2, 4-trichlorobenzene (1,2,4-TCB) with alkyl acetates namely methyl acetate, ethyl acetate, propyl acetate, butyl acetate and pentyl acetate have been done over the entire composition range at four different temperatures $(T = 303.15, 308.15, 313.15$ and 318.15 K) and pressure $(P = 0.1$ MPa). The intermolecular interactions present in these mixtures were briefly explained through the calculated excess molar volume (V_m^E), excess isentropic compressibility (κ_S^E) and excess speeds of sound (u^E). The ideal and excess parameters were correlated with Redlich-Kister polynomial equation. Different theoretical models such as PFP theory, CFT and FLT have been used to analyze the experimental results of V_m^E and u values respectively. The strength of intermolecular interactions between the component molecules have been confirmed using the excess properties and the results were further analyzed with FT-IR spectroscopic technique.

< Previous   Next >

Keywords

Binary mixtures; 1, 2, 4-trichlorobenzene; Densities; Excess thermodynamic properties; Speeds of sound; FTIR studies

---

Recommended articles

Cited by (0)

View full text

Keywords

Binary mixtures; 1, 2, 4-trichlorobenzene; Densities; Excess thermodynamic properties; Speeds of sound; FTIR studies

Journal Pre-proof

Quantum cutting and near-infrared emissions in Ho^{3+}/Yb^{3+} codoped transparent glass-ceramics

P. Babu, I.R. Martín, V. Lavín, U.R. Rodríguez-Mendoza, Hyo Jin Seo, K. Venkata Krishanaiah, V. Venkatramu

Please cite this article as: P. Babu, I.R. Martín, V. Lavín, U.R. Rodríguez-Mendoza, H.J. Seo, K.V. Krishanaiah, V. Venkatramu, Quantum cutting and near-infrared emissions in Ho^{3+}/Yb^{3+} codoped transparent glass-ceramics, *Journal of Luminescence* (2020), doi: https://doi.org/10.1016/j.jlumin.2020.117424.

CRediT author statement

P. Babu: Conceptualization, Investigation, Writing – original/Revised draft preparation.

I.R. Martin: Methodology, Investigation.

V. Lavin: Investigation, Writting - Reviewing and Editing.

U.R. Rodriguez-Mendoza: Formal analysis.

Hyo Jin Seo: Methodology, Resources.

K. Venkata Krishnaiah: Software, Data curation.

V. Venkatramu: Validation

Quantum cutting and near-infrared emissions in Ho^{3+}/Yb^{3+} codoped transparent glass-ceramics

P. Babu[1,*], I.R. Martín[2], V. Lavín[2], U.R. Rodríguez-Mendoza[2],
Hyo Jin Seo[3], K. Venkata Krishanaiah[4], V. Venkatramu[5,6]

[1]*Department of Physics, Government Degree College, Palamaner-517408, India*
[2]*Departamento de Física, MALTA Consolider Team, IMN, and IUdEA, Universidad de la Laguna,
Apartado de Correos 456, E-38200 San Cristóbal de La Laguna, Santa Cruz de Tenerife, Spain*
[3]*Department of Physics, Pukyong National University, Busan, Republic of Korea*
[4]*Department of Physics, RGM College of Engineering and Technology, Nandyal – 518501, India*
[5]*Department of Physics, Yogi Vemana University, Kadapa-516 005, India*
[6]*Department of Physics, Krishna University Dr. MRAR PG Centre, Nuzvid -521 201, India*

Abstract

Visible to near-infrared quantum cutting and 2.0 µm near-infrared emissions have been obtained in Ho^{3+}/Yb^{3+} co-doped oxyfluoride transparent glass-ceramic, containing cubic CaF$_2$ nanocrystals, under 473 nm excitation. The formation of CaF$_2$ nanocrystals and the incorporation of Ho^{3+}/Yb^{3+} ions into these nanocrystals have been confirmed from x-ray diffraction and photoluminescence studies, respectively. Lifetime of 1.2 µm emission has been enhanced by three orders of magnitude in the glass-ceramic compared to that of the precursor glass. Time-resolved near-infrared quantum cutting emission of Yb^{3+} ions at different delay times under 532 nm laser excitation has also been obtained. Studies reveal that the infrared quantum cutting emission of Yb^{3+} and Ho^{3+} ions in the CaF$_2$ nanocrystalline glass-ceramic could improve the efficiency of crystalline-Si solar cells, and that the 1.2 µm emission could be useful for further enhancing transmission windows using optical amplifiers.

_____

Keywords: Oxyfluoride glass-ceramics; Ho^{3+}/Yb^{3+} ions; CaF$_2$ nanocrystals; Downconversion; Near-infrared quantum cutting

*Corresponding authors: drbabu64@gmail.com (P. Babu)

1. INTRODUCTION

A transparent oxyfluoride glass-ceramic (TGC) is a two-phase material containing fluoride nanocrystals that precipitate in an amorphous environment during the controlled thermal treatment of the precursor glass. In recent years, TGCs have attracted great deal of interest due to their potential applications in diverse fields of science and technology [1-3]. Alumina-silicate based glasses are most suitable for precipitation of fluoride nanocrystals due to their excellent thermal, chemical and mechanical properties compared to phosphate or fluoride glasses. Further, in these TGCs, the host for the trivalent lanthanide (Ln^{3+}) ions corresponds to fluoride crystals with low phonon energy and, hence, low multiphonon probabilities, which results in increasing the luminescence efficiency of these materials compared to their precursor glasses [3]. Ln^{3+} ions doped TGCs are widely investigated as they exhibit both upconversion (UC) and downconversion (DC) processes besides excellent Ln^{3+} ion solubility [4]. Recently, TGCs containing fluoride nanocrystals have been explored for laser cooling applications as they show extraordinary properties, including high photoluminescence quantum yield and low background absorption [5-7].

Trivalent holmium, Ho^{3+}, ion is suitable for infrared-to-visible upconversion since it has two pumping energy levels, $^5F_5$ and $^5I_4$, along with a relatively long lived intermediate energy level, $^5I_7$, that acts as a good population reservoir for upconversion processes. As a result, in recent times there is significant amount of interest in Ho^{3+}-doped glasses and crystals as possible upconversion materials. Further, Ho^{3+}-doped glass fibers are found to emit continuous wave upconversion laser under red light pumping [8]. In addition, Yb^{3+} ion has a relatively simple energy level structure with the $^2F_{7/2}$ level as ground state and the $^2F_{5/2}$ level as excited state. Its broad emission, ranging between 900 and 1100 nm, overlaps with the crystalline silicon´s band

2

gap of ~1.12 eV, making Yb^{3+} ion an important candidate for near-infrared (NIR) quantum cutting (QC) materials to improve the efficiency of crystalline-silicon (C-Si) solar cells [9]. Materials co-doped with Yb^{3+} ions and other Ln^{3+} ions are attractive for the development of upconversion devices. In the specific case of Ln^{3+} (Er^{3+}, Tm^{3+} or Ho^{3+}) ions, resonance energy transfer is facilitated by the energy matching of their excited states with that of Yb^{3+} ion [10]. The Yb^{3+} ion is found to be efficient sensitizer for Ho^{3+} lasers [2], due to considerable energy match between Yb^{3+} and Ho^{3+} ions and hence, Ho^{3+}/Yb^{3+} couple is a good choice for NIR QC investigations [11]. The NIR QC, which converts one UV-blue photon into two NIR photons of ~1.0 µm, has attracted more attention for their application in plasma display, mercury free fluorescent tubes, and solar cells [11,12]. In recent times, more emphasis has been focused on NIR QC in different systems with the combination of different Ln^{3+} ions with Yb^{3+} ions, for example, Nd^{3+}/Yb^{3+} [13], Tb^{3+}/Yb^{3+} [14-17], Er^{3+}/Yb^{3+} [18,19], Tm^{3+}/Yb^{3+} [20], Pr^{3+}/Yb^{3+} [13,21] Ho^{3+}/Yb^{3+} [9,22,23], and Yb^{2+}/Yb^{3+} [24] to enhance the efficiency of solar cells. On the other side, solid state laser working in the infrared region at 2 µm is attracting increasing interest for its wide range of applications such as remote sensing, optical parametric oscillators, eye safe LIDAR, biomedical applications, environmental sensing, etc. [2,25]. Among the Ln^{3+} ions, Ho^{3+} is one of the important active ions that can emit at 2 µm through the $^5I_7 \rightarrow {}^5I_8$ transition.

In the present work, Ho^{3+}/Yb^{3+} codoped TGCs containing CaF_2 nanocrystals have been synthesized through post-thermal treatment method and their visible, QC and NIR emissions have been measured exciting at 473 nm. NIR QC emissions are observed at 1.0 and 1.2 µm wavelengths under 473 nm excitation and their possible mechanisms are discussed. The NIR emission spectra at 2.0 µm have been measured in glass and GCs and explained their variation

with respect to size of the nanocrystals. Absorption and emission cross-sections and figure of merit for the 1.2 µm and 2.0 µm emissions have also been calculated.

2. EXPERIMENTAL DETAILS

Precursor Ho^{3+}/Yb^{3+} co-doped oxyfluoride glass, with composition (in mol%) $45SiO_2$ - $20Al_2O_3$ - $8CaO$ - $24CaF_2$ - $2Yb_2O_3$ - $1Ho_2O_3$, was prepared by the melt-quenching technique at 1400 °C for 2 h using a covered platinum crucible. The melt was poured onto a pre-heated brass mold kept just below the glass transition temperature (T_g), at which glass samples were annealed, and slowly cooled to room temperature to avoid thermal stress and strains. Finally, glass samples were annealed for 4h at 650, 675, 700 and 725 °C (hereafter referred to as GC1, GC2, GC3 and GC4, respectively), close to the onset of crystallization temperature T_c (675 °C) of CaF_2 nanocrystals to transform them into glass-ceramics. Structural differences between the precursor glass and glass-ceramics were identified by using X-ray diffraction technique, performed with a Thermo ARL X'TRA powder diffractometer with Cu-K_α radiation (1.54 Å).

Visible and NIR quantum cutting emissions were obtained by pumping with a cw laser at 473 nm and the emission was collimated and focalized in an optical fiber coupled to a ANDOR spectrograph, a SR-303i-B equipped with a Newton 970EMCCD camera for the visible range, and an SR-500i-B2 with a iDusInGaAs photodiode array for the NIR range. The time-resolved fluorescence was obtained by exciting the samples with an EKSPLA 10 ns pulsed Optical Parametric Oscillator (OPO) laser and recording the luminescence with a Jobin-Yvon 320 spectrometer equipped with a Hamamatsu NIR-extended photomultiplier connected to a Lecroy digital storage oscilloscope.

4

3. RESULTS AND DISCUSSION

3.1. *X-ray diffraction spectra*

X-ray diffraction (XRD) patterns of Ho^{3+}/Yb^{3+}-doped precursor glass and glass-ceramics are shown in Fig. 1. The profile of the precursor glass contains two broad curves typical of an amorphous structure, whereas the GCs contain several additional sharp peaks related to the diffraction pattern of a crystalline structure, which can be identified as the CaF_2 cubic phase with *Pm3m* ($\alpha = \beta = \gamma = 90°$) space group, by comparing with standard data (JCPDS Card No. 35-0816). These crystals form nanostructures that are found to precipitate from the precursor aluminosilicate glass through a suitable thermal treatment that, from the XRD peak widths and using the Scherer's formula [26], sizes of the nanocrystals are found to be around 8, 10, 13 and 18 nm for GC1, GC2, GC3 and GC4, respectively. Samples exhibit only the cubic phase and no second phase is detected in the XRD pattern, indicating the successful formation of CaF_2 nanocrystals.

3.2. *Emission spectra and decay curves*

3.2.1. *Visible emission spectra*

Visible emission spectra of glass (G) and glass-ceramics (GCs) are measured exciting the $^5I_8 \rightarrow ^5F_3$ transition of the Ho^{3+} ion under 473 nm laser excitation, and are shown in Fig. 2. Spectra consist of three bands centered at ~542, ~648 and ~752 nm corresponding to the $^5S_2, ^5F_4 \rightarrow ^5I_8$, $^5F_5 \rightarrow ^5I_8$ and $^5S_2, ^5F_4 \rightarrow ^5I_7$ transitions, respectively. When samples are excited, Ho^{3+} ions reach the $^5F_3$ level, from which a fast non-radiative decay takes place and ions reach the $^5S_2, ^5F_4$ metastable multiplets, resulting in green emission at ~542 nm and red emission at ~752 nm. From the $^5S_2, ^5F_4$ levels further non-radiative deexcitation processes populates the $^5F_5$ level, resulting in $^5F_5 \rightarrow ^5I_8$ emission at ~648 nm. Mechanisms of excitation and emissions are

5

shown in Fig. 3. Lin *et al*. [27] obtained similar emission spectra in Ho^{3+}/Yb^{3+} co-doped GC with YF_3 nanocrystals under 488 nm excitation. Out of these three transitions, the green emission is more intense than the other two. As can be seen from Fig. 2, the emission intensity and splitting of the bands increases from glass to GC4, indicating the progressive incorporation of Ho^{3+} ions into the CaF_2 nanocrystals and the increase in size of the nanocrystals.

3.2.2. *Quantum cutting and 1.2 µm emission spectra*

As already mentioned, when the samples are excited with a 473 nm cw laser, the Ho^{3+} ions are excited to the $^5F_3$ level, followed by a non-radiative relaxation to the $^5S_2, ^5F_4$ level. From this level, the following resonant cross-relaxation energy transfer, denoted as CR1 in Fig. 3, occurs:

$$^5S_2, ^5F_4 (Ho^{3+}) + {}^2F_{7/2} (Yb^{3+}) \rightarrow {}^5I_6 (Ho^{3+}) + {}^2F_{5/2} (Yb^{3+})$$
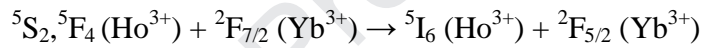
and one Ho^{3+} 1180 nm photon (from the $^5I_6$ level) and one Yb^{3+} 980 nm photon (from the $^2F_{5/2}$ level) are emitted.

Further, non-radiative multiphonon relaxations from the $^5S_2, ^5F_4$ levels populate the $^5F_5$ one and, from this level, another resonant cross-relaxation energy transfer, shown as CR2 in Fig. 3, takes place as follows:

$$^5F_5 (Ho^{3+}) + {}^2F_{7/2} (Yb^{3+}) \rightarrow {}^5I_7 (Ho^{3+}) + {}^2F_{5/2} (Yb^{3+})$$
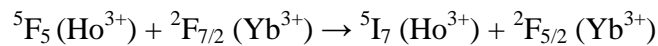
resulting in the emission of one Ho^{3+} 2.0 µm photon (from the $^5I_7$ level) and one Yb^{3+} 980 nm photon (from the $^2F_{5/2}$ level). All these excitations, CR and emissions channels are shown in the partial energy level diagram of Yb^{3+} and Ho^{3+} ions in Fig. 3. It is worth noting that Zhou *et al*. [26] and Lin *et al*. [27] proposed similar mechanisms to explain QC processes in Ho^{3+}/Yb^{3+} codoped glass-ceramics.

Emissions from Yb^{3+} ($^2F_{5/2} \rightarrow {}^2F_{7/2}$) and Ho^{3+} ($^5S_2, {}^5F_4 \rightarrow {}^5I_6$) ions overlap giving a wide band in the range of 950-1100 nm, as shown in Fig. 4. Additionally, Yb^{3+} emissions consist of two peaks, a sharp one at ~980 nm and broader one at ~1020 nm, attributed to emission from the lowest Stark level of $^2F_{5/2}$ multiplet to the lowest and next higher Stark levels of the $^2F_{7/2}$ ground multiplet, respectively [28]. The intensity of Yb^{3+} emissions increases, due to the change of the Ln^{3+} local structure, from glass to glass-ceramic GC3, and then decreases marginally for GC4, which could be due to back transfer processes from Yb^{3+} to Ho^{3+} ions. The $^5I_6 \rightarrow {}^5I_8$ transition gives emission at ~1.2 μm and is also shown in Fig. 4 for the glass and GCs. Their intensities are higher compared to those of 1.0 μm, and increase monotonically from the glass to the glass-ceramic GC4 with the increase in size of the nanocrystals and the progressive incorporation of Ho^{3+} ions into low phonon energy CaF_2 nanocrystals.

As can be seen from Figs. 2 and 4, in moving from glass to GC4, the enhancement factor of the intensity is higher for the $^5I_6 \rightarrow {}^5I_8$ emission band compared to the $^5S_2, {}^5F_4 \rightarrow {}^5I_7$ band of Ho^{3+} ions. This can be explained taking into account that the energy difference between the $^5S_2, {}^5F_4$ and $^5F_5$ levels is ~3020 cm^{-1} whereas the difference between the $^5I_6$ and $^5I_7$ levels is ~3540 cm^{-1} (from absorption spectrum). Larger energy gap results in lower multiphonon relaxation from the upper level. In moving from glass to GC4, phonon energy of the host progressively decreases. As a result of this, there is progressive increase in radiative emission from the $^5I_6$ level compared to the $^5S_2, {}^5F_4$ level in moving from glass to GC4. Another reason for higher enhancement factor of the $^5I_6 \rightarrow {}^5I_8$ emission could be increase in CR1 process, in moving from glass to GC4, which depopulates the $^5S_2, {}^5F_4$ level and populates the $^5I_6$ one.

Quantum cutting (QC) is a process in which one photon of high energy converts into two photons of lower energy. This process in the Ho^{3+} ions, where each photon at 473 nm that is absorbed can produce two NIR photons, given by $^2F_{5/2} \rightarrow {}^2F_{7/2}$ & $^5I_6 \rightarrow {}^5I_8$ (1.0 & 1.2 μm) and $^2F_{5/2} \rightarrow {}^2F_{7/2}$ & $^5I_7 \rightarrow {}^5I_8$ (1.0 & 2.0 μm). The low energy photons (~1.2 and ~2.0 μm) are more intense and efficient as they occur only between Ho^{3+} ions, whereas the former ones (~1.0 μm) involves energy transfer from Ho^{3+} to Yb^{3+} ions and, hence, they are weaker.

The effect of Yb^{3+} ions can be analyzed using the decay curves of the $^2F_{5/2}$ level of Yb^{3+} ions in glass and GC3. These decays are measured by exciting them with a 944 nm laser radiation and monitoring the emission at ~1020 nm, where there is shoulder in the Yb^{3+} ions emission, and are shown in Fig. 5. Both decay curves are clearly non-exponential and the average lifetimes [11] are found to be ~15 and ~28 μs for glass and GC3, respectively. It is interesting to note that the lifetime in GC3 increases significantly, almost by a factor of 2, due to the presence of Yb^{3+} ions in a low phonon energy CaF_2 nanocrystalline environment.

Decay curves for the $^5I_6 \rightarrow {}^5I_8$ transition of Ho^{3+} ions at 1.2 μm measured in the glass and the glass-ceramics, under 473 nm laser excitation, are shown in Fig. 6. As can be seen, all decay curves are non-exponential in nature and consists of short and long components. The short component corresponds to ions that reside in the glass matrix and are not incorporated in the nanocrystals. But, as can be seen from Fig. 6, this component is reduced from GC1 to GC4. Lifetime of the long component of 1.2 μm decay, which is due to ions present in CaF_2 nanocrystals, increases with the increase in the size of nanocrystals from 15 μs (Glass/GC1) to 1.586 ms (GC4). It is worth noting that the lifetime in GC4 is three orders of magnitude (~1006 times) longer compared to that of the glass, due to the presence of Ho^{3+} ions in low phonon energy CaF_2 nanocrystals. The present lifetime of the 1.2 μm emission of Ho^{3+} ion in GC4 is

longer compared to other reported Ho^{3+} doped matrices, such as $CaSc_2O_4$ ceramic [29] or water-free fluorotellurite glasses [30].

Fig. 7 shows the time-resolved NIR QC emission of Yb^{3+} ions at different delay times after exciting with a 532 nm laser light, resonant with the $^5I_8 \rightarrow {^5F_4, ^5S_2}$ transition of Ho^{3+} ions. The emission spectra consist of overlapped bands at ~894, ~911, ~980 and ~1020 nm due to Stark's splitting of the excited $Yb^{3+}:^2F_{5/2}$ multiplet and the $^5F_4, ^5S_2 \rightarrow {^5I_6}$ transition of Ho^{3+} ions at ~1010 nm. The energy transfer from Ho^{3+} ions is responsible for the emission of Yb^{3+} ions. The emission intensity and full width at half maximum of the 980 nm emission band increases with the increase in delay time, due to population differences among the thermally coupled levels of Yb^{3+} ions in the matrix.

In order to study the energy transfer process more accurately, luminescence decay curves are obtained by exciting $^5I_8 \rightarrow {^5F_4, ^5S_2}$ transition at 532 nm of the Ho^{3+} ions and monitoring the emissions at ~975 and ~1010 nm, respectively, as shown in Fig. 8. The decay curves indicate that the energy transfer process is predominant at higher delay times because the Yb^{3+} ions are excited through CR1 or CR2 processes from Ho^{3+} ions. The rising edge in the decay curve (975 nm) of Fig. 8 indicates the slow population process of the $^2F_{5/2}$ level of Yb^{3+} ions through energy transfer from Ho^{3+} ions. This provides a strong evidence for the energy transfer from the Ho^{3+} to Yb^{3+} ions [31]. On the contrary, in the emission at ~1010 nm, associated with the $^5F_4, ^5S_2 \rightarrow {^5I_6}$ transition, predominates the emission coming from Ho^{3+} ions initially excited.

The emission cross-section between a high energy level and a lower energy level can be derived using the McCumber [32] theory,

$$\sigma_{em}(\lambda) = \sigma_{ab}(\lambda)\frac{Z_l}{Z_u}\exp\left(\frac{h\nu - E_{ZL}}{k_B T}\right) \quad (1)$$

where σ_{ab} is absorption cross-section, $\sigma_{ab} = \alpha(\lambda)/N$, where $\alpha(\lambda)$ is the experimental absorption coefficient and N is the concentration of Ho^{3+} ions; Z_l and Z_u are the partial functions of lower and upper levels, respectively; k_B is Boltzmann's constant; $E_j - E_i = h\nu - E_{ZL}$ is the energy separation between the two levels; and E_{ZL} is the 'zero line' energy, i.e. the energy of the transition from the lowest Stark sublevels of upper and lower manifold.

Absorption and emission cross-sections ($\times 10^{-20}$ cm^2) are calculated for the 1.2 μm emission of the Ho^{3+} ion and are found to be 0.93 and 5.2 for the precursor glass and 1.16 and 6.7 for the glass-ceramic GC4. Values of emission-cross-sections of glass and GC4 are much larger than those of TZNF60 glass (0.63 $\times 10^{-20}$ cm^2) [30] and oxyfluoride nano glass-ceramic (0.27 $\times 10^{-20}$ cm^2) [33]. Figure of merit (FOM), defined as the product of experimental lifetime and emission cross-section [34], for the 1.2 μm emission is found to be 0.08 $\times 10^{-23}$ cm^{-2}.s for glass and 10720 $\times 10^{-23}$ cm^{-2}.s for the glass-ceramic GC4. The FOM for GC4 is found to be about 1000 times higher than that of glass. The higher value of FOM indicates higher gain for the 1.2 μm emission in GC4.

3.2.3. 2.0 μm emission spectra

NIR emission spectra of the oxyfluoride glass and the glass-ceramics at around 2.0 μm are measured by exciting $^5I_8 \rightarrow ^5F_3$ transition using a 473 nm laser light and are shown in Fig. 9. As can be seen, the intensity of the bands increases from the glass to the glass-ceramic GC3 and then decreases slightly for GC4. This could be due to decrease in the magnitude of the cross-relaxation processes, CR2 in GC4, which feeds $^5I_7$ level, due to decrease in multiphonon relaxation from $^5S_2, ^5F_4$ to $^5F_5$ level. The full width at half maximum (FWHM) of the all the

10

emissions of the present study, from glass to GC4, is found to be around 153 nm (386 cm^{-1}), which is slightly larger than 149 nm found in TZNF60 glass [26] but less than 171 nm found in germinate glass [35].

Absorption and emission cross-sections (x10^{-20} cm^2) of the 2.0 μm band calculated using Eq. (1) are found to be 2.1 and 5.39 for the precursor glass and 2.09 and 5.79 for the glass-ceramic GC4, respectively. The absorption and emission cross-sections (x10^{-20} cm^2) of the present study are larger than those found in oxyfluoride glass (σ$_{ab}$= 0.498, σ$_{em}$= 0.47) and glass-ceramic GC C (σ$_{ab}$= 0.56, σ$_{em}$= 0.66) [2] and TZNF60 glass (σ$_{ab}$= 0.68, σ$_{em}$= 0.72) [26].

The wavelength dependent gain cross-section can be expressed as:

$$\sigma_g(\lambda) = \gamma \sigma_{em}(\lambda) - (1-\gamma)\sigma_{ab}(\lambda)$$

(2)

where σ_{em} and σ_{ab} represents emission and absorption cross-sections, respectively, and γ (0 to 1 with an increments of 0.1) represents the population of Ho^{3+} ions. Gain cross-section spectra of the $^5I_8 \leftrightarrow ^5I_7$ transitions of Ho^{3+} ion at 2.0 μm as a function of population inversion for a glass and the glass-ceramic GC4 are shown in Figs.10 (a) and (b), respectively. Gain is positive when the population inversion is equal or greater than 0.3. However, broadening is more predominant for GC4 compared to glass. The gain is found to be 5.79 cm^{-2} for GC4 which is higher than that of glass, 5.35 cm^{-2}. The value of gain is very high compared to those of reported tellurite [35] and fluorophosphate [37] glasses. It is observed from the gain spectra that a tunable wavelength range of 1900-2100 nm is expected when the population inversion is greater than or equal to 0.5. These results reveal that the Ho^{3+}-doped glass-ceramics have potential for optical amplifiers.

4. CONCLUSIONS

The Ho^{3+}-Yb^{3+} co-doped transparent oxyfluoride glass and glass-ceramics containing CaF_2 nanocrystals have been investigated. X-ray diffraction patterns confirm the formation of CaF_2 nanocrystals in the glass matrix. The size of the nanocrystals increases from 8 to 18 nm with increasing the thermal treatment temperature of the precursor glass. Near-infrared quantum cutting as well as 2.0 µm eye safe emissions are obtained in Yb^{3+} ions and Ho^{3+} ions, respectively by exciting with 473 nm laser at the $^5F_2$ level of Ho^{3+} ions. The similar emission is also achieved at different delay times by exciting the $^5F_4$ level of Ho^{3+} ions at 532 nm. The decay curves of Yb^{3+} emission evidences the energy transfer process from Ho^{3+} to Yb^{3+} ions. It is worth noting that lifetime of 1.2 µm emission has been enhanced by three order of magnitude in GC4 sample compared to that of the precursor glass. Intense Yb^{3+} and Ho^{3+} near-infrared emissions indicate that the present oxyfluoride glass-ceramics containing CaF_2 nanocrystals have potential application in realizing the solar spectrum to enhance the efficiency of c-Si solar cells.

ACKNOWLEDGEMENTS

REFERENCES

[1]. F. Lahoz, S.E. Hernández, N.E. Capuz, D. Navarro-Urrios, Appl. Phys. Lett 90 (2007) 201117-1-201117-3.

[2]. J. Pan, R. Xu, Y. Tian, K. Li, L. Hu, J. Zhang, Opt. Mater. 32 (2010) 1451-1455.

[3]. G. Gorni, J.J. Velazquez, J. Mosa, G. C. Mather, A. Serrano, M. Vila, G.R. Castro, D. Bravo, R. Balda, J. Fernandez, A. Duran, Y. Castro, Nano Mater. 9 (2019) 530-545.

[4]. L.M. Almeida, *Fluoride glasses*, Handbook on the Physics and Chemistry of Rare-Earths, In: K.A. Gschneidner Jr, L. Eyring (Eds.), Vol. 5, Elsevier Science Publishers, 1991, p. 287-346.

[5]. K. Venkata Krishnaiah, E.S. de L. Filho, Y. Ledemi, G. Nemova, Y. Messaddeq, R. Kashyap, Sci. Reports 6 (2016) 21905-1-21905-12.

[6]. E. S. de L. Fiilho, K. Venkata Krishnaiah, Y. Ledemi, Y.J. Yu, Y. Messaddeq, G. Nemova, R. Kashyap, Opt. Exp. 23 (2015) 4630-4640.

[7]. K. Venkata Krishnaiah, Y. Ledemi, E.S. de L. Filho, G. Nemova, Y. Messaddeq, R. Kashyap, Opt. Eng. 56 (2017) 011103-1-011103-5.

[8]. J.C. Boyer, F. Vetrone, J.A. Capobianco, A. Speghini, and M. Bettinelli, J. Appl. Phys. 93 (2003) 9460-9465.

[9]. D.C. Yu, X.Y. Huang, S. Ye, Q.Y. Zhang, J. Alloys Compds. 509 (2011) 9919-9923.

[10]. A. Volokitina, P. Loiko, O. Dymshits, M. Tsenter, S. Zapalova, K. Bogdanov, A. Baranov, A. Zhilin, J. Phys. Conf. Series 917 (2017) 062024-062027.

[11]. L. Guo, Y. Wang, J. Zhang, Y. Wang, P. Dong, Nano Scale Res. Lett. 7 (2012) 636-642.

[12]. D. Chen, Y. Wang, Y. Yu, P. Huang, F. Weng, Opt. Lett. 33 (2008) 1884-1886.

[13]. L.J. Borrero-González, L.A.O. Nunes, J. Phys.: Condens. Matter 24 (2012) 385501-1-385501-7.

[14]. S. Ye, B. Zhu, J. X. Chen, J. Luo, J.R. Qiu, Appl. Phys. Lett. 92 (2008) 141112-1-141112-3.

[15]. Y. Wang, L. Xie, H. Zhang, J. Appl. Phys. 105 (2009) 023528-1-023528-4.

[16]. Q.Y. Zhang, C.H. Yang, Y.X. Pan, Appl. Phys. Lett. 90 (2007) 021107-1-021107-3.

[17]. Y. Arai, T. Yamashidta, T. Suzuki, Y. Ohishi, J. Appl. Phys. 105 (2009) 083105-1-083105-6.

[18]. A.L. Arrts, O.M. vander Ende, A. Meijerink, J. Appl. Phys. 106 (2009) 023522-1-023522-6.

[19]. J.J. Eilers, D. Biner, J.T.V. Wijngaarden, K. Kramer, H.U. Gudel, A. Meijerink, Appl. Phys. Lett. 96 (2010) 151106-1-151106-3.

[20]. L. Xie, Y. Wang, H. Zhang, Appl. Phys. Lett. 94 (2009) 061905-1-061905-3.

[21]. B. Bryan, M. van der Ende, L. Aarts, A. Meijerink, Adv. Mater. 21 (2009) 3073-3077.

[22]. K. Deng, T. Gong, L. Hu, X. Wei, Y. Chen, M. Yin, Opt. Express 19 (2011) 1749-1754.

[23]. Z. Hou, H. Li, Z. Xue, M. Wang, X. Hu, S. Wang, J. Alloys Compds. 640 (2015) 311-316.

[24]. Y. Teng, J. Zhou, X. Liu, S. Ye, J. Qiu, Opt. Exp. 18 (2010) 9671-9676.

[25]. J. He, H. Zhan, Z. Zhou, A. Zhang, A. Lin, Opt. Mater. 35 (2013) 2573-2576.

[26]. X. Zhou, Y. Wang, X. Zhao, L. Li, Z. Wang, Q. Li, J. Am. Ceram. Soc., 97 (2014) 179-184.

[27]. H. Lin, D. Chen, Y. Yu, A. Yang, Y. Wang, Opt. Lett. 36 (2011) 876-878.

[28]. K. Venkata Krishnaiah, C.K. Jayasankar, S. Chaurasia, C.G. murali, L.J. Dhareshwar, Sci. Advan. Mater. 5 (2013) 276-284.

[29]. Ş. Georgescu, A. Ştefan, O. Toma, A.-M. Voiculescu, J. Lumin. 162 (2015) 174-179.

[30]. J. He, H. Zhan, Z. Zhou, A. Zhang, A. Lin, Opt. Commun. 320 (2014) 68-72.

[31]. Q. Zou, P. Huang, W. Zheng, W. You, R. Li, D. Tu, J. Xu, X. Chen, Nanoscale 9 (2017) 6521-6528.

[32]. D.E. McCumber, Phys. Rev. A, 136 (1964) A954-A957.

[33]. K. Driesen, V.K. Tikhomirov, C.G.Walrand, V.D. Rodriguez, Appl. Phys. Lett. 88 (2006) 073111-1-073111-3.

[34]. A.S. Pinheiro, A.M. Freitas, G.H. Silva, M.J.V. Bell, V. Anjos, A.P. Carmo, N.O. Dautas, Chem. Phys. Lett. 592 (2014) 164-169.

[35]. M. Cai, B. Zhou, F. Wang, Y. Tian, J. Zhou, S. Xu, J. Zhang, Opt. Mater. Exp. 5 (2015) 1431-1439.

[36]. K. Damak, El Sayed Yousef, A.S. Al-Shihri, H.J. Seo, C. Rüssel, R. Maâle, Solid State Sci. 28 (2014) 74-80.

[37]. L.X. Yi, M. Wang, S.Y. Feng, Y.K. Chen, G.N. Wang, L.L. Hu, J.J. Zhang, Opt. Mater. 31 (2009) 1586-1590.

Figures
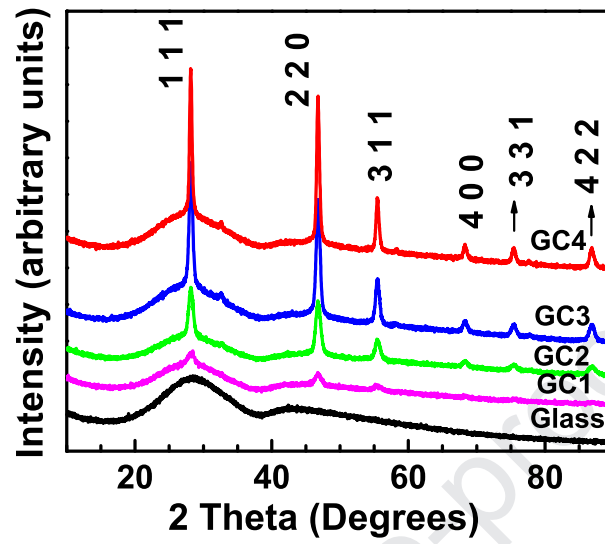
Fig.1. X-ray diffraction patterns of the oxyfluoride glass and glass-ceramics.
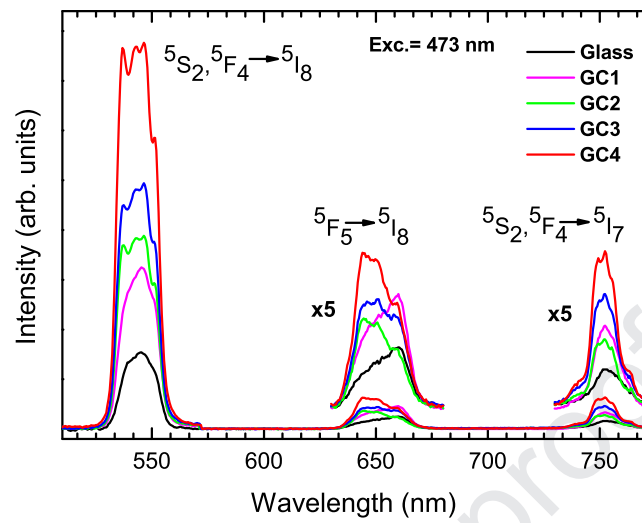
Fig. 2. Visible emissions of Ho^{3+} ions in the oxyfluoride glass (G) and glass-ceramics (GC) under 473 nm laser excitation.
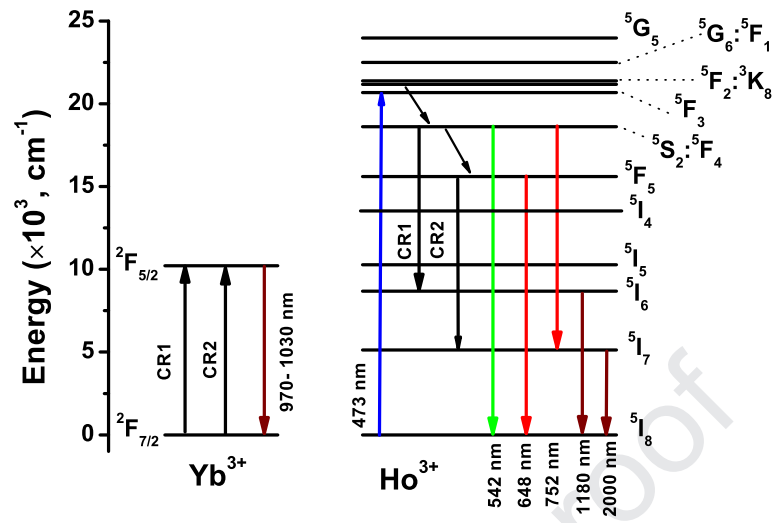
Fig.3. Partial energy level diagram of the oxyfluoride glass and glass-ceramics. CR indicates a cross-relaxation channel.
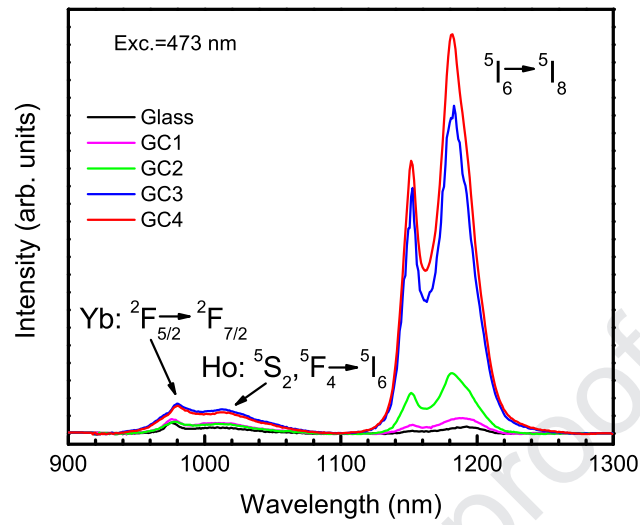
Fig. 4. Quantum cutting emissions of Yb^{3+} and Ho^{3+} ions in the oxyfluoride Glass (G) and glass-ceramics (GC) under 473 nm laser excitation.
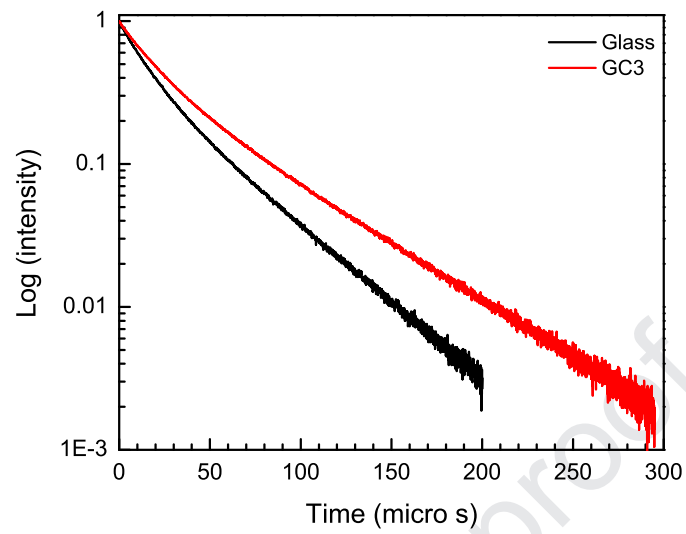
Fig. 5. Decay curves of the Yb^{3+} ions in the oxyfluoride glass (G) and glas-ceramic (GC3) exciting at 944 nm and monitoring the emission at 1020 nm, where there is shoulder in the Yb^{3+} emission.
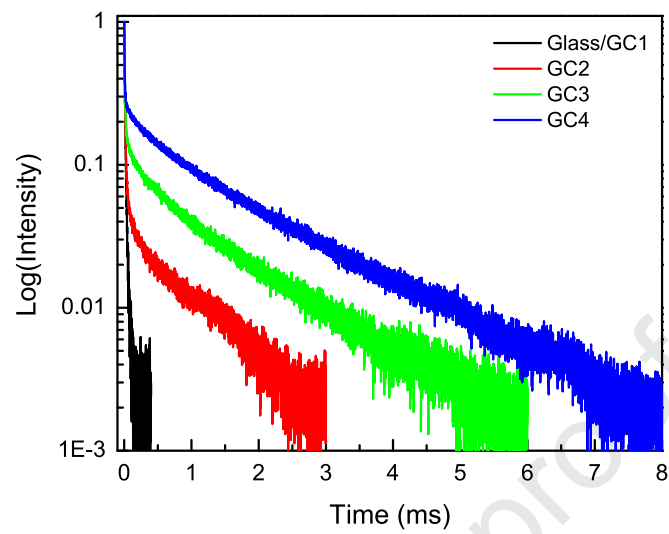
Fig. 6. Decay curves of the Ho^{3+} ion in the oxyfluoride glass (G) and glass-ceramics (GC) exciting at 473 nm and monitoring the emission at 1.2 μm.
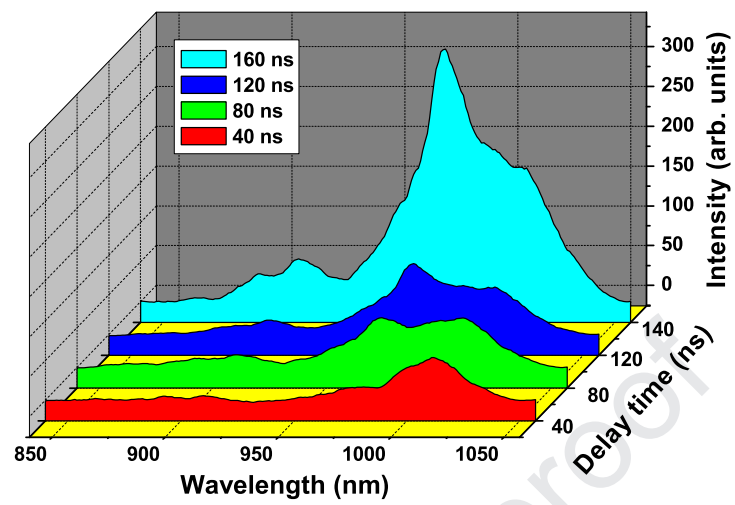
Fig. 7. Time-resolved near-infrared quantum cutting emissions of Yb^{3+} ions at different delay times after a 532 nm pulsed-laser excitation in a glass-ceramic (GC3).
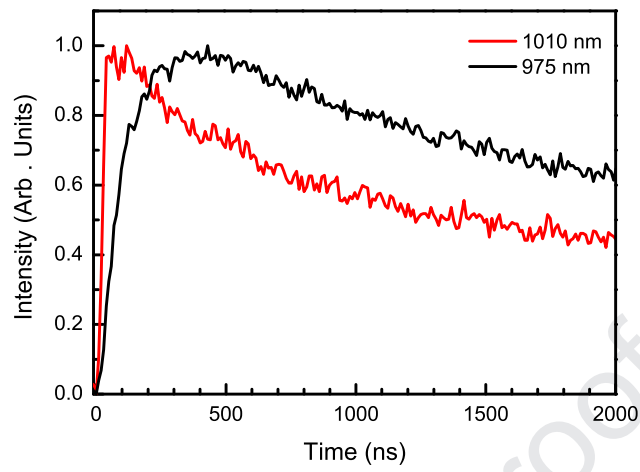
Fig. 8. Decay curves of Yb^{3+} (975 nm) and Ho^{3+} (1010 nm) ions in glass-ceramic (GC3) under 532 nm pulsed laser excitation.
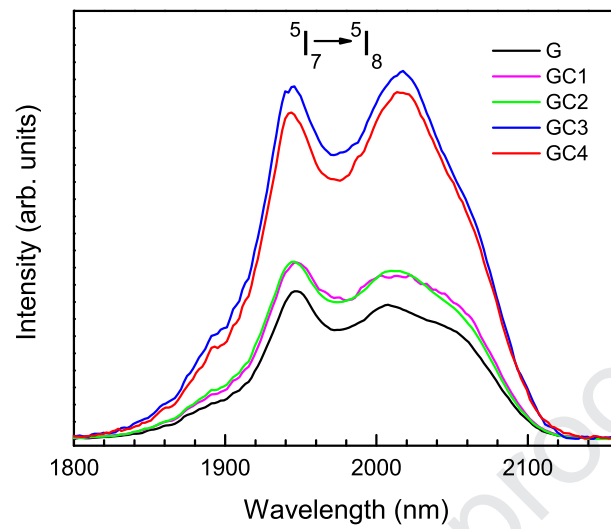
Fig. 9. Near infrared emissions of Ho^{3+} ions in the oxyfluoride glass (G) and glass-ceramics (GC) under 473 nm laser excitation.

(a)

(b)
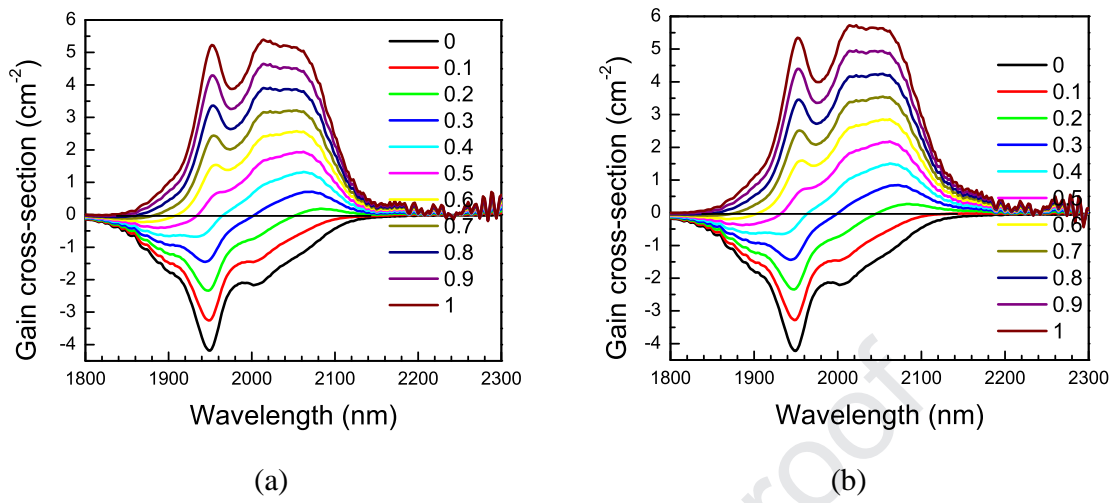
Fig. 10. Gain cross-section spectra of Ho^{3+} ion at 1950 nm in Ho^{3+}/Yb^{3+}-doped oxyfluoride (a) glass and (b) glass-ceramic (GC4).

Research Highlights:

- Ho^{3+}-Yb^{3+} co-doped oxyfluoride glass and glass-ceramics (GC) have been synthesized.

- Samples show quantum cutting (QC) and near infrared emissions under 473 nm excitation.

- Lifetime of 1.2 μm emission has been enhanced by three orders of magnitude in GC compared to precursor glass.

- 1.0 μm QC emission of Yb^{3+} ions could improve the efficiency of Si solar cells.

- 1.2 μm QC emission of Ho^{3+} ions could be useful for enhancing transmission windows of optical amplifiers.

<u>Declaration of interests</u>

The authors declare that they have no known competing financial interests or personal relationships that could have appeared to influence the work reported in this paper.

Optical Absorption and NIR Photoluminescence of Nd^{3+}-Activated Strontium Phosphate Glasses

R.N.A. PRASAD,[1] N. VIJAYA,[2] P. BABU,[3] N. KRISHNA MOHAN,[1]
and R. PRAVEENA [ID][4,5]

1.—Department of Physics, Akkineni Nageswara Rao College, Gudivada 521 301, India.
2.—Department of Physics, Sri Venkateswara University, Tirupati 517 502, India.
3.—Department of Physics, Government Degree College, Palamaner 517 408, India.
4.—Department of Physics, Gayatri Vidya Parishad College of Engineering (A), Visakhapatnam 530 048, India. 5.—e-mail: praveena@gvpce.ac.in

Strontium phosphate glasses with various concentrations of Nd$_2$O$_3$ have been prepared by melt quenching method. Absorption and photoluminescence spectra and lifetime measurements have been carried out to obtain the optical properties of these glasses. From the absorption spectrum, intensity and radiative parameters have been evaluated using Judd–Ofelt analysis. Near-infrared photoluminescence spectra consist of three bands centered at 875 nm, 1056 nm and 1327 nm, among which the highest intensity has been noticed for the band at 1056 nm that corresponds to the $^4F_{3/2} \rightarrow {}^4F_{11/2}$ transition of Nd^{3+} ion. Laser parameters such as branching ratio, band width, stimulated emission cross section and gain bandwidth for the $^4F_{3/2} \rightarrow {}^4F_{11/2}$ transition are found to be 0.52, 28 nm, 2.31 × 10^{-20} cm^2 and 6.5 × 10^{-26} cm^3, respectively. Decay curves of the $^4F_{3/2}$ level of Nd^{3+} ions exhibit a single exponential nature at lower concentrations, while they become non-exponential at higher concentrations ($\geq$ 0.1 mol.%) due to non-radiative energy transfer processes. This feature is also associated with shortening of lifetime from 307 μs to 82 μs when the Nd^{3+} ion concentration increases from 0.1 mol.% to 4.0 mol.%. The results have been compared with those of barium and magnesium phosphate glasses and commercial glasses. The results suggest that these glasses have potential applications as infrared laser materials at 1.05 μm.

Key words: Nd^{3+} ion, strontium phosphate glasses, JO parameters, NIR luminescence, laser applications

INTRODUCTION

Trivalent lanthanide (Ln^{3+}) ion-doped glasses have attracted much attention as they have potential applications in the fields of plasma display panels, photovoltaics, antibacterial activity, optical detectors, fiber grating, drug carriers, photocatalysis, lasers, fiber amplifiers, waveguides and telecommunications.[1–3] Owing to the optical properties of the Ln^{3+}-doped glasses and with the prompt evolution of the diode-pumped solid-state lasers,

investigation on newly developed laser glasses has gained more attention.[4,5] Among the various Ln^{3+} ions, Nd^{3+} ion is one of the important and most extensively studied ions for near-infrared (NIR) lasers as it emits very useful wavelengths at 880 nm, 1050 nm, 1350 nm and 1800 nm corresponding to $^4F_{3/2} \rightarrow {}^4I_{J/2}$ (J = 9, 11, 13 and 15) transitions, respectively. Out of these four transitions, the $^4F_{3/2} \rightarrow {}^4I_{11/2}$ transition at 1050 nm is the most intense one and has several practical applications. The other laser transitions at 800 nm and 1350 nm are being used in diode lasers and telecommunications, respectively.

On the other hand, petawatt (PW)-scale laser facilities based on ultrahigh-intensity lasers have

been fabricated around the world in the last few decades.[6,7] Nd^{3+}-doped glass amplifiers are being used to develop these ultrahigh-intensity lasers.[8] But the commercially available Nd^{3+}-doped silicate and phosphate[9,10] glasses and even the hybrid glass structure[11] are unable to shorten the pulse duration and enhance the peak power of the laser pulses to the required level (exawatt-level pulse or 10–15 PW in a single beam) due to their narrow emission bandwidth (around 25 nm)[12] and short fluorescence lifetime. Hence, it is important to develop the new Nd laser glasses that can give an ultra-wide emission band for constructing high-energy ultrashort pulse lasers. Therefore, selecting a suitable glass host as an active medium for the laser action is also an important criterion to achieve the desired characteristics, including minimum optical losses, high gain and high-energy storage capability. These characteristics in turn depend on the stimulated emission cross section, band width, coupling efficiency of the pump source and lifetime of the excited level.[13,14]

Of all the optical glasses, phosphate glasses have been extensively studied due to their exclusive advantages such as low melting point, low dispersion, low softening temperatures, high mechanical, thermal and electrochemical stability, high refractive index, high ionic conductivity, high solubility of Ln^{3+} ions resulting in less clustering, extensive transparency in the ultraviolet-infrared (UV-IR) spectral region, etc.[15,16] Nevertheless, the hygroscopic nature and poor chemical durability of these glasses are the drawbacks for their practical application as laser gain media. Addition of alkaline earth metals (Mg, Ca, Sr and Ba) to the phosphate glass as a network modifier leads to a disruption of the glass network and enhances the creation of non-bridging oxygen (NBO) defects.[17]

In view of the above merits, the authors systematically prepared the Nd^{3+}-doped phosphate glasses modified by BaO, MgO and SrO individually as a single modifier. Spectroscopic investigations of Nd^{3+}-doped BaO (P_2O_5-BaO-Nd_2O_3: PBN) and MgO (P_2O_5-MgO-Nd_2O_3: PMN) modified phosphate glasses have already been reported earlier[18,19] by our group. In this report, absorption and NIR photoluminescence properties of Nd^{3+}-doped SrO (P_2O_5-SrO-Nd_2O_3: PSN) modified phosphate glasses are studied, and the results obtained are compared with those of BaO- and MgO-modified glasses along with the other reported SrO-based Nd^{3+}-doped phosphate glasses as well as commercial glasses. The effect of concentration on the photoluminescence properties of these glasses has also been presented. For the past decade, phosphate glasses with two or three modifiers have been studied so far. To the best of the authors' knowledge, the photoluminescence properties of phosphate glasses with a single modifier (i.e. SrO) have not been reported so far. Therefore, the present work can provide the basis to understand the fundamentals that underlie the composition dependent luminescence properties of phosphate glasses.

EXPERIMENTAL TECHNIQUES

Nd^{3+}-doped strontium phosphate (PSN) glasses of composition $(50 - x/2)$ $P_2O_5 + (50 - x/2)$ SrO + x Nd_2O_3 (where x = 0.05 mol.%, 0.1 mol.%, 0.5 mol.%, 1.0 mol.%, 2.0 mol.%, 3.0 mol.% and 4.0 mol.%) were prepared by the melt quenching method following the procedure described in our earlier paper.[18] High-purity chemicals of strontium metaphosphate ($Sr(PO_3)_2$) and neodymium oxide (Nd_2O_3) from Sigma-Aldrich were taken as initial materials. Prepared glass samples were labeled as PSN005, PSN01, PSN05, PSN10, PSN20, PSN30 and PSN40 for 0.05 mol.%, 0.1 mol.%, 0.5 mol.%, 1.0 mol.%, 2.0 mol.%, 3.0 mol.% and 4.0 mol.% concentration of Nd_2O_3, respectively.

Refractive index was measured with an Abbe refractometer at the wavelength of 589.3 nm. Archimedes' drainage method was used to obtain the density of glass samples using distilled water. The density and concentration of Nd^{3+} ion in the PSN10 glass were found to be 3.298 g cm^{-3} and 0.2641×10^{20} ions cm^{-3}, respectively. The UV-visible-NIR absorption spectrum of the PSN10 glass was recorded on a Perkin–Elmer Lambda 950 UV/VIS/NIR spectrophotometer with a spectral resolution of ± 1 nm. An Edinburgh UV-VIS-NIR (FLS 980) spectrophotometer equipped with an 808-nm pulsed laser diode (excitation source) was used to record NIR luminescence spectra and decay curves. All these measurements were made at room temperature.

RESULTS AND DISCUSSION

The refractive index of the PSN10 glass is found to be 1.586 which is slightly lower than 1.0 mol.% of Nd_2O_3-doped BaO (PBN10) (1.598)[18] and higher than MgO-modified (PMN10) (1.581)[19] phosphate glasses. It is observed that the refractive index increases with increase in cationic radius of the network modifier element. It is also well known that the NBO with increasing polarizability can enhance the index of refraction in the glass host. Therefore, the low refractive index shows the presence of a relatively low concentration of NBOs in the present PSN10 glass compared to that of PBN10 glass.[18] Optical absorption spectrum of Nd^{3+}-doped PSN10 glass is depicted in Fig. 1. All the absorption bands fall in the visible-NIR region, whereas the absorption edge is in the ultraviolet (UV) region ($\sim$ 300 nm). No sharp absorption edge is observed, which is evidence for the glassy state. It can be seen that the Stark structure is weakly resolved in the glasses due to the inhomogeneous broadening, and hence most of the transitions often overlap in the spectrum. Upon excitation, Nd^{3+} ions are pumped from the ground state ($^4I_{9/2}$) to the different excited levels of $4f^3$–$4f^3$ electronic transitions. Eleven bands
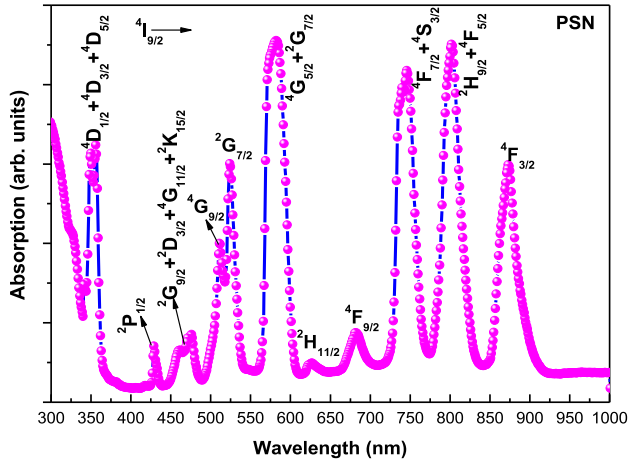
Fig. 1. Optical absorption spectrum of Nd^{3+}-doped PSN10 glass.

centered at 352 nm, 430 nm, 468 nm, 510 nm, 524 nm, 581 nm, 626 nm, 682 nm, 745 nm, 802 nm and 874 nm are observed in the absorption spectrum, which are assigned to the $^4I_{9/2} \rightarrow$ ($^4D_{1/2} + {}^4D_{3/2} + {}^4D_{5/2}$), ($^2P_{1/2} + {}^2D_{5/2}$), ($^2G_{9/2} + {}^2D_{3/2} + {}^4G_{11/2} + {}^2K_{15/2}$), $^4G_{9/2}$, $^2G_{7/2}$, ($^4G_{5/2} + {}^2G_{7/2}$), $^2H_{11/2}$, $^2F_{9/2}$, ($^4F_{7/2} + {}^4S_{3/2}$), ($^4F_{5/2} + {}^2H_{9/2}$) and $^4F_{3/2}$ transitions, respectively. The absorption spectrum is similar to those of the reported Nd^{3+} glasses,[9–12,18,19] except for small changes in their relative peak positions, intensities and broadening due to changes in the ligand field around the Nd^{3+} ions in different glass matrices. The Nd^{3+}–ligand bond influences the position of the absorption band due to the nephelauxetic effect. The nephelauxetic ratio (β) and bonding parameter (δ) are calculated using the following expressions:[20,21]

$$\beta = \frac{v_c}{v_a} \qquad (1)$$

$$\delta = \left[\frac{1 - \bar{\beta}}{\bar{\beta}} \times 100 \right] \qquad (2)$$

where 'v_c' and 'v_a' are the energies of the respective transitions in the glass system and aqua solution. The assignment of energy levels of the Nd^{3+} ions in the PSN10 glass and the aquo-ion are made using the reports of Carnall et al.[22] as these values are host-independent. The $\bar{\beta}$ is the average of all the β values of the observed transitions in the absorption spectrum. Positive or negative values of δ specify the covalent or ionic nature of the Nd^{3+}–O bond, respectively.[23] The experimental energies and δ values are given in Table I. A positive value of δ in this PSN10 glass shows that the bonding of Nd^{3+} ions with their surrounding ligand field is covalent. It is noticed that the δ value is lower compared to those of PBN10[18] and PMN10[19] glasses, indicating that Nd^{3+} ions experience relatively weak covalence in the PSN glass and that the covalence is increased in the order of PSN < PBN < PMN.

Among the absorption transitions, $^4I_{9/2} \rightarrow$ ($^4G_{5/2} + {}^2G_{7/2}$) is the most intense and is hypersensitive transition (HST). Generally, the HST is more sensitive to the chemical surroundings of the Nd^{3+} ion in the glass matrix. This transition normally has higher values of doubly reduced matrix elements and oscillator strengths compared to other transitions. Experimental oscillator strengths (f_{exp}) of various absorption transitions of Nd^{3+} ion in the PSN10 glass are evaluated by integrating each band as given in Ref. 24. Using these f_{exp} values, Judd–Ofelt (JO)[25,26] analysis has been performed for the PSN10 glass to obtain the calculated oscillator strengths (f_{cal}) and intensity parameters (Ω_λ, $\lambda = 2,4,6$) following the least square method.[24] The value of root-mean-square deviation [$\sigma(N)$] indicates the quality of the fit. The values of f_{exp}, f_{cal} and $\sigma(N)$ are given in Table I and are compared to those of PMN10[18] and PBN10[19] glasses. From Table I, it is noticed that the value of $\sigma(N)$ is $\pm 0.87 \times 10^{-6}$ which indicates that f_{exp} and f_{cal} are in good agreement. As expected, the oscillator strengths for the HST are high and it is also noticed that these are relatively higher in PBN10[18] and lower in the present PSN10 glasses, suggesting that a relatively lower nonsymmetric electric field component is acting on the Nd^{3+} ions in the PSN glass.

The obtained intensity parameters (Ω_2, Ω_4 and Ω_6) from JO analysis for the present PSN10 glass are presented in Table II along with the values of other reported Nd^{3+}-doped glasses.[18,19,27–31] Generally, intensity parameters do not vary much as a function of Nd^{3+} ion concentration. Hence, it is usual practice to calculate the intensity parameters for a 1.0 mol.% doped sample (which is the optimum concentration to obtain reasonable intensities for absorption bands of Ln^{3+} ions) and are used to evaluate radiative properties of the emitting levels of Ln^{3+} ions. It is reported that Ω_2 is more sensitive to the ligand field, and, in turn, the composition of the glass and its value is a measure of the amount of covalent bonding between Nd^{3+} ions and surrounding ligands and site symmetry as well.[32] As can be seen from Table II, it is observed that the Ω_2 value is decreasing in the order STPN[30] > PKSAN[27] > PKSAFN[27] > PKSABFN[27] > PKSFAN[28] > LG-750[31] > LHG-8[31] > LG-770[31] > LHG-80[31] > PBN[18] > PMN[19] > PCBSN[29] > PSN. It is clear that the Ω_2 value in PSN10 glass is lowest compared to those of the glass systems presented in Table II,[18,19,27–31] suggesting that there is higher symmetry at the Nd^{3+} ion site and weaker covalence of the Nd^{3+}–ligand bond. The higher symmetry at the Nd^{3+} ion site (due to the close packing of oxygen atoms around the Nd^{3+} ion) in the PSN10 glass is also evident from the lower values of oscillator strengths. The weaker Nd–O covalence in the PSN10 glass is also consistent with the result obtained from the nephelauxetic effect. Therefore, both JO theory and the nephelauxetic effect indicate that Nd^{3+} ions in the PSN10 glass experience relatively weaker covalence, and both approaches give the

Table I. Experimental energies (E_{exp}, cm^{-1}), experimental (f_{exp}) and calculated (f_{cal}) oscillator strengths ($\times 10^{-6}$) and bonding parameter (δ) of PSN10, PMN10 and PBN10 glasses

| Transition | Energy | Oscillator strengths | | | | | |
| | | PSN10 | | PMN10 | | PBN10 | |
$^4I_{9/2} \rightarrow$	E_{exp}	f_{exp}	f_{cal}	f_{exp}	f_{cal}	f_{exp}	f_{cal}
$^4F_{3/2}$	11,456	2.56	1.85	1.54	1.93	2.20	2.67
$^4F_{5/2} + {}^2H_{9/2}$	12,469	4.43	4.74	5.89	5.82	7.34	6.79
$^4F_{7/2} + {}^4S_{3/2}$	13,405	4.51	4.46	5.78	5.96	5.85	6.34
$^4F_{9/2}$	14,663	0.51	0.36	0.63	0.46	0.43	0.51
$^2H_{11/2}$	15,974	0.15	0.10	0.16	0.13	0.09	0.14
$^4G_{5/2} + {}^2G_{7/2}$	17,212	9.55	9.61	13.20	13.29	16.30	16.34
$^4G_{7/2}$	19,084	3.54	2.39	4.48	2.74	4.22	3.58
$^4G_{9/2}$	19,531	3.11	1.08	3.01	1.23	2.58	1.57
$^4G_{11/2} + {}^2D_{3/2} + {}^2G_{9/2} + {}^2K_{15/2}$	21,008	1.69	0.89	1.30	1.03	1.74	1.29
$^2P_{1/2} + {}^2D_{5/2}$	23,310	0.38	0.50	0.46	0.49	0.74	0.72
$^4D_{1/2} + {}^4D_{3/2} + {}^4D_{5/2}$	28,090	7.77	9.05	8.56	9.10	12.68	13.07
$\sigma(N)^a$ ($\times 10^{-6}$)		± 0.87 (11)		± 0.79 (11)		± 0.48 (11)	
δ		0.3714		0.6036		0.4016	

$^a\sigma(N)$ is the root mean square (r.m.s) deviation between experimental and calculated energy levels, and N is the number of levels considered in the fitting.

Table II. Comparison of JO parameters (Ω_λ, $\times 10^{-20}$ cm^2), spectroscopic quality factor (χ), radiative (τ_R, μs), experimental (τ_{exp}, μs) lifetimes, quantum efficiency (η, %), bandwidth ($\Delta\lambda_{eff}$, nm), emission cross section [$\sigma(\lambda_p)$, $\times 10^{-20}$ cm^2], gain band width [$\Delta\lambda_{eff} \times \sigma(\lambda_p)$, $\times 10^{-26}$ cm^3] in various Nd^{3+}-doped phosphate glasses

Glass	Composition	Ω_2	Ω_4	Ω_6	χ	τ_R	τ_{exp}	η	$\Delta\lambda_{eff}$	$\sigma(\lambda_p)$	$\Delta\lambda_{eff} \times \sigma(\lambda_p)$	References
PSN	P_2O_5, SrO, Nd_2O_3	1.16	3.78	3.00	1.25	451	256	57	28.2	2.31	6.5	Present work
PBN	P_2O_5, BaO, Nd_2O_3	2.62	5.47	4.24	1.29	331	180	54	24.0	2.79	6.7	18
PMN	P_2O_5, MgO, Nd_2O_3	2.55	3.74	4.12	0.91	394	232	59	25.0	3.26	8.2	19
PKSAN	P_2O_5, K_2O, SrO, Al_2O_3, Nd_2O_3	6.74	3.86	6.35	0.61	319	172	54	27.95	4.05	11.3	27
PKSFAN	P_2O_5, K_2O, SrO, SrF, Al_2O_3, Nd_2O_3	5.24	4.30	5.81	0.74	326	211	65	32.6	3.29	10.7	28
PKSAFN	P_2O_5, K_2O, SrO, Al_2O_3, Al_2F_3, Nd_2O_3	6.63	5.07	5.98	0.85	290	188	65	23.7	5.08	12.0	27
PKSABFN	P_2O_5, K_2O, SrO, Al_2O_3, BaF, Nd_2O_3	6.50	4.64	5.99	0.77	306	194	63	23.5	4.72	11.1	27
PCBSN	P_2O_5, CaO, BaO, SrO, Nd_2O_3	2.17	2.46	3.07	0.80	354	284	80	27.5	3.90	10.7	29
STPN	SrO, TiO_2, P_2O_5, Nd_2O_3	7.75	4.74	6.05	0.78	282	238	84	26.0	4.89	12.7	30
LHG-80	–	3.6	5.0	5.5	0.91	326	–	–	23.9	4.20	10.0	31
LHG-8	P_2O_5, Al_2O_3, K_2O, BaO	4.4	5.1	5.6	0.91	351	–	–	26.5	3.60	9.5	31
LG-770	P_2O_5, Al_2O_3, K_2O, MgO	4.3	5.0	5.6	0.89	349	–	–	25.4	3.90	9.9	31
LG-750	P_2O_5, Al_2O_3, K_2O, BaO	4.6	4.8	5.6	0.86	367	–	–	25.3	3.70	9.3	31

same conclusion. Chanthima et al.[33] also observed that the asymmetric nature around the Ln^{3+} ion is more in MgO-modified phosphate glass than that of the SrO-modified glass. Further, from Table II, it is also observed that with the addition of K_2O, Al_2O_3,[27]

fluorine content[27,28] and TiO_2[30] to the phosphate glasses, the covalence of the Nd–O bond increases drastically.

It is also well known that Ω_4 depends on the long-range effects and is related to the bulk properties of

glass, and Ω_6 is related to the rigidity of the glass host, which are influenced by the vibronic transitions of the Ln^{3+} ions bound to the ligand atoms. As can be seen from Table II, the Ω_6 value is found to be lowest in the PSN10 glass compared to those of the other reported glasses, indicating that PSN glass has a less rigid nature. Generally, in the case of Nd^{3+} ions, a higher value of Ω_4 parameter favors an intense $^4F_{3/2} \rightarrow {}^4I_{9/2}$ transition, while the Ω_6 parameter improves intensity of the $^4F_{3/2} \rightarrow {}^4I_{11/2}$ transition. In fact, the ratio of Ω_4/Ω_6, called spectroscopic quality factor (χ), is a very important parameter, and it provides the information about the means through which $^4F_{3/2}$ level of Nd^{3+} ion can relax to the ground state. In order to get the highest luminescence for $^4F_{3/2} \rightarrow {}^4I_{11/2}$ transition, Ω_6 should be slightly greater than Ω_4. In the PSN10 glass, the χ value is found to be 1.25 which falls within the normal range of 0.2–1.5. As can be seen from Table II, $\Omega_6 > \Omega_4$ for all the reported glasses, except for PSN10 and PBN10[18] glasses; consequently, the χ value is greater than that for the PSN10 and PBN10 glasses. This result is similar to those found in borate,[34] LiPbAlB,[35] Nb1,[36] tellurite,[37] fluorophosphate[38] and ZBSN4[39] glasses. Hence, in these glasses, the $^4F_{3/2} \rightarrow {}^4I_{9/2}$ transition also plays an important role in relaxing the $^4F_{3/2}$ level. Moreover, this high-intensity laser at 875 nm corresponding to the $^4F_{3/2} \rightarrow {}^4I_{9/2}$ transition is also useful to produce blue light-emitting devices by the monolithic integration of laser emission.[40]

Further, the JO intensity parameters (Ω_λ) are used to evaluate the radiative properties like radiative transition probability (A_R), branching ratio (β_R) and radiative lifetime (τ_R) for the $^4F_{3/2} \rightarrow {}^4I_{9/2,11/2,13/2}$ transitions of Nd^{3+} ion in the PSN10 glass. Radiative lifetime for the $^4F_{3/2}$ level of Nd^{3+} ion in the PSN10 glass is found to be 451 μs which is the highest value compared to those of the other reported glasses presented in Table II. This indicates that the excited level slowly depopulates in the PSN10 glass, which favors the population inversion and, consequently, stimulated emission.

NIR luminescence spectra of PSN glasses were obtained by exciting the samples with an 808-nm laser and are shown in Fig. 2. A partial energy level diagram of the Nd^{3+} ions is shown in Fig. 3 which explains the mechanism involved in NIR luminescence in the Nd^{3+}-doped PSN glasses. When excited at 808 nm, initially, the Nd^{3+} ions were pumped to the $^4F_{9/2}$ level, from which they made fast non-radiative transition and reached a $^4F_{3/2}$ metastable state, as shown in Fig. 3. Thereafter, they made radiative transitions to lower-lying energy levels whose wavelength lies in NIR region. NIR luminescence spectra consisting of three bands at 875 nm, 1056 nm and 1327 nm correspond to the $^4F_{3/2} \rightarrow {}^4I_{J/2}$ ($J = 9$, 11 and 13) transitions, respectively. Among them, the $^4F_{3/2} \rightarrow {}^4I_{11/2}$ transition at 1056 nm is the most intense and prominent one which has many practical applications as a four-
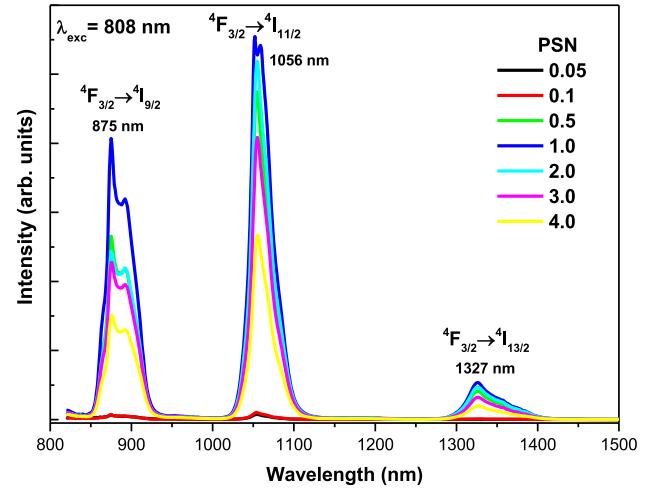
Fig. 2. NIR luminescence spectra of Nd^{3+}-doped PSN glasses under 808-nm excitation.
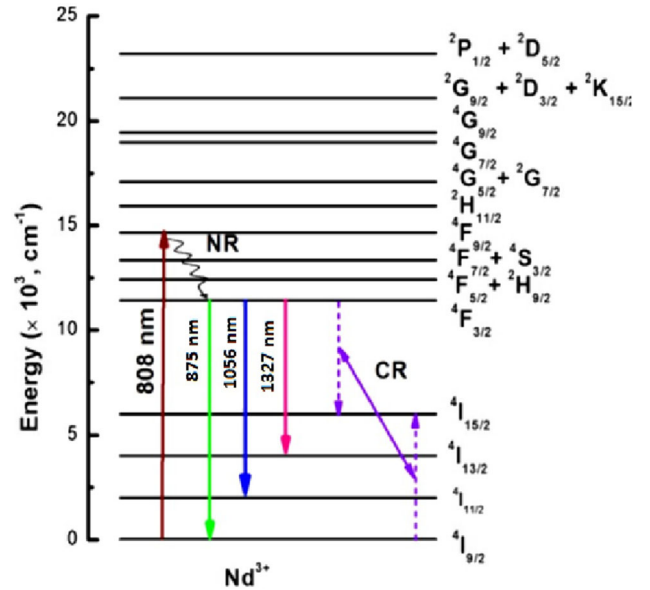
Fig. 3. Partial energy level diagram of Nd^{3+} ions in PSN glasses.

level laser system. The emission band at 875 nm split into two bands, which describes the specificity of the glass host. Intensities of all three transitions with respect to Nd^{3+} ion concentration are depicted in Fig. 4a. As can be seen, at very low concentrations (from 0.05 mol.% to 0.1 mol.%), no change is observed in the intensity, but the intensities of all three transitions increase rapidly from 0.1 mol.% to 1.0 mol.% and then decreases with increase in concentration. This luminescence quenching behavior at higher concentrations above 1.0 mol.% is due to the enhanced energy transfer between the neighboring Nd^{3+} ions via cross-relaxation channels, through $^4F_{3/2} + {}^4I_{9/2} \rightarrow {}^4I_{15/2} + {}^4I_{15/2}$ (Fig. 3).[41] Therefore, 1.0 mol.% is the optimum concentration in the present Nd^{3+}: PSN glasses. Further, the
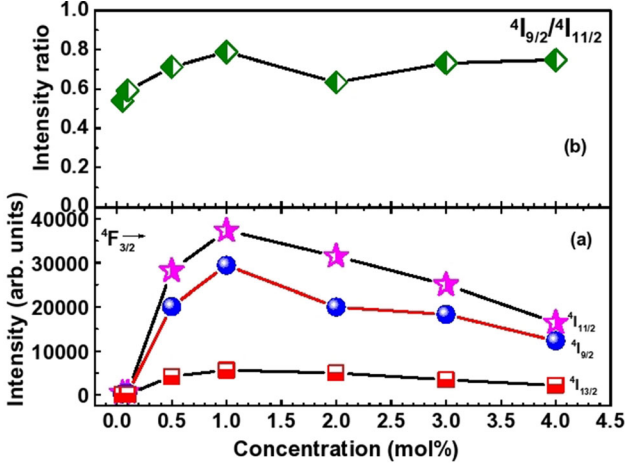
Fig. 4. (a) Variation of peak intensity of $^4F_{3/2} \rightarrow \, ^4I_{9/2}$, $^4I_{11/2}$ and $^4I_{13/2}$ transitions and (b) relative intensity ratio of $^4F_{3/2} \rightarrow \, ^4I_{9/2}/^4F_{3/2} \rightarrow \, ^4I_{11/2}$ transitions in Nd^{3+}-doped PSN glasses as a function of concentration.

Fig. 5. Bandwidth (nm) in various Nd^{3+}-doped phosphate glasses.

Table III. Emission peak position (λ_p, nm), effective bandwidth ($\Delta\lambda_{eff}$, nm), radiative transition probability (A_R, s^{-1}), peak stimulated emission cross section ($\sigma(\lambda_p)$, $\times 10^{-20}$ cm^2) and experimental and calculated branching ratios (β_R) for $^4F_{3/2} \rightarrow \, ^4I_J$ (J = 9/2, 11/2 and 13/2) transitions in PSN10 glass

Transition $^4F_{3/2} \rightarrow$	λ_p	$\Delta\lambda_{eff}$	A_R	$\sigma(\lambda_p)$	β_R Exp.	β_R Cal.
$^4I_{9/2}$	875	36.26	1012	0.86	0.40	0.46
$^4I_{11/2}$	1056	28.21	1010	2.31	0.52	0.46
$^4I_{13/2}$	1327	46.74	182	0.63	0.08	0.08

relative intensity ratio of $^4F_{3/2} \rightarrow \, ^4I_{9/2}/^4F_{3/2} \rightarrow \, ^4I_{11/2}$ transitions is also high at 1.0 mol.% concentration of Nd^{3+} ions, as shown in Fig. 4b.

From the NIR luminescence spectra, effective bandwidth ($\Delta\lambda_{eff}$, nm), radiative transition probability (A_R, s^{-1}), peak stimulated emission cross section [$\sigma(\lambda_p)$, $\times 10^{-20}$ cm^2] and experimental branching ratio (β_R) for $^4F_{3/2} \rightarrow \, ^4I_{J/2}$ (J = 9, 11 and 13) transitions in PSN10 glass are evaluated and are given in Table III. As can be seen, radiative transition probabilities for both $^4F_{3/2} \rightarrow \, ^4I_{9/2}$ and $^4I_{11/2}$ transitions are more or less similar, which indicates that the $^4F_{3/2} \rightarrow \, ^4I_{9/2}$ transition is competing with the $^4F_{3/2} \rightarrow \, ^4I_{11/2}$ transition in the PSN10 glasses, as discussed above. Another essential parameter that characterizes the power of the laser transition is the branching ratio. In Table III, the experimental β_R values are obtained from the ratio of area under the corresponding emission band and total integrated area of all the emission bands (Fig. 2), while the calculated β_R values are obtained from the JO analysis. It is noticed that the

experimental and calculated β_R values are in good agreement. It is observed from the literature that the β_R values for $^4I_{9/2,11/2,13/2}$ levels of Nd^{3+} ion in many glasses[42–44] are approximately in the ratio of 35:55:10, respectively. In the present case, calculated β_R values are in the ratio of 46:46:8 (Table III) as observed in the case of lanthanum sodium zinc tellurite glass.[45] This is also evident from the values of χ and A_R. However, experimental β_R values are in the ratio of 40:52:8 indicating that the $^4F_{3/2} \rightarrow \, ^4I_{11/2}$ transition of Nd^{3+} ion in PSN glass is dominant and is more efficient laser transition than the other two transitions. Furthermore, experimental β_R values (hence the intensity of emission bands) varied marginally in the PBN10,[18] PMN10[19] and PSN10 glasses. However, the β_R value for $^4F_{3/2} \rightarrow \, ^4I_{9/2}$ transition is slightly decreased in the order of PMN > PSN > PBN, while it is increased in the order of PMN < PSN < PBN for the $^4F_{3/2} \rightarrow \, ^4I_{11/2}$ transition of Nd^{3+} ion. This trend indicates that with increasing cationic radius of the network modifier ions ($Mg^{2+} < Sr^{2+} < Ba^{2+}$), the intensity of $^4F_{3/2} \rightarrow \, ^4I_{11/2}$ transition increases. This may be due to greater depolymerization of BaO network modifier oxide.[46]

A low value of $\Delta\lambda_{eff}$ and high value of $\sigma(\lambda_p)$ are preferable for an efficient laser transition. In the present case, lower $\Delta\lambda_{eff}$ and higher $\sigma(\lambda_p)$ values for the $^4F_{3/2} \rightarrow \, ^4I_{11/2}$ transition of Nd^{3+} ion in PSN10 glass compared to other two transitions infers that $^4F_{3/2} \rightarrow \, ^4I_{11/2}$ transition is a sharp and efficient laser transition. Therefore, based on the above observations, the potential laser transition at 1056 nm in the Nd^{3+}-doped PSN glass can be used for low-threshold and high-gain applications. The $\Delta\lambda_{eff}$ and $\sigma(\lambda_p)$ values for $^4F_{3/2} \rightarrow \, ^4I_{11/2}$ transition of Nd^{3+} ion in PSN10 glass are compared with those reported for the other glasses[18,19,27–31] in Table II. But for the high-energy ultrashort pulse lasers, high radiative lifetime and emission bandwidth values are required. It is observed that the value
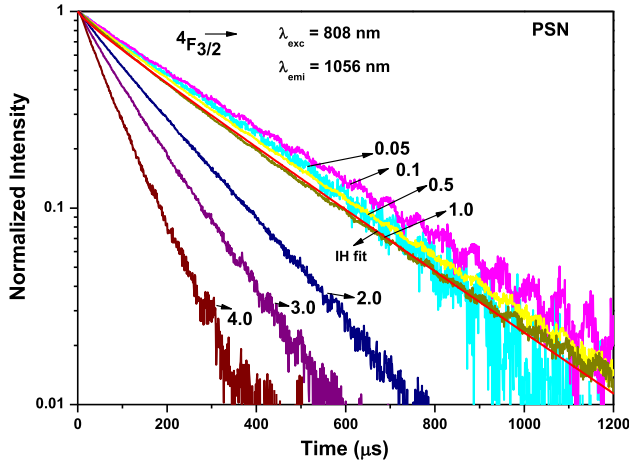
Fig. 6. Decay curves of the $^4F_{3/2}$ level for different concentrations of Nd³⁺ ions in PSN glasses under 808-nm excitation, monitoring the emission at 1056 nm. Inokuti–Hirayama (IH) model fit for 1.0 mol.% decay curve is also shown.

of $\Delta\lambda_{\text{eff}}$ is slightly higher in the PSN glass compared to those of other glasses, including commercial glasses except for PKSFAN glass[28] (see Fig. 5). Hence, based on the higher radiative lifetime and emission bandwidth values, the present PSN glasses doped with Nd³⁺ ions can find application as high-energy ultrashort pulse laser material. However, the value of $\sigma(\lambda_p)$ for the $^4F_{3/2} \rightarrow {}^4I_{11/2}$ transition is found to be lowest in the PSN glass compared to those of other glasses listed in Table II. This could be due to the slightly higher value of $\Delta\lambda_{\text{eff}}$ in the PSN glass. However, the magnitude of $\sigma(\lambda_p)$ is found to be higher in the PSN glass than that of barium fluorophosphate,[47] phosphate,[48] LG-650,[48] L-41,[48] lead fluorosilicate[49] and NaF-Na₂O-B₂O₃[50] glasses, indicating the importance of PSN glass as a potential laser host material. Further, the product of $\Delta\lambda_{\text{eff}} \times \sigma(\lambda_p)$, known as gain bandwidth, is an essential parameter for the design of optical amplifiers. The gain bandwidth is found to be 6.5×10^{-26} cm³ for the $^4F_{3/2} \rightarrow {}^4I_{11/2}$ transition of Nd³⁺ ion in the present PSN10 glass. The gain bandwidth is increasing in the order of PSN < PBN < PMN glasses. Further, it is observed that addition of TiO₂, K₂O, Al₂O₃ and AlF₃ modifiers[27–30] to the strontium phosphate glass greatly enhances the gain bandwidth. Therefore, the present glass forms the basis to understand the modifier effect on the gain bandwidth which will help to improve the function of optical amplifiers. The gain band width value is higher in PSN10 glass than those reported for bismuth borate,[51] fluoroborate[52] and zinc phosphate[53] glasses, indicating that the present PSN glasses can also find application in optical amplifiers.

In order to get more quantitative information on luminescence quenching behavior, the decay curves for the $^4F_{3/2}$ level of Nd³⁺ ion in PSN glasses are measured. Figure 6 shows the decay curves of the $^4F_{3/2} \rightarrow {}^4I_{11/2}$ transition under 808-nm excitation.

As can be seen, the decay curves are single exponential at lower concentrations up to 0.1 mol.% and turn into non-exponential for higher concentrations of Nd³⁺ ions. The non-exponential decay curves are well fitted to the expression[54] (see the supplementary Figures S1 to S6):

$$I(t) = A_1 \exp\left(-\frac{t}{\tau_1}\right) + A_2 \exp\left(-\frac{t}{\tau_2}\right) \qquad (3)$$

where A_1 and A_2 are constants; τ_1 and τ_2 are extracted from the fitted curves which represent the fast and slow components of decay and are attributed to the radiative and the migration stages of emission, respectively. Therefore, the experimental (τ_{exp}) or average (τ_{avg}) lifetimes of the $^4F_{3/2}$ level in these glasses are computed by using the following expression and are presented in Table IV.

$$\tau_{\text{avg}} = \frac{A_1 \tau_1^2 + A_2 \tau_2^2}{A_1 \tau_1 + A_2 \tau_2} \qquad (4)$$

As can be seen from Table IV, the experimental lifetimes of the $^4F_{3/2}$ level initially increases from 0.05 mol.% to 0.1 mol.% of Nd³⁺ ions and then decreases for higher concentrations. This initial rise and then fall in lifetimes with increasing concentration was also observed for tellurite[55] and PKBA[56] glasses. This could be due to either radiative trapping[55] or differential site occupancy. Variations in the ligand fields around the Nd³⁺ ion may give raise to differences in the lifetimes. The shortening of lifetimes at higher concentrations could be due to the concentration quenching between Nd³⁺ ions. The τ_{exp} values of PSN glasses are compared with those of PBN[18] and PMN[19] glasses and are given in Table IV and shown in Fig. 7. It is also noticed that with increasing concentration, the lifetime values are relatively slowly decreasing in PSN glass compared to those of PBN[18] and PMN[19] glasses. This could be due to the higher symmetry and weaker covalence experienced by the Nd³⁺ ion in the PSN glass compared to PMN and PBN glasses. The τ_{exp} value is found to be higher in PSN10 glass compared to those of other glasses shown in Table II except for PCBSN.[29] It is observed that addition of K₂O, Al₂O₃ and fluorine content[27,28] may lower the lifetime, while CaO + BaO[29] and TiO₂[30] may enhance the lifetime in the SrO-based phosphate glasses.

On the other hand, in PSN10 glass, considerable variation between τ_{exp} and τ_R for the $^4F_{3/2}$ level has been observed, which emphasizes that some non-radiative energy transfer processes (W_{nr}) are involved. W_{nr} values in the PSN glasses are presented in Table IV, which are evaluated using the following expression:

$$W_{\text{nr}} = \left(\frac{1}{\tau_{\text{exp}}} - \frac{1}{\tau_R}\right) \qquad (5)$$

Table IV. Lifetime (τ_{exp}, μs), non-radiative energy transfer rate (W_{nr}, μs^{-1}), quantum efficiency (η, %), energy transfer parameter (Q), critical distance (R_o, A°) and donor–acceptor interaction parameter (C_{DA}, × 10^{-40} cm^6 s^{-1}) of Nd^{3+}-doped PSN glasses

Concentration		τ_{exp}							
(mol.%)	(ions cc^{-1})	PSN	PMN	PBN	W_{nr}	η (%)	Q	R_o	C_{DA}
0.05	0.069	273	346	260	1.652	61	–	–	–
0.1	0.147	307	315	235	1.469	68	0.047	7.55	6.03
0.5	0.682	282	300	224	1.599	63	0.157	6.78	3.16
1.0	1.306	256	232	180	1.762	57	0.250	6.38	2.20
2.0	2.597	167	170	151	2.701	37	0.701	7.14	4.32
3.0	3.964	124	–	88	3.637	27	1.087	7.18	4.46
4.0	5.366	82	57	74	5.500	18	1.650	7.46	5.61
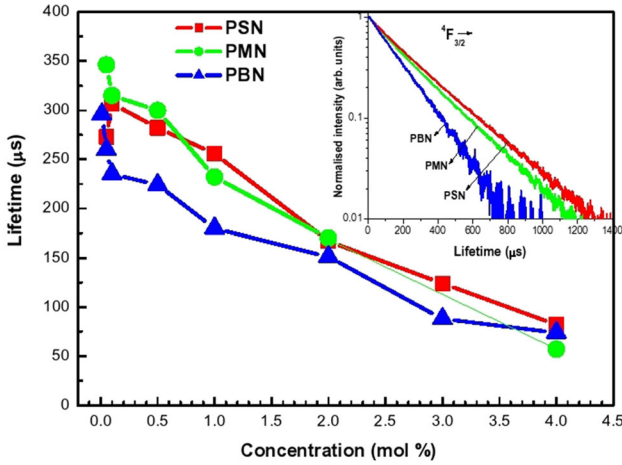
Fig. 7. Variation of lifetime (τ_{exp}) of the $^4F_{3/2}$ level of Nd^{3+} ion in PSN, PMN and PBN glasses. The inset shows the decay profiles of Nd^{3+} ion in PSN10, PMN10 and PBN10 glasses.

As can be seen from Table IV, W_{nr} values are increasing consistently with increase in concentration of Nd^{3+} ions after 0.1 mol.%. It is well known that there are four decay processes, namely multiphonon relaxation (MPR), concentration quenching, energy transfer and presence of OH content, which are responsible for the observed decrease of lifetime through non-radiative energy transfer. It is observed from the literature that the phonon energy of phosphate glass is around 1300 cm^{-1}[57], and, hence, four to five phonons are required to overcome the gap between the $^4F_{3/2}$ level and its lower $^4I_{15/2}$ level ($\sim$ 5250 cm^{-1}). Hence, MPR is one of the processes that contributes to the decrease of lifetime in the present PSN glasses. Concentration quenching is mainly due to the increase in Nd^{3+} ion concentration, which involves two mechanisms: The first one is due to the cross-relaxation where the donor (which is in an excited state) and nearby acceptor (which is in a ground state) exchange energy, and the second one is due to the energy migration between donor to donor and then to traps.

In the present case, the former is playing a dominant role and is evident from the decrease of emission intensities with increasing concentration. Finally, the non-exponential behavior of the decay curves represents the presence of energy transfer. In order to explain the type of energy transfer mechanism, the decay curves are analyzed in the framework of the Inokuti–Hirayama (IH) model following the same procedure given in Ref. 58. The non-exponential decay curves are well-fitted to the IH model for $S = 6$, which confirms the nature of interaction between Nd^{3+} ions is dipole–dipole. The IH fit for the decay curve of 1.0 mol.% is included in Fig. 6. The calculated energy transfer parameter (Q), critical distance (R_o) and donor-to-acceptor energy transfer interaction parameter (C_{DA}) are given in Table IV, which are important to assess the strength of the interaction between donor and acceptor. Generally, with increase in R_o value, Q and C_{DA} parameters will increase. As can be seen from Table IV, the Q value is increasing consistently with increase in Nd^{3+} ion concentration, while the values of R_o and C_{DA} decrease initially up to 2.0 mol.% and then increase for higher concentrations.

Further, in order to determine whether the concentration quenching of lifetime of the $^4I_{15/2}$ level of Nd^{3+} ions in the present PSN glasses is due to a diffusion-limited or fast diffusion process, the decay curves have been analyzed based on the theory developed by Auzel et al.[59,60] The diffusion-limited process represents strong self-quenching,[59] whereas the fast diffusion process represents weak self-quenching[60] between Nd^{3+} ions in the glass host. According to Auzel's theory, for electric dipole–dipole interaction, the self-quenching by a diffusion-limited process can be calculated using the expression[59]

$$\tau(N) = \frac{\tau_0}{1 + \frac{9}{2\pi}\left(\frac{N}{N_0}\right)^2} \tag{6}$$

and self-quenching by fast diffusion can be calculated by the expression[60]
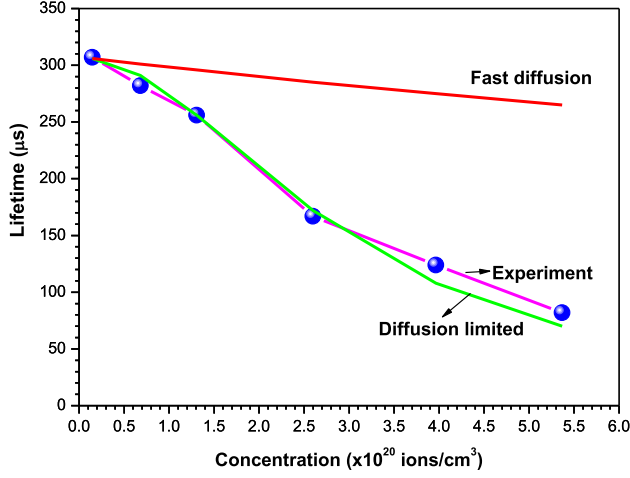
Fig. 8. Quenching of lifetime of the $^4F_{3/2}$ level as a function of of Nd^{3+} ion concentration in PSN glasses along with the simulated curves using Eqs. 6 and 7.

$$\tau(N) = \frac{\tau_0}{1 + 1.45 \frac{N}{N_c} e^{-\frac{\beta \Delta E}{4}}} \qquad (7)$$

where N is the concentration of Nd^{3+} ion, τ_o is the experimental lifetime at very low concentration, N_o is the critical sensitizer concentration for self-quenching, N_c is the critical concentration for the diffusion step between active ions, β is the exponential parameter for multiphonon-assisted energy transfers in the considered host and ΔE is the energy gap between the $^4F_{9/2}$ and $^4I_{15/2}$ levels of the Nd^{3+} ion.

In the present study, N_c was taken to be equal to N_o (3.5×10^{20} ions/c.c.), which is calculated from the Eq. 6 for 1.0 mol.% of Nd^{3+} ions by taking $\tau_o = 307$ μs (experimental lifetime of 0.1 mol.% Nd^{3+}-doped glass). The β value (2.0×10^{-3} cm) was calculated from the equations given in Ref. 61, by taking the values of phonon energy as 1300 cm^{-1}[57,58] and the electron phonon coupling constant (g) as 0.054.[57] By substituting the appropriate values, Eqs. 6 and 7 are used to simulate the lifetimes of the $^4F_{3/2}$ level for different Nd^{3+} ion concentrations in the PSN glasses. The results are depicted in Fig. 8. As can be seen from Fig. 8, it is understood that the concentration quenching in the present PSN glasses is purely diffusion-limited up to 2.0 mol.% and then slightly deviated towards fast diffusion for higher Nd^{3+} ion concentrations. This indicates a gradual decrease of the diffusion-limited process and onset of the fast diffusion processes at higher Nd^{3+} ion concentration in the PSN glasses.

Quantum efficiency (η, %) can be known from the ratio of experimental and calculated lifetimes ($= \tau_{exp}/\tau_R$) which gives the conversion efficiency in laser performance as it is equal to the ratio of number of emitted photons to the number of absorbed photons. The values of η calculated using the above relation are given in Table IV. It is noticed that the magnitude of η is decreasing as a function of concentration. The η value is found to be lower in the present PSN10 glass than those of glasses that are compared in Table II but higher than those of tellurite,[62] bismuth borate,[51,63] fluoroborate,[52] fluorophosphate,[38] lead borate,[64] BiZNd[65] and borate sodium[66] glasses. Finally, the important laser parameter, figure of merit (FOM), defined as the product of $\sigma(\lambda_p) \times \tau_{exp}$, is proportional to the slope efficiency and inversely proportional to the threshold pump power. Hence, a higher value of FOM is required to achieve high gain for a laser material. FOM values vary in the order of PBN (9.23×10^{-24} cm^2 s) $<$ PSN (10.42×10^{-24} cm^2 s) $<$ PMN (12.84×10^{-24} cm^2 s). The FOM value is found to be increasing with decrease in the cationic radius of the network modifier.

CONCLUSIONS

Nd^{3+}-doped strontium phosphate glasses with different concentrations have been prepared by melt quenching method. Absorption and NIR luminescence spectra and lifetime measurements are made to characterize these glasses. JO analysis has been carried out on the 1.0 mol.% of Nd^{3+}-doped PSN glass to derive intensity parameters and in turn to determine radiative properties. Both JO and nephelauxetic parameters show that Nd^{3+} ions experience higher symmetry and weaker covalence in the PSN10 glass. The spectroscopic quality factor is found to lie within the normal range. The values of χ, calculated β_R and A_R reveal that $^4F_{3/2} \rightarrow {}^4I_{9/2}$ transition is competing with the $^4F_{3/2} \rightarrow {}^4I_{11/2}$ transition of Nd^{3+} ion in the PSN10 glass. A higher value of τ_R for the $^4F_{3/2} \rightarrow {}^4I_{11/2}$ transition indicates that the excited level of Nd^{3+} ion slowly depopulates in the PSN10 glass that favors the population inversion.

The NIR luminescence spectra consist of three bands in which the $^4F_{3/2} \rightarrow {}^4I_{11/2}$ transition at 1056 nm is the most intense one. Luminescence intensity is found to be higher for the 1.0 mol.% Nd^{3+}-doped PSN glass. Higher values of experimental β_R ($> 50\%$) and $\sigma(\lambda_p)$ and lower value of $\Delta\lambda_{eff}$ for the $^4F_{3/2} \rightarrow {}^4I_{11/2}$ transition compared to other two transitions infer that the $^4F_{3/2} \rightarrow {}^4I_{11/2}$ transition of Nd^{3+} ion in PSN10 glass is a sharp and efficient laser transition. The value of $\Delta\lambda_{eff}$ of the $^4F_{3/2} \rightarrow {}^4I_{11/2}$ transition is relatively higher compared to all strontium-based phosphate glasses and also commercial glasses, suggesting the possible application of the present glass in high-energy ultrashort pulse generation. Decay profiles are single exponential at lower concentration and then become non-exponential at higher concentrations accompanied by a decrease in lifetimes. Non-exponential decay curves are analyzed using the IH model, which infers that the energy transfer between Nd^{3+} ions is of a dipole–dipole type. Diffusion-limited processes are responsible for the observed decrease in the lifetimes of the $^4F_{3/2}$ level of Nd^{3+} ion in PSN

glass. Higher values of the FOM show better potential of PSN glasses for NIR laser applications.

ACKNOWLEDGMENTS

CONFLICT OF INTEREST

The authors declare that they have no conflict of interest.

ELECTRONIC SUPPLEMENTARY MATERIAL

The online version of this article (https://doi.org/ 10.1007/s11664-020-08383-5) contains supplementary material, which is available to authorized users.

REFERENCES

1. A.A. Menazea, A.M. Abdelghany, N.A. Hakeem, W.H. Osman, and F.H. Abd El-Kader, *J. Electron. Mater.* 49, 826 (2020).
2. S. Gopi, P. Remya Mohan, E. Sreeja, N.V. Unnikrishnan, C. Joseph, and P.R. Biju, *J. Electron. Mater.* 48, 4300 (2019).
3. D. Van Hau, D.T.T. Nhan, N. Van Duc, V.P. Tuyen, T.-D. Nguyen, T. Thai Hoa, and N. Duc Cuong, *J. Electron. Mater.* 48, 329 (2019).
4. M.M. Ismail, I.K. Batisha, L. Zur, A. Chiasera, M. Ferrari, and A. Lukowiak, *Opt. Mater.* 99, 109591 (2020).
5. M. Soharab, I. Bhaumik, R. Bhatt, A. Saxena, S. Khan, and A.K. Karnal, *Opt. Mater.* 92, 379 (2019).
6. C. Danson, D. Hillier, N. Hopps, and D. Neely, *High Power Laser Sci. Eng.* 3, e3 (2015).
7. V. Bagnoud and F. Wagner, *High Power Laser Sci. Eng.* 4, e39 (2016).
8. A.A. Kuzmin, E.A. Khazanov, and A.A. Shaykin, *Opt. Express* 19, 14223 (2011).
9. D.F. de Sousa, L.A.O. Nunes, J.H. Rohling, and M.L. Baesso, *Appl. Phys. B Lasers Opt.* 77, 59 (2003).
10. L. Hu, D. He, H. Chen, X. Wang, T. Meng, L. Wen, J. Hu, Y. Xu, S. Li, Y. Chen, W. Chen, S. Chen, J. Tang, and B. Wang, *Opt. Mater.* 63, 213 (2017).
11. G.R. Hays, E.W. Gaul, M.D. Martinez, and T. Ditmire, *Appl. Opt.* 46, 4813 (2007).
12. J.P. Zou, C. Le Blanc, D.N. Papadopoulos, G. Chériaux, P. Georges, G. Mennerat, F. Druon, L. Lecherbourg, A. Pellegrina, P. Ramirez, F. Giambruno, A. Fréneaux, F. Leconte, D. Badarau, J.M. Boudenne, D. Fournet, T. Valloton, J.L. Paillard, J.L. Veray, M. Pina, P. Monot, J.P. Chambaret, P. Martin, F. Mathieu, P. Audebert, and F. Amiranoff, *High Power Laser Sci. Eng.* 3, e2 (2015).
13. S. Surendra Babu, R. Rajeswari, K. Jang, E.J. Cho, K.H. Jang, H.J. Seo, and C.K. Jayasankar, *J. Lumin.* 130, 1021 (2010).
14. C. Tian, X. Chen, and Y. Shuibao, *Solid State Sci.* 48, 171 (2015).
15. R.O. Omrani, S. Krimi, J.J. Videau, I. Khattech, A. El Jazouli, and M. Jemal, *J. Non Cryst. Solids* 390, 5 (2014).
16. A. Jha, B. Richards, G. Jose, T.T. Fernandez, P. Joshi, X. Jiang, and J. Lousteau, *Prog. Mater. Sci.* 57, 1426 (2012).
17. W. Vogel, *Glass Chemistry* (Berlin: Springer, 1994).
18. P. Ravi, N. Vijaya, and N. Krishna Mohan, *Int. J. Sci. Res. Phys. Appl. Sci.* 6, 45 (2018).
19. R.N.A. Prasad, R. Praveena, N. Vijaya, P. Babu, and N. KrishnaMo han, *Mater. Res. Express* 6, 096204 (2019).
20. C.K. Jorgensen, *Orbitals in Atoms and Molecules* (London: Academic Press, 1962).
21. S.P. Sinha, *Complexes of the Rare Earths* (Oxford: Pergamon, 1966).
22. W.T. Carnall, P.R. Fields, and K. Rajnak, *J. Chem. Phys.* 49, 4424 (1968).
23. E. Rukmini and C.K. Jayasankar, *Phys. B* 212, 167 (1995).
24. R. Praveena, R. Vijaya, and C.K. Jayasankar, *Spectrochim. Acta A* 70, 577 (2008).
25. B.R. Judd, *Phys. Rev.* 127, 750 (1962).
26. G.S. Ofelt, *J. Chem. Phys.* 37, 511 (1962).
27. K. Upendra Kumar, P. Babu, K.H. Jang, H.J. Seo, C.K. Jayasankar, and A.S. Joshi, *J. Alloys Compd.* 458, 509 (2008).
28. R. Vijaya, V. Venkatramu, P. Babu, L. Rama Moorthy, and C.K. Jayasankar, *Mater. Chem. Phys.* 117, 131 (2009).
29. Z. Mazurak, M. Czaja, R. Lisiecki, and A. Meijerink, *J. Mater. Sci. Eng. Adv. Technol.* 5, 1 (2012).
30. D.V.R. Murthy, T. Sasikala, B.C. Jamalaiah, A.M. Babu, J.S. Kumar, M. Jayasimhadri, and L.R. Moorthy, *Opt. Commun.* 284, 603 (2011).
31. J.H. Campbell and T.I. Suratwala, *J. Non Cryst. Solids* 263, 318 (2000).
32. C.K. Jorgensen and R. Reisfeld, *J. Less Common Met.* 93, 107 (1983).
33. N. Chanthima, Y. Tariwong, T. Sareein, J. Kaewkhao, and N.W. Sangwaranatee, *Appl. Mech. Mater.* 879, 27 (2018).
34. E.W.J.L. Omen and A.M.A. Van Dungeon, *J. Non Cryst. Solids* 111, 205 (1989).
35. N. Deopa, A.S. Rao, M. Gupta, and G. Vijaya Prakash, *Opt. Mater.* 75, 127 (2018).
36. M. Zambelli, A. Speghini, G. Ingletto, C. Locatelli, M. Bettinelli, F. Vetrone, J.C. Boyer, and J.A. Capobianco, *Opt. Mater.* 25, 215 (2004).
37. E. Pecoraro, J.A. Sampaio, L.A.O. Nunes, S. Gama, and M.L. Baesso, *J. Non Cryst. Solids* 277, 73 (2000).
38. J.H. Choi, A. Margaryan, A. Margaryan, and F.G. Shi, *J. Lumin.* 114, 167 (2005).
39. I. Pal, A. Agarwal, S. Sanghi, M.P. Aggarwal, and S. Bhardwaj, *J. Alloys Compd.* 587, 332 (2014).
40. T.F. Xue, L.Y. Zhang, J.J. Hu, M.S. Liao, and L.L. Hu, *Opt. Mater.* 47, 24 (2015).
41. A.D. Sontakke, K. Biswas, A.K. Mandal, and K. Annapurna, *Appl. Phys. B* 101, 235 (2010).
42. J. Azevedo, J. Coelho, G. Hungerford, and N. Sooraj Hussain, *Phys. B* 405, 4696 (2010).
43. I. Pal, A. Agarwal, S. Sanghi Sanjay, and M.P. Aggarwal, *Indian J. Pure Appl. Phys.* 51, 18 (2013).
44. B. Karthikeyan, R. Philip, and S. Mohan, *Opt. Commun.* 246, 153 (2005).
45. M. Sobczyk, *J. Quant. Spectrosc. Rad. Transf.* 119, 128 (2013).
46. S. Srihari Sastry and B.R. Venkateswara Rao, *Indian J. Pure Appl. Phys.* 52, 491 (2014).
47. G.A. Kumar, A. Martinez, and E.D.L. Rosa, *J. Lumin.* 99, 141 (2002).
48. G.A. Kumar, P.R. Biju, C. Venugopal, and N.V. Unnikrishnan, *J. Non Cryst. Solids* 221, 47 (1997).
49. K. Zou, H. Guo, M. Lu, W. Li, C. Hou, W. Wei, J. He, B. Peng, and B. Xiangli, *Opt. Express* 17, 10001 (2009).
50. B. Karthikeyan and S. Mohan, *Mater. Res. Bull.* 39, 1507 (2004).
51. K. Mariselvam, R. Arun Kumar, and P. Manasa, *Inf. Phys. Technol.* 91, 18 (2018).
52. K. Mariselvam, R. Arun Kumar, and K. Suresh, *Physica B* 534, 68 (2018).
53. D.D. Ramteke, R.E. Kroon, and H.C. Swart, *J. Non Cryst. Solids* 457, 157 (2017).
54. T. Fuji, K. Kodaira, O. Kawauchi, N. Tanaka, H. Yamashita, and M. Anpo, *J. Phys. Chem. B* 101, 10631 (1997).

55. S. Shen, M. Naftaly, and A. Jha, *Opt. Commun.* 205, 101 (2002).
56. P. Babu, H.J. Seo, K.H. Jang, R. Balakrishnaiah, C.K. Jayasankar, K.S. Lim, and V. Lavin, *J. Opt. Soc. Am. B* 24, 2218 (2007).
57. P. Babu, H.J. Seo, K.H. Jang, R. Balakrishnaiah, C.K. Jayasankar, and A.S. Joshi, *J. Phys. Condens. Matter* 17, 4859 (2005).
58. R. Praveena, K.H. Jang, C.K. Jayasankar, and H.J. Seo, *J. Alloys Compd.* 496, 335 (2010).
59. F. Auzel, F. Bonfigli, S. Gagliari, and G. Baldacchini, *J. Lumin.* 94–95, 293 (2001).
60. F. Auzel, G. Baldacchini, L. Laversenne, and G. Boulon, *Opt. Mater.* 24, 103 (2003).
61. N. Yamada, S. Shionoya, and T. Kushida, *J. Phys. Soc. Jpn.* 32, 1577 (1972).
62. Z. Zhou, Y. Zhou, M. Zhou, X. Su, and P. Cheng, *J. Non Cryst. Solids* 470, 122 (2017).
63. Y. Che, Y. Huang, M. Huang, R. Chen, and Z. Luo, *J. Am. Ceram. Soc.* 88, 19 (2005).
64. J. Pisarska, W.A. Pisarski, and W.R. Romanowski, *Opt. Laser Technol.* 42, 805 (2010).
65. G. Gupta, A.D. Sontakke, P. Karmakar, K. Biswas, S. Balaji, R. Saha, R. Sen, and K. Annapurna, *J. Lumin.* 149, 163 (2014).
66. R.T. Karunakaran, K. Marimuttu, S. Arumugam, S. Surendra Babu, S.F. Leon-Luis, and C.K. Jayasankar, *Opt. Mater.* 32, 1035 (2010).
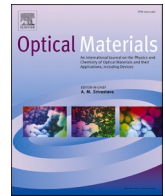
Role of excitation wavelength and dopant concentration on white light tunability of dysprosium doped titania-fluorophosphate glasses

N. Ravi [a], G. Neelima [a,b], Nanda Kumar Reddy Nallabala [c], Venkata Krishnaiah Kummara [d,e,*], R. Ravanamma [a,b], V. John Reddy [b,j], M. Prasanth [b,f], K. Suresh [a], P. Babu [g], V. Venkatramu [h,i]

[a] Department of Physics, Rajeev Gandhi Memorial College of Engineering & Technology, Nandyal-518501, India
[b] Department of Physics, JNT University, Anantapuramu-515002, India
[c] Department of Physics, Madanapalle Institute of Technology and Science, Madanapalle-517 325, India
[d] Laser Applications Research Group, Ton Duc Thang University, Ho Chi Minh City, Viet Nam
[e] Faculty of Applied Sciences, Ton Duc Thang University, Ho Chi Minh City, Viet Nam
[f] Department of Physics, JNTUACE, Kalikiri-517234, India
[g] Department of Physics, SVCR Government Degree College, Palamaner-517408, India
[h] Department of Physics, Yogi Vemana University, Kadapa-516 005, India
[i] Department of Physics, Krishna University Dr. MRAR PG Centre, Nuzvid-521 201, India
[j] Department of H&S (Physics), Nalla Narasimha Reddy Educational Society's Group of Institutions, Hyderabad, India

ARTICLE INFO

ABSTRACT

Dysprosium-doped fluorophosphate glasses (P_2O_5–CaF_2–BaF_2–TiO_2-Dy_2O_3) have been prepared using melt-quenching technique and characterized their optical, structural, thermal and photoluminescence properties. Thermal stability (128 °C) of 0.5 mol% Dy_2O_3-doped glass has been estimated using Differential thermal analysis. Functional groups for 0.5 mol% Dy_2O_3-doped glass have been studied by Fourier Transform Infrared spectrum. Absorption spectra have been utilized for estimating the Judd-Ofelt (JO) parameters and allied properties. Several excitation wavelengths (350, 365, 387, 425, 452 and 472 nm) have been used for pumping the Dy^{3+} ions and analyzed for white luminescence. Intense emission has been observed for 0.5 and 1.5mol% of Dy_2O_3-doped glasses under 387 nm excitation. The $^4F_{9/2} \rightarrow ^6H_{13/2}$ transition at 573 nm has unveiled a high stimulated emission cross-section (σ_{SE}) of 41.52×10^{-22} cm^2 for 0.5 mol% Dy_2O_3-doped glass. CIE coordinates fall close to the white region in CIE diagram, and hence these glasses are suitable for cold white light emitting diode applications.

1. Introduction

In the present market, white light emitting diodes (WLEDs) are premier light sources rather than the conventional fluorescent and incandescent light sources owing to their low power consumption, long operating lifetime, high brightness, higher efficiency, excellent reliability and environmental responsive characteristics [1–3]. Higher photoluminescence efficiency is essential to meliorate for these types of opto-electronic device applications [4]. In general, trivalent lanthanide (Ln^{3+}) ions are active centers of luminescence in photonics and opto-electronics device applications. However, researchers are motivated extensively towards Ln^{3+}:glasses for evolving the devices such as plasma displays, lasers, amplifiers, optical temperatures and WLEDs [5].

Trivalent dysprosium (Dy^{3+}) ($4f^9$) ion is one of the exciting Ln^{3+}ions

for exploring the luminescence properties owing to their usage in laser devices [6], telecommunication [7] and color display applications [8]. Moreover, Dy^{3+} ions exhibit intense yellow emission due to the $^4F_{9/2} \rightarrow ^6H_{13/2}$ (electric dipole) transition than blue emission due to the $^4F_{9/2} \rightarrow ^6H_{15/2}$ (magnetic dipole) transition [9–13]. Consequently, at the suitable ratio yellow-to-blue (Y/B) intensity ratio, Dy^{3+} ions are more fascinated for WLEDs. Therefore, it is recommended to use Dy^{3+} ions for white light sources.

Phosphate (P_2O_5) glasses are the prominent host materials for embedding Ln^{3+} ions for lighting applications among other glass formers due to their advantages such as reasonably low phonon energy and good stability. Oxyfluoride glasses have been offered their predominant properties by reason of collective advantages of matrices of oxide and fluoride such as low melting point, a low index of refraction and a low

---

N. Ravi et al.

phonon energy, hence enhances the radiative transitions [14,15]. In addition, fluorophosphate glasses have been studied as dominant materials for solid state lasers. The influence of excitation wavelengths on color tunability of oxyfluorosilicate glasses modified with CaF_2 have been discussed for WLEDs [2]. Photoluminescence (PL) studies have been performed for Dy^{3+}-doped oxyfluorosilicate glasses modified with BaF_2 [16]. In this work, Dy^{3+}-doped titania fluorophosphate glasses are obtained by modifying phosphate network with CaF_2 and BaF_2.

Dy^{3+}-doped glasses with various glass formers and modifiers are made with different molar ratios for the WLEDs applications, which include tellurite glasses: $47TeO_2–25WO_3 – 25Li_2O–3Dy_2O_3$ ($TWLD_{3.0}$) [2], germanate glasses: $30B_2O_3–40GeO_2 - 29Gd_2O_3–1Dy_2O_3$ ($BGGD_{1.0}$) [17], silicate glasses $35.7SiO_2 - 25.5B_2O_3–17BaO - 3.4K_2O_3–4Al_2O_3$ $–15BaCl_2 -0.5$ Dy_2O_3 ($SBBaKABlDy_{0.5}$) [18], borate glasses: $50B_2O_3$ - $xLiF - (30-x)CaO–20Bi_2O_3-1.0Dy_2O_3$ ($BLfCBiDy_{1.0}$) [19], phosphate glasses: $70P_2O_5–10Bi_2O_3 – 10Na_2CO_3–9SrCO_3 – 1.0Dy_2O_3$ ($NaBiSrPDy_{1.0}$) [20], $69.4P_2O_5–5B_2O_3 – 25BaO - 0.6Dy_2O_3$ ($PBBaDy_{0.6}$) [21], $65P_2O_5–17NaF - 17Gd_2O_3–1.0Dy_2O_3$ ($PNfGdDy_{1.0}$) [22], $44P_2O_5–17K_2O –9Al_2O_3 - 28$ $Nb_2O_5 – 2.0Dy_2O_3$ ($PKANbDy_{2.0}$) [23].

The present research aims to examine the influence of Dy^{3+} ion concentration and excitation wavelengths on photoluminescence properties in particular white light tunability. From the differential thermal analysis (DTA) spectrum of $PCBTD_{0.5}$ glass, glass transition temperature, crystalline temperature and thermal stability are evaluated. By using Fourier transform infrared (FTIR) spectrum, the functional groups of Dy^{3+} ion doped titaniafluorophosphate glasses are assessed. The optical, PL and spectroscopic properties of PCBTD glasses are analyzed. Lifetimes of the Dy^{3+} ions for various concentrations are estimated by means of the decay profiles. Color tunability of these glasses has been studied based on various concentrations of Dy^{3+} ions and pump wavelengths.

2. Experimental details

2.1. Glass synthesis

Melt-quenching technique [24] has been used for the synthesis of glasses with a composition of 60 P_2O_5 (99.9%) - 20 CaF_2 (99.5%) - 15 BaF_2 (99.0%) - 5 TiO_2 (99.0%) - xDy_2O_3 (99.8%) (x = 0.5, 1.0, 1.5, 2.0 and 2.5 mol %). The glasses were designated as $PCBTD_{0.5}$, $PCBTD_{1.0}$, $PCBTD_{1.5}$, $PCBTD_{2.0}$ and $PCBTD_{2.5}$ for 0.5, 1.0, 1.5, 2.0 and 2.5 mol % Dy_2O_3, respectively. 10 g of chemicals were thoroughly mixed by grinding for 1 h, then transferred to an alumina crucible and placed in a rectangular box-type heating furnace at 1300 °C at a rate of 10 °C/min for 90 min. The melt is poured into a pre-heated brass plate, maintained at 500 °C and rapidly quenched. Then the glass was annealed at 500 °C for 4 h and cooled to room temperature (RT). These glasses are polished for their optical quality and are used for optical characterization.

2.2. Characterization techniques

The DTA was performed by PerkinElmer (model- Diamond TG/DTA) from room temperature (RT) to 1000 °C at a heating rate of 10 °C/min. The Fourier transform infrared (FTIR) spectra were obtained at RT (in the range of 500–3900 cm^{-1}) by a Thermofisher Scientific (model: Nicolet 6700 FTIR spectrometer). Absorption spectrum of $PCBTD_{2.0}$ glass was obtained by VARIAN Cary 5000 spectrophotometer in the region of 350–1900 nm. PL spectra were measured by Edinburg Spectrofluorometer (FLS-980) with Xe lamp as an excitation source. Decay curves were measured with the same spectrometer under the Xe lamp excitation in the pulsed mode. Typical density (ρ) and thickness (t) of the glasses are found to be 3.11 gm/cm^3 and 0.37 cm respectively.

3. Results and discussion

3.1. Thermal studies

The DTA curve of $PCBTD_{0.5}$ glass in Fig. 1 shows an endothermic peak corresponding to the glass transition temperature (T_g) at 552 °C and the exothermic peak at 704 °C associated to the peak crystalline temperature (T_c). The onset crystallization temperature (T_x at 629 °C) of $PCBTD_{0.5}$ glass is assessed by plotting a tangent in the straight section of the crystalline peak. The thermal stability (ΔT) of the glass, T_x-T_g, is an essential parameter for the optical fiber drawing. The glass should exhibit ΔT as high as possible to decrease scattering losses thereby increase optical performance of the fiber. The thermal stability (ΔT) is found to be 128 °C which is higher than 103 °C of calcium fluoride modified oxyfluophosphate glass [25].

3.2. FTIR analysis

FTIR vibrational profile of $PCBTD_{0.5}$ glass at RT in the energy region of 500–3900 cm^{-1} is shown in Fig. 2. The spectrum shows numerous absorption bands around 752, 902, 1091, 1563, 1635, 2331, 3440 and 3755 cm^{-1}. Usually, the IR bands in the range of 1200–1300 cm^{-1} is due to P = O bonds from phosphate polymerization units. Phosphate (P–O^-) stretching bands reflected the energy range of 900–1100 cm^{-1} because of non-bridging oxygens (NBOs) and band at ∼ 750 cm^{-1} owing to the bridging oxygens (BOs) of P–O–P vibrations [26]. The peaks at around ∼3755 and 3440 cm^{-1} are attributed to H–O–H stretching hydroxyl groups vibrations owing to NBOs in phosphate because of its high hygroscopic nature. The vibrational band ∼2331 cm^{-1} is owing to asymmetric stretching vibrations of the O–H bond. The absorption bands at 1590 cm^{-1} and 1695 cm^{-1} are because of the bending vibrations of H–O–H bonds due to moisture during the preparation and/or inherent present of OH ions in phosphate compounds. In general, IR spectrum of the glass sample is measured by the KBr pellet technique and is likely to be influenced by number of factors, including the atmospheric conditions around the IR spectrophotometer. In particular, the atmospheric moisture is easily absorbed by the sample or by the pellet, causing the appearance of IR bands belonging to H_2O molecules although the sample under investigation does not contain H_2O as a unit in the network. It is anticipated that IR bands of water arise mainly because of the hygroscopic nature of the glasses with higher phosphate content, and change in these bands with composition is indicative of changes in their hygroscopicity and hence changes in the glass structure or vice versa [27]. The intensity of the band at 1091 cm^{-1} is accredited to the end groups (Q^0) species of symmetric vibrations of (PO_3). The vibration of Ca/Ba–O–P bonds is assigned to the band at 902 cm^{-1} due to asymmetric
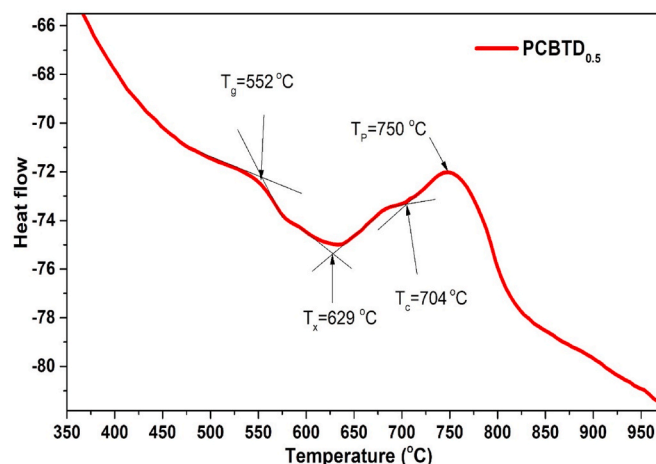

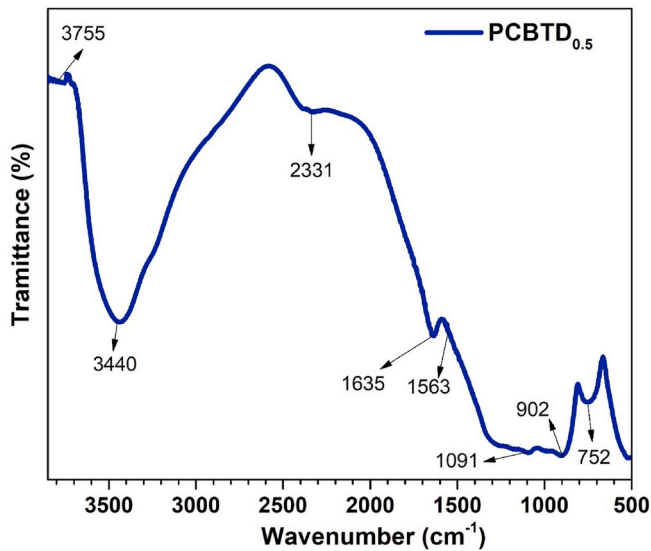**Fig. 1.** DTA thermograph of $PCBTD_{0.5}$ glass.

Fig. 2. FTIR profile of the PCBTD$_{0.5}$ glass in the energy range of 500–3900 cm^{-1}.

stretching from metaphosphate of $(PO_4)^{3-}$ groups. In addition, the band at 752 cm^{-1} is for P–O–Ti symmetrical stretching mode [28].

3.3. Optical properties - optical absorption spectrum

The optical absorption spectrum (UV–Visible–NIR) of PCBTD$_{2.0}$ glass in the wavelength range of 350–1900 nm is shown in Fig. 3. The spectrum exhibits eleven bands positioned at around 377, 387, 424, 452, 472, 748, 797, 894, 1093, 1268 and 1675 nm assigned to the transitions from ground $^6H_{15/2}$ level to the different higher energy states, $^4M_{19/2}$, $^4K_{17/2}$, $^4G_{11/2}$, $^4I_{15/2}$, $^4F_{9/2}$, $^6F_{3/2}$, $^6F_{5/2}$, $^6F_{7/2}$, $^6F_{9/2} + ^6H_{7/2}$, $^6F_{11/2} + ^6H_{9/2}$ and $^6H_{11/2}$ of Dy^{3+} ions, respectively. From these bands, the 1268 nm band with an energy of 7886 cm^{-1} corresponds to the $^6H_{15/2} \rightarrow ^6F_{11/2} + ^6H_{9/2}$ transition which is referred as hypersensitive transition because of its highest intensity compared to rest of the bands. It follows the selection rules ($|\Delta S| = 0$, $|\Delta L| \leq 2$ and $|\Delta J| \leq 2$) owing to the degree of asymmetry about Dy^{3+} ions [1,2]. Further, the strength of the $^6H_{15/2} \rightarrow ^6F_{11/2} + ^6H_{9/2}$ transition is highly sensitive to the ligand field of the Dy^{3+} ions. This absorption band shows the interaction of electric and
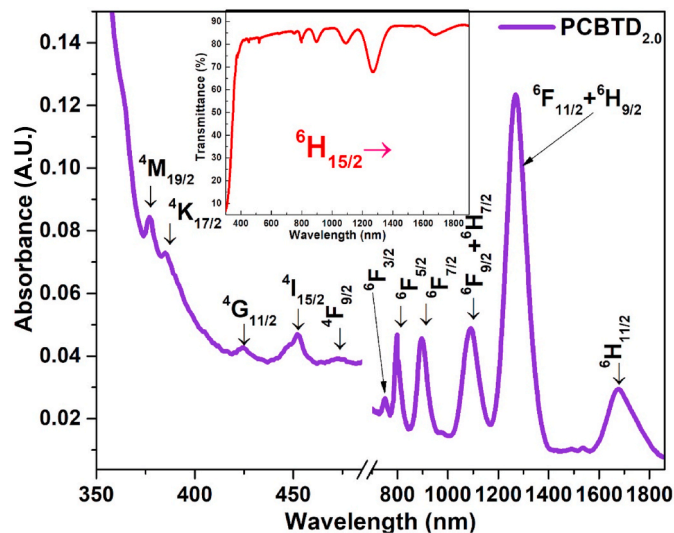
magnetic dipoles, which leads to the transfer of energy (ET) during mutual relaxation (CR) between Dy^{3+} ions. In addition, the PCBTD$_{2.0}$ glass transmittance spectrum shows about 90% of the most preferred transparency for optical applications, as shown in the inset of Fig. 3.

3.4. Judd-Ofelt theory

By applying the Judd-Ofelt (JO) theory [29,30] to the absorption spectrum of PCBTD$_{2.0}$ glass, the JO intensity parameters are obtained from the JO theory. Intensity parameters and oscillator strengths are assessed by least square fitting method. Moreover, the optical absorption strength of the Dy^{3+} ions are associated to the JO parameters Ω_λ ($\lambda = 2$, 4, 6). These parameters illustrate the electric and magnetic-dipole strengths of the ligand field in the glass matrix [31]. Root mean square (rms) eccentricity between the experimental (f_{exp}) and calculated (f_{cal}) oscillator strengths is estimated as $\pm 0.287 \times 10^{-6}$ which indicates a good quality of fit between f_{exp} and f_{cal}. In addition, it shows a trend of $\Omega_2 > \Omega_4 > \Omega_6$ and are compared with the other glass trends shown in Table 1. The present glass exhibits higher covalence of Dy–O bonds. As can be seen, most of the Dy^{3+}-doped phosphate glasses follow a similar trend in JO parameters.

Some of the evaluated parameters of the PCBTD$_{2.0}$ glass such as radiative lifetime (τ_{rad}), experimental lifetime (τ_{exp}), emission cross-section (σ_{SE}, cm^2) and gain bandwidth are presented in Table 2. The gain bandwidth ($\sigma_{SE} \times \Delta\lambda_{eff}$, 10^{-28}, cm^3) for the $^4F_{9/2} \rightarrow ^6H_{13/2}$ transition of Dy^{3+} ions shows higher for the PCBTD$_{0.5}$ glass among the glasses under study. It is found that the $^4F_{9/2} \rightarrow ^6H_{13/2}$ transition displays a higher peak emission cross-section of 41.52 $\times$ 10^{-22} cm^2 at 573 nm for PCBTD$_{0.5}$ glass among the glasses in the present investigation. This value obtained is found to be higher compared to 9.53 $\times$ 10^{-22} for YCaSBDy$_{0.5}$ [33], 20.93 $\times$ 10^{-22} for BGGD$_{1.0}$ [17], 21.3 $\times$ 10^{-22} for BaBPDy$_{0.4}$ [21] and 39.4 $\times$ 10^{-22} for PPBGaDy$_{2.5}$ [38] glasses whereas lower than 42.95 $\times$ 10^{-22} for TZPPNDy$_{1.0}$ [36], 61.28 $\times$ 10^{-22} for DyNaFGdP$_{1.0}$ [22], 62.86 $\times$ 10^{-22} for ZTFBD$_{0.5}$ [37], 64 $\times$ 10^{-22} for PKANbDy$_{2.0}$ [23] and 90.1 for NaBiSrPDy$_{1.0}$ [20] glasses, as shown in Table 2.

3.5. Photoluminescence excitation

The excitation (λ_{ex}) spectrum of PCBTD$_{0.5}$ glass is measured by monitoring the emission at 573 nm and is depicted in Fig. 4. The Dy^{3+} ion bands perceived in the excitation spectrum are centered at 350, 365, 387, 425, 452 and 472 nm and their associated transitions are $^6H_{15/2} \rightarrow ^6P_{7/2}$, $^6P_{5/2}$, $^4M_{19/2} + ^4K_{17/2} + ^4M_{21/2} + ^4I_{13/2} + ^4F_{7/2}$, $^4G_{11/2}$, $^4I_{15/2}$ and $^4F_{9/2}$, respectively. A broad and intense excitation band is perceived at 387 nm due to the combination of five deconvoluted bands 377, 387, 389, 393 and 396 nm which resembles to the transition $^6H_{15/2} \rightarrow ^4M_{19/2} + ^4K_{17/2} + ^4M_{21/2} + ^4I_{13/2} + ^4F_{7/2}$ resolved in the inset of Fig. 4. Moreover, the band at 387 nm is selected for exciting the Dy^{3+} ions in PCBTD glasses.

Fig. 3. Absorption spectrum in the UV–visible–NIR region of PCBTD$_{2.0}$ glass. Inset shows the transmittance spectrum of the same glass.

Table 1
Assessment of Judd-Ofelt (JO) intensity parameters (Ω_2, Ω_4 and Ω_6, $\times$ 10^{-20} cm^2), their trend for the PCBTD$_{2.0}$ glass and other reported Dy^{3+}: glasses.

Glass	Ref.	Ω_2	Ω_4	Ω_6	Trend
PCBTD$_{2.0}$	[PW]	20.25	9.61	8.92	$\Omega_2 > \Omega_4 > \Omega_6$
TWLD$_{3.0}$ (Tellurite)	[2]	16.00	2.39	3.75	$\Omega_2 > \Omega_6 > \Omega_4$
MgB2O3Dy$_{0.7}$ (Borate)	[9]	23.02	12.86	12.17	$\Omega_2 > \Omega_4 > \Omega_6$
BGGD$_{1.0}$ (Germanate)	[17]	3.65	0.65	1.57	$\Omega_2 > \Omega_6 > \Omega_4$
NaBiSrPDy$_{1.0}$ (Phosphate)	[20]	2.48	0.82	0.61	$\Omega_2 > \Omega_4 > \Omega_6$
BaBPDy$_{0.4}$ (Phosphate)	[21]	4.47	1.27	0.99	$\Omega_2 > \Omega_4 > \Omega_6$
DyNaFGdP$_{1.0}$ (Phosphate)	[22]	16.83	8.87	6.25	$\Omega_2 > \Omega_4 > \Omega_6$
PKANbDy$_{2.0}$ (Phosphate)	[23]	23.01	0.72	3.53	$\Omega_2 > \Omega_6 > \Omega_4$
GePbfDyf$_{10}$ (Germanate)	[32]	6.41	1.02	2.25	$\Omega_2 > \Omega_6 > \Omega_4$
YCaSBDy$_{0.5}$ (Borate)	[33]	2.84	0.15	0.95	$\Omega_2 > \Omega_6 > \Omega_4$
AYCBSMTD$_{2.0}$ (Tellurite)	[34]	3.09	0.88	2.19	$\Omega_2 > \Omega_6 > \Omega_4$
PbAlSiDy$_{1.0}$ (Silicate)	[35]	15.71	0.92	2.83	$\Omega_2 > \Omega_6 > \Omega_4$

N. Ravi et al.

Table 2

Comparison of radiative (τ_{rad}, ms) and experimental (τ_{exp}, ms) lifetimes of $^4F_{9/2}$ level, stimulated emission cross sections (σ_{SE}, $\times 10^{-22}$ cm^2) and gain bandwidth ($\sigma_{SE} \times \Delta\lambda_{eff}$ 10^{-28} cm^2) of $^4F_{9/2} \rightarrow {}^6H_{13/2}$ transition and Y/B ratios of Dy^{3+}-doped PCBTD$_{0.5}$ glass with other reported Dy^{3+}:glasses.

Glass matrix	Ref.	τ_R (ms)	τ_{exp} (ms)	$\sigma_{em} \times 10^{-22}$ cm^2	Y/B	$\sigma_{SE} \times \Delta\lambda_{eff}$ 10^{-28} cm^3
PCBTD$_{0.5}$	[PW]	0.78	0.15	41.52	3.10	39.77
TWLD$_{3.0}$	[2]	0.075	0.05	–	2.46	–
BGGD$_{1.0}$	[17]	0.84	0.38	20.93	2.25	40.83
NaBiSrPDy$_{1.0}$	[20]	0.13	0.06	90.1	–	126
BaBPDy$_{0.4}$	[21]	2.01	0.65	21.3	–	28.71
DyNaFGdP$_{1.0}$	[22]	0.61	0.53	61.28	1.94	–
PKANbDy$_{2.0}$	[23]	0.44	0.17	64.00	5.08	118.97
YCaSBDy$_{0.5}$	[33]	1.78	0.69	9.53	1.30	17.08
TZPPNdy$_{1.0}$	[35]	0.37	0.33	42.95	–	59.25
ZTFBD$_{0.5}$	[36]	0.89	0.40	62.86	1.11	45.11
PPBGaDy$_{2.5}$	[38]	0.55	0.44	39.4	2.05	58.3
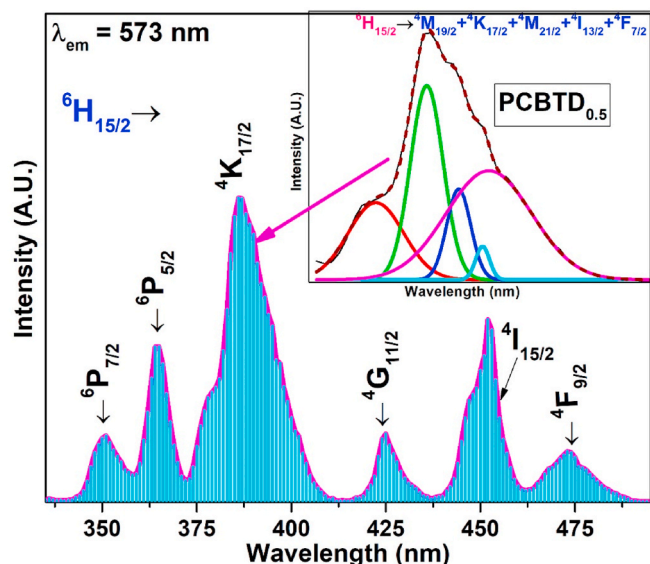
Fig. 4. PL excitation spectrum of PCBTD$_{0.5}$ glass upon monitoring the emission at 573 nm.

3.6. Photoluminescence spectra

The luminescence spectra of the Dy^{3+} ions doped PCBTD glasses are obtained from 400 to 800 nm by exciting at 387 nm and are shown in Fig. S1 (provided in the supplementary information). Four emission bands are observed in the spectra at 483, 573, 662 and 753 nm correspond to the $^4F_{9/2} \rightarrow {}^6H_{15/2}$, $^6H_{13/2}$, $^6H_{11/2}$, and $^6H_{9/2}$ transitions, respectively. Among these, the $^4F_{9/2} \rightarrow {}^6H_{15/2}$ transition ($\Delta J = 3$) is due to magnetic-dipole (MD) that gives blue emission with low emission intensity and the $^4F_{9/2} \rightarrow {}^6H_{13/2}$ transition ($\Delta J = \pm 2$) is due to electric-dipole (ED) that yields highest intensity, among the other transitions, known as hypersensitive transition [19,20]. Moreover, the PCBTD$_{0.5}$ glass gives intense yellow emission for the $^4F_{9/2} \rightarrow {}^6H_{15/2}$ transition. Gradual decrease in the intensity of yellow emission was noticed with the increase of Dy^{3+} ions up to 2.5 mol% concentration from 0.5 mol%. The PCBTD$_{0.5}$ glass is optimum under 387 nm excitation as it gives intense emission for 0.5 mol% of Dy$_2$O$_3$, which can be further exploited under different excitation wavelengths.

PL spectra of PCBTD glasses upon several excitation wavelengths are shown in Fig. 5. Further, to optimize the white light emission of these glasses, the optimum glass (PCBTD$_{0.5}$) is excited by several excitation wavelengths. In fact, for PCBTD$_{0.5}$ glass exhibits an intense emission that can be excited under different wavelengths which include 350, 365, 387,
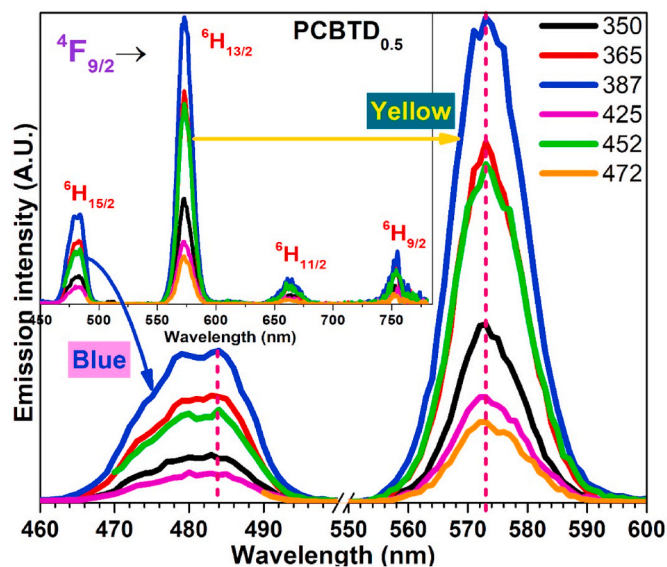
Fig. 5. PL emission spectra of two transitions of Dy^{3+} ions in PCBTD$_{0.5}$ glass under 350, 365, 387, 425, 452 and 472 nm excitations. Inset demonstrations the PL spectra of the same glass in the range of 450–810 nm under different excitation wavelengths.

425, 452 and 472 nm. When the excitation wavelength increased from 350 to 387 nm, the peak position for the $^4F_{9/2} \rightarrow {}^6H_{13/2}$ transition shifts slightly towards higher wavelengths (lower energy) and later the shift decreases with increase in the excitation wavelength, as shown in Fig. 5. The PL spectra of PCBTD$_{0.5}$ glass is obtained upon several excitation wavelengths. It is observed that the strength of the bands is significantly high at the excitation wavelength of 387 nm. Similar trend is also observed for blue emission.

The Dy^{3+} ions are pumped to the higher states in the glass, the peak positions of the emission spectra shift slightly from their mean positions. Yellow emission intensity of various Dy^{3+} ion concentration is influenced by different excitation wavelengths, as displayed in Fig. 6. Consequently, 0.5 mol% of Dy$_2$O$_3$-doped glass conveyed high emission intensity under 387 nm excitation, however for 1.0 mol% Dy$_2$O$_3$-doped glass high intensity was perceived for the excitation wavelength of 365 nm compared to 387 nm. Moreover, the glass with 2.5 mol% Dy$_2$O$_3$ content shows an intense yellow emission under the 452 nm excitation wavelength compared to the 387 nm. For the rest of the concentrations, intense emission was reported for the excitation wavelength of 387 nm. This is because of the manifestation of high concentration of Dy^{3+} ions.

For various Dy^{3+} ions concentrations, the shift of peak positions under several excitation wavelengths is presented in Fig. S2. Intense yellow emission at 573 nm for the $^4F_{9/2} \rightarrow {}^6H_{13/2}$ transition of Dy^{3+} ions doped glasses is obtained under different excitation wavelengths. It is interesting to note that under 387 nm excitation, a blue shift is observed for yellow emission with increase of Dy^{3+} ions concentration. A red shift known as Stokes shift towards higher wavelengths from 573 nm to 574.09 nm ($\Delta\lambda = 1.09$ nm) is observed for 1.0 mol% of Dy$_2$O$_3$-doped glass under different excitations. Furthermore, at higher concentrations of 2.0 and 2.5 mol% of Dy$_2$O$_3$, the yellow emission was shifted in the range of 571.9–573 nm ($\Delta\lambda = 1.1$ nm) and 571.99–574 nm ($\Delta\lambda = 2.0$ nm) that is towards blue shift known as anti-Stokes shift which may be owing to increase of Dy^{3+} ions. Shift in the peak positions is around 2 nm which is significantly more at higher Dy^{3+} ions concentration (2.5 mol%) compared to 0.51 nm at low concentrations (0.5 mol%). Over all, a red shift is observed when Dy^{3+} ions concentration is increased in these glasses.

On the other hand, full width at half maxima (FWHM) and integrated area (intensity) for yellow emission are shown in Figs.S3 (a) and (b). The FWHM increases in the range of 13.0–14.4 nm with increase in the
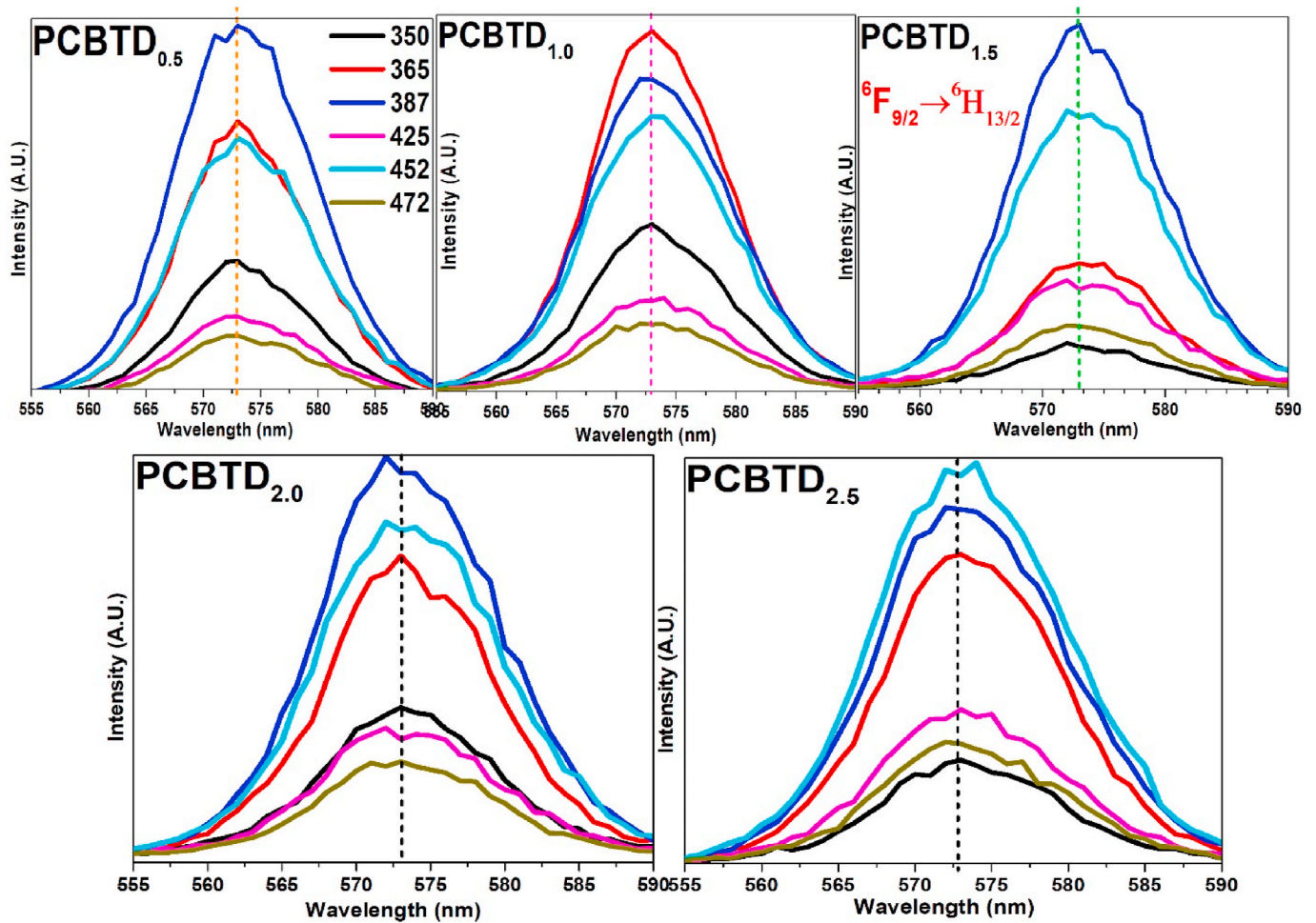
N. Ravi et al.

Fig. 6. PL emission spectra for several concentrations of Dy^{3+}-doped PCBTD glasses upon different λ_{ex} = 350, 365, 387, 425, 452 and 472 nm.

excitation wavelengths in the range of 350–472 nm for $PCBTD_{0.5}$ glass. Later, it decreases to a value of 13.9 nm for 425 nm wavelength excitation and increases slightly to 14.1 nm for the excitation wavelengths 452 and 472 nm. On the other hand, for $PCBTD_{0.5}$ glass, under 350 & 387 nm excitation wavelengths, the integrated intensity increases significantly and then decrease for higher excitation wavelengths.

Y/B ratio is obtained by exploring the integrated area of the two prominent transitions, $^4F_{9/2} \rightarrow {}^6H_{13/2}$ and $^4F_{9/2} \rightarrow {}^6H_{15/2}$. This is used to know the material that has the co-ordination number and equilibrium around the Dy^{3+} ions [39]. The Y/B intensity ratio increases till 1.5 mol % of Dy_2O_3 content and declines with further increase of Dy^{3+} ions concentration, as shown in Fig. S4. Usually, the behavior of Y/B intensity ratio be contingent on the trend of PL intensity in regard to Dy^{3+} concentration. Among the present glass systems, the $PCBTD_{0.5}$ glass shows an intense emission with a higher value of FWHM (14.39 nm). On the other hand, Y/B ratio declines with the increase of Dy^{3+} ion concentration beyond 1.5 mol% Dy_2O_3. This is due to concentration quenching which leads to the ET between the Dy^{3+} ions. Similar results were discerned for the other glasses [40].

Energy level diagram of Dy^{3+} ions in PCBTD glasses including the radiative and non-radiative channels is shown in Fig. 7. Several excitation wavelengths that includes 350, 365, 387, 425, 452, and 472 nm are employed to vary the emission colors of Dy^{3+} ions. Under 350 nm excitation, Dy^{3+} ions are excited to the $^6P_{7/2}$ from the $^6H_{15/2}$ level. They de-excite to the $^4F_{9/2}$ meta-stable state (whose lifetime is relatively high) through non-radiative transitions because of short lifetime and low energy separation among the higher energy levels [38]. Similar phenomena is applicable to all excitation wavelengths except 472 nm, in this
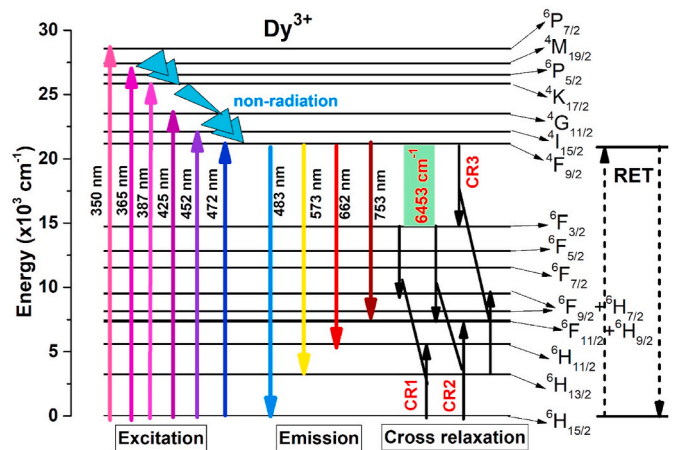
Fig. 7. Partial energy level structure of Dy^{3+} ions in PCBTD glasses. The various excitation, emission and CR channels are also shown along with non-radiation processes. RET: Resonance energy transfer.

case the Dy^{3+} ions are excited resonantly to $^4F_{9/2}$ level. From the $^4F_{9/2}$ level, radiative emission transitions, $^4F_{9/2} \rightarrow {}^6H_{15/2}$, $^6H_{13/2}$, $^6H_{11/2}$ and $^6H_{9/2}$ occur giving rise to blue, yellow, red and NIR emissions, respectively. At higher concentrations, the energy transfer (ET) through cross-relaxations (CR1, CR2 and CR3) between the adjacent Dy^{3+} ions occur because of multi-polar interaction, which leads to concentration

quenching of luminescence. In general, CR1, CR2 and CR3 occurs when the ET from the emission transitions perfectly counterparts with transitions of the absorption [25].

CR1: $^6F_{3/2}$, $^6H_{15/2} \rightarrow {}^6F_{9/2} + {}^6H_{7/2}$, $^6H_{11/2}$

CR2: $^6F_{3/2}$, $^6H_{15/2} \rightarrow {}^6F_{11/2} + {}^6H_{9/2}$

CR3: $^4F_{9/2}$, $^6H_{13/2} \rightarrow {}^6F_{3/2}$, $^6F_{9/2} + {}^6H_{7/2}$

Resonant energy transfer (RET) is established among the Dy^{3+} ion levels $^4F_{9/2} \leftrightarrow {}^6H_{15/2}$ and vice versa. The luminescence properties are changed due to RET, CR1, CR2 and CR3 with an increase in the concentration of Dy^{3+} ions. This can be confirmed by analyzing the decay curves, as shown in the next sections.

3.7. Fluorescence decay curves

Decay profiles of level $^4F_{9/2}$ of Dy^{3+} ions in PCBTD glass were measured upon 387 nm excitation by monitoring emission at 573 nm and are presented in Fig. 8. The decay curves show a non-exponential pattern for all the concentrations of Dy^{3+} ions. This is due to ET attributable to dipole-dipole interactions among the Dy^{3+} ions via CR channels. These curves were fitted using the following Eq. (1),

$$I(t) = A_1 \exp(-t/\tau_1) + A_2 \exp(-t/\tau_2) \tag{1}$$

where A_1 & A_2 and τ_1 & τ_2 are the constants and decay times correspond to the slow and fast components of the decay curves, respectively. τ_{exp} is experimental lifetime for the $^4F_{9/2}$ level, evaluated with the following Eq. (2),

$$\tau_{exp} = \frac{A_1\tau_1^2 + A_2\tau_2^2}{A_1\tau_1 + A_2\tau_2} \tag{2}$$

Decrease of τ_{exp} values for Dy^{3+} ions are noticed with increase of Dy^{3+} ions concentration which are found to be 151, 145, 129, 35 and 20 μs for the PCBTD$_{0.5}$, PCBTD$_{1.0}$, PCBTD$_{1.5}$, PCBTD$_{2.0}$ and PCBTD$_{2.5}$ glasses, respectively. The PCBTD$_{0.5}$ glass discloses a higher lifetime of 151 μs compared to the rest of the studied glasses. In the case of glasses doped with RE^{3+} ions, ET through CR mechanism is accountable for the behavior of non-exponential. However, the decrease of lifetime in PCBTD glasses indicates the presence of ET from excited to neighboring unexcited Dy^{3+} ions [40].
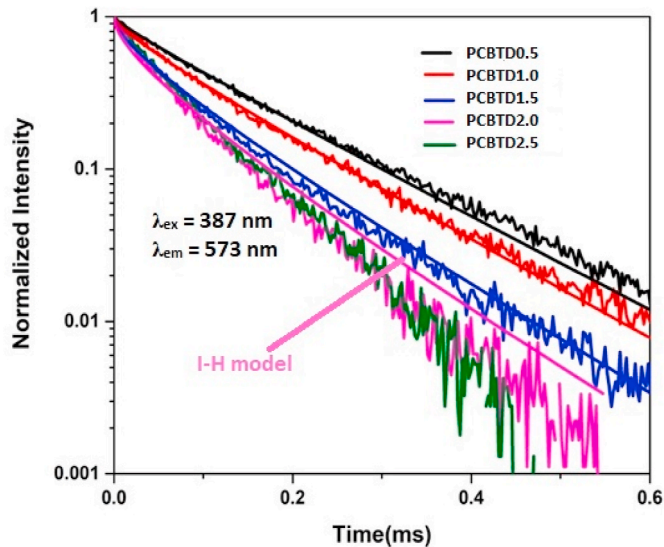
Fig. 8. Decay profiles for the excited state, $^4F_{9/2}$ of Dy^{3+} ions in PCBTD glasses under 387 nm excitation. Solid lines are fittings of the non-exponential curves to the I–H model.

The Inokuti-Hirayama (IH) model [41] is utilized when the ET process between an activator and sensitizer ions is much faster than energy diffusion. According to IH model, the PL intensity is defined by the following Eq.,

$$I(t) = I_0 \exp\left\{ -\frac{t}{\tau_0} - Q\left(\frac{t}{\tau_0}\right)^{3/s} \right\} \tag{3}$$

where $S = 6$, 8 and 10, t is the time afterward excitation, τ_0 is the intrinsic decay time of the activators in the absence of acceptors, Q is the ET parameter given by Eq.,

$$Q = \frac{4\pi}{3}\Gamma\left(1 - \frac{3}{S}\right)N_0R_0^3 \tag{4}$$

where $S = 6$, 8 and 10 for dipole-dipole ($\Gamma(x) = 1.77$), dipole-quadrupole ($\Gamma(x) = 1.43$) and quadrupole-quadrupole ($\Gamma(x) = 1.3$) interactions, respectively. N_0 is activator ion concentration and R_0 is the critical transfer distance between the activator and sensitizer. The activator-sensitizer interaction parameter (C_{DA}) is defined by Eq.,

$$C_{DA} = \frac{R_0^S}{\tau_0} \tag{5}$$

The decay curve is well correlated with Eq. (3) when S = 6, which shows that the ET in CR among the Dy^{3+} ions in the PCBTD glass is dipole, as shown in Fig. 8. The energy transfer parameter (Q), activator-sensitizer interaction parameter (C_{DA}) and critical distance (R_0) are evaluated for 2.0 mol% Dy_2O_3 doped glass and are found to be 0.433, 4.45×10^{-42} cm^6/s and 8.5 Å, respectively.

3.8. CIE color coordinate diagram

Emission color of Dy^{3+}-doped PCBTD glasses is examined with CIE (Commission Internationale de l'Elcairage) 1931 chromaticity diagram. The color coordinates of CIE (x, y) were estimated according to the procedure described elsewhere [42] and are presented in Table 3 and Fig. 9. The chromaticity coordinates (x, y) are found to be (0.4, 0.45), (0.4, 0.45), (0.41, 0.46), (0.41, 0.45) and (0.4, 0.46) for the PCBTD$_{0.5}$, PCBTD$_{1.0}$, PCBTD$_{1.5}$, PCBTD$_{2.0}$ and PCBTD$_{2.5}$ glasses, respectively. In addition, the corresponding correlated color temperature (CCT) values are calculated for different excitation wavelengths to know the emitted light is either "cold" or "warm" in nature. According to the McCamy's approach [43], the CCT value for the PCBTD glass is evaluated from the following Eq. (6).

$$CCT = -449n^3 + 3525n^2 - 6823n + 5520.33 \tag{6}$$

where $n = (x-x_e)/(y-y_e)$ is the converse slope line, $x_e = 0.332$ and $y_e = 0.186$ are the epicenter. Table 3 presents the color coordinates and CCT values of Dy^{3+}-doped glasses under different excitation wavelengths. The CCT values are obtained in the region of 3814–4057 K. Basically, light sources with CCT less than or equal to 3200 K usually exhibit a warm white light, whereas the light sources with CCT ~3700–5000 K emit pure white light, as displayed in Fig. 9. In these PCBTD glasses, the CCT values of 4000 K indicates the emission of pure white light. Location of the color coordinates with magnification is shown in the inset of Fig. 9.

As can be seen, color coordinates of the PCBTD$_{0.5}$ glass are almost close to the region of white light under different excitation wavelengths and are shown in Fig. 10. The emission color of the glass shifts from warm white to pure white light region as can be seen from their CCT values which are obtained in the range of 3413–4752 K. For all excitation wavelengths, the emission chromaticity is almost same. However, owing to higher CCT values around 3814–6332 K for PCBTD$_{2.0}$ glass, i. e., emission chromaticity is very near to the white light region and shifts from pure white to cool white light region. Especially, for the several excitation wavelengths of 350, 365 and 425 nm, the emission appeared

N. Ravi et al.

Table 3
CIE chromaticity (x, y) coordinates and CCT values of PCBTD glasses at several excitation wavelengths.

λ_{ex} (nm)	PCBTD$_{0.5}$			PCBTD$_{1.0}$			PCBTD$_{1.5}$			PCBTD$_{2.0}$			PCBTD$_{2.5}$		
	x	y	CCT	x	y	CCT	x	y	CCT	x	y	CCT	x	y	CCT
350	0.4	0.45	4006	0.4	0.45	4006	0.38	0.42	4278	0.34	0.41	5294	0.38	0.43	4328
365	0.4	0.45	4006	0.4	0.45	4006	0.4	0.45	4006	0.37	0.41	4475	0.39	0.45	4207
387	0.4	0.45	4006	0.4	0.45	4006	0.41	0.46	3870	0.41	0.45	3814	0.4	0.46	4057
425	0.37	0.49	4752	0.36	0.48	4929	0.36	0.48	4929	0.31	0.38	6332	0.35	0.48	–
452	0.42	0.47	3747	0.41	0.47	3923	0.42	0.47	3747	0.38	0.44	4374	0.41	0.47	3923
472	0.46	0.52	3413	0.46	0.52	3413	0.46	0.52	3413	0.4	0.53	–	0.45	0.52	3549
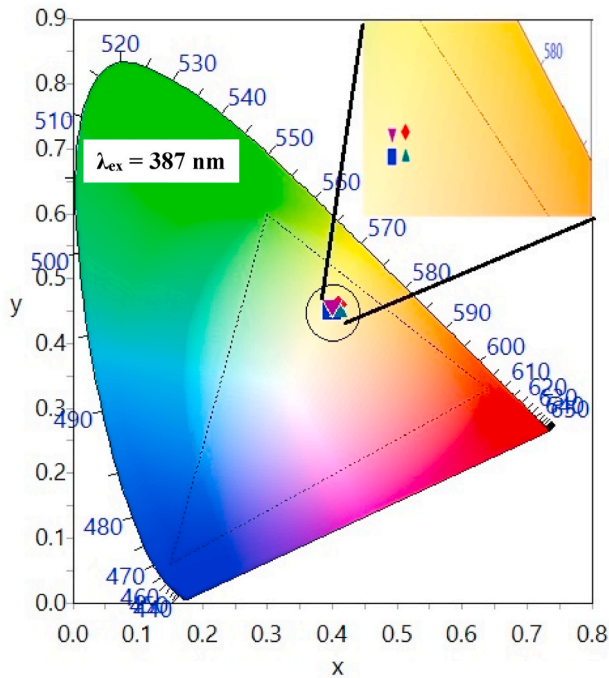
Fig. 9. Position of emission color Dy^{3+} -doped PCBTD glasses through CIE diagram. Inset shows the magnified region of the color coordinates.

almost in the white light region and is presented in Fig. 10. The study revealed that the effect of excitation wavelengths is more significant on emission color of Dy^{3+} ions compared to the Dy^{3+} ion concentrations. The 2.0 and 2.5 mol% of Dy^{3+} ions doped glasses are most significant samples for the fabrication of w-LEDs. Effect of different excitation wavelengths on emission properties were reported for Dy^{3+}-doped oxyfluoride silicate [3], borogermante [17], calcium alumina-borosilicate [5], oxyfluoride glass [42] and sodium-aluminum phosphate [44] glasses.

4. Conclusion

Dy^{3+}-doped titaniafluorophosphate (PCBTD) glasses have been fabricated by usual melt-quenching procedure and investigated their structural, optical and photoluminescence properties. DTA analysis of PCBTD$_{0.5}$ glass shows that the glass exhibits a good thermal stability (128 °C). FTIR analysis revealed the presence of functional groups of the phosphate network and other vibrational and stretching structural units. JO intensity parameters have been evaluated for the PCBTD$_{2.0}$ glass. Intense yellow (573) and moderate-intense blue (483) emissions were observed under 387 nm excitation. Yellow to blue (Y/B) intensity ratios and CIE color coordinates are estimated from emission spectra for several Dy^{3+} ions concentrations and excitation wavelengths which show feasibility for the extraction of white light. Fluorescence decay rates of the $^4F_{9/2}$ level of the Dy^{3+} ions show a progressive non-exponential behavior associated with quenching of lifetimes with increase in Dy^{3+} ions concentration due to the increase in ET process between Dy^{3+} ions. Effect of different excitation wavelengths and various Dy^{3+} ion concentrations on color coordinates and CCT values are discussed and displayed in CIE diagram. Different excitation wavelengths are used for the white light tunability of these glasses.
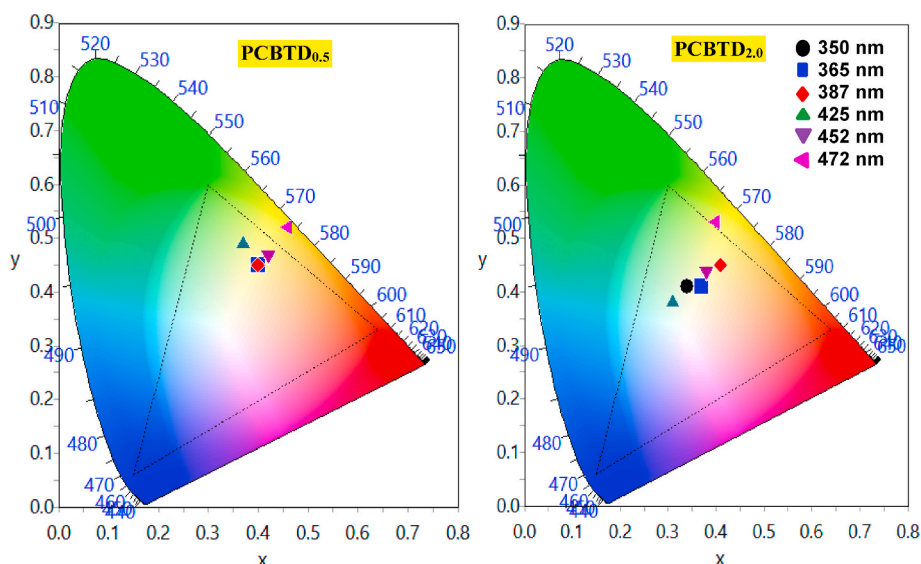
Fig. 10. Location of CIE color coordinates of PCBTD$_{0.5}$ and PCBTD$_{2.0}$ glasses under different excitation wavelengths.

CRediT authorship contribution statement

N. Ravi: Conceptualization, Data curation, Roles/, Writing - original draft, Formal analysis, Investigation, Resources, Supervision. **G. Neelima:** Methodology, Formal analysis. **Nanda Kumar Reddy Nallabala:** Formal analysis, Writing - review & editing. **Venkata Krishnaiah Kummara:** Conceptualization, Data curation, Roles/, Writing - original draft, Formal analysis, Investigation, Resources, Supervision. **R. Ravanamma:** Methodology, Formal analysis. **V. John Reddy:** Software, Validation, Visualization. **M. Prasanth:** Software, Validation, Visualization. **K. Suresh:** Software, Validation, Visualization. **P. Babu:** Formal analysis, Writing - review & editing. **V. Venkatramu:** Formal analysis, Writing - review & editing.

Declaration of competing interest

The authors declare that they have no known competing financial interests or personal relationships that could have appeared to influence the work reported in this paper.

Acknowledgements

Appendix A. Supplementary data

Supplementary data related to this article can be found at https ://doi.org/10.1016/j.optmat.2020.110593.

References

[1] U. Caldiño, A. Lira, A.N. Meza-Rocha, I. Camarillo, R. Lozada-Morales, Development of sodium-zinc phosphate glasses doped with Dy^{3+}, Eu^{3+} and Dy^{3+}/Eu^{3+} for yellow laser medium, reddish-orange and white phosphor applications, J. Lumin. 194 (2018) 231–239.

[2] O. Kıbrısl, A.E. Ersundu, M. Çelikbilek Ersundu, Dy^{3+} doped tellurite glasses for solid-state lighting: an investigation through physical, thermal, structural and optical spectroscopy studies, J. Non-Cryst. Solids 513 (2019) 125–136.

[3] Chaofeng Zhu, Xianghua Zhang, Hongli Ma, Claire Timlin, Sb-, Dy-, and Eu-doped oxyfluoride silicate glasses for light emitting diodes, J. Alloys Compd. 647 (2015) 880–885.

[4] Yukio Narukawa, Masatsugu Ichikawa, Daisuke Sanga, Masahiko Sano, Takashi Mukai, White light emitting diodes with super-high luminous efficacy, J. Phys. Appl. Phys. 43 (35) (2010) 354002.

[5] Yao Zhou, Chaofeng Zhu, Meimei Zhang, Jianan Liu, Optical properties of Eu- and Dy-doped calcium aluminoborosilicate glasses for LED applications, J. Alloys Compd. 688 (2016) 715–720.

[6] Y. Fujimoto, O. Ishii, M. Yamazaki, Yellow laser oscillation in Dy^{3+}-doped waterproof fluoro-aluminate glass fibre pumped by 398.8 nm GaN laser diodes, Electron. Lett. 46 (2010) 586–587.

[7] Ralph H. Page, Kathleen I. Schaffers, Stephen A. Payne, William F. Krupke, Dy-doped chlorides as gain media for 1.3 μm telecommunications amplifiers, J. Lightwave Technol. 15 (1997) 786–793.

[8] Chaofeng Zhu, Jia Wang, Meimei Zhang, Xiaorong Ren, Jianxing Shen, Yuanzheng Yue, Eu-, Tb-, and Dy-doped oxyfluoride silicate glasses for LED applications, J. Am. Ceram. Soc. 97 (3) (2014) 854–861.

[9] A. Ichoja, S. Hashim, S.K. Ghoshal, I.H. Hashim, R.S. Omar, Physical, structural and optical studies on magnesium borate glasses doped with dysprosium ion, J. Rare Earths 36 (12) (2018) 1264–1271.

[10] Sk Nayab Rasool, L. Rama Moorthy, C.K. Jayasankar, Optical and luminescence properties of Dy3+ ions in phosphate based glasses, Solid State Sci. 22 (2013) 82–90.

[11] P. Babu, Kyoung Hyuk Jang, Eun Sik Kim, Liang Shi, R. Vijaya, V. Lavin, C.K. Jayasankar, Hyo Jin Seo, Optical properties and energy transfer in Dy3+-doped transparent oxyfluoride glasses and glass ceramics, J. Non-Cryst. Solids 356 (4–5) (2010) 236–243.

[12] N. Vijaya, K. Upendra Kumar, C.K. Jayasankar, "Dy3+ -doped zinc fluorophosphate glasses for white luminescence applications," Spectrochim, Acta Mol. Biomol. Spectrosc. 113 (2013) 145–153.

[13] P. Babu, Kyoung Hyuk Jang, Ch Srinivasa Rao, Liang Shi, C.K. Jayasankar, Víctor Lavín and Hyo Jin Seo, "White light generation in Dy3+-doped oxyfluoride glass and transparent glass-ceramics containing CaF2 nanocrystals,", Optic Express 19 (3) (2011) 1836–1841.

[14] Haruka George, Nisha Deopa, Sumandeep Kaur, Aman Prasad, M. Sreenivasulu, M. Jayasimhadri, A.S. Rao, Judd-Ofelt parametrization and radiative analysis of Dy^{3+} ions doped Sodium Bismuth Strontium Phosphate glasses, J. Lumin. 215 (2019) 116693.

[15] C. T. Lin, S. W. Yung, J. Lin, W. S. Chen, C. H. Lai, Y. M. Lee, J. S. Lin, Luminescence properties of Tm^{3+}/Dy^{3+} co-doped zinc-aluminum phosphate glasses for white LED, Adv. Mater. Res., Vol. 602–604, pp 821-828.

[16] G. Lakshminarayana, Jianrong Qiu, Photoluminescence of Pr^{3+}, Sm^{3+} and Dy^{3+}-doped SiO_2–Al_2O_3–BaF_2–GdF_3 glasses, J. Alloys Compd. 476 (2009) 470–476.

[17] Melis Gokce, Deniz Kocyiğit, Spectroscopic investigations of Dy^{3+} doped borogermanate glasses for laserand wLED applications, Opt. Mater. 89 (2019) 568–575.

[18] Nilanjana Shasmal, Basudeb Karmakar, White light-emitting Dy^{3+}-doped transparent chloroborosilicate glass: synthesis and optical properties, Journal of Asian Ceramics Societies 7 (2019) 42–52.

[19] P. Narwal, Manjeet S. Dahiya, A. Yadav, A. Hooda, A. Agarwal, S. Khasa, Improved white light emission in Dy^{3+} doped LiF–CaO–Bi_2O_3–B_2O_3 glasses, J. Non-Cryst. Solids 498 (2018) 470–479.

[20] Haruka George, Nisha Deopa, Sumandeep Kaur, Aman Prasad, M. Sreenivasulu, M. Jayasimhadri, A.S. Rao, Judd-Ofelt parametrization and radiative analysis of Dy^{3+} ions doped Sodium Bismuth Strontium Phosphate glasses, J. Lumin. 215 (2019) 116693.

[21] Sujita Karki, C.R. Kesavulu, H.J. Kim, J. Kaewkhao, N. Chanthima, S. Kothan, S. Kaewjaeng, Physical, optical and luminescence properties of the Dy^{3+}doped barium borophosphate glasses, J. Non-Cryst. Solids 521 (2019) 119483.

[22] S. Ravangvong, N. Chanthimaa, R. Rajaramakrishna, H.J. Kim, N. Sangwaranatee, J. Kaewkhao, Dy^{3+} ions doped (Na_2O/NaF)-Gd_2O_3–P_2O_5 glasses for solid state lighting material applications, Solid State Sci. 97 (2019) 105972.

[23] T. Srihari, C.K. Jayasankar, Fluorescence properties and white light generation from Dy^{3+} -doped niobium phosphate glasses, Opt. Mater. 69 (2017) 87–95.

[24] G. Neelima, , Venkata Krishnaiah Kummara, C.S. Dwaraka Viswanath, K. Thyagarajan, N. Ravi, T. Jayachandra Prasad, Ceram. Int. 44 (13) (2018) 15304–15309.

[25] S. Cui, J. Massera, M. Lastusaari, L. Hupa, L. Petit, Novel oxyfluorophosphate glasses and glass-ceramics, J. Non-Cryst. Solids 445–44 (2016) 40–44.

[26] K.P. Muller, Struktur and eigenschaften von glasern und glasbildenden schmelzen. Teil III. Untersuchungen über die struktur abgeschreckter alkaliborat-undAlkaliphosphatglaser mittels infrarot, Glasteeh. Bet. 42 (1969) 83.

[27] C. Dayanand, G. Bhikshamaiah, V. Jaya Tyagaraju, M. Salagram, A.S.R. Krishna Murthy, Structural investigations of phosphate glasses: a detailed infrared study of the x(PbO)-(1 - x)P_2O_5, vitreous system, J. Mater. Sci. 31 (1996) 1945–1967.

[28] D. Toloman, D.A. Magdas, I. Bratu, L.M. Giurgiu, I. Ardelean, Infrared spectra of calcium phosphate glasses, Int. J. Mod. Phys. B 24 (3) (2010) 351–358.

[29] B.R. Judd, Optical absorption intensities of rare earth ions, Phys. Rev. 127 (1962) 750–761.

[30] G.S. Ofelt, Intensities of crystal spectra of rare earth ions, J. Chem. Phys. 37 (1962) 511–520.

[31] M. Brian, Walsh, Judd-Ofelt theory: principles and practices, Advances in Spectroscopy for Lasers and Sensing (2006) 403–433.

[32] B. Klimesz, G. Dominiak-Dzik, M. Zelechower, W. Ryba-Romanowski, Optical study of GeO_2–PbO–PbF_2 oxyfluoride glass single doped with lanthanide ions, Opt. Mater. 30 (2008) 1587–1594.

[33] C.R. Kesavulu, H.J. Kim, S.W. Lee, J. Kaewkhao, N. Chanthima, Y. Tariwong, Physical, vibrational, optical and luminescence investigations of Dy^{3+}-doped yttrium calcium silicoborate glasses for cool white LED applications, J. Alloys Compd. 726 (2017) 1062–1071.

[34] Feifei Huang, Lili Hu, Danping Chen, Observation of 2.8 μm emission from diode-pumped Dy^{3+}-doped fluoroaluminate glasses modified by, TeO_2 40 (8) (2014) 12869–12873.

[35] M. Sundara Rao, V. Sudarsan, M.G. Brik, Y. Gandhi, K. Bhargavi, M. Piasecki, I.V. Kityk, N. Veeraiah, De-quenching influence of aluminum ions on Y/B ratio of Dy^{3+} ions in lead silicate glass matrix, J. Alloys Compd. 575 (2013) 375–381.

[36] Kamel Damak, El Sayed Yousef, Christian Rüssel, Ramzi Maâlej, White light generation from Dy^{3+} doped tellurite glass, J. Quant. Spectrosc. Radiat. Transfer 134 (2014) 55–63.

[37] P. Suthanthirakumar, K. Marimuthu, Investigations on spectroscopic properties of Dy^{3+} doped zinc telluro-fluoroborate glasses for laser and white LED applications, J. Mol. Struct. 1125 (2016) 443–452.

[38] G. Chinna Ram, T. Narendrudu, G. Suresh, A. Suneel Kumar, M.V. Sambasiva Rao, V. Ravi Kumar, D. Krishna Rao, Investigation of luminescence and laser transition of Dy^{3+} ion in P_2O_5-PbO-Bi_2O_3-R_2O_3 (R = Al, Ga, In) glasses, Opt. Mater. 66 (2017) 189–196.

[39] Marta Kuwik, Agata Górny, Joanna Pisarska, A. Wojciech, Pisarski, Lead-based glasses doped with Dy^{3+} ions for W-LEDs, Mater. Lett. 254 (2019) 62–64.

[40] C.R. Kesavulu, C.K. Jayasankar, White light emission in Dy^{3+}-doped lead fluorophosphate glasses, Mater. Chem. Phys. 130 (2011) 1078–1085.

[41] M. Inokuti, F. Hirayama, Influence of energy transfer by the exchange mechanism on donor luminescence, J. Chem. Phys. 43 (1965) 1978–1989.

[42] K. Venkata Krishnaiah, K. Upendra Kumara, C.K. Jayasankar, Spectroscopic properties of Dy^{3+}-doped oxyfluoride glasses for white light emitting diodes, Materials Express 3 (1) (2013) 61–70.

[43] C.S. McCamy, Correlated color temperature as an explicit, Function of Chromaticity Coordinates 17 (2) (1992) 142–144.

[44] A. Amarnath Reddy, M. Chandra Sekhar, K. Pradeesh, S. Surendra Babu, G. Vijaya Prakash, Optical properties of Dy^{3+}-doped sodium–aluminum–phosphate glasses, J. Mater. Sci. 46 (2011) 2018–2023.

Optical and white light emission properties of Dy^{3+} ions doped zinc oxyfluorotellurite glasses

P. Babu [a,*], V. Chandrappa [b], N. Vijaya [b], C.K. Jayasankar [b,**], Hyo Jin Seo [c]

[a] Department of Physics, SVCR Government Degree College, Palamaner - 517408, India
[b] Department of Physics, Sri Venkateswara University, Tirupati - 517 502, India
[c] Department of Physics, Pukyong National University, Busan 608-737, Republic of Korea

A B S T R A C T

The dysprosium ions-doped zinc oxyflluorotellurite glasses of three different compositions have been synthesized and analyzed their vibrational, thermal, optical and white light emission properties. The differential thermal analysis curves, Fourier Transform Infrared, absorption, emission and excitation spectra and lifetimes from the luminescent level ($^4F_{9/2}$) have been measured and analyzed. Absorption spectra have been characterized in the frame of Judd-Ofelt model to determine essential radiative properties namely, transition probabilities, calculated lifetimes and branching ratios of the $^4F_{9/2}$ luminescent level. Photoluminescence spectra of the glasses are measured by exciting with 388 nm broad band and 355 nm laser. The glasses emit intense white luminescence with 388 nm broad band excitation. The CIE chromaticity color coordinates of one of the glass are nearer to the equal energy point. Decay time profiles of the $^4F_{9/2}$ state are non-exponential for three glasses under study where their effective lifetimes have been evaluated. Quantum efficiencies of the glasses vary from 30 to 62% with change in ZnF$_2$ content.

1. Introduction

Glass is an interesting material for research and development and as host for rare-earths (RE) because of its wide potential uses as high-power solid state lasers, sensors, and in optical communication, etc. Recently, considerable studies have been focused on the RE^{3+}-doped TeO$_2$ based glasses to enhance their photoluminescence (PL) properties [1,2]. These properties can be tuned by changing the modifier, and/or activator ion concentration in the host glass. Such modifications yield the host network stronger and acquire necessary properties which will have potential applications in the fields of medicine and industry.

Tellurite glasses are potential candidates as hosts for RE^{3+} ions because of their lower phonon energies (700-800 cm^{-1}) and higher refractive indices than those of other oxide glasses (such as borate, phosphate and silicate). These properties are highly useful for higher radiative emission rates of RE^{3+} ions. Further, tellurite glasses have additional merits such as better transparency in the 0.35–6 μm region, better glass stability and RE^{3+} ions doping. Oxyfluoride tellurite glasses are characterized by the favourable properties such as lower phonon energies and a relatively higher thermal stability, higher chemical

durability and ease of preparation. Also, tellurite glasses are useful for fabrication of planar waveguides and optical fibers [1–6]. Rare earth ions-doped tellurite glasses find potential applications as optical devices such as optical fibers, optical amplifiers, display devices, solid state lasers, waveguides, optical modulators and frequency doublers. These matrices have good optical quality and are stable against atmospheric moisture over other oxide glasses [7–12].

The Dy^{3+} ion emits several interesting wavelengths that covers the region from visible to near-infrared (NIR) and are useful for the fabrication of photonic components and devices. The visible emission of Dy^{3+} ion primarily exhibit two strong bands, blue and yellow, corresponding to the $^4F_{9/2} \rightarrow {}^6H_{15/2}$ and $^4F_{9/2} \rightarrow {}^6H_{13/2}$ transitions, respectively. In these, the $^4F_{9/2} \rightarrow {}^6H_{15/2}$ transition is hypersensitive in principle and its intensity vary mainly depending on the nature of host. This gives rise to characteristic yellow (Y)-to-blue (B), (Y/B), intensity ratios which vary significantly with Dy^{3+} ions concentration and/or with glass composition. At a suitable ratio of Y/B, the Dy^{3+} ions will produce white luminescence [13]. The emission at 1.32 μm is useful for application in fiber amplifiers used in optical communication systems [14,15]. Dy^{3+}-doped BaYF$_5$ nanoparticles are found to have potential application as

temperature sensor [13]. Further, the Dy^{3+} ions can emit mid-IR luminescence from 2.9 to 4.4 μm [14–16] with proper excitations.

In view of the importance of tellurite glasses and interesting luminescence properties of Dy^{3+} ions, several authors investigated Dy^{3+}-doped tellurite glasses of different compositions and Dy^{3+} ion concentrations [1–10,20–34]. Kibrisli et al. [2], studied Dy_2O_3-doped tellurite glasses, with the composition of $50TeO_2$–$25WO_3$–$25Li_2O$, for solid state lighting applications through physical, thermal, structural and optical spectroscopy. They concluded that lower Dy_2O_3 content is necessary for an improved colour purity, quantum efficiency and non-radiative transition rate in this glass system. Structural, thermal, optical and white light emission properties of Dy^{3+}-doped titanium-tungstate-tellurite glasses were investigated and found that the glasses were suitable for generation of white light [3]. The Er^{3+}-doped tellurite glasses of the composition, TeO_2–ZnO–Na_2O–Er_2O_3, were investigated and found that these were promising materials for laser and optical amplifiers [4].

Heavy metal germanium tellurite glasses containing silver nano particles doped with Dy^{3+} ions were investigated under 454 nm excitation and were found to emit efficient warm yellowish-white light [6]. Tellurite glasses with the composition TeO_2–Tl_2O–ZnO were found to exhibit second harmonic generation [7]. Erbium doped niobic-tungsten-tellurite glasses were investigated [8] for laser and amplifier device applications through thermal stability and spectroscopic properties. Tellurite glasses co-doped with Dy^{3+} and Eu^{3+} ions were studied and were found to be promising for the UV and blue converted white light emitting diodes [9]. Tuyen et al. [10], studied Dy^{3+}-doped alumina lithium telluroborate glasses through JO analysis, spectroscopic and energy transfer properties. They also investigated white light emission properties and found that Y/B ratio depends strongly on the components of host and weekly on the concentration of Dy^{3+}-ions. Several other authors were also investigated RE^{3+}-doped tellurite glasses [17–32] to explore their thermal, structural, optical and white light emission properties.

Present work focuses on the preparation and characterization of Dy^{3+}-doped oxyfluorotellurite glasses via differential thermal analysis (DTA), Fourier Transform Infrared (FTIR), absorption, excitation and emission spectra and lifetime analyses. The obtained results are analyzed and compared with the similar properties of studied Dy^{3+}:glass systems.

2. Experimental details

Three different compositions of Dy^{3+} in oxyfluorotellurite (TZNDy) glasses having a composition (in mol %) of (74-x) TeO_2 + 20 ZnO + x ZnF_2 + 5 Na_2O + 1 Dy_2O_3, x = 0, 10 and 20, referred as $TZNDy_{1.0}$, $T10ZofNDy_{1.0}$ and $T20ZofNDy_{1.0}$ glasses, respectively, were made by traditional melt and sudden quenching method. About 20 g of the batch was mixed well in an agate mortar and thoroughly mixed batch so obtained was kept in a platinum crucible and placed in an high temperature furnace maintained at 860 °C for 1 h. The bubble free and homogenous melt thus obtained was poured on to a preheated stainless steel mould kept at 250 °C and the resulting glass samples were annealed at 250 °C for 6 h to free them from thermal strain and stress. Refractive indices and densities of the samples were determined by Brewster angle and Archimedes' methods, respectively. The thermal properties of the glasses were measured by using DTA at 10 °C/min heating rate under a N_2 atmosphere (TG-DTA 2020, Bruker AXS K.K.). The FTIR spectra were recorded on Nicolet Magna 550 IR spectrometer.

Absorption spectra were recorded using Lambda-950 Perkin Elmer Spectrophotometer. The luminescence spectra were measured using JOBIN YVON Fluorolog-3 Spectrofluorimeter exciting at 388 nm and also using 355 nm line of Nd:YAG (Spectron Laser Sys. SL802G) laser. For laser excitation, the signal was detected through a 0.75 m monochromator (Acton research Corp. Pro-750) by using a PMT (Hamamatsu R928). Lifetimes were evaluated by exciting at 355 nm with LeCroy 9310 digital storage oscilloscope connected to a computer.

3. Theory

The intensities of absorption bands are expressed in terms of experimental oscillator strengths (f_{exp}) by the expression [2,10,12,35],

$$f_{exp} = 4.318X10^{-9} \int \varepsilon(\nu)d\nu \tag{1}$$

where $\varepsilon(\nu)$ is the molar absorptivity at energy $\nu(cm^{-1})$ which can be obtained by Beer-Lambert's law [10].

Theoretical oscillator strengths (f_{cal}) for the induced electric dipole transition from the ground state to an excited state can be calculated from the Judd-Ofelt (JO) theory using the expression [2,10,12,35],

$$f_{cal} = \frac{8\pi^2 mc\nu}{3h(2J+1)} \frac{(n^2+2)^2}{9n} \sum_{\lambda=2,4,6} \Omega_\lambda \|U^\lambda\|^2 \tag{2}$$

where J is the total angular momentum of the ground state, n is the refractive index of the material, $\Omega_\lambda(\lambda = 2,4,6)$ are the JO intensity parameters and $\|U^\lambda\|^2$ are the squared doubly reduced matrix elements of the unit tensor operator of the rank $\lambda = 2,4,6$. These elements are independent of the host and hence are taken from our earlier studies [35].

Radiative properties such as radiative transition probability (A_R), branching ratio (β_R), calculated lifetime (τ_R), peak stimulated emission cross-section ($\sigma(\lambda_p)$) can be calculated from the JO intensity parameters as follows:

Radiative transition probability (A_R) from an initial level, ψJ to a final level $\psi' J'$ can be obtained using the following expression [2,3],

$$A_R(\psi J, \psi' J') = \frac{64\pi^4 e^2 \nu^3}{3h(2J+1)} \left[\frac{n(n^2+2)^2}{9} S_{ed} + n^3 S_{md} \right] \tag{3}$$

where S_{ed} is electric dipole and S_{md} is the magnetic dipole line strengths of a given transition. S_{ed} and S_{md} values can be determined using the expressions [2],

$$S_{ed}(\psi J, \psi' J') = e^2 \left(\sum_{\lambda=2,4,6} \Omega_\lambda (\psi J \|U^\lambda\| \psi' J')^2 \right) \tag{4}$$

$$S_{md}(\psi J, \psi' J') = \left(\frac{e^2}{4m^2c^2} \right) \Omega_\lambda (\psi J \|L + 2S\| \psi' J')^2 \tag{5}$$

Calculated branching ratio β_{cal}, can be determined using the following relation [2,3,35],

$$\beta_{cal}(\psi J, \psi' J') = \frac{A_R(\psi J, \psi' J')}{A_T(\psi' J')} \tag{6}$$

where A_T is the total radiative transition probability which is the sum of all A_R values from an excited state. The experimental branching ratio β_{exp}, values are determined from the ratio of integrated area of corresponding emission band to the total integrated area of emission.

The calculated lifetime of an excited state can be evaluated using the relation [2,35],

$$\tau_{cal} = \frac{1}{A_T(\psi' J')} \tag{7}$$

Peak stimulated emission cross-section, $\sigma(\lambda_p)$, can be calculated for each emission peak wavelength using the expression [2,3,35],

$$\sigma(\lambda_p)(\psi J, \psi' J') = \frac{\lambda_p^4}{8\pi cn^2 \Delta\lambda_{eff}} A_R(\psi J, \psi' J') \tag{8}$$

where $\Delta\lambda_{eff}$ is the effective bandwidth of corresponding emission band calculated by deviding the band area by height.

4. Results and discussion

4.1. Physical and thermal properties

Physical properties of the TZNDy glasses such as densities (d), concentration (C) of Dy^{3+} ions and refractive indices (n) are presented in Table 1. As can be seen, 'd' and 'n' values follow the same trend of increase from $TZNDy_{1.0}$ to $T10ZofNDy_{1.0}$ and then decrease for $T20ZofNDy_{1.0}$. The 'd' and 'n' values of TZNDy are slightly lower compared to those of $49TeO_2 + 25WO_3 + 25Li_2O + 1Dy_2O_3$ ($TWLDy_{1.0}$) [2] and $74TeO_2 + 10TiO_2 + 15WO_3 + 1Dy_2O_3$ ($TTiWDy_{1.0}$) [3] glasses.

Differential thermal analysis profiles of TZNDy glasses are depicted in Fig. 1. Glass transition (T_g) and onset of crystallization (T_x) temperature, and the difference between T_x and T_g (called thermal stability factor, $\Delta T = T_x - T_g$) of TZNDy glasses are shown in Fig. 1 and also in Table 1. It is found that, with the replacement of TeO_2 by ZnF_2 from 0 to 20 mol %, both T_g and T_x are gradually increased whereas the value of ΔT decreased from 122 to 119 °C. The thermal stability factor ΔT is one of the most important criterion for fiber drawing. The larger the value of ΔT, better the glass stability [23]. Larger value of ΔT minimizes the scattering loss caused by the crystallization of drawn fiber [3]. In general, glass host with $\Delta T > 100$ °C is suitable for drawing conventional fiber. The present results indicate that the $TZNDy_{1.0}$ glass has a better glass forming ability than the other glasses and is suitable for fiber drawing and for other optical devices.

4.2. FTIR spectral analysis

The FTIR spectral analysis is one of the spectroscopic techniques used to study the structure of the glasses. Fig. 2 illustrates the FTIR spectra of TZNDy glasses. As can be seen, five FTIR bands peaking at 460, 702, 1045, 1635 and 3490 cm^{-1} are observed distinctly. These peaks are found to be almost at the same positions for all the present glasses indicating that there may not be any change in structure of the glass with the increase of ZnF_2 content. The broad band at 3490 cm^{-1} corresponds to the OH stretching (ν_{OH}). This band may be due to presence of the inclusion of water molecules in the pores [24]. The band in the range of 445–465 cm^{-1} belong to the symmetrical stretching and bending modes of continuous chains of corner sharing sites of TeO_3, TeO_4 and TeO_{3+1} polyhedra [25,26]. This indicates that in these glasses, the vibrations of the Te–O–Te linkage are caused by the transformation of TeO_4 into TeO_3 groups. The band at 702 cm^{-1} corresponds to the asymmetric vibrations of the continuous network structure by the joining of TeO_4 trigonal bipyramids and Te–O–Te bond consisting of a long short Te–O bond [27]. Two overtones of peaks at 460 and 702 cm^{-1} are observed at around 1090 and 1635 cm^{-1}, respectively.

4.3. Absorption spectra and Judd-Ofelt analysis

Absorption spectra of the TZNDy glasses along with their band assignments in the wavelength range of 400–1950 nm are given in Fig. 3. The peaks originate from the ground level, $^6H_{15/2}$ to different excited states (shown in Fig. 3) belong to the $4f^9$ (Dy^{3+}) electronic configuration. As can be seen, the profile and the peak position of each transition remain unchanged with the addition of ZnF_2 content. The absorption level peaked at 1281 nm, corresponds to the $^6H_{15/2} \rightarrow {}^6F_{11/2}$ transition,
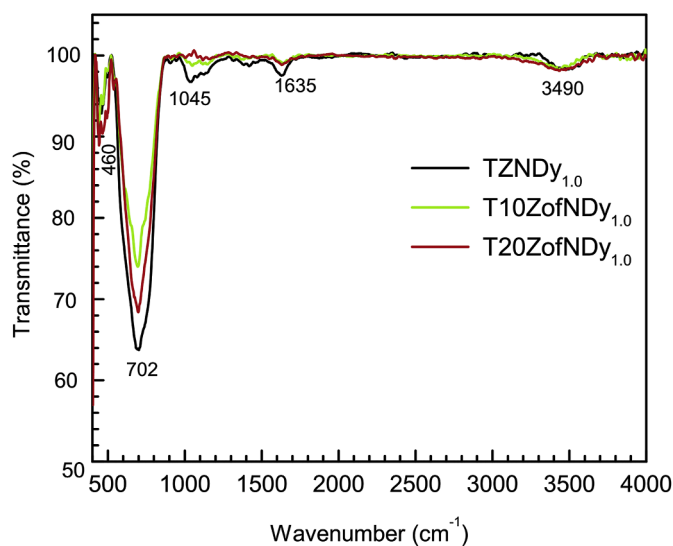

Fig. 1. DTA curves of TZNDy glasses.

Fig. 2. FTIR spectra of TZNDy glasses.

is dominant and obeys the selection rule, $|\Delta L| \leq 2$, $|\Delta S| = 0$ and $|\Delta J| \leq 2$. This is called hypersensitive transition (HST) and its intensity is more sensitive to the local environment surrounding the Dy^{3+} ions.

At first, the experimental oscillator strengths (f_{exp}) for the absorption transitions of Dy^{3+} ion are determined from the absorption spectrum by calculating the integrated area of each absorption band following the procedure described in our earlier works [36]. The JO model [37,38] has been used to evaluate the calculated (f_{cal}) oscillator strengths. The f_{exp} and f_{cal} values of all absorption peaks for the present TZNDy glasses along with other reported tellurite based glasses [2,3,28–30] are presented in Table 2. As can be seen, the magnitude of oscillator strength is higher for the $^6H_{15/2} \rightarrow {}^6F_{11/2}$ transition as it is a HST. The f_{exp} values of HSTs of TZNDy glasses varies with glass composition as $T10ZofNDy_{1.0} > T20ZofNDy_{1.0} > TZNDy_{1.0}$ and are higher than those of the reported Dy^{3+}:glasses [2,3,28,29]. These variations in f_{exp} values of HSTs are due to change in environment in the vicinity of the Dy^{3+} ions in the glasses. For other transitions, f_{exp} values of the titled glass systems are comparable to those of reported ones. Finally, three important parameters, called JO (Ω_λ, $\lambda = 2, 4$ and 6) parameters are calculated from the electric-dipole and magnetic-dipole components of f_{exp} and f_{cal} using
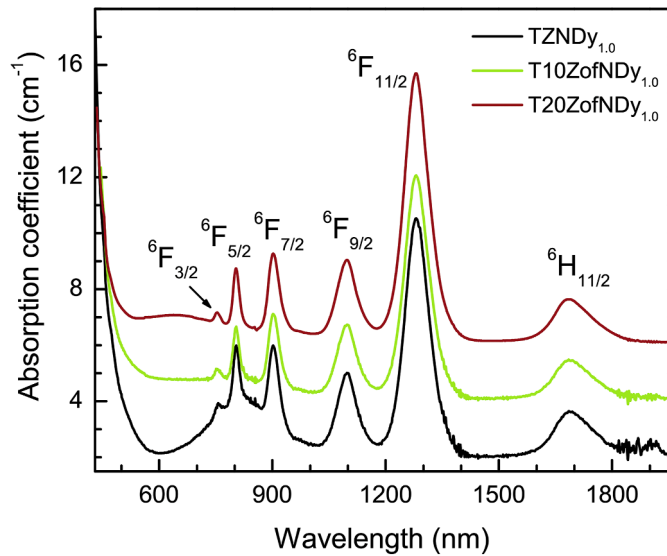
Table 1

Densities (d, gcm^{-3}), concentrations (C, $\times 10^{20}$ ions/cc), refractive indices (n), glass transition temperature (T_g, ^{0}C), onset of crystallization temperature (T_x, ^{0}C) and glass stability factors ($\Delta T = T_x - T_g$, ^{0}C) of TZNDy glasses.

Glass Label	d	C	n	T_g	T_x	$\Delta T = T_x - T_g$
$TZNDy_{1.0}$	4.63	1.975	1.96	292	414	122
$T10ZofNDy_{1.0}$	4.81	2.136	2.00	296	416	120
$T20ZofNDy_{1.0}$	4.50	2.181	1.89	309	428	119

Fig. 3. Optical absorption spectra of Dy^{3+} ions in TZNDy glasses.

least squares fitting approach for all the three TZNDy glasses and are presented in Table 3.

The JO parameters are very useful to evaluate the local structural geometry and bonding nature in the surroundings of RE^{3+} ions. The JO parameters of TZNDy glasses are shown in Table 3 along with those of studied Dy^{3+}-doped tellurite based glasses: $TWLDy_{1.0}$ [2], $TTiWDy_{1.0}$ [3], $39H_3BO_3 + 30TeO_2 + 30PbF_2 + 1Dy_2O_3$ ($BTPfDy_{1.0}$) [28], $76TeO_2 + 10ZnO + 9PbO + 1PbF_2 + 3Na_2O + 1Dy_2O_3$ ($TZPofNDy_{1.0}$) [29], $60TeO_2 + 12Pb_2O_5 + 20ZnF_2 + 3Nb_2O_5 + 5Dy_2O_3$ ($TPbZfNbDy_{5.0}$) [30], $59B_2O_3 + 10TeO_2 + 15CaO + 10Nb_2O_5 + 5ZnO + 1Dy_2O_3$ ($BTCNbZDy_{1.0}$) [31] and $40TeO_2 + 29B_2O_3 + 15MgO + 15K_2O + 1Dy_2O_3$ ($TBMKDy_{1.0}$) [32]. Generally, the parameter Ω_2 is related to the effects of short-range coordination and the other parameters Ω_4 and Ω_6 depend on the effect of long-range. The Ω_2 is a measure of the symmetry of ligand field in any glass host. The Ω_2 value depends on the covalence nature of RE-ligand bond while Ω_6 is inversely proportional to the covalence of RE-ligand bond and it also measure the rigidity of the host matrix [33,34]. The JO parameters follow the similar trend as $\Omega_2 > \Omega_4 > \Omega_6$ for both $T10ZofNDy_{1.0}$ and $T20ZofNDy_{1.0}$ glasses, whereas they follow $\Omega_2 > \Omega_6 > \Omega_4$ trend for $TZNDy_{1.0}$ glass indicating that the addition of ZnF_2 changes the surrounding ligand field of Dy^{3+}:glass. The larger value of Ω_2 is an indication for the higher asymmetry and covalency of local environment around the Dy^{3+} ions [33]. From Table 3, one can notice that the magnitude of Ω_2 ($\times 10^{-20}$ cm^2) increases from 5.94 to 11.62 with the increase in ZnF_2 component from 0 to 20 mol %. Moreover, larger variation in Ω_2 parameter indicates its strong dependence on the surroundings of the Dy^{3+} ion than the other two parameters (Ω_4 and Ω_6). The value of Ω_2 in $T20ZofNDy_{1.0}$ glass is found to be higher than those of $TZNDy_{1.0}$ and $T10ZofNDy_{1.0}$ glasses as well as those of reported Dy^{3+}:glasses [2,3,28–32] shown in Table 3, indicating the

existence of higher covalance between Dy^{3+} ion and surrounding ligand environment. On the other hand the Ω_4 and Ω_6 magnitude in the titled glass systems are comparable to those of the reported ones in Table 3.

Using the refractive index and JO parameters, important radiative characteristics such as transition probabilities (A), branching ratios (β_R) and lifetimes (τ_R) associated with transitions from the $^4F_{9/2}$ luminescent level to the next lower lying ^6H_J (J = 11/2, 13/2 and 15/2) levels are evaluated for all the TZNDy glasses and are presented in Table 4. From Table 4, one can see that, 'A' value of the $^4F_{9/2} \rightarrow ^6H_{13/2}$ level is the highest compared to those of other two levels indicating its highest transition probability which is reflected in the emission spectrum, where the band corresponding to this transition is most intense. For all the three transitions, maximum 'A' values are found for $T10ZfNDy_{1.0}$ glass and minimum values for $TZNDy_{1.0}$ glass. The calculated β_R values for all the three TZNDy glasses are in the order of $^4F_{9/2} \rightarrow ^6H_{11/2} < ^4F_{9/2} \rightarrow ^6H_{15/2} < ^4F_{9/2} \rightarrow ^6H_{13/2}$. The quantity of radiative (calculated) lifetimes

Table 3
Judd-Ofelt parameters ($\Omega_\lambda \pm 5\%$, $\times 10^{-20}$ cm^2) of TZNDy glasses along with those of some reported Dy^{3+}:glasses.

Glass	Ω_2	Ω_4	Ω_6	Trend
$TZNDy_{1.0}$ [Present work]	5.94	1.39	1.87	$\Omega_2 > \Omega_6 > \Omega_4$
$T10ZofNDy_{1.0}$ [Present work]	10.56	3.00	2.95	$\Omega_2 > \Omega_4 > \Omega_6$
$T20ZofNDy_{1.0}$ [Present work]	11.62	2.88	2.48	$\Omega_2 > \Omega_4 > \Omega_6$
$TWLDy_{1.0}$ [2]	5.90	0.93	1.22	$\Omega_2 > \Omega_6 > \Omega_4$
$TTiWDy_{1.0}$ [3]	3.37	0.30	1.07	$\Omega_2 > \Omega_6 > \Omega_4$
$BTPfDy_{1.0}$ [28]	7.75	2.31	2.70	$\Omega_2 > \Omega_6 > \Omega_4$
$TZPofNDy_{1.0}$ [29]	5.66	0.84	2.17	$\Omega_2 > \Omega_6 > \Omega_4$
$TPbZfNbDy_{5.0}$ [30]	2.32	0.64	4.64	$\Omega_2 > \Omega_6 > \Omega_4$
$BTCNbZDy_{1.0}$ [31]	11.30	3.30	2.60	$\Omega_2 > \Omega_4 > \Omega_6$
$TBMKDy_{1.0}$ [32]	9.23	1.15	1.56	$\Omega_2 > \Omega_6 > \Omega_4$

Table 4
Effective bandwidths ($\Delta\lambda_{eff} \pm 0.1$, nm) of the emission bands under 355 nm excitation, radiative transition probabilities ($A_R \pm 2\%$, s^{-1}), peak stimulated emission cross-sections ($\sigma(\lambda_p) \pm 0.2$, $\times 10^{-21}$ cm^2), experimental and calculated branching ratios ($\beta_R \pm 2\%$) for the $^4F_{9/2} \rightarrow ^6H_J$ (J = 11/2, 13/2,15/2) transitions and radiative lifetime ($\tau_R \pm 2\%$, µs) of the $^4F_{9/2}$ level of Dy^{3+} ions in TZNDy glasses.

Glass Transition $^4F_{9/2} \rightarrow$	$\Delta\lambda_{eff}$	A	$\sigma(\lambda_p)$	β_R Exp.	β_R Cal.	τ_R
$TZNDy_{1.0}$						
$^6H_{11/2}$	12.23	155	0.86	0.03	0.08	
$^6H_{13/2}$	10.83	1299	4.52	0.64	0.73	483
$^6H_{15/2}$	12.26	333	5.97	0.33	0.19	
$T10ZofNDy_{1.0}$						
$^6H_{11/2}$	12.80	589	1.40	0.03	0.08	
$^6H_{13/2}$	10.91	2445	8.13	0.62	0.74	267
$^6H_{15/2}$	12.26	589	0.86	0.35	0.18	
$T20ZofNDy_{1.0}$						
$^6H_{11/2}$	11.21	240	1.56	0.02	0.09	
$^6H_{13/2}$	10.95	2059	7.64	0.62	0.76	326
$^6H_{15/2}$	12.79	411	0.69	0.36	0.15	

Table 2
Absorption levels, band positions (λ_p, nm), experimental (f_{exp}) and calculated (f_{cal}) oscillator strengths ($\times 10^{-6}$) of TZNDy glasses and experimental oscillator strengths of some reported Dy^{3+}:glasses. All the transitions are from the ground state, $^6H_{15/2}$.

Level	λ_p	$TZNDy_{1.0}$ f_{exp}	$TZNDy_{1.0}$ f_{cal}	$T10ZofNDy_{1.0}$ f_{exp}	$T10ZofNDy_{1.0}$ f_{cal}	$T20ZofNDy_{1.0}$ f_{exp}	$T20ZofNDy_{1.0}$ f_{cal}	$TWLDy_{1.0}$ [2]	$TTiWDy_{1.0}$ [3]	$BTPfDy_{1.0}$ [28]	$TZPofNDy_{1.0}$ [29]	$TPbZfNbDy_{5.0}$ [30]
$^6H_{11/2}$	1685	1.12	1.42	2.08	2.42	1.76	2.08	1.59	0.61	1.27	1.53	2.29
$^6H_{9/2}+F_{11/2}$	1281	7.70	7.66	14.44	14.39	13.86	13.82	6.53	4.74	6.76	7.31	4.04
$^6H_{7/2}+F_{9/2}$	1098	2.46	2.57	4.60	4.75	3.76	3.89	1.49	1.18	2.65	2.81	4.90
$^6F_{7/2}$	902	2.54	2.22	4.30	3.78	3.37	2.94	0.77	1.68	2.16	2.48	2.10
$^6F_{5/2}$	804	0.56	1.05	2.20	1.72	1.86	1.30	0.34	0.10	1.38	1.69	0.28
$^6F_{3/2}$	752	1.18	0.20	0.46	0.32	0.37	0.25	0.06	0.29	0.19	0.23	0.21
δ_{rms}		± 0.49		± 0.33		± 0.33						

of the $^4F_{9/2}$ level first decreases and then increases with increase in ZnF_2 component. This could be caused by the structural modifications in the surrounding of the Dy^{3+} ions.

4.4. Luminescence properties

Selection of proper excitation wavelength is an important parameter to analyze the emission properties of any RE^{3+} ion. The absorption spectrum of present Dy^{3+}-doped glasses do not show any bands in ultraviolet–visible region because of the dominant absorption of tellurite host in this region. Excitation spectrum, measured in the range of 300–550 nm for the T20ZofNDy$_{1.0}$ glass, monitoring the well known emission of the Dy^{3+} ion at 577 nm which belongs to the $^4F_{9/2} \rightarrow ^4H_{13/2}$ level, is shown in Fig. 4. The excitation peaks centered at 351, 367, 387, 428, 454 and 473 nm are attributed to the $^6H_{15/2} \rightarrow ^6P_{7/2}$, $^4P_{3/2}$, $^4I_{13/2}$, $^6G_{11/2}$, $^4I_{15/2}$ and $^4F_{9/2}$ levels, respectively. It is well-known that excitation energy corresponding to the intense excitation peak can give better luminescence. The excitation bands peaked at 354, 388 and 453 nm are found to be most intense in UV–visible region. However, our experimental facilities are limited to UV excitation only. Hence, the luminescence spectra are recorded using 355 nm and 388 nm excitation wavelengths.

Photoluminescence (PL) spectra of TZNDy are measured in the spectral region of 430–700 nm with 388 nm broad band and 355 nm laser excitations and are shown in Figs. 5 and 6, respectively. The luminescence spectra show principal characteristic emission peaks of Dy^{3+} ion consisting of the band, $^4F_{9/2} \rightarrow ^6H_{15/2}$ at 482 nm (due to magnetic-dipole) and the band $^4F_{9/2} \rightarrow ^6H_{13/2}$ at 575 nm (due to electric-dipole) and a relatively feeble band, $^4F_{9/2} \rightarrow ^6H_{11/2}$ at 666 nm. It is well known that the yellow emission of Dy^{3+} belongs to the HST follows the selection rule $|\Delta J| \leq 2$, and is highly sensitive to the surroundings of the active Dy^{3+} ions. The blue emission marginally varies with the crystal-field effect surrounding the Dy^{3+} ion. When Dy^{3+} is kept in a low-symmetry local site, the yellow emission usually dominates in the emission spectrum, and when it is in a high-symmetry site, the blue emission dominates in the de-excitation spectrum [39,40]. Further, higher Y/B ratio is an indication for the higher degree of covalency between Dy^{3+} ion and surrounding oxygen ions [37]. The Y/B ratios for TZNDy glasses, under 388 and 355 nm excitations are evaluated and are presented in Table 5. From Table 5, Y/B ratios of the present glass systems are <1 for broadband excitation and ~2 for 355 nm laser excitation. The Y/B ratios of TZNDy are compared to those of reported 1.0 mol

Fig. 5. Luminescence spectra of TZNDy glasses under 388 nm broadband excitation.
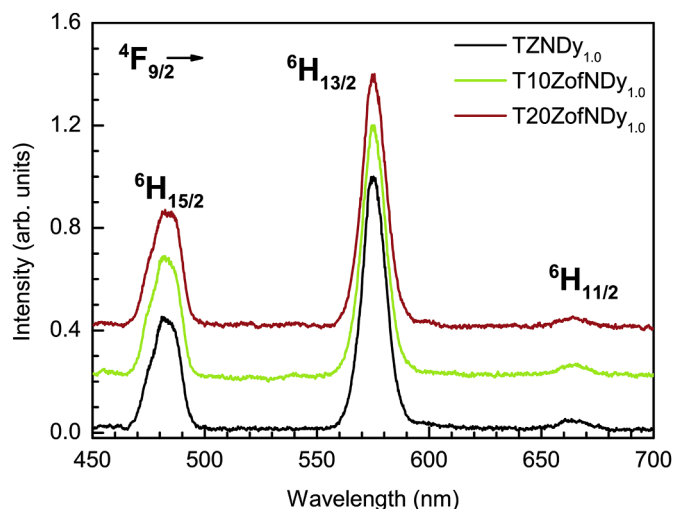

Fig. 6. Luminescence spectra of TZNDy glasses under 355 nm laser excitation.

% Dy^{3+}-doped glasses [1–3,29,31], $41P_2O_5 + 17K_2O + 8Al_2O_3 + 23ZnF_2 + 10LiF + 1Dy_2O_3$ (PKAZfLfDy$_{1.0}$) [41], $30KH_2PO_4 + 24(NaPO_3)_6 + 25TiO_2 + 20CaCl_2 + 1Dy_2O_3$ (PKNTiClDy$_{1.0}$) [42], $30KH_2PO_4 + 24(NaPO_3)_6 + 25TiO_2 + 20SrCl_2 + 1Dy_2O_3$ (PKNTiSlDy$_{1.0}$) [42], $(60-x)TeO_2 + 25WO_3 + 15PbF_2 + 1Dy_2O_3$ (TWPfDy$_{1.0}$) [43], $46.7SiO_2 + 35.9BaO + 1.0Al_2O_3 + 4.03(Li_2O + Na_2O + K_2O) + 11.22Y_2O_3 + 1.15Dy_2O_3$ (SBALNKYDy$_{1.15}$) [44] in Table 5. Among the reported glasses shown in Table 5, laser excitation was used only for TTiWDy$_{1.0}$ [3] and TZPofNDy$_{1.0}$ [29] and for the remaining systems, broadband excitation was used.

From the PL spectra, other radiative properties such as experimental branching ratio, effective bandwidth ($\Delta\lambda_{eff}$), and stimulated emission cross-sections ($\sigma(\lambda_p)$) for the $^4F_{9/2} \rightarrow ^6H_{11/2,13/2,15/2}$ transitions of TZNDy glasses are determined and are presented in Table 4. From Table 4, one can see that, $\Delta\lambda_{eff}$ values of the $^4F_{9/2} \rightarrow ^6H_{13/2}$ band are lower compared to those of other two bands. Also, the values of $\sigma(\lambda_p)$ and calculated branching ratios (β_{cal}) for the $^4F_{9/2} \rightarrow ^6H_{13/2}$ (HST) are higher than those of other transitions. Moreover, the $\sigma(\lambda_p)$ ($\times 10^{-21}$ cm^2) value of this HST changes from 4.52 to 8.13 with change in ZnF_2 content. The luminescence branching ratio is one of the crucial parameter that indicates the lasing nature of a transition and it was shown that an emission level with $\beta_R \geq 60\%$ is relatively more potential for laser

Fig. 4. Excitation spectrum of T20ZofNDy$_{1.0}$ glass monitoring the 577 nm emission.

Table 5

Yellow to blue intensity ratios (Y/B), chromaticity color coordinates (x, y) and correlated color temperature (CCT, K) of TZNDy glasses under 388 nm broadband and 355 nm laser excitations and those of some reported 1.0 mol % Dy^{3+}-doped glasses.

System	Y/B	Chromaticity co-ordinates		CCT (K)
		x	Y	
388 nm Excitation				
$TZNDy_{1.0}$	0.83	0.341	0.387	5222
$T10ZofNDy_{1.0}$	0.71	0.321	0.366	5950
$T20ZofNDy_{1.0}$	0.74	0.325	0.372	5782
355 nm Excitation				
$TZNDy_{1.0}$	1.93	0.394	0.429	4003
$T10ZofNDy_{1.0}$	1.77	0.390	0.420	4040
$T20ZofNDy_{1.0}$	1.76	0.385	0.427	4187
Reported				
$TWLDy_{1.0}$ [2]	2.40	0.38	0.43	4221
$TTiWDy_{1.0}$ [3]	2.02	0.38	0.41	–
$TZPofNDy_{1.0}$ [29]	0.88	0.38	0.43	4312
$BTCNbZDy_{1.0}$ [31]	0.65	0.31	0.36	6439
$PKAZfLfDy_{1.0}$ [41]	0.77	0.32	0.37	5992
$PKNTiClDy_{1.0}$ [42]	1.23	0.33	0.34	5609
$PKNTiSlDy_{1.0}$ [42]	1.38	0.33	0.34	5609
$TWPfDy_{1.0}$ [43]	1.02	0.34	0.40	5270
$SBALNKYDy_{1.15}$ [44]	2.03	0.385	0.437	4233

action. As can be seen from Table 4, there is reasonably good coincidence between calculated and experimental β_R values which indicates the accuracy of the calculations. The value of β_R (both experimental and calculated) for the $^4F_{9/2} \rightarrow {}^6H_{13/2}$ level in all the TZNDy glasses is estimated to be >60%, showing the suitability of present glass systems for lasing applications at this wavelength.

The $\Delta\lambda_{eff}$, $\sigma(\lambda_p)$ and β_{cal} of the $^4F_{9/2} \rightarrow {}^6H_{13/2}$ level as well as radiative predicted lifetime (τ_R) of the $^4F_{9/2}$ luminescent state of Dy^{3+} ion in various tellurite based glasses [3,28–32] are compared in Table 6. As can be seen, relatively larger value of $\sigma(\lambda_p)$ for $^4F_{9/2} \rightarrow {}^6H_{13/2}$ channel in $T10ZofNDy_{1.0}$ glass, compared to already studied Dy^{3+}:glasses, indicate that this glass is a suitable gain media for potential laser emission in yellow spectral region. The value of τ_R is found to decrease from 483 to 267 and then increase to 326 µs when ZnF_2 increased from 0 to 20 mol % and these values are comparable with other reported glasses [29,30] shown in Table 6. Out of all the Dy^{3+}:tellurite glasses [3,28–32] compared in Table 6, TZNDy glasses show lower $\Delta\lambda_{eff}$ and higher $\sigma(\lambda_p)$ values. The β_{cal} values of TZNDy glasses are higher than all the compared glass systems except that of $BTCNbZDy_{1.0}$ [31] glass. Calculated lifetimes of the $^4F_{9/2}$ state in the present glasses are comparable to those of $TZPofNDy_{1.0}$ [29] and $TPbZfNbDy_{5.0}$ [30] glasses and are less than those

Table 6

Effective bandwidths ($\Delta\lambda_{eff}\pm0.1$, nm) of the emission bands under 355 nm excitation, stimulated emission cross-section ($\sigma(\lambda_p)\pm0.2$, x 10^{-21} cm^2) and calculated branching ratio (β_{cal}) of $^4F_{9/2} \rightarrow {}^6H_{13/2}$ transition, radiative lifetime ($\tau_R\pm2\%$, µs) of the $^4F_{9/2}$ level, gain bandwidth ($\sigma(\lambda_p)$ x $\Delta\lambda_{eff}$), x10^{-27} and optical gain ($\sigma(\lambda_p)$ x τ_R), x10^{-24} of the $^4F_{9/2}$ level of Dy^{3+} ions in various tellurite based glasses.

Glass	$\Delta\lambda_{eff}$	σ	β_{cal}	τ_R	$\sigma(\lambda_p)$ x $\Delta\lambda_{eff}$	$\sigma(\lambda_p)$ x τ_R
$TZNDy_{1.0}$ [Present work]	10.83	4.52	0.73	483	4.90	2.18
$T10ZofNDy_{1.0}$ [Present work]	10.91	8.13	0.74	267	8.87	2.17
$T20ZofNDy_{1.0}$ [Present work]	10.95	7.64	0.76	326	8.37	2.49
$TTiWDy_{1.0}$ [3]	16	2.4	0.53	–	3.84	–
$BTPfDy_{1.0}$ [28]	16	2.86	0.63	–	4.58	–
$TZPofNDy_{1.0}$ [29]	14.56	4.07	0.63	374	5.93	1.52
$TPbZfNbDy_{5.0}$ [30]	–	–	0.61	453	–	–
$BTCNbZDy_{1.0}$ [31]	17.06	3.22	0.83	999	5.49	3.22
$TBMKDy_{1.0}$ [32]	13.11	6.05	0.69	778	7.93	2.51

of $BTCNbZDy_{1.0}$ [31] and $TBMKDy_{1.0}$ [32] glasses.

The parameters, optical gain ($\sigma(\lambda_p) \times \tau_R$) and gain bandwidth ($\sigma(\lambda_p) \times \Delta\lambda_{eff}$) are very essential ones to predict the amplification of the RE^{3+} ions doped medium. An optical amplifier is characterized by higher quantities of gain bandwidth and optical gain [31]. As can be noticed from Table 6, $\sigma(\lambda_p) \times \tau_R$ and $\sigma(\lambda_p) \times \Delta\lambda_{eff}$ of the titled TZNDy are nearer to those of the Dy^{3+}:tellurites [3,28–32]. Out of all the glasses compared in Table 6, $T10ZofNDy_{1.0}$ and $T20ZfNDy_{1.0}$ glasses show higher values of gain bandwidth.

4.5. CIE chromaticity coordinates

The emission spectrum of Dy^{3+} ion under UV excitation exhibits two prominent bands in the blue and yellow regions. By properly adjusting the intensities of these bands one can generate the white luminescence. In view of this, an attempt is made to measure luminescence from TZNDy glasses by changing the excitation wavelength. Emission spectra of TZNDy glasses are recorded by exciting at 388 nm broadband and 355 nm laser excitations and are shown in Figs. 5 and 6, respectively. From Figs. 5 and 6, one can see that the blue band is dominant under broadband excitation whereas the yellow band is found to be more intense than blue under laser excitation. This clearly indicates that the symmetry sites occupied Dy^{3+} can be changed by excitation source also rather than changing the composition.

The white light emission properties of TZNDy glasses are examined with the help of chromaticity co-ordinate of colors under different excitation sources. These co-ordinates are obtained by converting the luminescence spectra of present glasses into standard CIE 1931 chromaticity co-ordinate graphs. The obtained graphs of colour are listed in Table 5 and located in chromaticity frame shown in Fig. 7. As can be seen, the co-ordinates falls in yellow region under 355 nm laser excitation. But intense white luminescence is noticed when the glasses are excited with 388 nm radiation. The CIE color co-ordinates of TZNDy glasses along with other reported 1.0 mol % Dy^{3+}-doped glasses [1–3, 29,31,41–44] are presented in Table 5. From Table 5, the evaluated co-ordinates of colour for the present glasses (for 388 nm excitation) are very nearer to white light illuminate and are comparable to those of studied Dy^{3+}:glasses. Further, the color coordinates of $T20ZofNDy_{1.0}$
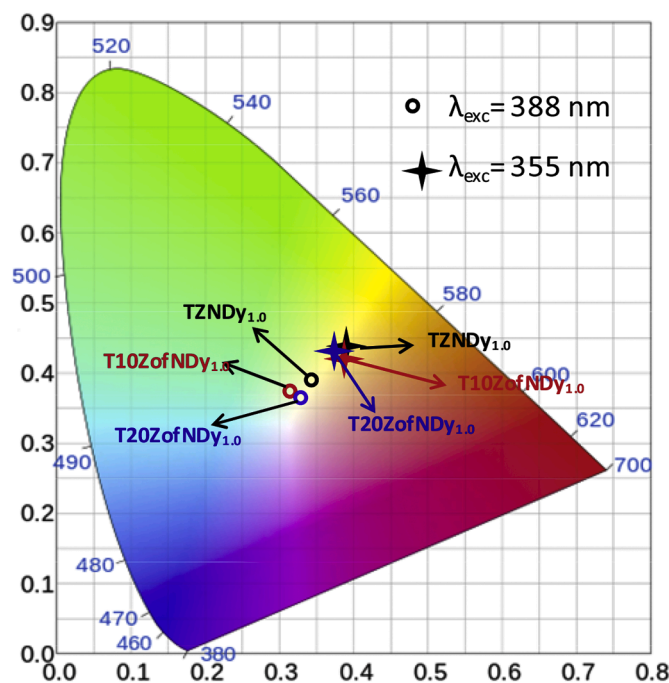
Fig. 7. CIE 1931 chromaticity diagram showing the chromaticity coordinates (x, y) of TZNDy glasses under 355 nm and 388 nm excitations.

glass (0.33, 0.37) are very nearer to the equal energy position (0.33, 0.33).

The quality of the light source is generally assessed by calculating correlated color temperature (CCT) [8], which indicates the temperature of a nearest Plankian black-body radiator to the operating position in the chromaticity graphical representation. The CCT values are determined based on the color coordinators through the Mc Camy's Eq. [45],

$$CCT = -449n^3 + 3525n^2 - 6823n$$
$$+ 5520.33 \qquad (9)$$

Here n = (x-x_e)/(y-y_e) indicates the inverse slope line where x_e = 0.332 and y_e = 0.186 relates the epicenter. The CCT values of the present glasses are calculated for 388 and 355 nm excitations and are collected in Table 5 along with the reported values of 1.0 mol % Dy^{3+}-doped glasses [2,3,29,31,41–44]. The CCT quantities calculated with 388 nm broadband source are closer to that of normal day light (5500 K) and those with 355 nm laser excitation are nearer to that of fluorescent tube (3935 K) [46]. From Table 5, CCT values of reported glass systems of $TWLDy_{1.0}$ [2], $TZPofNDy_{1.0}$ [29] and $SBALNKYDy_{1.15}$ [44] are nearer to that of fluorescent tube and the rest of the systems [1,31,41–43] are nearer to that of day light.

4.6. Decay curves

Decay curves of the $^4F_{9/2}$ state of Dy^{3+} ion in TZNDy glasses are recorded by exciting with 355 nm laser and observing the emission at 577 nm which are presented in Fig. 8. All the decay profiles exhibit non-exponential behaviour and hence, the average lifetime (τ) is determined using the below Eqn.,

$$\tau_{exp} = \int \frac{tI(t)dt}{I(t)dt} \qquad (10)$$

and are found to be 145, 166 and 163 μs for $TZNDy_{1.0}$, $T10ZofNDy_{1.0}$ and $T20ZofNDy_{1.0}$ glasses, respectively. It is observed that there is no significant variation in experimental lifetimes with increase in ZnF_2 content from 10 to 20% where as significant variation is noticed for the radiative lifetime. The quantum efficiency is expressed as the ratio of number of emitted to the absorbed photons. In the case of RE^{3+} ions-doped systems, it is taken as the ratio of τ_{exp} to τ_R for the given states ($\eta = \frac{\tau_{exp}}{\tau_R} X100$). The quantity of η for the $^4F_{9/2}$ state of Dy^{3+} in the present $TZNDy_{1.0}$, $T10ZofNDy_{1.0}$ and $T20ZofNDy_{1.0}$ glasses are found to be 30, 62 and 50, respectively. Out of the three glasses, 'η' is maximum (62) for the $T10ZofNDy_{1.0}$ glass and minimum (30%) for the $TZNDy_{1.0}$ glass. The 'η' values of the present Dy^{3+} glasses are comparable to those of the studied ones, $PKAZfLfDy_{1.0}$ (55) [41] and $TWLDy_{1.0}$ (61) [2] but less than that of $TTiWDy_{1.0}$ (90) glass [3].

5. Conclusions

Thermal, structural, optical and white light emission properties of TZNDy glasses have been systematically investigated using DTA curves, FTIR, absorption, excitation and emission spectra and decay times. It is found that thermal stability factor decreases from 122 to 119 °C with the replacement of TeO_2 by ZnF_2 from 0 to 20 mol %. By applying the Judd-Ofelt model to the absorption spectra of TZNDy glasses, three JO parameters are evaluated and are in turn used to predict the radiative properties of the emitting level, $^4F_{9/2}$, such as radiative transition probabilities, branching ratios, calculated lifetimes and peak stimulated emission cross-sections. From the emission spectra, obtained with 388 nm excitation, experimental branching ratios are evaluated and are found to be in good agreement with the calculated ones. The CIE chromaticity co-ordinates of colour are determined from the emission spectra. It is found that the titled glasses emit bright white light under
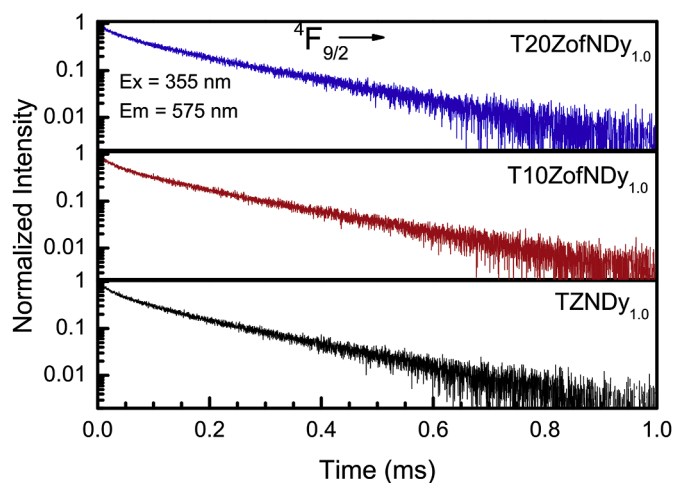

Fig. 8. Decay curves for the $^4F_{9/2}$ level of Dy^{3+} ions in TZNDy glasses.

388 nm broadband excitation. Among the glass systems studied, the color coordinates of the $T20ZofNDy_{1.0}$ glass are very nearer to the equal energy point. The decay curves of the $^4F_{9/2}$ state of Dy^{3+} ions show non-exponential behavior for the studied glasses. Quantum efficiency for the $^4F_{9/2}$ state is found to be maximum for the $T10ZofNDy_{1.0}$ glass. The results obtained in the present study can find potential applications in the design of optical display devices.

CRediT author statement

P. Babu, Conceptualization, Invesitigation, Writting - Writing – original draft. V. Chandrappa, Methodology, Investigation. N. Vijaya, Formal analysis, Investigation. C.K. Jayasankar, Resources, Writting – Writing – review & editing. Hyo Jin Seo, Resourses, Supervision.

Declaration of competing interest

The authors declare that they have no known competing financial interests or personal relationships that could have appeared to influence the work reported in this paper.

References

[1] M. Walas, A. Pastwa, T. Lewandowski, A. Synak, I. Gryczynski, W. Sadowski, B. Koscielska, Luminescent properties of Ln^{3+} doped tellurite glasses containing AlF_3, Opt. Mater. 59 (2016) 70–75, https://doi.org/10.1016/j.optmat.2016.01.040.

[2] O. Kibrisli, A.E. Ersundu, M. Celikbilek Ersundu, Dy^{3+} doped tellurite glasses for solid state lighting: an investigation through physical, thermal, structural and optical spectroscopy studies, J. Non-Cryst. Solids 513 (2019) 125–136, https://doi.org/10.1016/j.jnoncrysol.2019.03.020.

[3] L. Jyothi, G. Upender, R. Kuladeep, D. Narayana Rao, Structural, thermal, optical properties and simulation of white light of titanium-tungstate-tellurite glasses doped with dysprosium, Mater. Res. Bull. 50 (2014) 424–431, https://doi.org/10.1016/j.materresbull.2013.11.013.

[4] I. Jlassi, H. Elhouichet, M. Ferid, C. Barthou, Judd-Ofelt analysis and improvement of thermal and optical properties of tellurite glasses by adding P_2O_5, J. Lumin. 130 (2010) 2394–2401, https://doi.org/10.1016/j.jlumin.2010.07.026.

[5] J.E. Stanworth, Tellurite glasses, J. Soc. Glass. Technol. 38 (1954) 425.

[6] C. Hua, L. Shen, E.Y.B. Pun, D. Li, H. Lin, Dy^{3+} doped tellurite glasses containing silver nanoparticles for lighting devices, Opt. Mater. 78 (2018) 72–81, https://doi.org/10.1016/j.optmat.2018.02.006.

[7] M. Soulis, J.-R. Dulclère, T. Haykawa, V. Courdec, M. Dutreilh-Colas, P. Thomas, Second harmonic generation induced by optical poling in new TeO_2-Tl_2O-ZnO

glasses, Mater. Res. Bull. 45 (2010) 551–557, https://doi.org/10.1016/j.materresbull.2010.01.024.

[8] N.G. Boetti, J. Lousteau, A. Chiasera, M. Ferrari, E. Mura, G.C. Scarpignato, S. Abrate, D. Milanese, Thermal stability and spectroscopic properties of erbium-doped niobic-tungsten-tellurite glasses for laser and amplifier devices, J. Lumin. 132 (2012) 1265–1269,, https://doi.org/10.1016/j.jlumin.2011.12.057.

[9] C. Yu, Z. Yang, A. Huang, Z. Chai, J. Qiu, Z. Song, D. Zhou, Photoluminescence properties of tellurite glasses doped Dy^{3+} and Eu^{3+} for the UV and blue converted WLEDs, J. Non-Cryst. Solids 457 (2017) 1–8, https://doi.org/10.1016/j.jnoncrysol.2016.11.025.

[10] V.P. Tuyen, V.X. Quang, P.V. Do, L.D. Thanh, N.X. Ca, V.X. Hoa, L.V. Tuat, L.A. Thi, M. Nogami, An in-depth study of the Judd-Ofelt analysis, spectroscopic properties and energy transfer of Dy^{3+} in alumino-lithium-telluroborate glasses, J. Lumin. 210 (2019) 435–443, https://doi.org/10.1016/j.jlumin.2019.03.009.

[11] D.V. Phan, V.X. Quang, H.V. Tuyen, T. Ngoc, V.P. Tuyen, L.D. Thanh, N.X. Ca, N.T. Hien, Structure, optical properties and energy transfer in potassium-alumino-borotellurite glasses doped with Eu^{3+} ions, J. Lumin. 216 (2019) 116748, https://doi.org/10.1016/j.jlumin.2019.116748.

[12] V.X. Quang, P.V. Do, N.X. Ca, L.D. Thanh, V.P. Tuyen, P.M. Tan, V.X. Hoa, N.T. Hien, Role of modifier ion radius in luminescence enhancement from $^5D_4$ level of Tb^{3+} ion doped alkali-alumino-telluroborate glasses, J. Lumin. 221 (2020) 117039, https://doi.org/10.1016/j.jlumin.2020.117039.

[13] A.N. Belsky, N.M. Khaidukov, J.C. Krupa, V.N. Makhov, A. Philippov, Luminescence of $CsGd_2F_7:Er^{3+}$, Dy^{3+} under UV excitation, J. Lumin. 94–95 (2001) 45–49.

[14] J.G. Choi, J. Heo, 1.3 μm emission and multiphonon relaxation phenomenon in $PbO-Bi_2O_3-Ga_2O_3$ glasses doped with rare-earths, J. Non-Cryst. Solids 217 (1997) 199–207.

[15] Z. Yang, W. Chen, L. Luo, Dy^{3+}-doped Ge-Ga-Sb-Se glasses for 1.3 μm optical amplifiers, J. Non-Cryst. Solids 351 (2005) 2513–2518, https://doi.org/10.1016/j.jnoncrysol.2005.07.008.

[16] Z. Cao, S. Zhou, G. Jiang, Y. Chen, C. Duan, M. Yin, Temperature dependent luminescence of Dy^{3+}-doped $BaYF_5$ nanoparticles for optical thermometry, Curr. Appl. Phys. 14 (2014) 1069–1071, https://doi.org/10.1016/j.cap.2014.05.020.

[17] Y. Tian, R. Xu, L. Hua, J. Zhang, Broadband 2.84 μm luminescence properties and Judd-Ofelt analysis in Dy^{3+}-doped ZrF_4-BaF_2-LaF_3-AlF_3-YF_3 glass, J. Lumin. 132 (2012) 128–131,, https://doi.org/10.1016/j.jlumin.2011.08.017.

[18] M. Zhang, A. Yang, Y. Peng, B. Zhang, H. Ren, W. Guo, Y. Yang, C. Zhai, Y. Wang, Z. Yang, D. Tang, Dy^{3+}-doped Ga-Sb-S chalcogenide glasses for mid-infrared lasers, Mater. Res. Bull. 70 (2015) 55–59, https://doi.org/10.1016/j.materresbull.2015.04.019.

[19] L. Gomes, J. Lousteau, D. Milanese, E. Mura, S.D. Jackson, Spectroscopy of mid-infrared (2.9 μm) fluorescence and energy transfer in Dy^{3+}-doped tellurite glasses, J. Opt. Soc. Am. B 31 (2014) 429–435, https://doi.org/10.1364/JOSAB.31.000429.

[20] Wojciech A. Pisarski, Joanna Pisarska, Lidia Zur, Tomasz Goryczka, Structural and optical aspects for Eu^{3+} and Dy^{3+} ions in heavy metal glasses based on $PbO-Ga_2O_3-XO_2$ (X = Te, Ge, Si), Opt. Mater. 35 (2013) 1051–1056, https://doi.org/10.1016/j.optmat.2012.12.012.

[21] M. Reza Dousti, S. Raheleh Hosseinian, Enhanced upconversion emission of Dy^{3+} doped tellurite glass by heat-treated silver nanoparticles, J. Lumin. 154 (2014) 218–223, https://doi.org/10.1016/j.jlumin.2014.04.028.

[22] M. Vijayakumar, K. Marimuthu, Tailoring the luminescence of Eu^{3+} co-doped Dy^{3+} incorporated aluminofluoro-borophosphate glasses for white light applications, J. Lumin. 178 (2016) 414–424, https://doi.org/10.1016/j.jlumin.2016.06.016.

[23] G. Wang, S. Xu, S. Dai, J. Yang, L. Hu, Z. Jiang, Thermal stability, spectra and laser properties of Yb:lead-zinc-telluride oxide glasses, J. Non-Cryst. Solids 336 (2004) 102–106,, https://doi.org/10.1016/j.jnoncrysol.2004.01.009.

[24] S.K.J. Al-Ani, S.S. Al-Rawi, A.H. Jassim, H.A. Al-Hilli, FTIR spectra of Molybdenum tellurite glasses, Iraqi J. Appl. Phys. 2 (2006) 23–25.

[25] H. Burger, K. Kneipp, H. Hobert, W. Vogel, V. Kozhukharov, S. Neov, Glass formation, properties and structure of glasses in the TeO_2-ZnO system, J. Non-Cryst. Solids 151 (1992) 134–142.

[26] T. Sekiya, N. Mochida, A. Ohtsuka, Raman spectra of $MO-TeO_2$ (M = Mg, Sr, Ba and Zn) glasses, J. Non-Cryst. Solids 168 (1994) 106–114.

[27] P. Wang, C. Wang, W. Li, M. Lu, B. Peng, Effects of Al_2O_3 on the thermal stability, glass configuration of Yb^{3+}-doped TeO_2-K_2O-ZnO-Al_2O_3 based tellurite laser glasses, J. Non-Cryst. Soids 359 (2013) 5–8,, https://doi.org/10.1016/j.jnoncrysol.2012.09.031.

[28] M.V. Vijaya Kumar, B.C. Jamalaiah, K. Rama Gopal, R.R. Reddy, Optical absorption and fluorescence studies of Dy^{3+}-doped lead telluroborate glasses, J. Lumin. 132 (2012) 86–90,, https://doi.org/10.1016/j.jlumin.2011.07.021.

[29] K. Damak, El S. Yousef, C. Rüssel, R. Maâlej, White light generation from Dy^{3+} doped tellurite glass, J. Quant. Spectrosc. Radiat. Transfer 134 (2014) 55–63, https://doi.org/10.1016/j.jqsrt.2013.10.013.

[30] B. Klimesz, W. Ryba-Romanowski, R. Lisiecki, Oxyfluorotellurite glasses doped by dysprosium ions. Thermal and optical properties, Opt. Mater. 42 (2015) 538–543, https://doi.org/10.1016/j.optmat.2015.02.012.

[31] O. Ravi, C. Madhukar Reddy, B. Sudhakar Reddy, B. Deva Prasad Raju, Judd-Ofelt analysis and spectral properties of Dy^{3+} ions doped niobium containing tellurium calcium zinc borate glasses, Opt Commun. 312 (2014) 263–268, https://doi.org/10.1016/j.optcom.2013.09.044.

[32] K. Maheshvaran, K. Marimuthu, Structural and optical investigations on Dy^{3+} doped boro-tellurite glasses, J. Alloys Compd. 509 (2011) 7427–7433, https://doi.org/10.1016/j.jallcom.2011.04.055.

[33] R. Cases, M.A. Chammaro, Judd-Ofelt analysis and multiphonon relaxations of rare earth ions in fluorohafnate glasses, J. Solid State Chem. 90 (1991) 313–319.

[34] A. Awang, S.K. Ghoshal, M.R. Sahar, M.R. Dousti, R.J. Amjad, F. Nawaz, Enhanced spectroscopic properties and Judd-Ofelt parameters of Er-doped tellurite glass: Effect of gold nanoparticles, Curr. Appl. Phys. 13 (2013) 1813–1818, https://doi.org/10.1016/j.cap.2013.06.025.

[35] P. Babu, C.K. Jayasankar, Spectroscopic properties of Dy^{3+} ions in lithium borate and lithium fluoroborate glasses, Opt. Mater. 15 (2000) 65–79.

[36] S. Surendra Babu, P. Babu, C.K. Jayasankar, Th. Tröster, W. Sievers, G. Wortmann, Optical properties of Dy^{3+}-doped phosphate and fluorophosphates glasses, Opt. Mater. 31 (2009) 624–631,, https://doi.org/10.1016/j.optmat.2008.06.019.

[37] B.R. Judd, Optical absorption intensities of rare-earth ions, Phys. Rev. 127 (1962) 750–761.

[38] G.S. Ofelt, Intensities of crystal spectra of rare-earth ions, J. Chem. Phys. 37 (1962) 511–520.

[39] M. Jian- Xin, Y. Chuang-Tao, C. Qing-Qing, Photoluminescence characterization of Ce^{3+} and Dy^{3+} doped Li_2CaGeO_4 phosphors, J. Lumin. 130 (2010) 1320–1323,, https://doi.org/10.1016/j.jlumin.2010.02.047.

[40] M. Yu, J. Lin, Z. Wang, J. Fu, S. Wang, H.J. Zhang, Y.C. Han, Fabrication, patterning and optical properties of nanocrystalline YVO_4:A (A = Eu^{3+}, Dy^{3+}, Sm^{3+}, Er^{3+}) phosphor films via sol-gel soft lithography, Chem. Mater. 14 (2002) 2224–2231.

[41] N. Vijaya, K. Upendra Kumar, C.K. Jayasankar, Dy^{3+}-doped zinc fluorophosphate glasses for white luminescence applications, Spectrochim. Acta A 113 (2013) 145–153, https://doi.org/10.1016/j.saa.2013.04.036.

[42] D.V.R. Murthy, B.C. Jamalaiah, A. Mohan Babu, T. Sasikala, L. Rama Moorthy, The luminescence properties of Dy^{3+}-doped alkaline earth titanium phosphate glasses, Opt. Mater. 32 (2010) 1112–1116,, https://doi.org/10.1016/j.optmat.2010.03.009.

[43] A. Mohan Babu, B.C. Jamalaiah, J. Suresh Kumar, T. Sasikala, L. Rama Moorthy, Spectroscopic and photoluminescence properties of Dy^{3+}-doped lead tungsten tellurite glasses for laser materials, J. Alloys Compd. 509 (2011) 457–462,, https://doi.org/10.1016/j.jallcom.2010.09.058.

[44] Xin-yuan Sun, Shi-ming Huang, Xiao-san Gong, Qing-chun Gao, Zi-piao Ye, Chun-yan Cao, Spectroscopic properties and simulation of white light in Dy^{3+}-doped silicate glass, J. Non-Cryst. Solids 356 (2010) 98–101,, https://doi.org/10.1016/j.jnoncrysol.2009.10.009.

[45] C.S. McCamy, Correlated color temperature as an explicit function of chromaticity coordinates, Color Res. Appl. 17 (1992) 142–144.

[46] E.C. Fuchs, C. Sommer, F.P. Wenzl, B. Bitschnau, A.H. Paultisch, A. Muhlanger, K. Gatterer, Polyspectral white light emission from Eu^{3+}, Tb^{3+}, Dy^{3+}, Tm^{3+} co-doped $GdAl_3(BO_3)_4$ phosphors obtained by combustion synthesis, Mater. Sci. Eng. B 156 (2009) 73–78,, https://doi.org/10.1016/j.mseb.2008.11.024.

Accepted Manuscript

Title: Dysprosium doped niobium zinc fluorosilicate glasses: Interesting materials for white light emitting devices

Authors: J. Prabhakar, Venkata Krishnaiah Kummara, K. Linganna, P. Babu, C.K. Jayasankar, Jihoon Kim, V. Venkatramu

Please cite this article as: Prabhakar J, Kummara VK, Linganna K, Babu P, Jayasankar CK, Kim J, Venkatramu V, Dysprosium doped niobium zinc fluorosilicate glasses: Interesting materials for white light emitting devices, *Optik* (2018), https://doi.org/10.1016/j.ijleo.2018.09.061

Dysprosium doped niobium zinc fluorosilicate glasses: Interesting materials for white light emitting devices

J. Prabhakar[1], Venkata Krishnaiah Kummara[2,3,*] kvkrishaniah@tdtu.edu.vn , K. Linganna[4], P. Babu[5], C.K. Jayasankar[6] Jihoon Kim[1], and V. Venkatramu[7*] vvramuphd@gmail.com

[1]Division of Advanced Materials Engineering, Kongju National University, Cheonan, Chungnam 31080, South Korea.
[2]Laser Applications Research Group, Ton Duc Thang University, Ho Chi Minh City, Vietnam.
[3]Faculty of Applied Sciences, Ton Duc Thang University, Ho Chi Minh City, Vietnam.
[4]Optical Lens Research Center, Korea Photonics Technology Institute, Cheomdan venture-ro 108-9, Buk-gu, Gwangju 61007, Republic of Korea.
[5]Department of Physics, SVCR Govt. Degree College, Palamaner 517408, India
[6]Department of Physics, Sri Venkateswara University, Tirupati – 517 502, India.
[7]Department of Physics, Yogi Vemana University, Kadapa-516 005, India.

*Corresponding authors

Abstract

Trivalent dysprosium doped niobium zinc fluorosilicate glasses modified with different Nb_2O_5/ZnF_2 molar ratios have been fabricated by the traditional melt-quenching technique and derived their structural, photoluminescence and decay properties using spectroscopic techniques. Induced structural modifications have been observed upon increasing content of Nb_2O_5. Maximum phonon energy of the glass matrix is found to be 1010 cm^{-1} from the Raman analysis. The emission spectra of these glasses exhibit two intense bands at 480 and 570 nm besides a weak red emission at 650 nm. The decay profiles of Dy^{3+} ion for the $^4F_{9/2}$ level exhibit a non-exponential behavior for all the glasses. The intrinsic lifetimes for the $^4F_{9/2}$ level of Dy^{3+} ion have been determined by using the Inokuti-Hirayama model and are found to be 409, 366 and 325µs for the glasses with Nb_2O_5/ZnF_2:10/30, 20/20 and 30/10 molar ratios, respectively. The color coordinates have been evaluated from the emission spectra of the glasses and found that the glass with Nb_2O_5/ZnF_2:30/10 molar ratio appears near to the equal energy point. The correlated color

temperature matches well to the summer sunlight region (4900-5600 K), indicating that the glasses could be a potential candidate for white light emitting devices.

1. Introduction

Trivalent dysprosium (Dy^{3+})-doped materials have potential applications in visible lasers [1, 2], mid infra-red lasers [3, 4], optical amplifiers [5] and white light emitting diodes (WLEDs) [6]. Of these, the WLEDs are playing a key role in solid state lighting technology and received a great attention for replacing the existing fluorescent and incandescent lamps because of their low production cost, high reliability, environmentally benign, low energy consumption and longer lifetime [7].

White light emission can be accomplished with co-doped and tri-doped systems through upconversion [8] and down-shifting [9] processes, by mixing three primary colors (Red, Green and Blue). However, it is difficult to optimize the concentrations co-doped and tri-doped systems to achieve the optimum intensities of the red, green and blue emissions for the production of white luminescence. An alternative way is to use single Dy^{3+}-doped systems through the optimization of yellow to blue (Y/B) intensity ratio. Further, the Dy^{3+} ion has strong absorption bands in the ultra-violet (UV) region suitable to pump with low-cost GaN and InGaN diodes. Previous studies have shown that the Y/B ratio could be controlled by changing the Dy^{3+} ion concentration [10-12], pump wavelength [13, 14] and glass matrix [15]. Recently, Sundara Rao *et al.* reported the effect of aluminum ions on Y/B ratio of Dy^{3+} ions in lead silicate glass matrix

2

under the excitation of 352 and 451 nm [16]. Pisarska *et al*. studied the variation of Y/B ratio as a function of B_2O_3/PbO ratio [15].

In our earlier work, Dy^{3+} ion concentration [12] and pump wavelength [14] dependence white luminescence studies have been demonstrated and reported that the 0.1 mol% Dy_2O_3-doped glasses exhibit a better white luminescence under 387 nm excitation. However, still there is a large scope to achieve ideal white light emission from these glasses through the optimization of glass composition. Moreover, optical transmittance of the glass in the visible region was increased with the addition of Nb_2O_5 content [17]. Hence, it is interesting to study the effect of composition on white light luminescence properties. In the present study, we have fabricated Nb_2O_5 dependence zinc fluorosilicate glasses and characterized for the white light emission applications since Nb_2O_5 modified glasses exhibited a high refractive index, good transparency from visible to infrared region, high glass transition temperature, high thermo-mechanical stability, relatively high non-linear optical properties [16, 18-20]. Luminescence properties of Eu^{3+}-doped niobium-borate glasses were enhanced significantly with increasing the Nb_2O_5 content [21].

Therefore, the present work focuses on the composition dependent 0.1 mol % Dy_2O_3-doped niobium zinc fluorosilicate glasses modified with different Nb_2O_5/ZnF_2 (10:30, 20:20 and 30:10) molar ratios for the better understanding and optimization of the white luminescence under the excitation of 350 and 387 nm. The Y/B intensity ratios, energy transfer parameters, chromaticity coordinates and correlated color temperatures were evaluated and compared to the glass with 20:20 molar ratio of Nb_2O_5/ZnF_2 [12,14] along with other reported ones [6,22-25].

3

2. Material and methods

Dy^{3+}-doped niobium zinc fluorosilicate glasses with different compositions ($29.9SiO_2$–$10Nb_2O_5$–$20K_2O$–$30ZnF_2$–$10LiF$–$0.1Dy_2O_3$, $29.9SiO_2$–$20Nb_2O_5$–$20K_2O$–$20ZnF_2$–$10LiF$–$0.1Dy_2O_3$ and $29.9SiO_2$–$30Nb_2O_5$–$20K_2O$–$10ZnF_2$–$10LiF$–$0.1Dy_2O_3$, labeled as Nb10:ZF30, Nb20:ZF20 and Nb30:ZF10, respectively) were fabricated by the melt-quenching technique [12, 14]. The precursor chemicals were thoroughly mixed in an agate mortar and then taken into a platinum crucible. The powders were then heated at 1300 °C for 3h in a muffle furnace under ambient atmosphere. The glass melt was casted onto a brass mold preheated at 510 °C and subsequently annealed at the same temperature for 12h in order to eliminate any residual internal stress and then allowed to cool room temperature. Finally, the glass samples were polished to get optical quality for optical characterization.

Raman spectra of the glasses were measured upon 786 nm diode laser excitation by using spectrometer (Renishaw inVia Raman microscope). The emission spectra were recorded by using HORIBA JOBIN YVON Fluorolog-3 spectrofluorimeter at room temperature. Decay curves were recorded by monitoring the emission at 573 nm under the 387 nm excitation.

3. Results and discussion

Raman spectra of niobium zinc fluorosilicate glasses at different molar ratios in the energy region of 220-1270 cm^{-1} are shown in Fig. 1. The well resolved spectra exhibit seven Raman modes at 244, 480, 596, 681, 818, 888 and 1010 cm^{-1} for the glass with 30:10 molar ratio of Nb_2O_5/ZnF_2 whereas the Raman modes at 681 and 818 cm^{-1} do not appear as resolved bands for the other two glasses. This may be due to presence of high Nb_2O_5 content. Density of the glass sample is found to be 3.44, 3.45, and 3.60 g/cm^3 for 10:30, 20:20 and 30:10 molar ratio of

Nb_2O_5/ZnF_2, respectively. The energy of high intense vibrational mode (phonon energy) decreases from the 888 cm^{-1} to 818 cm^{-1} with the increase in the content of Nb_2O_5 from 10 to 30 mol%, respectively. In other words, it is also perceived that the vibrational energy at 888 cm^{-1} decreases with the decrease in the content of ZnF_2 from 30 to 10, respectively. The band at 1010 cm^{-1} is not related to the Nb vibrations [26], but it could be assigned to the stretching vibrations of silicon tetrahedra. This is also supported by the decrease in the relative intensity of Raman band at 1010 cm^{-1} with increasing the molar ratio of Nb_2O_5/SiO_2 [27]. It is interesting to note that the intensity of Raman bands increases with the increase of Nb_2O_5 content for all the vibrational modes. Initially, high intense band is observed at 888 cm^{-1} and then the intensity of the band at 815 cm^{-1} is increased with increasing Nb_2O_5 content. An enhancement of 815 cm^{-1} peak intensity is an indication of increase in the Nb-O bonds and non-bridging oxygens [28]. Moreover, the other bands and a shoulder of spectra are resolved for the glass with high Nb_2O_5 content. The vibrations at 815 cm^{-1} and 888 cm^{-1} correspond to the non-bridging oxygen and Nb-O-Si, respectively, in the glass matrix [29]. This vibration chain extended to Nb-O-Si-(O-M) due to the presence of alkali ions (M = K and Li). The intermediate frequency band around at 681 cm^{-1} is attributed to the vibrational modes of Si-O-Si bonds attached to the bending vibrational modes of Nb-O bonds in NbO_6 octahedron without non-bridging oxygen [29]. The vibrational bands at 244, 480 and 596 cm^{-1} are ascribed to purely niobium octahedron (NbO_6) through bridging bonds Nb-O-Nb [30]. With increasing of Nb_2O_5 content in the glass matrix, there is a great enhancement of bandwidth due to the Nb-related vibrational modes [31]. Moreover, the degree of bonding is increased between various structural groups in the glass network with the increase of Nb_2O_5 content [17].

The excitation spectra were obtained by monitoring the emission at 570 nm are shown in Fig. 2. Spectra exhibit more or less similar behavior to the glass with 20:20 molar ratio of Nb_2O_5/ZnF_2 [12, 13] except variation in their intensities due to non-bridging oxygens as evidenced from Raman spectra. The spectra are normalized with respect to the $^6H_{15/2} \rightarrow ^4K_{17/2}$ transition. It is noticed that the $^6H_{15/2} \rightarrow ^6P_{7/2}$ transition possesses higher intensity for the glass with 10:30 molar ratio whereas lower intensity for the glass with 30:10 molar ratio.

Normalized luminescence spectra of Dy^{3+}-doped niobium zinc fluorosilicate glasses with varying Nb_2O_5/ZnF_2 ratio, obtained by exciting the glass samples at 350 nm and 387 nm and are shown in Figs. 3(a) and (b), respectively. Emission spectra were exhibited three well known bands at 486, 577 and 669 nm which originated from the $^4F_{9/2} \rightarrow ^6H_{15/2}$, $^4F_{9/2} \rightarrow ^6H_{13/2}$ and $^4F_{9/2} \rightarrow$ $^6H_{11/2}$ transitions, respectively. Emission spectra are normalized to observe the spectral variation of the electric-dipole transition (ED), $^4F_{9/2} \rightarrow ^6H_{15/2}$ (blue). From the emission spectra, the intensities of blue and yellow emissions are found to be more or less similar for the glasses with different molar ratios. However, the blue emission is predominant for the glasses with 20:20 and 10:30 ratio of Nb_2O_5/ZnF_2 under the excitation wavelengths 350 and 387 nm. High intensity of blue emission could be due to high covalence between Dy-O bonds and the presence of Dy^{3+} ion in different sites under suitable excitation wavelength. The Y/B ratios under 350 nm excitation are found to be 1.77, 0.82 and 1.15 for the glass with 10:30, 20:20 and 30:10 molar ratios of Nb_2O_5/ZnF_2, respectively. As can be seen, the blue emission is dominant for a glass with 20:20 molar ratio. On the other hand, under 387 nm excitation, the Y/B ratios are found to be 0.56, 0.86, and 0.92 for the glasses with 10:30, 20:20 and 30:10 molar ratios of Nb_2O_5/ZnF_2, respectively, and higher the blue emission is observed for 10:30 molar ratio. The higher

6

magnitudes of Y/B ratio indicate that higher degree of covalency between Dy^{3+} ions and their ligand environment. The Y/B ratios (1.15 and 0.92) are close to unity for a glass with 30:10 molar ratios of Nb_2O_5/ZnF_2 under both 350 and 387 nm excitations. This could be due to the presence of higher non-bridging oxygens and/or lower phonon energy around the Dy^{3+} ions. High value of Y/B ratio indicates the larger concentration of dissociated Dy^{3+} ions from Dy-O-Dy bonds and the possibility for high degree of de-polymerization in the glass matrix [32]. In our glass system, high value of Y/B ratio of 1.77 for the glasses with 10:30 ratio of Nb_2O_5/ZnF_2 indicates a large amount of dissociated Dy^{3+} ions from Dy-O-Dy bonds. This could be due to the increase of non-bridging oxygens or the formation of the Dy-F-Dy or Nb-F-Nb bonds (decrease of Dy-O-Dy or Nb-O-Nb bonds) in the glass matrix. This is also evidenced from the Raman mode at 888 cm^{-1} which purely related to the Nb-F(O) vibrations. The Y/B ratio of 0.1 mol% Dy^{3+}-doped glasses are compared to those of other Dy^{3+}:systems in Table 1 and found to be comparable to LBO:Dy glass (0.93) [6] and lower than silicate glass (1.96) [24].

The luminescence decay profiles of Dy^{3+} ions for the $^4F_{9/2}$ level under 387 nm excitation are shown in Fig. 4 and are found to be non-exponential. The lifetime for the $^4F_{9/2}$ level of Dy^{3+} ion is evaluated from the equation, $\langle \tau \rangle = \dfrac{\int tI(t)dt}{\int I(t)dt}$ and is found to be 281, 265 and 245 μs for the glasses with 20:20, 10:30 and 30:10 molar ratios of Nb_2O_5/ZnF_2, respectively. It is noticed that the lifetime decreases with varying Nb_2O_5/ZnF_2 molar ratio due to the increase in non-radiative processes of Dy^{3+} ions. The lower lifetime for 30:10 of Nb_2O_5/ZnF_2 ratio indicates more covalent Dy-O bonds in the glass network as evidenced from the Raman spectra, leading to increase in the intensity and broadening of vibrational frequencies. This can be understood from the Raman analysis. The non-exponential decay profiles are analyzed under the frame of Inokuti-Hirayama

7

(IH) model [33] by taking the intrinsic lifetime, τ_0 as 0.41 ms [12] found for 20:20 molar ratio. According to this model, the luminescence intensity $I(t)$ of the de-excited ion is given by

$$I(t) = I_0 \exp\left[-\left(\frac{t}{\tau_0}\right) - Q\left(\frac{t}{\tau_0}\right)^{3/S} \right]$$

(1)

where τ_0 is the inherent decay time of the donors without the acceptors, S (=6, 8 or 10) relates the mechanism of the interaction, i.e. dipole–dipole, dipole-quadrupole or quadrupole-quadrupole, respectively and Q is the energy transfer parameter. The decay curves are fitted to the Eq. (1) by varying τ_0 and Q. The best fit is obtained for $S = 6$, indicating that the nature of interaction between Dy^{3+} ions is dipole-dipole type. From the fitting, Q values are estimated to be 0.54, 0.27 and 0.34 for the glasses with 10:30, 20:20, and 30:10 molar ratios of Nb_2O_5/ZnF_2, respectively. It is noticed that the lifetime of Dy^{3+} for the $^4F_{9/2}$ level decreases with increasing Nb_2O_5 content, due to increase in non-radiative processes.

The combination of blue and yellow emissions from the Dy^{3+}-doped material can produce a white luminescence. Dy^{3+}-doped glasses can be considered as an attractive materials for two-color phosphors since Dy^{3+} ion exhibits intense emissions at blue (482 nm, $^4F_{9/2} \rightarrow {}^6H_{15/2}$) and yellow (573 nm, $^4F_{9/2} \rightarrow {}^6H_{13/2}$) regions. It is well known that the $^4F_{9/2} \rightarrow {}^6H_{13/2}$ transition of Dy^{3+} ions is hypersensitive and its intensity strongly depends on the nature of the host, whereas the intensity of magnetic-dipole allowing the $^4F_{9/2} \rightarrow {}^6H_{15/2}$ transition is less sensitive to the host. Therefore, the intensity ratio (Y/B) of these transitions can be tailored such that the Dy^{3+}-doped materials would generate white light. The white light produced by the emission of Dy^{3+}-doped glass samples can be analyzed in the frame of the chromaticity coordinates of colors. The procedure established by the Commission International de I'Eclairage (CIE) is the most widely

8

used method to describe the composition of any color in terms of three primaries colors i.e. Red, Green and Blue (RGB). Artificial "colors", denoted by X, Y, Z, also called tristimulus values, can be added to produce real spectral colors (RGB). The chromaticity color coordinates is obtained from the following equations:

$$x = \frac{X}{X+Y+Z}, \quad y = \frac{Y}{X+Y+Z}; \text{ and } z = \frac{Z}{X+Y+Z} \qquad (2)$$

where X, Y, and Z are the tristimulus values given by: $X = \int E(\lambda)\bar{x}(\lambda)d\lambda \quad Y = \int E(\lambda)\bar{y}(\lambda)d\lambda$ and $Z = \int E(\lambda)\bar{z}(\lambda)d\lambda$; $\bar{x}$, $\bar{y}$, and $\bar{z}$ are matching functions of CIE, to define the chromatic characteristics of a visible source and they can be thought of as the spectral sensitivity curves of three linear light detectors yielding the CIE tristimulus values X, Y and Z.

The CIE chromaticity color coordinates are evaluated from the emission spectra and are presented in Figs. 4(a) and (b) under 387 and 350 nm excitations, respectively. The McCamy equation has been used to compute correlated color temperature (CCT) [34, 35] from the CIE chromaticity coordinates. The (x, y) chromaticity coordinates and CCT values are found to be (0.282, 0.329), (0.332, 0.372) and (0.332, 0.371) and, 8267, 5520 and 5520 K for the glasses with 10:30, 20:20 and 30:10 molar ratios of Nb_2O_5/ZnF_2, respectively, under 387 nm excitation. On the other hand, under 350 nm excitation, the (x, y) chromaticity coordinates and CCT are found to be (0.352, 0.388), (0.331, 0.374) and (0.333, 0.377) and 4891, 5556 and 5485 K for the glasses with 10:30, 20:20 and 30:10 molar ratios, respectively. The CCT values, obtained at 350 nm excitation, are comparable to those of lithium borate (0.25 mol%, 5169 K) [6], silicate (0.5 mol%, 4324 K) [24] glasses (which are evaluated from the reported CIE chromaticity coordinates), apart from the reported oxyfluoride (0.25 mol%, 13750 K) [24] glass, which falls

9

under clear blue sky light source. Under 387 nm excitation, the CCT values for the investigated glasses are higher than those of other reported glasses including LBO:Dy (5101 K) [6], oxyfluoride (2115 K) [22], SZBPDy (3756 K) [36], sodium borate (3756 K) [37] and TSWD2 (4971 K) [38]. The CCT values of the investigated glasses match well in the region of the light sources such as summer sunlight (4900-5600 K) and clear blue sky (8000-27000 K). The above results indicate that these glasses find potential applications for the development of summer sunlight white light sources.

4. Conclusions

Luminescence properties of Dy^{3+}-doped oxyfluoride glasses modified with different Nb_2O_5/ZnF_2 molar ratios have been studied under 350 and 387 nm excitations for the white luminescence. The maximum phonon energy is found to be 1010 cm^{-1} for a glass with high content of Nb_2O_5 content. The emission spectra exhibited two intense bands at 480 and 570 nm corresponding to the $^4F_{9/2}\rightarrow^6H_{15/2}$ (blue) and $^4F_{9/2}\rightarrow^6H_{13/2}$ (yellow) transitions, respectively, besides a weak red emission attributed to the $^4F_{9/2}\rightarrow^6H_{11/2}$ transition. Higher Y/B ratio has been noticed for the glass with 10:30 molar ratio of Nb_2O_5/ZnF_2 compared to the other glasses of the present study. The decay curve analysis reveals that the mechanism of interaction for the energy transfer between the Dy^{3+} ions is of dipole-dipole type. The color coordinates and correlated color temperature for the glass with 30:10 (Nb_2O_5/ZnF_2) molar ratio is found to be nearer to the ideal white light and hence, it could be a potential candidate for the generation of white light sources under 350 and 387 nm excitations.

Acknowledgments

References

1. J. Limpert, H. Zellmer, P. Riedel, G. Mazé, A. Tünnermann, Electron. Lett. 36 (2000) 1386–1387.

2. Y. Fujimoto, O. Ishii, M. Yamazaki, Electron. Lett. 46 (2010) 586–7.

3. I.V. Kityk, J. Wasylak, J. Kucharski, D. Dorosz, J. Non-Crystalline Solids, 297 (2002) 285-289.

4. Laércio Gomes, Joris Lousteau, Daniel Milanese, Emanuele Mura and Stuart D. Jackson, J. Opt. Soc. Am. B, 31 (2014) 429-435.

5. Zhiyong Yang, Wei Chen, Lan Luo, J. Non-Crystalline Solids, 351 (2005) 2513-18.

6. Xin-Yuan Sun, Shuai Wu, Xi Liu, Pan Gao, Shi-Ming Huang, J. Non-Crystalline Solids, 368 (2013) 51-54.

7. J.S. Kim, K.T. Lim, Y. Jeong, P. Jeon, J. Choi, H. Park, Solid State Commun. 135 (2005) 21-24.

8. N.K. Giri, D. K. Rai, and S. B. Rai, J. Appl. Phys. 104 (2008) 113107.

9. G Lakshminarayana, R Yang, J R Qiu, M G Brik, G A Kumar and I V Kityk, J. Phys. D: Appl. Phys. 42 (2009) 015414-12.

10. Y. Ji, J. Cao, Z. Zhu, J. Li, Y. Wang, and C. Tu, , J. Lumin.132 (2012) 702-706.

11. J. Pisarska, R. Lisiecki, W. Ryba-Romanowski, T. Goryczka, W.A. Pisarski, Chem. Phys. Lett., 489 (2010) 198-201.

12. K. Venkata Krishaniah and C.K. Jayasankar, Proc. SPIE, 8001 (2011) 80012N1-8

13. M. Jayasmhadrai, K. Jang, H. S. Lee, B. Chen, S. S. Yi, and J. H. Jeong, J. Appl. Phys. 106 (2009) 013105-4.

14. K. Venkata Krishnaiah, K. Upendra Kumar and C.K. Jayasankar, Mater. Express, 3 (2013) 61-70.

15. J. Pisarska, Opt. Mater. 31 (2009) 1784-1786.

16. Z. Chun, Z. Qin-Yuan, P. Yue-Xiao, and J. Zhong-Hong, Chin. Phys. 15 (2016) 2158.

17. A. Siva Sesha Reddy, A. Ingram, M.G. Brik, M. Kostrzewa, P. Bragiel, V. Ravi Kumar and N. Veeraiah, J Amer. Ceram. Soc. 100 (2017) 4066-4080

18. S. W. Yung, Y. S. Huang, Yi-Mu Lee and Y. S. Lai, RSC Adv., 3 (2013) 21025.

19. Q. Zhang, X. Du, S. Tan, D. Tang, K. Chen, T. Zhang, Sci. Rep. 7 (2017) 5355.

20. S. Rani, S. Sanghi, A. Agarwa, S. Khasa, IOP Conf. Series: Mater. Sci. Engineering 2 (2009) 012041.

21. Y. Attafi, S. Liu, J. Non-Crystal. Solids, 447 (2016) 74.

22. H. Xia, J. Zhang, J. Wang, and Y. Zhang, Chin. Opt. Lett. 4 (2006) 476.

23. M. Sundara Rao, V. Sudarsan, M.G. Brik, Y. Gandhi, K. Bhargavi, M. Piasecki, I.V. Kityk, N. Veeraiah, J. Alloys Compounds, 575 (2013) 375-381.

24. Xin-yuan Sun, Shi-ming Huang, Xiao-san Gong, Qing-chun Gao, Zi-piao Ye, Chun-yan Cao, J. Non-Crystalline Solids, 356 (2010) 98-101.

25. Chaofeng Zhu, Jia Wang, Meimei Zhang, Xiaorong Ren, Jianxing Shen, and Yuanzheng Yue, J. Am. Ceram. Soc., 97 (2014) 854-861.

26. P. McMillan, B. Piriou, Bull. Mineral. 106 (1983) 57.

27. A. Aronne, V.N. Sigaev, B. Champagnon, E. Fanelli, V. Califano, L. Z. Usmanova, P. Pernice, J. Non-Crystalline Solids 351 (2005) 3610–3618.

28. S. Fukui, S. Sakida, Y. Benino and T. Nanba, Jpn. J. Ceram. Soc. 120 (2012) 530.

29. K. Fukumi, S. Sakka, J. Mater. Sci. 23 (1988) 2819.

30. A.A. Lipovskii, D.K. Tagantsev, A.A. Vetrov, O.V. Yanush, Optical Materials 21 (2003) 749–757.

31. M. G. Donato, M. Gagliardi, L. Sirleto, G. Messina, A. A. Lipovskii, D. K. Tagantsev, and G. C. Righini, Appl. Phys. Lett. 97, (2010) 231111.

32. Valluri Ravi kumar, G. Giridhar, N. Veeraiah, Opt. Mater. 60 (2016) 594-600

33. M. Inokuti, F. Hirayama, J. Chem. Phys. 43 (1965) 1978-1989.

34. S. S. McCamy, Color Res. Appl. 17 (1992) 142-144.

35. E. Fred Schubert, Light-Emitting Diodes, 2nd edn., Cambridge University Press, New York (2006), Chap. 17, p. 309-310.

36. N. Kiran and A. Suresh Kumar, J Mol. Struct. 1054–1055 (2013) 6–11.

37. K. Liggins, V.M. Edwards and B. Rami Reddy, Proc. SPIE 10100 (2017) 101001W-1-7.

38. V. Himamaheswara Rao, P. Syam Prasad, M. Mohan Babu, P. Venkateswara Rao, T. Satyanarayana, Luís F. Santos, N. Veeraiah, Spectrochimica Acta Part A 188 (2018) 516.

Figures
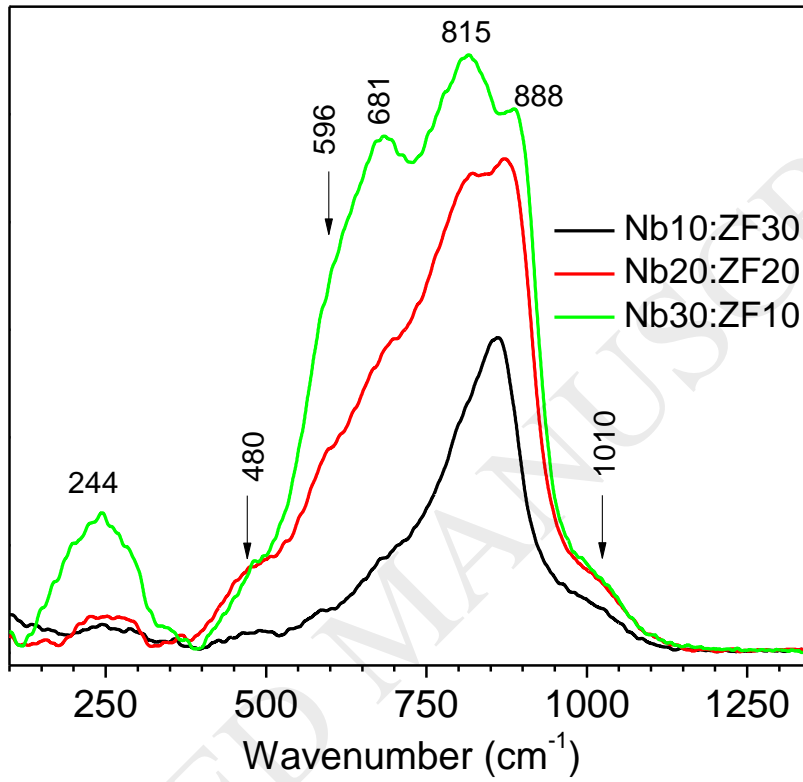
Fig. 1. Raman spectra of glasses modified with 10:30, 20:20 and 30:10 molar ratios of Nb_2O_5 and ZnF_2.
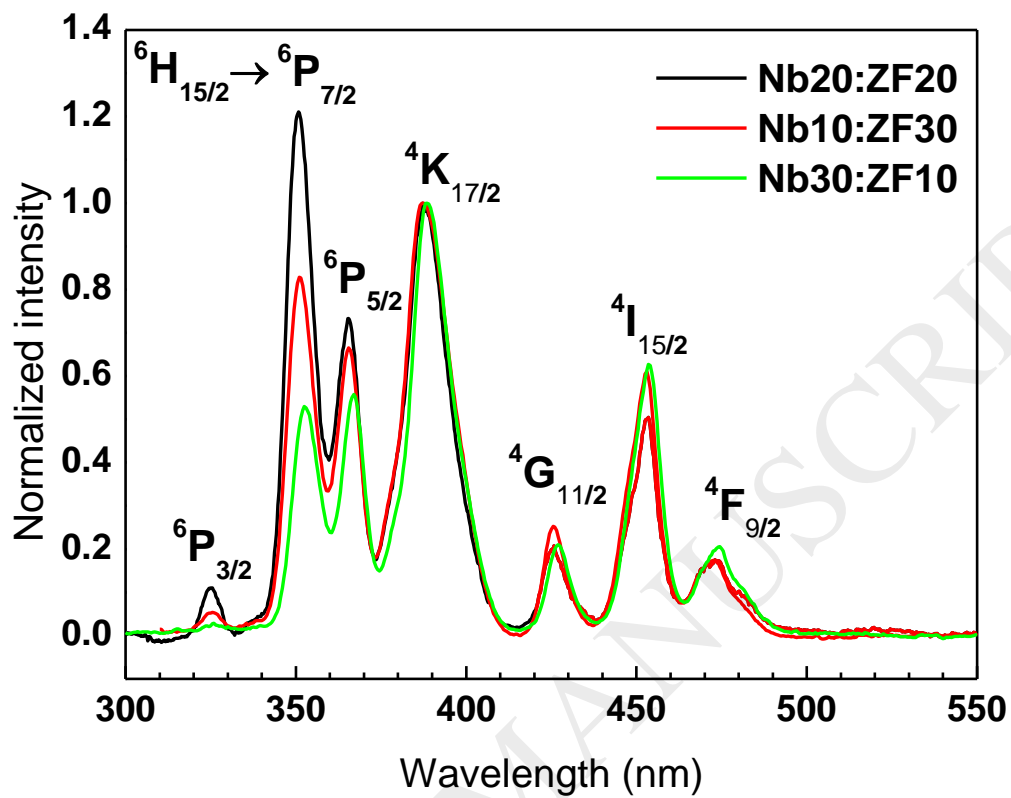
Fig. 2. Normalized (with respect to $^6H_{15/2} \rightarrow {}^6K_{17/2}$) excitation spectra of 0.1 mol % Dy^{3+}-doped oxyfluoride glasses for different molar ratios.
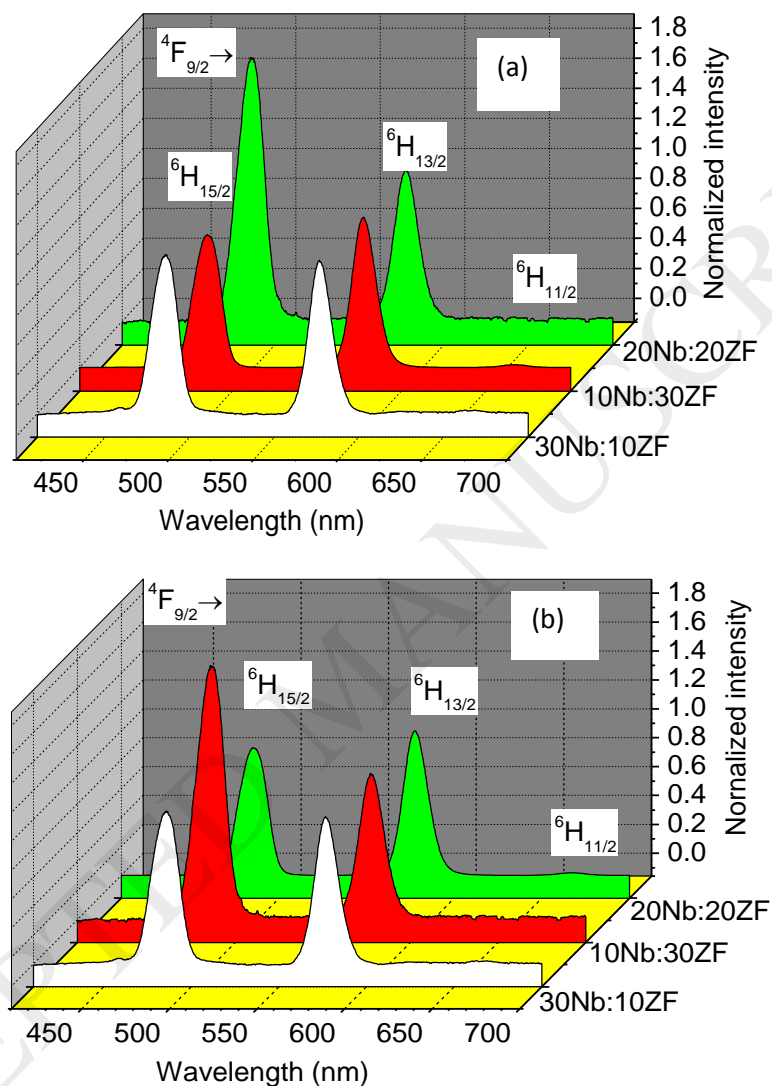
Fig. 3. Luminescence spectra of 0.1 mol % Dy^{3+} -doped oxyfluoride glasses under (a) 350 nm and (b) 387 nm excitations. The spectra normalized to the maximum intensity of the $^4F_{9/2} \rightarrow ^6H_{13/2}$ transition and compared with Nb_2O_5/ZnF_2 : 20/20 molar ratio.
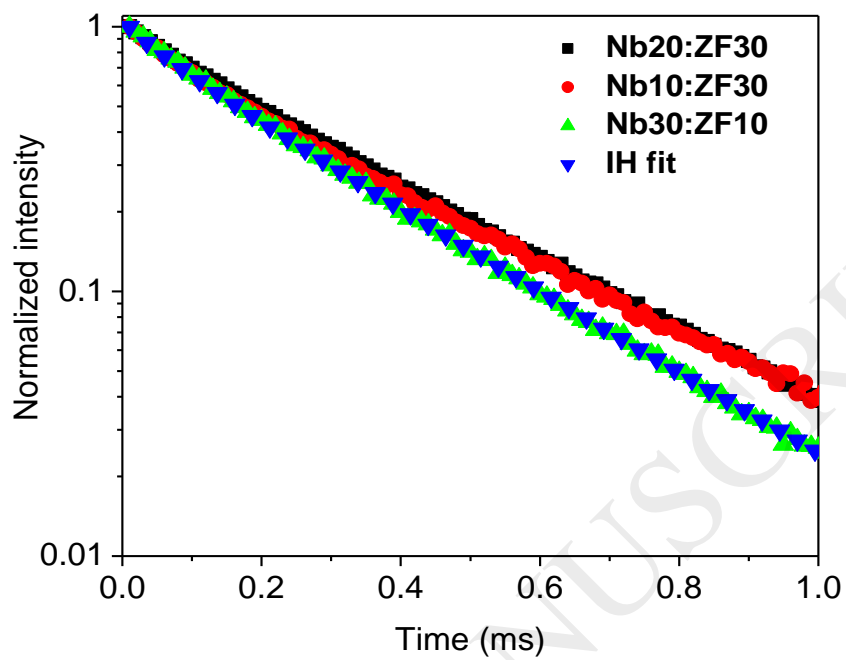
Fig. 4. Decay curves for the $^4F_{9/2}$ level of Dy^{3+} ion under 387 nm excitation along with IH fit for $S = 6$.

18
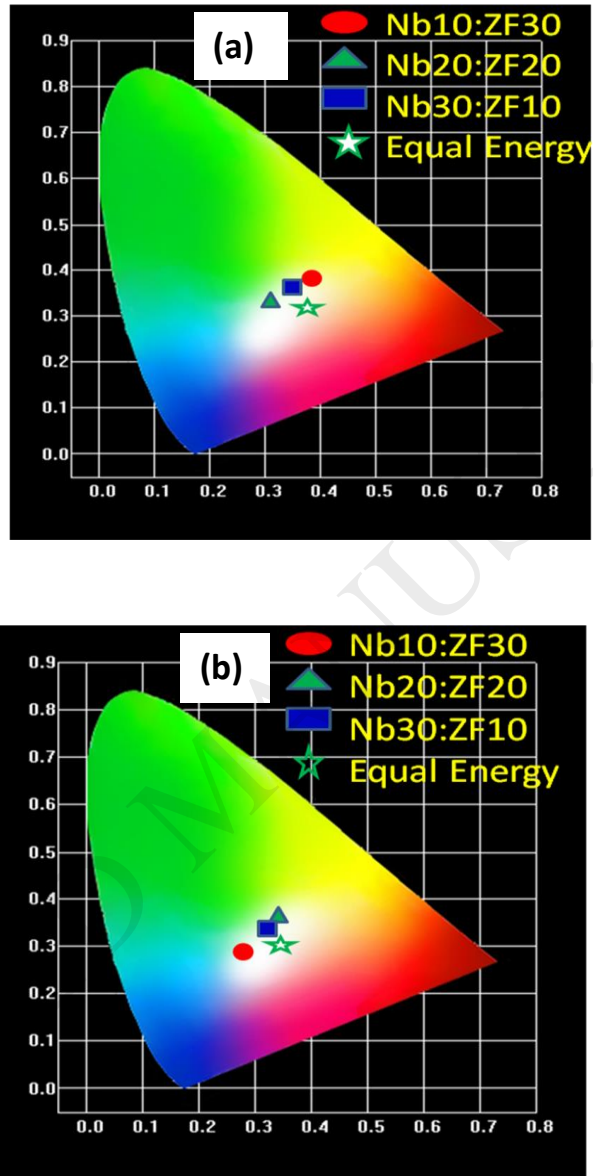
Fig. 5. Representation of CIE chromaticity color coordinates of Dy^{3+}-doped Nb_2O_5/ZnF_2:20/20 molar ratio glasses under (a) 350 nm and (b) 387 nm excitations.

Table 1. Comparison of Y/B ratios, (*x*,*y*) chromaticity color coordinates, correlated color temperature (CCT, K) of Dy^{3+}:systems under 350 and 387 nm excitations.

Glass system (Dy^{3+} ion concentration)	Y/B ratio		(*x*,*y*)		CCT		Reference
	350 nm	387 nm	350 nm	387 nm	350 nm	387 nm	
Nb20:ZF20 (0.1 mol %) Nb10:ZF30 (0.1 mol %) Nb30:ZF10 (0.1 mol %)	0.82 1.77 1.15	0.86 0.56 0.90	(0.331, 0.374) (0.352, 0.388) (0.333, 0.377)	(0.332, 0.371) (0.282, 0.329) (0.332, 0.372)	5556 4891 5485	5520 8267 5520	Present work
LBO:Dy (0.25 mol%)	0.93	0.95	(0.342, 0.371)	(0.344, 0.371)	5169*	5101*	[6]
Silicate (0.5 mol %)	1.96	-	(0.381,0.434)	-	4324*	-	[23]
Oxyfluoride (0.25 mol%)	-	-	(0.23,0.31)	(0.38,0.40)	13750	4163	[24]
SLBPDy (1.0 mol%)	-	0.72	-	(0.45,0.42)	-	2115	[36]
Sodium Borate (1.5 mol%)	-	-	-	(0.44, 0.50) @ 375nm excitation	-	3756 @ 375nm excitation	[37]
TSWD2 (0.2 mol%)	-	1.51@ 452 nm	-	(0.35,0.40) @ 452 nm	-	4971 @ 452 nm	[38]

*Indicates the values are evaluated from the data mentioned in the papers.

Investigation of modifier effect on the spectroscopic properties of Sm^{3+} ions in binary boro-bismuth glasses

K. Udaya Kumar[a], C.R. Kesavulu[a,b,c,*], P. Babu[d], C.K. Jayasankar[a,**]

[a] *Department of Physics, Sri Venkateswara University, Tirupati 517 502, India*
[b] *Department of Physics, Kyungpook National Univeristy, Daegu 41566, Republic of Korea*
[c] *SiC Laboratory, Centre for Materials for Electronics Technology (C-MET), Cherlapally, Hyderabad 500 051, India*
[d] *Department of Physics, SVCR Govt. Degree College, Palamaner 517 408, India*

ABSTRACT

Trivalent samarium (Sm^{3+})-doped boro-bismuth glass systems are prepared using the well-known melt quenching technique and studied their physical and spectroscopic properties. Theoretical optical basicity of the glasses are evaluated using the glass compositions. The optical absorption spectra are used to predict the optical band gap and bonding parameters of glasses. The ultra violet (UV) cutoff wavelength is increasing towards the higher wavelength side with increase in bismuth concentration. Judd-Ofelt parameters are obtained from absorption spectrum and are inturn used to estimate radiative properties for various excited states of the Sm^{3+} ions in boro-bismuth glasses. Luminescence decay curves of the $^4G_{5/2}$ level in the Sm^{3+}-doped boro-bismuth glasses are measured under 402 nm excitation. The decay times exhibit single exponential nature for lower concentrations (≤ 0.1 mol%) and tends towards non-exponential with increase in Sm^{3+} concentrations (≥ 0.5 mol %). The non-exponential decay curves of higher Sm^{3+}-doped glasses are fitted to the Inokuti-Hiriyama model to know the nature of interaction for energy transfer between the Sm^{3+} ions. The chromaticity color coordinates for present glass systems are also evaluated and found that the luminescence color falls in the reddish-orange region.

1. Introduction

Rare-earth (RE) ion doped glasses are fascinating systems for the growth of numerous optoelectronic devices such as short wavelength lasers, display devices, sensors and hole burning high density storage devices, etc. [1]. The broad applications of the RE-doped glasses stimulate the search for novel systems and examination of their optical analysis. Glasses doped with various RE ions exhibit valuable information that include spectroscopic properties such as energy level structure, emission cross-section, optical gain, etc. [2,3]. These results play a significant role to improve the existing or to design new optical devices.

Among several RE ions, Sm^{3+} have prospective applications for high-density optical data storage, under sea communication and color displays [4,5]. Moreover, the Sm^{3+} ions exhibit wide emission of $^4G_{5/2} \rightarrow {}^6H_J$ (J = 5/2, 7/2, 9/2 and 11/2) transitions in any host matrix. Furthermore, the orange-red emission around 600 nm can be obtained because of the large energy difference between the

$^4G_{5/2}$ meta-stable level and its next lower lying level [6,7]. Boro-bismuth glasses show high transparency, low melting point, high thermal stability and good glass forming nature. Borate glasses are the better hosts for RE ions doping compared to various other traditional glass materials. However, borate glasses have high phonon energies, resulting in enhanced non-radiative processes that reduces luminescence efficiency. Such high phonon energies possessed by the borate glasses can be conveniently reduced by adding heavy metal oxides such as bismuth and lead oxides [8].

Recently, bismuth containing glasses were investigated for feasible use in glass scintillators, radiation detectors for applications in high energy Physics [9,10]. Bismuthate glasses have large infrared transmission windows besides high refractive index which are suitable for optical components [9,10]. Pure bismuth is not considered as a glass former since it has lower field strength (0.53). However, the combination of $B_2O_3/SiO_2/TeO_2/P_2O_5$ with Bi_2O_3 can form glasses in comparatively more compositional ranges which results in increase in non-bridging oxygen and refractive indices [11]. Boro-bismuth glass systems were also

* Corresponding author at: Department of Physics, Sri Venkateswara University, Tirupati 517 502, India.
** Corresponding author.
E-mail addresses: crkesavulu2005@gmail.com (C.R. Kesavulu), ckjaya@yahoo.com (C.K. Jayasankar).

recognized as an outstanding host matrices for doping of RE oxides because of their excellent glass forming ability at low temperature compared to various traditional glass formers such as silicate, phosphate, germanate, vanadate, tellurite, etc., [12–16]. In the present work, optical properties of the Sm^{3+}-doped boro-bismuth (BBiSm) glasses (20–70 mol % of Bi_2O_3) are reported. The present work also deals with the preparation of Sm^{3+}-doped bismuth glasses and to study their various physical properties such as density and refractive index and spectroscopic properties that include radiative transition probabilities, stimulated emission cross-sections, lifetimes and CIE chromaticity coordinates. All the obtained results are compared with those of reported systems in the literature [17–54].

2. Sample preparation and measurements

Glass samples with the compositions (mol%) of:

B80Bi20Smx: $(80 - x/2)H_3BO_3 + (20 - x/2)Bi_2O_3 + xSm_2O_3$;

B70Bi30Smx: $(70 - x/2)H_3BO_3 + (30 - x/2)Bi_2O_3 + xSm_2O_3$;

B60Bi40Smx: $(60 - x/2)H_3BO_3 + (40 - x/2)Bi_2O_3 + xSm_2O_3$;

B50Bi50Smx: $(50 - x/2)H_3BO_3 + (50 - x/2)Bi_2O_3 + xSm_2O_3$;

B40Bi60Smx: $(40 - x/2)H_3BO_3 + (60 - x/2)Bi_2O_3 + xSm_2O_3$;

B30Bi70Smx: $(30 - x/2)H_3BO_3 + (70 - x/2)Bi_2O_3 + xSm_2O_3$

(where x = 0.01, 0.05, 0.1, 0.5, 1.0 and 2.0) were prepared by melt-quenching method. H_3BO_3, Bi_2O_3 and Sm_2O_3 chemicals used were of analytical reagent grade. Batch composition of chemicals of 25 g were taken and thoroughly grinded by agate mortar to get homogeneous mixture. The fine powder was placed in an alumina crucible and kept in an electric furnace at 850 °C for 2 h. The molten liquid was suddenly quenched on preheated brass mold at 310 °C and annealed at the same temperature for 12 h.

The prepared glass systems were polished to measure their physical and optical properties. The refractive indices were measured by Brewster's angle method using diode laser (λ = 650 nm). The densities were measured by the Archimedes' method utilizing twofold refined water as a submersion fluid. The X-ray diffraction (XRD) spectra were recorded with JEOL 8030 X-beam diffractometer utilizing $CuK\alpha$ radiation. The absorption specta were measured with Perkin Elmer Lambda-950 spectrophotometer. The excitation and emission spectra and lifetimes were measured with an Endinburgh FLS980 spectrofluorimeter with xenon lamp as a light source in continuous and pulsed mode. All the measurements were made at room temperature.

For computation of errors, all the above experiments are measured three times and are used to compute mean and standard deviation (σ) using the expression,

$$(\sigma) = \sqrt{\frac{\sum (x - y)^2}{N}}$$

where x is the actual measurement reading, y is the mean reading and N is the number of measurements.

3. Results and discussion

3.1. Physical properties

The density of a host is a unique property to assess the strength of the glass, which gives information about the structural softening or compactness of the system [17]. The densities (d) of the BBiSm glasses were measured by Archimedes's principle using double distilled water as an immersion liquid and various physical properties of the BBiSm glasses are calculated using relevant expressions reported elsewhere [18,19]. Table 1 presents the measured and calculated physical properties of BBiSm glasses and are compared with

Table 1
Physical properties of the Sm^{3+}-doped glasses.

Physical properties	B80Bi20Sm0.5	B70Bi30Sm0.5	B60Bi40Sm0.5	B50Bi50Sm1.0	B40Bi60Sm1.0	B30Bi70BSm0.5	BNCfSm1.0 [20]	B40BiCfSm1.0 [20]
Density, d (g/cm⁻³) (± 0.02)	4.71	5.60	6.39	7.10	7.53	7.75	3.00	6.29
Refractive index, n (at 532 nm) (± 0.01)	1.76	1.91	2.02	2.16	2.21	2.24	1.52	1.79
Sm^{3+} ion concentration ($\times 10^{20}$ ions/cm³) (± 0.01)	1.85	1.72	1.61	3.02	2.78	1.25	4.23	3.30
Inter-molecular distance, r_i (Å) (± 0.01)	17.54	17.98	18.38	14.91	15.32	19.99	13.32	14.47
Field strength, F ($\times 10^{14}$ cm⁻²) (± 0.02)	6.01	5.71	5.46	8.31	7.87	4.62	10.41	8.83
Molar volume, V_m (g. cm⁻³) (± 0.02)	30.39	32.75	35.02	37.30	40.52	44.55	28.48	36.48
Molar refractivity, R_m (cm⁻³) (± 0.02)	12.51	15.36	17.74	20.51	22.86	27.02	8.70	15.38
Electric polarizability, α_e ($\times 10^{-22}$ cm³) (± 0.01)	5.31	6.52	7.52	4.35	4.84	11.57	1.73	3.05
Dielectric constant, ε (± 0.02)	3.09	3.64	4.08	4.67	4.88	5.66	2.32	3.19
Reflection losses, R (%) (± 0.01)	7.58	9.78	11.41	13.48	14.21	16.52	4.30	7.95
Metallization factors, M (± 0.02)	0.59	0.53	0.49	0.45	0.44	0.39	–	–

$40B_2O_3 + 40Na_2O + 19CaF_2 + 1.0Sm_2O_3$ (BNCfSm1.0) and $40B_2O_3 + 40Bi_2O_3 + 19CaF_2 + 1Sm_2O_3$ (B40BiCfSm1.0) glasses [20]. The physical properties are calculated for all the compositions and are compared only to those combinations which gives better luminescence properties. From Table 1, it can be observed that as bismuth content increases in glass matrix, the density increases which is due to replacement of lighter mass of B_2O_3 (M.W = 61.98 g) content by heavier mass of Bi_2O_3 (M.W = 465.96 g). Similar results were also observed by Mariyappan et al. [20] in boro-bismuth glasses (Table 1). It can also be observed that in the present systems, the values of refractive index increases from 1.76 to 2.24 ± 0.01 with increase in bismuth content from 20 to 70 mol%. Hence, it clearly shows that addition of bismuth content to the glass matrix causes increase in refractive index. Similar results were also observed by Agarwal et al. [21].

The refractive index is an important parameter, which affects the performance of optical fibers [22]. From the Table 1, it can be observed that the present B40Bi60Sm1.0 (2.21) and B30Bi70Sm0.5 (2.24) glasses have the higher refractive indices compared to zinc bismuth borate: ((79-x) $B_2O_3 + xBi_2O_3 + 20ZnO + 1Sm_2O_3$, x = 15, 20, 25, 30, 35) (1.72–1.99) [21], zinc lithium borate: $25Li_2CO_3 + 64H_3BO_3 + 10ZnF_2 + 1Sm_2O_3$ (1.48) [23] and zinc bismuth silicate: $(20ZnO + (79.5-x) Bi_2O_3 + xSiO_2 + 0.5Sm_2O_3$, x = 20, 30, 40, 50 (2.18–2.08) [24]) glasses. Hence, it can be said that the higher refractive index in the present boro-bismuth glasses is more suitable for fiber drawing and waveguide applications [22].

3.2. Theoretical optical basicity

Theoretical optical basicity (Λ) can be predicted from the composition of the glass, according to Duffy and Ingram [25]. Optical basicity parameter (Λ) defines the electron donating power of the oxygen in an oxide glass [25]. This analysis can be made from the glass composition with basicity moderating parameter (γ_i). Also, γ_i can be computed from the relation (γ_i) = 1.36 (X_i − 0.26), where X_i is the Pauling electronegativity of the cations in the glass composition [25,26]. The optical basicity of the boro-bismuth glasses are evaluated from the expression [25,26],

$$\Lambda_{glass} = \frac{X(Bi_2O_3)}{\gamma_A} + \frac{X(B_2O_3)}{\gamma_B} + \frac{X(Sm_2O_3)}{\gamma_C} \qquad (1)$$

In the above expression, B80Bi20Sm0.5: (0.1975, 0.7975, 0.005); B70Bi30Sm0.5: (0.2975, 0.6975, 0.005); B60Bi40Sm0.5: (0.3975, 0.5975, 0.005); B50Bi50Sm0.5: (0.495, 0.495, 0.01); B40Bi60Sm0.5: (0.5950, 0.3950, 0.01) and B30Bi70Sm0.5: (0.6975, 0.2975, 0.005) are the ratios of the oxygen atoms ($X(Bi_2O_3)$, $X(B_2O_3)$ and $X(Sm_2O_3)$, respectively. These are participating to the total oxygen atom content in the BBiSm glasses. The basicity moderating parameters (γ_i) are evaluated by taking the X_i values represented by Pauling [27] and are found to be $\gamma_i(Bi)$ = 2.2304, $\gamma_i(B)$ = 2.3664 and $\gamma_i(Sm)$ = 1.2376. Fig. 1 shows the variation of Λ with bismuth concentration. It can be observed that the value of Λ linearly increases with increase in bismuth concentration. Therefore, the studied BBiSm glasses possess relatively high optical basicity at high bismuth content [28].

3.3. X-ray diffraction

The recorded XRD profile of 0.5 mol% Sm^{3+}-doped boro-bismuth (B30Bi70BSm0.5) glass is shown in Fig. 2 and is similar to all other glasses (BBiSm). It is confirmed that the prepared samples are amorphous in nature due to lack of sharp peaks in the XRD profile.

3.4. Absorption spectra

Absorption spectra of the Sm^{3+}-doped BBiSm glasses are recorded in the ultra-violet (UV) to near infrared (NIR) range. Figs. 3(A) and (B)

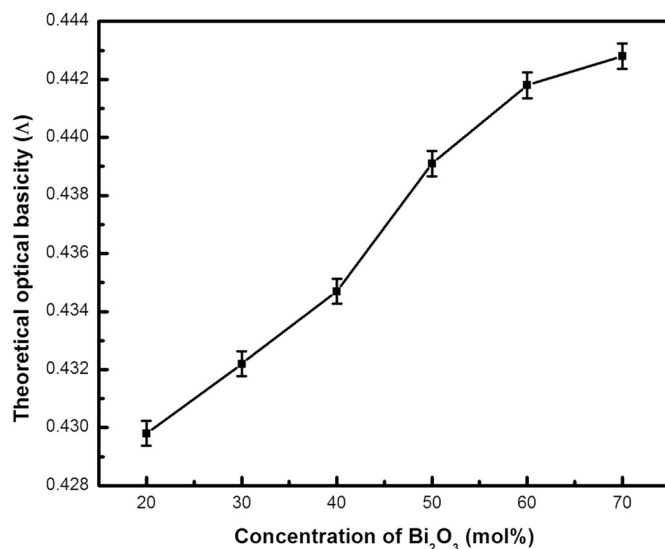**Fig. 1.** Variation of evaluated theoretical optical basicity (Λ) with bismuth concentration (mol%).
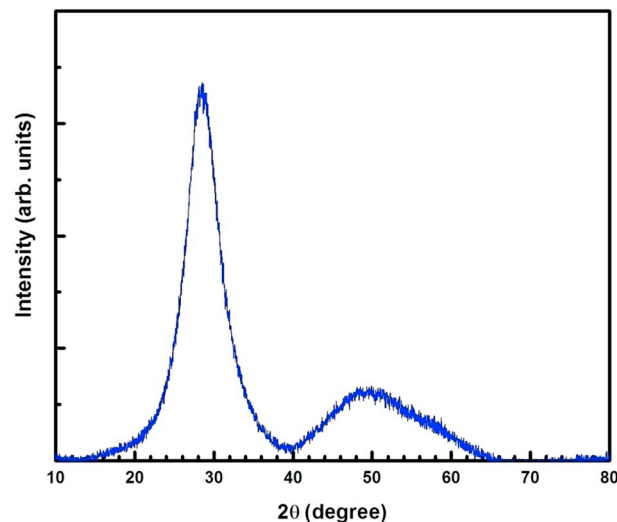

Fig. 2. XRD patterns of B30Bi70Sm0.5 glass.

show the absorption spectra in the UV–visible (300–800 nm) and NIR (850–2000 nm) regions, respectively. This spectral region of the present BBiSm glasses are comparable to other reported Sm^{3+}-doped glasses [29–33]. The various absorption transitions originate from the $^6H_{5/2}$ ground state to the various upper energy states. From Fig. 3(A), it can be observed that the UV–visible region is more sensitive to bismuth concentration although the Sm^{3+} ions concentration was kept constant at 0.5 mol% in B80Bi20Sm0.5, B70Bi30Sm0.5 and B60Bi40Sm0.5 glasses. At lower Bi content glasses, few prominent transitions $^6H_{5/2} \rightarrow ^6P_{3/2}$ (402 nm), $^6H_{5/2} \rightarrow ^6P_{5/2}$ (416 nm), $^6H_{5/2} \rightarrow ^4I_{11/2}$ (479 nm) and $^6H_{5/2} \rightarrow ^4I_{11/2}$ (479 nm) are clearly observed. When the bismuth content reaches to 40 mol%, UV–visible transitions disappear. It clearly shows that bismuth content significantly affects UV–visible transitions of Sm^{3+} ions owing to high absorption of hosts in the UV range. From the inset of Fig. 3(A), it can be observed that UV cutoff wavelength increases towards the higher wavelength side from 383 to 463 nm in moving from B80Bi20Sm0.5 to B30Bi70Sm0.5. This may also be one of the reasons for the absence of the Sm^{3+} ion absorption transitions in UV–visible range. It can be said that bismuth content can be used in borate glasses for UV cutoff applications.

Fig. 3(B) shows NIR transitions (above 10,706 cm^{-1}) which are

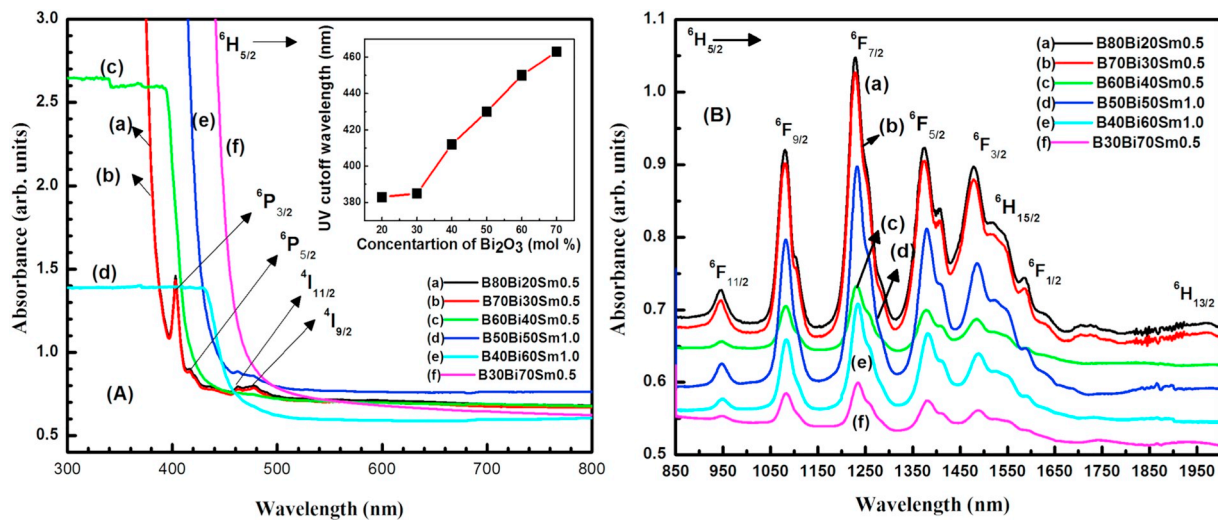**Fig. 3.** (A). UV–VIS absorption spectra (inset shows the UV-VIS cutoff wavelength with Bi_2O_3 concentration) (B). NIR absorption spectra of Sm^{3+}-doped bor-o-bismuth glasses.

Table 2
Observed band positions (± 2, cm^{-1}) and bonding parameters ($\overline{\beta}$ and δ, ± 0.0001) of the Sm^{3+}-doped boro-bismuth glasses.

Transition $^6H_{5/2} \rightarrow$	B80Bi20Sm0.5	B70Bi30Sm0.5	B60Bi40Sm0.5	B50Bi50Sm1.0	B40Bi60Sm1.0	B30Bi70Sm0.5	Aquo-ion [37]
$^6H_{13/2}$	5079	–	–	–	–	–	5042
$^6F_{1/2}$	6317	6313	6289	6278	6302	6270	6397
$^6F_{3/2}$	6771	6757	6743	6729	6725	6720	6630
$^6F_{5/2}$	7283	7273	7241	7246	7236	7246	7100
$^6F_{7/2}$	8143	8143	8130	8103	8104	8110	8000
$^6F_{9/2}$	9294	9234	9259	9251	9225	9242	9200
$^6F_{11/2}$	10,605	10,593	10,560	10,560	10,537	10,560	10,500
$^4I_{9/2}$	20,877	20,964	20,964	20,964	–	–	20,526
$^4I_{11/2}$	21,645	21,598	21,692	21,692	–	–	21,600
$^4P_{5/2}$	24,039	23,981	–	–	–	–	24,050
$^4P_{3/2}$	24,876	24,814	–	–	–	–	24,999
$\overline{\beta}$	0.7356	0.7347	0.7340	0.7333	1.0063	1.0064	
δ	0.3594	0.3611	0.3624	0.3636	−0.0063	−0.0064	
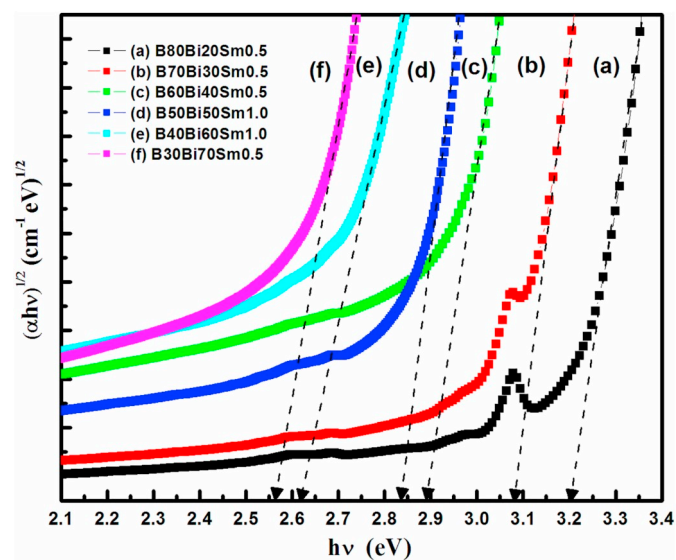
Fig. 4. Tauc's plots for the prepared Sm^{3+}-doped boro-bismuth glasses.

sharp and more intense because 4f electrons in the Sm^{3+} ions are adequately protected by the 5 s and 5p filled shells [34]. Eight absorption transitions are found in NIR region which originates from the $^6H_{5/2}$ ground state to the various excited states, $^6F_{11/2}$ (~943 nm), $^6F_{9/2}$

(~1082 nm), $^6F_{7/2}$ (~1228 nm), $^6F_{5/2}$ (~ 1373 nm), $^6F_{3/2}$ (~1478 nm), $^6H_{15/2}$ (~ 1524), $^6F_{1/2}$ (~1587 nm) and $^6H_{13/2}$ (~1967 nm). In the present glass systems, the ground state of all the absorption transitions begin because of electric-dipole involvement and they obey the selection rule $\Delta J \leq 6$. The $^6H_{5/2} \rightarrow {}^6F_{7/2}$ transition is magnetic-dipole in nature and comply with the selection rule $\Delta J = 0, \pm 1$ [35]. As can be seen from Fig. 3(B), absorption band corresponding to the $^6H_{5/2} \rightarrow {}^6F_{7/2}$ transition acquire higher intensity and is known as a hypersensitive transition. From the observed transitions of the absorption spectra, the Judd-Offelt (JO) parameters [40,41] are calculated using the oscillator strengths of the absorption transitions and squared doubly reduced matrix elements.

3.4.1. Nephelauxetic effect - Bonding parameter

The nephelauxetic ratios ($\overline{\beta}$) and bonding parameters (δ) are calculated to find the nature of bonding between the Sm^{3+} ions and their surrounding metal-ligands [36,37]. The bonding parameter 'δ' is determined where $\delta = (1 - \overline{\beta})/\overline{\beta}$. The $\overline{\beta}$ and δ values are presented in Table 2. The bonding property in host matrix could be covalent/ionic depending on the $+/-$ sign of δ value. From the Table 2, it can be seen that the nephelauxetic ratios ($\overline{\beta}$) are found to decrease with the increase in bismuth content up to 50 mol% and increases thereafter. The evaluated $\overline{\beta}$ values are found to be 0.7356 ± 0.0001, 0.7347 ± 0.0001, 0.7340 ± 0.0001, 0.7333 ± 0.0001, 1.0063 ± 0.0001 and 1.0064 ± 0.0001 for the B80Bi20Sm0.5, B70Bi30Sm0.5, B60Bi40Sm0.5, B50Bi50Sm1.0, B40Bi60Sm1.0 and B30Bi70Sm0.5 glasses, respectively. The positive values of 'δ' for lower bismuth content (≤ 50 mol%) indicates the

Table 3

Trasition assignments, experimental (f_{exp}) and calculated (f_{cal}) oscillator strengths ($\pm$ 5%, $\times 10^{-6}$), Judd-Ofelt intensity parameters ($\Omega_\lambda \pm$ 5%, λ = 2, 4 and 6, $\times 10^{-20}$ cm^2) and root mean square deviation (δ_{RMS}) values of Sm^{3+}-doped boro-bismuth glasses along with reported Sm^{3+}:glasses.

Transition $^6H_{5/2} \rightarrow$	B80Bi20Sm0.5		B70Bi30Sm0.5		B60Bi40Sm0.5		B50Bi50Sm1.0		B40Bi60Sm1.0		B30Bi70Sm0.5		BiSPbSm0.5 [48]		BLNfSm1.0 [54]	
	f_{exp}	f_{cal}	f_{exp}	f_{cal}	f_{exp}	f_{cal}	f_{exp}	f_{cal}	f_{exp}	f_{cal}	f_{exp}	f_{cal}	f_{exp}	f_{cal}	f_{exp}	f_{cal}
$^6P_{3/2}$	1.10	0.67	1.10	0.06	–	–	–	–	–	–	–	–	–	–	8.20	9.12
$^6P_{5/2}$	1.05	0.00	1.05	0.00	–	–	–	–	–	–	–	–	–	–	0.65	0.29
$^4I_{11/2}$	0.58	1.04	0.58	1.05	–	–	–	–	–	–	–	–	–	–	2.90	1.96
$^4I_{9/2}$	0.05	0.08	0.05	0.08	–	–	–	–	–	–	–	–	–	–	0.36	0.32
$^6F_{11/2}$	0.88	1.04	0.88	1.05	0.82	0.88	0.99	0.91	0.50	0.74	1.62	2.07	1.23	1.43	0.92	0.76
$^6F_{9/2}$	6.80	6.31	6.80	6.45	5.22	5.34	5.22	5.58	4.54	4.65	12.5	12.6	1.82	1.67	7.42	6.94
$^6F_{7/2}$	8.52	8.68	8.52	8.77	7.64	7.41	8.03	7.79	6.55	6.44	18.0	18.0	3.14	3.23	8.94	8.64
$^6F_{5/2}$	3.68	3.67	3.68	3.66	2.92	3.32	3.42	3.50	2.58	2.82	8.00	8.42	2.79	3.12	5.64	4.76
$^6P_{3/2}$	1.87	1.76	1.87	1.75	2.4	1.80	1.25	0.04	1.85	1.45	4.88	4.16	1.67	1.72	2.92	3.48
$^6F_{1/2}$	0.09	1.16	0.09	0.17	0.09	0.45	0.06	0.04	0.03	0.27	0.14	0.58	–	–	–	–
$^6H_{13/2}$	0.00	0.64	–	–	–	–	–	–	–	–	–	–	–	–	–	–
δ_{RMS}	$\pm$ 0.45		$\pm$ 0.34		$\pm$ 0.25		$\pm$ 0.47		$\pm$ 0.28		$\pm$ 0.57		$\pm$ 0.94		$\pm$ 0.51	
Ω_2	0.46		0.43		0.93		0.12		0.85		1.49		2.54		3.92	
Ω_4	5.64		4.27		4.30		4.33		4.59		3.01		4.28		8.17	
Ω_6	6.39		5.780		4.40		4.22		4.41		2.84		4.54		5.82	

Table 4

Comparison of Judd-Ofelt ($\Omega_\lambda \pm$ 5%, $\times 10^{-20}$ cm^2) parameters of Sm^{3+}:boro-bismuth glasses with reported Sm^{3+}:glasses.

Glass	JO intensity parameters			Trend
	Ω_2	Ω_4	Ω_6	
79.75B$_2$O$_3$ + 19.75Bi$_2$O$_3$ + 0.5Sm$_2$O$_3$ (B80Bi20Sm0.5) [Present work, PW]	0.46	5.64	6.39	$\Omega_6 > \Omega_4 > \Omega_2$
69.75B$_2$O$_3$ + 29.75Bi$_2$O$_3$ + 0.5Sm$_2$O$_3$ (B70Bi30Sm0.5) [PW]	0.43	4.27	5.78	$\Omega_6 > \Omega_4 > \Omega_2$
59.75B$_2$O$_3$ + 39.75Bi$_2$O$_3$ + 0.5Sm$_2$O$_3$ (B60Bi40Sm0.5) [PW]	0.93	4.30	4.40	$\Omega_6 > \Omega_4 > \Omega_2$
49.50B$_2$O$_3$ + 49.50Bi$_2$O$_3$ + 1.0Sm$_2$O$_3$ (B50Bi50Sm1.0) [PW]	0.12	4.33	4.22	$\Omega_4 > \Omega_6 > \Omega_2$
39.50B$_2$O$_3$ + 59.50Bi$_2$O$_3$ + 1.0Sm$_2$O$_3$ (B40Bi60Sm1.0) [PW]	0.85	4.59	4.41	$\Omega_4 > \Omega_6 > \Omega_2$
29.75B$_2$O$_3$ + 69.75Bi$_2$O$_3$ + 0.5Sm$_2$O$_3$ (B30Bi70Sm0.5) [PW]	1.49	3.01	2.84	$\Omega_4 > \Omega_6 > \Omega_2$
60B$_2$O$_3$ + 15ZnO + 10BaF$_2$ + 10CaF$_2$ + 4.9 Al$_2$O$_3$ + 0.1Sm$_2$O$_3$ (BZBfCfASm0.1) [11]	0.59	4.18	4.27	$\Omega_6 > \Omega_4 > \Omega_2$
52.33PbO + 26.66B$_2$O$_3$ + 16GeO$_2$ + 4Bi$_2$O$_3$ + 1.0Sm (PbBGBiSm1.0) [18]	0.42	2.65	2.48	$\Omega_4 > \Omega_6 > \Omega_2$
64B$_2$O$_3$ + 15Bi$_2$O$_3$ + 20ZnO + 1.0Sm$_2$O$_3$ (BZBiSm1.0) [21]	1.93	1.84	1.79	$\Omega_2 > \Omega_4 > \Omega_6$
83.5SiO$_2$ + 10Bi$_2$O$_3$ + 5Na$_2$CO$_3$ + 1.5Sm$_2$O$_3$ (SBiNSm1.5) [30]	2.26	3.46	2.09	$\Omega_4 > \Omega_2 > \Omega_6$
60B$_2$O$_3$ + 9Bi$_2$O$_3$ + 20ZnO + 10Al$_2$O$_3$ + 1.0Sm$_2$O$_3$ (BBiZASm1.0) [31]	1.17	4.14	8.52	$\Omega_6 > \Omega_4 > \Omega_2$
40Bi$_2$O$_3$ + 25MgHPO$_4$ + 24B$_2$O$_3$ + 10PbO + 1.0Sm$_2$O$_3$ (BiPBPbMgSm1.0) [44]	0.20	3.47	4.37	$\Omega_6 > \Omega_4 > \Omega_2$
39H$_3$BO$_3$ + 30TeO$_2$ + 30PbF$_2$ + 1.0Sm$_2$O$_3$ (BTPfSm1.0) [45]	0.21	1.42	1.87	$\Omega_6 > \Omega_4 > \Omega_2$
41P$_2$O$_5$ + 17K$_2$O + 23ZnF$_2$ + 10LiF + 8Al$_2$O$_3$ + 1.0Sm$_2$O$_3$ (PKZfLfASm1.0) [46]	4.50	7.40	3.93	$\Omega_4 > \Omega_2 > \Omega_6$
59B$_2$O$_3$ + 20PbO + 5BaO + 5ZnO + 10LiF + 1.0Sm$_2$O$_3$ (BPbBaZLfSm1.0) [47]	0.32	3.29	1.93	$\Omega_4 > \Omega_6 > \Omega_2$
69.5Bi$_2$O$_3$ + 10SiO$_2$ + 20PbO + 0.5Sm$_2$O$_3$ (BiSPbSm0.5) [48]	2.54	4.28	4.54	$\Omega_6 > \Omega_4 > \Omega_2$
49B$_2$O$_3$ + 20Bi$_2$O$_3$ + 15Li$_2$O + 10SrO + 5SrF$_2$ + 2.0Sm$_2$O$_3$ (BBiLSofSm2.0) [49]	3.17	5.97	6.22	$\Omega_6 > \Omega_4 > \Omega_2$
33.33B$_2$O$_3$ + 53.33PbO + 13.33PbF$_2$ + 0.7Sm$_2$O$_3$ (BPofSm0.7) [50]	3.41	2.92	2.17	$\Omega_2 > \Omega_4 > \Omega_6$
49B$_2$O$_3$ + 25Na$_2$O + 10CaF$_2$ + 10AlF$_3$ + 5LaF$_3$ + 1.0SmF$_3$ (BNCfAfLafSf1.0) [51]	3.51	3.48	4.56	$\Omega_6 > \Omega_2 > \Omega_4$
69.75H$_3$BO$_3$ + 20Li$_2$CO$_3$ + 10CaCO$_3$ + 0.25Sm$_2$O$_3$ (BLCSm0.25) [52]	4.77	10.79	6.22	$\Omega_4 > \Omega_6 > \Omega_2$
69.5H$_3$BO$_3$ + 29.50Li$_2$CO$_3$ + 1.0Sm$_2$O$_3$ (BLSm1.0) [53]	6.81	10.16	6.93	$\Omega_4 > \Omega_6 > \Omega_2$
49B$_2$O$_3$ + 25Li$_2$O + 25NaF + 1.0Sm$_2$O$_3$ (BLNfSm1.0) [54]	3.92	8.17	5.82	$\Omega_4 > \Omega_6 > \Omega_2$

predominant covalent environment of the bonding between Sm^{3+} ions and ligands. As bismuth content increases beyond 50 mol% in the pure borate glass, 'δ' values become negative and nature of the bonds tends towards ionic nature.

3.4.2. Optical band gap energy

The absorption at slightly higher energies (optical absorption edge) provides information on the combined density of states at the valence-band and conduction-band edges (optical band gap) of the materials [38]. The absorption coefficient $\alpha(\lambda)$, near the edge of the absorption spectra can be evaluated by using the below relation,

$$\alpha(\lambda) = (1/t)In(I/I_0) \tag{2}$$

where 't' is the thickness and $In(I/I_0)$ is the to absorbance of the sample. The relation between $\alpha(\lambda)$ and photon energy of the incident radiation, 'hν' is given by [39],

$$\alpha(\lambda) = A(h\nu - E_{opt})^r/h\nu \tag{3}$$

where E_{opt} is the optical band gap (eV), A is a constant and 'r' is an index. According to the Tauc's relations for glassy systems, indirect

transition (r = 2) is valid [39]. The values of indirect optical band gap energy (E_{opt}) for the given glass can be determined by the extrapolation of straight line portion of $(\alpha(\lambda)h\nu)^{1/2}$ vs. $h\nu$ curve to zero. Fig. 4 shows the evaluated Tauc's plots for B80Bi20Sm0.5 (2.56 $\pm$ 0.01 eV), B70Bi0Sm0.5 (2.62 $\pm$ 0.01 eV), B60Bi40Sm0.5 (2.84 $\pm$ 0.01 eV), B50Bi50Sm0.5 (2.89 $\pm$ 0.01 eV), B40Bi60Sm0.5 (3.08 $\pm$ 0.01 eV) and B30Bi70Sm0.5 (3.21 $\pm$ 0.01 eV) glasses. As can be seen the value of 'E_{opt}' for boro-bismuth glasses increases from 2.56 to 3.21 $\pm$ 0.01 eV with increase in bismuth content from 20 to 70 mol%. The present values show that increase of bismuth content in borate glass can enhance the E_{opt} value of the glass system.

3.4.3. Oscillator strengths and Judd–Ofelt intensity parameters

The experimental oscillator strengths (f_{exp}) are calculated by integrating the area of each band in the absorption spectra using the following expression,

$$f_{exp} = \frac{2.303mc^2}{N\pi e^2} \int \varepsilon(\upsilon)d\upsilon = 4.318 \times 10^{-9} \int \varepsilon(\upsilon)d\upsilon \tag{4}$$

and theoretical oscillator strengths (f_{cal}) are calculated by using the

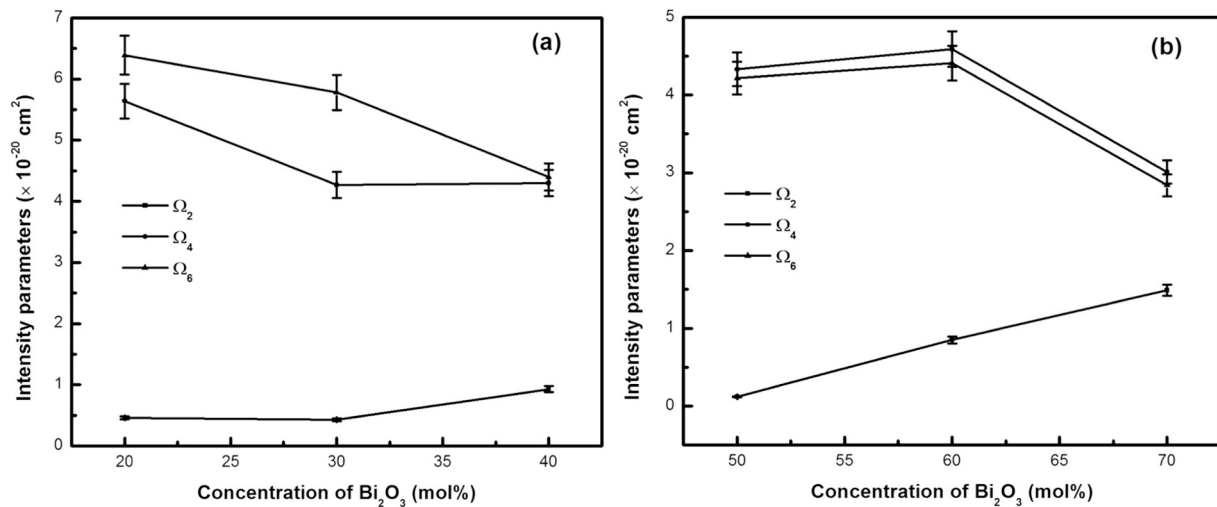**Fig. 5.** Variation of intensity parameters (Ω_2, Ω_4 and Ω_6) with Bi_2O_3 concentration (mol%) in boro-bismuth glasses. B80Bi20Sm, B70Bi30Sm and B60Bi40Sm (b) B50Bi50Sm, 40Bi60Sm and B30Bi70Sm boro-bismuth glasses.
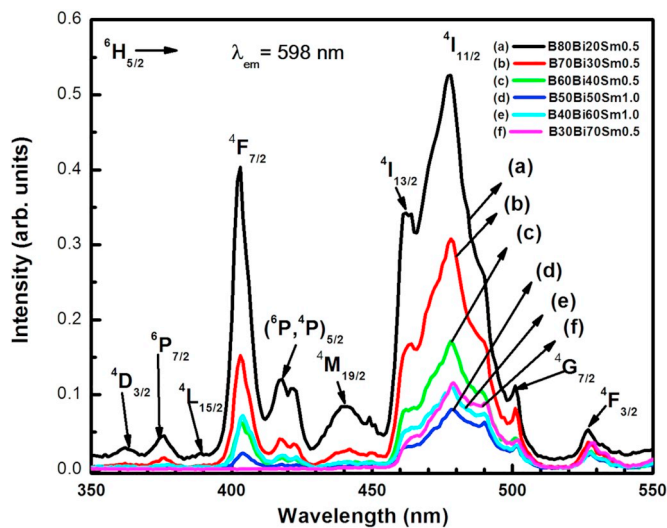

Fig. 6. Excitation spectra of boro-bismuth glasses (λ_{em} = 598 nm).

Judd-Ofelt (JO) theory [40,41],

$$f_{cal} = \frac{8\pi^2 mc\upsilon}{3h(2J+1)} \frac{(n^2+2)^2}{9n} \sum_{\lambda=2,4,6} \Omega_\lambda(\psi J \| U^\lambda \| \psi'J')^2 \tag{5}$$

all the notations and symbols in Eq. (5) carry the same meaning as in Refs. [40, 41]. The values of f_{exp} and f_{cal} are listed in Table 3. The JO intensity parameters, Ω_λ (λ = 2, 4 and 6) are determined by using the least square fitting method as carried out in earlier works. The root-mean-square deviation is defind as,

$$\delta_{RMS} = \sum [(f_{exp} - fcal)^2/N]^{1/2} \tag{6}$$

where N is the number of levels included in the fit and also have been used to determine the accuracy of the intensity parameters. As can be seen from the Table 3, the δ_{RMS} values are found to be ± 0.45, ± 0.34, ± 0.25, ± 0.47, ± 0.28, ± 0.57, ± 0.94 and ± 0.51 for B80Bi20Sm0.5, B70Bi30Sm0.5, B60Bi40Sm0.5, B50Bi50Sm1.0, B40Bi60Sm1.0, B30Bi70Sm0.5, BiSPbSm0.5 [48] and BLNfSm1.0 [54], respectively, and show that experimental intensity values are in good agreement with the calculated values. Table 4 compares the calculated JO parameters with those of reported systems [11,18,21,30,31,44–54]. The JO intensity parameter Ω_2 describes the covalency between RE^{3+} ions and ligand (O^-) anions. Similarly, the parameters Ω_4 and Ω_6 are

related to the host matrix properties such as rigidity and viscosity [42].

Figs. 5(a) and (b) represent the variation of the intensity parameters with respect to bismuth content. It can be observed that the JO parameters for Sm^{3+}:glasses follow two different trends. When the bismuth content is ≤ 40 mol%, JO parameters are following the trend as $\Omega_6 > \Omega_4 > \Omega_2$, and when bismuth content is ≥ 50 mol%, intensity parameters are following the trend as $\Omega_4 > \Omega_6 > \Omega_2$. In both the cases, Ω_2 value is increasing with increasing of bismuth content where as Ω_4 and Ω_6 values are decreasing. This indicates that up to 40 mol%, the rigidity of the glass system decreases with increase in bismuth content and the similar trend was also observed in bismuth system reported by Pal et al. [24]. As can be seen from Fig. 5, for higher content of bismuth, the rigidity of the glass system is also increasing up to 60 mol%, after that sudden decrement was observed in Ω_4 and Ω_6 values, which may be due to the non availability of boran linkages leading to less possibility of glass formation. In the present case, 70 mol% of bismuth glass shows less transparency. From Table 4, the Ω_2 values of investigated glasses are comparable to those of reported bismuth and borate systems. It can be observed that the present glass systems have more or less similar value for covalency nature compared to BZBfCfASm1.0 [11], PbBGBiSm1.0 [18], BiPBPbMgSm1.0 [44], BTPfSm1.0 [45] and BPbBaZLfSm1.0 [47]. Besides this, the Ω_2 values are found to be lower compared to those reported for BBiZSm1.0 [21], SBiNSm1.5 [30], BBiZASm1.0 [31], PKZfLfASm1.0 [46], BiSPbSm0.5 [48], BBiLSofSm2.0 [49], BPofSm0.7 [50], BNCfAfLafSf1.0 [51], BLCSm0.25 [52], BLSm1.0 [53] and BLNfSm1.0 [54] glasses indicating that the symmetry around the Sm^{3+} ion is higher in the present glasses compared to those of reported glas systems.

3.5. Excitation, emission and radiative properties

The excitation spectra, measured in the range of 350–550 nm, by monitoring the emission at 601 nm, are shown in Fig.6. The bands observed from excitation spectra are at 360, 375, 388, 403, 416, 441, 461, 479, 501 and 526 nm which correspond to the transitions of $^6H_{5/2} \rightarrow {}^4D_{3/2}$, $^6P_{7/2}$, $^4L_{15/2}$, $^4F_{7/2}$, $(^6P,^4P)_{5/2}$, $^4M_{19/2}$, $^4I_{13/2}$, $^4I_{11/2}$, $^4G_{7/2}$ and $^4F_{3/2}$, respectively. Among all excitation transitions, the $^6H_{5/2} \rightarrow {}^4I_{11/2}$ transition at 479 nm is having highest intensity and is prominent to investigate the photoluminescence emission spectra of all Sm^{3+}-doped boro-bismuth glasses.

The emission spectra of all the Sm^{3+}-doped BBiSm glasses are presented in Fig. 7. The emission spectra exhibit four emission bands corresponding to the $^4G_{5/2} \rightarrow {}^6H_{5/2}$ (~561 nm), $^4G_{5/2} \rightarrow {}^6H_{7/2}$ (~598 nm), $^4G_{5/2} \rightarrow {}^6H_{9/2}$ (~647 nm) and $^4G_{5/2} \rightarrow {}^6H_{11/2}$ (~705 nm)
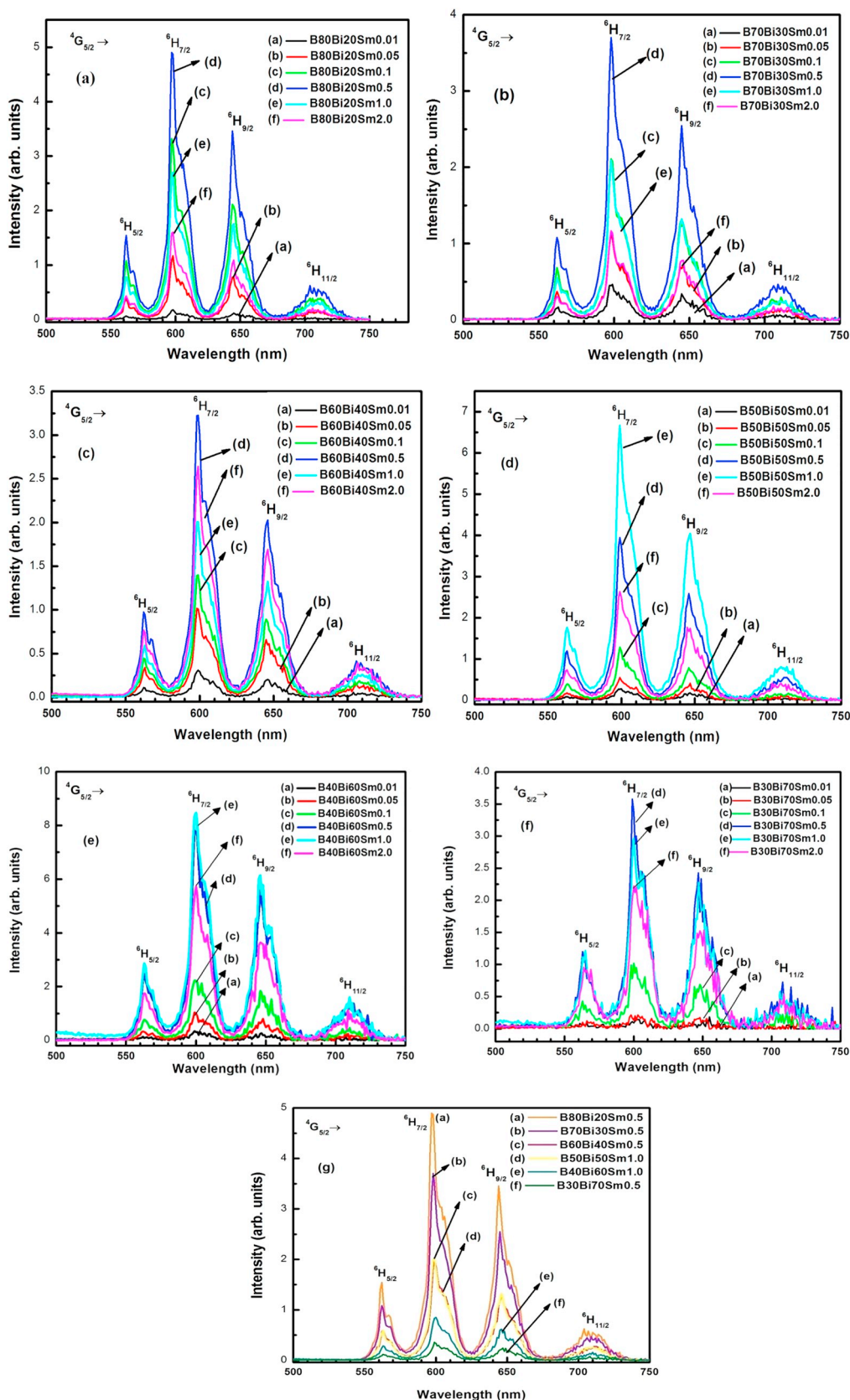
Fig. 7. Emission spectra of BBiSm glasses (λ_{ex} = 479 nm).

transitions irrespective of variation in concentration. Out of these four bands, the $^4G_{5/2} \rightarrow {}^6H_{7/2}$ is more intense and $^4G_{5/2} \rightarrow {}^6H_{11/2}$ is weeker in intensity. As can be seen from Fig. 7, the emission spectral intensity

of Sm^{3+} ions in titled glasses increase gradually up to 0.5 mol% of Sm^{3+} and then decreases for all the peaks in the glass compositions of B80Bi20Sm, B70Bi30Sm, B60Bi40Sm and B30Bi70Sm. Similarly, the
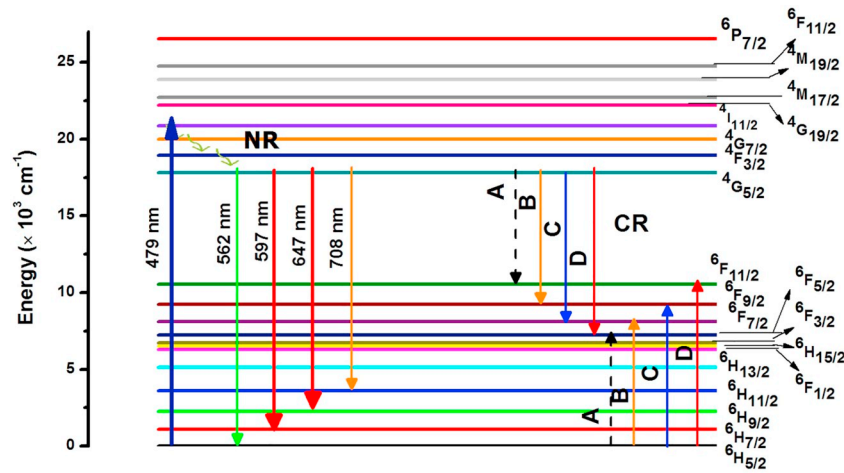
Fig. 8. Partial energy level diagram of Sm^{3+} − doped boro-bismuth glasses.

Table 5
Peak wavelength ($\lambda_p \pm 0.2$, nm), effective linewidth ($\Delta\lambda_{eff} \pm 0.01$, nm), radiative transition probability ($A_R \pm 2$, s^{-1}), stimulated emission cross-section (σ_e (λ_p) ± 0.2, $\times 10^{-21}$ cm²), experimental ($\beta_R(Exp) \pm 2\%$) and calculated (($\beta_R(Cal) \pm 2\%$) branching ratio corresponding to the $^4G_{5/2}$ emission transitions.

Transitions	Parameters	B80Bi20Sm0.5	B70Bi30Sm0.5	B60Bi40Sm0.5	B50Bi50Sm1.0	B40Bi60Sm1.0	B30Bi70Sm0.5
$^4G_{5/2} \rightarrow {}^6H_{5/2}$	λ_p	562	561	562	562	561	561
	$\Delta\lambda_{eff}$	11.24	10.06	9.60	9.60	9.34	12.24
	$\sigma_e(\lambda_p)$	2.31	2.96	2.99	3.16	3.73	2.89
	A_R	70	71	89	101	129	151
	$\beta_R(Exp)$	0.11	0.09	0.09	0.08	0.09	0.10
	$\beta_R(Cal)$	0.10	0.05	0.11	0.12	1.12	0.12
$^4G_{5/2} \rightarrow {}^6H_{7/2}$	λ_p	597	598	597	597	598	598
	$\Delta\lambda_{eff}$	13.73	14.66	14.14	14.59	14.52	14.02
	$\sigma_e(\lambda_p)$	4.25	4.37	5.15	4.27	5.59	5.90
	A_R	117	213	176	163	234	274
	$\beta_R(Exp)$	0.46	0.48	0.48	0.48	0.45	0.44
	$\beta_R(Cal)$	0.30	0.52	0.23	0.20	0.22	0.22
$^4G_{5/2} \rightarrow {}^6H_{9/2}$	λ_p	644	647	644	644	647	647
	$\Delta\lambda_{eff}$	14.95	15.98	15.97	16.30	17.65	16.70
	$\sigma_e(\lambda_p)$	12.84	13.83	4.85	13.62	14.54	15.69
	A_R	295	304	139	429	539	634
	$\beta_R(Exp)$	0.34	0.35	0.35	0.35	0.37	0.37
	$\beta_R(Cal)$	0.42	0.21	0.49	0.52	0.51	0.50
$^4G_{5/2} \rightarrow {}^6H_{11/2}$	λ_p	708	705	708	708	705	705
	$\Delta\lambda_{eff}$	19.38	21.17	17.83	18.69	20.19	27.22
	$\sigma_e(\lambda_p)$	2.00	1.53	2.18	2.12	2.13	1.67
	A_R	31	42	48	52	64	78
	$\beta_R(Exp)$	0.09	0.09	0.08	0.09	0.10	0.11
	$\beta_R(Cal)$	0.05	0.12	0.06	0.06	0.06	0.60

spectral intensity increase gradually up to 1.0 mol% of Sm^{3+} and then decreases for all peaks in the compositions of B50Bi50Sm and B40Bi60BSm glasses. This concentration quenching could be due to enhanced interaction between Sm^{3+} ions leading energy transfer through the cross-relaxation [55]. Among these glasses, emission cross-section is maximum for B80Bi20Sm0.5 glass. This glass has a very distinct orange-red luminescence, which is mainly due to the intense $^4G_{5/2} \rightarrow {}^6H_{7/2}$ transition at 598 nm (16,722 cm^{-1}) and $^4G_{5/2} \rightarrow {}^6H_{9/2}$ transition at 647 nm (15,456 cm^{-1}). These transitions are useful in high-density optical data storage, color display and medical diagnostics. The partial energy level diagram drawn for BBiSm glasses are shown in Fig. 8.

The intensity of orange-red luminescence emitted by BBiSm glasses increases with the concentration of Sm^{3+} ions up to 0.5 mol% and then decreases. The $^4G_{5/2} \rightarrow {}^6H_{5/2}$ (563 nm) is predominantly magnetic-dipole in character where as the $^4G_{5/2} \rightarrow {}^6H_{9/2}$ (644 nm) transition is predominantly electric-dipole in character. The transition $^4G_{5/2} \rightarrow {}^6H_{7/2}$ (598 nm) is mainly electric-dipole in character although the transition is magnetic-dipole allowed. In the present work, spectral intensity of the electric-dipole

transition, $^4G_{5/2} \rightarrow {}^6H_{9/2}$, of the Sm^{3+} ion is higher than the magnetic-dipole transition, $^4G_{5/2} \rightarrow {}^6H_{5/2}$. The relative intensities of these transitions are known to be sensitive to the variations in the local field around the Sm^{3+} ions [46].

Using Ω_λ parameters, radiative transition probabiliy (A_{rad}) for spontaneous emission, radiative lifetime of the excited state from which fluorescence is observed and branching ratios (β_R) of transitions are calculated and are presented in Table 5 for the $^4G_{5/2} \rightarrow {}^6H_{5/2}$ (561 nm), $^4G_{5/2} \rightarrow {}^6H_{7/2}$ (598 nm), $^4G_{5/2} \rightarrow {}^6H_{9/2}$ (647 nm) and $^4G_{5/2} \rightarrow {}^6H_{11/2}$(705 nm) transitions. A_{rad}, which depend on the JO parameters and refractive index (n) of the host system through the local field correction is increasing with Bi_2O_3 content [3]. Among the four emission transitions, $^4G_{5/2} \rightarrow {}^6H_{7/2}$ (~597) and $^4G_{5/2} \rightarrow {}^6H_{9/2}$ (~ 644) transitions are more intense for BBiSm0.5 and BBiSm1.0 glasses. The peak stimulated emission cross-section ($\sigma_e(\lambda_p)$) of an emission band having transition probability of $A_R(\Psi J, \Psi'J')$ can be expressed as

$$\sigma_e(\lambda_p)(\Psi J, \Psi'J') = \frac{\lambda_p{}^4}{8\pi c n^2 \, \Delta\lambda_{eff}} A_R(\Psi J, \Psi'J')$$

(7)

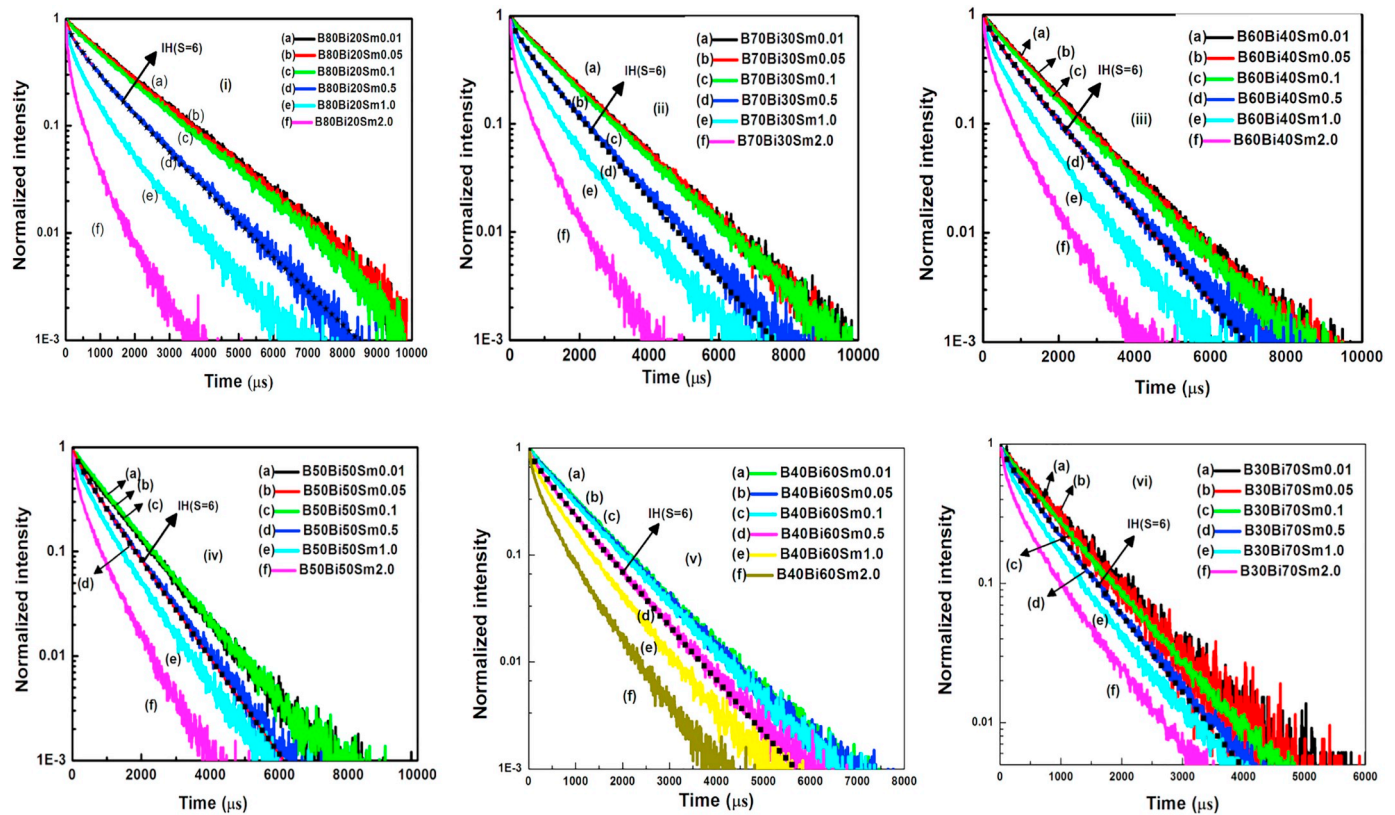**Fig. 9.** Decay curves for different concentrations of Sm_2O_3 ions in ((i) B80Bi20Sm, (ii) B70Bi30Sm, (iii) B60Bi40Sm, (iv) B50Bi50Sm, (v) B40Bi60Sm and (vi) B30Bi70Sm) boro-bismuth glasses.

here λ_p is the transition peak wavelength and $\Delta\lambda_{eff}$ is its effective linewidth found by dividing the area of the emission band by its average height. The values of $\sigma_e(\lambda_p)$ are given in Table 5. The large $\sigma_e(\lambda_p)$ is an attractive element for low-threshold and high gain laser applications, which are utilized to attain CW laser action. Among the four emission transitions, the $^4G_{5/2} \rightarrow$ $^6H_{9/2}$ transition has high $\sigma_e(\lambda_p)$ for all the titled glasses.

The luminescence branching ratio (β_R) is another essential parameter which plays an important role in deciding the lasing potentiality of an emission transition. It is well known that the emission transition having the $\beta_R > 50\%$ is considered to be more potential for laser emission [46]. Hence, in the labelled glass systems, $^4G_{5/2} \rightarrow {}^6H_{7/2}$ transition fullfil the above conditions necessary for a good laser transition. The experimental branching ratios (β_R (Exp)) and calculated branching ratios (β_R(Cal)) are given in Table 5. It is evident that the $^4G_{5/2} \rightarrow {}^6H_{7/2}$ transition is more intense compared to other transitions and therefore the BBiSm glasses could be used for the development of light emitting diodes (LEDs) in optical communication [33]. The laser characteristic parameters such as branching ratios (β_R) and stimulated emission cross-sections ($\sigma_e(\lambda_p)$) for the B70Bi30Sm0.5 glass are compared with those of other glasses in Table 5. From the Table 5, it is evident that the $^4G_{5/2} \rightarrow {}^6H_{9/2}$ transition of B30Bi70Sm0.5 glass has the higher $\sigma_e(\lambda_p)$ of 15.69×10^{-21} cm^2, which could be a favorable feature for the development of visible laser around at around 647 nm [46].

3.6. Decay curve analysis

The decay times of the fluorescence level of $^4G_{5/2}$ in Sm^{3+}-doped boro-bismuth glasses are measured under the excitation of 402 nm. As 402 nm can excite the Sm^{3+} ions to above the $^4G_{5/2}$ level, the excited ions will make fast decay to $^4G_{5/2}$ level, through non-radiative transition as the energy separation between these levels are too small. From the $^4G_{5/2}$ level, there will be radiative emission and the mechanism is shown in Fig. 8. Figs. 9(a)–(d) show the decay times for the $^4G_{5/2}$ level

for different Sm^{3+} ion concentrations (0.01–2.0 mol%) in boro-bismuth glasses with varying host composition. It can be seen that the decay curves exhibit single exponential for lower concentrations ($\leq$ 0.1 mol %) and turns into non-exponential with increasing concentration ($\geq$ 0.5 mol%). For lower Sm^{3+} concentrations ($\leq$ 0.1 mol%), the decay curves are well fitted to single function,

$$I = A\exp(-t/\tau) \tag{8}$$

where I is the luminescence intensity, A is constant, t is the time after excitation and τ is the intrinsic lifetime of the donors in the absence of the acceptors [4]. The single exponential nature of the decay curves for the lower concentrations is due to negligible interaction between donor and acceptor ions. The deviation from the exponential behavior increases with the increase in the doping concentration of Sm^{3+} ions due to non-radiative energy transfer between Sm^{3+} ions through cross-relaxation (CR) channels (see Fig. 8). In the case of non-exponential decay curves, experimental lifetimes (τ_{exp}) can be calculated using the following Eq. [9,56]

$$\tau_{exp} = (A_1 t_1^2 + A_2 t_2^2)/(A_1 t_1 + A_2 t_2) \tag{9}$$

The experimental lifetimes of the prepared boro-bismuth glasses are found to decrease with the increase in Sm^{3+} ion concentration and the values are found to be 1.63–0.34 ± 0.01 ms; 1.36–0.45 ± 0.01 ms; 1.18–0.51 ± 0.01 ms, 1.03–0.47 ± 0.01 ms; 0.93–0.37 ± 0.01 ms and 0.86–0.27 ± 0.01 ms for B80Bi20Sm0.01-B80Bi20Sm2.0; B70Bi30Sm0.01-B70Bi30Sm2.0; B60Bi40Sm0.01-B60Bi40Sm2.0; B50Bi50Sm0.01-B50Bi50Sm2.0; B40Bi60Sm0.01-B40Bi60Sm2.0 and B30Bi70Sm0.01-B30Bi70Sm2.0 glasses, respectively (Table 6). As can be seen, the lifetime of the $^4G_{5/2}$ level of the Sm^{3+} ions in the boro-bismuth glasses are found to decrease linearly with increase in Sm^{3+} ion concentrations as well as increase in bismuth content. This may be caused by the increase in non-radiative energy transfer (ET) between different Sm^{3+} ions through CR process [57,58]. The rate of non-

Table 6

Experimental lifetime ($\tau_{exp} \pm 0.01$, ms), energy transfer parameter ($Q \pm 0.01$), critical distance ($R_0 \pm 0.02$, Å), dipole–dipole interaction parameter ($C_{DA} \pm 0.01$, $\times 10^{-40} cm^6/s$), luminescence cross-relaxation rate ($W_{CR} \pm 0.01, s^{-1}$) and quantum efficiency ($\eta, \pm 2\%$) for the $^4G_{5/2}$ energy level of the Sm^{3+} doped boro-bismuth glasses.

Glass	τ_{exp}	Q	R_0	C_{DA}	W_{CR}	η
B80Bi20Sm0.01	1.63	–	–	–	1.50	99
B80Bi20Sm0.05	1.61	–	–	–	10.71	98
B80Bi20Sm0.1	1.54	–	–	–	36.52	94
B80Bi20Sm0.5	1.13	0.75	10.08	9.28	272	69
B80Bi20Sm1.0	0.73	1.62	10.32	16.45	754	45
B80Bi20Sm2.0	0.34	3.74	11.05	54.14	2364	21
B70B30Sm0.01	1.36	–	–	–	17.57	98
B70B30Sm0.05	1.35	–	–	–	20.86	97
B70B30Sm0.1	1.34	–	–	–	23.07	97
B70B30Sm0.5	1.07	0.55	9.33	6.20	163	82
B70B30Sm1.0	0.79	1.17	9.46	9.01	645	53
B70B30Sm2.0	0.45	2.47	9.62	17.61	2255	24
B60Bi40Sm0.01	1.18	–	–	–	89.60	89
B60Bi40Sm0.05	1.51	–	–	–	110	87
B60Bi40Sm0.1	1.11	–	–	–	140	84
B60Bi40Sm0.5	0.88	0.42	8.70	4.06	375	67
B60Bi40Sm1.0	0.78	1.02	9.28	8.06	518	60
B60Bi40Sm2.0	0.51	1.94	9.08	12.48	1205	39
B50Bi50Sm0.01	1.03	–	–	–	154	85
B50Bi50Sm0.05	1.02	–	–	–	165	83
B50Bi50Sm0.1	0.98	–	–	–	201	80
B50Bi50Sm0.5	0.80	0.39	8.72	5.53	442	65
B50Bi50Sm1.0	0.71	0.80	8.73	6.23	591	58
B50Bi50Sm2.0	0.47	1.66	8.83	10.01	1294	39
B40Bi60Sm0.01	0.93	–	–	–	153	86
B40Bi60Sm0.05	0.91	–	–	–	170	83
B40Bi60Sm0.1	0.88	–	–	–	214	79
B40Bi60Sm0.5	0.74	0.40	9.01	7.19	452	61
B40Bi60Sm1.0	0.58	0.67	8.47	6.32	612	56
B40Bi60Sm2.0	0.37	1.14	8.23	7.19	1323	48
B30Bi70Sm0.01	0.86	–	–	–	151	87
B30Bi70Sm0.05	0.83	–	–	–	193	84
B30Bi70Sm0.1	0.79	–	–	–	255	80
B30Bi70Sm0.5	0.68	0.33	8.78	6.76	464	69
B30Bi70Sm1.0	0.56	0.64	8.39	7.08	781	56
B30Bi70Sm2.0	0.27	1.11	8.18	11.10	2706	27

Table 7

Color chromaticity coordinates (x, y) of bismuth-borate glasses doped with Sm^{3+} ions.

Glass	x	y
B80Bi20Sm0.01	0.599	0.399
B80Bi20Sm0.05	0.604	0.395
B80Bi20Sm0.1	0.603	0.396
B80Bi20Sm0.5	0.606	0.393
B80Bi20Sm1.0	0.605	0.395
B80Bi20Sm2.0	0.606	0.394
B70B30Sm0.01	0.600	0.399
B70B30Sm0.05	0.602	0.397
B70B30Sm0.1	0.605	0.394
B70B30Sm0.5	0.607	0.392
B70B30Sm1.0	0.608	0.391
B70B30Sm2.0	0.609	0.390
B60Bi40Sm0.01	0.595	0.404
B60Bi40Sm0.05	0.604	0.395
B60Bi40Sm0.1	0.603	0.396
B60Bi40Sm0.5	0.607	0.392
B60Bi40Sm1.0	0.608	0.390
B60Bi40Sm2.0	0.609	0.393
B50Bi50Sm0.01	0.597	0.402
B50Bi50Sm0.05	0.593	0.406
B50Bi50Sm0.1	0.605	0.395
B50Bi50Sm0.5	0.608	0.391
B50Bi50Sm1.0	0.609	0.389
B50Bi50Sm2.0	0.608	0.391
B40Bi60Sm0.01	0.580	0.419
B40Bi60Sm0.05	0.599	0.399
B40Bi60Sm0.1	0.602	0.398
B40Bi60Sm0.5	0.608	0.392
B40Bi60Sm1.0	0.609	0.391
B40Bi60Sm2.0	0.603	0.397
B30Bi70Sm0.01	0.549	0.449
B30Bi70Sm0.05	0.580	0.419
B30Bi70Sm0.1	0.591	0.408
B30Bi70Sm0.5	0.603	0.396
B30Bi70Sm1.0	0.598	0.402
B30Bi70Sm2.0	0.596	0.403

Fig. 10. The CIE 1931 color chromaticity diagram of the Sm^{3+} ions doped boro-bismuth glasses.

radiative ET can be calculated from the well known Eq.

$$W_{ET} = W_{CR} = (1/\tau_{exp}) - (1/\tau_{rad}) \qquad (10)$$

where τ_{exp} is the experimental lifetime and τ_{rad} is the radiative lifetime calculated from the JO theory. In the present case, non-radiative energy transfer occurs mainly through cross-relaxation channels, A: $(^4G_{5/2}, {}^6H_{5/2}) \rightarrow (^6F_{11/2}, {}^6F_{5/2})$; B: $(^4G_{5/2}, {}^6H_{5/2}) \rightarrow (^6F_{9/2}, {}^6F_{7/2})$; C: $(^4G_{5/2}, {}^6H_{5/2}) \rightarrow (^6F_{7/2}, {}^6F_{9/2})$ and D: $(^4G_{5/2}, {}^6H_{5/2}) \rightarrow (^6F_{5/2}, {}^6F_{11/2})$, shown in Fig. 8. There is a good energy matching between these levels and also large energy separation (7000 cm^{-1}) between the $^4G_{5/2}$ and $^6F_{11/2}$ levels of the Sm^{3+} ion. The ET rates linearly increases with the increase in Sm^{3+} ion concentration in boro-bismuth samples and are given in Table 6. The quantum efficiency (η) of the $^4G_{5/2}$ excited level for all the prepared samples has been calculated using the equation $\eta = (\tau_{exp}/\tau_{rad}, \%)$ and are tabulated in Table 6. As can be seen, measured quantum efficiency linearly decreases with the increase in Sm_2O_3 concentration and the values are found to be in the range of 99–21 ± 2%, 98–24 ± 2%, 89–39 ± 2%, 85–39 ± 2%, 86–48 ± 2% and 87–27 ± 2% for the B80Bi20Sm0.01-B80Bi20Sm2.0; B70Bi30Sm0.01-B70Bi30Sm2.0; B60Bi40Sm0.01-B60Bi40Sm2.0; B50Bi50Sm0.01-B50Bi50Sm2.0; B40Bi60Sm0.01-B40Bi60Sm2.0 and B30Bi70Sm0.01-B30Bi70Sm2.0 glasses, respectively (see Table 6). The non-exponential nature of the decay times for higher concentration (≥ 0.5 mol%) of Sm^{3+} ions in boro-bismuth glasses arises from donor (Sm^{3+})-acceptor (Sm^{3+}) interactions. The non-exponential decay curves are fitted in the frame of Inokuti-Hirayama (IH) model [59]. According to IH model, the fluorescence intensity I(t) is given by
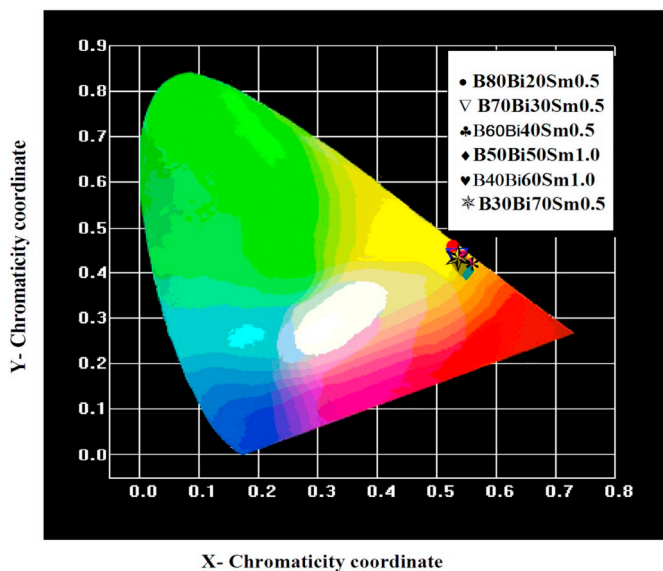
$$I(t) = I_0 \exp[-\frac{t}{t_0} - Q(\frac{t}{t_0})^{\frac{3}{S}}] \tag{11}$$

where 't' is the decay time after excitation, τ_0 is the intrinsic decay time of the excited Sm^{3+} ions (donor) in the absence of acceptors. The value of S = 6 is attributed to dipole-dipole, S = 8 is to dipole-quadrupole and S = 10 is to quadrupole-quadrupole of the interaction mechanisms. All the decay curves above 0.5 mol% of Sm_2O_3 are well-fitted to IH model for S = 6 (Fig. 9), indicating that the interaction between Sm^{3+} and Sm^{3+} ions is of dipole-dipole type. The energy transfer parameter (Q) can be calculated by using the Eq.

$$Q = \frac{4\pi}{3}\Gamma(1 - \frac{3}{S})N_0 R_0^3 \tag{12}$$

where, gamma function $\Gamma(x)$ is equal to 1.77 for S = 6, 1.43 for S = 8 and 1.3 for S = 10. N_0 is the concentration of acceptors (ions/cc) and R_0 is the critical transfer distance defined as donor-acceptor separation. The donor-acceptor energy transfer parameter (C_{DA}) can be obtained by using the Eq.

$$C_{DA} = R_0^6 \tau_0^{-1} \tag{13}$$

the τ_{exp}, Q, R_0, C_{DA} and W_{CR} values are collected in Table 6. As can be seen, R_0, Q and W_{CR} values increases with increase in Sm_2O_3 concentration. With increase in Sm_2O_3 concentrations, the non-radiative ET increases resulting in decrease of lifetimes [60,61].

3.7. CIE chromaticity coordinates

Sm^{3+}-doped materials can be used for display device applications [62–66]. In addition to the spectroscopic parameters such as $\sigma_e(\lambda_p)$ and η, the color chromaticity coordinates of the glass systems are also significant parameters for evaluating the color emitted by the Sm^{3+}-doped boro-bismuth glasses. Color chromaticity coordinates of a sample are evaluated from the emission spectra of the bismuith-borate glasses by using the frame work of de L'Eclairage procedure [66]. The evaluated CIE (x,y) color coordinates of the B80Bi20Sm0.5 (0.606, 0.393), B70Bi30Sm0.5 (0.607, 0.392), B60Bi40Sm0.5 (0.607, 0.392), B50Bi50Sm1.0 (0.609, 0.389), B40Bi60Sm1.0 (0.609, 0.391) and B30Bi7Sm0.5 (0.603, 0.396) glasses are shown in the CIE chromaticity diagram of Fig. 10. The CIE diagram for present glass systems confirms that all boro-bismuth glasses produce emissions in the reddish-orange region, indicating that these glasses can be of potential use for display applications [62–66].

4. Conclusions

The optical properties of Sm^{3+}-doped boro-bismuth glasses, measured through absorption, photoluminescence and decay curves have been analysed and compared with similar reported systems. The higher refractive index of the present boro-bismuth glasses indicate that these glasses are more suitable for fiber drawing and waveguide applications. The high optical basicity for higher bismuth content glasses indicate that the high amount of oxide ions transfer electrons to the nearby cations. Increase in cutoff wavelength with increasing bismuth content shows that these glasses can be useful for UV cutoff applications. The positive values of 'δ' for lower bismuth content (< 50 mol%) indicate the predominant covalent nature of the bonding between Sm^{3+} ions and their nearby ligands, and for higher bismuth content the bonding nature turns in to ionic. The value of E_{opt} for present glasses increases from 2.56 to 3.21 eV with increase in bismuth content that can enhance the value of optical band gap. The evaluated JO parameters show that for lower content of bismuth, the covalency nature between Sm^{3+} − ions and ligands increases with increase in bismuth content. Among the studied boro-bismuth glass systems, B80Bi20Sm0.5 glass exhibit higher β_R and $\sigma_e(\lambda_p)(\times 10^{-21} \text{ cm}^2)$ values for the $^4G_{5/2} \rightarrow ^6H_{7/2}$ transition and it can act as a promising reddish-orange emitting

material when excited at 479 nm. The non-exponential nature of the luminescence decay curves (≥ 0.5 mol% of Sm_2O_3) reveal that the mechanism of interaction among Sm^{3+} ions is of dipole-dipole type. The CIE diagram confirms that all Sm^{3+}-doped boro-bismuth glasses produces reddish-orange color, which indicates that these glasses can be useful for the display device applications (Table 7).

References

[1] G. Blasse, B.C. Grabmaier, Luminescent Materials, Springer Verlag, Berlin, 1994.
[2] R. Vijaya, V. Venkatramu, P. Babu, C.K. Jayasankar, U.R. Rodríguez-Mendoza, V. Lavín, J. Non-Cryst. Solids 365 (2013) 85–92.
[3] Ch. Srinivasa Rao, C.K. Jayasankar, Opt. Commun. 286 (2013) 204–210.
[4] C. Gorller-Walrand, K. Binnemans, K.A. Gschneidner, Jr.L. Eyring (Eds.), Handbook on the Physics and Chemistry of Rare Earths, vol. 25, North-Holland, Amsterdam, 1998, pp. 101–264 (Chapter 167).
[5] M. Liao, L. Hu, Y. Fang, J. Zhang, H. Sun, S. Xu, L. Zhang, Spectrochim. Acta A 68 (2007) 531–535.
[6] M.C. Fearries, P.R. Morkel, J.E. Townsend, Electron. Lett. 24 (1988) 709–711.
[7] G. Turky, M. Dawy, Mater. Chem. Phys. 77 (2002) 48–59.
[8] M. Veeramohan Rao, B. Shanmugavelu, V.V. Ravi Kanth Kumar, J. Lumin. 181 (2017) 291–298.
[9] S.E. Van Kirk, S.W. Martin, J. Am. Ceram. Soc. 75 (1992) 1028–1031.
[10] J. Fu, H. Yatsuda, Phys. Chem. Glasses 36 (1995) 211–215.
[11] Sk. Mahamuda, K. Swapna, M. Venkateswarlu, A. Srinivasa Rao, Suman Latha Shakya, G. Vijaya Prakash, J. Lumin. 154 (2014) 410–424.
[12] J. Pisarska, L. Zur, T. Goryczka, W.A. Pisarski, J. Rare Earths 29 (2011) 1157–1160.
[13] G. Okada, H. Masai, A. Torimoto, S. Kasap, T. Yanagid, J. Ceram. Process. Res. 17 (2016) 148–151.
[14] J. Zmojda, M. Kochanowicz, P. Miluski, J. Dorosz, J. Pisarska, W.A. Pisarski, D. Dorosz, J. Lumin. 170 (2016) 795–800.
[15] S.Y. Choi, B. Ryu, J. Non-Cryst. Solids 431 (2016) 112–117.
[16] L. Bolundut, L. Pop, M. Bosca, N. Tothazan, G. Borodi, E. Culea, P. Pascuta, R. Stefan, J. Alloys Compd. 692 (2017) 934–940.
[17] A. Wagh, Y. Raviprakash, V. Upadhyaya, S.D. Kamath, Spectrochim. Acta A Mol. Biomol. Spectrosc. 151 (2015) 696–706.
[18] A. Herrera, R.G. Fernandes, A.S.S. Decamargo, A.C. Hernandes, S. Buchner, C. Jacinto, N.M. Balzaretti, J. Lumin. 171 (2016) 106–111.
[19] P. Chimalawong, J. Kaewkhao, C. Kedkaew, P. Limsuwan, J. Phys. Chem. Solids 71 (2010) 965–970.
[20] M. Mariyappan, S. Arunkumar, K. Marimuthu, J. Mol. Struct. 1105 (2016) 214–224.
[21] A. Agarwal, I. Pal, S. Sanghi, M.P. Aggarwal, Opt. Mater. 32 (2009) 339–344.
[22] R. Rolli, K. Gatterer, M. Wachtler, M. Bettinelli, A. Speghini, D. Ajò, Spectrochim. Acta A Mol. Biomol. Spectrosc. 57 (2001) 2009–2017.
[23] Sunil Thomas, Sk. Nayab Rasool, M. Rathaiah, V. Venkatramu, Cyriac Joseph, N.V. Unnikrishnan, J. Non-Cryst. Solids 376 (2013) 106–116.
[24] I. Pal, A. Agarwal, S. Sanghi, M.P. Aggarwal, Spectrochim. Acta A 101 (2013) 74–81.
[25] J.A. Duffy, M.D. Ingram, J. Inorg, Nucl. Chem. 37 (1975) 1203–1206.
[26] C.H. Kam, S. Buddhudu, J. Quant. Spectrosc. Radiat. Transf. 87 (2004) 325–337.
[27] L. Pauling, The Nature of Chemical Bond, third ed., Cornell University Press, New York, 1960, p. 93.
[28] M. Abdel-Baki, F. El-Diasty, F.A. Abdel Wahab, Opt. Commun. 261 (2006) 65–70.
[29] I.I. Kindrat, B.V. Padlyak, A. Drzewiecki, J. Lumin. 166 (2015) 264–275.
[30] V. Thomas, R.G.S. Sofin, M. Allen, H. Thomas, P.R. Biju, G. Jose, N.V. Unnikrishnan, Spectrochim. Acta A 171 (2017) 144–148.
[31] K. Swapna, Sk. Mahamuda, A. Srinivasa Rao, S. Shakya, T. Sasikala, D. Haranath, G. Vijaya Prakash, Spectrochim. Acta A 125 (2014) 53–60.
[32] S. Arunkumar, K. Marimuthu, J. Alloys Compd. 565 (2013) 104–114.
[33] C.K. Jayasankar, E. Rukmini, Opt. Mater. 8 (1997) 193–205.
[34] Y.K. Sharma, S.S.L. Surana, R.K. Singh, J. Rare Earths 27 (2009) 773–780.
[35] K. Wang, J. Zhang, J. Wang, W. Yu, H. Zhang, Z. Wang, Z. Shao, Mater. Res. Bull. 41 (2006) 1695–1700.
[36] S.P. Sinha, Complexes of the Rare Earths, Pergamon Press, Oxford, 1966, pp. 89–96.
[37] W.T. Carnall, P.R. Fields, K. Rajnak, J. Chem. Phys. 49 (1968) 4450–4455.
[38] N.F. Mott, E.A. Davis, Electronic Processes in Non-Cryst. Mater, Second ed., Clarendon Press, Oxford, 1979, pp. 272–300.
[39] J. Tauc, Amorphous and Liquid Semiconductor, Plenum Press, NY, 1974.
[40] B. Judd, Phys. Rev. 127 (1962) 750–761.
[41] G. Ofelt, J. Chem. Phys. 37 (1962) 511–520.
[42] C.K. Jorgensen, R. Reisfeld, Judd-Ofelt parameters and chemical bonding, J. Less Common Met. 93 (1983) 107–112.
[43] D. Rajeswara Rao, G. Sahaya Baskaran, P. Ramesh Babu, Y. Gandhi, N. Veeraiah, J. Mol. Struct. 1073 (2014) 164–173.

[44] Y.N.Ch. Ravi Babu, P. Sreeram Naik, K. Vijaya Kumar, N. Rajesh Kumar, A. Suresh Kumar, J. Quant. Spectrosc. Radiat. Transf. 113 (2012) 1669–1675.

[45] B.C. Jamalaiah, M.V. Vijaya Kumar, K. Rama Gopal, Opt. Mater. 33 (2011) 1643–1647.

[46] Ki-Soo Lim, N. Vijaya, C.R. Kesavulu, C.K. Jayasankar, Opt. Mater. 35 (2013) 1557–1563.

[47] Sd. Zulfiqar Ali Ahamed, C. Madhukar Rddy, B. Deva Prasad Raju, Spectrochim. Acta A 103 (2013) 246–254.

[48] S. Bhardwaj, R. Shukla, S. Sanghi, A. Agarwal, I. Pal, Spectrochim. Acta A 117 (2014) 191–197.

[49] D. Rajesh, A. Balakrishna, Y.C. Ratnakaram, Opt. Mater. 35 (2012) 108–116.

[50] A.G.S. Filho, J.M. Filho, F.E.A. Melo, M.C.C. Custódio, R. Lebullenger, A.C. Hernandes, J. Phys. Chem. Solids 61 (2000) 1535–1542.

[51] D. Umamaheswari, B.C. Jamalaiah, T. Sasikala, Il-Gon Kim, L. Rama Moorthy, J. Non-Cryst. Solids 358 (2012) 782–787.

[52] G. Tripathi, V.K. Rai, S.B. Rai, Appl. Phys. B Lasers Opt. 84 (2006) 459–464.

[53] C.K. Jayasankar, P. Babu, J. Alloys Compd. 307 (2000) 82–95.

[54] I.A. Rayappan, K. Selvaraju, K. Marimuthu, Physica B 406 (2011) 548–555.

[55] Marcin Sobczyk, Damian Szymanski, J. Lumin. 142 (2013) 96–102.

[56] C.R. Kesavulu, H.J. Kim, S.W. Lee, J. Kaewkhao, N. Wantana, S. Kothan, S. Kaewjaeng, J. Non-Cryst. Solids 474 (2017) 50–57.

[57] P. Raghava Rao, G. Murali Krishna, M.G. Brik, Y. Gandhi, N. Veeraiah, J. Lumin. 131 (2011) 212.

[58] C.R. Kesavulu, C.K. Jayasankar, J. Lumin. 132 (2012) 2802–2809.

[59] M. Inokuti, F. Hirayama, J. Chem. Phys. 43 (1965) 1978–1989.

[60] C.R. Kesavulu, C.K. Jayasankar, Mater. Chem. Phys. 130 (2011) 1078–1085.

[61] Ch. Basavapoornima, C.K. Jayasankar, J. Lumin. 153 (2014) 233–241.

[62] E. Malchukova, B. Boizot, D. Ghaleb, G. Petite, Nucl. Instrum. Methods Phys. Res. 537 (2005) 411–414.

[63] F. Vetrone, J.C. Boyer, J.A. Capobianco, A. Sepghini, M. Bettinelli, Appl. Phys. Lett. 80 (2002) 1752–1754.

[64] P.R. Biju, G. Jose, V. Thomas, V.P.N. Nampoori, N.V. Unnikrishnan, Opt. Mater. 24 (2004) 671–677.

[65] S. Schweizer, L.W. Hobbs, M. Secu, J.M. Spaeth, A. Edgar, G.V.M. Williams, Appl. Phys. Lett. 83 (2003) 449–451.

[66] W.M. Yen, S. Shionoya, Phosphors, Hand Book, CRC Press, New York, 1999, pp. 805–809.

Near-infrared and upconversion luminescence of Tm^{3+} and Tm^{3+}/Yb^{3+}-doped oxyfluorosilicate glasses

C.S. Dwaraka Viswanath[a], P. Babu[b], I.R. Martín[c], V. Venkatramu[d], V. Lavín[c], C.K. Jayasankar[a],*

[a] Department of Physics, Sri Venkateswara University, Tirupati 517 502, India
[b] Department of Physics, SVCR Government Degree College, Palamaner 517 408, India
[c] Department of Physics, MALTA-Consolider Team, IMN, and IUdEA, Universidad de la Laguna, Apdo. 456, E-38200 San Cristóbal de La Laguna, Santa Cruz de Tenerife, Spain
[d] Department of Physics, Yogi Vemana University, Kadapa 516 005, India

ABSTRACT

Oxyfluorosilicate glasses-doped with different concentrations of Tm^{3+} and Tm^{3+}/Yb^{3+} ions have been synthesized and characterized their absorption, photoluminescence, luminescence decay and upconversion properties. The Judd-Ofelt intensity parameters have been obtained from the absorption spectrum of Tm^{3+} single-doped glass and are in turn used to calculate radiative properties such as transition probabilities, branching ratios and lifetimes for the fluorescent levels of Tm^{3+} ions. Visible and near-infrared emission spectra of Tm^{3+} and Tm^{3+}/Yb^{3+}-doped glasses have been measured under 473 nm laser excitation. The quenching of emission intensities at higher concentrations of Tm^{3+} ions has been found to be due to cross-relaxation mechanisms. The Tm^{3+}/Yb^{3+} co-doped glasses show upconverted emissions under 975 nm laser excitation. The mechanism of upconversion has been explained based on the pump power dependence of upconversion luminescence. The results reveal that the co-doped glasses are promising for optical fiber amplifiers operating at the relatively low-loss wavelength regions.

1. Introduction

In recent years, researchers focused on oxyfluoride glasses due to their combined advantages of both oxide and fluoride matrices having high stability and low phonon energies, respectively [1–3]. Oxyfluoride glasses doped with trivalent rare-earth (RE^{3+}) ions exhibit attractive luminescence properties, with high transparency, and are found to be potential materials for upconversion luminescence and optical amplification [4–8]. Trivalent thulium (Tm^{3+}) is one of the most attractive RE^{3+} ions that gives visible and infrared luminescence in glasses. Particularly, 1.2 μm emission corresponding to the $^1G_4 \rightarrow {}^3H_4$ transition of Tm^{3+} ions is useful for optical fiber amplifiers [9].

Spectroscopic investigations on Tm^{3+}-doped glass systems that include silicate [1,5,10–12], bismuth silicate [13], phosphorous silicate [14], fluorophosphate [15–17], metaphosphate [18], borate [19], fluoroborate [20,21], lead borate [3], phosphate [22–24], borophosphate [25], fluoroindate [26], tellurite [27–30], bismuthate [31], fluorozirconate [32], gallate-bismuth-lead [33], heavy metals [34] and germinate [25,35–37] have been reported. Because of simple energy level scheme, long lifetime and large absorption and emission cross-

sections, ytterbium (Yb^{3+}) is used as a sensitizer in RE^{3+}-doped glasses, and co-doping of Tm^{3+} with Yb^{3+} significantly enhances the emission intensities of Tm^{3+} ion [9]. Recently, Tm^{3+}/Yb^{3+} co-doped glass systems that include phosphate [38], fluorophosphate [9,39], fluoride, gallate, aluminate, germinate [39], silicate [39,40], tellurite [41,42], leadfluoroborate [43] and fluorozirconate [44] have been reported. It is worth noting that there are only a few reports on the 1.2 μm emission in Tm^{3+} and Tm^{3+}/Yb^{3+} co-doped oxyfluorosilicate glasses.

The concentration of hydroxyl (OH^-) impurities to an acceptable level in silica fibers has been optimized to minimize the losses (~ 0.5 dB/km) at around 1.2 μm wavelength region [45]. However, not much attention has been paid for the study of emission/amplification at ~1.2 μm wavelength region. Ytterbium fiber laser pumped Raman fiber laser is a powerful method to generate ~1.2 μm laser action, but it is not a broad band light source and requires a very long fiber Raman cavity [27,46].

From the energy level diagram, Tm^{3+} ion has got two metastable excited states, $^1D_2$ and $^1G_4$, which emits blue emission either from their normal emission or by upconversion processes [3]. The latter processes involves the conversion of near-infrared (NIR) light into visible one

---

* Corresponding author.
  E-mail address: ckjaya@yahoo.com (C.K. Jayasankar).

which attracts much attention, in recent times, in the design of optical devices. In optical telecommunications, the RE^{3+}-doped fiber amplifiers are playing a vital role [15,41]. Silicate hosts are very interesting because it is easier to integrate into existing silica fiber networks with low transmission loss. Further, silicate glasses are chemically and mechanically stable and can be fabricated from bulk (rod) to a miniature (fiber) size [6,11,47]. In addition, oxyfluoride glasses possess combined advantages of oxide as well as fluoride glasses like low phonon energy, excellent chemical durability and high mechanical strength. Recently, Zhou et al. [27,46] demonstrated the optical amplification at around 1.2 μm based on Tm^{3+}: $^{1}G_4 \rightarrow {}^{3}H_4$ emission in tellurite and gallo-germanate glasses.

The present work reports the absorption and emission spectra, as well as lifetimes of the emitting levels, of Tm^{3+} ions in single and Tm^{3+}/Yb^{3+} co-doped oxyfluorosilicate glasses, including the fluorescence characteristics of 1.2 and 1.6 μm emissions. Upconversion luminescence properties of Tm^{3+}/Yb^{3+} co-doped oxyfluorosilicate glasses with 0.1 mol% of Tm^{3+} and 0.1, 0.5, 1.0 and 2.0 mol% of Yb^{3+} have also been studied.

2. Experimental details

Oxyfluorosilicate glasses with the composition (in mol%) of 41 SiO$_2$ + 10 Al$_2$O$_3$ + (26-x) LiF + 23 SrF$_2$ + x Tm$_2$O$_3$ (x = 0.01, 0.05, 0.1, 0.5 and 1.0, denoted as SALSTmx) and 41 SiO$_2$ + 10 Al$_2$O$_3$ + (25.9-x) LiF + 23 SrF$_2$ + 0.1 Tm$_2$O$_3$ + x Yb$_2$O$_3$ (x = 0.1, 0.5, 1.0 and 2.0, denoted as SALSTm0.1Ybx) were prepared by the conventional melt quenching technique. Batches of 25 g chemicals were well-mixed in an agate mortar and melted in platinum rhodium crucible with lid at 1450 °C (1723 K) for 2 h. Then the glass melt was poured on to a preheated brass mold and annealed at 450 °C (723 K) for 18 h and then cooled down to room temperature to remove thermal stress and strain. After cutting, grinding and polishing, these glass samples were used for optical characterization. Densities of the prepared glasses were measured by the Archimedes method using distilled water as an immersion liquid. Refractive indices were measured using an Abbe-refractometer using 1-bromonapthalene as contact liquid. Absorption spectra in UV–visible-NIR region were measured using a spectrophotometer (Cary 5000). Visible and NIR emission spectra were obtained by exciting at 473 nm using diode pumped solid-state laser and analyzing the emission with a 500 mm focal length spectrograph (Andor Shamrock 500i) equipped with intensified CCDs and InGaAs cameras. Decay curves for the $^{1}G_4$ and $^{3}H_4$ levels were measured by exciting at 473 and 776 nm laser, respectively, using optical parametric oscillator (EKSPLA/NT342/3/UVE) and the signal was detected with the help of a digital oscilloscope (Tekronix 2430). All measurements were done at room temperature and were corrected from instrument responses.

For computation of errors, all the above experiments are measured three times and are used to compute mean and standard deviation (σ) using the expression,

$$(\sigma) = \sqrt{\frac{\sum (x - y)^2}{N}} \tag{1}$$

where x is the actual measurement reading, y is the mean reading and N is the number of measurements.

3. Results and discussion

3.1. Optical absorption spectra and Judd-Ofelt theory

The absorption spectra of SALSTm1.0 and SALSTm0.1Yb0.1 glasses, shown in Fig. 1, were measured in the wavelength range of 340–2000 nm. As can be seen, the absorption peaks at 356, 465, 658, 683, 790, 1210 and 1643 nm correspond to the transitions from $^{3}H_6$

ground level of Tm^{3+} to the $^{1}D_2$, $^{1}G_4$, $^{3}F_2$, $^{3}F_3$, $^{3}H_4$, $^{3}H_5$ and $^{3}F_4$ excited levels, respectively. The absorption peak at 1210 nm corresponds to the $^{3}H_6 \rightarrow {}^{3}H_5$ transition shows both electric and magnetic-dipole contributions, whereas the other transitions show the electric-dipole contribution only. The $^{3}H_6 \rightarrow {}^{3}F_4$ transition is said to be hypersensitive in nature [3], as it is very sensitive to changes in the local environment of the optically active ion, i.e. it obeys the selection rules: $|\Delta S| = 0$, $|\Delta L| \leq 2$, and $|\Delta J| \leq 2$. In addition, the intense band at 976 nm, observed in Tm^{3+}/Yb^{3+} co-doped glass, belongs to the absorption of Yb^{3+} ions from the $^{2}F_{7/2}$ ground state to the $^{2}F_{5/2}$ excited state. The Judd-Ofelt (JO) theory [48,49] has been widely used to predict the spectroscopic properties of RE^{3+} ions. The JO intensity parameters have been obtained from the absorption spectrum of 1.0 mol% Tm$_2$O$_3$-doped glass. The experimental oscillator strengths, f_{exp}, of all the absorption bands of Tm^{3+} are determined using the Smakula formula [50]. These f_{exp} values are in turn used to evaluate the JO intensity parameters (Ω_2, Ω_4, Ω_6) by a least-square fitting method [20]. The expressions used for the calculation of JO parameters and other radiative properties are given below [18,20,48,49].

The oscillator strength of an absorption transition (f_{exp}) is directly proportional to the area under the absorption curve and is expressed as

$$f_{exp} = 4.32 \times 10^{-9} \int \varepsilon(\upsilon) d\upsilon \tag{2}$$

where $\varepsilon(\upsilon)$ is the molar absorptivity of a band at a wave number υ (cm^{-1}).

According to JO theory, the calculated oscillator strength for the absorption band corresponding to the electronic transition from the ground state, ΨJ, (assumed that all the crystal-field levels of the ground state are equally populated) to an excited state, $\Psi' J'$, is given by

$$f_{cal} = \frac{8\pi^2 mc\upsilon}{3h(2J+1)} \frac{(n^2+2)^2}{9n} \sum_{\lambda=2,4,6} \Omega_{\lambda}(\Psi J \, \|U^{\lambda}\| \, \Psi' J')^2 \tag{3}$$

where 'm' is the mass of the electron, 'c' is the speed of light in vacuum, 'υ' is the wavenumber (cm^{-1}) associated with the transition, 'h' is the Planck's constant, 'n' is the refractive index of the host lattice, $\frac{(n^2+2)^2}{9n}$ is the local field correction for the effective field induced by the host lattice, 'J' is the total angular momentum of the ground state, Ω_2, Ω_4 and Ω_6 are called JO intensity parameters and $\|U^{(\lambda)}\|^2$ are the squared doubly reduced matrix elements evaluated from the intermediate coupling approximation for a transition, $\Psi J \rightarrow \Psi' J'$. The oscillator strengths of the various observed transitions are evaluated through Eq. (2) and are used in Eq. (2). A least-square fitting approximation is then used for Eq. (3) to determine Ω_{λ} ($\lambda = 2, 4$ and 6) parameters, which give the best fit between experimental and calculated oscillator strengths. The theoretical oscillator strengths (f_{cal}) are then determined using Ω_{λ} and Eq. (2).

The radiative transition probability (A) for a transition $\Psi J \rightarrow \Psi' J'$ can be expressed by

$$A(\Psi J, \Psi' J') = \frac{64\pi^4 \upsilon^3}{3h(2J+1)} \frac{n(n^2+2)^2}{9} S_{ed} + \frac{64\pi^4 \upsilon^3}{3h(2J+1)} n^3 S_{md} \tag{4}$$

where, S_{ed} and S_{md} represents the electric-dipole and magnetic-dipole linestrengths, respectively between the ground state and particular excited state. For electric-dipole transitions,

$$S_{ed} = e^2 \sum_{\lambda=2,4,6} \Omega_{\lambda}(\Psi J \, \|U^{\lambda}\| \, \Psi' J')^2 \tag{5}$$

For magnetic-dipole transitions,

$$S_{md} = \frac{e^2 h^2}{16\pi^2 m^2 c^2}(\Psi J \, \|L + 2S\| \, \Psi' J')^2 \tag{6}$$

The total radiative transition probability (A_T) for an excited state is the sum of the $A(\Psi J, \Psi' J')$ terms calculated over all the terminal states

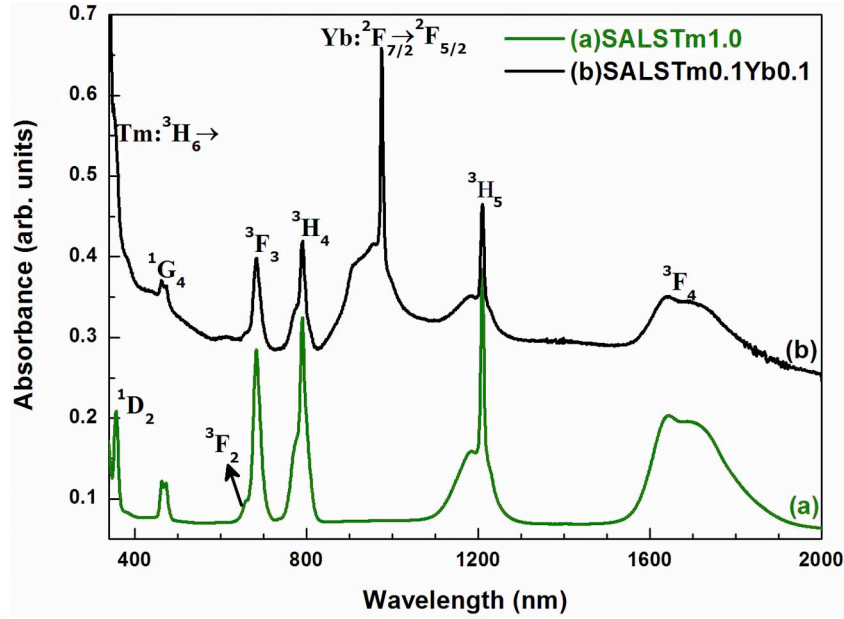$$A_T(\Psi J) = \sum A(\Psi J, \Psi' J') \tag{7}$$

Fig. 1. Absorption spectra of (i) SALSTm1.0 and (ii) SALSTm0.1Yb0.1 glasses in UV- visible-NIR regions.

A_T is related to the radiative lifetime (τ_R) of an excited state by

$$\tau_{rad}(\Psi J) = \frac{1}{A_T(\Psi J)} \quad (8)$$

The branching ratio (β_R) corresponding to the emission from an excited $\Psi' J'$ level to its lower level ΨJ is given by

$$\beta_R(\Psi J, \Psi' J') = \frac{A(\Psi J, \Psi' J')}{A_T(\Psi J)} \quad (9)$$

The peak stimulated emission cross-section, $\sigma(\lambda_p)$ ($\Psi J, \Psi' J'$), between the states ΨJ and $\Psi' J'$ having a probability of $A(\Psi J, \Psi' J')$ can be expressed as

$$\sigma(\lambda_p)(\Psi J, \Psi' J') = \frac{\lambda_p^4}{8\pi c n^2 \Delta\lambda_{eff}} A(\Psi J, \Psi' J') \quad (10)$$

where λ_p is the transition peak wavelength and $\Delta\lambda_{eff}$ is its effective linewidth found by dividing the area of the emission band by its average height.

The Ω_λ values thus obtained are used to calculate the theoretical oscillator strengths f_{cal} of the absorption transitions of Tm^{3+} ion. The f_{exp} and f_{cal} values of absorption transitions in SALSTm1.0 glass along with reported f_{exp} values for SBZT10 [14], NBWT10 [15], PKBAT10 [18], PBAWTm [19], BZL [20] and AT$_{10}$ [47] glasses are presented in Table 1. Smaller root-mean-square deviation, ($\pm 0.51 \times 10^{-6}$), for the

SALSTm1.0 glass indicates the good fit between experimental and calculated oscillator strengths. The evaluated JO parameters ($\times 10^{-20}$ cm^2) are $\Omega_2 = 5.55$, $\Omega_4 = 2.95$ and $\Omega_6 = 2.20$. The larger value of Ω_2 suggests more asymmetry at the Tm^{3+} ion site and the larger Tm-O covalence in the SALSTm1.0 glass. The lower value of Ω_6 indicates the higher rigidity of SALSTm1.0 glass matrix. The JO intensity parameters and their trends in different Tm^{3+}-doped glasses that include TS3 [1], STE [2], SPL and SPS [10], NBWT10 [15], PBAWTm [19], TPBL [27], TWTm [28], ZBLANTm [32], SLNS [39] and GeBL [46], are compared in Table 2. As can be seen, the JO parameters of the present glass systems are comparable to those of reported Tm^{3+}:glass systems.

The JO parameters are in turn used to determine radiative properties, such as radiative transition probabilities A, branching ratios β_R, and radiative lifetimes τ_R of the excited states of Tm^{3+} ions in SALSTm glasses under study, and are listed in Table 3. As can be seen, the spontaneous emission probability of the 1.2 µm emission (Tm^{3+}:$^1G_4 \rightarrow$ $^3H_4$) is high (206 s^{-1}), indicating its largest intensity.

The τ_R values for various excited emitting levels ($^1D_2$, $^1G_4$, $^3H_4$, and $^3F_4$) in SALSTm1.0 glass is presented in Table 4, along with those of other reported glass systems. As can be seen, τ_R value for the $^1G_4$ level in present glass is close to PKBAT [18], higher than that of NBWT10 [15], PBAWTm [19], BZL [20], TWTm [28], TNZLTm [29] and PBATm [38], and smaller than ZBLANTm [32] and SCBLTm [40] glass systems.

Table 1
Transition energies (λ, nm), experimental (f_{exp}) and calculated (f_{cal}) oscillator strengths ($\pm 5\%$, $\times 10^{-6}$) for SALSTm1.0 glass and f_{exp} for some reported Tm^{3+}-doped glasses.

Transition			λ(nm)	SALSTm1.0 [Present work]		f_{exp}					
				f_{exp}	f_{cal}	ZnTm [14]	NBWT10 [15]	PKBAT [18]	PBAWTm [19]	BZL [20]	AT$_{10}$ [47]
$^3H_6$	$\rightarrow$	$^1D_2$	356	3.34	3.81	0.41	–	2.13	–	1.91	–
		$^1G_4$	465	1.67	1.33	0.49	0.84	0.96	0.52	0.70	0.99
		$^3F_2$	658	0.52	1.04	0.13	–	0.20	–	1.48	–
		$^3F_3$	683	4.34	4.89	0.96	2.44[a]	1.56	4.32[a]	7.88	7.43[a]
		$^3H_4$	790	4.00	4.48	1.52	2.78	2.28	3.13	7.09	8.22
		$^3H_5$	1210	3.51	2.66	0.45	1.65	2.00	2.09	4.50	3.91
		$^3F_4$	1643	4.09	4.12	1.21	2.28	3.03	2.24	5.62	3.68

[a] The sum of oscillator strengths for $^3F_{2,3}$ transitions.

Table 2

Comparison of Judd-Ofelt intensity parameters (Ω_2, Ω_4 and Ω_6 $\pm$ 5%, $\times 10^{-20}$ cm^2) and their trends in Tm^{3+}-doped glasses.

Glasses	$\times 10\Omega_2$	Ω_4	Ω_6	Trend
SALSTm1.0 [Present work]	5.57	2.94	2.21	$\Omega_2 > \Omega_4 > \Omega_6$
TS3 [1]	3.08	0.99	0.40	$\Omega_2 > \Omega_4 > \Omega_6$
STE [2]	3.25	1.22	0.38	$\Omega_2 > \Omega_4 > \Omega_6$
SPS [10]	3.60	0.79	0.78	$\Omega_2 > \Omega_4 > \Omega_6$
SPL [10]	3.03	0.92	0.79	$\Omega_2 > \Omega_4 > \Omega_6$
NBWT10 [15]	5.28	2.32	1.16	$\Omega_2 > \Omega_4 > \Omega_6$
PBAWTm [19]	2.93	0.58	1.60	$\Omega_2 > \Omega_6 > \Omega_4$
TPBL [27]	4.72	1.35	1.21	$\Omega_2 > \Omega_4 > \Omega_6$
TWTm [28]	6.8	2.0	2.2	$\Omega_2 > \Omega_6 > \Omega_4$
ZBLANTm [32]	2.57	1.90	0.84	$\Omega_2 > \Omega_4 > \Omega_6$
SLNS [39]	3.26	1.20	0.46	$\Omega_2 > \Omega_4 > \Omega_6$
GeBL [46]	4.65	1.51	1.42	$\Omega_2 > \Omega_4 > \Omega_6$

Table 3

Emission transitions, energies ($\nu \pm 2$, cm^{-1}), predicted radiative transition probabilities (A $\pm$ 2, s^{-1}), branching ratios ($\beta_R \pm 2\%$) and lifetimes (τ_R, μs) for the excited levels of SALSTm1.0 glass.

Transition			ν	A	β_R	τ_R
$^1D_2$	$\rightarrow$	$^1G_4$	6689	159	0.0068	42
		$^3F_2$	12,859	885	0.0379	
		$^3F_3$	13,455	888	0.0380	
		$^3H_4$	15,401	1462	0.0626	
		$^3H_5$	19,760	125	0.0054	
		$^3F_4$	22,183	11,990	0.5137	
		$^3H_6$	28,011	7833	0.3356	
$^1G_4$	$\rightarrow$	$^3F_2$	6170	12	0.0061	501
		$^3F_3$	6766	54	0.0272	
		$^3H_4$	8712	206	0.1030	
		$^3H_5$	13,071	668	0.3347	
		$^3F_4$	15,494	164	0.0821	
		$^3H_6$	21,322	892	0.4469	
$^3F_2$	$\rightarrow$	$^3F_3$	596	0	0	726
		$^3H_4$	2542	13	0.0093	
		$^3H_5$	6901	228	0.1653	
		$^3F_4$	9324	505	0.3669	
		$^3H_6$	15,152	632	0.4586	
$^3F_3$	$\rightarrow$	$^3H_4$	1946	4	0.0016	425
		$^3H_5$	6305	262	0.1117	
		$^3F_4$	8728	88	0.0377	
		$^3H_6$	14,556	1994	0.8489	
$^3H_4$	$\rightarrow$	$^3H_5$	4359	23	0.0207	885
		$^3F_4$	6782	96	0.0850	
		$^3H_6$	12,610	1010	0.8943	
$^3H_5$	$\rightarrow$	$^3F_4$	2423	6	0.0278	4356
		$^3H_6$	8251	223	0.9722	
$^3F_4$	$\rightarrow$	$^3H_6$	5828	208	1.0000	4814

Table 4

Predicted radiative lifetimes (τ_R, μs) for various transitions ($^1D_2$, $^1G_4$, $^3H_4$ and $^3F_4$) in SALSTm1.0 glass along with those of reported Tm^{3+}-doped glasses.

Glass	$^1D_2$	$^1G_4$	$^3H_4$	$^3F_4$
SALSTm1.0 [present work]	42	501	885	4814
NBWT10 [15]	34	454	642	4028
PKBAT [18]	36	515	932	4168
PBAWTm [19]	31	293	497	3636
BZL [20]	20	200	351	2078
TWTm [28]	–	144	966	185
TZNLTm [29]	–	164	316	1727
ZBLANTm [32]	56	774	1310	6020
PBATm [38]	29	430	882	906
SCBLTm [40]	–	570	980	4990
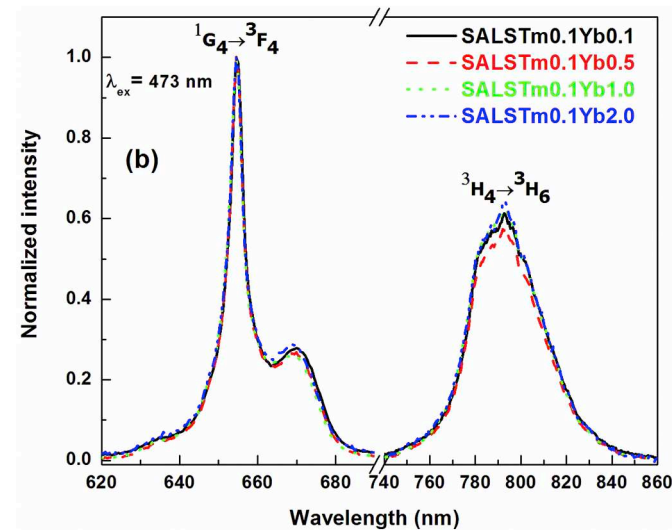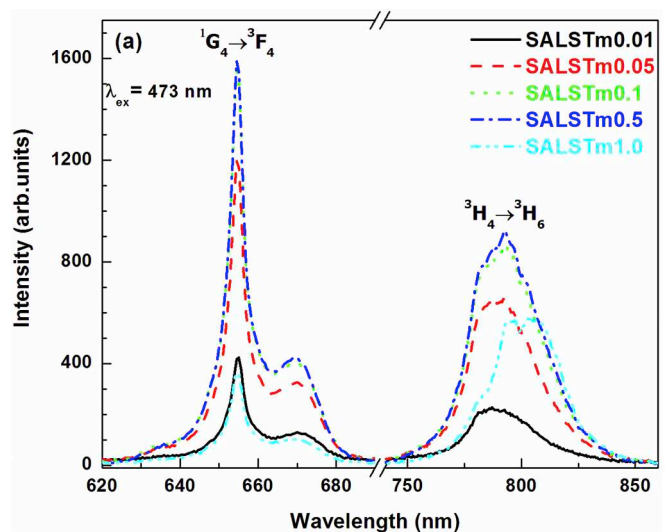
Fig. 2. Visible emission spectra of (a) Tm^{3+}-doped and (b) Tm^{3+}/Yb^{3+} co-doped SALS glasses under 473 nm laser excitation.

Higher τ_R value of a given level indicates its lower spontaneous emission probability and higher stimulated emission probability under suitable conditions. Hence, higher τ_R value of $^1G_4$ level in SALSTm1.0 glass compared to those of most of the compared systems indicates its higher stimulated emission probability.

3.2. Visible and near-infrared spectra

The visible emission spectra, shown in Figs. 2 (a) and (b) in the wavelength range of 600–900 nm, are measured under the 473 nm laser excitation for the Tm^{3+} and Tm^{3+}/Yb^{3+} co-doped SALS glasses with different concentrations of optically active ions. Fig. 3 shows the partial energy level diagram of Tm^{3+} and Yb^{3+} in SALS glass along with excitation, de-excitation and cross-relaxation channels.

Emission spectra consist of two intense bands at around 650 and 790 nm corresponding to the $^1G_4 \rightarrow {}^3F_4$ and $^3H_4 \rightarrow {}^3H_6$ transitions, respectively. As can be seen, in Tm^{3+} single doped glasses, with increase in Tm^{3+} ions concentration from 0.01 to 0.5 mol%, intensities of both ~650 and ~790 nm emissions follow the same increasing trend but for 1.0 mol% doped glass, they decrease non-uniformly. The ~650 nm emission decreases below that of 0.01 mol% doped one and ~790 nm
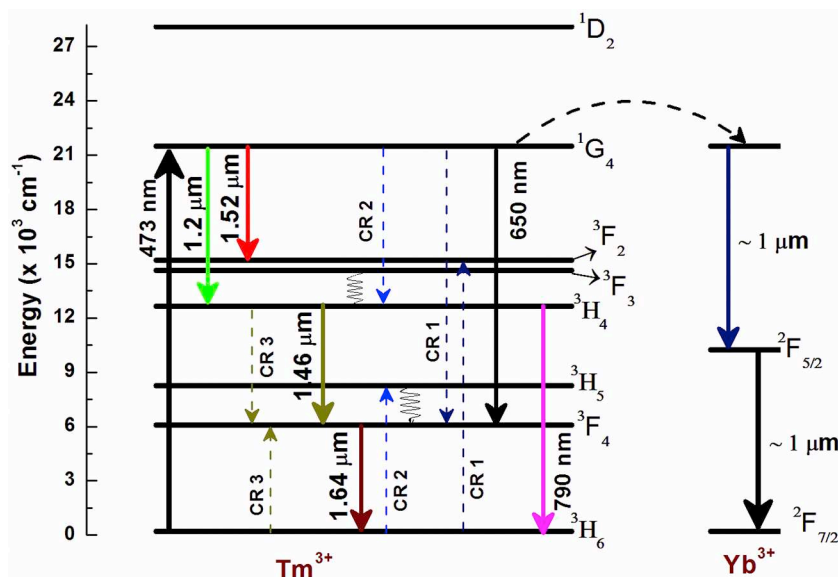
Fig. 3. Partial energy level diagram of Tm^{3+} and Yb^{3+} ions showing transitions of excitation, emission and cross-relaxation channels.
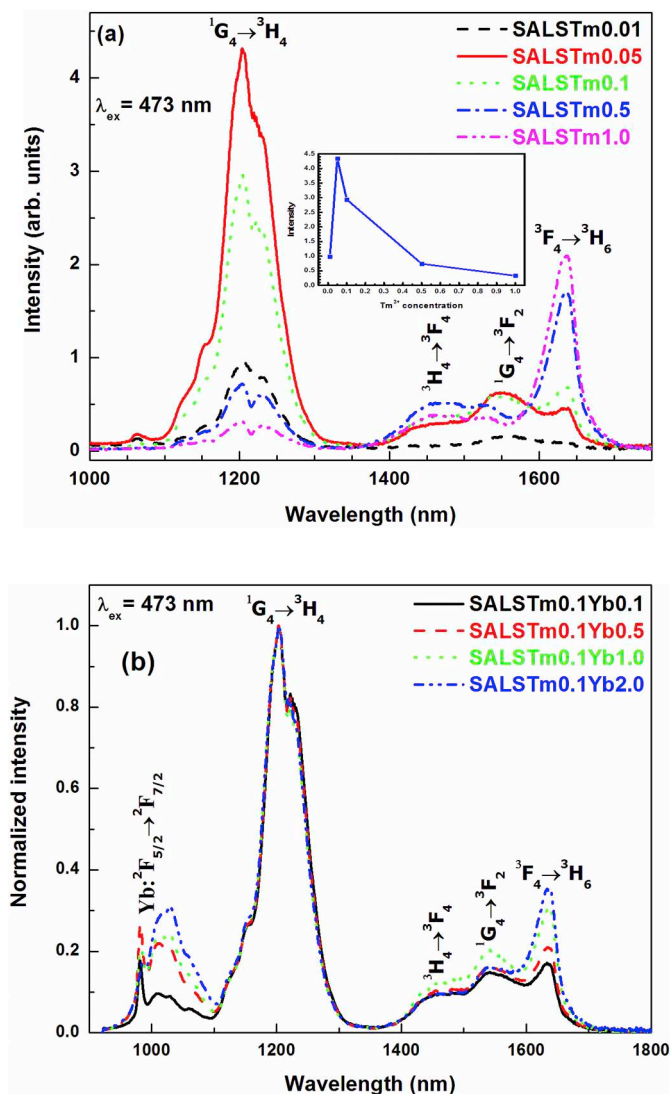

Fig. 4. NIR emission spectra of (a) Tm^{3+}-doped and (b) Tm^{3+}/Yb^{3+} co-doped SALS glasses under 473 nm laser excitation. The inset of the Fig. 4 (a) shows the variation of 1.2 μm emission intensity with Tm^{3+} ions concentration.

emission is > 0.01 mol% doped one but < 0.05 mol% doped glass with slight red shift in band position compared to those of other concentrations. The increase in intensities of the emissions with Tm^{3+} ions concentration up to 0.5 mol% can be explained as due to availability of more ions in the ground state for pumping to excited state. But when the Tm^{3+} ions concentration reaches 1.0 mol%, cross-relaxation energy transfer processes CR1 ($^1G_4, ^3H_6 \rightarrow ^3F_4, ^3F_2$), CR2 ($^1G_4, ^3H_6 \rightarrow ^3H_4, ^3H_5$) and CR3 ($^3H_4, ^3H_6 \rightarrow ^3F_4, ^3F_4$), shown in Fig. 3, becomes dominant resulting in reduced and non-uniform emissions at 650 and 790 nm. The CR1 channel populates the $^3F_2$ and $^3F_3$ thermalized levels, which in turn populates the $^3H_4$ multiplet through multiphonon relaxation and CR2 directly populates $^3H_4$ level causing increase in the intensity of 790 nm emission. This is also evident from the lowest intensity of the $^1G_4 \rightarrow ^3H_4$ transition at 1.0 mol% Tm^{3+} concentration [see Fig. 4(a)], as it will be discussed later. But CR3 process depopulates the $^3H_4$ level and populates the $^3F_4$ level causing reduced emission at 790 nm. Energy migration among Tm^{3+} ions and then transfer to traps may also be the reason for overall reduction of emissions of SALSTm1.0 glass. The visible emission spectra of Tm^{3+}/Yb^{3+} co-doped glasses, under 473 nm excitation, is shown in Fig. 2(b) and are normalized to the maximum intensity of the $^1G_4 \rightarrow ^3F_4$ transition. As can be seen, the intensity of the $^3H_4 \rightarrow ^3H_6$ transition undergoes only marginal changes with increase in Yb^{3+} ions concentration which could be due to small variations in energy transfer processes between Tm^{3+} and Yb^{3+} ions.

The NIR emission spectra of Tm^{3+} and Tm^{3+}/Yb^{3+} — doped oxy-fluorosilicate glasses with different concentrations of active ions are measured under 473 nm laser excitation and are shown in Figs. 4 (a) and (b), respectively. As can be seen from Fig. 4 (a), there is a broad and intense emission at 1.2 μm associated with the $^1G_4 \rightarrow ^3H_4$ transition of the Tm^{3+} ion. The intensity of this emission first increases significantly from 0.01 to 0.05 mol% of Tm_2O_3 and then decreases monotonically up to 1.0 mol% Tm_2O_3. The initial increase in intensity is due to availability of more number of Tm^{3+} ions for excitation in to the $^1G_4$ emitting level. The decreasing of intensity of the 1.2 μm emission band at higher Tm^{3+} ion concentrations is attributed to increase in the strength of cross-relaxation CR1 ($^1G_4, ^3H_6 \rightarrow ^3F_4, ^3F_2$), and CR2 ($^1G_4, ^3H_6 \rightarrow ^3H_4, ^3H_5$) energy transfer channels (see Fig. 3). The CR energy transfer processes increase with Tm^{3+} ions concentration and lead to the depopulation of the $^1G_4$ level of Tm^{3+} ions. Zhou et al. also observed similar result of decreasing intensity of the 1.2 μm emission with increase in Tm^{3+} ions concentration in tellurite glasses [27].

In the NIR spectra shown in Fig. 4(a), there are three more

overlapped bands at around 1.46, 1.52 and 1.64 μm regions, assigned to the $^3H_4 \rightarrow {}^3F_4$, $^1G_4 \rightarrow {}^3F_2$ and $^3F_4 \rightarrow {}^3H_6$ transitions, respectively [27]. With increase in Tm^{3+} ions concentration, the 1.64 μm emission increases monotonically from 0.01 to 1.0 mol% which is clear evidence for increase in CR process with increase in Tm^{3+} concentration as all of them are populating the $^3F_4$ level. The variation of 1.52 μm emission is similar to that of 1.2 μm emission as they are from the same emitting level. The 1.46 μm emission follows the same trend as that of 1.64 μm up to 0.5 mol% of Tm^{3+} ions concentration and then decreases for 1.0 mol% of Tm^{3+} ions. This decrease could be due to activation of the CR3 ($^3H_4, {}^3H_6 \rightarrow {}^3F_4, {}^3F_4$) channel [39].

To understand the energy transfer process from Tm^{3+} to Yb^{3+} ions in co-doped glasses, emission spectra are measured, exciting at 473 nm, in the range of 925–1750 nm and are shown in Fig. 4(b). The spectra are normalized to the maximum of the 1.2 μm emission. As can be seen, there are emission bands at around 1 μm corresponding to Yb^{3+} ions emission ($^2F_{5/2} \rightarrow {}^2F_{7/2}$) and their intensities increases continuously with increase in Yb^{3+} ions concentration. The only source of Yb^{3+} ions excitation is energy transfer from the Tm^{3+} ions. As CR1 and CR2 channels populate $^3H_4$ level of Tm^{3+} ions, the most probable path of energy transfer from Tm^{3+} to Yb^{3+} ions is Tm ($^3H_4$) + Yb ($^2F_{7/2}$) → Tm ($^3H_6$) + Yb ($^2F_{5/2}$). The amount of energy transfer is found to increase with Yb^{3+} ions concentration, as evidenced from the increase in intensity of the Yb^{3+} ions $^2F_{5/2} \rightarrow {}^2F_{7/2}$ emission at around 1 μm, which is very much useful for enhancing the efficiency of silicon solar cells [51]. The 1.64 μm emission follows the same trend as the Yb^{3+} ions 1 μm emission, with increase in Yb^{3+} ions concentration, as the energy of the excited $^1G_4$ level is the source of both the emissions. Intensities of both the 1.46 and 1.52 μm emissions follow that of 1.64 μm emission up to 1.0 mol% and then decreases for 2.0 mol% of Yb^{3+} ions due to increase in strength of CR3 process. Overall, 1.2 μm emission is the dominant one in both the single-doped and co-doped glass systems.

The stimulated emission cross-sections $\sigma(\lambda_p)$ of the intense 1.2 μm emission have been evaluated by using the expression [28],

$$\sigma(\lambda_p) = \frac{\lambda_p{}^4}{8\pi c n^2 \Delta\lambda_{eff}} A \tag{11}$$

where λ_p is the peak wavelength; 'n' is the refractive index of the glass; $\Delta\lambda_{eff}$ is the effective bandwidth; and 'A' is the spontaneous emission probability for the $^1G_4 \rightarrow {}^3H_4$ transition.

The $\sigma(\lambda_p)$ value for the $^1G_4 \rightarrow {}^3H_4$ transition in SALSTm0.01, SALSTm0.05 and SALSTm0.1 glasses are presented in Table 5 along with those of reported Tm^{3+}-doped TPBL [27], TWTm [28], GeBL [46] and AT$_{10}$ [47] glasses. As can be seen, the $\sigma(\lambda_p)$ values of the present glasses decreases with the increase in Tm^{3+} ions concentration and are higher than those of reported ones in TWTm [28], GeBL [46] and AT$_{10}$ [47] glass systems. For efficient lasers, figure of merit i.e., product of emission cross-section and lifetime (FOM = $\sigma(\lambda_p)$ x τ_{exp}) should be as high as possible. Its value is proportional to the slope efficiency and inversely proportional to the threshold pump power of the laser. The FOM of 1.2 μm emission has been evaluated for three concentrations of Tm^{3+}-doped glasses and are presented in Table 5. As can be seen, FOM

Table 5
Comparison of stimulated emission cross-sections ($\sigma(\lambda_p)$ ± 0.2, x10^{-21} cm^2) and figure of merit (FOM, x10^{-24} cm^{2}s) for Tm^{3+}: $^1G_4 \rightarrow {}^3H_4$ transition in Tm^{3+}-doped glasses.

S. No.	Glass	$\sigma(\lambda_p)$	FOM
1	SALSTm0.01 [present work]	3.12	1.43
2	SALSTm0.05 [present work]	3.08	1.16
3	SALSTm0.1 [present work]	3.06	0.85
4	TPBL [27]	4.70	
5	TWTm [28]	5.8	
6	GeBL [46]	2.85	
7	AT$_{10}$ [47]	1.2	
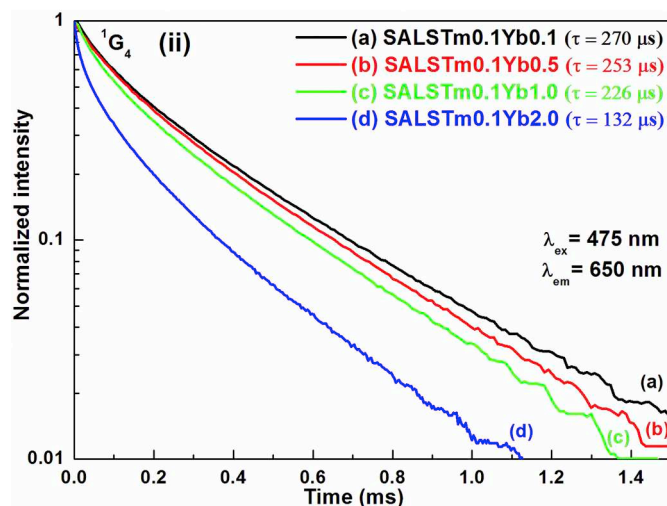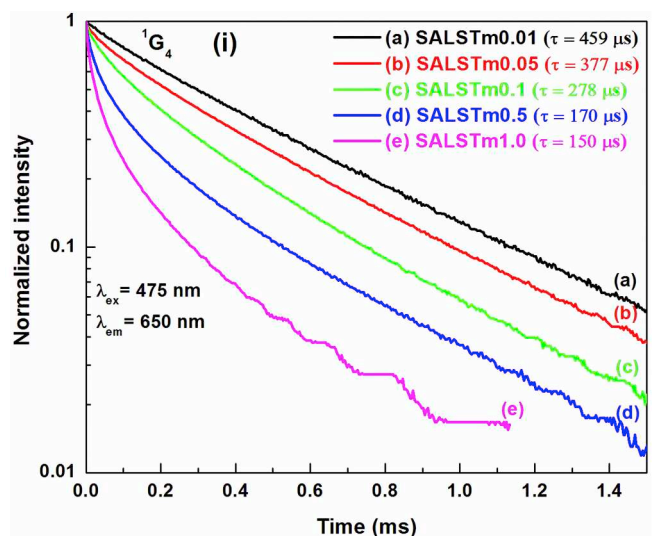
Fig. 5. Decay curves of the $^1G_4$ level of (i) Tm^{3+}-doped and (ii) Tm^{3+}/Yb^{3+} co-doped SALS glasses under 475 nm laser excitation.

for the 1.2 μm emission is maximum for SALSTm0.01 glass. These results indicate that the present glasses are useful for optical amplification applications at around 1.2 μm wavelength.

3.3. Luminescence decays

Decay curves for the $^1G_4$ level of Tm^{3+} and Tm^{3+}/Yb^{3+} co-doped glasses under 475 nm laser excitation are shown in Figs. 5(i) and (ii), respectively, whereas Figs. 6(i) and (ii) show the decay curves for the $^3H_4$ level of Tm^{3+} and Tm^{3+}/Yb^{3+} co-doped glasses, respectively, under 776 nm laser excitation. From Figs. 5 and 6, it is noticed that all the decay curves exhibits non-exponential behavior, indicating the presence of energy transfer processes.

Experimental lifetime (τ_{exp}) values for the $^1G_4$ and $^3H_4$ levels in Tm^{3+}-doped glasses and the $^2F_{5/2}$ level of Yb^{3+} ions in Tm^{3+}/Yb^{3+} co-doped glasses have been evaluated from the measured decay curves using the Eqn. [18],

$$\tau = \int \frac{t I(t) dt}{I(t)} \tag{12}$$

At higher concentrations of Tm^{3+} ions, the interactions between them increase, resulting in a quenching of lifetimes of the $^1G_4$ and $^3H_4$ levels. The difference between the values of τ_{exp}, obtained at low concentrations, and τ_R can be understood by the presence of non-radiative
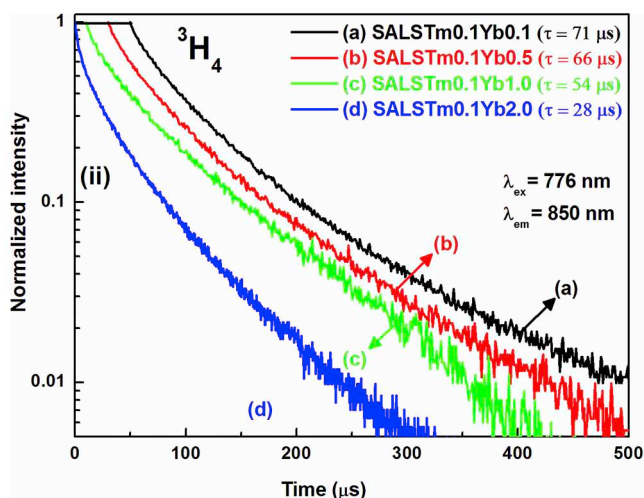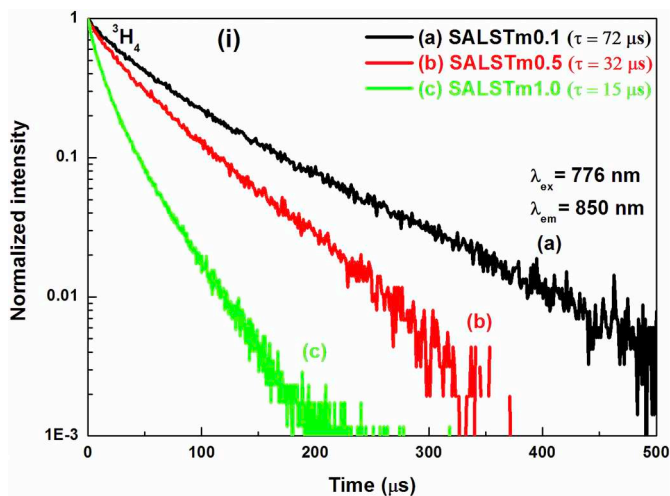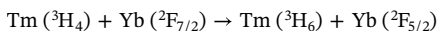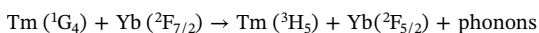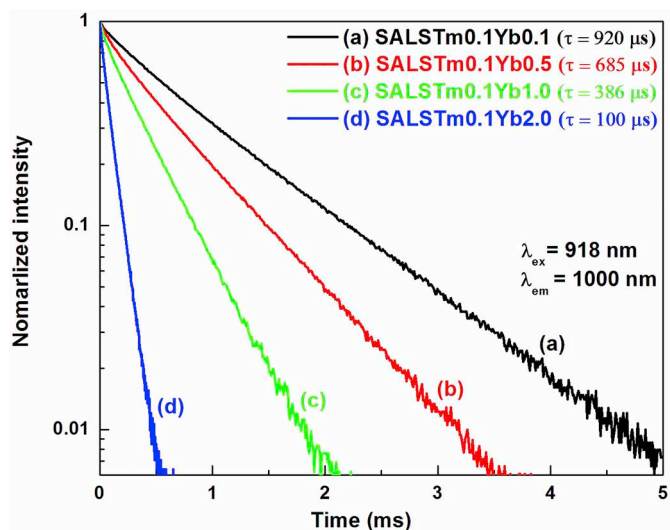
Fig. 7. Decay curves for the $^2F_{5/2}$ level of Yb^{3+} ion in SALSTmYb glasses under 918 nm excitation, monitoring the emission at 1000 nm.

Fig. 6. Decay curves of the $^3H_4$ level of (i) Tm^{3+}-doped and (ii) Tm^{3+}/Yb^{3+} co-doped SALS glasses under 776 nm laser excitation, monitoring the emission at 850 nm. In Fig (ii) the excitation cutoff has been shifted for clarity.

processes between the transitions [15]. In co-doped samples, lifetime of the $^2F_{5/2}$ level of Yb^{3+} ions decreases with increase in concentration. This could be due to concentration quenching of Yb^{3+} ions due to energy transfer processes between them and then transfer to traps/defects. The decrease in lifetimes of the $^1G_4$ and $^3H_4$ levels of Tm^{3+} ions in co-doped systems, even though the concentration of Tm^{3+} ions is kept constant at 0.1 mol%, could be due to the existence of following energy transfer channels from Tm^{3+} to Yb^{3+} ions:

$$Tm\ (^1G_4) + Yb\ (^2F_{7/2}) \rightarrow Tm\ (^3H_5) + Yb(^2F_{5/2}) + phonons$$

$$Tm\ (^3H_4) + Yb\ (^2F_{7/2}) \rightarrow Tm\ (^3H_6) + Yb\ (^2F_{5/2})$$

To know the energy transfer from Tm^{3+} to Yb^{3+} ions, the energy transfer efficiency η is an important parameter and it can be calculated using the Eqn. [40],

$$\eta = 1 - \frac{\tau}{\tau_0} \tag{13}$$

where, τ and τ_0 are the experimental lifetimes of the $^1G_4$ level in co-doped and 0.1 mol% Tm_2O_3 single-doped samples, respectively. The η value for SALSTm0.1Yb2.0 glass is 53% and is higher compared to 32% for zinc barium glass ($0.75Tm^{3+}/2Yb^{3+}$) and 40% for zinc lanthanum glass ($0.75Tm^{3+}/2Yb^{3+}$) [44].

To understand the energy transfer processes effectively, decay

curves for the $^2F_{5/2}$ emitting level of Yb^{3+} ions are measured exciting at 918 nm and monitoring the emission at 1.0 μm in co-doped glasses, and are shown in Fig. 7. The decrease in lifetimes with increase in Yb^{3+} ions concentration is an evidence for the energy transfer from Yb^{3+} to Tm^{3+} ions and/or concentration quenching of Yb^{3+} ions.

3.4. Upconversion luminescence

The upconversion (UC) luminescence is observed in Tm^{3+}/Yb^{3+} co-doped glasses exciting at 975 nm in the wavelength range of 325–700 nm and is shown in Fig. 8. Four emission bands are observed at 362, 450, 474 and 650 nm, which correspond to the $^1D_2 \rightarrow {}^3H_6$, $^1D_2 \rightarrow {}^3F_4$, $^1G_4 \rightarrow {}^3H_6$ and $^1G_4 \rightarrow {}^3H_4$ transitions of Tm^{3+} ion, respectively. Among these four emission bands, it is observed that the red emission at 650 nm is relatively weaker than the blue at 474 nm. From Fig. 8, it is observed that the UC luminescence intensity increases with the Yb^{3+} concentration up to 1.0 mol% and decreases thereafter. The variation of 474 and 650 nm UC emission intensities with Yb^{3+} concentration is shown in inset of Fig. 8. For both wavelengths, the UC emission intensity is highest for 1.0 mol% of Yb^{3+} ions and decreases thereafter. The increase in UC luminescence intensity up to 1.0 mol% of Yb^{3+} ions can be explained as due to increase in the efficiency of energy transfer processes from Yb^{3+} to Tm^{3+} ions. The decrease in UC luminescence intensity at higher concentrations of Yb^{3+} ions is caused by concentration quenching through energy migration among the Yb^{3+} ions and then transfer to traps.

In upconversion processes, the relationship between upconversion emission intensity and the intensity of the excitation is given by $I_{UP} \propto I_{IR}^n$, where n is the number of IR photons absorbed per visible photon emitted. The graph between log upconversion intensity (log I_{UP}) and IR excitation intensity (log I_{IR}) shows a straight line with slope n. Fig. 9 shows the plot for log I_{UP} versus log I_{IR} for the 362, 474 and 650 nm emissions. The values of 2.7, 2.0 and 1.9 are obtained for the slopes of 362, 464 and 650 nm emissions, respectively, indicating that emission from the $^1D_2$ level is a three photon process and emissions from the $^1G_4$ level is a two photon one [42].

The mechanism of upconversion can be explained using the partial energy level diagram of Tm^{3+} and Yb^{3+} ions shown in Fig. 10. The pump power dependence of UC emission indicates that $^1G_4$ and $^1D_2$ levels are populated by absorption of two and three NIR photons, respectively. When the co-doped samples are excited with 975 nm laser, Yb^{3+} ions are excited to the $^2F_{5/2}$ level and energy is transferred to Tm^{3+} ions by three different routes. First one is energy transfer to $^3H_5$
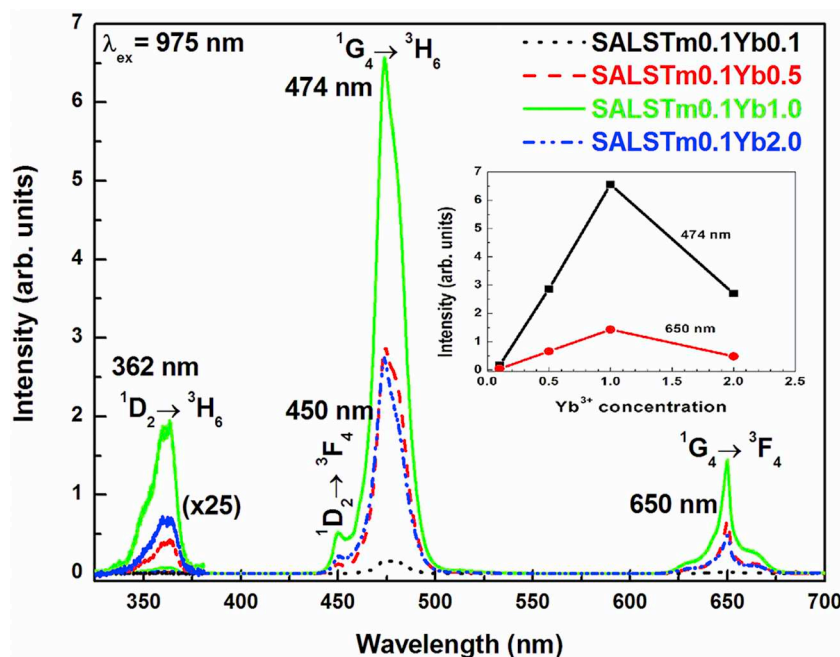
Fig. 8. Upconversion spectra of Tm^{3+}/Yb^{3+} co-doped SALS glasses under 975 nm laser excitation. Inset shows the variation of 474 and 650 nm upconversion emission intensities with Yb^{3+} concentration.
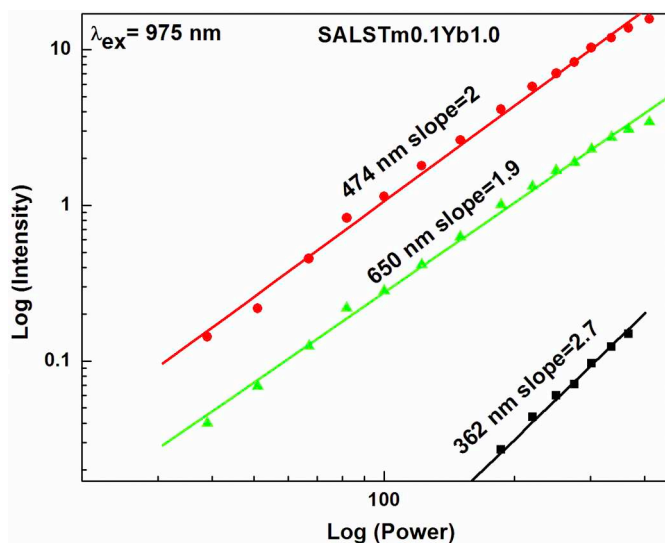

Fig. 9. Pump power dependence of up-converted emissions at 362, 474 and 650 nm in Tm^{3+}/Yb^{3+} co-doped SALS glasses.

level by ET1 process followed by nonradiative relaxation (NR) to the $^3F_4$ level. Energy transfer upconversion from this level (ETU1) populates the $^3F_{2,3}$ levels followed by NR to the $^3H_4$ level. Another possibility is energy transfer from Yb^{3+} ions directly to $^3H_4$ level of Tm^{3+} through ET2 process and from there another NIR photon populates $^1G_4$ level (ETU2 or ET3). The $^1G_4$ level can also be populated by two photon absorption (TPA) at 975 nm from two Yb^{3+} ions [52]. Both processes supports that excitation to the $^1G_4$ level is a two photon process, reflected in the slope value of 2.0 for the 474 nm emission (Fig. 9). From the $^1G_4$ level two main radiative decay processes takes place resulting in 650 (red) and 474 nm (blue) emissions corresponding to the $^1G_4 \rightarrow {}^3F_4$ and $^1G_4 \rightarrow {}^3H_6$ transitions, respectively.

The ET3 energy transfer from Yb^{3+} ions $^2F_{5/2}$ level causes ETU3 from $^1G_4$ to populate the $^1D_2$ level, although energy matching in this case is poor compared to those of ETU1 and ETU2. Alternatively, the

cross-relaxation (CR) channel, $^1G_4$, $^3H_4 \rightarrow {}^3F_4$, $^1D_2$, may also populates the $^1D_2$ level because of a better energy matching. The $^1D_2$ level also gives two radiative emissions at 362 and 450 nm corresponding to the $^1D_2 \rightarrow {}^3H_6$ and $^1D_2 \rightarrow {}^3F_4$ transitions shown in Fig. 8. However, intensities of emissions from the $^1D_2$ level are relatively weaker than those of the $^1G_4$ level. This could be due to the weaker efficiency of the excitation processes that populates the $^1D_2$ level. The three photon excitation process of the $^1D_2$ level is also reflected in the value of slope (2.7) of the 362 nm emission (Fig. 9).

The dynamics of upconversion has also been investigated by measuring decay curves of the $^1G_4$ level, exciting at 475 nm and monitoring the emission at 650 nm (Stokes emission); and exciting at 975 nm and monitoring the emission at 475 nm (upconversion), and are shown in Fig. 11 for the SALSTm0.1Yb0.5 glass. As can be seen, in the case of Stokes emission, the lifetime of the $^1G_4$ level is 253 μs and in the case of upconversion, there is clear rise time of 165 μs and the decay time is 1070 μs, around 4 times more than the normal lifetime. The upconversion decay time reflect population change of feeder level, i.e., $^3F_4$, which populates $^1G_4$ through upconversion process. The rise time of upconversion emission reflect the time scale of energy transfer processes [37]. From the above results, it is evident that there is transfer of energy from Yb^{3+} to Tm^{3+} ions under 975 nm excitation because NIR level with longer lifetime ($^3F_4$) is involved in the upconversion process. On the other hand, if the $^3F_4$ level is involved in the upconversion, the slopes should be about 3 and 4 for the levels $^1G_4$ and $^1D_2$, respectively, but in the present case they are only about 2 and 3. This is because of saturation effect in Yb^{3+}-Tm^{3+} upconversion processes which causes population and depopulation of the $^3F_4$ level [53,54].

4. Conclusions

Oxyfluorosilicate glasses doped with different concentrations of Tm^{3+} and Tm^{3+}/Yb^{3+} ions have been prepared and investigated their absorption and emission spectra, lifetimes of the luminescent levels and upconversion properties. From absorption spectrum of the 1.0 mol% Tm_2O_3-doped glass, intensity analysis has been made using the Judd-Ofelt theory and calculated various radiative properties of the emitting levels and compared with those of similar reported systems. Relative
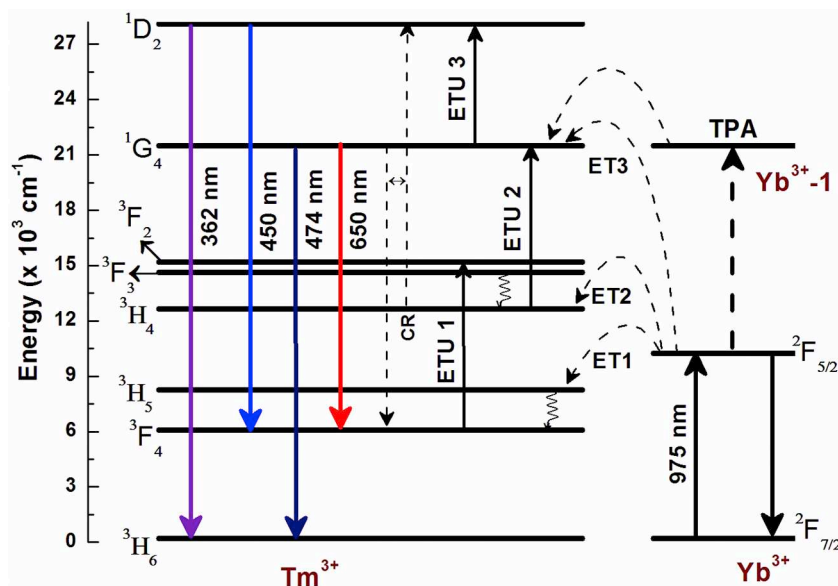
Fig. 10. Partial energy level diagram of Tm^{3+} and Yb^{3+} ions showing the mechanism of upconversion luminescence (TPA: two photon absorption and Yb^{3+}-1 represents a second Yb^{3+} ion).
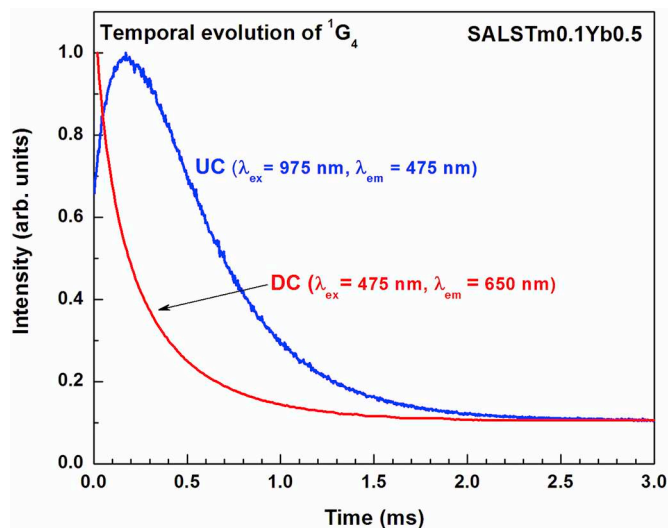

Fig. 11. Temporal evolution of the $^1G_4$ level emissions in SALSTm0.1Yb0.5 glass under 475 nm excitation (Stokes emission) and under 975 nm excitation (upconversion).

variations of the visible and NIR emission spectra with change in concentrations of active ions have been explained as due to variations of different cross-relaxation processes. Lifetimes of the 650 and 790 nm emissions have been measured and are found to decrease with increase in Tm^{3+} ions concentration in single-doped glasses, due to concentration quenching, and with the increase of Yb^{3+} ions concentration in co-doped glasses due to energy transfer from Tm^{3+} to Yb^{3+} ions. The 1.2 μm emission band in NIR spectra of single as well as co-doped glasses is very broad and intense and finds application in optical amplifiers. The NIR emission spectra of co-doped glasses show emission at around 1.0 μm which increases with increase in Yb^{3+} ions concentration. The decrease in lifetimes of the $^2F_{5/2}$ level of Yb^{3+} ions with increase in Yb^{3+} ions concentration is explained as due to energy transfer process/concentration quenching. The 1.0 μm emission is useful to enhance Si solar cell efficiency. Finally, the Tm^{3+}/Yb^{3+} co-doped glasses show upconversion emissions under 975 nm excitation. Relative variations of upconversion emissions, their pump power dependencies, mechanism and dynamics have been explained based on energy transfer

processes. Overall, the visible, NIR and upconversion emissions of the studied glasses are very much useful for the design of photonic devices.

References

[1] M. Li, G. Bai, Y. Guo, L. Hu, J. Zhang, Investigation on Tm^{3+}-doped silicate glasses for 1.8 μm emission, J. Lumin. 132 (2012) 1830–1835, https://doi.org/10.1016/j.jlumin.2012.02.022.

[2] M. Li, X. Liu, Y. Guo, W. Hao, L. Hu, J. Zhang, ~2μm fluorescence radiative dynamics and energy transfer between Er^{3+} and Tm^{3+} ions in silicate glass, Mater. Res. Bull. 51 (2014) 236–270, https://doi.org/10.1016/j.materresbull.2013.12.021.

[3] T. Suhasini, B.C. Jamalaiah, T. Sasikala, G.V. Lokeswara Reddy, L. Rama Moorthy, Study on visible luminescence of the Tm^{3+}: $^1D_2 \rightarrow ^3F_4$ emission state in lead borate titanate glasses, Opt. Commun. 285 (2012) 1229–1232, https://doi.org/10.1016/j.optcom.2011.11.056.

[4] X. Li, S. Bo, X. Shengchun, L. Jingwen, Up-conversion luminescence of Tm^{3+}/Yb^{3+} co-doped oxy-fluoride glasses, J. Rare Earths 28 (2010) 194–197, https://doi.org/10.1016/S1002-0721(09)60079-X.

[5] D.C. Yu, J.P. Zhang, Q.J. Chen, W.J. Zhang, Z.M. Yang, Q.Y. Zhang, Three-photon near-infrared quantum cutting in Tm^{3+}-doped transparent oxyfluoride glass ceramics, Appl. Phys. Lett. 101 (2012), https://doi.org/10.1063/1.4764005 171108-1-4.

[6] F.C. Guinhos, P.C. Nóbrega, P.A. Santa-Cruz, Compositional dependence of upconversion process in Tm^{3+}-Yb^{3+} codoped oxyfluoride glasses and glass-ceramics, J. Alloys Compd 323-324 (2001) 358–361, https://doi.org/10.1016/s0925-8388(01)01036-2.

[7] H. Zheng, D. Gao, X. Zhang, E. He, X. Zhang, Fluorescence characteristics of Tm^{3+} in different local environments, J. Appl. Phys. 104 (2008), https://doi.org/10.1063/1.2953063 013506-1-4.

[8] J. Pisarska, L. Zur, Wojciech A. Pisarski, Optical spectroscopy of Dy^{3+} ions in heavy metal lead-based glasses and glass-ceramics, J. Mole. Struct. 993 (2011) 160–166, https://doi.org/10.1016/j.molstruc.2010.12.022.

[9] Y. Tian, R. Xu, L. Hu, J. Zhang, Mid-infrared luminescence and energy transfer of

Tm^{3+}/Yb^{3+} doped fluorophosphates glass, Mat. Chem. Phy. 133 (2012) 340–345, https://doi.org/10.1016/j.matchemphys.2012.01.035.

[10] X. Wang, S. Fan, K. Li, L. Zhang, Sh. Wang, L. Hu, Compositional dependence of the 1.8 μm emission properties of Tm^{3+} ions in silicate glass, J. Appl. Phys. 112 (2012), https://doi.org/10.1063/1.4766908 103521-1-7.

[11] X. Wang, K. Li, Ch. Yu, D. Chen, L. Hu, Effect of Tm_2O_3 concentration and hydroxyl content on the emission properties of Tm doped silicate glasses, J. Lumin. 147 (2014) 341–345, https://doi.org/10.1016/j.jlumin.2013.11.025.

[12] T.M. Hau, R. Wang, X. Yu, D. Zhou, Zh. Song, Zh. Yang, X. He, J. Qiu, Near-infrared broadband luminescence and energy transfer in Bi-Tm-Er co-doped lanthanum aluminosilicate glasses, J. Phys. Chem. Solids 73 (2012) 1182–1189, https://doi.org/10.1016/j.jpcs.2012.04.006.

[13] G. Zaho, Y. Tian, X. Wang, H. Fan, L. Hu, Spectrosccopic properties of 1.8 μm emission in Tm^{3+} doped bismuth silicate glass, J. Lumin. 134 (2013) 837–841, https://doi.org/10.1016/j.jlumin.2012.06.040.

[14] K.S.V. Sudhakar, T. Satyanarayana, L. Srinivasa Rao, M. Srinivasa Reddy, N. Veeraiah, Optical absorption and self activated up conversion fluorescence spectra of Tm^{3+} ions in antimony borate glass systems, Sol. Stat. Sci. 146 (2008) 441–445, https://doi.org/10.1016/j.ssc.2008.04.008.

[15] G. Poirier, V.A. Jerez, B. Cid, Y. De Araujo, S.J.L. Ribeiro Messaddeq, M. Poulain, Optical spectroscopy and frequency upconversion properties of Tm^{3+}-doped tungstate fluorophosphate glasses, J. Appl. Phys. 93 (2003) 1493–1497, https://doi.org/10.1063/1.1536017.

[16] R. Li, C. Tian, Y. Tian, T. Wei, B. Li, X. Jing, F. Ruan, F. Wang, Mid-infrared emission properties and energy transfer evaluation in Tm^{3+} doped fluorophosphate glasses, J. Lumin. 162 (2015) 58–62, https://doi.org/10.1016/j.jlumin.2015.02.016.

[17] A. Mallik, B. Pal, Studies on preparation and property evaluation of some Tm^{3+}-ion doped oxyfluorophosphate glasses, Mater. Sci. Engin. B 179 (2014) 77–83, https://doi.org/10.1016/j.mseb.2013.10.005.

[18] P. Babu, H.J. Seo, K.H. Jang, R. Balakrishnaiah, C.K. Jayasankar, A.S. Joshi, Optical spectroscopy and energy transfer in Tm^{3+}-doped metaphosphate laser glasses, J. Phys. Condens. Matter 17 (2005) 4859–4876, https://doi.org/10.1088/0953-8984/17/32/001.

[19] W.A. Pisarski, J. Pisarska, G. Dominiak-Dzik, W. Ryba-Romanowski, Visible and infrared spectroscopy of Pr^{3+} and Tm^{3+} ions in lead borate glasses, J. Phys.: Condens. Matter 16 (2004) 6171–6184, https://doi.org/10.1088/0953-8984/16/34/016.

[20] K.-S. Lim, P. Babu, C.K. Jayasankar, S.-K. Lee, Van-Thai Pham, H.-J. Seo, Optical spectroscopy of thulium-doped oxyfluoroborate glass, J. Alloys Compd. 385 (2004) 12–18, https://doi.org/10.1016/j.jallcom.2004.04.133.

[21] K. Pavani, L. Rama Moorthy, J. Suresh Kumar, A. Mohan Babu, Energy transfer and luminescence properties of Tm^{3+} ions in calcium fluoroborate glasses for fiber amplifiers, J. Lumin. 136 (2013) 383–388, https://doi.org/10.1016/j.jlumin.2012.12.014.

[22] Z. Mazurak, M. Czaja, R. Lisiecki, J. Gabrys-Pisarska, Optical properties of the Tm^{3+} and energy transfer between $Tm^{3+} \rightarrow Pr^{3+}$ ions in P_2O_5-CaO-SrO-BaO phosphate glass, Opt. Mater. 33 (2011) 506–510, https://doi.org/10.1016/j.optmat.2010.10.031.

[23] A. Kermaoui, F. Pelle, Synthesis and infrared spectroscopic properties of Tm^{3+}-doped phosphate glasses, J. Alloys Compd. 469 (2009) 601–608, https://doi.org/10.1016/j.jallcom.2008.02.024.

[24] R. Praveena, Kyoung Hyuk Jang, C.K. Jayasankar, H.J. Seo, Optical absorption and fluorescence properties of Tm^{3+}-doped K-Mg-Al phosphate glasses for laser applications, J. Alloys Compd. 496 (2010) 335–340, https://doi.org/10.1016/j.jallcom.2010.02.007.

[25] G. Turri, V. Sudesh, M. Richardson, M. Bass, A. Toncelli, M. Tonelli, Temperature-dependent spectroscopic properties of Tm^{3+} in germanate, silica, and phosphate glasses: a comparative study, J. Appl. Phys. 103 (2008), https://doi.org/10.1063/1.2912952 093104-1-7.

[26] W. Ryba-Romanowski, S. Golab, G. Dominiak-Dzik, M. Zelechower, J. Gabrys-Pisarska, Excited state relaxation dynamics and non-radiative energy transfer in fluoroindate glass singly doped with thulium and doubly doped with thulium and terbium, J. Alloys Compd. 325 (2001) 215–222, https://doi.org/10.1016/s0925-8388(01)01265-8.

[27] B. Zhou, H. Lin, E. Yue-Bun Pun, Tm^{3+}-doped tellurite glasses for fiber amplifiers in broadband optical communication at 1.20 μm wavelength region, Opt. Express 18 (2010) 18805–18810, https://doi.org/10.1346/oe.18.018805.

[28] G. Ozen, A. Aydinli, S. Cenk, A. Sennaroglu, Effect of composition on the spontaneous emission probabilities, stimulated emission cross-sections and local environment of Tm^{3+} in TeO_2-WO_3 glass, J. Lumin. 101 (2003) 293–306, https://doi.org/10.1016/s0022-2313(02)00572-0.

[29] R. Lachheb, K. Damak, A.A. Assadi, A. Herrmann, E. Yousef, C. Russel, R. Maalej, Characterization of Tm^{3+}-doped TNZL glass laser material, J. Lumin. 161 (2015) 281–287, https://doi.org/10.1016/j.jlumin.2014.12.069.

[30] V. Kumar Rai, L. de S. Menezes, Cid B. De Araujio, Spectroscopy, energy transfer, and frequency upconversion in Tm^{3+}-doped TeO_2-PbO glass, J. Appl. Phys. 102 (2007), https://doi.org/10.1063/1.2769788 043505-1-4.

[31] H. Fan, G. Gao, G. Wang, J. Hu, L. Hu, Tm^{3+}-doped Bi_2O_3 GeO_2-Na_2O glasses for 1.8 μm fluorescence, Opt. Mater. 32 (2010) 627–631, https://doi.org/10.1016/j.optmat.2009.12.012.

[32] E.W.J.L. Oomen, Up-conversion of red light in to blue light in thulium doped fluorozirconate glasses, J. Lumin. 50 (1992) 317–332, https://doi.org/10.1016/0022-2313(92)90081-j.

[33] Q.Y. Zhang, T. Li, Z.H. Jiang, X.H. Ji, S. Buddhudu, 980 nm laser-diode-excited intense blue upconversion in Tm^{3+}/Yb^{3+}-codoped gallate-bismuth-lead glasses, Appl. Phys. Lett. 87 (2005), https://doi.org/10.1063/1.2115082 171911-1-3.

[34] A. Kos, I. Czopek, J. Pisarska, W.A. Pisarski, R. Lisiecki, W. Ryba-Romanowski, Energy transfer processes from Yb^{3+} to Ln^{3+} (Ln = Er or Tm) in heavy metal glasses, J. Rare Earths 32 (2014) 273–276, https://doi.org/10.1016/S1002-0721(14)60064-8.

[35] S. Gao, X. Liu, X. Fan, X. Li, T. Xue, K. Li, M. Liao, L. Hu, ~2 μm emission properties and non-radiative process of Tm^{3+} in germinate glass, J. Appl. Phys. 116 (2014) 173108-1-6, https://doi.org/10.1063/1.4900534.

[36] Y.-P. Peng, X. Yuan, J. Zhang, L. Zhang, The effect of La_2O_3 in Tm^{3+}-doped germinate-tellurite glasses for ~2 μm emission, Sci. Rep. 4 (2014) 1–5, https://doi.org/10.1038/srep05256.

[37] B.M. Walsh, N.P. Barnes, D.J. Reichle, Sh. Jiang, Optical properties of Tm^{3+} ions in alkali germinate glass, J. Non-Cryst. Solids 352 (2006) 5344–5352, https://doi.org/10.1016/j.jnoncrysol.2006.08.029.

[38] X. Bo, Y. Bin, Z. Yuepin, X. Haiping, W. Jinhao, Cooperative energy transfer in Tm^{3+} and Yb^{3+} co-doped phosphate glasses, J. Rare Earths 31 (2013) 164–168, https://doi.org/10.1016/S1002-0721(12)60252-X.

[39] X. Zou, T. Izumitani, Fluorescence mechanisms and dynamics of Tm^{3+} singly doped and Yb^{3+}, Tm^{3+} doubly doped glasses, J. Non-Cryst. Solids 162 (1993) 58–67, https://doi.org/10.1016/0022-3093(93)90741-f.

[40] Ruijie Cao, Yu Lu, Ying Tian, Feifei Huang, Yanyan Guo, Shiqing Xu, Junjie Zhang, Mid-infrared luminescence and energy transfer of Tm^{3+} in silicate glass by co-doping with Yb^{3+} ions, Opt. Lasertech. 94 (2017) 106–111, https://doi.org/10.1016/j.optlastec.2017.03.026.

[41] A. Mohan Babu, B.C. Jamalaiah, T. Chengaiah, G.V. Lokeswara Reddy, L. Rama Moorthy, Upconversion luminescence in Tm^{3+}/Yb^{3+} co-doped lead tungstate tellurite glasses, Physica B 406 (2011) 3074–3078, https://doi.org/10.1016/j.physb.2011.05.010.

[42] Q. Nie, X. Li, Sh. Dai, T. Xu, Z. Jin, X. Zhang, Energy transfer and upconversion luminescence in Tm^{3+}/Yb^{3+} co-doped lanthanum-zinc-lead-tellurite glasses, J. Lumin. 128 (2008) 135–141, https://doi.org/10.1016/j.jlumin.2007.06.001.

[43] J. Pisarska, R. Lisiecki, W. Ryba-Romanowski, G. Dominiak-dzik, W.A. Pisarski, Up-converted luminescence in Yb-Tm co-doped lead fluoroborate glasses, J. Alloys Compd. 451 (2008) 226–228, https://doi.org/10.1016/j.jallcom.2007.04.168.

[44] O. Maalej, A. Lukowiak, A. Bouajaj, A. Chiasera, G.C. Righini, M. Ferrari, B. Boulard, Blue to NIR down-conversion in Tm^{3+}/Yb^{3+} co-doped fluorozirconate glasses compared to Pr^{3+}/Yb^{3+} ion-pair, J. Lumin. 193 (2018) 22–28, https://doi.org/10.1016/j.jlumin.2017.09.021.

[45] G.A. Thomas, B.I. Shraiman, P.F. Glodis, M.J. Stephen, Towards the clarity limit in optical fibre, Nature 404 (2000) 262–264, https://doi.org/10.1038/35005034.

[46] B. Zhou, L. Tao, Y.H. Tsang, E. Yue-Bun Pun, Broadband 1.20 μm emission in Tm^{3+}-doped and Tm^{3+} / Tb^{3+}, Eu^{3+} codoped gallogermanate glasses, Opt. Mater. 34 (2012) 1776–1780, https://doi.org/10.1016/j.optmat.2012.04.022.

[47] Y. Gandhi, M.V. Ramachandra Rao, Ch. Srinivasa Rao, I.V. Kityk, N. Veeraiah, Role of Al_2O_3 in upconversion and NIR emission in Tm^{3+} and Er^{3+} codoped calcium fluoro phosphorous silicate glass system, J. Lumin. 131 (2011) 1443–1452, https://doi.org/10.1016/j.jlumin.2011.03.046.

[48] B.R. Judd, Optical absorption intensities of rare-earth ions, Phys. Rev. 127 (1962) 750–761, https://doi.org/10.1103/physrev.127.750.

[49] G.S. Ofelt, Intensities of crystal spectra of rare-earth ions, J. Chem. Phys. 37 (1962) 511–520, https://doi.org/10.1063/1.1701366.

[50] A. Smakula, About excitement and discoloration of photoelectrically conductive alkali halides, Z. Phys. 59 (1930) 603–614.

[51] Q. Zhang, B. Zhu, Y. Zhuang, G. Chen, X. Liu, G. Zhang, J. Qiu, D. Chen, Quantum cutting in Tm^{3+}/Yb^{3+}-codoped lanthanum aluminum germanate glasses, J. Am. Ceram. Soc. 93 (2010) 654–657, https://doi.org/10.1111/j.1551-2916.2009.03483.x.

[52] Y. Ledemi, A.A. Trudel, Victor A.G. Rivera, S. Chenu, E. Veron, L.A. Nunes, M. Allix, Y. Messaddeq, White light and multicolor emission tuning in triply doped $Yb^{3+}/Tm^{3+}/Er^{3+}$ novel fluoro-phosphate transparent glass-ceramics, J. Mater. Chem. C 2 (2014) 5046–5056, https://doi.org/10.1039/c4tc00455h.

[53] F.W. Ostermayer, J.P. Vanderziel, H.M. Marcos, L.G. Vanuiter, J.E. Geusic, Frequency upconversion in YF_3-Yb^{3+},Tm^{3+}, Phys. Rev. B 3 (1971) 2698–2705, https://doi.org/10.1103/PhysRevB.3.2698.

[54] J. Mendez-Ramos, F. Lahoz, I.R. Martin, A.B. Soria, A.D. Lozano-Gorrin, V.D. Rodriguez, Optical properties and upconversion in Yb^{3+}-Tm^{3+} co-doped oxyfluoride glasses and glass ceramics, Mol. Phys. 101 (2003) 1057–1065, https://doi.org/10.1080/0026897021000046915.
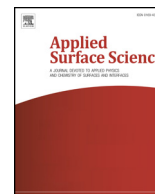
Full length article

Infrared-laser precipitation of Dy^{3+}-Yb^{3+} codoped SrF_2 nanocrystals in glass and upconversion luminescence

Gangseon Ji[a], Gi-joon Hong[a], Chang-hyuck Bae[a], Palamandala Babu[b], Ki-Soo Lim[a,*]

[a] *Department of Physics, Chungbuk National University, Cheongju 28644, Republic of Korea*
[b] *Department of Physics, SVCR Govt. Degree College, Palamaner 517408, India*

ABSTRACT

Oxyfluoride glass-ceramics containing SrF_2 nanocrystals have been prepared by a CO_2 laser treatment on the glass prepared by high temperature melt quenching. The optimized scan speed and laser power produced nanocrystals with sizes of ~10 nm. Energy dispersive spectroscopy mapping analysis showed that Dy^{3+} and Yb^{3+} ions are highly populated inside the SrF_2 nanocrystals. We also report a substantially enhanced down-converted visible emission from the 4F9/2 state of Dy3+ ions, including some violet emissions from the higher energy states under 365 nm excitation in the glass-ceramics, as compared to the as-made glass. Moreover, 980 nm laser diode excitation produced strong green and red emissions from the $^4I_{15/2}$ state and blue and yellow emissions from the $^4F_{9/2}$ state. A model has been proposed to interpret the upconversion emissions through the multistep-excitation of Dy^{3+} ions and energy transfers from, efficient sensitizers, Yb^{3+} ions to Dy^{3+} ions.

1. Introduction

Rare-earth ion doped glass-ceramics may become potentially useful for optoelectronic applications. Glass-ceramics offer the ease of melt processing like conventional glasses, but rare earth ion segregation to crystalline regions results in spectral and laser properties similar to those of single crystals and ceramics [1]. Oxyfluoride glass-ceramics have attracted much attention due to their combined advantages of oxide glasses and fluoride glasses [2,3] and their maintenance of good chemical and thermal stabilities [4]. Thus, numerous studies on oxyfluoride glass-ceramics containing fluoride nanocrystals doped with rare-earth ions have been reported thus far [3,5–8]. Fluoride nanocrystals have much less phonon energy (~360 cm^{-1}) [9], yielding a large quantum efficiency.

Most oxyfluoride glass-ceramics are fabricated using controlled heat treatments in an electric furnace in order to form nanocrystals in the interior of glass [10]. Recently, the laser annealing of glass has been reported as an alternative method for glass-ceramics formation with the advantage of spatially selected structural modification and crystallization inside glass with ultraviolet, visible, near-infra-red, and mid-infrared lasers [5,11–13]. Laser-heated glass-ceramics formation with an infrared laser hold some potential for optical device applications of oxyfluoride glasses with fluoride nanocrystals, because the infrared laser can treat selective regions upon the surface of the glass.

The infrared-to-visible up-conversion behavior of the glass-ceramics codoped with (Yb, Er) [14], (Yb, Tm) [15], (Yb, Ho) [16], or (Yb, Eu) [17] prepared by furnace treatment has been recently reported for display and solar-cell applications [18]. However, only a few studies on glass-ceramics co-doped with (Yb, Dy) have been reported thus far [19], and the blue-violet emissions still need further investigation before their origin can be clarified. Dy^{3+} ion exhibits intense blue and yellow colors as well as white light emission, and Yb^{3+} ions are widely used in infrared-to-visible upconversion applications [20]. In this work, CO_2 laser-induced crystallization technique has been used to a multi-component SiO_2-Al_2O_3-SrF_2-LiF oxyfluoride glass doped with rare-earth ions prepared by the melt-quenching process [15]. We report the precipitation of spatially selective glass-ceramics containing SrF_2 nanocrystals doped with Dy^{3+} and Yb^{3+} ions, as well as the enhancements of down-conversion and upconversion emissions of Dy^{3+} ions. The optimized conditions were achieved for emission enhancement by controlling the power and scan speed of the laser beam.

2. Experimental

The nominal composition of precursor glass (as-melted) used in this study was $40SiO_2$-$12Al_2O_3$-$23SrF_2$-24LiF-$0.5Yb_2O_3$-$0.5Dy_2O_3$ (mol.%). The raw materials used for preparation were fine grained powders from high purity (3 N) commercial chemicals. The starting batches were

thoroughly mixed and melted at 1450 °C for 1 h in a covered platinum crucible under normal atmosphere. The melt was then cast into an iron mold prior to being annealed at 530 °C for 10 h, in order to release inner stress. Finally, the glass was cut and polished into the glass samples with a thickness of 1 mm. For thermal treatment to induce SrF_2 nanocrystals, we used a CO_2 laser employing various powers ranging from 0.9 to 1.3 W and scan speeds ranging from 0.1 to 0.3 mm/s.

The samples studied here are glass-ceramics prepared by the laser treatments of 1.3W_0.3 mm/s, 1.3 W_0.2 mm/s, 1.3W_0.1 mm/s, or 0.9W_0.3 mm/s, denoted by G1, G2, G3, and G4, respectively. The laser beam was focused on the surface of the glass. The selective area had a ~100 μm diameter. We employed micro-x-ray diffraction (μ-XRD, D/MAX RAPID-S) analysis for the irradiated regions in order to examine the formation of SrF_2 crystals. Furthermore, in order to clarify the size and crystallization of nanocrystals, we performed transmission electron microscopy (TEM, Titan G2 60-300) and EDS (Energy Dispersive Spectroscopy) analysis for the laser-treated surface. Photoluminescence and upconversion emission spectra for Dy^{3+} ions under 365 nm LED and 980 nm LD excitations were measured respectively for both unirradiated and irradiated glass area in order to confirm whether the ions are doped inside the nanocrystals.

3. Results and discussion

Micro- x-ray diffraction patterns of the glasses exposed to CO_2 laser with 0.3 mm/s scan speed and 1.3 W and 0.9 W powers (GC1 and GC4) are shown in Fig. 1, indicating the diffraction pattern of SrF_2 crystalline phase [21]. The XRD peaks were observed only in the CO_2 laser exposed area. The sharp and relatively intense peaks of the exposed area of glass can easily be assigned to the diffractions from the (111), (200), (220), (311), (222), (400), (331), and (420) planes of spinel SrF_2 phase (JCPDS No. 06-0262). This implies that the treated volume of the glass by CO_2 laser irradiation was changed into glass-ceramic. Although the x-ray beam has a slightly smaller size than the laser beam of ~100 μm on the surface and penetrates through the sample, the laser thermal treatment is only effective on the surface because of the low thermal conductivity of glass.

The average size of the nanocrystals has been calculated using the Scherrer formula [22] for XRD data of the lattice plane (hkl), using the full width at half maximum β, diffraction angle θ, and x-ray wavelength λ,

$$D(hkl) = \frac{0.9\lambda}{\beta\cos\theta} \tag{1}$$

The sizes of nanocrystals obtained with GC1 and GC4 are estimated at 15 and 13 nm, respectively. This implies that the laser thermal energy increases the sizes of the nanocrystals. The increase of XRD peaks indicates the increased density of nanocrystals in the glass. This implies that with increase in laser exposure time nucleation continues and the volume concentration of crystalline SrF_2 increases. In the TEM image of Fig. 2(a), the round-shaped nanocrystal with a size of ~300 nm can observed, with the background corresponding to the glassy phase. It is not a single domain, but seems to consist of many nanocrystals. In order to confirm the crystalline phases, high-resolution transmission electron microscopy (HRTEM) was employed. The HRTEM image in Fig. 2(b), which was collected by focusing an electron beam on the dark domain of Fig. 2(a), shows a well-defined lattice structure of the SrF_2 crystal with random orientation. The average size of nanocrystals is about 8 nm, which is smaller than the estimated value obtained from the Scherrer equation. A large temperature gradient in the laser-treated region originates from the inhomogeneous thermal distribution due to the use of the Gaussian laser beam. It produces various sizes of nanocrystals depending on the position [23]. Thus, the CO_2 laser irradiation energy was not sufficient to grow large nanoparticles of a single domain. Thus, we suggest that the larger crystallite size in Fig. 2(a) is due to the aggregation of nanocrystals.

The spatial distributions of Sr, F, Dy, and Yb ions are verified by EDS, as shown in Fig. 2(c)–(f), respectively. Fig. 2(c) and (d) show a large portion of Sr and F ions in the crystal displayed in Fig. 2(a), revealing the formation of SrF_2 crystal. It has been reported that the real fluorine concentration is somewhat lower than the nominal one, owing to the volatility of fluoride components at high temperature and the escape of fluorine from the melt [24]. Thus, a relatively low concentration of fluorine ions is expected as compared their initial doping concentration. Dy and Yb ions are located in the SrF_2 crystal domain as well as on the surface of the crystallites. The absorption spectrum of the glass in Fig. 3 shows the absorption peaks of Dy^{3+} and Yb^{3+} ions, implying that both ions have the absorption at 980 nm.

The emission spectra in Fig. 4 are obtained under 365 nm excitation reaching the $^6P_{5/2}$ state of Dy^{3+} ion. Laser heating could help to populate the $^6P_{7/2}$ state. The dominant blue (482 nm) and yellow (574 nm) bands are attributed to the transitions from the excited state of $^4F_{9/2}$ to the lower states of $^6H_{15/2}$ and $^6H_{13/2}$, respectively. Beyond that, we also observed weak emissions at 409, 418, 430, 445, 456, 660, and 725 nm, which correspond to $^6P_{7/2}$–$^6H_{13/2}$, $^6P_{5/2}$–$^6H_{11/2}$, $^4G_{11/2}$–$^6H_{15/2}$, $^4I_{13/2}$–$^6H_{13/2}$, $^4I_{15/2}$–$^6H_{15/2}$, $^4F_{9/2}$–$^6H_{11/2}$, and $^4F_{9/2}$–$^6H_{9/2}$ transitions from the glass-ceramics. Most of these violet emissions have not been reported under ultraviolet excitation for Dy^{3+} and Yb^{3+} co-doped glass or phosphors [25,26] because of the nonradiative relaxation from the $^6P_{5/2}$ and $^6P_{7/2}$ excited state to the $^4F_{9/2}$ state. This is further evidence for the emissions from nanocrystals doped with Dy^{3+} ions. The relatively strong blue and yellow emission intensities increased with laser exposure in the glass-ceramics (from GC1 to GC3). The GC3 shows more than 17 times enhancement of the overall visible emissions as compared to those from the untreated glass. The increase in emission intensities with laser exposure is evidence for the formation of Dy^{3+}-doped SrF_2 nanocrystals which causes lowering of nonradiative relaxation of rare-earth ions incorporated into SrF_2 nanocrystals with very low phonon energy [9]. In addition, energy transfer can effectively occur among the neighboring Dy^{3+} ions inside SrF_2 nanocrystals because of the shorter distance between doped ions. The blue emission of the $^4F_{9/2}$–$^6H_{15/2}$ transition is mainly magnetically allowed and insensitive to the crystal field around the ions, whereas the yellow emission of $^4F_{9/2}$–$^6H_{13/2}$ transition is a forced electric dipole transition and allowed only at low symmetries with no inversion center. Dy^{3+} ion can be incorporated in the interior of SrF_2 nanocrystals because the radius of Dy^{3+} ion is smaller than that of SrF_2. However, its site
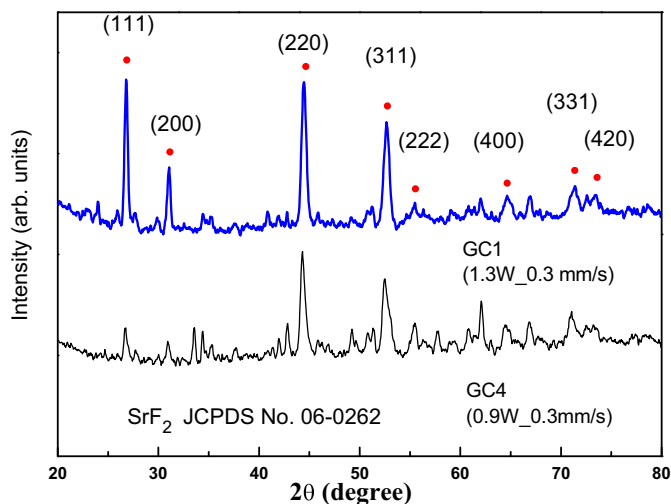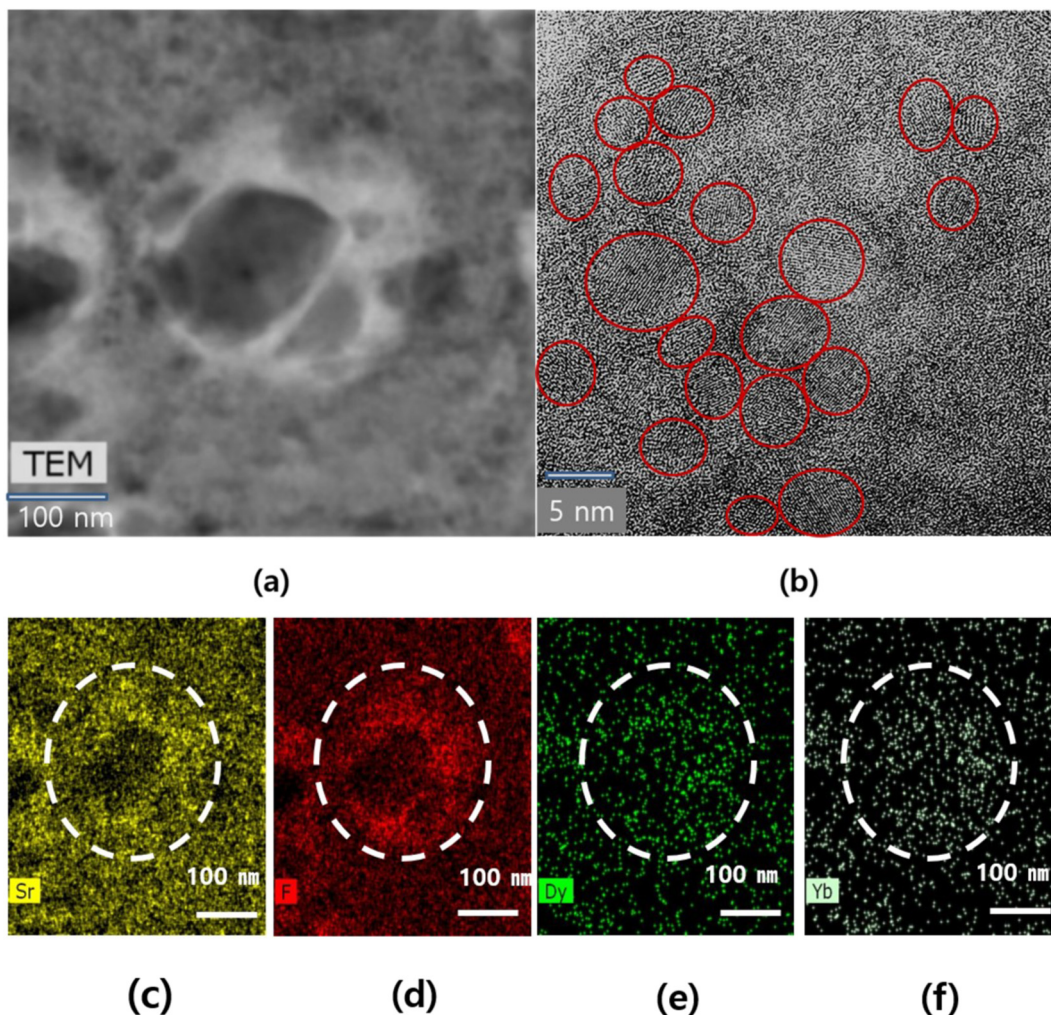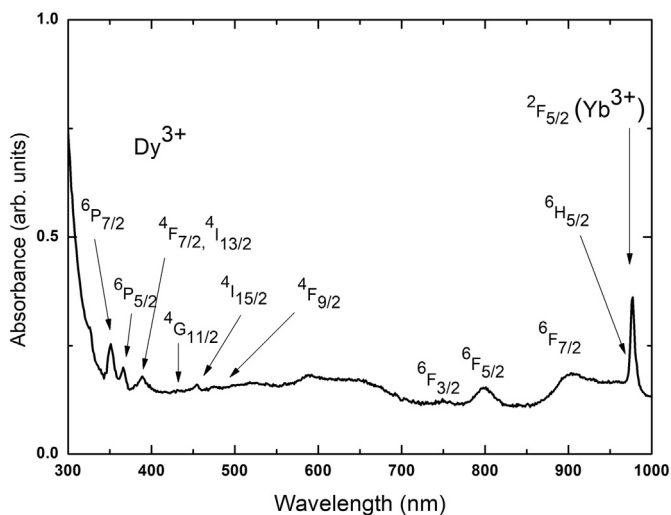

Fig. 1. XRD patterns of SrF_2 nanocrystals precipitated in glass by CO_2 laser irradiation with the power of 1.3 and 0.9 W (GC1 and GC4) and the same scan speed of 0.3 mm/s.
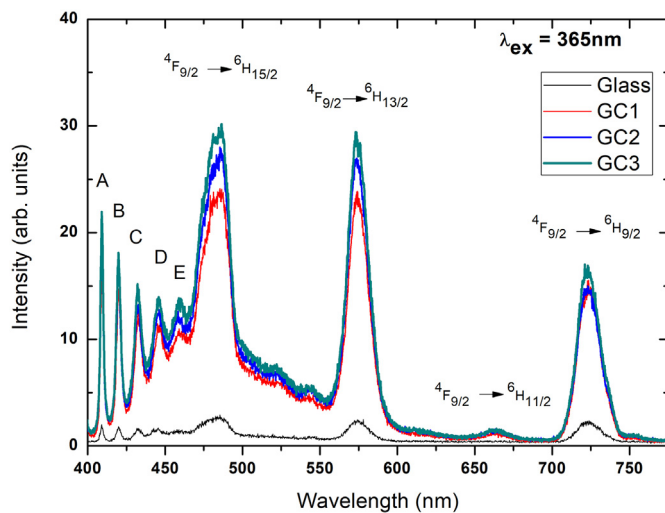
Fig. 2. (a) TEM micrograph of crystallites, (b) HRTEM image of crystalline area, and (c-f) EDS element maps of Sr, F, Dy, and Yb ions in the area of (a) in the GC3 precipitated by CO_2 laser irradiation.

Fig. 3. Absorption spectrum of the as-made glass.

Fig. 4. Down-conversion emission spectra of Dy^{3+} obtained under 365 nm excitation of glass and glass-ceramics. The emissions of A, B, C, D, and E indicate the transitions of $^6P_{7/2}$–$^6H_{13/2}$, $^6P_{5/2}$–$^6H_{11/2}$, $^4G_{11/2}$–$^6H_{15/2}$, $^4I_{13/2}$–$^6H_{13/2}$, and $^4I_{15/2}$–$^6H_{15/2}$ respectively.

symmetry regarding the crystal field may not have inversion symmetry due to a charge compensator which is needed for charge balance, as is the case in CaF_2 [27]. Furthermore, some Dy^{3+} ions can be populated on the surface of SrF_2 nanocrystals, resulting in low site symmetry.

Thus, the yellow emission is stronger than the blue emission. The energy level diagram in Fig. 5 shows the possible transitions for the
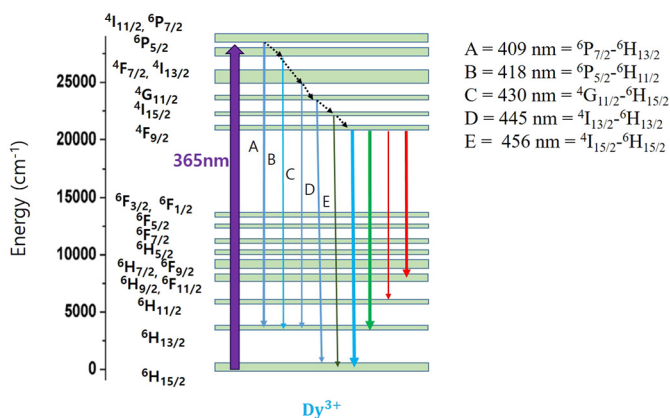
Fig. 5. The energy level diagram to explain the possible transitions for the observed emissions under 365 nm excitation.
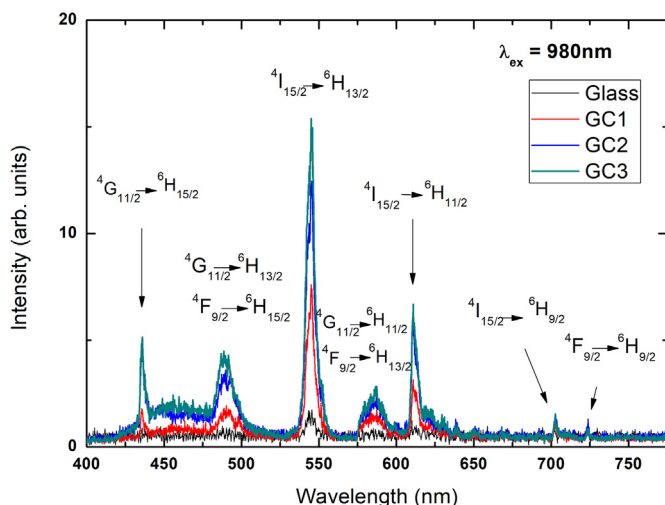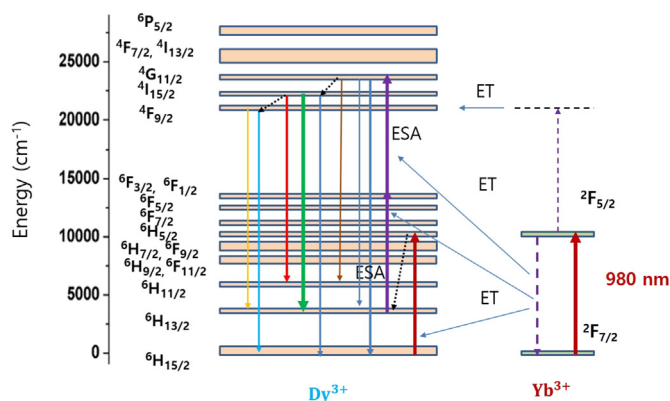

Fig. 7. Energy level diagram of Dy^{3+} and Yb^{3+} ions explaining the main energy transfer processes of Dy^{3+}-Yb^{3+} ions and excited state absorptions in Dy^{3+} ions under 980 nm excitation (ESA: excited state absorption; ET: energy transfer; dot lines: nonradiative relaxations).

Fig. 6. Upconversion emission spectra of Dy^{3+} obtained under 980 nm excitation of glass and glass-ceramics.

observed emissions under 365 nm excitation.

Upconversion emission spectra of the glass-ceramics obtained under the excitation of the $^2F_{5/2}$ state of Yb^{3+} at 980 nm are shown in Fig. 6. The GC3 produced much stronger visible upconversion emission from the surface, as compared to the as-made glass. The strong upconversion emission from the limited surface region is further evidence for the effective nanocrystal formation. Through the incorporation of Dy^{3+} and Yb^{3+} ions into the SrF_2 crystal phases, the energy transfers can also effectively occur among the neighboring Dy^{3+}–Yb^{3+} ions, because of the shorter distance between doped ions inside nanocrystals. It is well known that the incorporation of Yb^{3+} ions into rare-earth ion doped optical materials is beneficial for infrared-to-visible upconversion emission because Yb^{3+} ions have a strong and broad absorption band around 980 nm. The feature of the upconversion emission spectra is much different from that of the down-conversion spectra in Fig. 4. First, the strongest emission at 542 nm corresponds to the $^4I_{15/2}$–$^6H_{13/2}$ transition. The other emissions of the $^4I_{15/2}$–$^6H_{15/2}$ and $^4I_{15/2}$–$^6H_{11/2}$ transitions also appear at 456 and 610 nm. As shown in Fig. 7, the 980 nm excitation populates both the $^6H_5$ (Dy^{3+}) and $^2F_{5/2}$ (Yb^{3+}) levels, although the $^6H_5$ has a very weak absorption at 980 nm. The electrons reached to the $^6H_{13/2}$ level by nonradiative relaxation from the $^6H_5$ can absorb both the 980 nm pump photons and the transferred energy from the $^2F_{5/2}$ level of Yb^{3+} ion, reaching the $^6F_{1/2}$ level of Dy^{3+} ion. Another absorption process from the $^6F_1$ to the $^4G_{11/2}$, followed by weak emissions of the $^4G_{11/2} \longrightarrow {}^6H_{15/2},$ $^6H_{13/2}$ and $^6H_{11/2}$

transitions. The rapid relaxation from the $^4G_{11/2}$ to $^4I_{15/2}$ level is followed by several emissions from the $^4I_{15/2}$ level, showing the relatively strong emission of the $^4I_{15/2}$–$^6H_{13/2}$ transition. Much of the enhanced emission is due to the crystal environment of Dy^{3+} ions. The non-radiative relaxation from the $^4I_{15/2}$ to $^4F_{9/2}$ level enables the well-known blue and yellow emissions of the $^4F_{9/2}$–$^6H_{15/2}$ and $^4F_{9/2}$–$^6H_{13/2}$ transitions. However, the yellow emission (574 nm) appears to be weaker than the blue emission (483 nm), which differs from the down-conversion in Fig. 4. We must consider the cooperative upconversion emission at 490 nm [28] to explain the difference. The virtual state of Yb^{3+} ions reached by two-step excitation via Yb^{3+}-Yb^{3+} energy transfer produces 490 nm emission, which is transferred to Dy^{3+} ions and overlapped with the blue emission from the $^4F_{9/2}$ level. This implies that the Dy^{3+} site still has non-inversion symmetry.

The band-width of the strongest emission at 542 nm is about 6 nm, which is one-third of the band-width of the yellow or blue band in the down-conversion emission in Fig. 4. The narrower band-width implies that the excited-state absorption and energy transfer are effective only for some subgroups matching the excitation of 980 nm among inhomogeneously distributed sites of Dy^{3+} and Yb^{3+} ions. The main energy transfer channels between Yb^{3+} and Dy^{3+} ions and two excited state absorptions in Dy^{3+} ions are suggested for the blue, green, yellow, and red emissions as displayed in Fig. 7.

4. Conclusions

Dy^{3+}/Yb^{3+} co-doped glass ceramic containing SrF_2 nanocrystals has been prepared by the CO_2 laser surface treatment of 40SiO$_2$-12Al$_2$O$_3$-23SrF$_2$-24LiF-0.5Yb$_2$O$_3$-0.5Dy$_2$O$_3$ glass. In this glass ceramic, SrF_2 nanocrystals are embedded in the glass matrix and Dy^{3+}/Yb^{3+} ions are incorporated into the SrF_2 nanocrystalline phase. The Dy^{3+} ions in SrF_2 nanocrystals exhibit much enhanced emission intensity, including new emission bands in the 400–460 nm range along with well-known blue and yellow emissions from the $^4F_{9/2}$ level under 365 nm excitation. The upconversion visible emission also showed stronger intensity than the precursor glass under 980 nm excitation, including 430–460 nm blue emission and strong green emission from the $^4I_{15/2}$ level. The substantial enhancement of the emission in glass-ceramics indicates the proper incorporation of Dy^{3+} and Yb^{3+} ions into a nanocrystalline environment. Detailed upconversion mechanisms for the observed emissions are suggested based on the observed emissions. The results may be applied to the patterned white-light imaging technology on the Dy^{3+}-Yb^{3+} co-doped thin glass.

Acknowledgement

References

[1] Adam J. Stevenson, Hélène Serier-Brault, Patrick Gredin, Michel Mortier, Fluoride materials for optical applications: single crystals, ceramics, glasses, and glass–ceramics, J. Fluor. Chem. 132 (2011) 1165–1173.

[2] Matthew J. Dejneka, The luminescence and structure of novel transparent oxy-fluoride glass-ceramics, J. Non-Cryst. Solids 239 (1998) 149–155.

[3] F. Lahoz, I.R. Martin, J. Mendez-Ramos, P. Nunez, Dopant distribution in a Tm^{3+}–Yb^{3+} codoped silica based glass ceramic: an infrared-laser induced upconversion study, J. Chem. Phys. 120 (2004) 6180–6190.

[4] Y. Wang, J. Ohwaki, New transparent vitroceramics codoped with Er^{3+} and Yb^{3+} for efficient frequency upconversion, Appl. Phys. Lett. 63 (1993) 3268–3270.

[5] S. Gonzalez-Perez, I.R. Martin, P. Haro-Gonzalez, Local devitrification on an oxy-fluoride glass doped with Ho^{3+} ions under argon laser irradiation, Opt. Mater. 31 (2009) 1373–1375.

[6] J.-P.R. Wells, R.J. Reeves, Upconversion fluorescence of Eu^{3+} doped alkaline earth fluoride crystals, J. Lumin. 66 (67) (2004) 219–223.

[7] Xvsheng Qiao, Xianping Fan, Jin Wang, Minquan Wang, Luminescence behavior of Er^{3+} in glass-ceramics containing CaF_2 nanocrystals, J. Non-Cryst. Solids 351 (2005) 357–363.

[8] Radosław Lisiecki, Elz̄bieta Augustyn, Witold Ryba-Romanowski, Michal Zelechower, Er-doped and Er, Yb co-doped oxyfluoride glasses and glass–ceramics, structural and optical properties, Opt. Mater. 33 (2011) 1630–1637.

[9] L.A. Riseberg, H.W. Moos, Multiphonon orbit-lattice relaxation of excited states of rare-earth ions in crystals, Phys. Rev. 174 (1968) 429–438.

[10] M. Secu, C.E. Secu, S. Polosan, G. Aldica, C. Ghica, Crystallization and spectroscopic properties of Eu-doped CaF_2 nanocrystals in transparent oxyfluoride glass-ceramics, J. Non-Cryst. Solids 355 (2009) 1869–1872.

[11] S.E. Mekhlouf, A. Boukenter, M. Ferrari, F. Goutaland, N. Ollier, Y. Ouerdane, UV assisted local crystallization in Er^{3+} doped oxy-fluoride glass, J. Non-Cryst. Solids 353 (2007) 506–509.

[12] M. Kusatsugu, M. Kanno, T. Honma, T. Komatsu, Spatially selected synthesis of LaF_3 and Er^{3+}-doped CaF_2 crystals in oxyfluoride glasses by laser-induced crystallization, J. Solid State Chem. 181 (2008) 1176–1183.

[13] V.P. Veiko, G.K. Kostyuk, N.V. Nikonorov, E.B. Yakovlev, Structural phase modification of glass-ceramic materials under CO_2 laser irradiation, Bull. Russ. Acad. Sci. Phys. 72 (2008) 167–171.

[14] Daqin Chen, Yuansheng Wang, En Ma, Yunlong Yu, Feng Liu, Partition, luminescence and energy transfer of Er^{3+}/Yb^{3+} ions in oxyfluoride glass ceramic containing CaF_2 nano-crystals, Opt. Mater. 29 (2007) 1693–1699.

[15] Su-A Song, Dong-Seon Kim, Hong-Myeong Jeong, Ki-Soo Lim, Upconversion in Nd–Tm–Yb triply doped oxyfluoride glass–ceramics containing CaF_2 nanocrystals, J. Lumin. 152 (2014) 75–78.

[16] A. Santana-Alonso, J. Méndez-Ramos, A.C. Yanes, J. del-Castillo, V.D. Rodríguez, Up-conversion in sol–gel derived nano-glass–ceramics comprising $NaYF_4$ nano-crystals doped with Yb^{3+}, Ho^{3+} and Tm^{3+}, Opt. Mater. 32 (2010) 903–908.

[17] E.V. Vilejshikova, P.A. Loiko, G.E. Rachkovskaya, G.B. Zakharevich, K.V. Yumashev, Up-conversion luminescence in oxyfluoride glass-ceramics with PbF_2:(Yb^{3+}, Eu^{3+}, RE^{3+}) (RE = Tm, Ho, or Er) nanocrystals, J. Appl. Spectrosc. 83 (2016) 723–729.

[18] Qiu Jianbei, Jiao Qing, Zhou Dacheng, Yang Zhengwen, Recent progress on up-conversion luminescence enhancement in rare-earth doped transparent glass-ceramics, J. Rare Earths 34 (2016) 341–367.

[19] Linlin Liu YanminYang, Shuzhen Cain, Fuyun Jiao, Chao Mi, Xianyuan Su, Jiao Zhang, Fang Yu, Xiaodong Li, Ziqiang Li, Up-conversion luminescence and near-infrared quantum cutting in Dy^{3+}, Yb^{3+} co-doped $BaGd_2ZnO_5$ nanocrystal, J. Lumin. 146 (2014) 284–287.

[20] Hao Dong, Ling-Dong Sun, Chun-Hua Yan, Energy transfer in lanthanide upconversion studies for extended optical applications, Chem. Soc. Rev. 44 (2015) 1608–1634.

[21] Weiwei Li, Bingchu Mei, Jinghong Song, Zhe Wang, Fabrication and optical property of highly transparent SrF_2 ceramic, Mater. Lett. 159 (2015) 210–212.

[22] A.L. Patterson, The Scherrer formula for x-ray particle size determination, Phys. Rev. 56 (1939) 978–981.

[23] Masaki Kanno, Tsuyoshi Honma, Takayuki Komatsuw, Two-dimensional mapping of Er^{3+} photoluminescence in CaF_2 crystal lines patterned by lasers in oxyfluoride glass, J. Am. Ceram. Soc. 92 (2009) 825–829.

[24] Mohammad Hassan Imanieh, Bijan Eftekhari Yekta, V. Marghussian, Saeed Shakhesi, I.R. Martín, Crystallization of nano calcium fluoride in CaF_2-Al_2O_3-SiO_2 system, Solid State Sci. 17 (2013) 76–82.

[25] O. Ravi, C. Madhukar Reddy, B. Sudhakar Reddy, B. Deva Prasad Raju, Judd–Ofelt analysis and spectral properties of Dy^{3+} ions doped niobium containing tellurium calcium zinc borate glasses, Opt. Commun. 312 (2014) 263–268.

[26] Ying Fang, Weidong Zhuang, Yunsheng Hua, Xinyu Ye, Xiaowei Huang, Luminescent properties of Dy^{3+} ion in $Ca_8Mg(SiO_4)_4Cl_2$, J. Alloys Compd. 455 (2008) 420–423.

[27] Qun Luo, Xvsheng Qiao, Xianping Fan, Shiqi Liu, Hui Yang, Xianghua Zhang, Reduction and luminescence of europium ions in glass ceramics containing $SrF2$ nanocrystals, J. Non-Cryst. Solids 354 (2008) 4691–4694.

[28] Xiuhong Pan, Jianding Yu, Yan Liu, Shinichi Yoda, Minghui Zhang, Fei Ai, Fei Jin, Huimei Yu, Weiqing Jin, Infrared to visible upconversion luminescence in Er^{3+}/Yb^{3+} doped titanate glass prepared by containerless processing, J. Lumin. 132 (2012) 1025–1029.

ACCEPTED MANUSCRIPT

Neodymium-doped magnesium phosphate glasses for NIR laser applications at 1.05 μm

Neodymium-doped magnesium based phosphate glasses for NIR laser applications at 1.05 μm

R.N.A.Prasad[1], R. Praveena[2,*], N. Vijaya[3], P. Babu[4], N. Krishna Mohan[1]

[1]Department of Physics, Akkineni Nageswara Rao College, Gudivada – 521 301, India.
[2]Department of Physics, GVP College of Engineering (A), Visakhapatnam – 530 048, India.
[3]Department of Physics, Chalapathi Institute of Engineering and Technology, Guntur- 522 034, India.
[4]Department of Physics, Government Degree College, Palamaner – 517 408, India.
*Corresponding author E-mail: praveena@gvpce.ac.in

Abstract

Neodymium-doped magnesium phosphate glasses with various concentrations of active ion are prepared by melt quenching method and characterized their spectroscopic properties using absorption and emission spectra and decay measurements. Using the Judd-Ofelt analysis, various spectroscopic parameters such as intensity parameters (Ω_λ, $\lambda = 2,4,6$), radiative transition probabilities, branching ratios and radiative lifetimes are evaluated. The near infrared emission spectra are measured by exciting the samples at 808 nm. In the emission spectra, maximum intensity is observed at 1054 nm which corresponds to the $^4F_{3/2} \rightarrow {}^4F_{11/2}$ transition of Nd^{3+} ion. The branching ratio, band width and stimulated emission cross-section for the above transition are found to be 0.51, 25 nm and 3.26×10^{-20} cm^2, respectively. The decay curves for the $^4F_{3/2}$ fluorescent level are single exponential nature with decreasing lifetime from 346 to 57 μs with increase in Nd^{3+} concentration from 0.05 to 4.0 mol%. The results suggest that PMN glasses could be useful as infrared laser sources at around 1.05 μm.

Key words: Neodymium, phosphate glass, Judd-Ofelt analysis, spectroscopic properties, NIR luminescence

1. Introduction

Lanthanide (Ln^{3+}) doped glasses are quite preferable in the scientific community due to their several technological applications as solid state lasers, waveguide lasers, light emitting diodes, flat panel technologies, sensors, optical amplifiers, optical detectors, optical fibers, opto-electronic and photonic devices [1-5]. Among the Ln^{3+} ions, Nd^{3+} ion has become one of the popular active ion for developing high power terawatt solid state lasers at 1.05 μm wavelength that corresponds to the transition $^4F_{3/2} \rightarrow {}^4I_{11/2}$ of Nd^{3+} ion. These lasers are useful in the fields of communication, radar, high energy weapon, medical, etc. [6-8]. Apart from this important emission at 1.05 μm, Nd^{3+} ion also exhibit laser transitions $^4F_{3/2} \rightarrow {}^4I_{9/2}$ and $^4I_{13/2}$, that gives raise to luminescence bands at ~ 0.9 and 1.3 μm, respectively. The laser band at 1.3 μm is useful for O-band optical amplifiers [9] while the laser band at 0.9 μm is useful to manufacture a device that emits blue light through the monolithic integration of laser emission [10]. Nd^{3+}-doped materials are also considered to be next generation near infra red (NIR) emitting scintillators [11]. In addition to these well-known NIR emissions, the upconversion (UC) emission from NIR to visible is also possible in the case of Nd^{3+}-doped glasses [12,13]. For example, infrared to visible UC in the regions of blue, green and orange has been observed from the $^4G_{7/2}$ level of Nd^{3+} ion in ZnO-Li_2O-Na_2O-P_2O_5 glasses [14]. Jimenez and Sendova have reported lasing action in the near ultra violet region in the Cu, Nd:co-doped phosphate glasses [15].

It is obvious that, optical properties of Nd^{3+} ion depend on the concentration of active ion and the composition of glass [16,17]. Hence, finding a suitable glass matrix that brings together advantageous of glass forming ability and excellent optical properties become the research hotspot in the areas of Lasers and fiber amplifiers. In this connection, phosphate glasses are more attractive because of their peculiar properties. New phosphate glasses are being developed enormously because of their excellent characteristics including wide range of the thermal expansion coefficient, low melting, high electrical conductivity, low cost and softening temperatures [18,19]. These glasses are also important due to their structural versatility to allow several cation and/or anion exchanges. Such type of properties make them worth-full candidates for laser hosts, fast ion conducting material, glass to metal seals and biocompatible materials. Addition of modifier oxides such as MgO into the glass matrix improves the chemical durability of the phosphate glasses by depolymerising the long phosphate chains as well as replaces the P-O-P bonds by more chemically stable bonds by forming the non-bridging oxygen ions [20]. Presence of MgO also tightens the glass network

2

compared to CaO due to its high ionic field strength values ($\sim$ 5 Å) and thereby enhances the glass mechanical strength and density [21]. Magnesium phosphate glasses are attractive due to their low density, high viscosity, high polarizability and high field intensity [22]. It also enhances the luminescence intensity [23,24].

In view of the above advantageous, Nd^{3+}-doped phosphate glasses have been prepared and characterised to realize their concentration dependent optical and laser properties. In addition, standard Judd-Ofelt (JO) analysis has been performed to calculate the JO parameters, line strength, radiative and non-radiative decay properties and efficiency of the Nd^{3+} ion in the present glass matrix. Specifically, luminescence properties of the phosphate glasses with the MgO as single modifier have been explored, which have not been reported so far to the best of authors' knowledge.

2. Experimental Methods

2.1 Preparation of glasses

Nd^{3+}-doped magnesium phosphate (PMN) glasses with the composition (50-x/2) P_2O_5 + (50-x/2) MgO + x Nd_2O_3 (where x = 0.05, 0.1, 0.5, 1.0, 2.0 and 4.0 (mol%)) were prepared by the conventional melt quenching method similar to that described in our previous paper [25]. Highest pure chemicals (Sigma-Aldrich) of magnesium metaphosphate ($Mg(PO_3)_2$) and neodymium oxide (Nd_2O_3) were used as starting materials. The glass samples were labelled as PMN005, PMN01, PMN05, PMN10, PMN20 and PMN40, for 0.05, 0.1, 0.5, 1.0, 2.0 and 4.0 mol% of Nd_2O_3, respectively.

2.2. Characterization of glasses

The optical path lengths of the PMN glasses were measured by digital Vernier callipers and refractive indices were meausred by using Abbe refractometer at the wavelength of 589.3 nm. Densities of all the glasses were measured with Archimedes' drainage method in distilled water. The physical properties such as path length, density, refractive index and concentration of Nd^{3+} ions of the PMN glasses are given Table 1. The UV-visible-NIR absorption spectra of the PMN glasses were measured on an Elico SL210 double beam spectrophotometer with a spectral repeatability of $\pm$ 0.2 nm. The NIR emission spectra and decay curves were recorded using Edinburgh UV−VIS−NIR (FLS 980) spectrophotometer using 808 nm pulsed laser diode as the excitation source. All the measurements were made at room temperature.

3

3. Results and Discussion

3.1 Optical absorption and covalency of Nd-O bond

Physical properties of Nd^{3+}-doped PMN glasses of the present study such as optical path length, density, concentration and refractive index are presented in Table 1. As can be seen and as expected, density, concentration of Nd^{3+} ions and refractive index increases with increase in concentration of Nd^{3+} ions. Figure 1 shows the UV-visible-NIR absorption spectra of PMN glasses measured in the wavelength range of 300-1000 nm which is similar to the reported results in the literature [26,27]. The observed bands in the absorption spectrum corresponds to the $4f^3 \rightarrow 4f^3$ transitions from the $^4I_{9/2}$ ground state to different excited states of Nd^{3+} ion in the glass matrix. As can be seen the band at 808 nm is very intense, indicating that this glass can be effectively excited at this wavelength. The intrinsic absorption cut-off sideband of the present glass is observed at 325 nm below which no absorption band can be seen. In addition, intensity of the transition $^4I_{9/2} \rightarrow {}^4G_{5/2}, {}^2G_{7/2}$ observed at 582 nm is very high since it is a hypersensitive transition (HST) following the selection rule $|\Delta S| = 0$; $|\Delta L| \leq$ 2 and $|\Delta J| \leq 2$. Generally, HSTs are very sensitive to the local field around the Nd^{3+} ion in the glass host. The nature of bonding between the Nd^{3+} ion and the ligand can be known from the values of Nephelauxetic ratio (β) and bonding parameter (δ). The formula for β is given by [28],

$$\beta = \frac{v_c}{v_a} \tag{1}$$

where 'v_c' is the energy of a specific absorption transition of the Nd^{3+} ion in the given glass host and 'v_a' is the energy of the same transition in the aqua solution. Energy levels of the Nd^{3+} ions in the glass host and the aquo-ion were assigned based on the reports of Carnall et al. [29].

The bonding parameter δ can be evaluated from the average values of β (referred as $\bar{\beta}$), using the below expression,

$$\delta = [\frac{1-\bar{\beta}}{\bar{\beta}}] \times 100 \tag{2}$$

the positive and negative values of δ indicate the covalent and ionic nature of the metal-ligand bond, respectively [30]. In the present case the positive value of δ (0.6036) indicates that the Nd^{3+}–ligand bond in the PMN10 glass is covalent nature.

The Judd-Ofelt (JO) [31,32] analysis can be used to determine JO parameters and radiative properties of Ln^{3+} ions in different host materials like glasses and crystals. Reader is suggested to refer our earlier papers for the necessary theory [33,34]. Table 2 presents the

4

experimental (f_{exp}) and calculated (f_{cal}) oscillator strengths of the absorption bands along with their peak positions (λ_P) of PMN10 glass. Least square fit between the f_{exp} and f_{cal} has been used to obtain the three JO parameters, Ω_λ ($\lambda = 2,4,6$). The obtained JO parameters ($\times 10^{-20}$ cm^2) for the PMN10 glass are $\Omega_2 = 2.55$, $\Omega_4 = 3.74$, $\Omega_6 = 4.12$ with the root mean square error of about 0.79×10^{-6}, which confirms the accuracy of calculation. These errors in fitting arise due to the difference in the reduced matrix elements and absorption spectrum. Among these JO parameters, Ω_2 represent the covalency of metal-ligand bond and depends on the intensity of HST. It also represents the asymmetry in the surroundings of Nd^{3+} ions in the glass host. The other two parameters, Ω_4 and Ω_6 represent the viscosity and rigidity of the glass matrix, respectively [35]. Table 3 presents Ω_λ values in various phosphate glasses [14,25,26,33,34,36-47] for comparison (here we excluded fluoro-phosphate glasses). In this table the composition of the glasses are presented in the increasing order of the Ω_2. As can be seen from Table 3, magnitude of Ω_2 for the present PMN10 glass is smaller than those of all other glasses including commercial laser glasses LG-750, LHG-8, LG-770 and LHG-80 [36], except CBP [38], ZLNP [14], PCBS [40] and PABKLiNbLa [41] glasses. Therefore, the smaller value of Ω_2 indicates moderate covalence of the Nd^{3+}-ligand bond [35] and lower asymmetry or higher symmetry around Nd^{3+} ions in the PMN10 glass. The covalency nature of the metal-ligand bond is also consistent with the result obtained from the Nephelauxetic effect. Also, the JO parameters in the PMN10 glass follows the trend as $\Omega_6 > \Omega_4 > \Omega_2$. This trend is similar to that of commercial laser glasses [36]. Further, from Table 3, the effect of modifier is more on the environment of Nd^{3+} ions in the phosphate glass which in turn determines most of their optical properties. From the values of Ω_2 given in Table 3, it is observed that the addition of modifiers such as $Al_2O_3/K_2O/TiO_2$ results in increase in the value of Ω_2 in phosphate glasses which in turn increases the covelency of the metal-ligand bond and asymmetry around Nd^{3+} ions.

One of the important laser parameters is spectroscopic quality factor (χ) which is given by the ratio of Ω_4/Ω_6. This parameter is useful to estimate the intrinsic intensity of the $^4F_{3/2} \rightarrow {}^4I_{11/2}$ transition [48]. In the case of $Nd^{3+}:{}^4F_{3/2}$ transitions, the reduced matrix elements $\langle \| U^2 \| \rangle$ are zero, hence stimulated emission parameters are directly influenced by the Ω_4 and Ω_6 but not the Ω_2. Previous reports suggest that if χ is less than 1, the intensity of $^4F_{3/2} \rightarrow {}^4I_{11/2}$ laser transition will be higher than that of the $^4F_{3/2} \rightarrow {}^4I_{9/2}$ transition in the glass host. Additionally, larger χ value indicates a stronger emission at 1.06 μm ($^4F_{3/2} \rightarrow {}^4I_{11/2}$). In the present work the χ value is 0.91 (less than 1) indicating that $^4F_{3/2} \rightarrow {}^4I_{11/2}$ is the dominant

5

lasing transition. The present χ value is compared with those of phosphate glasses shown in Table 3. As can be seen from Table 3, the χ value is similar to PZAL [45] and commercial LHG-8 [36], LHG-80 [36] glasses, smaller than PANK [42], PBN [25], PAN [46] and PAKBPb [39] glasses and higher than that of the remaining glasses. But in the PBN, PAN and PAKBPb glasses χ value is even more than 1, hence these are not suitable for lasers at 1.06 μm. Figure 2 shows the variation of χ value in different phosphate glasses in which the glass composition is arranged in the increasing order of χ value. It is worth noting that the magnitude of χ value in the MgO based phosphate glasses varies in the order MgTP < PKMAN < LG-770 < PMN glasses. This could be due to the higher symmetry around the Nd^{3+} ions in PMN glass which varies in the order PMN > LG-770 > PKMAN > MgTP glasses. Therefore, the present PMN glass can be used as a diode-pump 1.05 μm laser.

Radiative properties such as radiative transition probability (A_R), radiative lifetime ($\tau_R = 1/\Sigma A_R$) of the $^4F_{3/2}$ level and branching ratios (β_R) are evaluated using JO parameters [34], and are also reported in Table 4. Some of these values are compared with those of the other phosphate glasses in Table 3.

3.2. NIR Luminance properties

Nd^{3+} ions get excited from the ground state ($^4I_{9/2}$) to the excited state ($^4F_{5/2}$) with the 808 nm excitation, which are then relaxed to the $^4F_{3/2}$ metastable state non-radiatively. NIR luminescence spectra of Nd^{3+}-doped PMN glasses are shown in Fig. 3. Three discrete emission bands at 876, 1054 and 1323 nm are observed, corresponding to the $^4F_{3/2} \rightarrow ^4I_{9/2}$, $^4I_{11/2}$ and $^4I_{13/2}$ transitions of Nd^{3+} ion, respectively. As expected, band corresponds to the $^4F_{3/2} \rightarrow ^4I_{11/2}$ transition at 1.05 μm is the sharpest and strongest compared to other two transitions. The luminescence intensities of these bands in most of the metaphosphate glasses varies around 30-40%, 50-60%, 5-10% and 0.5% for the radiative transitions $^4F_{3/2} \rightarrow ^4I_{9/2}$, $^4I_{11/2}$, $^4I_{13/2}$ and $^4I_{15/2}$, respectively. The luminescence intensities of all these bands are increase consistently with increase in Nd^{3+} ion concentration up to 0.5 mol% and then quenched with further increase in concentration. As can be seen from the Fig. 2 the band at 876 nm consists of two parts centred at 876 and 894 nm, respectively. This rare phenomenon may be related to the specificity of the glass host.

The laser parameters such as effective bandwidths ($\Delta\lambda_{eff}$), stimulated emission cross-sections ($\sigma(\lambda_P)$), spontaneous transition probabilities (A_R), gain band widths ($\sigma(\lambda_P) \times \Delta\lambda_{eff}$), measured ($\beta_{mes}$) and calculated ($\beta_R$) branching ratios are calculated and are given in Table 4.

6

From Table 4 and Fig. 3, the $^4F_{3/2} \to ^4I_{11/2}$ transition is found to be the most efficient for lasing action, due to its higher stimulated emission cross-section. The $\sigma(\lambda_p)$ value of PMN glass is higher than that of CBP [38], PABKLiNbLa [41] and PBN [25] glasses and is slightly lower than that of the MgO based phosphate glasses [26,36,37]. But the $\Delta\lambda_{eff}$ is comparable to those observed in the MgO based phosphate glasses.

Similar to χ parameter, the radiative branching ratios (β_R) of the $^4F_{3/2} \to ^4I_{11/2}$ transition depends only on Ω_4/Ω_6 ratio and independent of Ω_2 parameter because of zero value of $\langle \|U^2\| \rangle$ matrix element of the $^4F_{3/2}$ level [49,50]. The β_R for Nd^{3+}-doped crystals and glasses can also be calculated based on the χ value using the following equations given by Lomheim and Shazer [51],

$$\beta_R \left(^4F_{3/2} \to ^4I_{9/2} \right) = \frac{0.3194\chi + 0.0767}{0.4247\chi + 0.4567}$$

$$\beta_R \left(^4F_{3/2} \to ^4I_{112} \right) = \frac{0.1053\chi + 0.2874}{0.4247\chi + 0.4567}$$

$$\beta_R \left(^4F_{3/2} \to ^4I_{13/2} \right) = \frac{0.0902}{0.4247\chi + 0.4567}$$

$$\beta_R \left(^4F_{3/2} \to ^4I_{15/2} \right) = \frac{0.0023}{0.4247\chi + 0.4567}$$

The β_R values calculated using the above Eqs. are comparable to those values calculated from the JO theory (Table 4).

On the other hand, for continuous wave laser operation, the input pump power is directly proportional to the saturation intensity I_s, that can be calculated as $I_s = hc/\lambda\ \sigma(\lambda_p) \times \tau_{exp}$ [52]. From the above Eqs. it is obvious that, the glass matrix with higher optical gain will have lower threshold power for laser operation. The I_s value for the $^4F_{3/2} \to ^4I_{11/2}$ laser transition in the present PMN10 glass is 1.39×10^8 W/m^2 which is slightly higher than those of LHG-80 (1.33×10^8) and LG-770 (1.38×10^8) commercial glasses [36]. In view of the above results, it can be concluded that the Nd^{3+}-doped PMN10 glass can be used as a potential NIR laser with relatively lower threshold power.

3.3 Luminescence decay curves

Fluorescence lifetime is one of the key parameters to accomplish laser gain media. Longer fluorescence lifetime indicates the possibility of attaining higher population inversion and hence stimulated emission. In order to measure lifetimes of the $^4F_{3/2}$ level, decay curves are measured for all the PMN glasses. Figure 4 shows decay profiles of the $^4F_{3/2} \to ^4I_{112}$ transition. All the decay curves exhibit single exponential nature indicating the absence of energy transfer between donor and acceptor ions. The single exponential nature of the decay

7

curves could be due to either fast decay of excited Nd^{3+} ions or the effect of ligands is minimal on Nd^{3+} ions [53]. In the present glass systems, experimental lifetimes (τ_{exp}) are found to decrease considerably from 346 to 57 μs with increase in Nd^{3+} ions concentration from 0.05 to 4.0 mol%. The τ_{exp} values for all the PMN glasses are reported in Table 5. Figure 5 represents the graph between lifetime verses concentration of Nd^{3+} ion in PMN glasses. The reason for decrease in lifetimes could be due to the onset of fast Nd^{3+}–Nd^{3+} diffusion processes [54], wherein energy is migrated from one Nd^{3+} ion to another and finally to traps. The lifetime values of the $^4F_{3/2}$ level in PMN10 glass is comparable to those of reported ones presented in Table 3 [14,25,26,33,34,36-47]. As can be seen, measured lifetime value for the PMN10 glass is found to be higher than those of ZLNP [14], PNL [44], PZAL [45], PKMAN [26], PKSAN [34], PKBAN [33] and PNK [44] glasses.

From the values of radiative and fluorescence lifetimes, the non-radiative decay rate can be determined by the relation,

$$W_{NR} = (\frac{1}{\tau_{exp}} - \frac{1}{\tau_R})$$

The non-radiative decay rates in the PMN glasses, calculated from the above Eq. are increase from 350 to 14960 s^{-1} as shown in Table 5 and Fig. 5.

In phosphate glasses, shortening of radiative lifetime is mainly due to four non-radiative decay processes, given by

$$W_{NR} = W_{ET} + W_{MP} + W_{CQ} + W_{OH}$$

where W_{ET}, W_{MP}, W_{CQ} and W_{OH} denote the non-radiative decay rates corresponding to the energy transfer, multiphonon relaxation, concentration quenching, and hydroxyl groups, respectively. The exponential decay curves of the present PMN glass system indicate the absence of direct energy transfer between donor and acceptor. From the literature, phosphate glass is found to have phonon energy of ~1300 cm^{-1} [55]. Nearly four to five phonons are needed to bridge the gap between the $^4F_{3/2}$ level and its lower $^4I_{15/2}$ level which is around 5500 cm^{-1}. Hence, multiphonon relaxation may contribute to the increase of non-radiative decay rate in the present Nd^{3+}-doped PMN glasses. Increase in Nd^{3+} ions concentration may also cause non-radiative decay by concentration quenching. In general, there are two relaxation mechanisms involved in the concentration quenching. The first one is cross-relaxation in which two neighbouring ions (donor and acceptor) exchange energy and the second one is migration of the excitation energy (donor to donor and then to traps or hopping mechanism) where the energy moves from one ion to the other till it finds the trap. Therefore,

8

concentration quenching due to energy migration from one Nd^{3+} ion to the other and then to traps plays a significant role for the fast decrease of lifetimes in the present PMN glasses.

The quantum efficiency (η), defined as the ratio of τ_{exp} and τ_R of the emitting level, depends on absorption and emission cross-sections, transition probabilities, ligand-field and concentration of active Ln^{3+} ions [56]. The variation of quantum efficiency in PMN glasses is shown in Table 5 and in the inset of Fig. 5. The quantum efficiencies of PMN glasses are found to decrease from 88 to 15% when the concentration of Nd^{3+} ion increase from 0.05 to 4.0 mol%, which is due to the increase in concentration quenching. The η values in various phosphate glasses are compared in Table 3. The product ($\sigma(\lambda_p) \times \tau_{exp}$) represents 'figure of merit' (FOM). For the PMN glasses, the evaluated ($\sigma(\lambda_p) \times \tau_{exp}$) values for the $^4F_{3/2} \to {}^4I_{11/2}$ transition are presented in Table 5. The FOM of PMN glasses are also compared with those of other phosphate glasses in Table 3. As FOM is proportional to the slope efficiency and inversely proportional to the threshold pump power, higher value of FOM is required to achieve high gain for a laser material [57]. That means, the higher value of the FOM shows better potentiality of PMN glasses for NIR laser applications.

4. Conclusions

Various concentrations of Nd^{3+}-doped megnesium phosphate glasses have been prepared by melt quenching method. The spectroscopic and laser properties of these glasses have been evaluated. The absorption and NIR emission spectra of Nd^{3+} ions in PMN glasses are identical to those of reported Nd^{3+}-doped phosphate glasses. The spectroscopic perameters of Nd^{3+}-doped PMN glasses have been compared with those of reprted Nd^{3+}-doped phosphate glasses. The smaller value of Ω_2 indicates weak covalency of metal-ligand bond and higher symmetry around Nd^{3+} ions in the PMN glasses. The χ value is found to be around 0.91 which indicates that there is intense emission from the $^4F_{3/2} \to {}^4I_{11/2}$ laser transition. The effective bandwidth and stimulated emission cross-section for the present PMN10 glass are in the same range as that of the LG-750 and LHG-8 commercial laser glasses. The maximum NIR lumineiscent intensity is obtained for the 0.5 mol% of Nd^{3+} ions in PMN glasses. In the present work, of all the glasses studied, $^4F_{3/2}$ level of Nd^{3+} ion exhibits single exponential decay. This is also followed by shortening of lifetime of the $^4F_{3/2}$ level with increase in Nd^{3+} concentration due to the increase in concentration quenching.

Acknowledgements

Refereces

1. A. Bajaj, A. Khanna, N.K. Kulkarni, S.K. Aggarwal, J. Am. Ceram. Soc. 92 (2009) 1036.

2. E.A. Lalla, U.R. Rodriguez-Mendoza, A.D. Lozano-Gorrin, A. Sanz-Arranz, F. Rull, V. Lavin, Opt. Mater. 51 (2016) 35.

3. V. Lupei and A. Lupei, J. Lumin. 169 (2016) 426.

4. F. Zaman, G. Rooh, N. Srisittipokakum, S. Ruengsri, H.J. Kim, J. Kaewkhao, J. Non-Cryst. Solids 452 (2016) 307;

5. A. Jha, B. Richards, G. Jose, T. Teddy-Fernandez, P. Joshi, X. Jiang, J. Lousteau, Prog. Mater. Sci. 57 (2012) 1426.

6. L. Bolundut, L. Pop, M. Bosca, N. Tothazan, G. Borodi, E. Culea, P. Pascutta, R. Stefan, J. Alloy. Compd. 692 (2017) 934.

7. I. Pal, A. Agarwal, S. Sanghi, M.P. Aggrawal, S. Bhardwaj, J. Alloy. Compd. 587 (2014) 332.

8. B. Shanmugavelu, V. Venkatramu, V.V. Ravi Kanth Kumar, Spectrochim. Acta A 122 (2014) 422.

9. H.K. Dan, D.C. Zhou, Z.W. Yang, Z.G. Song, X. Yu, J.B. Qiu, J. Non-Cryst. Solids 414 (2015) 21.

10. T.F. Xue, L.Y. Zhang, J.J. Hu, M.S. Liao, L.L. Hu, Opt. Mater. 47 (2015) 24.

11. D. Nakauchi, G. Okada, M. Koshimizu, T. Yanagida, J. Rare Earths 34 (2016) 757.

12. S. Guo, M.K. Tsang, W.S. Lo, J. Hao, W.T. Wong, Nanoscale 10 (2018) 2790.

13. Q. Zhu, T. Sun, M.N. Chung, X. Sun, Y. Xiao, X. Qiao, F. Wang, Dalton Trans. 47 (2018) 8581.

14. D.D. Ramteke, R.E. Kroon, H.C. Swart, J. Non-Cryst. Solids 457 (2017) 157.

15. J.A. Jimenez and M. Sendova, J. Chem. Phys. 162 (2015) 425.

16. M.J. Weber, J. Non-Cryst. Solids 123 (1990) 208.

17. R. Reisfeld, Struct. Bond. 22 (1975) 123.

18. S. Tanabe, N. Sugimoto, S. Ito, T. Hanada, J. Lumin. 87 (2000) 670.

19. A. Mori, T. Sakamoto, K. Kobayashi, K. Shikano, K. Oikawa, K. Hoshino, T. Kanamori, Y. Ohishi, M. Shimizu, J. Lightwave Technol. 20 (2002) 794.

20. F. Wu, S. Li, Z. Chang, H. Liu, S. Huang, Y. Yue, J. Mol. Stru. 1118 (2016) 42.

21. M. Diba, F. Tapia, A.R. Boccaccini, L.A. Strobel, Int. J. App. Gla. Sci. 3 (2012) 221.

22. M. Liao, H. Sun, L. Wen, Y. Fang, L. Hu, Mat. Chem. Phys. 98 (2006) 154.

23. F. Ahmadi, R. Hussin, S.K. Ghoshal, J. Non-Cryst. Solids 448 (2016) 43.

24. F. Ahmadi, R. Hussin, S.K. Ghoshal, J. Non-Cryst. Solids 452 (2016) 266.

25. P. Ravi, N. Vijaya, N. Krishna Mohan, Int. J. Sci. Res. in Phys. Appl. Sci. 6 (2018) 45.

26. S. Surendra Babu, P. Babu, C.K. Jayasankar, A.S. Joshi, A. Speghini, M. Bettinelli, J. Phys.: Condens. Matter 18 (2006) 3975.

27. S. Kang, X. Wang, W. Xu, X. Wang, D. He, L. Hu, Opt. Mat. 66 (2017) 287.

28. S.P. Sinha, Complexes of the rare earths, Pergamon Press, Oxford, London, 1966.

29. W.T. Carnall, P.R. Fields, K. Rajnak, Electronic energy levels in the trivalent lanthanide aquo ions, J. Chem. Phys. 49 (1968) 4424.

30. E. Rukmini and C K Jayasankar, Physica B 212 (1995) 167.

31. B.R. Judd, Phys. Rev. B 127 (1962) 750.

32. G.S. Ofelt, J. Chem. Phys. 37 (1962) 511.

33. R. Balakrishaniah, P. Babu, C.K. Jayasankar, A.S. Joshi, A. Speghini, M. Bettinelli, J. Phys.:Condens. Matter 18 (2006) 165.

34. K. Upendra Kumar, P. Babu, K.H. Jang, Hyo Jin Seo, C.K. Jayasankar, A.S. Joshi, J. Alloys and Compds. 458 (2008) 509.

35. C.K. Jorgensen, R. Reisfeld, J. Less-Common Met. 93 (1983) 107.

36. J.H. Campbell and T.I. Suratwala, J. Non-Cryst. Solids 263 (2000) 318

37. D.V.R. Murthy, T. Sasikala, B.C. Jamalaiah, A.M. Babu, J.S. Kumar, M. Jayasimhadri, L.R. Moorthy, Opt. Commun. 284 (2) (2011) 603.

38. N. Chanthima, J. Kaewkhao, Y. Tariwong, N. Sangwaranatee, N.W. Sangwaranatee, Materials Today proc. 4 (2017) 6091.

39. Q. Yin, S. Kang, X. Wang, S. Li, D. He, L. Hu, Opt. Mat. 66 (2017) 23.

40. Z. Mazurak, M. Czaja, R. Lisiecki, A. Meijerink, J. Mat. Sci. Eng. Adv. Tech. 5 (2012) 1.

41. J. Dong and M. Bass, J. Opt. Soc. Am. B 21 (2004) 454.

42. N.O. Dantas, E.O. Serqueira, A.C.A. Silva, A.A. Andrade, S.A. Lourenco, Braz. J. Phys. 43 2013) 230.

43. Mao Yan-Li, Sun Zhen-Rong, Jiang Xiu-Li, Deng Pei-Zhen, Gan Fu-Xi, Chin. Phys. 11 (2002) 613.

44. M. Seshadri, K.Venkata Rao, J. Lakshmana Rao, K.S.R. Koteswara Rao, Y.C. Ratnakaram, J. Lumin. 130 (2010) 536.

45. M. Bouderbala, H. Mohmoh, A. Bahtat, M. Bahtat, M. Ouchetto, M. Duretta, B. Elouadi, J. Non-Cryst. Solids 259 (1999) 23.

46. V.M. Martins, D.N. Messoas, J.L. Doualan, A. Braud, P. Camy, N.O. Dantas, T. Catunda, V. Pilla, A.A. Andrade, R. Moncorge, J. Lumin. 162 (2015) 104.

47. R. Laskshmikantha, N.H. Ayachit, R.V. Anavekar, Solid State Physics: Proce. 57th DAE SSPS 2012, AIP Conf. Proc. 1512 (2013) 530.

48. R.R. Jacobs and M.J. Weber, IEEE J. Quantum Electron. 12 (1976) 102.

49. A. Flórez, J.F. Martinez, M. Flórez, P. Porcher, J. Non-Cryst. Solids 284 (2001) 261.

50. D.F. de Sousa, F. Batalioto, M.J.V. Bell, S.L. Oliveira, L.A.O. Nunes, J. Appl. Phys. 90 (2001) 3308.

51. T.S. Lomheim and L.G. De Shazar, Opt. Commun. 24 (1978) 89.

52. J. Azkargorta, I. Iparraguirre, R. Balda, J. Fernandez, E. Denoue, J.L. Adam, J. IEEE, Quantum Electron. 30 (1994) 1862.

53. R. Balda, J. Fernandez, A. De Pablos, J.M. Fdez-Navaro, M.A. Arriandiaga, Phys. Rev. B. 53 (1996-I) 5181.

54. J. Azkargorta, I. Iparraguirre, R. Balda, J. Fernandez, E. Denoue, J.L. Adam, IEEE J. Quant. Electron. 30 (1994) 1862.

55. P. Babu, H.J. Seo, K.H. Jang, R. Balakrishnaiah, C.K. Jayasankar, A.S. Joshi, J. Phys.:Condens. Matter 17 (2005) 4859.

56. A.A. Kaminskii, Laser Crystals Their Physics and Properties, first ed., Springer, New York, 1981.

57. K. Linganna, R. Narro-Garcia, H. Desirena, E. De la Rosa, Ch. Basavapoornima, V. Venkatramu, C.K. Jayasankar, J. Alloys Compds. 684 (2016) 322.

Table 1. Physical properties of the Nd^{3+}-doped PMN glasses

S.No.	Glass label	Optical path length (mm)	Density (gm/c.c)	Concentration (x 10^{20} ions/c.c.)	Refractive index
1	PMN005	4.06	2.4023	0.0013	1.564
2	PMN01	3.85	2.4270	0.0066	1.569
3	PMN05	3.67	2.4470	0.0134	1.577
4	PMN10	3.50	2.4564	0.0670	1.581
5	PMN20	4.39	2.4949	0.1356	1.585
6	PMN40	3.73	2.5191	0.2718	1.587

Table 2. Experimental energies (E_{exp}, cm^{-1}), experimental (f_{exp}) and calculated (f_{cal}) oscillator strengths ($\times 10^{-6}$) and JO intensity parameters of PMN10 glass.

Transition $^4I_{9/2} \rightarrow$	Energy E_{exp}	Oscillator strengths	
		f_{exp}	f_{cal}
$^4F_{3/2}$	11429	1.54	1.93
$^4F_{5/2}+^2H_{9/2}$	12453	5.89	5.82
$^4F_{7/2}+^4S_{3/2}$	13405	5.78	5.96
$^4F_{9/2}$	14663	0.63	0.46
$^2H_{11/2}$	15949	0.16	0.13
$^4G_{5/2}+^2G_{7/2}$	17182	13.20	13.29
$^4G_{7/2}$	19048	4.48	2.74
$^4G_{9/2}$	19531	3.01	1.23
$^4G_{11/2}+^2D_{3/2}+ ^2G_{9/2} + ^2K_{15/2}$	21186	1.30	1.03
$^2P_{1/2}+^2D_{5/2}$	23310	0.46	0.49
$^4D_{1/2}+^4D_{3/2}+^4D_{5/2}$	28011	8.56	9.10
$\sigma\ (N)^a$		$\pm 0.79\ (11)$	
Ω_2	2.55×10^{-20} cm^2		
Ω_4	3.74×10^{-20} cm^2		
Ω_6	4.12×10^{-20} cm^2		

[a]σ indicates root mean square deviation between experimental and calculated energy values and N represents the number of energy levels used in the fitting.

13

Table 3. Comparison of JO parameters (Ω_λ, $\times$ 10^{-20} cm^2), spectroscopic quality factor (χ), radiative (τ_R) and experimental (τ_{exp}) lifetimes (μs), quantum efficiency (η, %), branching ratio (β_R), bandwidth ($\Delta\lambda_{eff}$, nm), emission cross-section ($\sigma(\lambda_p)$, $\times$ 10^{-20} cm^2), figure of merit (FOM, $\times$ 10^{-20} cm^2) in various Nd^{3+}-doped phosphate glasses.

S.No	Host	Modifiers	mol/Wt %	Ω_2	Ω_4	Ω_6	$\Sigma\Omega_\lambda$	χ	τ_R	τ_{exp}	η	β_R	$\Delta\lambda_{eff}$	$\sigma(\lambda_p)$	FOM	Ref.
1	CBP	CaO, BaO	1	1.09	1.97	3.37	6.43	0.58	595	-	-	0.69	-	0.92	-	[38]
2	ZLNP	ZnO, Li$_2$O, Na$_2$O	1	1.58	1.10	3.47	6.15	0.32	693	206	30	0.53	36.7	69.22	14259	[14]
3	PCBS	CaO, BaO, SrO	0.5	2.17	2.46	3.07	7.7	0.80	354	284	80	0.65	27.5	3.90	1108	[40]
4	PABKLiNbLa	Al$_2$O$_3$, Li$_2$O, K$_2$O, BaO, Nb$_2$O$_5$, La$_2$O$_3$	3	2.47	4.25	5.30	12.02	0.80	332	300	90	0.50	23.4	0.79	237	[41]
5	PMN	MgO	1	2.55	3.74	4.12	10.41	0.91	394	232	59	0.51	25	3.26	756	PW
6	PBN	BaO	1	2.62	5.47	4.24	12.33	1.29	313	-		0.54	24	2.79	-	[25]
7	PANK	Al$_2$O$_3$, Na$_2$O, K$_2$O	1	2.62	2.87	2.92	8.41	0.98	~375	~360	96			4.12	1483	[42]
8	PAKBPb	Al$_2$O$_3$, K$_2$O, BaO, PbO	1	3.08	6.31	5.45	14.84	1.16	644	-	-	0.47	20.6	4.43	-	[39]
9	LHG-80	-		3.6	5.0	5.5	14.1	0.91	326	-	-	-	23.9	4.2	-	[36]
10	PABKLiNbLa	Al$_2$O$_3$, Li$_2$O, K$_2$O, BaO, Nb$_2$O$_5$, La$_2$O$_3$	2.2	3.9	4.6	5.3	13.8	0.87	330	~360	109	0.48	25	4.0	1440	[53]
11	LG-770	Al$_2$O$_3$, K$_2$O, MgO		4.3	5.0	5.6	15	0.89	349	-	-	-	25.4	3.9	-	[36]
12	PNL	Li$_2$O, Na$_2$O	1	4.32	3.66	6	13.98	0.61	-	79	-	0.52	36.23	3.73	295	[44]
13	LHG-8	Al$_2$O$_3$, K$_2$O, BaO		4.4	5.1	5.6	15.1	0.91	351	-	-	-	26.5	3.6	-	[36]
14	PZAL	Al$_2$O$_3$, ZnO, La$_2$O$_3$	2	4.53	3.67	4.02	12.22	0.91	320	117	37	0.49	28.4	-	-	[45]
15	LG-750	Al$_2$O$_3$, K$_2$O, BaO		4.6	4.8	5.6	15	0.86	367	-	-	-	25.3	3.7	-	[36]
16	PAN	Al$_2$O$_3$, Na$_2$CO$_3$	1	4.7	6.0	5.4	16.1	1.1	330	-	-	0.46	-	-	-	[46]
17	PKMAN	Al$_2$O$_3$, K$_2$O, MgO	1	6.22	5.95	6.83	19	0.87	262	194	74	0.68	28.8	4.41	856	[26]
18	PKSAN	Al$_2$O$_3$, K$_2$O, SrO	1	6.74	3.86	6.35	19.44	0.61	319	172	54	0.75	27.95	4.05	697	[34]
19	MgTP	TiO$_2$, MgO	1	7.11	3.62	5.60	16.33	0.65	339	244	72	0.52	27	4.71	1149	[37]
20	CaTP	TiO$_2$, CaO	1	7.49	3.88	5.64	17.01	0.69	323	243	75	0.51	27	4.55	1106	[37]
21	PNK	Na$_2$O, K$_2$O	1	7.68	8.96	11.71	28.35	0.77	-	40	-	0.52	41.5	8.67	347	[44]
22	SrTP	TiO$_2$, SrO	1	7.75	4.74	6.05	18.54	0.78	282	238	84	0.50	26	4.89	1164	[37]
23	PKBAN	Al$_2$O$_3$, K$_2$O, BaO,	1	9.23	7.00	8.74	24.97	0.80	214	144	67	0.59	25.5	6.48	933	[33]
24	PZP2	ZnO, PbO	1	13.06	6.83	11.64	31.53	0.59	-	-	-	-	-	-	-	[47]

14

Table 4. Emission band positions (λ_p, nm), effective bandwidths ($\Delta\lambda_{eff}$, nm), radiative transition probabilities (A_R, s^{-1}), peak stimulated emission cross-sections ($\sigma(\lambda_p)$, $\times 10^{-20}$ cm^2), gain band widths ($\sigma(\lambda_p) \times \Delta\lambda_{eff}$, x$10^{-26}$ cm^3) experimental and calculated branching ratios (β_R) for $^4F_{3/2} \rightarrow {^4I_J}$ (J = 9/2, 11/2 and 13/2) transitions in PMN10 glass.

Transition $^4F_{3/2} \rightarrow$	λ_p	$\Delta\lambda_{eff}$	A_R	$\sigma(\lambda_p)$	$\sigma(\lambda_p) \times \Delta\lambda_{eff}$	β_R Exp.	Cal.	$\beta_R{}^*$
$^4I_{9/2}$	876	37	1045	0.88	3.26	0.41	0.41	0.44
$^4I_{11/2}$	1054	25	1243	3.26	8.15	0.51	0.49	0.45
$^4I_{13/2}$	1324	51	245	0.78	3.98	0.08	0.10	0.11

*Lomhein and De Shazer method values

Table 5. Lifetimes (τ_{exp}, μs), non-radiative decay rates (W_{NR}, s^{-1}), quantum efficiencies (η, %) and figure of merits (FOM) ($\sigma(\lambda_p) \times \tau_{exp}$, $\times 10^{-26}$ cm^{2}s) of PMN glasses.

Glass Label	τ_{exp}	W_{NR}	η	FOM
PMN005	346	350	88	1128
PMN01	315	630	80	1027
PMN05	300	800	76	978
PMN10	232	1770	59	756
PMN20	170	3340	43	554
PMN40	57	14960	15	186
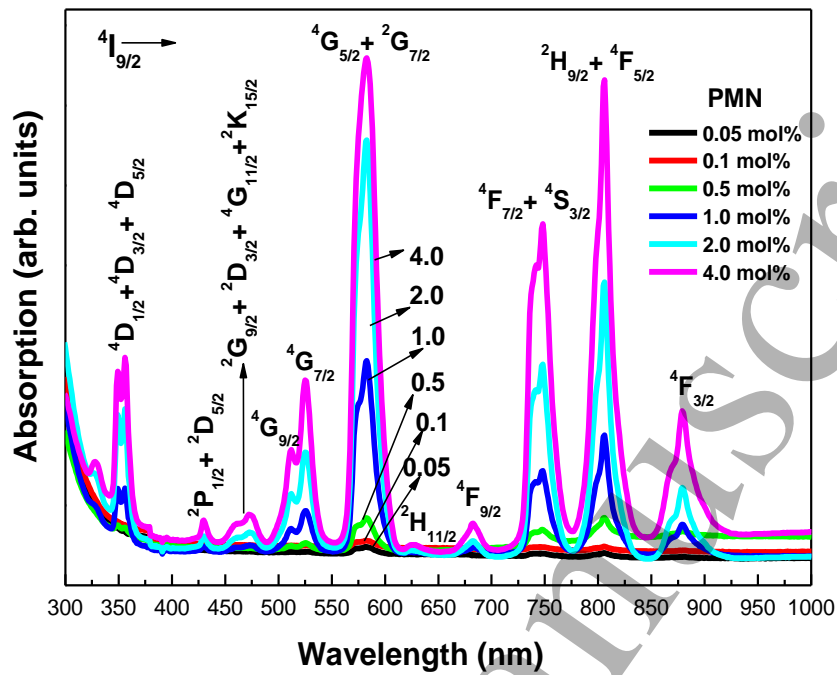
Fig. 1. Absorption spectra of Nd^{3+} ions in PMN glasses.
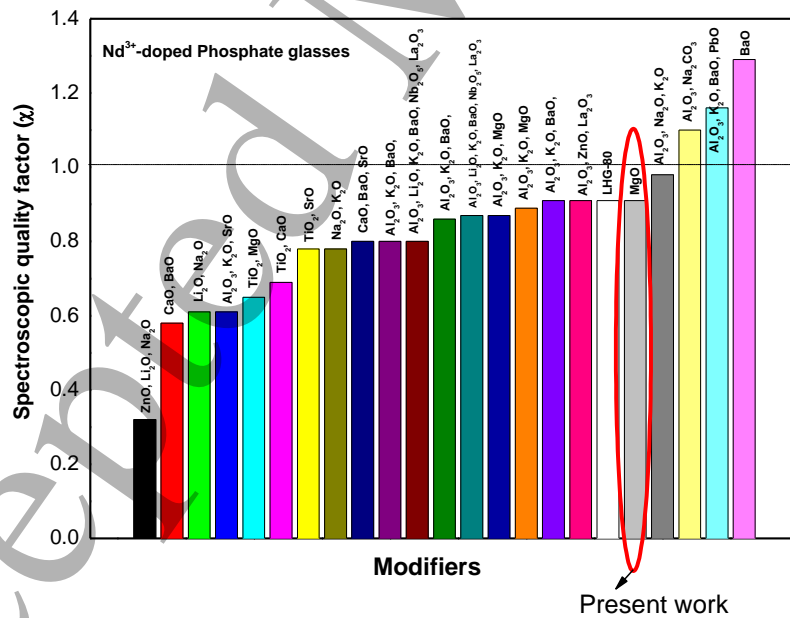
Fig. 2. Comparison of spectroscopic quality factor values in various Nd^{3+}-doped phosphate glasses.

16
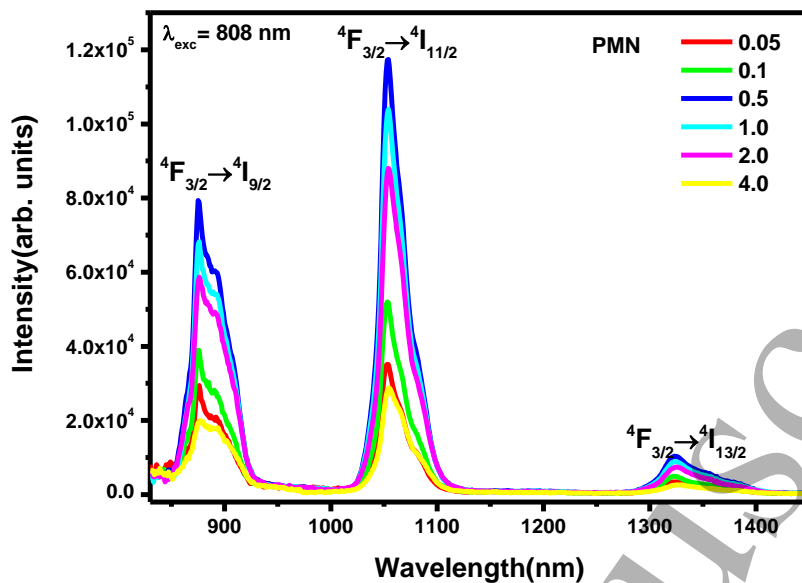
Fig. 3. Emission spectra of PMN glasses doped with different concentrations of Nd^{3+} ions.
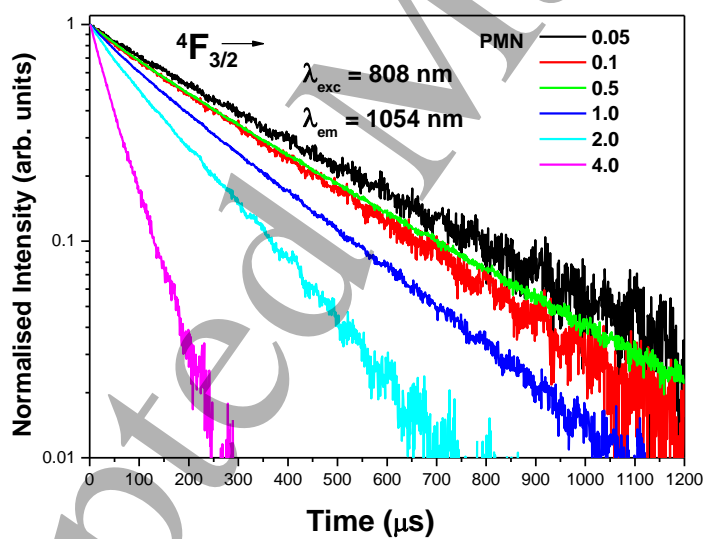
Fig. 4. Normalised decay curves of the $^4F_{3/2}$ level of Nd^{3+} ions in PMN glasses doped with different concentrations of Nd^{3+} ions.

17
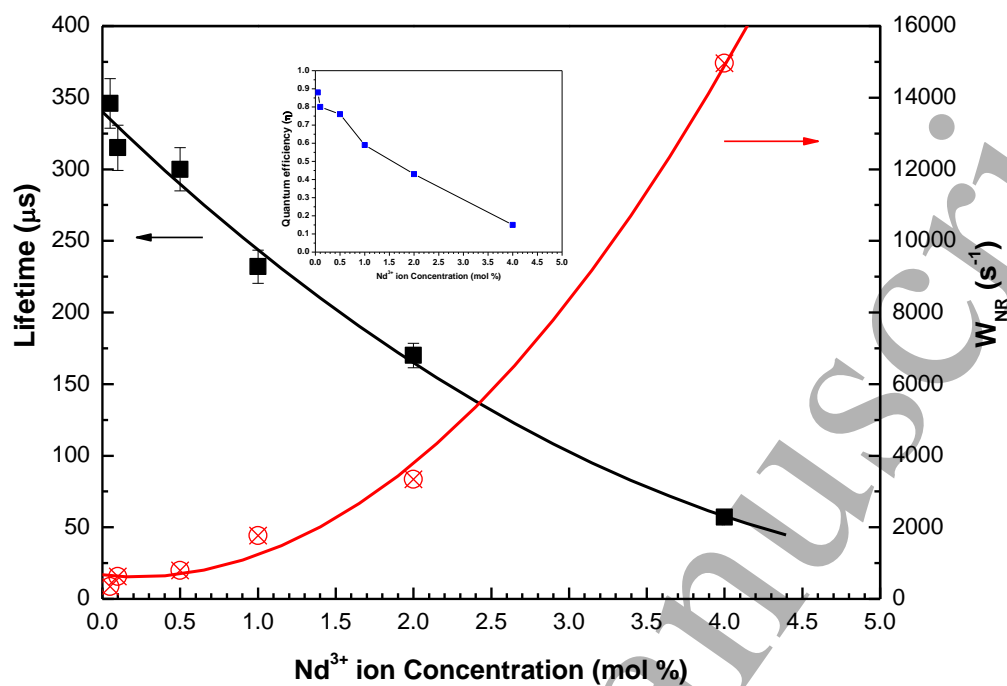
Fig. 5. Variation of lifetime, non-radiative decay rate of the $^4F_{3/2}$ level and the in the inset quantum efficiency with respect to concentration of Nd^{3+} ions in PMN glasses.

Study of excess thermodynamic properties of binary systems containing cinnamaldehyde with alcohols supported by ATR-FTIR spectral studies

R. Prathibha [a], P. Bhanuprakash [a,b], C. Narasimha rao [a], N.V.V. Jyothi [a,*], K. Sivakumar [c,*]

[a] *Department of Chemistry, Sri Venkateswara University, Tirupati, 517502, A.P., India*
[b] *Department of Chemistry, S.V.C.R. Govt. Degree College, Palamaner, 517408, A.P., India*
[c] *Department of Chemistry, S.V. Arts Degree & P.G. College (T.T.D'S), Tirupati, 517502, A.P., India*

ARTICLE INFO

ABSTRACT

The thermophysical behavior of the binary mixtures trans-cinnamaldehyde (CA) with alcohols namely, methanol (MO), ethanol (EO), propanol (PO), isopropanol (IPO) has been studied through the measurement of density (ρ), speed of sound (u), over the entire mole fraction range at T = (298.15, 303.15, 308.15, 313.15) K under atmospheric pressure. Excess volume (V^E) and excess isentropic compressibilities (κ_S^E) were also calculated and correlated with Redlich–Kister equation. Except for CA with MO and EO, the remaining investigated systems exhibit positive values of V^E and all the four systems exhibit negative κ_S^E values over the entire composition range. Moreover, all the systems behave differently when the temperature is raised. Besides, ATR-FTIR spectroscopy is used for finding molecular interactions in component molecules.

© 2019 Elsevier B.V. All rights reserved.

Specifications table

Subject area	Chemical thermodynamics, chemical engineering
Compounds	Cinnamaldehyde with methanol, ethanol, propanol, isopropanol
Data category	Physicochemical properties, density, speed of sound
Data acquisition format	FTIR spectral analysis
Data type	Calculated, analyzed
Procedure	Density measured by using Rudolph Research Analytical Digital Densimeter (DDM-2911 model), Speeds of sound (u) estimated with single crystal ultrasonic interferometer (model F-05) from Mittal Enterprises, New Delhi, India
Data accessibility	Data is with this article

1. Rationale

The knowledge on thermodynamic properties of organic liquid mixtures at a wide range of temperatures is of great importance. The studies on properties of the liquid mixtures are important to develop the thermodynamic models which are

widely applied in chemical, pharmaceutical, garment, tannery and other industries. Thermodynamic data plays an important role in many industrial applications such as the design and separation of solvents in chemical industries; oil refinery and gas industries for flow assurance and purification of oils; and solvent extraction in pharmaceutical and polymer industries [1]. The sign and magnitude are important parameters for binary mixtures to find out the specific interactions between the component molecules [2,3]. The study of molecular interaction in organic mixtures containing alcohol as one of the components is very important because alcohols are strongly self associated with a three dimensional network of hydrogen bonds [4] as well as capable to associate with any other group having degree of polar attraction [5].

The trans-cinnamaldehyde (CA) which consists of a phenyl group attached to an unsaturated aldehyde has greater significance as an intermediate in pharmaceutical industry because of its stability due to extended conjugation and strong polar nature of aldehyde group. The capsules of CA are used in food supplements to reduce blood sugar levels in diabetic patients. Furthermore, the study of the properties of mixtures containing CA becomes significant because of their extensive use in agriculture as pesticides and fungicides, in nuclear energy industries, pharmaceutical industries, engineering and in textile industries [6]. Alcohols are polar, self-associated liquids and the dipolar association of alcohols decrease when they are mixed with polar compounds due to the existence of specific intermolecular interactions between the hydroxyl group of alcohols and polar molecules. Alcohols are inexpensive and easily available at high purity [7]. Further, versatile alcohol solvents are widely used in a variety of industrial and consumer applications such as perfumes, cosmetics, paints varnish, drugs, fuel, explosives, fats, waxes, resin, plastics, rubber, detergents, DDT etc. The molecular interaction in binary liquid mixtures of CA and a series of alcohols namely methanol (MO), ethanol (EO), propanol (PO), isopropanol (IPO) has been studied in this present work. A survey of the literature [9] had reported that speed of sound, density and viscosity data at 303.15 K were measured for the binary systems of cinnamaldehyde and a series of alcohols namely methanol (MA), ethanol (EA), n-propyl alcohol (NPA), iso-propyl alcohol (IPA), n–butyl alcohol (NBA), iso-butyl alcohol (IBA), secondary butyl alcohol (SBA) and tertiary butyl alcohol (TBA).

Our study has attempted to demonstrate the nature of interactions between CA with alcohols through density and speed of sound measurements at temperatures ranging from 298.15 K to 313.15 K. The measured data is used to calculate the excess quantities like excess volume (V^E) and excess isentropic compressibility (κ_S^E) which are then fitted to Redlich–Kister polynomial equation [8] to estimate the coefficients and standard error. The experimental results were interpreted in terms of intermolecular interactions between component molecules, supported by ATR-FTIR spectral studies.

2. Procedure

2.1. Reagents

The chemicals CA (Avra, India, ≥0.980), MO (Sigma-Aldrich, India, ≥0.999), EO (Changshu Hongsheng Fine Chemicals, China, ≥0.999), PO (S.D. fine chemicals, India, ≥0.995) and IPO (Sigma-Aldrich, India, ≥0.995) of Analytical Reagent (AR) grade are procured and used without further purification. The specification of pure components are shown in Table 1. To verify the purity of chemicals, their densities (ρ) and speeds of sound (u) were experimentally determined and compared in Table 2 with the literature values [9–33]. The chemicals were stored over 0.4 nm molecular sieves for about 72 h to reduce water content, if any and then degassed just before use. The binary liquid mixtures of CA with MO, EO, PO, IPO were prepared gravimetrically in glass bottles with air tight stoppers in order to minimize losses by evaporation. The mass measurements were performed on digital electronic balance (Afcoset, ER-120A, India) with an uncertainty of $\pm 1 \times 10^{-4}$ g. The resulting uncertainty in mole fraction was found to be less than 5×10^{-4}. The properties of the freshly prepared liquid mixtures were measured on the same day to prevent evaporation loss.

2.2. Measurements

Densities (ρ) of the pure solvents and their mixtures were measured by using Rudolph Research Analytical Digital Densimeter (DDM-2911 model). The instrument has a built-in solid-state thermostat and a resident program with accuracy in temperature of ± 0.02 K. The densities were automatically measured at the specified temperature by transferring the homogeneous and bubble free sample into the U-tube of the densimeter with the help of a medical syringe. The uncertainty in

Table 1
The CAS number, source, mass fraction purity, water content and molar mass of pure liquids used in the present study.

| Components	CAS number	Source	Purity in mass fraction[a]	Water content in mass fraction	Molar mass (g mol^{-1})
CA	14371-10-9	Avra, India	0.980	0.002	132.16
MO	67-56-1	Sigma-Aldrich, India	0.999	0.0003	32.04
EO	64-17-5	Changshu Hongsheng Fine Chemicals, China	0.999	0.001	46.06
PO	71-23-8	S.D. fine chemicals, India	0.995	0.002	60.09
IPO	67-63-0	Sigma-Aldrich, India	0.995	0.001	60.09

[a] As received from the supplier.

Table 2

Comparison of experimental and literature values of density (ρ) and speed of sound (u) of the pure liquids along with their molar heat capacity (C_p) at 298.15 K $\leq$ T $\leq$ 313.15 K.

components	T/K	$10^{-3}\rho$/(Kg m^{-3})		u/(m s^{-1})		C_P /(J K^{-1} mol^{-1})
		Exp.	Lit.	Exp.	Lit.	
CA	298.15	1.06309	–	1542.6	–	221.67 [a]
	303.15	1.05893	1.05890 [9]1.0427 [24]	1538.6	1537.6 [9]1543.0 [24]	223.63 [a]
	308.15	1.05475	–	1534.5	–	225.59 [a]
	313.15	1.05055	–	1530.6	–	227.53 [a]
MO	298.15	0.78709	0.7869 [25]0.786710[26]0.7868 [11]0.78720 [23]	1104.3	1104.23 [22]1104.30[19]1104 [23]	81.11[10]
	303.15	0.78222	0.7822 [11]0.78199 [27]	1086.1	1086 [11]1088.5 [15]	82.12 [10]
	308.15	0.77736	0.7772 [29]0.77703 [13]	1073.4	1073 [11]	83.17 [10]
	313.15	0.77247	0.7723 [12]0.77221 [14]0.77231 [22]	1054.5	1054.49[22]	84.28 [10]
EO	298.15	0.78524	0.78525 [29]0.78528 [16]0.78530 [17]0.7852 [11]0.78506 [22]	1142.7	1142.5 [17]1142.8 [18]	113.38 [17]
	303.15	0.78096	0.78096 [16]0.7809 [21]0.78080 [29]	1125.3	1125.5 [17]	115.29 [17]
	308.15	0.77667	0.77661 [16]0.77650 [21]0.77643 [31]	1108.8	1108.6 [17]1109.1 [18]	117.46 [17]
	313.15	0.77228	0.77223 [16]0.77250 [22]0.77220 [29]	1091.5	1091.8 [17]	119.70 [17]
PO	298.15	0.79991	0.80001 [19]0.79977 [20]0.79975 [30]	1206.1	1205.93[19]1206.17[20]1207 [33]	144.47 [19]
	303.15	0.79594	0.79597 [19]0.79560[13]0.79548 [14]	1189.1	1189.26[19]	147.80 [19]
	308.15	0.79196	0.79189 [19]0.79158 [13]	1172.2	1172.37[19]1171.41[18]	150.05 [19]
	313.15	0.78797	0.78777 [19]0.78754 [20]	1155.4	1155.53[19]1155.36[20]	153.58 [19]
IPO	298.15	0.78089	0.78070 [12]0.78136 [30]0.78098 [28]	1139.3	1138 [12]1140 [33]	154.59 [13]
	303.15	0.77692	0.77695 [14]	1122.3	1122 [11]	157.93[a]
	308.15	0.77294	0.77306 [13]0.77246 [14]0.77275 [32]	1097.5	1097[11]	160.18 [a]
	313.15	0.76895	0.7678 [12]0.76896 [13]	1085.6	1085 [11]	163.71 [a]

The standard uncertainties are u (ρ) = $\pm 5 \times 10^{-5}$ g cm^{-3}, u (u) = ± 0.5 m s^{-1}, u (T) = ± 0.02 K for density, u (T) = ± 0.05 K for speed of sound and u (p) = 1 k Pa.

[a] Estimated using group contribution additivity.
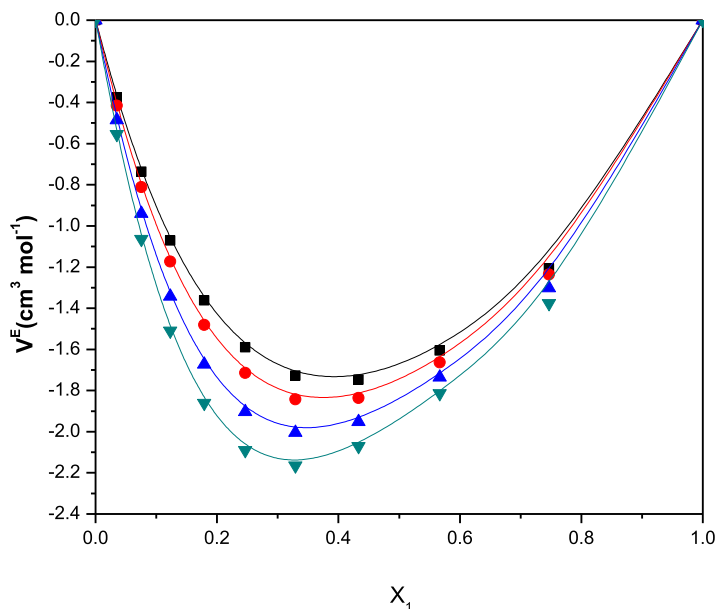
Fig. 1. Plot of excess volumes (V^E) vs mole fraction (x_1) for binary liquid mixtures of CA+MO at T = 298.15 K (■), T = 303.15 K (•), T = 308.15 K (▲), and T = 313.15 K (▼).

density was found to be $\pm 5 \times 10^{-5}$ g cm^{-3}. All the density measurements were made at atmospheric pressure. The calibration of the instrument was done on each day with air, double-distilled and de-ionized water as standards.

The speeds of sound (u) were estimated with single crystal ultrasonic interferometer (model F-05) from Mittal Enterprises, New Delhi, India, and operated at a 2 MHz frequency at the specified temperatures. The temperatures were controlled to ±0.02 K with the help of circulating well-stirred water around the cell form the thermostat. The uncertainty of speed of sound is ±0.5 m s^{-1}.

3. Data, value, and validation

3.1. Excess volumes (V^E)

The excess volumes (V^E) are calculated for the investigated binary mixtures by using the following equation:

$$V^E/\text{m}^3.\text{mol}^{-1} = \frac{x_1 M_1 + x_2 M_2}{\rho} - \left[\frac{x_1 M_1}{\rho_1} + \frac{x_2 M_2}{\rho_2} \right] \tag{1}$$

where, $x_1, x_2, \rho_1, \rho_2, M_1, M_2$ represents the mole fraction, density, molecular weight of components liquids namely CA and alcohols respectively and ρ_{mix} is the density of the binary mixture.

The mole fraction (x_1) of CA, experimental densities (ρ), excess volumes (V^E) for the binary mixtures of CA with MO, EO, PO, and IPO were presented in Table 3. An examination of curves in Figs. 1–4 reveal that V^E data is negative for the binary mixture of CA with MO and the property exhibits an inversion of sign with EO. The V^E data is completely positive over the entire composition range in mixtures of CA that contain PO and IPO.

The mixing behavior of these binary systems with composition has been qualitatively explained by considering the following possible opposing factors: (i) Disruption of self-associated molecules through dipole-dipole or hydrogen bonding interactions due to the addition of second component (ii) Formation of strong interactions like dipole-dipole, hydrogen bonding or complex formation between unlike molecules and (iii) packing effect between the component molecules due to their difference in the size and shape. The factor (i) causes expansion in volume and factors (ii) and (iii) leads to contraction in volume of the binary mixtures.

The sign and magnitude of excess volume of a binary system depends on the relative strength of volume expansion and volume contraction factors between two liquid components. If the volume expansion factors outweigh the contraction factors, then V^E becomes positive. On the other hand, if the volume contraction terms dominate the expansion factors then V^E becomes negative. In CA+MO system, the negative V^E values suggest that volume contraction factors dominate the expansion factors. The positive experimental V^E data of CA with PO, IPO over the entire composition range at all the investigated temperatures suggests that volume expansion factors outweigh the contraction factors. The inversion of sign of V^E for the binary mixtures of CA with MO indicates that both the factors are competing with each other in varying degrees. The addition of polar solvents like alcohols to CA leads to breaking of the dipolar-dipolar associates. It is assumed that positive V^E

Table 3

Mole fraction (x_1) of CA (1) density (ρ), experimental and predicted excess molar volumes (V^E), speed of sound (u), isentropic compressibility (κ_S) and experimental and predicted excess isentropic compressibility (κ_S^E) for the binary mixtures of alcohol (2) at 298.15 K to 313.15 K.

x_1	10^{-3} ρ (Kg m^{-3})	V^E Expt. 10^6/m^3 mol^{-1}	V^E Redlich–Kister	u (expt.) (m s^{-1})	κ_S (T Pa^{-1})	κ_s^E Expt. T Pa^{-1}	κ_s^E Redlich–Kister
CA+MO298.15 K							
0.0351	0.82177	−0.3757	−0.3756	1140.1	936.2	−42.57	−42.56
0.0757	0.85568	−0.7365	−0.7364	1182.5	835.7	−79.56	−79.67
0.1231	0.88854	−1.0704	−1.0704	1231.2	742.4	−109.20	−109.09
0.1792	0.91998	−1.3616	−1.3615	1284.2	659.1	−128.43	−128.21
0.2467	0.94970	−1.5893	−1.5891	1337.3	588.8	−134.35	−134.31
0.3294	0.97744	−1.7278	−1.7276	1385.8	532.7	−125.61	−125.36
0.4331	1.00307	−1.7466	−1.7464	1423.9	491.6	−101.48	−101.95
0.5671	1.02660	−1.6060	−1.6058	1460.4	456.7	−70.89	−70.82
0.7466	1.04775	−1.2069	−1.2068	1515.1	415.8	−45.87	−45.80
303.15 K							
0.0351	0.81757	−0.4155	−0.4155	1123.1	969.6	−47.32	−47.30
0.0757	0.85207	−0.8111	−0.8110	1167.3	861.3	−88.54	−88.53
0.1231	0.88535	−1.1726	−1.1724	1218.1	761.2	−121.26	−121.23
0.1792	0.91702	−1.4814	−1.4813	1273.8	672.1	−142.53	−142.51
0.2467	0.94675	−1.7142	−1.7140	1329.9	597.2	−149.24	−149.34
0.3294	0.97428	−1.8428	−1.8428	1380.7	538.4	−139.33	−139.48
0.4331	0.99954	−1.8369	−1.8369	1421.3	495.2	−113.44	−113.64
0.5671	1.02270	−1.6627	−1.6627	1459.2	459.2	−80.03	−79.32
0.7466	1.04366	−1.2362	−1.2361	1514.5	417.7	−51.55	−51.74
308.15 K							
0.0351	0.81394	−0.4856	−0.4856	1110.9	995.4	−51.61	−51.64
0.0757	0.84940	−0.9392	−0.9391	1156.4	880.4	−96.75	−96.74
0.1231	0.88331	−1.3426	−1.3425	1209.2	774.3	−132.66	−132.65
0.1792	0.91522	−1.6730	−1.6728	1268.0	679.5	−156.71	−156.27
0.2467	0.94476	−1.9031	−1.9029	1327.3	600.8	−164.31	−164.36
0.3294	0.97175	−2.0042	−2.0039	1381.2	539.4	−154.23	−154.53
0.4331	0.99632	−1.9521	−1.9519	1424.8	494.3	−127.22	−127.59
0.5671	1.01895	−1.7349	−1.7347	1465.2	457.1	−92.00	−91.52
0.7466	1.03991	−1.3017	−1.3015	1523.4	414.3	−61.81	−61.88
313.15 K							
0.0351	0.81021	−0.5543	−0.5543	1092.3	1034.5	−56.02	−56.09
0.0757	0.84661	−1.0649	−1.0648	1138.6	911.1	−105.29	−105.18
0.1231	0.88114	−1.5097	−1.5096	1193.0	797.3	−144.57	−144.42
0.1792	0.91329	−1.8618	−1.8616	1254.1	696.2	−170.69	−170.41
0.2467	0.94267	−2.0904	−2.0901	1316.7	611.8	−179.54	−179.65
0.3294	0.96916	−2.1657	−2.1655	1374.1	546.4	−169.03	−169.51
0.4331	0.99309	−2.0707	−2.0707	1421.4	498.4	−140.54	−140.67
0.5671	1.01526	−1.8146	−1.8146	1463.3	459.9	−101.99	−101.51
0.7466	1.03623	−1.3769	−1.3769	1522.9	416.0	−68.37	−68.40
CA+EO298.15 K							
0.0498	0.80363	0.7243	0.7242	1182.4	894.9	−23.09	−23.29
0.1055	0.82767	1.0409	1.0407	1222.3	816.6	−44.08	−43.93
0.1682	0.85691	0.9504	0.9502	1263.5	741.7	−61.45	−60.99
0.2393	0.89045	0.4956	0.4957	1301.1	671.6	−73.82	−73.37
0.3206	0.92663	−0.2115	−0.2115	1341.9	607.6	−79.90	−79.77
0.4144	0.96274	−0.9626	−0.9622	1384.7	550.9	−78.50	−78.80
0.5240	0.99503	−1.4307	−1.4311	1425.5	502.5	−68.71	−69.23
0.6537	1.01988	−1.2306	−1.2307	1461.5	462.4	−50.36	−50.65
0.8094	1.03765	−0.2526	−0.2526	1501.1	428.9	−25.22	−24.96
303.15 K							
0.0498	0.80004	0.6752	0.6751	1166.3	924.5	−26.32	−26.44
0.1055	0.82471	0.9409	0.9409	1207.5	840.6	−49.70	−49.57
0.1682	0.85451	0.7995	0.7996	1250.2	760.8	−68.67	−68.36
0.2393	0.88852	0.2961	0.2962	1289.1	686.7	−81.88	−81.64
0.3206	0.92509	−0.4548	−0.4547	1331.3	619.4	−88.08	−88.09
0.4144	0.96144	−1.2386	−1.2386	1375.3	560.1	−86.13	−86.37
0.5240	0.99374	−1.7206	−1.7205	1417.4	509.4	−75.19	−75.44
0.6537	1.01822	−1.4980	−1.4981	1454.7	467.8	−55.14	−55.17
0.8094	1.03513	−0.4377	−0.4376	1495.7	433.2	−27.82	−27.70
308.15 K							
0.0498	0.79686	0.5923	0.5921	1150.7	954.1	−29.81	−29.86
0.1055	0.82255	0.7726	0.7721	1192.8	864.5	−55.80	−55.70
0.1682	0.85332	0.5435	0.5439	1236.2	780.1	−76.55	−76.41
0.2393	0.88821	−0.0439	−0.0439	1275.9	702.0	−90.73	−90.72

(continued on next page)

Table 3 (*continued*)

x_1	$10^{-3}\ \rho$ (Kg m^{-3})	V^E Expt. 10^6/m^3 mol^{-1}	V^E Redlich–Kister	u (expt.) (m s^{-1})	κ_S (T Pa^{-1})	κ_s^E Expt. T Pa^{-1}	κ_s^E Redlich–Kister
0.3206	0.92551	−0.8709	−0.8711	1319.0	631.5	−97.13	−97.28
0.4144	0.96234	−1.7133	−1.7132	1363.9	569.6	−94.65	−94.82
0.5240	0.99465	−2.2191	−2.2193	1406.8	517.2	−82.49	−82.45
0.6537	1.01848	−1.9606	−1.9605	1445.1	474.3	−60.57	−60.35
0.8094	1.03382	−0.7584	−0.7584	1486.9	439.1	−30.80	−30.86
313.15 K							
0.0498	0.79356	0.5096	0.5094	1135.2	985.4	−34.43	−34.36
0.1055	0.82028	0.6042	0.6037	1178.9	888.7	−63.79	−63.71
0.1682	0.85199	0.2896	0.2888	1224.1	798.3	−86.72	−86.82
0.2393	0.88777	−0.3828	−0.3831	1265.6	715.3	−102.01	−102.34
0.3206	0.92581	−1.2862	−1.2862	1310.4	640.9	−108.51	−108.87
0.4144	0.96311	−2.1867	−2.1864	1356.9	576.0	−105.24	−105.28
0.5240	0.99546	−2.7163	−2.7167	1401.7	521.4	−91.45	−90.95
0.6537	1.01865	−2.4214	−2.4215	1441.6	477.1	−67.19	−66.56
0.8094	1.03243	−1.0777	−1.0782	1485.2	441.0	−34.41	−34.72
CA+PO298.15 K							
0.0629	0.82203	0.3998	0.3998	1239.5	794.6	−18.63	−18.41
0.1312	0.84519	0.7095	0.7091	1273.0	734.7	−32.39	−32.48
0.2057	0.86946	0.9217	0.9214	1307.9	679.2	−41.62	−42.05
0.2872	0.89482	1.0328	1.0327	1339.0	627.8	−46.63	−47.12
0.3767	0.92124	1.0426	1.0425	1373.6	580.4	−47.65	−47.85
0.4755	0.94862	0.9556	0.9554	1410.1	536.7	−44.92	−44.59
0.5851	0.97677	0.7834	0.7832	1444.5	496.5	−38.61	−37.93
0.7074	1.00545	0.5467	0.5465	1474.1	459.7	−28.91	−28.45
0.8447	1.03433	0.2748	0.2747	1507.4	426.0	−15.98	−16.31
303.15 K							
0.0629	0.81848	0.3577	0.3577	1223.8	819.0	−20.83	−20.57
0.1312	0.84199	0.6330	0.6328	1258.6	755.0	−36.10	−36.21
0.2057	0.86647	0.8205	0.8201	1294.8	696.1	−46.24	−46.76
0.2872	0.89195	0.9165	0.9165	1327.3	641.8	−51.63	−52.22
0.3767	0.91835	0.9227	0.9226	1363.1	591.9	−52.59	−52.82
0.4755	0.94560	0.8431	0.8434	1400.8	546.1	−49.40	−49.02
0.5851	0.97353	0.6905	0.6905	1436.6	504.1	−42.32	−41.51
0.7074	1.00190	0.4826	0.4827	1467.5	465.8	−31.57	−31.03
0.8447	1.03045	0.2447	0.2448	1502.1	430.8	−17.38	−17.77
308.15 K							
0.0629	0.81524	0.2857	0.2856	1208.2	844.1	−23.54	−23.21
0.1312	0.83927	0.5060	0.5061	1244.3	775.6	−40.60	−40.73
0.2057	0.86407	0.6576	0.6573	1281.7	713.1	−51.75	−52.40
0.2872	0.88966	0.7363	0.7362	1315.5	655.8	−57.51	−58.27
0.3767	0.91601	0.7425	0.7425	1352.6	603.4	−58.31	−58.65
0.4755	0.94304	0.6800	0.6797	1391.7	555.5	−54.53	−54.14
0.5851	0.97063	0.5569	0.5565	1428.6	511.8	−46.52	−45.60
0.7074	0.99861	0.3876	0.3877	1460.8	471.9	−34.58	−33.94
0.8447	1.02672	0.1946	0.1945	1496.7	435.6	−18.98	−19.44
313.15 K							
0.0629	0.81196	0.2137	0.2134	1192.6	870.1	−26.44	−26.06
0.1312	0.83650	0.3808	0.3809	1230.1	797.0	−45.38	−45.56
0.2057	0.86161	0.4975	0.4979	1268.8	730.6	−57.58	−58.37
0.2872	0.88730	0.5610	0.5608	1303.9	670.2	−63.70	−64.60
0.3767	0.91358	0.5676	0.5676	1342.5	615.2	−64.32	−64.69
0.4755	0.94042	0.5195	0.5190	1382.5	565.1	−59.93	−59.39
0.5851	0.96773	0.4207	0.4204	1420.8	519.4	−50.96	−49.80
0.7074	0.99535	0.2843	0.2839	1454.3	478.0	−37.78	−37.01
0.8447	1.02307	0.1315	0.1317	1491.5	440.4	−20.70	−21.30
CA+IPO298.15 K							
0.0644	0.80427	0.4811	0.4809	1179.3	899.3	−28.33	−28.24
0.1340	0.82891	0.8464	0.8462	1219.5	819.2	−49.48	−49.53
0.2097	0.85480	1.0923	1.0921	1261.1	746.4	−63.27	−63.74
0.2921	0.88193	1.2187	1.2184	1299.0	679.2	−71.42	−70.96
0.3823	0.91021	1.2299	1.2296	1340.3	620.4	−71.20	−71.54
0.4815	0.93951	1.1359	1.1357	1383.4	565.8	−66.54	−66.17
0.5909	0.96963	0.9521	0.9519	1424.5	517.3	−55.94	−55.81
0.7123	1.00035	0.6972	0.6970	1460.8	472.6	−41.35	−41.48
0.8478	1.03148	0.3844	0.3843	1500.7	431.1	−23.52	−23.53
303.15 K							
0.0644	0.80073	0.4378	0.4377	1163.6	928.0	−31.78	−31.60
0.1340	0.82569	0.7678	0.7677	1205.1	843.0	−54.69	−55.18

Table 3 (*continued*)

x_1	$10^{-3} \, \rho$ (Kg m^{-3})	V^E Expt. 10^6/m^3 mol^{-1}	V^E Redlich–Kister	u (expt.) (m s^{-1})	κ_S (T Pa^{-1})	κ_s^E Expt. T Pa^{-1}	κ_s^E Redlich–Kister
0.2097	0.85182	0.9876	0.9874	1248.0	764.7	−70.83	−70.67
0.2921	0.87905	1.0984	1.0982	1287.2	695.1	−78.25	−78.22
0.3823	0.90733	1.1055	1.1053	1329.7	633.1	−78.02	−78.38
0.4815	0.93651	1.0197	1.0194	1374.1	576.1	−72.71	−72.05
0.5909	0.96640	0.8562	0.8559	1416.5	526.2	−60.26	−60.45
0.7123	0.99681	0.6315	0.6313	1454.1	478.9	−44.98	−44.82
0.8478	1.02760	0.3542	0.3541	1495.4	436.0	−25.46	−25.53
308.15 K							
0.0644	0.79747	0.3637	0.3636	1140.9	970.8	−36.43	−36.41
0.1340	0.82294	0.6392	0.6391	1184.5	876.8	−63.52	−63.54
0.2097	0.84936	0.8242	0.8241	1229.4	792.0	−81.41	−81.25
0.2921	0.87671	0.9191	0.9190	1270.7	716.8	−89.53	−89.79
0.3823	0.90492	0.9280	0.9280	1315.3	649.3	−89.97	−89.76
0.4815	0.93389	0.8589	0.8589	1361.7	590.4	−81.70	−82.25
0.5909	0.96348	0.7237	0.7237	1406.2	535.8	−69.11	−68.71
0.7123	0.99352	0.5354	0.5353	1445.9	486.7	−50.82	−50.65
0.8478	1.02390	0.3005	0.3006	1489.3	441.5	−28.58	−28.67
313.15 K							
0.0644	0.79417	0.2915	0.2914	1129.8	994.7	−39.34	−39.33
0.1340	0.82012	0.5140	0.5138	1174.2	896.3	−68.34	−68.43
0.2097	0.84683	0.6650	0.6648	1219.9	807.6	−87.57	−87.23
0.2921	0.87428	0.7441	0.7439	1262.0	729.4	−96.13	−96.04
0.3823	0.90245	0.7533	0.7533	1307.4	660.7	−95.19	−95.61
0.4815	0.93123	0.6983	0.6983	1354.6	598.9	−87.23	−87.2
0.5909	0.96055	0.5875	0.5875	1399.8	543.5	−72.85	−72.59
0.7123	0.99026	0.4316	0.4316	1440.4	493.1	−53.36	−53.43
0.8478	1.02024	0.2383	0.2383	1484.6	446.1	−30.33	−30.33

The standard uncertainties are $u(x) = \pm 1 \times 10^{-4}$, $u(\rho) = \pm 5 \times 10^{-5}$ g cm^{-3}, $u(T) = 0.02$ K and the combined expanded uncertainties Uc are $Uc(V^E) = 0.002$ cm^3 mol^{-1}, $Uc(\kappa_s^E) = 0.03$ T Pa^{-1} (0.95 level of confidence) respectively.

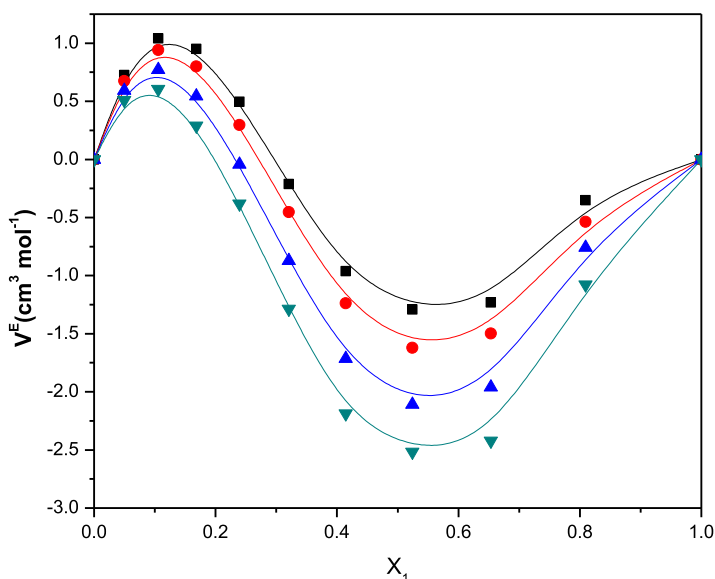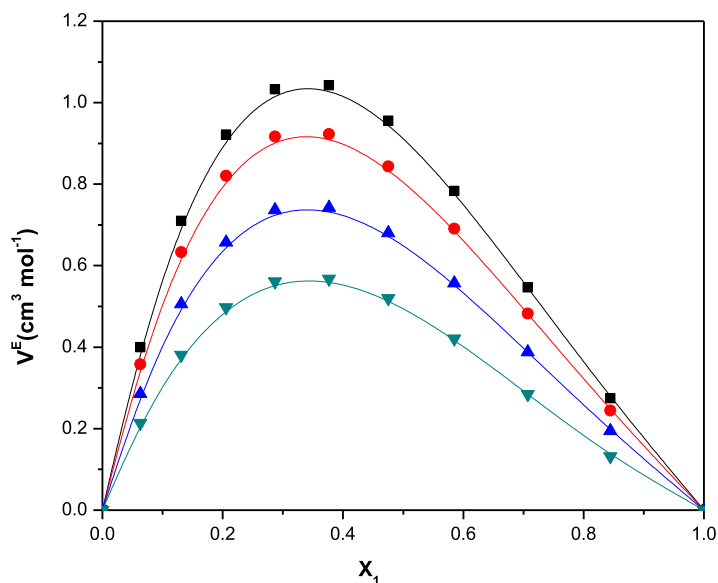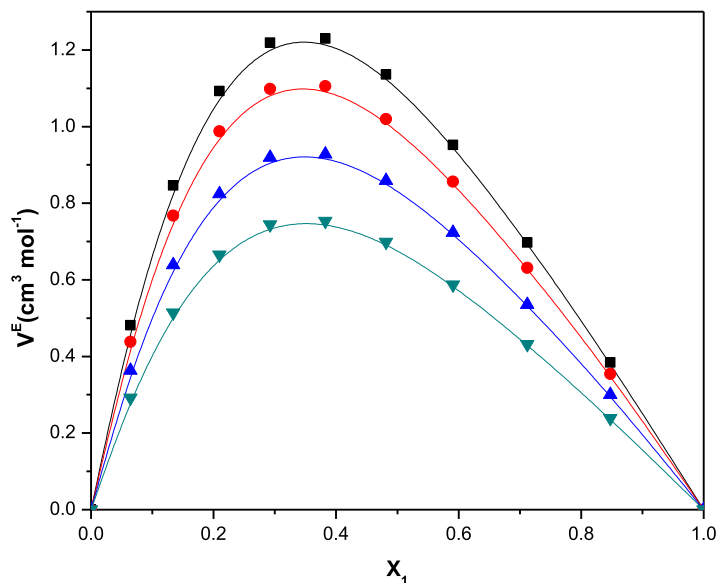**Fig. 2.** Plot of excess volumes (V^E) vs mole fraction (x_1) for binary liquid mixtures of CA+EO at T = 298.15 K (■), T = 303.15 K (•), T = 308.15 K (▲), and T = 313.15 K (▼).

data arises from the breakup interactions between like molecules namely, depolymerization of hydrogen bonded network of alcohols and the loosening of the dipolar interactions between CA molecules. The transition $V^E < 0$ to $V^E > 0$ from MO to IPO reveal that a steric effect increases the mixture volume. The degree of association [34] in alcohols decreases as the carbon chain length increases from MO to PO. The strength of the hydrogen bond between CA and alcohol molecule should follow the sequence: MO > EO > PO. This may be conveniently explained by considering CA as a proton acceptor forms hydrogen bond more effectively with MO, which is a good proton donor when compared to PO, which is a poor proton donor due to their bigger alkyl group size [35,36]. A similar trend was reported in the literature [37,38] for the mixtures
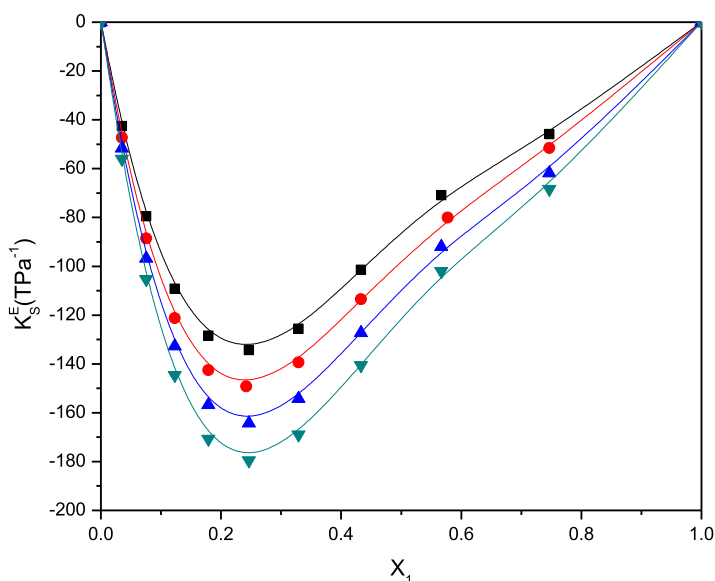
Fig. 3. Plot of excess volumes (V^E) vs mole fraction (x_1) for binary liquid mixtures of CA+PO at T = 298.15 K (■), T = 303.15 K (•), T = 308.15 K (▲), and T = 313.15 K (▼).

Fig. 4. Plot of excess volumes (V^E) vs mole fraction (x_1) for binary liquid mixtures of CA+IPO at T = 298.15 K (■), T = 303.15 K (•), T = 308.15 K (▲), and T = 313.15 K (▼).

of N,N-dimethyl formamide with n-alkanols and toluene with n-alkanols. The comparison of V^E data between PO and IPO suggests that the later mixture exhibit more positive deviation. This may be attributed to the branching of the alkyl group in IPO, which increases the steric hindrance [39] for the favorable cross hydrogen bonding formation between IPO and CA.

As the chain length of alcohols molecule increases from MO to IPO, the strength of hydrogen bonding formation decreases. The self-associated polymer aggregates of higher alcohols are relatively easier to break with increase in chain length of alcohols. The more negative V^E for the binary mixture containing MO suggest that the cross hydrogen bonding interactions between oxygen atom of CA and hydroxyl group of MO supersedes the structure breaking of polymer aggregates of MO. Positive to negative V^E values for CA+EO suggests that the structure breaking and structure making factors are competing with each other in varying degrees. The initial addition of CA molecules results in the disruption of self associated EO molecule leading to the positive V^E. With increase in the composition of CA, it results in the formation of cross H-bonding between CA and EO molecules leading to negative V^E values. The positive V^E for the binary mixture of CA with PO and

Fig. 5. Plot of excess isentropic compressibilities ($\kappa_s{}^E$) vs mole fraction (x_1) for binary liquid mixtures of CA+MO at T = 298.15 K (■), T = 303.15 K (•), T = 308.15 K (▲), and T = 313.15 K (▼).

IPO suggest that the disruption of self-associated PO and IPO outweighs the cross hydrogen bonding between the unlike molecules.

A comparison of V^E values for the binary mixtures of CA with 1-alcohols namely MO, EO, PO and IPO with the data reported earlier [40] for the binary mixtures of furfural with the same alcohols indicate that, the unlike interactions are very effective and stronger in the latter case resulting in the formation of intermolecular complexes through hydrogen bonding.

The perusal of Figs. 1 and 2 shows that the excess volumes (V^E) for the binary mixtures of CA with MO and EO become more negative with the increase in temperature. Figs. 3 and 4 illustrate that the excess volumes (V^E) for the binary mixtures of CA with PO and IPO become less positive with the increase in temperature. This may be attributed due to fact that the interactions between two like molecules might decrease more with temperature than the interactions between two unlike molecules. Further, increase in temperature enlarges the interstices, which lead to more efficient packing between unlike molecules.This result in increased contraction in volume leading to more negative V^E values in CA with MO and EO, and less positive V^E values in CA with PO and IPO.

3.2. Excess isentropic compressibility (κ_S^E)

The isentropic compressibility (κ_s), and excess isentropic compressibility (κ_S^E) values for each mixture were calculated from u and ρ of pure liquids and mixtures with the following expression:

$$\kappa_s = (u^2\rho)^{-1} \tag{2}$$

The excess isentropic compressibilities (κ_S^E) were calculated as

$$\kappa_S^E = \kappa_S - \kappa_S^{id} \tag{3}$$

where, $\kappa_s{}^{id}$ is the ideal isentropic compressibility value, which was calculated from the following equation recommended by Benson and Kiyohara [41] and Douheret et al. [42]

$$\kappa_s{}^{id} = \sum_{i=1}^{2} \phi_i\left[\kappa_{s.i} + TV_i\left(\alpha_i{}^2\right)/C_{p.i}\right] - \left\{ T\left(\sum_{i=1}^{2} x_iV_i\right)\left(\sum_{i=1}^{2} \phi_i\alpha_i\right)^2 / \sum_{i=1}^{2} x_iC_{p.i} \right\} \tag{4}$$

In which the ϕ_i, $\kappa_{s.i}$, V_i, C_{pi} and α_i are the volume fraction, isentropic compressibility, molar volume, molar heat capacity and the thermal expansion coefficient respectively of the pure component i, T represents temperature and x_i represents the mole fraction of i in the binary mixture. The values of C_p for the investigated liquids were obtained from the literature [10,13,17,19].

The experimental speeds of sound (u), isentropic compressibilities (κ_s) and excess isentropic compressibilities (κ_S^E) for the binary mixtures over the whole range of composition at T = 298.15–313.15 K were presented in Table 3. The plots of κ_S^E against x_1, for the binary mixtures of CA with MO, EO, PO, IPO at T = 298.5–313.5 K are depicted in Figs. 5–8. From the Table 3 and Figs. 5–8, it is evident that κ_S^E values are negative over the entire composition range for the mixtures of CA
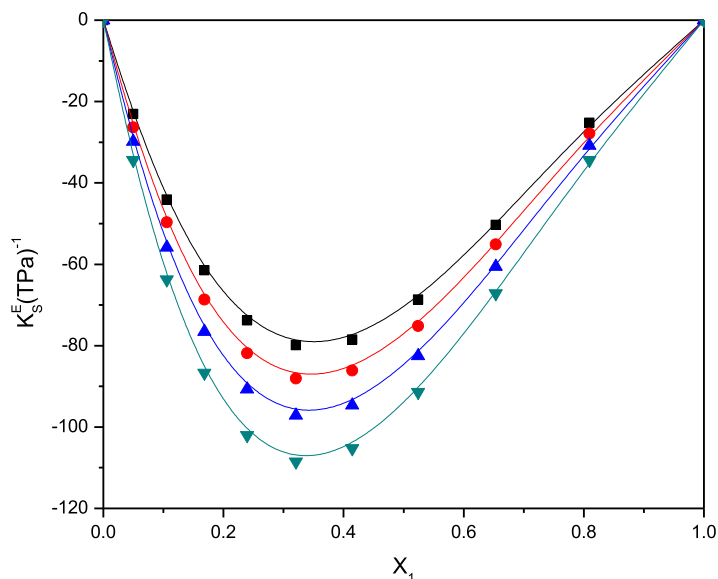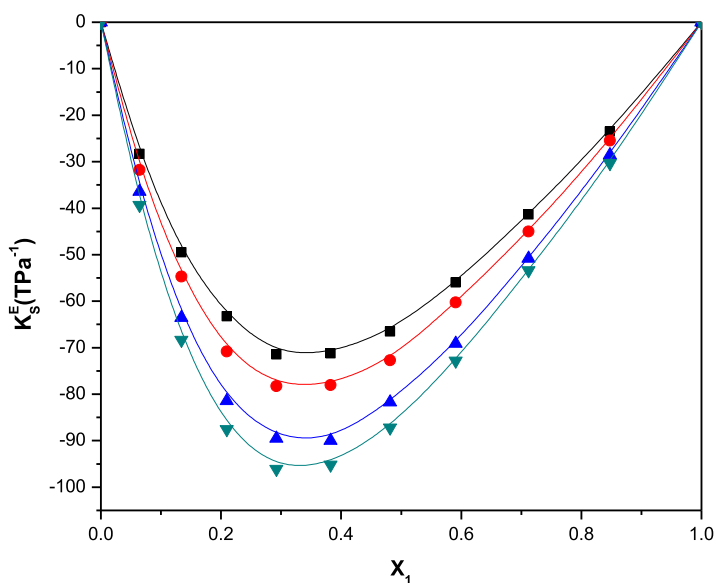
Fig. 6. Plot of excess isentropic compressibilities (κ_s^E) vs mole fraction (x_1) for binary liquid mixtures of CA+EO at T = 298.15 K (■), T = 303.15 K (•), T = 308.15 K (▲), and T = 313.15 K (▼).
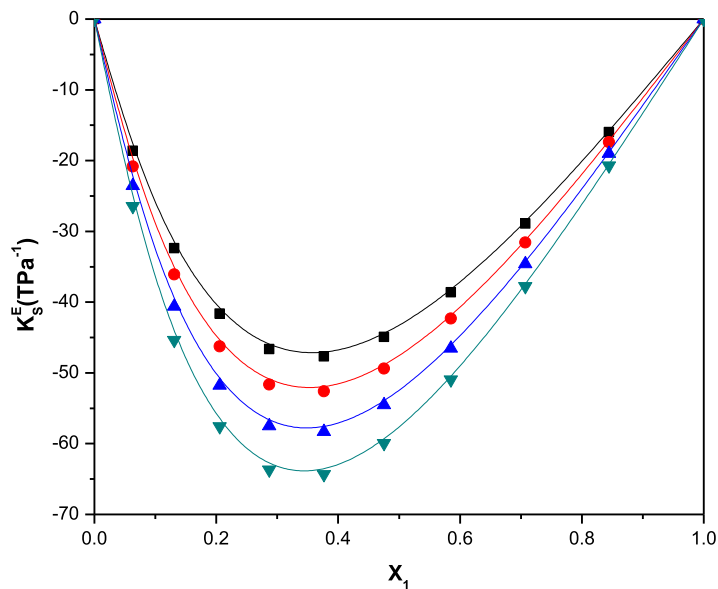

Fig. 7. Plot of excess isentropic compressibilities (κ_s^E) vs mole fraction (x_1) for binary liquid mixtures of CA+PO at T = 298.15 K (■), T = 303.15 K (•), T = 308.15 K (▲), and T = 313.15 K (▼).

with MO, EO, PO, and IPO at all the investigated systems. The sign and magnitude of excess isentropic compressibility data of any liquid mixtures may be explained in terms of dipole-dipole interactions and charge transfer complex formation between CA and alcohol molecules leading to increase in sound velocity and decrease in isentropic compressibility. As already suggested by many researchers [41,43,44] that the sign of excess isentropic compressibility is the result of several opposing effects. A strong molecular attraction through charge transfer, dipole induced dipole and dipole- dipole interactions, interstitial accommodation and orientational order in component molecules lead to a more compact structure which contributes to negative deviation in excess isentropic compressibility. The breaking up of solvent structure due to dipole–dipole association and the rupturing of hydrogen bond in the liquid structure contributes to the positive deviation in excess isentropic compressibilities.

The algebraic data of κ_S^E for the binary mixtures of CA with alcohols fall in the order.

MO > EO > IPO > PO

Fig. 8. Plot of excess isentropic compressibilities (κ_s^E) vs mole fraction (x_1) for binary liquid mixtures of CA+IPO at T = 298.15 K (■), T = 303.15 K (•), T = 308.15 K (▲), and T = 313.15 K (▼).
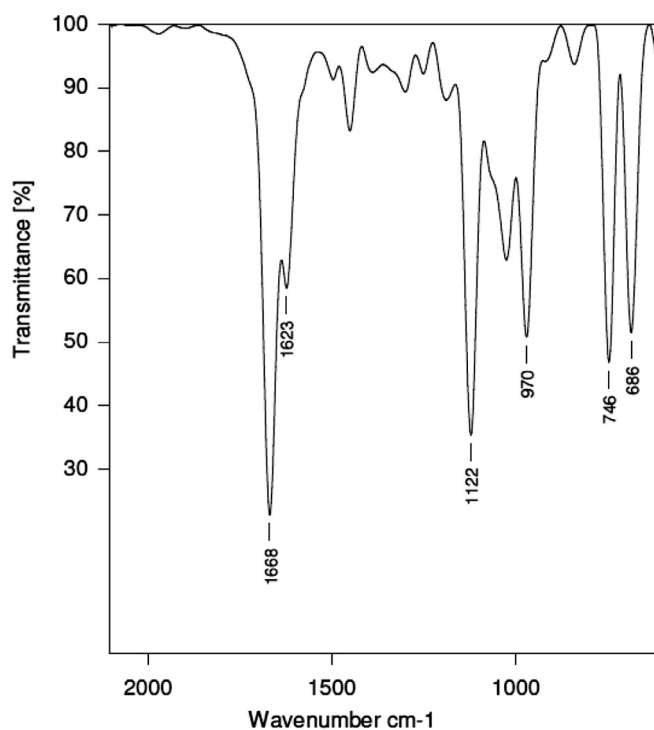
Fig. 9. Partial ATR-FTIR spectra of (CA+MO) binary mixture.

The negative κ_S^E values for all the systems imply that solvent molecules around the solute are less compressible than the solvent molecules in the bulk. The above order indicates that on the addition of an interactive molecule to CA, decluster the molecular order of the other, releasing several dipoles causing cross-molecular interactions. Thus, the structural arrangements of molecule results in increasing the negative excess isentropic compressibility as the chain length of alcohol molecule increase from MO to PO. As the size of the alkyl group of 1-alcohol increases, the steric hindrance increases leading to less efficient packing between bulkier CA and the smaller 1-alcohol molecules. Hence, the less negative κ_s^E values for CA+MO

Table 4

Coefficients a_0, a_1 and a_2 of the Redlich–Kister type polynomial equation (Eq. 6) and the corresponding standard deviations σ (Y^E) for the binary systems CA with alcohols.

Excess function	T (K)	Redlich–Kister			
		a_0	a_1	a_2	σ (Y^E)
CA+MO					
$V^E \times 10^6$ /m^3 mol^{-1}	298.15 K	−6.779	2.136	−2.69	0.0002
	303.15 K	−7.071	2.647	−3.163	0.0001
	308.15 K	−7.429	3.301	−4.438	0.0002
	313.15 K	−7.811	3.893	−5.706	0.0001
$\kappa_s^E \times 10^{-10}$/T Pa^{-1}	298.15 K	−342.1	473.4	−548.8	0.2440
	303.15 K	−382.1	522	−611.9	0.3205
	308.15 K	−434.3	548.4	−671.3	0.3312
	313.15 K	−480.4	595.6	−719.3	0.3214
CA+EO					
$V^E \times 10^6$/m^3 mol^{-1}	298.15 K	−5.508	−5.707	19.33	0.0002
	303.15 K	−6.664	−5.801	19.37	0.0001
	308.15 K	−8.655	−5.994	19.45	0.0003
	313.15 K	−10.64	−6.185	19.53	0.0005
$\kappa_s^E \times 10^{-10}$/T Pa^{-1}	298.15 K	−287.8	213.1	−15.32	0.4108
	303.15 K	−313.9	239.4	−36.09	0.2294
	308.15 K	−343.3	267.3	−57.86	0.1530
	313.15 K	−379.1	304.4	−89.63	0.4080
CA+PO					
$V^E \times 10^6$/m^3 mol^{-1}	298.15 K	3.689	−2.853	0.783	0.0003
	303.15 K	3.255	−2.545	0.769	0.0002
	308.15 K	2.624	−2.045	0.565	0.0003
	313.15 K	2.001	−1.625	0.26	0.0004
$\kappa_s^E \times 10^{-10}$/T Pa^{-1}	298.15 K	−173.3	109.8	−56.27	0.4882
	303.15 K	−190.3	124.5	−65.31	0.5756
	308.15 K	−209.9	142.8	−77.27	0.6909
	313.15 K	−230	161.8	−92.45	0.8507
CA+IPO					
$V^E \times 10^6$/m^3 mol^{-1}	298.15 K	4.437	−2.975	1.264	0.0003
	303.15 K	3.983	−2.665	1.272	0.0002
	308.15 K	3.358	−2.189	1.021	0.0001
	313.15 K	2.73	−1.781	0.736	0.0001
$\kappa_s^E \times 10^{-10}$/T Pa^{-1}	298.15 K	−258.7	168.2	−84.08	0.3512
	303.15 K	−281.4	190.8	−101.7	0.3975
	308.15 K	−321	223.6	−117.3	0.3224
	313.15 K	−340.2	243.6	−132.9	0.2493

and the more negative κ_S^E values for CA+PO systems. The more negative κ_S^E for CA+IPO than CA+PO is attributed to the fact that more branched IPO fit into the voids of the CA more easily than linear PO.

The κ_s^E values become more negative with increase in the temperature for the studied systems. The increase in temperature enlarges the interstices, which lead to more efficient packing between CA and alcohols. As a result, the binary systems become more resistant to compression resulting in more negative κ_s^E values.

The experimental excess volume and excess isentropic compressibility values were correlated with Redlich–Kister [8] equation.

Redlich–Kister equation:

$$Y^E = x_1(1 - x_1)[a_0 + a_1(2x_1 - 1) + a_2(2x_1 - 1)^2] \tag{5}$$

where, Y^E is any excess property (κ_S^E or V^E) and x_1 is the mole fraction of CA. The adjustable parameters a_0, a_1 and a_2 in Redlich–Kister equation were obtained by the method of least squares and were reported along with values of standard deviation between the experimental and calculated values of the respective excess functions in Table 4.

The standard deviation σ (Y^E) values for the studied excess parameters were calculated by using the following relation:

$$\sigma\left(Y^E\right) = \left[\frac{\sum\left(Y^E{}_{\exp} - Y^E{}_{cal}\right)^2}{n - p}\right]^{\frac{1}{2}} \tag{6}$$

where, n is the number of data points and p is the number of adjustable parameters.

The calculated values of V^E and κ_s^E from Redlich–Kister equation were also included in Table 3. From comparing the experimental and calculated excess properties, it was clear that Redlich–Kister model correlates the experimental data satisfactorily.
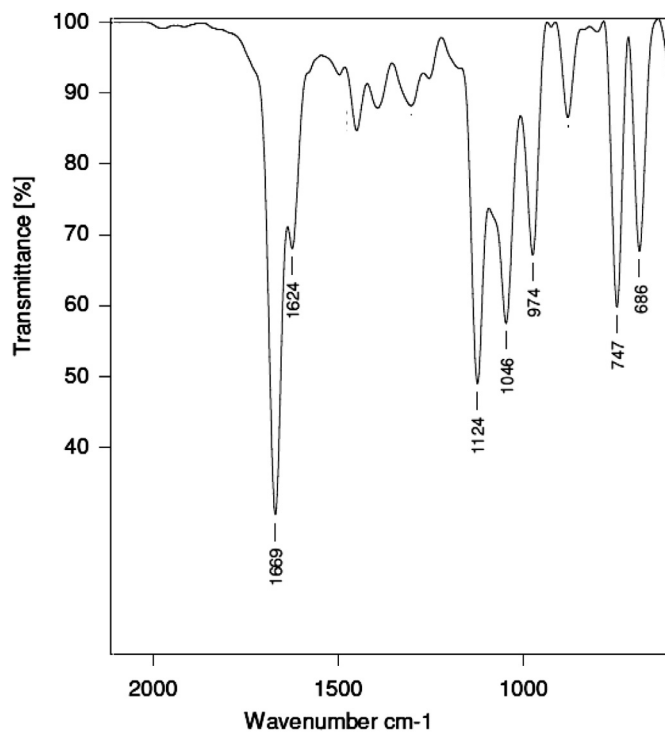
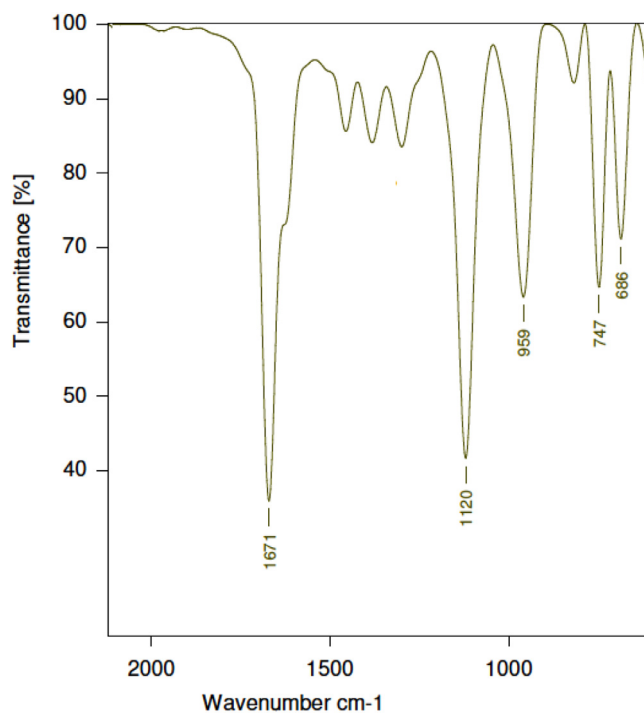**Fig. 10.** Partial ATR-FTIR spectra of (CA+EO) binary mixture.

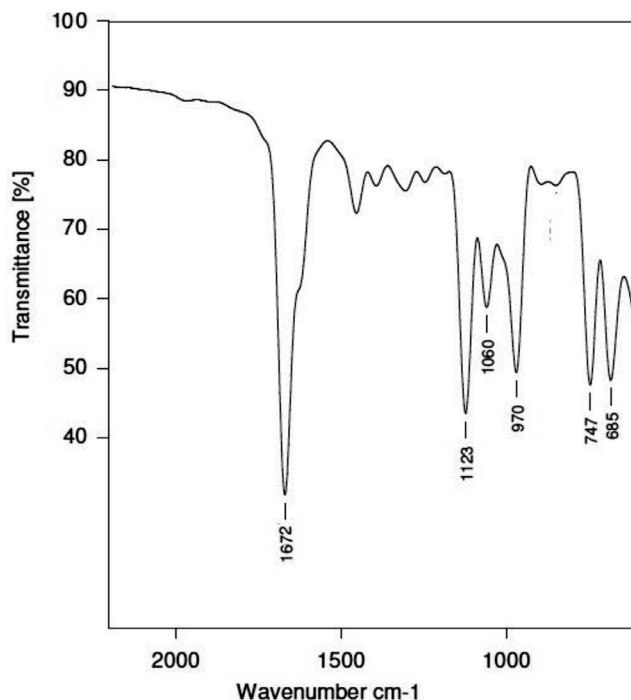**Fig. 11.** Partial ATR-FTIR spectra of (CA+PO) binary mixture.

Fig. 12. Partial ATR-FTIR spectra of (CA+IPO) binary mixture.

3.3. ATR-FTIR spectral studies

Among the spectroscopic techniques, ATR-FTIR is an effective tool used to investigate the intermolecular interactions like hydrogen bonding between the component molecules of the binary liquid mixtures by analyzing the position and shifts of the absorption band [45,46]. In the present investigation, the negative excess properties observed in the CA+MO and CA+EO systems may be attributed to intermolecular H-bonding between CA and alcohols. The strength of these chemical interactions in the studied systems can be analyzed by the comparison of the shift in stretching frequency of carbonyl group, v (C=O) of CA with the corresponding v (C=O) bands in their pure states.

In general, the polar C=O group produce a large change in dipole moment and hence results in a more intense v (C=O) absorption band. From the IR spectra of CA [47], it can be observed that v (C=O) band appear at 1685 cm^{-1}, v (C=C) at 1630 cm^{-1}, and v (C–O) at 1120 cm^{-1}. ATR-FTIR spectra of equimolar binary mixtures of CA with alcohols were recorded and the partial ATR-FTIR spectra of CA+alcohols in the v (C=O) region were shown in Figs. 9–12. The absorption bands of carbonyl group v (C=O) in Figs. 9–12, revealed a shift of stretching frequency (Δv) to lower frequency. The stretching frequency of v (C=O) bands for the equimolar mixtures of CA with MO, EO, PO and IPO were found to be 1668 cm^{-1}, 1669 cm^{-1}, 1671 cm^{-1},and 1672 cm^{-1} respectively and their corresponding Δv (C=O) values were in the order of −17 cm^{-1},−16 cm^{-1}, −14 cm^{-1}, and −13 cm^{-1} respectively.

The red shift of stretching frequency was a measure of the strength of hydrogen bond [46]. The red shift of v (C=O) peak strongly reveals that intermolecular H-bonding exists in the above systems investigated. The higher shift in v (C=O) absorption band in CA+MO, suggests the existence of stronger intermolecular H-bonding (C=O···H−O) than in the other three systems leading to more volume contraction and more negative excess volume. Hence, it can be concluded that the results of the excess thermodynamic properties have been supported by ATR-FTIR spectroscopic studies.

4. Conclusions

The densities (ρ), speed of sound (u), excess volume (V^E), excess isentropic compressibility (κ_S^E) of binary mixtures of CA with MO, EO, PO, and IPO were measured at T = (298.15, 303.15, 308.15, 313.15) K over the entire composition range. The values of V^E and κ_S^E are well correlated with Redlich–Kister equation. The excess properties were analyzed in terms of intermolecular interactions between component molecules. The thermodynamic conclusions of the binary systems have been supported by ATR-FTIR spectral studies.

References

[1] L. Venkatramana, C. Narasimha Rao, L. Ramesh Gardas, K. Siva Kumar, FT-IR study of excess thermodynamic properties of binary liquid mixtures of p-xylene with 1-alkanols at 303.15K, J. Mol. Liq. 207 (2015) 171–176.

[2] A. Ali, A.K. Nain, M. Ibrahim, Theoretical evaluation of ultrasonic velocity in binary liquid mixtures using various approaches, J. Pure Appl. Ultrason. 19 (1997) 41–46.

[3] J.D. Pandey, P. Jain, V. Vyas, Isothermal compressibility and sound velocity of binary liquid systems: application of hard sphere models, Pramana J. Phys. 43 (1994) 361–372.

[4] A. Ali, A.K. Nain, D. Chand, R. Ahmad, Volumetric, ultrasonic, viscometric and refractive index behavior of binary mixtures of 2,2,4-trimethylpentane with aromatic hydrocarbons: an experimental and theoretical study, J. Mol. Liq. 128 (2006) 32–41.

[5] L. Mosteiro, L.M. Casas, J.L. Legido, Surface tension, density, and speed of sound for the ternary mixture {diethyl carbonate + p-xylene + decane}, J. Chem. Thermodyn. 41 (2009) 695–704.

[6] O.P. Chimankar, N.R. Pawar, Ultrasonic investigation of bio-liquid mixtures of methanol with cinnamaldehyde by interferometric method operated in the frequency range 1MHz-10MHz, Int. J. Res. Eng.Tech. 3 (2014) 315–324.

[7] K.A. Kurnia, B. Ariwahjoedi, M.I. Abdul Mutalib, T. Murugesan, Density and excess molar volume of the protic ionic liquid Bis (2-hydroxyethyl) ammonium acetate with alcohols, J. Sol. Chem. 40 (2011) 470–480.

[8] O. Redlich, A.T. Kister, Algebraic representation of thermodynamic properties and the classification of solutions, J. Ind. Eng. Chem. 40 (1948) 345–348.

[9] G. Padmanabhan, R. Kumar, V. Ulagendran, V. Kannappan, S. Jayakumar, Molecular interaction studies of cinnamaldehyde with certain alcohols by ultrasonic method at 303.15 K, Indian J. Pure Appl. Phys. 50 (2012) 899–906.

[10] T.S. Khasanshin, T.B. Zykova, Heat capacity of saturated monovalent alcohols, Inzh.Fiz.Zh. 56 (1989) 991–994.

[11] T.M. Aminabhavi, I.A. Mrityunjaya, B.H. Shivaputrappa, H.B. Ramachandra, Densities, viscosities, refractive indices, and speeds of sound for methyl acetoacetate + aliphatic alcohols (C_1-C_8), J. Chem. Eng. Data 38 (1993) 31–39.

[12] J.G. Emilio, G. Begona, N. Calvar, D. Angeles, Physical properties of binary mixtures of the ionic liquid 1-ethyl-3-methylimidazolium ethyl sulfate with several alcohols at T = (298.15, 313.15, and 328.15) K and atmospheric pressure, J. Chem. Eng. Data 52 (2007) 1641–1648.

[13] J.A. Riddick, W.B. Bunger, T.K. Sakano, Organic Solvents; Physical Properties and Methods of Purification, 11, Fourth ed., Wiley-Interscience, New York, 1986.

[14] S.N. Pandharinath, N. Laxman Shirsat, M. Hasan, Density and viscosity studies of binary mixtures of acetonitrile with methanol, ethanol, propan-1-ol, propan-2-ol, butan-1-ol, 2- methylpropan-1-ol, and 2-methylpropan-2-ol at (298.15, 303.15, 308.15, and 313.15) K, J. Chem. Eng. Data 43 (1998) 732–737.

[15] M.N. Roy, S. Anuradha, S. Biswajit, Excess molar volumes, viscosity deviations and isentropic compressibility of binary mixtures containing 1, 3-dioxolane and monoalcohols at 303.15 K, J. Sol. Chem. 34 (2005) 1311–1325.

[16] L. Zhang, X. Lu, D. Ye, Y. Guo, W. Fang, Density and viscosity for binary mixtures of the ionic liquid 2,2-diethyl-1,1,3,3-tetramethylguanidinium ethyl sulfate with water, methanol, or ethanol, J. Chem. Eng. Data 61 (2016) 1023–1031.

[17] G. Garcia-Miaja, J. Troncoso, L. Romani, Excess properties for binary systems ionic liquid + ethanol: experimental results and theoretical description using the ERAS model, Fluid Phase Equilib. 274 (2008) 59–67.

[18] E. Vercher, A.V. Orchilles, P.J. Miguel, A. Martinez-Andreu, Volumetric and ultrasonic studies of 1-ethyl-3-methylimidazolium trifluoromethanesulfonate ionic liquid with methanol, ethanol, 1-propanol, and water at several temperatures, J. Chem. Eng. Data 52 (2007) 1468–1482.

[19] S. Singh, M. Aznar, N. Deenadayalu, Densities, speeds of sound, and refractive indices for binary mixtures of 1-butyl-3-methylimidazolium methyl sulphate ionic liquid with alcohols at T = (298.15, 303.15, 308.15, and 313.15) K, J. Chem. Thermodyn. 57 (2013) 238–247.

[20] S. Mrad, M. Hichri, I. Khattech, C. Lafuente, Thermophysical study of the binary mixtures of N, N-dimethylacetamide with 1-propanol and 1-butanol, J. Mol. Liq. 231 (2017) 168–173.

[21] A. Estrella, A. Cancela, R. Maceiras, J.M. Navaza, R. Taboas, Density, viscosity, excess molar volume, and viscosity deviation of three amyl alcohols + ethanol binary mixtures from 293.15 to 323.15K, J. Chem. Eng. Data 51 (2006) 940–945.

[22] Sahar Mard, Carlos Lafuente, Monia Hichri, Ismail Khattech, Density, speed of sound, refractive index, and viscosity of the binary mixtures of N,N-dimethylacetamide with ethanol and 1-butanol, J. Chem. Eng. Data 61 (2016) 2946–2953.

[23] B. Gonzalez, A. Dominguez, J. Tojo, Dynamic viscosities, densities, and speed of sound and derived properties of the binary systems acetic acid with water, methanol, ethanol, ethyl acetate and methyl acetate at T = (293.15, 298.15, and 303.15) K at atmospheric pressure, J. Chem. Eng. Data 49 (2004) 1590–1596.

[24] R. Kumar, R. Mahesh, B. Shanmugaoriyan, V. Kannappan, Volumetric, viscometric, acoustic and refractometric studies of molecular interactions in certain binary systems of o-chlorophenol at 303.15K, Indian J. Pure Appl. Phys. 50 (2012) 633–640.

[25] R.M. Naessems, R.A. Clara, A.C.G. Marigliano, Density, viscosity, excess molar volume and viscosity deviation for [chloroform (1) + methanol (3)] binary system and [chloroform (1) + di-isopropylether (2) + methanol (3)] ternary system at 298.15K, Chem. Data Coll 7-8 (2017) 68–79.

[26] V.H. Alvarez, S. Mattedi, M. Martín-Pastor, M.I. Aznar, Thermophysical properties of binary mixtures of {ionicliquid 2-hydroxy ethylammonium acetate plus (water, methanol, or ethanol)}, J. Chem. Thermodyn. 43 (2011) 997–1010.

[27] Z.P. Visak, A.G.M. Ferreira, I.M.A. Fonseca, Densities and viscosities of the ternary mixtures water + butyl acetate + methanol and water + ethyl propionate + methanol at 303.15K, J. Chem. Eng. Data 45 (2000) 926–931.

[28] A. Mohammad, H. Iloukhani, Density, viscosity and refractive indices of binary mixtures of acetophenone and 2- alkanols, J. Chem. Eng. Data 55 (2010) 1416–1420.

[29] A.C. Gomez, H.N. Solimo, Density, viscosity, excess molar volume, viscosity deviation, and their correlations for formamide + three alkan-1-ols binary systems, J. Chem. Eng. Data 47 (2002) 796–800.

[30] TRC, Data Bases for Chemistry and Engineering: TRC Thermodynamic Tables, Ver. 1996- IS, Jan 1996, Thermodynamic Research Center, Texas A & M University: College station, TX, 1996.

[31] M.T. Zafarani-Moattar, R. Majdan-Cegincara, Density, speed of sound, and viscosity of binary mixtures of poly (propylene glycol) 400 + ethanol and + 2-propanol at different temperatures, J. Chem. Eng. Data 53 (2008) 2211–2216.

[32] M. Venkatesh, L.S. Manjeshwar, M. Sairam, T.M. Aminabhavi, Thermodynamic interactions in binary mixtures of anisole with ethanol, propanol-1-ol, propanol-2-ol, and butanol-1-ol, pentanol-1-ol, and 3-methylbutan-1-ol at T = (298.15, 308.15, and 318.15) K, J. Chem. Thermodyn. 38 (2006) 1620–1628.

[33] A. Arce, E. Rodil, A. Soto, Physical and excess properties for binary mixtures of 1- methyl-3-octylimidazolium tetrafluoroborate, [Omim][BF$_4$], ionic liquid with different alcohols, J. Sol. Chem. 35 (1) (2006) 63–78.

[34] G.A. Krestov, Thermodynamics of Salvation, Ellis Horwood limited, England, 1991.

[35] M.A. Rauf, M. Afran, Farhataziz, excess molar volumes of (N,N- dimethyl formamide + an aliphatic alcohol) at 298.15K, J. Chem. Thermodyn. 15 (1983) 1021–1023.

[36] A. Ali, N. Anil Kumar, S. Vinod Kumar, S. Ahmad, Molecular interactions in binary mixtures of tetrahydrofuran with alkanols (C_6,C_8,C_{10}):An ultrasonic and volumetric study, Indian, J. Pure Appl. Phys. 42 (2004) 666–673.

[37] A. Ali, K. Tiwari, A.K. Nain, V. Chakravorthy, Study of intermolecular interaction in dimethyl sulphoxide + 1-alkanols (1-butanol, 1-hexanol, 1-octanol) at 303.15K, Phy, Chem. Liq. 38 (2000) 459–473.

[38] G.N. Swamy, G. Dharmaraju, G.K. Raman, Excess volumes of toluene mixtures with some alcohol at 303.15K, Can. J. Chem. 58 (1980) 229–230.

[39] B.D. Djordjevic, I.R. Radovic, M.L. Kijevcanin, A.Z. Tasic, S.P. Serbanovic, Molecular interaction studies of the volumetric behavior of binary liquid mixtures containing alcohols, J. Serb. Chem. Soc. 74 (5) (2009) 477–491.

[40] H. Nao rem, Nand kishore, S.K. Suri, Excess molar volumes, speeds of sound and isentropic compressibility's of binary mixtures of furfural with some aliphatic alcohols, Can. J. Chem 67 (1989) 648–650.

[41] G.C Benson, O. Kiyohara, Evaluation of excess isentropic compressibilities and isochoric heat capacities, J. Chem. Thermodyn. 11 (1979) 1061–1064.

[42] G. Douheret, C. Moreau, A. Villard, Excess thermodynamic quantities in binary systems of non electrolytes. I. Different ways of calculating excess compressibilities, Fluid Phase Equilib. 22 (1985) 277–287.

[43] P. Madhusudhana reddy, K. Siva Kumar, P. Venkatesu, Densities, and ultrasonic studies for binary mixtures of tetrahydrofuran with chlorobenzene, chlorotoluene and nitrotoluenes at 298.15K, Fluid Phase Equilib. 310 (2011) 74–81.

[44] A.S. Al- Jimaz, J.A. Al- Kandary, M. Abdul - Haq, Abdul -Latif, Acoustical and excess properties of {chlorobenzene + 1-hexanol, or 1-heptanol, or 1-oc- tanol, or 1-nonanol, or 1-decanol} at (298.15, 303.15, 308.15, and 313.15) K, J. Chem. Eng. Data 52 (2007) 206–214.

[45] P. Bhanuprakash, N.V.V. Jyothi, C. Narasimharao, M. Raveendra, K. Sivakumar, Elucidation of molecular interactions in the mixtures of benzyl alcohol with (C2-C4) alkyl acetates through volumetric, ultrasonic, theoretical and ATR-FTIR spectroscopic studies at T=(298.15,303.15,308.15,313.15) K, J. Mol. Liq. 234 (2017) 49–63.

[46] Q. Wei, X. Guo, Y. Wang, H. Yang, Temperature dependent FTIR study on three kinds of hydrogen bonded benzoic acid dimmers in their melt states, J. Mol. Liq. 177 (2013) 225–228.

[47] Jag Mohan, Organic Spectroscopy Principles and Applications, Second ed., CRC Press, 2004.

Spectroscopic studies on Yb³⁺-doped tungsten-tellurite glasses for laser applications

G. Venkataiah[a], P. Babu[b], I.R. Martín[c], K. Venkata Krishnaiah[d], K. Suresh[a], V. Lavín[c], C.K. Jayasankar[a],*

[a] Department of Physics, Sri Venkateswara University, Tirupati 517 502, India
[b] Department of Physics, SVCR Government Degree College, Palamaner 517408, India
[c] Departamento de Física, MALTA-Consolider Team, IMN, and IUdEA, Universidad de La Laguna, Apdo. 456, E-38200 San Cristóbal de La Laguna, Santa Cruz de Tenerife, Spain
[d] Department of Physics, RGM College of Engineering and Technology, Nandyal 518501, India

ARTICLE INFO

ABSTRACT

Tungsten tellurite glasses (TeO₂-WO₃-ZrO₂) doped with various concentrations of Yb³⁺ ions have been prepared by the conventional melt-quenching method and systematically studied their spectroscopic and laser properties. The spectroscopic properties and some of the laser parameters have been evaluated from the measured absorption and emission spectra. Emission cross-sections evaluated from the McCumber and the Fuchtbauer-Ladenburg methods are found to be in good agreement. The absorption and emission cross-sections are found to be in the range of 2.78–1.30 ($\times 10^{-20}$ cm²) and 3.64–1.83 ($\times 10^{-20}$ cm²), respectively, when Yb³⁺ ions concentration increases from 0.01 to 3.0 mol%. A significant change in luminescence spectral profile for higher concentration (> 0.1 mol%) of Yb³⁺ ions has been explained as due to reabsorption effects. An initial increase of lifetime for the $^2F_{5/2}$ level up to 0.5 mol% and decrease thereafter for higher concentrations (> 0.5 mol%) of Yb³⁺ ions has been explained with a suitable mechanism. The results of spectroscopic and laser parameters indicate that tungsten-tellurite glasses have potential applications as gain media for lasers and optical amplifiers.

1. Introduction

In recent years, an increasing importance of trivalent rare-earth (RE³⁺)-doped glasses as possible lasing materials have created a significant interest in the study of optical and spectroscopic properties for their applications in glass [1], fiber [2] and waveguide lasers [3]. Among the RE³⁺ ions, ytterbium (Yb³⁺) ion has attracted a great interest for its excellent properties such as (a) low non-radiative decay rate, (b) simple electronic structure, i.e., the $^2F_{7/2}$ ground state and the $^2F_{5/2}$ excited state, which can avoid non-radiative processes such as excited-state absorption and upconversion, (c) very good sensitizer for other 980 nm pumped RE³⁺ ions [4] and (d) broad absorption and emission bandwidths. These properties can be utilized for the development of high-power (> 50 W cm⁻²), high-efficiency ($> 50\%$) and ultrafast laser emission [5]. Very recently, the Yb³⁺-doped glass-ceramics have been utilized for laser cooling of solid state as they exhibit lower maximum phonon energy, higher photoluminescence quantum efficiency and lower background absorption compared to their parent glasses [6,7].

Among different types of glass hosts such as borate, phosphate, silicate and tellurite, the latter have many advantages such as (i) a wider transmission range (0.35–5 μm) compared to silicate glasses (0.2–3 μm), (ii) better corrosion resistance than fluoride glasses [8], (iii) high linear refractive indices (1.8–2.3) and (iv) lower phonon energy among oxide glass hosts (800 cm⁻¹), and (v) high solubility of dopant RE³⁺ ions [9]. The Yb³⁺-doped tellurite glasses have better spectroscopic properties such as large absorption and emission cross-sections as well as wide fluorescence effective line widths compared to other oxide glasses, and are considered as ideal host materials for fiber lasers and amplifiers [10]. The higher value of linear and non-linear refractive indices and the lower value of phonon energy make the tellurite glasses better suitable for non-linear laser and amplifier applications [7,11].

Tellurium dioxide (TeO₂) is a conditional glass former, the TeO₂ alone cannot form a glass, unlike other glass systems such as silicate and phosphate, because of lone pair of electrons in one of the equatorial positions of the [TeO₄] polyhedron [12,13]. A metal oxide or a transition metal oxide is necessary as an intermediate network modifier to

form tellurite glasses [14]. Addition of network modifier oxides such as WO_3 and ZrO_2 increases the glass forming ability of the TeO_2 [14,15]. The physical and optical properties of undoped glasses [16] and visible upconversion and broadband near-infrared luminescence properties of Er^{3+}-doped tellurite-tungsten glasses [17] were reported in the literature. However, in the present study spectroscopic and laser properties of Yb^{3+} ions in these glasses are investigated to check their suitability for laser and optical amplifier applications.

In this paper, the effect of Yb^{3+} ions concentration on spectroscopic properties of Yb^{3+}-doped tungsten-tellurite glasses has been investigated by considering the reabsorption effects. From the measured absorption spectra, emission and laser performance properties are evaluated. The emission cross-sections, evaluated from McCumber and Futchbauer-Landenburg methods, have been compared to those of other reported Yb^{3+}-doped glasses. The better emission and laser properties show that these glasses are promising candidates as gain medium for high power solid state laser applications [18].

2. Experimental

The starting chemicals of TeO_2, WO_3, ZrO_2 and Yb_2O_3 with a purity of 99.99% (Aldrich, USA) were weighed in an electronic balance, with an accuracy of ± 0.0001, according to the molar composition of $70TeO_2$-$(25-x)WO_3$-$5ZrO_2$-xYb_2O_3, where x = 0.01, 0.05, 0.1, 0.5, 1.0, 2.0 and 3.0 mol% and hereafter referred as TWZYbx. A 30 g batch was fairly mixed in agate mortar for getting a homogeneous mixture. The well-mixed powder was taken in a platinum crucible and melted in the temperature range of 940–980 °C (± 1 °C), depending on the Yb^{3+} concentration, for 50 min using a high temperature furnace. Glasses were suddenly quenched on preheated brass mold at 320 °C. Annealing was done at 320 °C for 16 h and then allowed to cool down to room temperature (RT) in steps of 20 °C per hour. Finally, the samples were cut and polished with a size of 20 × 20 × 2.15 mm³ for optical and spectroscopic measurements.

Densities of TWZYb glasses were measured by Archimedes' method using water as an immersion liquid with an accuracy of ± 0.0001 g. The refractive indices were measured by Brewster's angle method using diode laser (λ = 650 nm) with a precision of 0.01. Optical absorption spectra were measured with a Perkin Elmer Lambda-950 spectrometer in the wavelength range of 870–1040 nm with a spectral resolution of 1.0 nm. The near infrared emission spectra were measured in the wavelength range of 900–1070 nm with 0.5 nm spectral interval by exciting the samples with 910 nm wavelength from a Ti: sapphire laser (Spectra Physics 3900S) pumped by a 10 W cw Ar^+ laser (Spectra Physics). The decay curves for the $^2F_{5/2}$ level were measured by exciting with a 950 nm laser from optical parametric oscillator (EKSPLA/NT342/3/UVE) and the signal was detected with the help of a digital oscilloscope (Tekronix 2430). All the measurements were made at RT.

3. Results and discussion

3.1. Absorption and emission cross-sections

Densities, refractive indices and nominal Yb-Yb inter-atomic distances of TWZYb glasses are collected in Table 1. As can be seen, the density increases from 4.788 to 5.634 with increase in Yb^{3+}-ion concentration from 0.01 to 3.0 mol%. This can be explained by considering the molecular weight of Yb_2O_3 (394.08 g/mol), which is higher than TeO_2 (159.6 g/mol), WO_3 (231.84 g/mol) and ZrO_2 (123.22 g/mol). With the gradual replacement of WO_3 by Yb_2O_3, the average molecular weight increases which results in higher densities. Decrease in inter-atomic distances also supports higher density of the glasses at higher Yb^{3+} concentrations. The values of refractive index of the TWZYb glasses are found to be in the range of 2.01–2.22 at 650 nm, which are found to be higher than those of TeO_2-ZnO (2.02–2.10 at 643.8 nm) [19] and TeO_2-$LiNbO_3$ (2.06–2.11 at 632.8 nm) [20]. The higher

Table 1
The glass label, molar composition and their physical properties (density (d ± 0.1%, g/cm³)), Yb^{3+} ions concentration (C ± 0.1%, × 10²⁰ ions/cm³), nominal Yb^{3+}-Yb^{3+} distance (r ± 1%, Å) and refractive index (n ± 1%, at 650 nm) of Yb^{3+}-doped tellurite tungsten glasses.

Label	Glass composition	d	C	r_i	n
TWZYb001	$70TeO_2$ + 24.99 WO_3 + $5ZrO_2$ + $0.01Yb_2O_3$	4.7882	0.0336	66.75	2.01
TWZYb005	$70TeO_2$ + 24.05 WO_3 + $5ZrO_2$ + $0.05Yb_2O_3$	4.8105	0.1661	39.18	2.06
TWZYb01	$70TeO_2$ + 24.9 WO_3 + $5ZrO_2$ + $0.1Yb_2O_3$	4.8248	0.3318	31.11	2.11
TWZYb05	$70TeO_2$ + 24.5 WO_3 + $5ZrO_2$ + $0.5Yb_2O_3$	4.8376	1.6487	18.23	2.15
TWZYb10	$70TeO_2$ + 24 WO_3 + $5ZrO_2$ + $1.0Yb_2O_3$	4.8651	3.3029	14.46	2.18
TWZYb20	$70TeO_2$ + 23 WO_3 + $5ZrO_2$ + $2.0Yb_2O_3$	4.9625	6.6759	11.44	2.20
TWZYb30	$70TeO_2$ + 22 WO_3 + $5ZrO_2$ + $3.0Yb_2O_3$	5.6342	11.2668	9.61	2.22

refractive index of TWZYb glasses might find application in optoelectronic devices [7,11,21].

The potential laser performance parameters of Yb^{3+}-doped glasses can be evaluated from the absorption and emission spectra [18]. The absorption spectra of present glass samples for different Yb^{3+}-concentrations in the NIR region are shown in Fig. 1(a). All the TWZYb samples show peak absorption centered at 977 nm corresponding to the $^2F_{7/2} \rightarrow ^2F_{5/2}$ transition. The absorption coefficient of the 977 nm peak increases with increasing Yb^{3+} concentration and is shown in inset of Fig. 1(a). A linear dependence in intensity confirms the incorporation of the Yb^{3+}-ions into the TWZ glass matrix [22]. Owing to positional disorder, the RE^{3+} luminescence centers in TWZ matrix are characterized by a marginal change in spectroscopic parameters resulting in small inhomogeneous broadening of spectral lines [see Fig. 1(a)]. The local environment of Yb^{3+} centers in the TWZ glass network also consists of O^{2-} anions with statistically-distributed structural parameters (rare earth ion oxygen inter-atomic distances and coordination numbers) in the first coordination shell (positional disorder) that is seen in the inhomogeneous broadening of the optical absorption and emission bands. Moreover, a glass network is characterized by a short-range order which in the second (cationic) coordination sphere around the luminescence centers leads to the further inhomogeneous broadening of spectral lines [23]. The Stark splitting for the ground and excited state manifolds of Yb^{3+} ions is shown in Fig. 1(b). Moreover, some of the important spectroscopic parameters are determined by using either the reciprocity method [24] or the Futchbauer-Landenburg formula [25]. On the basis of the reciprocity method described by McCumber [24], the emission cross-section can be obtained from measured absorption spectrum. The absorption cross-section for the $^2F_{7/2} \rightarrow ^2F_{5/2}$ transition of Yb^{3+} ions can be obtained by using the following Eqs. [26,27],

$$\alpha = \frac{2.303 \log\left(\frac{I_0}{I}\right)}{l} \tag{1}$$

$$\sigma_{abs} = \frac{\alpha}{N} \tag{2}$$

where N is the Yb^{3+} ion concentration (in ions/cm³) and l is the thickness (in cm) of the glass sample. The emission cross-section can be calculated using the reciprocity method described by McCumber [24] from the measured absorption cross-section (σ_{abs}),

$$\sigma_{em}(\lambda) = \sigma_{abs}(\lambda) \frac{Z_l}{Z_u} \exp\left(\frac{E_{ZL} - hc\lambda^{-1}}{KT}\right) \tag{3}$$

where Z_i and Z_u are the partition functions of the lower and upper levels, respectively, and E_{ZL} is the zero line energy, which is equal to the energy gap between the lowest Stark components of the upper and
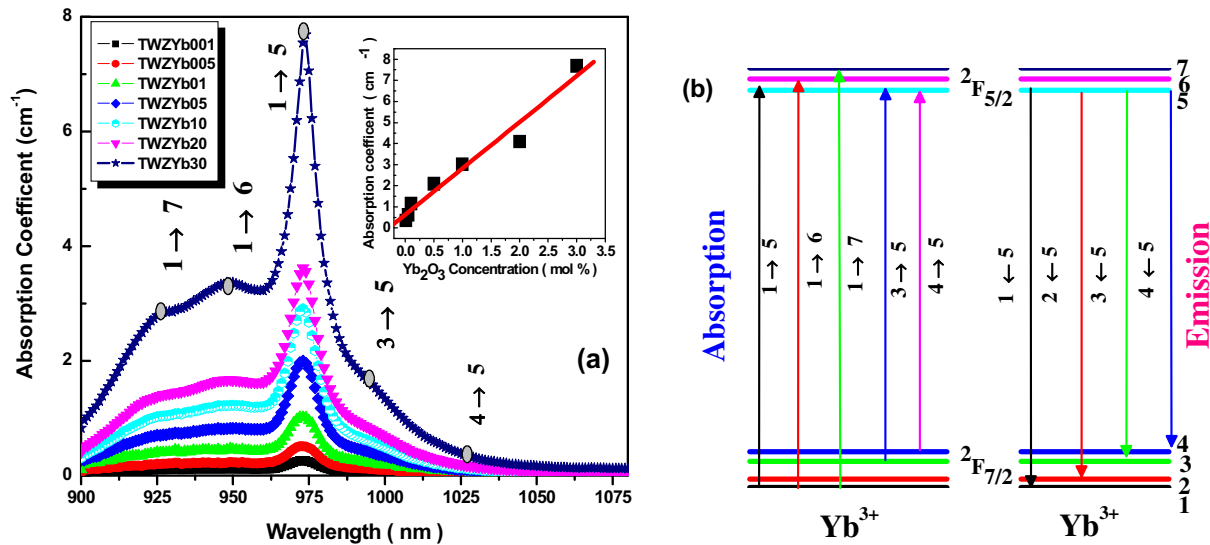
G. Venkataiah et al.

Fig. 1. (a) Absorption spectrum of TWZYb10 glass. Inset shows the variation of absorption coefficient with Yb_2O_3 concentration. (b) Energy level diagram of Yb^{3+} ions in TWZ glasses.
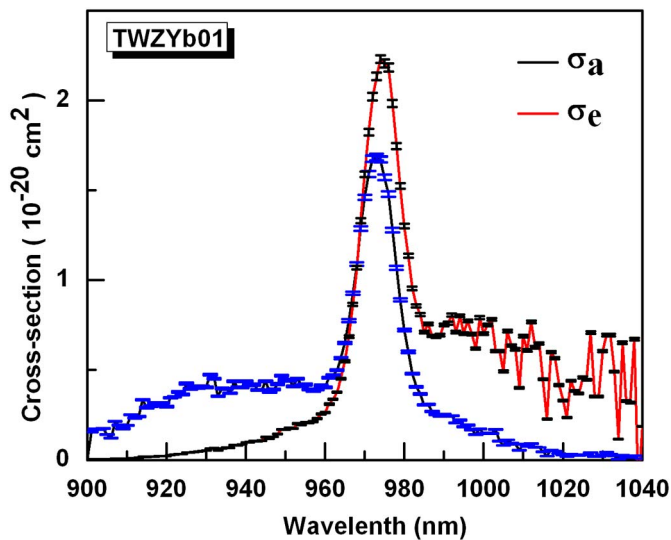

Fig. 2. Absorption and emission cross-sections of TWZYb01 glass, calculated from McCumber theory along with error bars.

Table 2
Comparison of emission cross-sections (± 1%) calculated from the Füchtbauer-Landenburg (F-L) and McCumber (McC) methods at primary (λ_p) and secondary (λ_s) wavelengths and their ratios for TWZYb glasses.

Glasses	Emission cross-section ($\times 10^{-20}$ cm^2)				$\sigma_{ems}/\sigma_{emp}$	
	F–L	McC	F–L	McC	F–L	McC
	($\sigma_{em\text{-}p}(\lambda_p)$)	($\sigma_{emp}(\lambda_p)$)	($\sigma_{em\text{-}s}(\lambda_s)$)	($\sigma_{ems}(\lambda_s)$)		
TWZYb001	3.78	3.64	1.85	1.63	0.49	0.45
TWZYb005	2.40	2.41	1.37	1.36	0.57	0.56
TWZYb01	2.11	2.24	1.10	0.92	0.52	0.41
TWZYb05	1.84	2.10	0.85	0.85	0.46	0.40
TWZYb10	1.42	2.07	0.75	0.75	0.53	0.36
TWZYb20	1.10	1.87	0.68	0.73	0.62	0.39
TWZYb30	1.08	1.83	0.67	0.68	0.62	0.31

lower levels of the Yb^{3+} ion. The constants h and K are the Planck's and Boltzmann's constants, respectively, and c is the velocity of the light. The ratio of the partition functions becomes the degeneracy weighing of the two states corresponding to the $^2F_{7/2} \rightarrow {}^2F_{5/2}$ transition and, since it does not change significantly with the change of the chemical
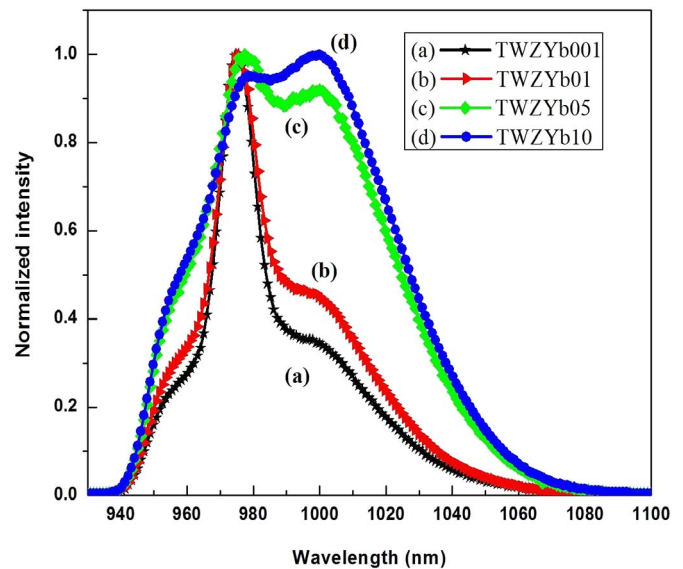

Fig. 3. Normalized emission spectra of TWZYb glasses for different concentrations of Yb_2O_3 (λ_{ex} = 915 nm).

composition and Yb^{3+} concentration, it is equal to 4/3 at RT. Absorption and emission cross-section spectra obtained through McCumber theory [Eqs. (1)–(3)] for TWZYb10 glass is shown in Fig. 2. The line shapes of the absorption and emission cross-sections spectra are similar for the remaining samples. The broad absorption and emission cross-sections of Yb^{3+} ions are due to electronic transitions involving the Stark sublevels of the $^2F_{7/2}$ and $^2F_{5/2}$ levels. The evaluated absorption and emission cross-sections through McCumber theory are listed in Table 2. As can be seen from the Table 2 with increase in Yb^{3+} ion concentration, a linear decrease in absorption and emission cross-sections has been observed for TWZYb glasses. The same behavior has also been observed in TPNxYb ($60TeO_2$-$30P_2O_5$-$10Na_2CO_3$-xYb_2O_3) glasses [18]. Fig. 3 shows the normalized emission spectra for TWZYb001, TWZYb01, TWZYb05 and TWZYb10 samples. To obtain the full Gaussian shape of the emission spectrum, all TWZYb glasses were excited with 915 nm instead of the intense absorption peak (~980 nm). As can be seen from Fig. 3, with increase in Yb^{3+} ions concentration, the emission spectral shape of TWZYb glasses changes which is due to reabsorption of emitted energy by the ground state Yb^{3+} ions as there is

maximum overlap of absorption and emission bands. The emission cross-section (σ_{em}) of the $^2F_{5/2} \rightarrow {}^2F_{7/2}$ transition of the Yb^{3+}-ions can also be obtained by using the Futchbauer-Landenburg model with the help of emission spectra shown in Fig. 3 [28], expressed as

$$\sigma_{em-p/s}(\lambda_{p/s}) = \frac{\lambda_p^4 \ A_R}{8\pi cn^2 \Delta\lambda_{eff}} \tag{4}$$

where A_R is spontaneous transition probability of the $^2F_{5/2} \rightarrow {}^2F_{7/2}$ transition and is determined from the absorption spectrum using the following expression [29],

$$A_R = \frac{1}{\tau_{rad}} = \frac{8\pi \ c \ n^2(2J'+1)}{\lambda_p^4 (2J+1)} \int \alpha(\lambda) \ d\lambda \tag{5}$$

where J' and J are the total angular momentum for the upper and lower levels, respectively, λ_p is the absorption peak wavelength, $\alpha(\lambda)$ is the absorption coefficient at the wavelength λ, n is the refractive index and τ_{rad} is the radiative lifetime. The $\Delta\lambda_{eff}$ is the effective linewidth expressed as

$$\Delta\lambda_{eff} = \int \frac{I(\lambda) \ d\lambda}{I_{max}} \tag{6}$$

where $I(\lambda)$ is the intensity at the wavelength λ, and I_{max} is the intensity at the peak wavelength.

The stimulated emission cross-sections are also evaluated by using the Futchbauer-Landenburg theory (Eqs.(4)–(6)) in order to confirm the validity of the evaluated results from the McCumber method [24]. Table 2 presents the calculated emission cross-sections at the primary (σ_{em-p} at 977 nm) and the secondary (σ_{em-s} at 1007 nm) peaks on the basis of above two methods. As can be seen, both McCumber and Futchbauer-Landenburg methods are in good agreement for lower concentrations (≤ 0.5 mol%), which may be due to the negligible effect of radiation trapping at these concentrations [30]. From Table 2, it is observed that the absorption and emission cross-sections at primary and secondary peaks decrease with increasing Yb^{3+} concentration.

The other evaluated spectroscopic parameters such as absorption cross-section at primary, $\sigma_{abs}(\lambda_p)$, and secondary, $\sigma_{abs}(\lambda_s)$ peaks, $\Delta\lambda_{eff}$, A_R and τ_{rad} for the TWZYb glasses are listed in Table 3. As can be seen from Table 3, there is a systematic decrease of radiative transition probabilities with increasing Yb^{3+} concentration. The absorption cross-section at λ_p and λ_s decreases from 2.78 to 1.30 ($\times 10^{-20}$ cm^2) and 0.38 to 0.18 ($\times 10^{-20}$ cm^2), respectively, with increasing Yb^{3+} concentration from 0.01 to 3.0 mol%. It is found that TWZYb05 glass exhibit higher absorption and emission cross-sections of 1.51×10^{-20} cm^2 (at λ_p) and 2.10×10^{-20} cm^2 (at λ_s), respectively, compared to those of the commercial Kigre QX/Yb glass: 1.06×10^{-20} (at λ_p) and 0.9×10^{-20} cm^2 (at λ_s) [31]. The $\Delta\lambda_{eff}$ values increase from 18 to 40 nm with increasing Yb^{3+} concentration which are comparable to those of commercial YB1 (51 nm) [32] and YP1 (52 nm) [32] laser glasses. The magnitude of A_R decreases from 2188 to 1484 s^{-1} with increasing Yb^{3+} concentration from 0.01 to 3.0 mol%. The same trend is noticed for the values of

$\sigma_{abs}(\lambda_p)$, $\sigma_{em}(\lambda_p)$ and A_R with increasing Yb^{3+} concentration in the case of other reported telluro-phosphate: $60TeO_2$-$30P_2O_5$-$10Na_2CO_3$-xYb_2O_3 (where x = 1, 3 and 5 mol%, referred as TPNxYb) [18], phosphate: $(59-x/2)P_2O_5$-$17K_2O$-$(15-x/2)BaO$-$9Al_2O_3$-xYb_2O_3 (where x = 0.05, 0.1 and 1.0 mol%, referred as PKBaAlxYb) [30], $80TeO_2$-$15(BaF_2$-BaO$)$-$(5-x)$ La_2O_3-xYb_2O_3 (where x ranges from 0.1 to 5.0 mol%, referred as TBa-BaFLaxYb) [33] and silicates: $(60SiO_2$-$20Al_2O_3$-$20CaF_2$-$xYbF_3$, where x = 0.2, 0.4 mol%, referred as SACaFx) [34] glasses.

3.2. Laser parameters

The complete assessment of Yb^{3+}-doped laser glasses involves determination of several significant parameters which characterize the lasing performance of the material [18]. First important laser parameter is β_{min}, which is defined as the minimum fraction of Yb^{3+} ions that are excited to balance the gain with the ground state absorption at lasing wavelength λ_s and is given by [25],

$$\beta_{min} = \frac{\sigma_{abs}(\lambda_s)}{\sigma_{em}(\lambda_s) + \sigma_{abs}(\lambda_s)} = \left\{ 1 + \frac{Z_l}{Z_u} \exp\left(\frac{E_{ZL} - hc\lambda_0^{-1}}{kT} \right) \right\}^{-1} \tag{7}$$

where the laser wavelength is considered as $\lambda_s = 1007$ nm. The calculated β_{min} values for TWZYb glasses are presented in Table 3 and are more or less similar. As can be seen from Tables 2 and 3, both emission and absorption cross-sections decreases with increase in Yb^{3+} ions concentration by a factor of 2 to 3.

The other important parameter is the pump saturation intensity, I_{sat}, that characterizes the pumping dynamics and requires an accurate measure of the absorption cross-section at the pump wavelength, $\sigma_{abs}(\lambda_p)$, and the fluorescence lifetime, τ_{exp}, of the Yb^{3+} ions and is given by [25],

$$I_{sat} = \frac{hc}{\lambda_p \sigma_{abs}(\lambda_p) \tau_{exp}} \tag{8}$$

where peak absorption wavelength, $\lambda_p = 977$ nm. As can be seen from Table 3, I_{sat} values increases with increasing Yb^{3+} concentration, which can be explained by the decrease of $\sigma_{abs}(\lambda_p)$ values.

The minimum absorbed pumping intensity, I_{min}, which characterizes the transparency to be achieved at the lasing wavelength, and is calculated by the following expression [25],

$$I_{min} = \beta_{min} \cdot I_{sat} \tag{9}$$

By using Eqs. (7) and (8), I_{min} values are determined and are shown in Table 3. As can be seen, the magnitude of I_{min} values increases with Yb^{3+} ions concentration. This may be due to the increase in I_{sat} values with increasing Yb^{3+} ions concentration. The same trend was also reported for PKBAxYb ($(54-x/2)$ P_2O_5-14 K_2O-$10KF$-$(13-x/2)$ BaO-$9Al_2O_3$-xYb_2O_3, where x = 0.1, 1.0, 2.0 and 4.0 mol%) [30] glasses.

Further, storage of optical energy in a laser material is also crucial for laser application perspectives. However, this can be feasible if the laser material satisfies high fluorescence lifetime, high Yb^{3+} ion

Table 3
Spectroscopic and some of the laser properties, (absorption cross-sections at primary peak ($\sigma_{ab}(\lambda_p) \pm 0.01$, $\times 10^{-20}$ cm^2)), absorption cross-sections at secondary peak ($\sigma_{ab}(\lambda_s) \pm 1\%$, $\times 10^{-20}$ cm^2), radiative transition probability ($A_R \pm 0.1\%$, s^{-1}), radiative lifetimes ($\tau_{rad} \pm 0.5\%$, μs), experimental lifetimes ($\tau_{exp} \pm 0.5\%$, μs), quantum efficiency ($\eta \pm 1\%$), fluorescence effective line width ($\Delta\lambda_{eff} \pm 1\%$, nm), the minimum fraction of Yb^{3+} ions excited to laser wavelength λ_s ($\beta_{min} \pm 1\%$), pump saturation intensity ($I_{sat} \pm 1\%$, kW/cm^2), minimum absorbed intensity ($I_{min} \pm 1\%$, kW/cm^2), pump intensity ($U_{sat} \pm 1\%$, W/cm^2) and minimum pulse duration ($\tau_{min} \pm 1\%$, fs) for different concentrations of Yb^{3+}-doped TWZ glasses.

Yb (mol%)	$\sigma_{ab}(\lambda_p)$	$\sigma_{ab}(\lambda_s)$	A_R	τ_{rad}	τ_{exp}	η	$\Delta\lambda_{eff}$	β_{min}	I_{sat}	I_{min}	U_{sat}	τ_{min}
0.01	2.78	0.38	2315	432	344	80	18	0.19	22.40	4.27	10.10	186
0.05	1.97	0.25	2237	442	349	78	26	0.17	28.44	4.42	12.67	128
0.1	1.69	0.19	2212	452	350	77	28	0.17	30.33	5.19	18.38	119
0.5	1.51	0.19	1848	541	418	77	26	0.17	32.87	5.75	19.62	93
1.0	1.50	0.18	1822	549	401	73	38	0.19	32.38	6.27	21.64	88
2.0	1.34	0.17	1786	560	357	64	40	0.19	33.84	6.39	22.68	83
3.0	1.30	0.18	1751	571	293	51	24	0.20	28.71	6.01	24.30	76

Table 4

Comparison of spectroscopic and laser performance parameters of Yb^{3+}-doped glasses (Yb^{3+} ions concertation (mol%), absorption cross-sections at the pump wavelength ($\sigma_{abs}(\lambda_p)$ ± 1%, × 10^{-20} cm^2), emission cross-section at the laser wavelength ($\sigma_{ems}(\lambda_s)$ ± 1%, × 10^{-20} cm^2), radiative transition probability (A_R ± 0.1%, s^{-1}), experimental lifetime (τ_{exp} ± 0.5%, μs), fluorescence effective bandwidth ($\Delta\lambda_{eff}$ ± 0.1%, nm) and minimum absorbed intensity (I_{min} ± 1%, kW/cm^{-2})).

Yb^{3+} glass systems	Yb^{3+} ions concentration	$\sigma_{ab}(\lambda_p)$	$\sigma_{ems}(\lambda_s)$	A_R	τ_{exp}	$\Delta\lambda_{eff}$	I_{min}
TWZYb001 [present work]	0.01	2.78	3.64	2315	344	18	4.27
TWZYb005 [present work]	0.05	1.97	2.41	2237	349	26	4.42
TWZYb01 [present work]	0.1	1.69	2.24	2212	350	28	5.19
TWZYb05 [present work]	0.5	1.51	2.10	1848	418	26	5.75
TWZYb10 [present work]	1.0	1.50	2.07	1822	401	38	6.27
TWZYb20 [present work]	2.0	1.34	1.88	1786	357	40	6.39
TWZYb30 [present work]	3.0	1.30	1.83	1751	293	24	6.01
TPN1Yb [18]	1.0 wt%	1.26	0	840	1260	–	1.79
TPN3Yb [18]	3.0 wt%	1.16	1.55	474	1150	–	2.14
TPN5Yb [18]	5.0 wt%	1.12	1.50	781	940	–	2.70
PKBAYb001 [30]	0.01	4.49	6.08	1195	1040	52	0.60
PKBAYb005 [30]	0.05	1.74	2.35	585	1090	54	1.05
PKBAYb01 [30]	0.1	1.71	2.31	535	1150	54	1.89
PKBAYb10 [30]	1.0	1.47	2.06	521	850	58	2.93
TBaBaFLa0.1Yb [33]	0.1	2.06	2.80	3246	432	55	3.79
TBaBaFLa0.5Yb [33]	0.5	1.98	2.68	2922	536	72	3.05
TBaBaFLa1.0Yb [33]	1.0	1.93	2.65	2701	634	76	2.74
TBaBaFLa3Yb [33]	3.0	1.78	2.33	2608	625	71	3.17
TBaBaFLa5Yb [33]	5.0	1.46	2.00	2498	449	66	5.14
SACF02 [34]	0.2	1.19	0.98	613	129	33	2.43
SACF04 [34]	0.4	1.17	0.61	506	143	42	1.51
Yb:YAG [35]	0.5	–	0.80	–	108	18	1.53
PbSiAl1Yb [37]	0.4	2.34	1.02	–	102	–	–
PbBiGaYb [38]	1.0 wt%	2.00	2.50	–	350	–	2.4

concentration and low emission cross-sections. These factors decide the depletion of stored energy due to spontaneous emission and pump power. The pump intensity required to create population inversion in a laser material is given by [35],

$$U_{sat} = \frac{hc}{\lambda_p \left[\sigma_{abs}(\lambda_s) + \sigma_{em-s}(\lambda_s) \right]} \qquad (10)$$

The U_{sat} values are calculated by considering the values of $\sigma_{abs}(\lambda_s)$ and $\sigma_{em-s}(\lambda_s)$, and are presented in Table 3. The U_{sat} value is found to be around 19.6 W/cm^2 for TWZYb05 glass and is higher than 14.02 W/cm^2 reported for niobium-tellurite (80TeO$_2$-10Nb$_2$O$_5$-5K$_2$O-5Li$_2$O-0.5Yb$_2$O$_3$) glass [36]. In addition, the minimum pulse duration is an important parameter to use the materials for ultrafast lasers. The minimum pulse duration is represented by the time bandwidth product, $\tau_{min} = 1/\Delta\upsilon$ [35] where $\Delta\upsilon$ is the emission bandwidth. The value of τ_{min} decreases from 186 to 76 fs with increasing of Yb^{3+} concentration from 0.01 to 3.0 mol% in TWZ glasses.

The spectroscopic parameters of TWZYb glasses are compared with different Yb^{3+}-doped systems in Table 4 [18,30,33,34,25,37,38]. As can be seen, the magnitude of $\sigma_{abs}(\lambda_p)$ of TWZYb05 glass is found to be higher than that of telluro-phosphate glasses [18] and comparable with phosphate glasses [30]. It is lower than that of oxyfluoride [33], lead silicate (PbSiAl1Yb; 40PbO-6Al$_2$O$_3$-54SiO$_2$-1Yb$_2$O$_3$) [37] and heavy metal oxide (PbBiGaYb; 46PbO-42Bi$_2$O$_3$-12Ga$_2$O$_3$-0.53Yb$_2$O$_3$) [38] glasses. The order of magnitude of $\sigma_{emp}(\lambda_p)$ for the reported glasses is following the trend as telluro-oxyflouride glass (0.1 mol%) [33] > heavy metal oxide glasses [38] > phosphate glass (0.1 mol%) [30] ≥ TWZYb05 > lead silicate [37] > telluro-phospahte [18] > silicate [34] glasses. The value of $\Delta\lambda_{eff}$ gradually increases with increasing Yb^{3+} concentration and the same trend was also observed in reported systems [30,33,25]. On the other hand, the value of $\Delta\lambda_{eff}$ for the TWZYb01 glass is higher than Yb:YAG crystal [25] and lower than phosphate [30], telluro-oxyflouride [33], and silicate [34] glasses.

Laser parameters I_{min} and $\sigma_{emp}(\lambda_p)$ together provides a spectroscopic measure to estimate the overall effective performance of the laser medium in the pulsed or CW operation [18]. From the laser operation point of view, it is favorable to have higher emission cross-section for larger gain, longer excited state lifetime to permit high inversion

density that relates to amplification, and higher absorption cross-section at pump wavelength for efficient pumping. The I_{min} should be as small as possible to minimize the threshold for Yb^{3+} laser material engaged in an oscillator type configuration, and also to offer the best extraction efficiency at the lasing wavelength [29,39]. Table 4 presents the comparison of some of the laser parameters of TWZYb glasses with other reported Yb^{3+}-doped systems [18,30,33,34,25,37,38]. As can be seen from Table 4, the I_{min} values for TWZYb glasses increase with increasing of Yb^{3+} concentration. The same behavior was also observed in telluro-phosphate [18], phosphate [30], TBaBaFLaxYb [33], and silicate glasses [34]. As can be seen form Table 4, the value of I_{min} for TWZYb05 glass is comparable to tellurophosphate glass [33].

Usually, the measured fluorescence lifetimes can be expressed as [40],

$$\frac{1}{\tau} = W_{tot} = W_{rad} + W_{non-rad} \qquad (11)$$

where W_{tot} is the sum of radiative, W_{rad}, and non radiative, $W_{non-rad}$, transition probabilities. On the other hand $W_{non-rad}$ is the sum of contributions from all non-radiative processes [41]

$$W_{non-rad} = W_{MP} + W_{ET},$$
$$W_{ET} = W_{Yb} + W_{OH} + W_{TM} + W_{RE} \qquad (12)$$

where W_{MP} is the multiphonon relaxation and is a critical loss parameter that depends on the temperature and glass matrix [42] and W_{ET} is the total energy transfer probability and is the sum of four terms given in Eq. (12). W_{Yb} represents the contribution of Yb^{3+} ions concentration quenching and caused by the energy exchange between Yb^{3+} ions due to possible clustering effect. W$_{OH}$, W$_{TM}$ and W$_{RE}$ refers to the interaction between Yb^{3+} ions and OH$^-$ group, transition-metal ions, and other RE^{3+} ions, respectively. Even though the starting materials are taken in high purity form, there is a possibility for some impurities in the present glasses [43]. If there exist some transition-metal or rare-earth impurities in a glass, then the system losses are given as a sum of the individual ion contributions [44].

The fluorescence decay curves for the $^2F_{7/2}$ level of Yb^{3+} ions are shown in Fig. 4. It is found that decay curves for all the concentrations exhibit single exponential nature. The excited state lifetime of the $^2F_{5/2}$ level has been estimated by finding the first e-folding times of the
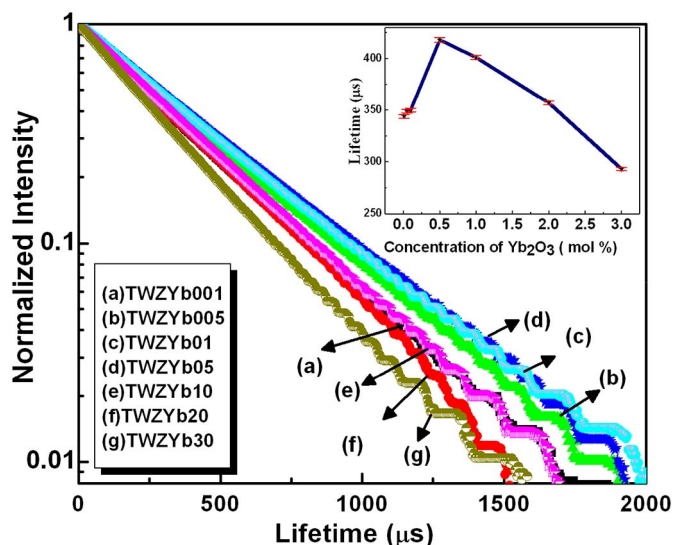
G. Venkataiah et al.

Fig. 4. Decay curves of TWZYb glasses for different concentrations of Yb_2O_3, monitoring the emission at 975 nm. Inset shows the variation of lifetime with concentration of Yb_2O_3 along with error bars.

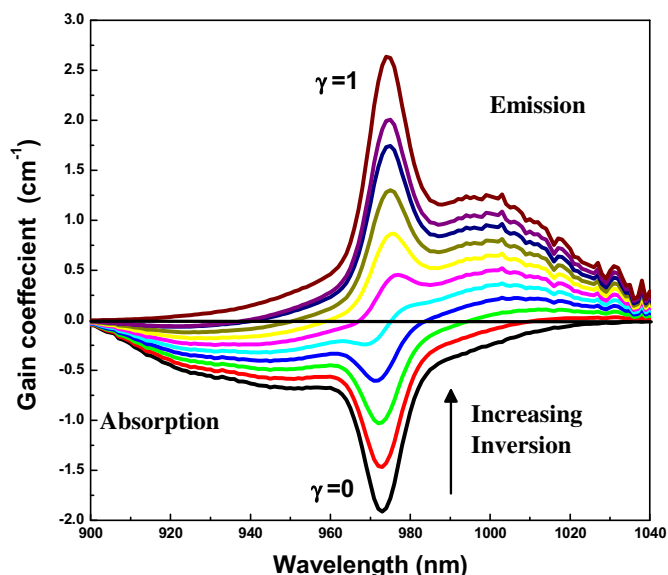**Fig. 5.** Gain cross-section spectra of 0.5 mol% Yb_2O_3-doped TWZ glass for different populations.

measured decay curves. A variation of lifetime with concentration is shown in inset of Fig. 4. It is found that lifetime initially increases from 0.01 to 0.5 mol% and then decreases for higher (≥ 0.5 mol%) concentrations with increasing Yb^{3+} concentration. The initial rise in the lifetime is due to the reabsorption or radiative trapping and decrease of lifetime could be due to the radiative energy transfer between adjacent Yb^{3+} ions [45,46]. From Eqs. (11) and (12), the decrease in lifetime at higher concentration could be due to energy transfer between Yb^{3+} ions/to transition metal ions/RE ions/to OH^- groups directly coupled with Yb^{3+} ions in the TWZYb glasses.

Overall, laser glass should possess higher value of product of σ_{ems} (λ_s) and τ_{exp} as large as possible to act as the gain media [47]. From Table 4, the product of σ_{ems} and τ_{exp} decreases from 1.25 to 0.54 pm^2 ms with increasing Yb^{3+} concentration from 0.01 to 3.0 mol%. The value of $\sigma_{ems} \times \tau_{exp}$ is found to be 0.88 pm^2 ms for TWZYb05 glass and is comparable to those of phosphate (0.63 to 0.18 pm^2 ms) [30], SACFYb04 (0.87 pm^2 ms) glass [34], Yb:YAG crystal (0.87 pm^2 ms) [35], PbSiAl1Yb (0.14 pm^2 ms) [37] and PbBiGaYb (0.88 pm^2 ms) [38]

although it is lower than telluro-oxyfluoride (1.20 to 0.89 pm^2 ms) [33] and telluro-phosphate (2.14 to 1.41 pm^2 ms) [18] glasses. From the spectroscopic and laser performance parameters, it can be concluded that TWZYb glasses in general are useful as a gain media for high-peak power and high average power lasers [47,25]. From the above evaluated σ_{ems} and τ_{exp} values TWZYb05 glass shows the higher lifetime (418 µs) and moderate emission cross-section (2.10×10^{-20} cm^2) than rest of TWZYb glasses, which shows that TWZYb05 glass is better one for laser gain media.

The internal gain coefficient $G(\lambda)$ at wavelength λ can be estimated by using the formula

$$G(\lambda) = \gamma N \sigma_{em}(\lambda) - (1 - \gamma) N \sigma_{abs}(\lambda) \tag{13}$$

where σ_{abs} and σ_{em} are the absorption and stimulated emission cross-sections obtained from McCumber theory at wavelength λ and γ denotes the population inversion which varies from 0 to 1. Fig. 5 shows the wavelength dependence of the gain coefficient for the $^2F_{5/2} \to {}^2F_{7/2}$ emission transition calculated for the TWZYb05 glass by varying the γ value from 0.0 to 1.0, with an increment of 0.1. It is worth noting that the gain coefficient is positive when γ is higher than 0.4. From Fig. 5, it can be concluded that a wide tunable range of 980–1050 nm is expected whenever the value of γ is > 0.4. The spectroscopic and laser performance properties indicate that the TWZYb05 glass is promising candidate for amplification and laser gain media.

4. Conclusions

Ytterbium-doped tungsten-tellurite glasses have been prepared and studied their concentration dependent spectroscopic and laser properties. The McCumber theory has been applied for evaluating absorption and emission cross-sections for the $^2F_{7/2} \to {}^2F_{5/2}$ and $^2F_{5/2} \to {}^2F_{7/2}$ transitions, respectively. The emission cross-sections evaluated from the McCumber and Futchbauer-Landenburg methods are found to be in good agreement for lower concentrations (≤ 0.5 mol%). Change in fluorescence spectra of Yb^{3+}-ions at higher Yb^{3+} ions concentrations (> 0.5) has been explained as due to increase in emission intensity to other Stark levels and to the reabsorption effect. An initial rise in lifetime (≤ 0.5 mol%) and decrease thereafter (> 0.5 mol%) can be explained as due to the reabsorption and radiative energy transfer between the neighboring Yb^{3+} ions. The 0.5 mol% Yb^{3+}-doped glass possesses moderate emission cross-section of 2.10×10^{-20} cm^2 and a higher lifetime of 418 µs. In addition to the spectroscopic properties, the minimum pulse duration (186–76 fs) and bandwidth (18–40 nm) suggest that these TWZYb glasses have potential applications as gain media for ultra short lasers and amplifiers.

References

[1] E. Snitzer, Optical maser action of Nd^{3+} in a barium crown glass, Phys. Rev. Lett. 7 (1961) 444–446.
[2] H.M. Pask, R.J. Carman, D.C. Hanna, A.C. Tropper, C.J. Mackechnie, P.R. Barber, J.M. Dawes, Ytterbium-doped silica fiber lasers: versatile sources for the 1–1.2 µm region, IEEE J. Sel. Top. Quantum Electron. 1 (1995) 2–13.
[3] C. Grivas, Prog. Quantum Electron. 35 (2011) 159.
[4] W.A. Pisarski, L. Grobelny, Joanna Pisarska, R. Lisiecki, W.R. Romanowski, Spectroscopic properties of Yb^{3+} and Er^{3+} ions in heavy metal glasses, J. Alloys Compd. 509 (2011) 8088–8092.

[5] A. Jouini, A. Brenier, Y. Guyot, G. Boulon, H. Sato, A. Yoshikawa, K. Fukuda, T. Fukuda, Spectroscopic and laser properties of the near-infrared tunable laser material Yb^{3+}-doped CaF_2 crystal, Am. Chem. Soc. 8 (2008) 808–811.

[6] K. Maheshvaran, S. Arunkumar, V. Sudarsan, V. Natarajan, K. Marimuthu, Structural and luminescence studies on Er^{3+}/Yb^{3+} co-doped boro-tellurite glasses, J. Alloys Compd. 561 (2013) 142–150.

[7] E.S. de Lima Filho, K. Venkata Krishnaiah, Y. Ledemi, Y.J. Yu, Y. Messaddeq, G. Nemova, R. Kashyap, Ytterbium-doped glass-ceramics for optical refrigeration, Opt. Express 23 (2015) 4630–4640.

[8] X. Feng, C. Qi, F. Lin, H. Hu, Tungsten-tellurite glass: a new candidate medium for Yb^{3+}-doping, J. Non-Cryst. Solids 256 & 257 (1999) 372–377.

[9] J.S. Wang, E.M. Vogel, E. Snitzer, Tellurite glass: a new candidate for fiber devices, Opt. Mater. 3 (1994) 187–203.

[10] C. Jiang, F.X. Gan, J.J. Zhang, P.Z. Deng, G.S. Huang, Yb: tellurite laser glass with high emission cross-section, Mater. Lett. 41 (1999) 209–214.

[11] M.B.M. El-Amraoui, Y. Ledemi, S. Morency, R. Vall'ee, Y. Messaddeq, Germanate-tellurite composite fibers with a high-contrast step-index design for nonlinear applications, Opt. Mater. Exp. 4 (2014) 1740–1746.

[12] R.A.H. El-Mallawany, Tellurite Glasses Handbook, CRC Press, Boca Raton/London/New York/Washington D.C., 2002, p. 17 (1st unit).

[13] V. Himamaheswara Rao, P. Syam Prasad, P. Venkateswara Rao, L.F. Santos, N. Veeraiah, Influence of Sb_2O_3 on tellurite based glasses for photonic applications, J. Alloys Compd. 687 (2016) 898–905.

[14] S.F. Mansour, El. Sayed Yousef, M.Y. Hassaan, A.M. Emara, The influence of oxides on the optical properties of tellurite glass, Phys. Scr. 89 (2014) 115812–115818.

[15] R. Braunstein, I. Lefkowitz, J. Snare, Dipole correlations in TeO_2-WO_3 glass, Solid State Commun. 28 (1978) 843–845.

[16] El. Sayed Yousef, Amin El-Adawy, N. El. Koshkhany, E.R. Shaaban, Optical and acoustic properties of TeO_2/WO_3 glasses with small amount of additive ZrO_2, J. Phys. Chem. Solids 67 (2006) 1649–1655.

[17] K. Venkata Krishnaiah, G. Venkataiah, J. Marques-Hueso, P. Dharmaiah, C.K. Jayasankar, B.S. Richards, Broadband near-infrared luminescence and visible upconversion of Er^{3+}-doped tungstate-tellurite glasses, Sci. Adv. Mater. 6 (2014) 1–9.

[18] P. Nandi, G. Jose, Ytterbium-doped P_2O_5 -TeO_5 glass for laser application, IEEE J. Quant. Electron. 42 (2006) 1115–1121.

[19] A. Ghosh, Memory switching in bismuth- vanadate glasses, J. Appl. Phys. 64 (1988) 2652–2655.

[20] S.K.J. Al-Ani, C.A. Hogarth, R. El Mallawany, A study of optical absorption in tellurite and tungsten – tellurite glasses, J. Mater. Sci. 20 (1985) 661–667.

[21] E.P. Golis, M. Reben, J. Wasylak, J. Filipecki, Investigations of tellurite glasses for optoelectronics devices, Opt. Appl. XXXVIII (1) (2008) 163–169.

[22] A.S. Pinheiro, A.M. Freitas, G.H. Silva, M.J.V. Bell, V. Anjos, A.P. Carmo, N.O. Dantas, Laser performance parameters of Yb^{3+} doped UV-transparent phosphate glasses, Chem. Phys. Lett. 592 (2014) 164–169.

[23] B. Padlyak, W. Ryba-Romanowski, R. Lisiecki, V. Adamiv, Y. Burak, I. Teslyuk, A. Banaszak-Piechowska, Optical spectra and luminescence kinetics of the Sm^{3+} and Yb^{3+} centres in the lithium tetraborate glasses, Opt. Appl. XL (2) (2010) 428–438.

[24] D.E. McCumber, Einstein relations connecting broadband emission and absorption spectra, Phys. Rev. 136 (1964) A954–A957.

[25] L.D. Deloach, S.A. Payne, L.L. Chase, L.K. Smith, W.L. Kway, W.F. Krupke, Evaluation of absorption and emission properties of Yb^{3+} doped crystals for laser applications, IEEE J. Quantum Electron. 24 (1993) 1179–1191.

[26] C. Görller-Walrand, K. Binnemans, K.A. Gschneidner, Jr.L. Eyring (Eds.), Handbook on the Physics and Chemistry of Rare Earths, vol. 25, 1998 (North Holland,

Amsterdam, (Ch.167)).

[27] S.A. Payne, L.L. Chase, L.K. Smith, W.L. Kway, W.F. Krupke, Infrared Cross - section measurements for crystals doped with Er^{3+}, Tm^{3+}, and Ho^{3+}, IEEE J. Quantum Electron. QE–28 (1992) 2619–2630.

[28] C.C. Ye, D.W. Hewak, M. Hempstead, B.N. Samson, D.N. Payne, J. Non-Cryst. Solids 56 (1996) 208.

[29] X. Zou, H. Toratani, Evaluation of spectroscopic properties of Yb^{3+}-doped glasses, Phys. Rev. B 52 (1995) 15889–15897.

[30] K. Venkata Krishnaiah, C.K. Jayasankar, S. Chaurasia, C.G. Murali, L.J. Dhareshwar, Preparation and characterization of Yb^{3+}-doped metaphosphate glasses for high energy and high power laser applications, Sci. Adv. Mater. 5 (2013) 276–284.

[31] http://www.toplent.com/ytterbium_laser_glass.htm.

[32] S. Dai, L. Hu, A. Sugiyama, Y. Izawa, L. Zhuping, Z. Jiang, Study of a new ytterbium doped phosphate laser glass, Chin. Sci. Bull. 47 (2002) 255–259.

[33] S. Balaji, A.D. Sontakke, K. Annapurna, Yb^{3+} ion Concentration effects on-1.0 μm emission in tellurite glass, J. Opt. Soc. Am. B 29 (2012) 1569–1579.

[34] Q. Zhang, J. Ding, B. Tang, J. Cheng, Y. Qiao, Q. Zhou, J. Qiu, Q. Chen, D. Chen, et al., J. Phys. D. Appl. Phys. 42 (235405) (2009) 1–4.

[35] L.C. Courrol, L.R.P. Kassab, A.S. Morais, C.M.S. Mendes, L. Gomes, N.U. Werrer, N.D. Vieira, F.C. Cassanjes Jr., Y. Messaddeq, S.J.L. Ribeiro, Study of the most suitable new glass laser to incorporate ytterbium: alkali niobium tellurite, lead fluorborate or heavy metal oxide, J. Lumin. 102–103 (2003) 106–111.

[36] P. Wang, C. Wang, W. Li, M. Lu, B. Peng, Effects of Al_2O_3 on the thermal stability, glass configuration of Yb^{3+}-doped TeO_2-K_2O-ZnO-Al_2O_3 based tellurite laser glasses, J. Non-Cryst. Solids 359 (2013) 5–8.

[37] M. Sundara Rao, Ch. Srinivas Rao, B.V. Ragavaiah, G. Sahaya Baskaran, V. Ravikumar, I.V. Kityk, N. Veeraiah, The role of ligand coordination on the spectral features of Yb^{3+} ions in lead aluminum silicate glasses, J. Mol. Struct. 1007 (2012) 185–190.

[38] L.R.P. Kassab, M.E. Fukumoto, V.D.D. Cacho, N.U. Wetter, N.I. Morimoto, Spectroscopic properties of Yb^{3+} doped PbO–Bi_2O_3–Ga_2O_3 glasses for IR laser applications, Opt. Mater. 27 (2005) 1576–1582.

[39] F. Auzel, G. Baldacchini, L. Laversenne, G. Boulon, Radiation trapping and self-quenching analysis in Yb^{3+}, Er^{3+}, and Ho^{3+} doped Y_2O_3, Opt. Mater. 24 (2003) 103–109.

[40] P.R. Ehrmann, J.H. Campbell, Nonradiative energy losses and radiation trapping in neodymium-doped phosphate laser glasses, J. Am. Ceram. Soc. 85 (2002) 1061–1069.

[41] J.H. Campbell, T.I. Suratwala, Nd-doped phosphate glasses for high-energy/high-peak-power lasers, J. Non-Cryst. Solids 263 & 264 (2000) 318–341.

[42] C.B. Layne, W.H. Lowdermilk, M.J. Weber, Multiphonon relaxation of rare-earth ions in oxide glasses, Phys. Rev. B 16 (1977) 10–20.

[43] P. Babu, I.R. Martín, G. Venkataiah, V. Venkatramu, V. Lavín, C.K. Jayasankar, Blue–green cooperative upconverted luminescence and radiative energy transfer in Yb^{3+}-doped tungsten tellurite glass, J. Lumin. 169 (2016) 233–237.

[44] P.R. Ehrmann, J.H. Campbell, T.I. Suratwala, J.S. Hayden, D. Krashkevich, K. Takeuchi, Optical loss and Nd^{3+} non-radiative relaxation by Cu, Fe and several rare earth impurities in phosphate laser glasses, J. Non-Cryst. Solids 263 & 264 (2000) 251–262.

[45] M. Ito, C. Goutaudier, Y. Guyot, K. Lebbou, T. Fukuda, G. Boulon, Crystal growth, Yb^{3+} spectroscopy, concentration quenching analysis and potentiality of laser emission in $Ca_{1-x}Yb_xF_{2+x}$, J. Phys. Condens. Matter 16 (2004) 1501–1521.

[46] S. Shen, M. Naftaly, A. Zha, Tungsten–tellurite-a host glass for broadband EDFA, Opt. Commun. 205 (2002) 101–105.

[47] C. Jiang, H. Liua, Q. Zeng, X. Tang, F. Gan, Yb: phosphate laser glass with high emission cross-section, J. Phys. Chem. Solids 61 (2000) 1217–1223.

ICAPMA_2017

Effect of concentration on spectral properties of lanthanide ions-doped fluorophosphate glasses

R. Vijaya[a,b], V. Venkatramu[c], P. Babu[d], C.K. Jayasankar[a,*], J. Kaewkhao[e], W. Lertlop[f]

[a]Department of Physics, Sri Venkateswara University, Tirupati-517 502, India.
[b]Department of Physics, Visvodaya Govt. Degree College. Venkatagiri – 524 132, India.
[c]Department of Physics, Yogi Vemana University, Kadapa – 516 003, India.
[d]Department of Physics, SVCR Govt. Degree College. Palamaner – 517 408, India.
[e]Center of Excellence in Glass Technology and Materials Science (CEGM), Nakhon Pathom Rajabhat University, Nakhon Pathom, 73000, Thailand
[f]Applied Physics, Faculty of Science and Technology, Suan Sunandha Rajabhat University, Bangkok 10300, Thailand.

Abstract

Concentration dependent spectroscopic properties of Ln^{3+} (Ln= Nd, Sm, Dy and Yb) -doped fluorophosphate glasses have been investigated. From the absorption spectra, Judd-Ofelt (JO) intensity parameters have been evaluated which are in turn used to predict radiative properties for the fluorescent levels of the said Ln^{3+} ions. For example, three JO intensity parameters (Ω_2, Ω_4 and Ω_6) for the Dy^{3+} ions in fluorophosphate glass are found to be $\Omega_2 = 12.34 \times 10^{-20}$ cm^2, $\Omega_4 = 2.67 \times 10^{-20}$ cm^2 and $\Omega_6 = 2.30 \times 10^{-20}$ cm^2. Using FTIR spectra, OH^- content in 1.0 mol % Nd_2O_3 -doped samples, responsible for quenching the lifetimes of Nd^{3+} ions, is found to be 2.01×10^{20} $ions/cm^3$ which is very much less compared to other reported glass systems. The decay profiles for the $^4G_{5/2}$ level of Sm^{3+} ions in the flurophosphate glasses are found to change from single exponential (0.1 mol%) to non-exponential (0.5, 1.0, 2.0, 4.0 and 6.0 mol%) with shortening of lifetimes. The Yb^{3+} -doped fluorophosphate glasses possess high absorption (2.55 cm^2) and emission (3.44 cm^2) cross-sections and high figure of merit (3.33). The analysis of the results confirm that the Ln^{3+} -doped fluorophosphate glasses could be useful for the development of photonic devices.
© 2018 Elsevier Ltd. All rights reserved.

Selection and/or Peer-review under responsibility of 3rd International Conference on Applied Physics and Materials Applications.

Keywords: Lanthanides; Fluorophosphate glasses; Judd-Ofelt theory; Luminescence properties; Photonic devices

* Corresponding author.
E-mail address: ckjaya@yahoo.com & wichan.le@ssru.ac.th.

1. Introduction

Research on lanthanide ions (Ln^{3+}) -doped optical quality transparent glasses are of great interest as they find applications in solid state lasers, optical amplifiers, upconverters, optical sensors, quantum cutters for solar energy harvesting, and phosphors [1-2]. The performance of these devices is limited by fast energy transfer, non-radiative de-excitation probabilities, clustering of Ln^{3+} ions at higher concentrations [3-4]. In order to improve their performance, it is necessary to limit the clustering of Ln ions. In this regard, the selection of chemical composition and concentration of Ln^{3+} ions plays vital role in the formation of clusters in glasses [5].

The optical properties of Ln^{3+} ions in glasses depend on the chemical composition of the glass, which determines the structure and nature of the bonds. Among different host materials, fluorophosphate (FPh) glasses are promising hosts because these glasses can combine the advantages of both fluoride and phosphate glasses such as lower phonon energy, better moisture resistance, physical and chemical stability, lower nonlinear refractive index and higher transparency from near UV to mid IR spectral range [6-8]. It was also found that a relatively higher degree of line broadening and smoother line shapes can be obtained [9] with FPh glass. These properties contribute to the applications of FPh glasses as Ln^{3+}-doped fiber laser. Many researchers have showed that Ln^{3+}-doped FPh glasses have promising features as laser gain media [10–12]. It is well known that the spectroscopic parameters such as absorption cross-section, emission cross-section and fluorescence lifetimes for metastable states of Ln^{3+} ions depend on their local environment in the glass matrix [13,14]. For FPh glasses, the local structure of Ln^{3+} ions can be modified over a large extent by varying P/F ratio and/or introducing other special ions [15,16].

2. Experimental details

Lanthanide (Ln^{3+}) -doped transparent fluorophosphate glasses with molar compositions of P_2O_5 +K_2O + MF + SrO + Al_2O_3 + Ln_2O_3 (where MF = $KF/MgF_2/SrF_2/AlF_3$; Ln = Nd/ Sm Dy/Yb) (x = 0.1, 0.5, 1.0, 2.0, 4.0 and 6.0 mol %) were prepared by conventional melt quenching technique. The method of preparation and experimental techniques for spectroscopic measurements [17].

3. Results and discussion

3.1. Absorption spectra

From the absorption spectrum, the experimental oscillator strengths of various absorption transitions are evaluated. A least-square fitting procedure has been used to determine the JO parameters following the procedure described elsewhere [17]. As can be seen from Table 1, the trend of the JO parameters is $\Omega_2 > \Omega_6 > \Omega_4$ for PKMFAN10 glass and $\Omega_6 > \Omega_2 > \Omega_4$ for PKSFAN10 glass. The larger value of Ω_2 is due to the relatively higher value of the oscillator strength of the hypersensitive transition. The parameter Ω_2 is affected by the covalency of the Ln-O bond as well as the asymmetry around the Ln^{3+} ion site. In the present case, the higher value of Ω_2 indicates less centrosymmetric coordination [18] and a strong covalence [19] nature of metal-ligand bond. The condition $\Omega_6 \gg \Omega_4$ favours the intense $^4F_{3/2} \rightarrow {}^4I_{11/2}$ transition at 1.06 µm and $\Omega_6 \ll \Omega_4$ favours the intense $^4F_{3/2} \rightarrow {}^4I_{9/2}$ transition at 0.89 µm [20] compared to other transitions in the emission spectra. For present glass systems, the spectroscopic quality factor ($\chi = \Omega_4/\Omega_6$) values are 0.70 (PKMFAN10) and 0.74 (PKSFAN10) which are presented in Table 1. For the PKFSASm10 glass system, the trend is $\Omega_2 > \Omega_4 > \Omega_6$, the higher value of Ω_2 indicates that PKFSAS10 glass has stronger covalent nature while the other parameters, Ω_4 and Ω_6 are related to the rigidity of the host. It is observed that the $^4G_{5/2} \rightarrow {}^6H_{9/2}$ transition exhibits higher $\sigma(\lambda_p)$ value for PKFSAS10 glass, which signifies the rate of energy extraction from the laser material. For the PKBAFDy10 glass, the larger value of Ω_2 indicates larger degree of covalency between the Dy^{3+} ion and the surrounding ligands and/or lower symmetry of the coordination structure surrounding the Dy^{3+} ion. As can be seen from Table1, for the PKBAFDy10 glass, the quantum efficiency exceeds 100%. This inconsistent result is attributed to the inherent uncertainty involved in the approximations of the JO theory.

Table 1. Refractive indices (n), concentrations (N_0, 10^{20} ions/cc), Judd-Ofelt parameters (Ω_λ, $\times10^{-20}$ cm^2), radiative (τ_R) and experimental (τ_{exp}) lifetimes (μs), quantum efficiencies (η) and stimulated emission cross-sections ($\sigma(\lambda_P)$, $\times10^{-22}$ cm^2) for 1.0 mol% Ln$_2$O$_3$-doped fluorophosphate glasses.

S.No.	Glass	n	N_0	Ω_2	Ω_4	Ω_6	Trend	τ_R	τ_{exp}	η %	$\sigma(\lambda_p)$
1.	PKSFANd10	1.540	2.48	5.24	4.30	5.81	$\Omega_6 > \Omega_2 > \Omega_4$	326	211	65	3.29
2.	PKMFANd10	1.524	2.55	4.41	2.88	4.06	$\Omega_2 > \Omega_6 > \Omega_4$	491	200	41	1.81
3.	PKFSASm10	1.515	2.69	8.36	7.42	4.37	$\Omega_2 > \Omega_4 > \Omega_6$	1840	1773	96	14.12
4.	PKBAFDy10	1.539	2.46	12.34	2.67	2.30	$\Omega_2 > \Omega_4 > \Omega_6$	669	732	109	4.76

3.2. Decay curve analysis

Luminescence decay curves of the Sm^{3+} ions have been measured by exciting with 476.5 nm laser and monitoring the 645 nm emission. The concentration dependent decay profiles for the $^4G_{5/2}$ level of Sm^{3+} ions in PKFSASm glasses are shown in Fig. 1. As can be seen, the decay curves change from single exponential to non-exponential with increase in Sm^{3+} ion concentration. Hence, the experimental lifetimes (τ_{exp}) of the $^4G_{5/2}$ level in PKFSASm glasses have been calculated as per the method described in Ref [17]. The τ_{exp} values of the $^4G_{5/2}$ level are found to be 2699, 1863, 1773, 1177, 331 and 108 μs for 0.1, 0.5, 1.0, 2.0, 4.0, 6.0 mol% Sm$_2$O$_3$ -doped PKFSA glasses, respectively. The observed non-exponential nature with shortening of lifetimes could be explained by the presence of an excitation energy transfer and cross-relaxation channels: ($^4G_{5/2}$, $^6H_{5/2}$) $\rightarrow$ ($^6F_{5/2}$, $^6F_{11/2}$) and ($^4G_{5/2}$, $^6H_{5/2}$) $\rightarrow$ ($^6F_{9/2}$, $^6F_{7/2}$) from Sm^{3+} ion being in the excited $^4G_{5/2}$ state to another one in the ground state. Later the two ions relax non-radiatively to their ground state, $^6H_{5/2}$. This transfer can occur either by exchange coupling or by electric multipolar interactions.
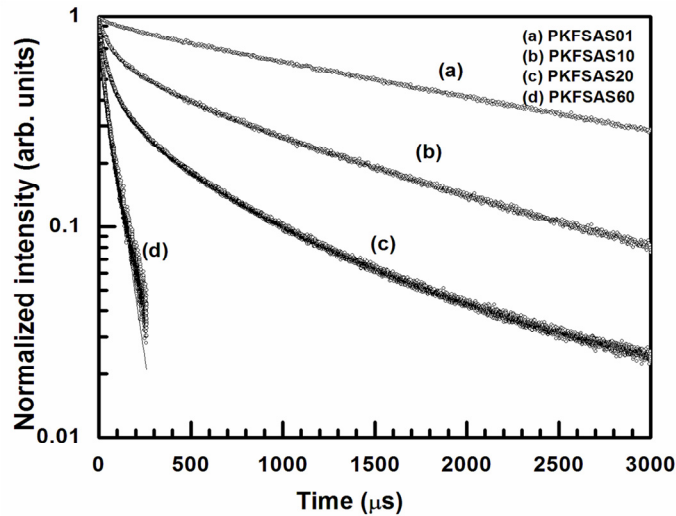

Fig.1. Decay curves of the $^4G_{5/2}$ level in (a) PKFSAS01 (b) PKFSAS10 (c) PKFSAS20 and (d) PKFSAS60 glasses.

3.3. FTIR spectra

The presence of OH$^-$ impurities in the studied glasses plays a key role in photonic device performance. In order to know the OH$^-$ concentrations in the glasses, the FTIR spectra are measured for 1.0 mol% Nd$_2$O$_3$ -doped glasses and are shown in Fig. 2.

From the FTIR spectra, OH$^-$ concentrations in 1.0 mol% Nd$_2$O$_3$ -doped glasses, responsible for quenching the lifetimes of Nd^{3+} ions, are calculated to be 2.01×10^{20} and 0.98×10^{20} ions/cm^3 in PKMFAN10 and PKSFAN10 glasses, respectively, which are very much less than 5.82×10^{20} ions/cm^3 reported for 0.1 mol% Er$_2$O$_3$-doped zinc tellurite glass [21]. From this analysis, it is clear that PKSFAN10 glass is having lower OH$^-$ content resulting in smaller

quenching effect on Nd^{3+} ions fluorescence in this glass. This is one of the reasons for the higher lifetimes of the $^4F_{3/2}$ level in PKSFAN glasses compared to PKMFAN glasses for all the three Nd^{3+} ion concentrations studied in the present work (Table 1).
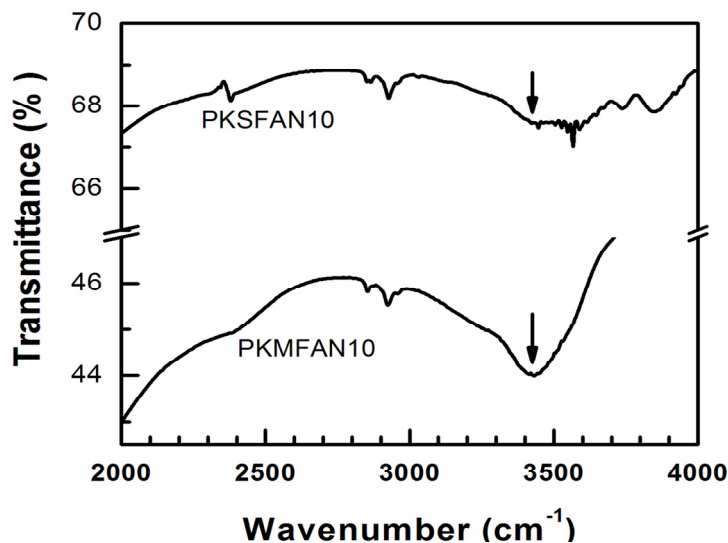

Fig. 2. The FTIR spectra of PKMFAN10 and PKSFAN10 glasses.

3.4. Laser performance parameters

In order to assess the potential of PKFSAYb glasses for laser devices, the laser performance parameters such as absorption (σ_{ab}) and emission (σ_{em}) cross-sections, lifetimes (τ), β_{min} (minimum fraction of Yb^{3+} ions that must be excited to balance the gain exactly with the ground state absorption at a laser wavelength), I_{sat} (pump saturation intensity) and I_{min} (minimum absorbed pumping intensity) have been determined following the procedure described elsewhere [22] and are shown in Table 2. As can be seen from Table 2, radiative lifetime (τ_R) increases with increase in Yb_2O_3 concentration in PKFSAYb glasses. The values of β_{min}, I_{sat} and I_{min} are in the range of 0.133 - 0.463, 9.52 - 100.4 kW/cm^2, 2.46 - 15.57 kW/cm^2, respectively. There is a considerable change in the value of β_{min} for the PKFSAYb glasses. It is desirable for I_{sat} to be as low as possible to minimize the minimum pumping intensity (I_{min}) as the emission cross-section is proportional to absorption cross-section. For a good laser glass, figure of merit ($\sigma_{em} \times \tau_{exp}$) and energy extraction efficiency are generally desirable to be as large as possible to provide high gain and the I_{min} to be as small as possible to minimize the pump losses. From Table 2, it is noticed that PKFSAYb01 glasses possess higher figure of merit value of 3.33, compared to reported glasses. Hence, PKFSAYb01 glass is more suitable for laser applications.

Table 2. Spectroscopic and laser performance parameters of Yb^{3+}-doped fluorophosphate glasses.

S. No.	Glass label	n	σ_{ab} (cm^2)	σ_{em} (cm^2)	τ_R (ms)	τ_{exp} (ms)	β_{min}	I_{sat} (kW/cm^2)	I_{min} (kW/cm^2)	$\sigma_{emi} \times \tau_{exp}$	SFL
1.	PKFSAYb01	1.515	2.55	3.47	1.02	0.96	0.463	9.52	4.41	3.33	0.755
2.	PKFSAYb05	1.516	1.74	2.31	1.14	0.86	0.159	15.51	2.46	1.99	0.809
3.	PKFSAYb10	1.517	1.63	2.18	1.19	0.64	0.142	22.27	3.18	1.39	0.440
4.	PKFSAYb20	1.517	1.61	2.16	1.30	0.47	0.133	30.54	4.07	1.01	0.251
5.	PKFSAYb40	1.526	1.29	1.72	1.53	0.29	0.140	62.51	8.75	0.50	0.057
6.	PKFSAYb60	1.529	1.10	1.48	1.46	0.21	0.155	100.40	15.57	0.31	0.020

4. Conclusions

The fluorophosphate glasses doped with various Ln^{3+} ions have been prepared by conventional melt-quenching technique and studied their concentration dependent spectroscopic and laser performance parameters. The spectroscopic quality factor for the present PKMFAN10 and PKSFAN10 glasses indicate that there is more probability for the $^4F_{3/2} \to {}^4I_{11/2}$ emission transition at around 1.06 μm. The larger value of Ω_2 indicates the larger asymmetry at the Sm^{3+} ion site as well as strong covalent nature of Sm-O bond in the PKFSAS10 glass. It is observed that the $^4G_{5/2} \to {}^6H_{9/2}$ transition possess higher emission cross-section ($\sigma(\lambda_p)$). The radiative properties derived from the JO theory as well as concentration dependent lifetimes of the $^4F_{9/2}$ level have been reported. It is found that the PKFSAYb01 glass possess higher absorption and emission cross-sections and higher figure of merit. The measured lifetime of $^2F_{5/2}$ level decreases from 0.96 to 0.21 ms in fluorophosphate glasses when Yb_2O_3 concentration is increased from 0.1 to 6.0 mol% due to energy transfer between Yb^{3+} ions and OH^- ions.

Acknowledgements

References

[1] C. Görller-Walrand, K. Binnemans, in: K. A. Gschneidner Jr., L. Eyring (Eds.), Handbook on the Physics and Chemistry of Rare Earths, Vol.25, North Holland, Amsterdam, 1998 (ch.167).
[2] X. Zou and H. Toratani, Phys. Rev. B 52 (1995) 15889-15897.
[3] B. J. Ainslie, S. P. Craig-Ryan, S. T. Davey, J. R. Armitage, C. G. Atkins, J. F. Massicot and R. Wyatt, IEEE Proc. 137 (1990) 205-208.
[4] P. Blixt, J. Nilsson, T. Carlnas and B. Jaskorzynska, IEEE Photon. Technol. Lett. 3 (1991) 996-998.
[5] K. Arai, H. Namikawa, K. Kumata, T. Honda, Y. Ishii and T. Handa, J. Appl. Phys. 59 (1986) 3430-3436.
[6] S.V.J. Lakshman, Y.C. Ratnakaram, Phys. Chem. Glasses 31(1990) 42-44.
[7] B. Viana, M. Palazzi, O. Lefol, J. Non-Cryst. Solids 215 (1997) 96-102.
[8] S. Jiang, T. Luo, B.C. Hwang, F. Smekatala, K. Seneschal, J. Lucas, N. Peyghambarian, J. Non-Cryst. Solids 263-264 (2000) 364-368.
[9] D. Ehrt, Proc. SPIE 1761 (1992) 213-222
[10] K. Lu, N.K. Dutta, J. Appl. Phys. 91 (2002) 576-581.
[11] L. Zhang, H.F. Hu, J. Non-Cryst. Solids 292 (2001) 108-114.
[12] H.B. Yin, P.Z. Deng, J.Z. Zhang, H.B. Yin, P.Z. Deng, J.Z. Zhang, J. Non-Cryst. Solids 210 (1997) 243-248.
[13] G.Y. Zhang, M.J. Poulain, G.Y. Zhang, M.J. Poulain, J. Alloys Compd. 275-277 (1998) 15-20.
[14] B. Karmakar, P. Kundu, R.N. Dwivedi, J. Non-Cryst. Solids 289 (2001) 155-162.
[15] D. Ehrt,W.Wintzer,W. Topfer, Proceedings of the XIII International Symposium on Non-oxide Glasses and New Optical Glasses, Pardubice, Czech Republic, 2002, p. 662.
[16] T. Murata, K. Mazeno, K. Morinaga, Sci. Technol. Adv. Mater. 3 (2002) 85-90.
[17] R. Vijaya, V. Venkatramu, P. Babu, C.K. Jayasankar, U. R. Rodríguez-Mendoza, V. Lavín, J. Non-Cryst. Solids 365 (2013) 85-92.
[18] Z. Jiang, J. Yang and S. Dai, J. Opt. Soc. Am. B 21 (2004) 739-743.
[19] C.K. Jorgensen and R. Reisfeld, J. Less-Common Met. 93 (1983) 107-112.
[25] R. C. Powell, Physics of Solid State Laser Materials, Springer, New York, 1998.
[21] S. Dai, J. Zhang, C. Yu, G. Zhou, G. Wang and L. Hu, Mater. Lett. 59 (2005) 2333-2336.
[22] L.D. Loach, S.A. Payne, L.K. Smith, W.L. Kway, W.F. Krupke, J. Opt. Soc. Am. B:Opt. Phys. 11 (1994) 269-276.

Accepted Manuscript

Temperature and composition dependence of the volumetric and acoustic properties of ionic liquid [emim][HSO$_4$] with polar protic and aprotic co-solvents

P. Bhanuprakash, N.V.V. Jyothi, C. Narasimharao, M. Raveendra, K. Sivakumar
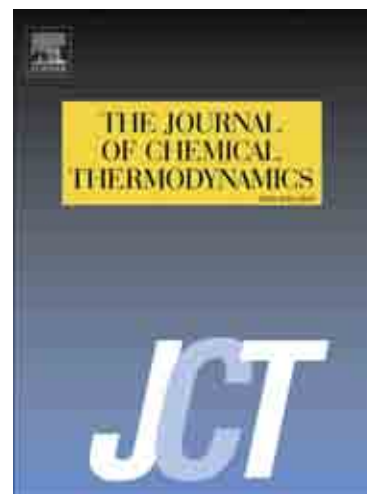
Please cite this article as: P. Bhanuprakash, N.V.V. Jyothi, C. Narasimharao, M. Raveendra, K. Sivakumar, Temperature and composition dependence of the volumetric and acoustic properties of ionic liquid [emim][HSO$_4$] with polar protic and aprotic co-solvents, *J. Chem. Thermodynamics* (2018), doi: https://doi.org/10.1016/j.jct.2018.03.007

Temperature and composition dependence of the volumetric and acoustic properties of ionic liquid [emim][HSO₄] with polar protic and aprotic co-solvents

P. Bhanuprakash[a,b], N.V.V. Jyothi[a,*], C. Narasimharao[a], M. Raveendra[c], K. Sivakumar[d,*]

[a]Department of Chemistry, S.V. University, Tirupati-517502, A.P., India.

[b]Department of Chemistry, S.V.C.R. Govt. Degree College, Palamaner-517408, A.P., India.

[c]Department of Chemistry, P.V.K.N. Govt. College, Chittoor-517002, A.P., India.

[d]Department of Chemistry, S.V. Arts Degree & P.G. College (T.T.D'S), Tirupati-517502, A.P., India.

Abstract

In the present paper, we report new experimental data on density (ρ) and speed of sound (u) in binary liquid mixtures of 1-ethyl-3-methylimidazolium hydrogen sulphate, [emim][HSO₄] with polar protic solvents ethanol (EtOH) and 1-propanol (n-PrOH) and aprotic solvent, dimethyl sulphoxide (DMSO) over the complete range of mole fraction at 298.15 K $\leq T \leq$ 313.15 K, every 5 K, and 0.1MPa pressure. The mixing behaviour of the binary systems of [emim][HSO₄] with EtOH, n-PrOH, and DMSO has been studied by computing the excess volumes (V^E) and excess isentropic compressibilities (κ_s^E) utilizing the measured densities (ρ) and speeds of sound (u). Further, the excess functions V^E and κ_s^E are correlated with mole fraction, using Redlich-Kister equation to derive the fitting parameters. For the systems studied, the excess thermodynamic properties (V^E and κ_s^E) are found to be negative over the whole range of composition at investigated temperatures. Also, the experimental results are discussed in terms of ion-ion, ion-dipole, hydrogen bonding interactions and interstitial accommodation between component molecules in the binary liquid mixtures. Moreover, the temperature dependence of the physicochemical and excess properties has been studied.

Keywords: 1-Ethyl-3-methylimidazolium hydrogen sulphate, Dimethyl sulphoxide, Excess volume, Speed of sound, Ion-dipole interaction.

----

*[a]Corresponding author. Tel.: +91 9912366219
E-mail addresses: nvvjyothi73@gmail.com (N. V. V. Jyothi)
*[d]Corresponding author. Tel.: +91 9290080843.
E-mail addresses: sivakumarkasi64@gmail.com (K. Sivakumar)

1. Introduction

Ionic liquids (ILs) are a new class of chemical compounds with low melting points, mainly below 373.15 K. They consist of larger and asymmetric cations like quaternary ammonium, imidazolium, thiazolium, pyridinium, piperidinium, pyrrolidinium, morpholinium, phosphonium and sulphonium ions bound with inorganic anions such as halides, hexafluorophosphate, nitrate, tetrafluoroborate, thiocyanate, dicyanamide, perchlorate, bis(trifluoromethylsulphonyl)imide, hexafluoroantimonate, or organic anions like acetate, benzoate, alkyl sulphate, tosylate, triflate etc. Their distinctive properties include negligible vapour pressure, wide liquid temperature range, non-flammability, high heat capacity, high polarity, high thermal stability and conductivity, good solvation capacity for organic and inorganic substances and potential recoverability [1, 2]. In particular, ILs have the ability to fine-tune their physicochemical properties for a specific application by the careful selection of the side chain length or the substituents and its position on the ring or chain, the possible combination, and size of organic cations and anions. This added advantage has led to term these liquids as "designer solvents" [3]. Mixing of two ionic liquids or an ionic liquid and organic solvent to form binary mixtures is an alternate approach to tune their remarkable properties. Ionic liquids are unique complex molecules in which, in addition to stronger Coulombic forces and covalent interactions, there are important hydrogen bonding interactions, π-stacking, and Van der Waals forces, which are not generally present in conventional organic solvents [4].

Their distinctive properties make ILs widely useful in catalysis as remarkable environmentally benign catalysts [5] and solvents [6] in the area of green chemistry. They are used increasingly in the field of nanomaterials as either solvent for the synthesis or stabilization of nanomaterials [7]. Since ILs contains ions, they have been used in a variety of electronic applications, including electrolyte materials for rechargeable batteries [8], electrochemical capacitors [9], fuel cells [10], dye-sensitized solar cells [11] and charge storage devices, as well as in light-emitting materials. In addition, they have also been employed in bio-catalysis [12], biomass dissolution, separation, and extraction technologies [13] and in the field of spectroscopy [14]. Similarly, ILs are finding their way in the area of polymers as solvents for polymerization and as modifiers of polymer morphology. They have been explored as materials for embalming and tissue preservation, adsorption films, thermal fluids [15], liquid crystals [16], fuel additives

and lubricants [17]. Further, they find application in protection from corrosion, evaporation, leakage and flame prevention [18].

The diverse applications of ILs in certain areas have been limited because of their high viscosity which in turn hinders its performance within reaction media. To go through this difficulty and expand the applications of ILs, the effective alternative method is dilute ILs by suitable co-solvents [19]. One of the main barriers to the design and development of ILs for novel industrial applications is the scarce knowledge of the thermophysical properties like, density, melting point, surface tension, speed of sound, viscosity, electrical conductivity, refractive index and self-diffusion coefficient etc of the pure ILs and its binary liquid mixtures with different solvents, in wide pressure and temperature ranges. Therefore, there is a clear need for systematic investigation of thermophysical properties of pure ILs or their mixtures to make them available for use as green solvents or as new materials for different industrial applications and also to design new ILs for specific purposes. The knowledge and understanding of structure-property relationships of binary systems through volumetric and acoustic properties is indispensable in many industrial, engineering and technological processes in designing and development of new processes and products, reliable correlations and predictive physical models in solution theories [20, 21]. The study on thermophysical properties of ILs and its solutions is required to contribute a quite large data to thermodynamic data bank [22]. However, the accurate experimental data on excess properties of (IL+ molecular solvents) is challenging and essential in understanding the nature and extent of interactions between them [23].

Among the commercially available ILs, the most prominently studied ILs are based on imidazolium cations with different anions such as $[X]^-$, $[BF_4]^-$, $[NTf_2]^-$, $[PF_6]^-$, $[CF_3COO]^-$, $[CF_3SO_3]^-$, $[ClO_4]^-$, alkyl sulphonates or alkyl sulphates. The imidazolium ILs, based on alkyl sulphate anions like $[HSO_4]^-$, $[MeSO_4]^-$, and $[EtSO_4]^-$ are easily synthesized in an atom-efficient and halide-free way. They also present an anion with a low toxicity in comparison with other ILs and are also suitable for applications in the large-scale because of their affordable prices. Moreover, they are hydrolysis-stable except under high temperatures and highly acidic conditions. They are the interesting green alternatives for polar solvents in industrial process and applications. Their solvent properties can easily be tunable by varying the alkyl chain length of the substituents at the nitrogen atoms on the imidazolium cation as well as the counter-ions. This allows for a fine manipulation of their polarity and hydrophilic-hydrophobic balance, which

3

makes them the real designer solvents. Alkyl sulphate based acidic ionic liquids have received a considerable interest to the catalysis community because they are hydrolysis-stable, water soluble, non-corrosive, recoverable and contain halogen-free anions [24, 25]. Imidazolium-based acidic ILs containing the sulphate anion, have been currently evaluated as eco-friendly catalysts in different organic reactions like esterification, carbonylation, polymerization, Friedel–Crafts, Beckmann and Diels–Alder reactions, biomass saccharification with excellent yield and selectivity [26]. The Bronsted acidic ILs with hydrogen sulphate anions possessing the favourable properties of solid and liquid acids have shown their potential applicability in various chemical reactions as catalysts and solvents and replace conventional acids like H_2SO_4 and HCl [27].

Dimethyl sulphoxide (DMSO) is a versatile colourless, polar aprotic solvent miscible with wide range of organic solvents [28]. Because of its good solvating capacity and non-toxicity, DMSO is commonly used as a solvent for chemical reactions notably for nucleophilic substitutions and polymerization reactions [1], in biological processes and in the field of medicine [29]. DMSO molecule has a trigonal pyramidal geometry with a non-bonded electron pair on the sulphur atom. It is a self-associated liquid through dipole-dipole interactions in its native state as shown in Figure1(a) due to its high dielectric constant ($\varepsilon = 46.7$ at T = 298.15 K) [19] and dipole moment ($\mu = 3.96$ D) [30]. The resonance structure of DMSO with a highly polar S=O group is shown in Figure 1(a). On the other hand, the self-association in DMSO is weaker when compared to the high degree of self-association through hydrogen bonding in alcohols in their pure state. On the other hand, it acts as a hydrogen bond acceptor due to its electron donating capacity [31].

1-Alkanols are polar protic solvents and self-associated liquids through intermolecular H-bonding in their pure state [32]. In its self-association, the hydroxyl group (-O-H) of alcohols act as hydrogen-bond donors as well as acceptors. The self-association of 1-alkanols presents equilibria consisting of a mixture of monomers, dimers and so on with cyclic as well as linear structures. But mostly, 1-alkanols exist as linear chain species as shown in Figure 1(b). The strength of the H-bonding in alcohols may differ depending on its concentration in the liquid state, the position of the functional group (-O-H), alkyl chain length, and on temperature [32-34]. Further, it was reported that the extent of self-association decreases with increase in the alkyl chain length of 1-alkanols [35, 36]. Due to its low cost and easy availability with high purity,

4

alkanols are mainly used as all-purpose solvents in varied applications, including chemical reactions and technological processes [37]. They are also used as fuels and as important precursors for many other organic compounds. They are considered as amphiphilic materials of great importance in the fields of biology, chemistry, and industry [38]. Hence, both the types of solvents, viz., DMSO and 1-alkanols are considered as "super solvents" due to their wide applications in industrial and medical fields [39].

Considering the above mentioned favourable and attractive properties of alkyl sulphate based ILs, DMSO and 1-alkanols and their wide range of applications, we are greatly motivated to investigate mixing behaviour of [emim][HSO$_4$] with a polar aprotic solvent (DMSO) and polar protic solvents (EtOH, n-PrOH) through excess thermodynamic properties derived from experimentally measured physicochemical properties. The present study aims at investigating the nature and extent of self and cross-association taking place between the [emim]$^+$ cation and [HSO$_4$]$^-$ anion of IL with an addition of molecular solvent through volumetric and acoustic properties. Further, the objective of the present investigation is to understand the effect of composition and temperature on the thermodynamic properties and on the strength of self and cross-association taking place in the binary systems.

An exhaustive survey of recent literature reveals that the physicochemical properties of [emim][EtSO$_4$] with water and ethanol [40], methanol, 1-propanol, and 2-propanol [41], (C$_6$-C$_9$)1-alkanols [42], acetonitrile, propylene carbonate, acetone, and dichloromethane [43], ethanoic and propanoic acid [44], 2-propoxyethanol [45], nitromethane [46] have been published. Further, some data is available on volumetric and acoustic properties of [emim][MeSO$_4$] with (C$_1$-C$_5$)1-alkanols and 2-propanol [47, 48], ethanoic and propanoic acid [49]. Excess thermodynamic properties of [bmim][MeSO$_4$] with ethanol [50] and nitromethane [46, 50] have been reported in the literature. However, currently there are no systematic measurements of volumetric and acoustic properties of [emim][HSO$_4$] with DMSO, EtOH, and n-PrOH as a function of composition and temperature. In the present study, the selected thermophysical properties (ρ and u) have been precisely measured for pure [emim][HSO$_4$] and its binary mixtures with DMSO, EtOH, and n-PrOH at 298.15 K $\leq T \leq$ 313.15 K, every 5 K. Further, excess volumes (V^E) and excess isentropic compressibilities (κ_s^E) for the binary liquid systems are computed and the corresponding values are correlated with Redlich−Kister equation [51] to derive the fitting parameters. Moreover, ion-dipole interactions, intermolecular hydrogen

5

bonds and the structural factors between [emim][HSO$_4$] and molecular solvents resulting in the binary mixtures are discussed by using the experimental results of excess thermodynamic functions. Likewise, a discussion about the temperature dependence of excess thermodynamic properties has been carried out.

2. Experimental

2.1. Materials

The Ionic liquid [emim][HSO$_4$], is obtained from Alfa Aesar, UK with mass fraction purity $\geq$ 0.980. The structure of the studied IL is presented in Figure 1(c).The physicochemical properties of ILs are very sensitive to water content and impurities present in it and hence [emim][HSO$_4$] is further subjected to vacuum at T = 343.15 K for 36 hours and the liquid salt is tightly sealed in an amber bottle under nitrogen gas prior to its use. The mass fraction of water content in the [emim][HSO$_4$] before and after vacuum drying, estimated by using Karl–Fischer Titrator are 0.0017 and 0.0005 respectively. The chemicals dimethyl sulphoxide (DMSO, Merck, purity $\geq$ 0.999), ethanol (EtOH, Merck, purity $\geq$ 0.999), 1-propanol (n-PrOH, Sigma-Aldrich, purity $\geq$ 0.997) of high purity are procured. All these molecular solvents are not further purified. The chemical names, acronyms, CAS numbers, molar mass, supplier, purification method, molecular purities and water content of the liquids used are reported in Table 1. The purity of the liquid solvents is further checked by comparison of the measured density (ρ) and speed of sound (u) data at 298.15 K $\leq T \leq$ 313.15 K with literature values [1, 52-61] as recorded in Table 2. It can be observed that the values of ρ and u for pure chemicals well agree with the values of literature.

2.2. Apparatus and procedure

2.2.1. Sample preparation

The binary homogeneous solutions of [emim][HSO$_4$] with the molecular organic solvents are prepared gravimetrically in airtight glass bottles with screw caps by using a digital analytical balance (ATY 224, Shimadzu, India) with a precision of $\pm 1 \times 10^{-4}$ g. The uncertainty in x_1 of each mixture is calculated as being about $u(x_1) = \pm 6 \times 10^{-3}$. Experimental measurements of ρ and u are done immediately after preparation of sample solutions.

2.2.2. Density (ρ) and speed of sound (u) measurements

The density (ρ) and speed of sound (u) measurements of pure components and the binary liquid mixtures of [emim][HSO$_4$] with DMSO, EtOH and n-PrOH are carried at temperatures ranging from 298.15 K to 313.15K, and at 0.1MPa pressure, using digital densimeter (Rudolph Research

Analytical, DDM-2911, USA) and ultrasonic interferometer (Mittal Enterprises, F-05, India) respectively. The working frequency for the speed of sound (u) measurement is 2 MHz. The desired temperature of the sample is maintained by a thermostat within $u(T) = \pm 0.02$ K. Further details about the experimental apparatus and procedure can be found in our previous papers [62]. The uncertainty in density (ρ) measurements and excess volumes (V^E) calculated from densities is estimated to be $\pm 1 \times 10^{-3}$ g·cm^{-3} and $\pm 5 \times 10^{-3}$ cm^3·mol^{-1} respectively. The uncertainty in the measured speeds of sound (u) and the derived excess isentropic compressibility (κ_s^E) values are found to be ± 0.5 m·s^{-1} and ± 0.05 TPa^{-1} respectively.

3. Results and discussion

3.1. Densities (ρ) and excess volumes (V^E)

Volumetric properties of mixtures containing ILs are complex properties which are sensitive to the composition, temperature, nature and extent of specific interactions, even on the shape, chemical nature, and size of the solute and solvent molecules [63]. The experimental densities (ρ) at 298.15 K $\leq T \leq$ 313.15 K, at 5 K interval for pure liquids [emim][HSO$_4$], DMSO, EtOH, and n-PrOH are compared with published literature values [1, 52-61] in Table 2. It is observed that the experimental density values correlate with the published data. The complete experimental density data (ρ) is presented in Table 3 and Figures 2-4 illustrates the density (ρ) *vs.* mole fraction of [emim][HSO$_4$] (x_1) for mixtures of (IL + organic solvents) at T= 298.15 K to 313.15 K. As expected, the densities increased with x_1 in all the studied mixtures because [emim][HSO$_4$] is much denser compared with organic solvents. This might be ascribed due to strong ion–ion or ion–dipole interactions in the binary mixtures. At a fixed temperature, ρ increases with an increase in x_1 and for a fixed composition (x_1), the values of ρ decrease with an increase in temperature for all the systems. With higher IL composition and lower temperature, the efficiency of packing between components increases in the mixture, resulting in high ρ values. Moreover, at the same temperature and composition, the ρ values are higher for the {[emim][HSO$_4$] + DMSO} mixture, moderate for {[emim][HSO$_4$] + EtOH} and lower in mixtures of the {[emim][HSO$_4$] + n-PrOH}. The high densities of the {[emim][HSO$_4$] + DMSO}system is attributed to stronger specific interactions between molecules of [emim][HSO$_4$] and DMSO. Further, with increasing temperature, the molecular agitations in binary solutions increase which weaken the intermolecular interactions, ensuing in a decrease in density values.

The excess volumes (V^E) for the liquid mixtures containing [emim][HSO$_4$] are calculated from the experimental densities (ρ) through the known relation:

$$V^E = \frac{x_1 M_1 + x_2 M_2}{\rho} - \left[\frac{x_1 M_1}{\rho_1} + \frac{x_2 M_2}{\rho_2} \right] \tag{1}$$

where ρ depicts the density of the binary system; ρ_1, x_1, M_1 and ρ_2, x_2, M_2 represent the density, mole fraction and molar mass of [emim][HSO$_4$] and organic solvents, respectively.

The V^E values rely on the balance between the following competing effects [32, 49, 63]:
(a) Chemical effect: Formation of the hydrogen bonds, ion-ion interactions, stronger dipole-dipole, ion-dipole interactions, donor–acceptor complexes, n-π interactions, π-π interactions among the components of the mixture contributes to the negative V^E values. The disruption of interactions between the constituents of mixture results in the positive values of V^E.
(b) Physical effect: The non-specific interactions caused mainly by weak Van der Waals forces or London dispersion forces between the components will mainly result in positive V^E values.
(c) Structural effect: Packing of smaller component molecules into others interstices because of their variation in shape, size, free volumes and molar volumes result in the negative V^E. On the other hand, a positive V^E is an indication of an ill-fitting between the mixed components.

The excess volumes (V^E) for {[emim][HSO$_4$] + organic solvents} against x_1 of [emim][HSO$_4$] at 298.15 K $\leq T \leq$ 313.15 K are displayed in Table 3 and Figures 5-7. It is noticed that V^E values are negative across the complete composition (x_1) at four studied temperatures. The V^E vs. x_1 curves of the above systems are asymmetric with their minima skewed towards organic solvents-rich mole fraction (i.e., at x_1 between 0.3 and 0.4.). When the (IL + organic solvent) mixtures are compared, the absolute values of V^E at the same temperature and composition are found to be:

[emim][HSO$_4$] + DMSO > [emim][HSO$_4$] + EtOH > [emim][HSO$_4$] + n-PrOH.

In [emim]$^+$ of IL, the carbon atoms C4- and C5- are almost neutral whereas C2-H is positively charged due to the electron deficiency in the C=N bond. The large positive charge is responsible for the highly acidic nature of hydrogen atom of C2-H in the imidazolium cation of IL. The repulsive interactions due to C=C bond explain the considerable electron releasing behaviour of C4- and C5- atoms [64]. The association within the pure [emim][HSO$_4$] liquid is mostly due to ion–ion attractions between the larger [emim]$^+$ and the smaller [HSO$_4$]$^-$ and π-π interactions between the imidazolium cations. After mixing the IL with an organic solvent, the

interactions between anions and solvent molecules and between cations and solvent molecules are generated. The excess volumes (V^E) for the three systems under study are influenced by the balance between the expansion and contraction effects arising due to mixing of ILs with polar organic solvents: (i) expansion of self-associated DMSO and alcohol due to disruption of dipole-dipole interactions and hydrogen bonds respectively (ii) expansion of associated [emim][HSO$_4$] due to weakening of ion-ion interactions and π-π interactions (iii) contraction due to ion-dipole interaction and H-bonding between [emim]$^+$ cation and oxygen atoms of organic solvents (iv) contraction due to ion-dipole interaction and H-bonding between [HSO$_4$]$^-$ anion and hydrogen atom of alcohol or sulphur atom of DMSO as illustrated in Figure 8, and (v) contraction due to the size difference between [emim][HSO$_4$] and organic solvents. The molar volumes (V_m) of [emim][HSO$_4$], DMSO, EtOH, n-PrOH are (152.47, 71.33, 58.67 and 75.13) cm^3·mol^{-1} respectively at T/K = 298.15. This significant difference in V_m values causes molecular arrangement of a relatively smaller organic molecule into the interstices of [emim][HSO$_4$] upon mixing. The negative V^E value suggests that the volume contraction factors (iii), (iv) and (v) outweigh the volume expansion factors (i) and (ii) in the mixtures. Hence, the structure making factors like ion–dipole interactions, cross H-bonding formation and also the molecular arrangement via packing effect between [emim] [HSO$_4$] and organic solvents govern the negative values of V^E in all the three systems. The minima in V^E for the three binary systems can be found in the organic solvent-rich region which might be interpreted as the favourable combination of strong inter-molecular bonds between the components in the mixture and a high degree of occupation of smaller organic solvent molecules into the interstices formed by the [emim][HSO$_4$] network [65].

In general, polar solvents of high dielectric constants (ε) show better miscibility and stronger inter-molecular interactions with ionic liquids [19]. The more negative V^E values of {[emim][HSO$_4$]+DMSO} than {[emim][HSO$_4$] + 1-alkanol} systems suggests the relatively stronger ion-dipole and cross H-bonding interactions between highly acidic proton of C2-H in the [emim]$^+$ cation and an oxygen atom of S=O group of DMSO. The higher dipole moment and dielectric constant for DMSO (ε =46.7, at T/K = 298.15) [19] than EtOH (ε = 24.2 at T/K = 298.15) and n-PrOH (ε =20.1 at T/K = 298.15) may be responsible for its stronger inter-molecular interactions with [emim][HSO$_4$] which in turn results in more negative V^E. The V^E values of (IL + ethanol) are more negative than (IL + 1-propanol) system. This indicates that the

9

(ion + dipole) interactions and packing efficiency decrease with increase in the alkyl chain length of 1-alkanol. Gonzalez *et al.* [41] found the similar result for the {[emim][EtSO$_4$] + alcohol} systems. In addition, similar behaviour was reported by Requejo *et al.* [47] and Wang *et al.* [48] for {[emim][MeSO$_4$]+ alcohol} systems. 1-Propanol has a lower dipole moment, lower dielectric constant, slightly hydrophobic and lesser capability to donate protons than ethanol. The larger aliphatic propyl (-C$_3$H$_7$) group in (IL + 1-propanol) system offers some steric hindrance for the interaction of -O-H group of 1-propanol with cation and anion of IL. This weakens the interactions between unlike molecules and results in lesser negative V^E than (IL + ethanol) system. Moreover, the more negative V^E of (IL + ethanol) system can be attributed to the fact that small ethanol molecules can effectively fill the free volume between the ionic networks of the ILs [66].

The temperature dependence of V^E is most evident in all the three IL mixtures with organic solvents. With an increase in temperature, the V^E values become more negative over the complete composition for the binary systems. The hydrogen bonds are more sensitive to temperature than the Coulombic interactions. At high temperatures, the Coulombic interactions might be stronger, but the hydrogen bonding interactions become weaker [67]. The more negative V^E values with increase in temperature may be ascribed due to the predominant weakening of the self-association between like molecules than the intermolecular interactions between [emim][HSO$_4$] and organic solvents. Further, the more negative V^E is also attributed to the more effective packing between [emim][HSO$_4$] and organic solvents due to enlargement of voids of IL molecules with temperature [43].

It may be expected that hydrogen sulphate (HSO_4^-) anion of [emim][HSO$_4$] reacts with ethanol and 1-propanol to produce ethyl sulphate ($EtSO_4^-$) and propyl sulphate ($PrSO_4^-$) respectively:

$$R - CH_2 - OH + HO - SO_3^- \rightarrow R - CH_2 - OSO_3^- + H_2O \tag{2}$$
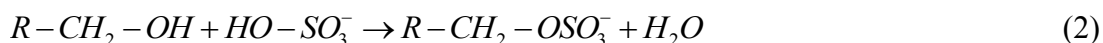
The possibility of reaction of HSO_4^- anion with alcohols is checked through ^{1}H-NMR spectral studies. ^{1}H-NMR spectra of the samples are recorded at 400 MHz by using JEOL, JNM-ECS400 NMR spectrometer. In this analysis, chemical shift (δ) values are reported and D$_2$O (H: δ = 4.69×10^{-6}) and CDCl$_3$ (H: δ = 7.33×10^{-6}) are used as a solvents.

The ^{1}H-NMR spectra of pure [emim][HSO$_4$], ethanol and 1-propanol are shown as Supplementary Information in Figures S1-S3. The ^{1}H-NMR spectra of the equimolar binary mixture of [emim][HSO$_4$] with ethanol and 1-propanol after 12 h of mixing are shown as Supplementary Information in Figures S4 and S5 respectively. The corresponding ^{1}H-NMR chemical shift (δ) values of the pure components and their equimolar binary liquid mixtures are as follows:

^{1}H-NMR ([emim][HSO$_4$]): δ=8.51 (C$_2$-H,1H), δ=7.29-7.22 (C$_{4,5}$-H,2H), δ=4.03 (N-CH$_2$, 2H), δ=3.69 (N-CH$_3$,3H), δ=1.29 (NCH$_2$CH$_3$,3H), and the proton of HSO$_4^-$ is exchanged with D$_2$O; ^{1}H-NMR(ethanol): δ=3.68 (O-CH$_2$-,2H), δ=3.11 (-O-H,1H) and δ=1.22 (CH$_3$-CH$_2$-,3H); ^{1}H-NMR (1-propanol): δ=3.57 (O-CH$_2$-,2H), δ=2.61 (-O-H,1H) , δ=1.57 (CH$_3$-CH$_2$-,2H), and δ=0.92 (CH$_3$-CH$_2$-,3H).^{1}H-NMR([emim][HSO$_4$]+ethanol): δ=8.47 (C$_2$-H,1H), δ=7.26-7.19 (C$_{4,5}$-H,2H), δ=3.98 (N-CH$_2$,2H), δ=3.65 (N-CH$_3$,3H), δ=3.37 (O-CH$_2$-,2H), δ=1.24 (N-CH$_2$-CH$_3$,3H), δ=0.91 (CH$_3$-CH$_2$-,3H), and the protons of -OH and HSO$_4^-$ are exchanged with D$_2$O; ^{1}H-NMR ([emim][HSO$_4$]+1-propanol): δ=8.51 (C$_2$-H,1H), δ=7.27 (C$_{4,5}$-H,2H), δ=4.03 (N-CH$_2$,2H), δ=3.69 (N-CH$_3$,3H), δ=3.35 (O-CH$_2$,2H), δ=1.34-1.28 (N-CH$_2$-CH$_3$,3H and O-CH$_2$-CH$_2$,2H), δ=0.68 (CH$_3$-CH$_2$-,3H), and the protons of -OH and HSO$_4^-$ are exchanged with D$_2$O solvent.

The formation of alkyl sulphate anions by the reaction of HSO_4^- with alcohols may be indicated by the appearance of a new peak for the $-CH_2-OSO_3^-$ protons in ^{1}H-NMR spectra of the equimolar binary mixture of [emim][HSO$_4$] with alcohols. In ^{1}H-NMR spectra of mixtures, no new peak corresponding to $-CH_2-OSO_3^-$ protons of alkyl sulphates are observed, which suggest the absence of formation of alkyl sulphate anions at the investigated temperatures. Moreover, this type of reaction is not reported in the liquid-liquid equilibria studies of ternary systems containing {[emim][HSO$_4$] + ethylacetate + ethanol} carried out at 313.2 K by Naydenov *et al.* [68]. It is also found in the literature that, in the esterification reaction of ethanol and 1-propanol with acetic acid in [emim][HSO$_4$] at temperatures of 60 $^\circ$C and 80 $^\circ$C respectively, alcohol may react with the HSO_4^- anion to produce very small amounts of corresponding alkyl sulphate anions in 24 h of reaction time [69].

3.2. Speed of sound (*u*) and excess isentropic compressibility (κ_s^E)

The speed of sound (*u*) has been claimed to be one of the important experimentally measured thermodynamic properties with good precision at different temperatures. It can be related with isentropic compressibility (κ_s) and excess isentropic compressibility (κ_s^E), which is frequently called for the design and development of several robust industrial processes. The results of the speed of sound (*u*) for {[emim][HSO$_4$] + organic solvents} as a function of composition and temperature are incorporated in Table 4. The variations of *u* against x_1, at 298.15 K $\leq T \leq$ 313.15 K for the three binary solutions are shown in Figures 9-11. The increase in *u* values with an increase in x_1 suggests the increase in compactness of that system. This may be attributed to the geometrical effects which allow the accommodation of organic molecules into [emim][HSO$_4$] network due to the significant variation in their molar volumes. A perusal of *u* data for the above systems reveals that the property decreases with increase in temperature. This may be attributed to the fact that with an increase in temperature, the availability of spaces for the interstitial accommodation of smaller organic solvent molecules into voids created by larger IL molecules increases.

Laplace-Newton's equation [70] is used to compute isentropic compressibility (κ_s) values of (IL + organic solvents) to assess molecular compactness:

$$\kappa_s = \frac{1}{u^2 \rho} \tag{4}$$

The excess isentropic compressibility (κ_s^E) values are derived from the ideal isentropic compressibilities (κ_s^{id}) by using the relation:

$$\kappa_s^E = \kappa_s - \kappa_s^{id} \tag{5}$$

The ideal isentropic compressibility (κ_s^{id}) is calculated through the following relation [71]:

$$\kappa_s^{id} = \sum_{i=1}^{2} \phi_i \left[\kappa_{s,i} + T V_i \left(\alpha_i^2 \right) / C_{p,i} \right] - \left\{ T \left(\sum_{i=1}^{2} x_i V_i \right) \left(\sum_{i=1}^{2} \phi_i \alpha_i \right)^2 / \sum_{i=1}^{2} x_i C_{p,i} \right\} \tag{6}$$

where x_i, V_i, $\kappa_{s,i}$, ϕ_i, α_i and $C_{p,i}$ represents the mole fraction, molar volume, volume fraction, isentropic compressibility, thermal expansivity and molar heat capacity of ith component in the binary mixture respectively. The molar heat capacity ($C_{p,i}$) values for the pure components are obtained from the literature [53,56,58,60] and are presented in Table 2. The isobaric thermal expansivity (α_i) of the investigated liquids at specified temperatures is evaluated from density (ρ)

12

data using eq (5). We obtained the α_i values of the studied liquids from the slope of the linear fitting of $\ln \rho$ versus T ($R^2 > 0.99$) and these values are shown in Table 2.

$$\alpha_i = \left(\frac{1}{V}\right)\left(\frac{\partial V}{\partial T}\right)_P = -\left(\frac{1}{\rho}\right)\left(\frac{\partial \rho}{\partial T}\right)_P = -\left(\frac{\partial \ln \rho}{\partial T}\right)_P \tag{7}$$

Table 4 also includes the experimental κ_s and κ_s^E values of {[emim][HSO$_4$] + organic solvents} over the complete composition at 298.15 K $\leq T \leq$ 313.15 K. The values of κ_s^E as the function of x_1 for the three binary series are plotted in Figures 12-14. The κ_s^E values have the same sign as that of the V^E values. The negative values of κ_s^E for the three binary solutions reveal that their structural order is higher and are less compressible when compared to ideal mixtures due to the stronger intermolecular interaction between the IL and organic solvents [72].

The magnitude of negative κ_s^E for the liquid mixtures follows the order:

[emim][HSO$_4$] + EtOH > [emim][HSO$_4$] + n-PrOH > [emim][HSO$_4$] + DMSO
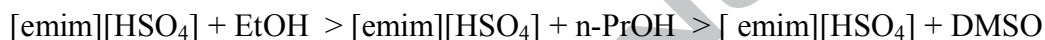
It can be observed that curves of κ_s^E *vs.* x_1 are asymmetric with a minimum in κ_s^E values skewed toward organic solvent-rich compositions, which are common in the binary systems containing component molecules with a large difference in their molar volumes. The negative κ_s^E values for the {[emim][HSO$_4$] + organic solvent} systems results from the contributions from chemical and structural effects of component molecules. The chemical effects include the disruption of self-associated pure liquids on mixing and simultaneous formation of new ion-dipole and H-bonding interactions between [emim][HSO$_4$] and polar organic solvents. This decreases the compressibility and in turn, leads to negative κ_s^E values for these liquid mixtures. The structural effect which involves the favourable geometrical fitting of organic solvents into the structural network of bigger [emim][HSO$_4$] molecules because of the considerable difference in molar volumes (V_m) of [emim][HSO$_4$] (=152.47 cm^3·mol^{-1}), DMSO (=71.33 cm^3·mol^{-1}), EtOH (=58.67 cm^3·mol^{-1}) and n-PrOH (=75.13 cm^3·mol^{-1}) also leads to the negative κ_S^E values. The more negative values of κ_S^E for {[emim][HSO$_4$] + EtOH} than the other two systems are the account of the better packing efficiency between the smaller EtOH molecules and bulkier [emim][HSO$_4$]. The less negative κ_s^E values for {[emim][HSO$_4$] + DMSO} system might be attributed to the fact that the large size of the sulphur atom in DMSO causes less efficient fitting into the interstices of [emim][HSO$_4$] [55].

13

At a fixed composition, the κ_s^E decreases with rise in temperature for all the investigated mixtures due to the decrease in solute-solute and solvent-solvent interactions more with temperature than that of solute-solvent interactions [73]. Moreover, increase in the temperature results in the enlargement of interstices, which in turn increases the packing efficiency between the dissimilar molecules [43, 74].

3.3. Correlation of derived properties

The experimental excess functions (V^E and κ_s^E) of {[emim][HSO$_4$] + organic solvents} at $T = (298.15, 303.15, 308.15,$ and $313.15)$ K are correlated with mole fraction, using the following form of Redlich-Kister polynomial equation [75]:

$$Y^E = x_1(1-x_1)\sum_{i=0}^{n} A_i \left(2x_1 - 1\right)^i \tag{8}$$

where $Y^E = V^E or \kappa_s^{E}$; x_1 is the mole fraction of pure [emim][HSO$_4$].

The values of adjustable parameters A_i of each excess property are evaluated by following the procedure of least-squares. The fitting parameter values together with respective standard deviations $\sigma(Y^E)$ are gathered in Table 5.

The standard deviation $\sigma(Y^E)$ is determined from the equation given below [76]:

$$\sigma\left(Y^E\right) = \left[\frac{\sum\left(Y_{exp}^E - Y_{cal}^E\right)^2}{(m-n)}\right]^{\frac{1}{2}} \tag{9}$$

where m and n represent the number of experimental measurements and adjustable parameters respectively.

The low values of standard deviations obtained at the investigated temperatures for {[emim][HSO$_4$] + organic solvents} systems indicate that the experimental excess properties are consistent.

4. Conclusion:

We report here on the composition and temperature dependence of density (ρ) and speed of sound (u) for the liquid mixtures of 1-ethyl-3-methylimidazolium hydrogen sulphate, [emim][HSO$_4$] with polar protic solvents ethanol (EtOH) and 1-propanol (n-PrOH) and polar aprotic solvent, dimethyl sulphoxide (DMSO) at $T = (298.15, 303.15, 308.15$ and $313.15)$ K.

14

The experimental values of ρ and u increase with the mole fraction of IL (x_1) and decreases with the temperature. From the experimental ρ and u data, excess volumes (V^E) and excess isentropic compressibilities (κ_s^E) are computed for {[emim][HSO$_4$] + organic solvents} systems. The V^E and κ_s^E values are negative at all the investigated temperatures for the systems. We have discussed the thermodynamic behaviour of the mixed solvents in terms of ion-dipole, cross H-bonding interactions and packing effects of component molecules. Moreover, we explained here the effect of temperature on the excess properties. It is deduced that the non-ideality of the investigated liquid mixtures increases with temperature.

Acknowledgement

References

1. D. Keshapolla, R.L. Gardas, Fluid Phase Equilib. 383 (2014) 32–42.

2. V. Govindaa, P. Venkatesua, I. Bahadur, Phys. Chem. Chem. Phys. 18 (2016) 8278-8326.

3. S.Y. Lee, A. Ogawa, M. Kanno, H. Nakamoto, T. Yasuda, M. Watanabe, J. Am. Chem. Soc. 132 (2010) 9764–9773.

4. S. Saha, H. Hamaguchi, J. Phys. Chem. B. 110 (2006) 2777–2781.

5. H.O. Bourbigou, L. Magna, D. Morvan, Appl. Catal. A 373 (2010) 1–56.

6. Marciniak, Fluid Phase Equilib. 294 (2010) 213–233.

7. W.H. Awad, J.W. Gilman, M. Nyden, R.H. Harris, Jr., T.E. Sutto, J. Callahan, P.C. Trulove, H.C. De Long, D.M. Fox, Thermochim. Acta 409 (2004) 3–11.

8. S. Seki, Y. Ohno, Y. Kobayashi, H. Miyashiro, A. Usami, Y. Mita, H. Tokuda, M. Watanabe, K. Hayamizu, S. Tsuzuki, M. Hattori, N. Terada, J. Electrochem. Soc. 154 (2007) A173–A177.

9. M. Ue, M. Takeda, T. Takahashi, M. Takehara, Electrochem. Solid State Lett. 5 (2002) A119–A121.

10. A. Noda, M.A.B.H. Susan, K. Kudo, S. Mitsushima, K. Hayamizu, M. Watanabe, J. Phys. Chem. B 107 (2003) 4024–4033.

11. D. Kuang, P. Wang, S. Ito, S.M. Zakeeruddin, M. Gratzel, J. Am. Chem. Soc. 128 (2006) 7732-7733.

12. T.L. Greaves, C.J. Drummond, Chem. Rev. 115 (2015) 11379-11448.

13. C. Jork, M. Seiler, Y.A. Beste, W. Arlt, J. Chem. Eng. Data 49 (2004) 852–857.

14. D.W. Armstrong, L.K. Zhang, L. He, M.L. Gross, Anal. Chem. 73 (2001) 3679–3686.

15. B. Wu, R.G. Reddy, R.D. Rogers, Proceedings of Solar Forum, 2001

16. J.D. Holbrey, K.R. Seddon, J. Chem. Soc. Dalton Trans. 13 (1999) 2133–2139.

17. H. Wang, Q. Lu, C. Ye, W. Liu, Z. Cui, Wear 256 (2004) 44–48.

18. S.A. Forsyth, J.M. Pringle, D.R. MacFarlane, Aust. J. Chem. 57 (2004) 113–119.

19. S. Hina, X. Zhu, Y. Chen, Y. Zhang, Chin. J. Chem. Eng. 23 (2015) 804-811.

20. M. Letcher, G.G. Redhi, Fluid Phase Equilib. 198 (1999) 257–266.

21. P. Bhanuprakash, N.V.V. Jyothi, C. Narasimharao, M. Raveendra, K. Sivakumar, J. Mol. Liq. 234 (2017) 49–63.

22. R.L. Gardas, M.G. Freire, P.J. Carvalho, I.M. Marrucho, I.M.A. Fonseca, A.G.M. Ferreira, J.A.P. Coutinho, J. Chem. Eng. Data 52 (2007) 80-88.

23. S. Parveen, S. Singh, D. Shukla, M. Yasmin, M. Gupta, J.P. Shukla, J. Solution Chem. 41 (2012) 156–172.

24. X. Nie, X. Liu, C. Song, X. Guo, J. Mol. Catal. A, 332 (2010) 145–151.

25. J.D. Holbrey, W.M. Reichert, R.P. Swatloski, G.A. Broker, W.R. Pitner, K.R. Seddon, R.D. Rogers, Green Chem. 4 (2002) 407–413.

26. S. Liu, C. Xie, S. Yu, M. Xian, F. Liu, Chin. J. Catal. 30 (2009) 401–406.

27. J. Safari, Z.N. Zarnegar, J. Chem. 38 (2014) 358–365.

28. J.A. Riddick, W.B. Bunger, T.K. Sakano, Organic Solvents, 4th ed., Wiley-Interscience, New York, 1986.

29. M.J.W. Povey, S.A. Hindle, J.D. Kennedy, Z. Stec, R.G. Taylor, Phys. Chem. Chem. Phys. 5 (2003) 73–78.

30. M.M. Palaiologou, G.K. Arianas, N.G. Tsierkezos, J. Solution Chem. 35 (2006) 1551–1565.

31. V. Govinda, P. Attri, P. Venkatesu, P. Venkateswarlu, J. Phys. Chem. B 117 (2013) 12535−12548.

32. B. Garcia, R. Alcalde, S. Aparicio, J.M. Leal, Phys. Chem. Chem. Phys. 4 (2002) 1170−1177.

33. G.P. Dubey, M. Sharma, S. Oswal, J. Chem. Thermodyn. 41 (2009) 849−858.

34. P. Venkatesu, Fluid Phase Equilib. 298 (2010) 173–191

35. A. Ali, N. Anilkumar, S. Vinodkumar, S. Ahmad, Acoust. Lett. 24 (2000) 9–16.

36. H. Funke, M. Wetzel, A. Heintz, Pure Appl. Chem. 61 (1989) 1429-1439.

37. K. Sreenivasulu, R.L. Gardas, P. Venkateswarlu, K. Sivakumar, J. Chem. Thermodyn. 67 (2013) 203–209.

38. C.D. Edas, J. Phys. Chem. B 104 (2000) 6653–6661.

39. A. Ali, S. Hyder, M. Tariq, Int. J. Thermophys. 26 (2005) 1537–1548.

40. E. Gomez, B. Gonzalez, N. Calvar, E. Tojo, A. Dominguez, J. Chem. Eng. Data 51 (2006) 2096–2102.

41. E.J. González, B. González, N. Calvar, A. Domínguez, J. Chem. Eng. Data 52 (2007) 1641–1648.

42. U. Domanska, M. Laskowska, J. Solution Chem. 37 (2008) 1271–1287.

43. J. Lehmann, M.H. Rausch, A. Leipertz, A.P. Fröba, J. Chem. Eng. Data. 55 (2010) 4068–4074.

44. S. Singh, I. Bahadur, G.G. Redhi, E.E. Ebenso, D. Ramjugernath, J. Mol. Liq. 199 (2014) 518–523.

45. M. Srinivasa Reddy, K. Thomas, S.S. Raju, A. Srinivasa Rao, N. Sharmila, B. Hari Babu J. Chem. Thermodyn.101 (2016) 139-149.

46. G. García-Miaja, J. Troncoso, L. Romaní, J. Chem. Thermodynamics 41 (2009) 334–341.

47. P.F. Requejo, E.J. Gonzalez, E.A. Macedo, A. Dominguez, J. Chem. Thermodyn. 74 (2014) 193–200.

48. J.Y. Wang, F.Y. Zhao, Y.M. Liu, X.L. Wang, Y.Q. Hu, Fluid Phase Equilib. 305 (2011) 114–120.

49. P. Bhanuprakash, C. Narasimha Rao, K. Sivakumar, J. Mol. Liq. 219 (2016) 79–87.

50. M.A. Iglesias-Otero, J. Troncoso, E. Carballo, L. Romani, J. Chem. Eng. Data 53 (2008) 1298–1301.

51. O. Redlich, A.T. Kister, Ind. Eng. Chem. 40 (1948) 345–348.

52. A.J.L. Costa, J.M.S.S. Esperanc, I.M. Marrucho, L.P.N. Rebelo, J. Chem. Eng. Data 56 (2011) 3433–3441.

53. L.E. Ficke, R.R. Novak, J.F. Brennecke, J. Chem. Eng. Data 55 (2010) 4946–4950.

54. S. Seki, S. Tsuzuki, K. Hayamizu, Y. Umebayashi, N. Serizawa, K. Takei, H. Miyashiro, J. Chem. Eng. Data 57 (2012) 2211−2216.

55. S. Bhagour, S. Solanki, N. Hooda, D. Sharma, V.K. Sharma, J. Chem. Thermodyn. 60 (2013) 76–86.

56. F. Comelli, R. Francesconi, A. Bigi, K. Rubini, J. Chem. Eng. Data 52 (2007) 639-644.

57. L. Zhang, X. Lu, D. Ye, Y. Guo, W. Fang, J. Chem. Eng. Data, 61 (2016) 1023–1031.

58. G. Garcia-Miaja, J. Troncoso, L. Romani, Fluid Phase Equilib. 274 (2008) 59–67.

59. E. Vercher, A.V. Orchilles, P.J. Miguel, A. Martinez-Andreu, J. Chem. Eng. Data 52 (2007) 1468–1482.

60. S. Singh, M. Aznar, N. Deenadayalu, J. Chem. Thermodyn. 57 (2013) 238–247.

61. S. Mrad, M. Hichri, I. Khattech, C. Lafuente, J. Mol. Liq. 231 (2017) 168–173.

62. L. Venkatramana, K. Sivakumar, R.L. Gardas, K. Dayananda Reddy, Thermochim. Acta 581 (2014) 123–132.

63. I. Bahadur, T.M. Letcher, S. Singh, G.G. Redhi, P. Venkatesu, D. Ramjugernath, J. Chem. Thermodyn. 82 (2015) 34–46.

64. P.A. Hunt, I.R. Gould, B. Kirchner, Aust. J. Chem. 60 (2007) 9-14.

65. A. Bhattacharjee, C. Varanda, M.G. Freire, S. Matted, L.M.N.B.F. Santos, I.M. Marrucho, J.A.P. Coutinho, J. Chem. Eng. Data 57 (2012) 3473–3482.

66. E.J. Gonzalez, P.F. Requejo, A. Dominguez, E.A. Macedo, J. Solution Chem. 42 (2013) 746–763.

67. L.P.N. Rebelo, V. Najdanovic-Visak, Z.P. Visak, M. Nunes da Ponte, J. Szydlowski, C.A. Cerdeiriña, J. Troncoso, L. Romani, J.M.S.S. Esperanca, Guedes, M.C. Sousa, Green Chem. 6 (2004) 369–381.

68. D. Naydenov, H.J. Bart, J. Chem. Eng. Data 52 (2007) 2375-2381.

69. D. Naydenova, H. Hasseb, G. Maurerb, H.J. Bart, Open Chem. Eng. J. 3 (2009) 17-26.

70. G. Douhheret, M.I. Davis, J.C.R. Reis, M.J. Blandamer, Chem. Phys. Chem. 2 (2001) 148–161.

71. G.C. Benson, O. Kiyohara, J. Chem. Thermodyn. 11 (1979) 1061–1064.

72. M.T.Z. Moattar, H. Shekaari, J. Chem. Eng. Data 50 (2005) 1694–1699.

73. Y. Zhong, H. Wang, K. Diao, J. Chem. Thermodyn. 39 (2007) 291–296.

74. S. Singh, I. Bahadur, G.G. Redhi, D. Ramjugernath, E.E. Ebenso, J. Mol. Liq. 200 (2014) 160–167.

75. O. Redlich, A.T. Kister, Ind. Eng. Chem. 40 (1948) 345–348.

76. M. Behroozi, H. Zarei, J. Chem. Thermodyn. 47 (2012) 276−287.

Figure captions

Figure 1 (a) Self association and resonance structure of DMSO (b) self-association of 1-alkanols and (c) chemical structure of 1-ethyl-3-methylimidazolium hydrogen sulphate.

Figure 2 Densities (ρ) of the {[emim][HSO$_4$] (1) + DMSO (2)} system against mole fraction (x_1) at T = 298.15 K (■), 303.15 K (●), 308.15 K (▲) and 313.15 K (▼).

Figure 3 Densities (ρ) of the {[emim][HSO$_4$] (1) + EtOH (2)} system against mole fraction (x_1) at T = 298.15 K (■), 303.15 K (●), 308.15 K (▲) and 313.15 K (▼).

Figure 4 Densities (ρ) of the {[emim][HSO$_4$] (1) + n-PrOH (2)} system against mole fraction (x_1) at T = 298.15 K (■), 303.15 K (●), 308.15 K (▲) and 313.15 K (▼).

Figure 5 Excess volumes (V^E) against mole fraction (x_1) for liquid mixtures of {[emim][HSO$_4$] (1) + DMSO (2)} at T = 298.15 K (■), 303.15 K (●), 308.15 K (▲) and 313.15 K (▼).

Figure 6 Excess volumes (V^E) against mole fraction (x_1) for liquid mixtures of {[emim][HSO$_4$] (1) + EtOH (2)} at T = 298.15 K (■), 303.15 K (●), 308.15 K (▲) and 313.15 K (▼).

Figure 7 Excess volumes (V^E) against mole fraction (x_1) for liquid mixtures of {[emim][HSO$_4$] (1) + n-PrOH (2)} at T = 298.15 K (■), 303.15 K (●), 308.15 K (▲) and 313.15 K (▼).

Figure 8 Ion-dipole and cross hydrogen bonding interactions between [emim][HSO$_4$] and DMSO or 1-alkanols in the binary mixtures.

Figure 9 Speeds of sound (u) of the {[emim][HSO$_4$] (1) + DMSO (2)} system against mole fraction at T = 298.15 K (■), 303.15 K (●), 308.15 K (▲) and 313.15 K (▼).

Figure 10 Speeds of sound (u) of the {[emim][HSO$_4$] (1) + EtOH (2)} system against mole fraction at T = 298.15 K (■), 303.15 K (●), 308.15 K (▲) and 313.15 K (▼).

Figure 11 Speeds of sound (u) of the {[emim][HSO$_4$] (1) + n-PrOH (2)} system against mole fraction at T = 298.15 K (■), 303.15 K (●), 308.15 K (▲) and 313.15 K (▼).

Figure 12 Plot of excess isentropic compressibilities (κ_s^E) *vs.* mole fraction (x_1) for binary systems of {[emim][HSO4] (1) + DMSO (2)} at T = 298.15 K (■), 303.15 K (●), 308.15 K (▲) and 313.15 K (▼).
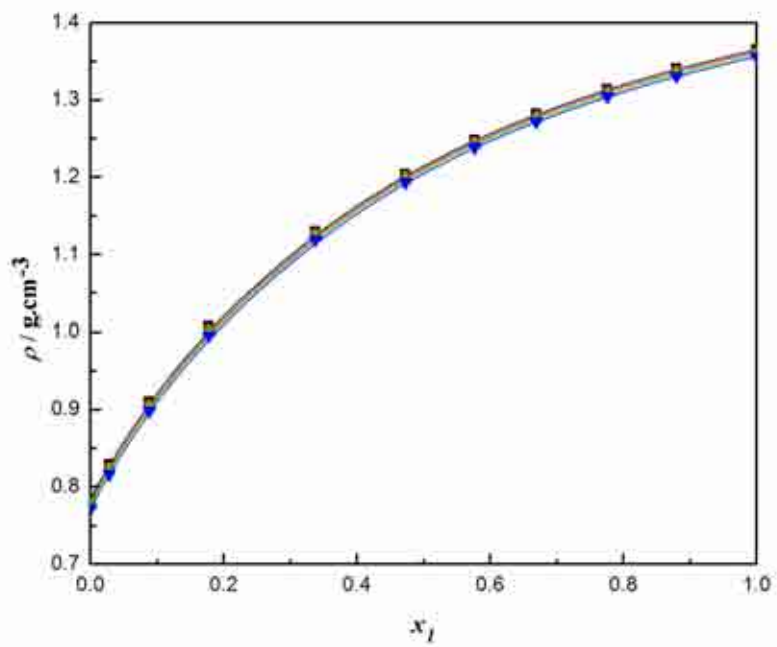
Figure 13 Plot of excess isentropic compressibilities (κ_s^E) *vs.* mole fraction (x_1) for binary systems of {[emim][HSO4] (1) + EtOH (2)} at T = 298.15 K (■), 303.15 K (●), 308.15 K (▲) and 313.15 K (▼).

Figure 14 Plot of excess isentropic compressibilities (κ_s^E) *vs.* mole fraction (x_1) for binary systems of {[emim][HSO4] (1) + n-PrOH (2)} at T = 298.15 K (■), 303.15 K (●), 308.15 K (▲) and 313.15 K (▼).
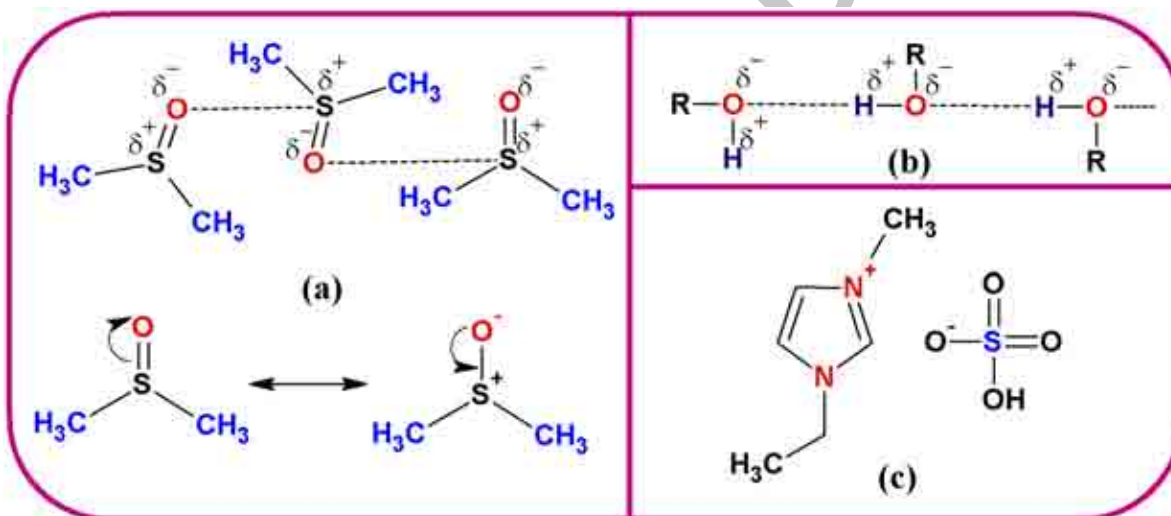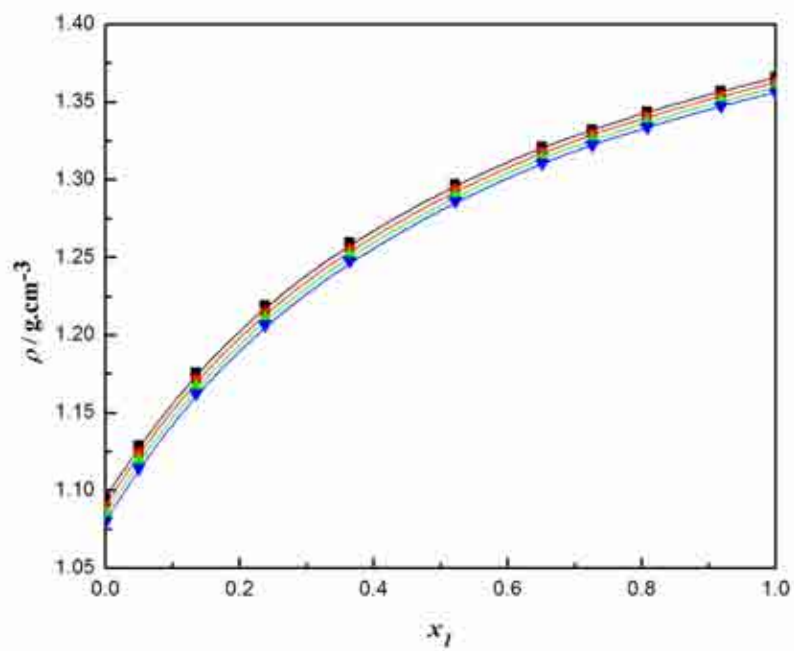
Figure 1

Figure 2

Figure 3
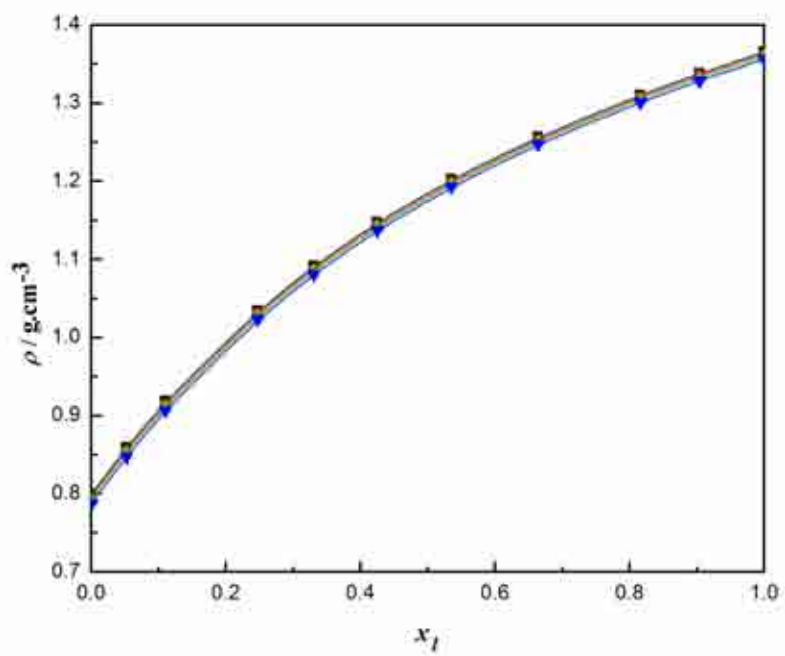
Figure 4
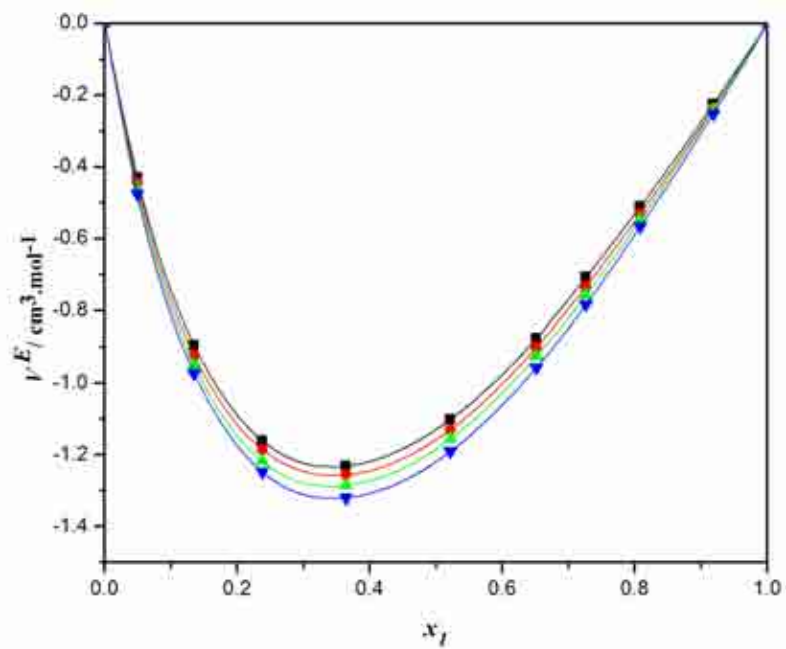
Figure 5
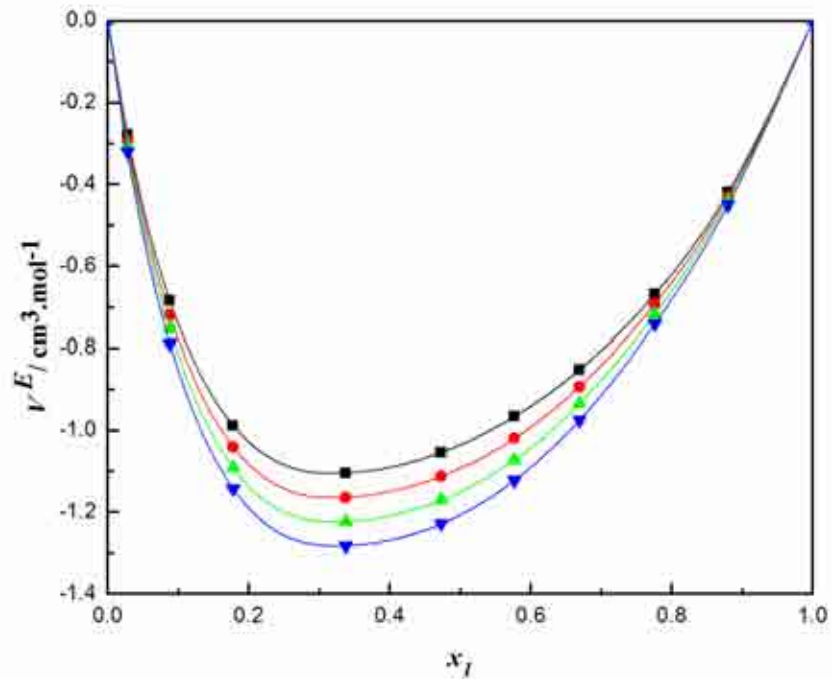
Figure 6
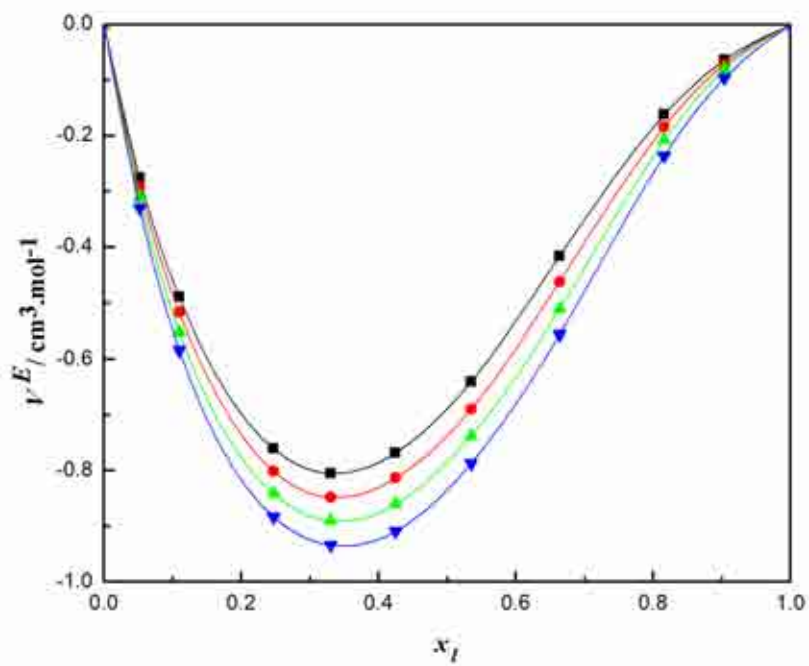
Figure 7
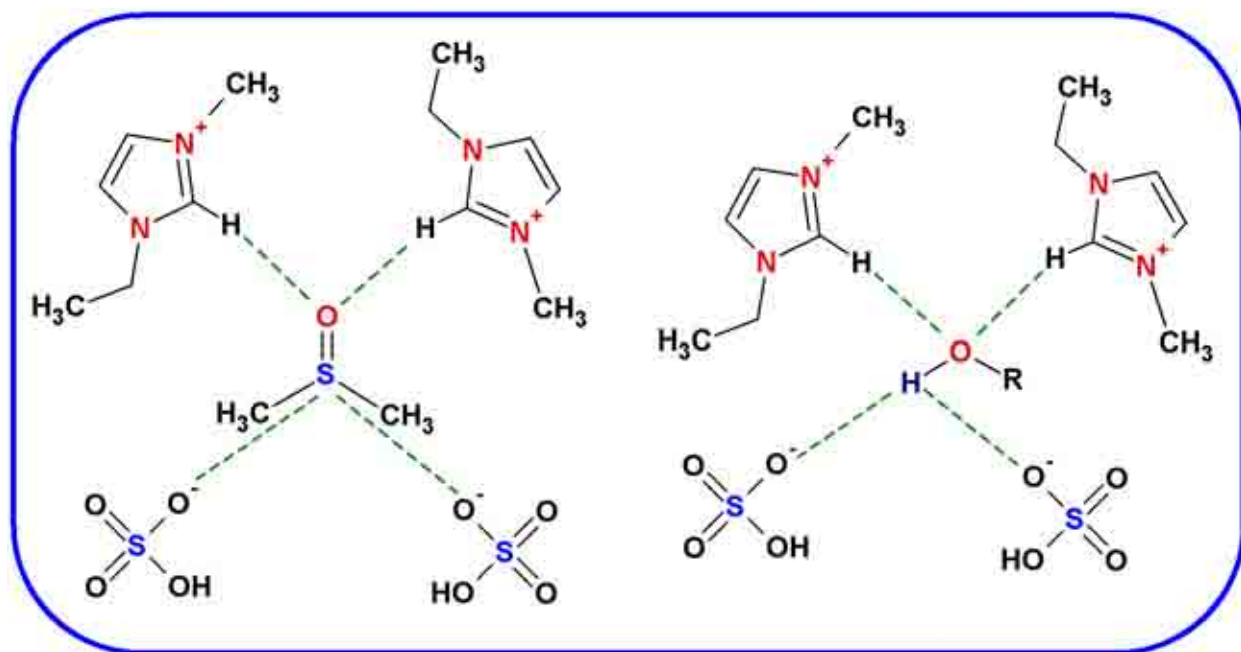
Figure 8
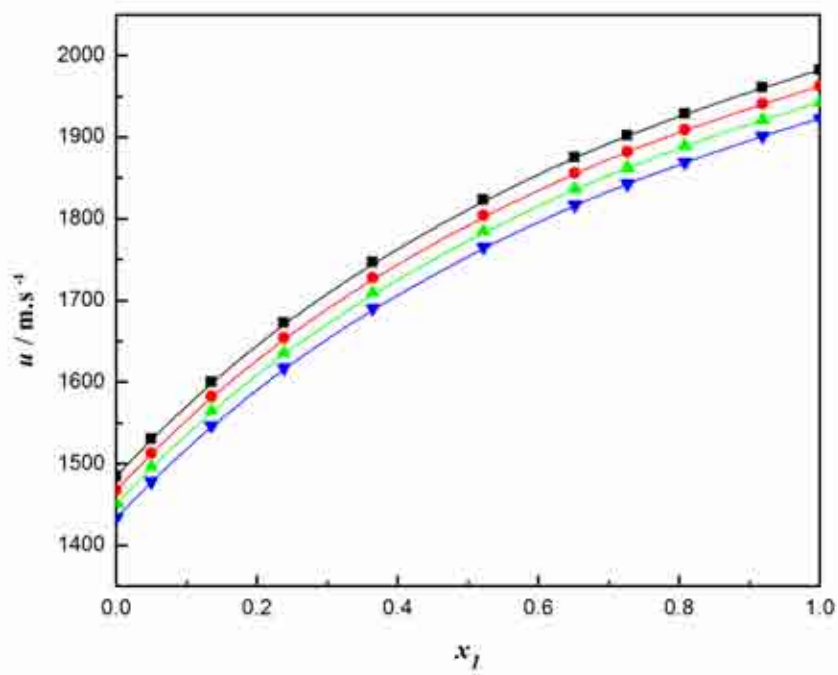
Figure 9
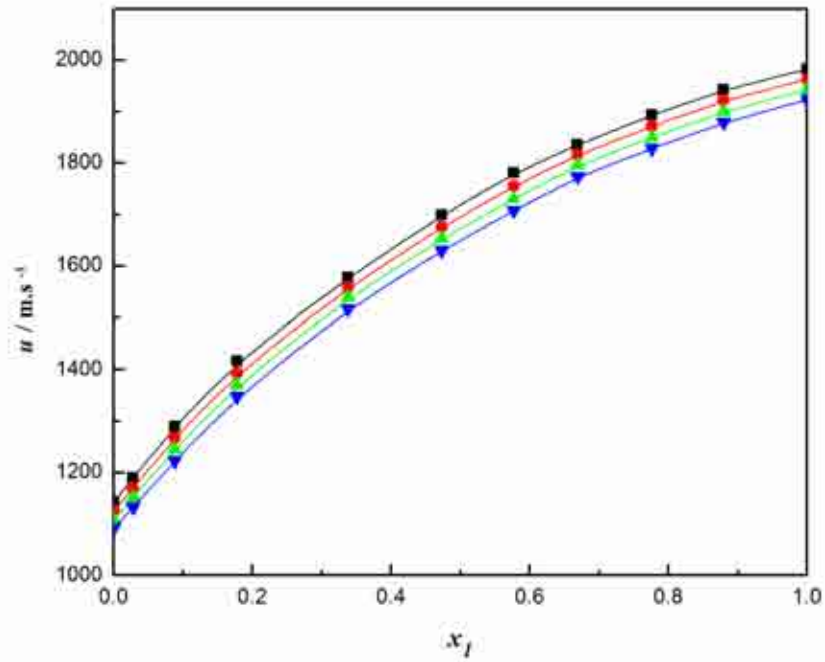
Figure 10
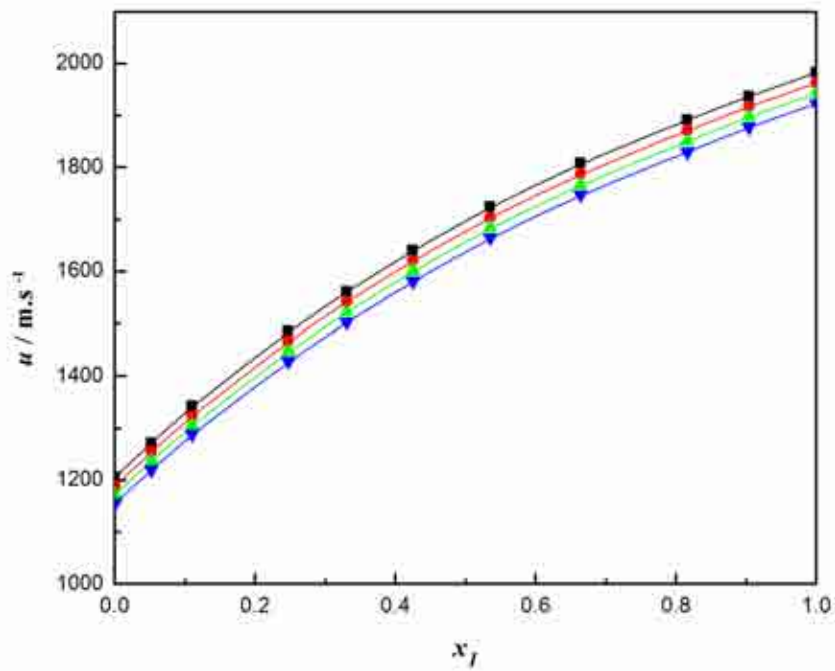
Figure 11
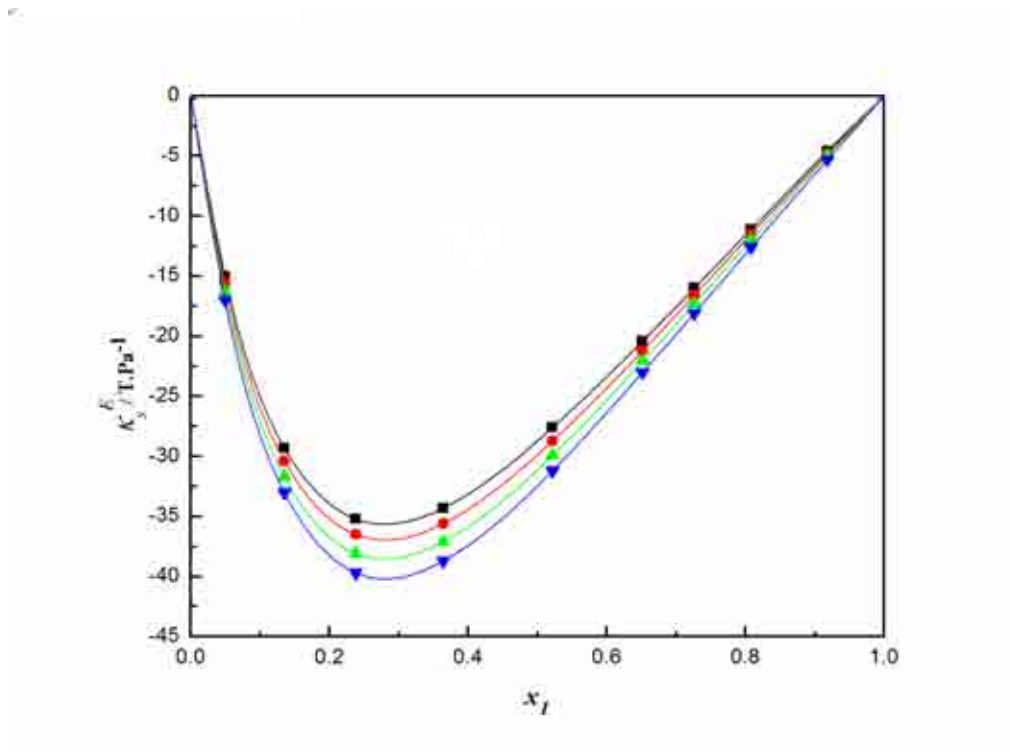
Figure 12
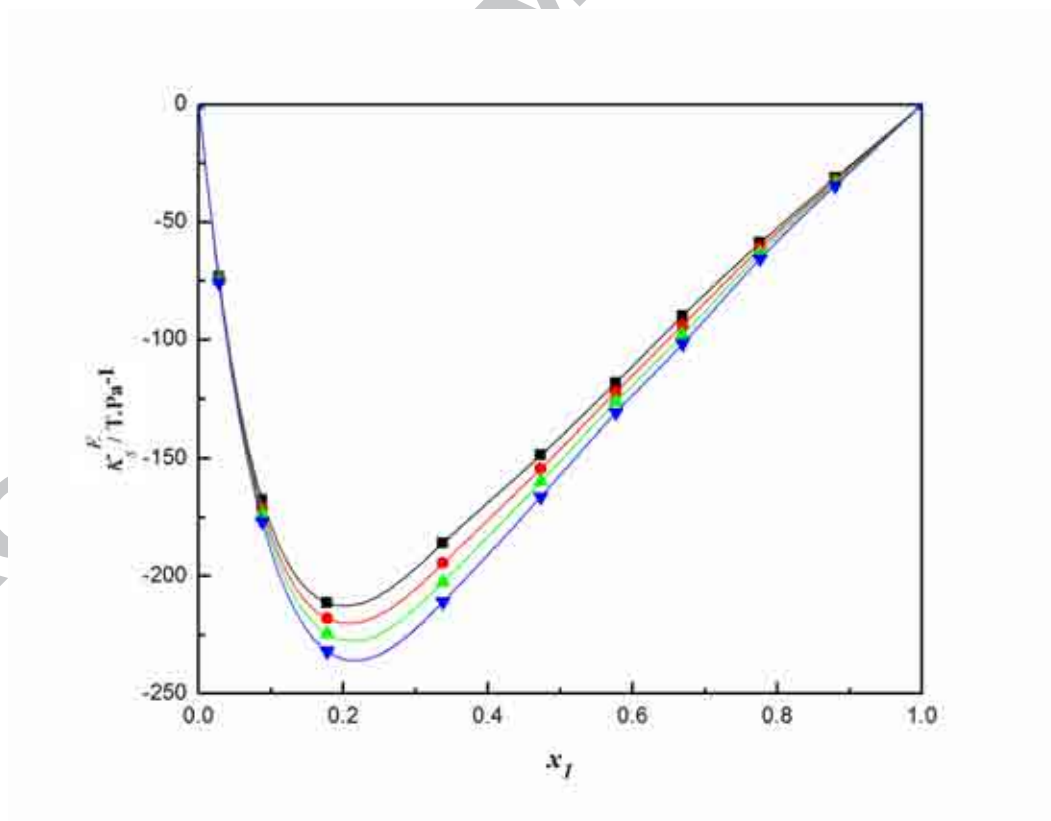
Figure 13
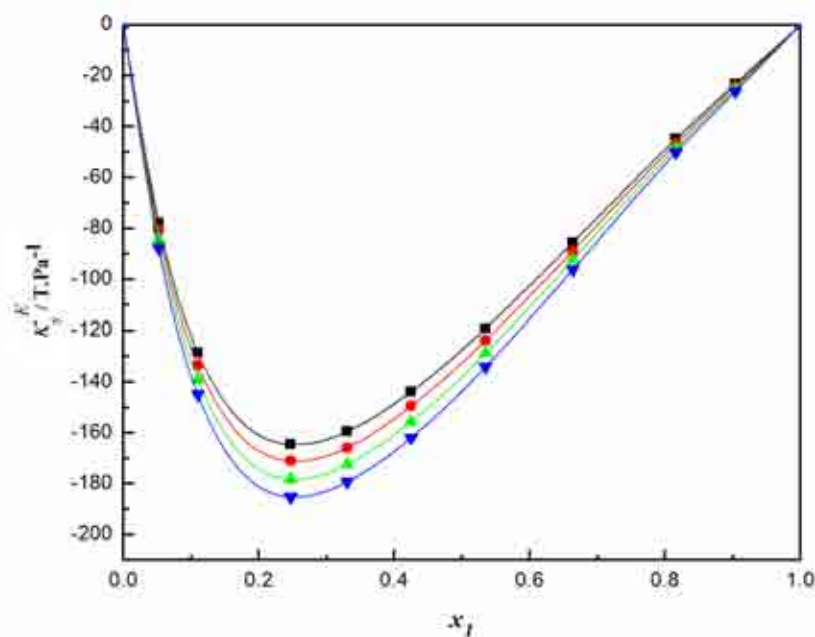
Figure 14

Table 1
Chemical name, acronym, CAS number, molar mass, source, purification method, mass fraction purity and water content of the pure liquids used in the present study.

Name of the chemical	Acronym	CAS Number	Molar mass / g·mol^{-1}	Source	Purification method	Mass fraction purity	Water content by KF /(%)
1-Ethyl-3-methylimidazolium hydrogen sulphate	[emim][HSO$_4$]	412009-61-1	208.24	Alfa Aesar, UK	Vacuum drying	0.980[a*]	0.05
Dimethyl sulphoxide	DMSO	67-68-5	78.13	Merck, India	None	0.999[b*]	0.05[*]
Ethanol	EtOH	64-17-5	46.07	Merck, India	None	0.999[b*]	0.01[*]
1-Propanol	n-PrOH	71-23-8	60.10	Sigma-Aldrich, India	None	0.997[b*]	0.05[*]

[a]Ion Chromatography analysis by supplier , [b]Gas Chromatography analysis by supplier, *Specified by supplier

Table 2

Comparison of experimental and literature values of density (ρ) and speed of sound (u) of the pure liquids along with their molar heat capacity (C_p) and thermal expansivity (α) values at 298.15 K $\leq T \leq$ 313.15 K and 0.1MPa pressure.

Pure compound	T/ K	ρ/g·cm^{-3}		u /m·s^{-1}		C_P/J·K^{-1}·mol^{-1}	α*/k·K^{-1}
		Exp.	Lit	Exp.	Lit		
[emim][HSO$_4$]	298.15	1.36575	1.36577[a] 1.36579[b] 1.3674[c]	1982.8	-	295.5[l]	0.4554
	303.15	1.36262	1.36267[a] 1.36263[b] 1.3643[c]	1962.9	-	297.0[b]	0.4565
	308.15	1.35953	1.35959[a] 1.3611[c]	1943.1	-	299.4[l]	0.4575
	313.15	1.35641	1.35690[a] 1.35627[b] 1.3578[c]	1923.2	-	302.0[b]	0.4586
Dimethyl sulphoxide	298.15	1.09533	1.095387[d] 1.09542[e]	1485.0	1485.97[d] 1486.26[e]	151.5[f]	0.9130
	303.15	1.09032	1.090367[d] 1.09040[e]	1468.3	1468.15[d] 1469.20[e]	152.2[f]	0.9172
	308.15	1.08531	1.085348[d] 1.08539[e]	1451.1	1451.28[d] 1452.66[e]	152.9[f]	0.9214
	313.15	1.08029	1.080327[d]	1434.2	1434.50[d]	153.7[f]	0.9257
Ethanol	298.15	0.78526	0.78528[g] 0.7853[h] 0.78510[i]	1142.7	1142.5[h] 1142.8[i]	113.3[h]	1.1018
	303.15	0.78098	0.78096[g] 0.7810[h]	1125.3	1125.5[h]	115.3[h]	1.1078
	308.15	0.77666	0.77661[g] 0.7767[h] 0.77644[i]	1108.8	1108.6[h] 1109.1[i]	117.5[h]	1.1140
	313.15	0.77228	0.77223[g] 0.7723[h]	1091.5	1091.8[h]	119.7[h]	1.1203
1-Propanol	298.15	0.79996	0.80001[j] 0.79977[k] 0.79956[i]	1206.1	1205.93[j] 1206.17[k] 1205.37[i]	144.47[j]	1.0198
	303.15	0.79592	0.79597[j]	1189.1	1189.26[j]	147.80[j]	1.0250
	308.15	0.79182	0.79189[j]	1172.2	1172.37[j]	150.05[j]	1.0303

		0.79146[i]			1171.41[i]		
313.15	0.78773	0.78777[j]	1155.4	1155.53[j]	153.58[j]	1.0356
		0.78754[k]			1155.36[k]		

Standard uncertainties are $u(\rho) = 1\times10^{-3}$ g·cm^{-3}, $u(u)= 0.5$ m·s^{-1}, $u(\alpha)=0.002$ k·K^{-1}, $u(T) = 0.02$ K and $u(P) = 1$ kPa

[a] Reference [52]
[b] Reference [53]
[c] Reference [54]
[d] Reference [1]
[e] Reference [55]
[f] Reference [56]
[g] Reference [57]
[h] Reference [58]
[i] Reference [59]
[j] Reference [60]
[k] Reference [61]
[l] Estimated using group contribution additivity.
*Derived from our measured densities.

Table 3

Mole fraction of [emim][HSO$_4$] (x_1), densities (ρ/g.cm^{-3}) and excess volumes (V^E/cm^3.mol^{-1}) for the binary liquid mixtures of [emim][HSO$_4$] with DMSO, EtOH and n-PrOH at 298.15 K ≤ T ≤ 313.15 K and 0.1MPa pressure.

x_1	ρ/g·cm^{-3}				V^E/cm^3·mol^{-1}			
	T/K=298.15	303.15	308.15	313.15	T/K=298.15	303.15	308.15	313.15
[emim][HSO$_4$] (1) + DMSO (2)								
0.0000	1.09533	1.09032	1.08531	1.08029	0.000	0.000	0.000	0.000
0.0494	1.12882	1.12411	1.11940	1.11468	-0.430	-0.445	-0.461	-0.476
0.1349	1.17573	1.17137	1.16699	1.16254	-0.895	-0.923	-0.950	-0.973
0.2377	1.21912	1.21491	1.21085	1.20672	-1.161	-1.185	-1.218	-1.248
0.3638	1.25943	1.25551	1.25166	1.24785	-1.231	-1.256	-1.285	-1.320
0.5219	1.29719	1.29361	1.29003	1.28651	-1.101	-1.129	-1.155	-1.190
0.6517	1.32097	1.31758	1.31421	1.31090	-0.875	-0.900	-0.925	-0.957
0.7261	1.33242	1.32914	1.32590	1.32264	-0.707	-0.732	-0.757	-0.783
0.8081	1.34371	1.34051	1.33732	1.33410	-0.510	-0.530	-0.548	-0.566
0.9182	1.35703	1.35389	1.35073	1.34761	-0.225	-0.236	-0.240	-0.252
1.0000	1.36575	1.36262	1.35953	1.35641	0.000	0.000	0.000	0.000
[emim][HSO$_4$] (1) + EtOH (2)								
0.0000	0.78526	0.78098	0.77666	0.77228	0.000	0.000	0.000	0.000
0.0281	0.82967	0.82550	0.82128	0.81700	-0.279	-0.293	-0.306	-0.320
0.0878	0.91066	0.90670	0.90270	0.89863	-0.684	-0.719	-0.753	-0.788
0.1779	1.00745	1.00374	0.99998	0.99614	-0.988	-1.040	-1.091	-1.142
0.3378	1.12995	1.12652	1.12306	1.11954	-1.104	-1.164	-1.223	-1.282
0.4731	1.20392	1.20065	1.19738	1.19405	-1.054	-1.112	-1.170	-1.228

0.5770	1.24874	1.24556	1.24238	1.23913	-0.966	-1.019	-1.072	-1.122
0.6689	1.28187	1.27869	1.27552	1.27231	-0.852	-0.893	-0.934	-0.975
0.7759	1.31438	1.31118	1.30800	1.30478	-0.668	-0.692	-0.717	-0.741
0.8797	1.34071	1.33751	1.33434	1.33114	-0.420	-0.430	-0.440	-0.450
1.0000	1.36575	1.36262	1.35953	1.35641	0.000	0.000	0.000	0.000
[emim][HSO$_4$] (1) + n-PrOH (2)								
0.0000	0.79996	0.79592	0.79182	0.78773	0.000	0.000	0.000	0.000
0.0519	0.85954	0.85559	0.85162	0.84765	-0.276	-0.292	-0.311	-0.330
0.1097	0.91850	0.91464	0.91080	0.90693	-0.490	-0.517	-0.552	-0.584
0.2473	1.03463	1.03095	1.02723	1.02351	-0.761	-0.801	-0.841	-0.883
0.3301	1.09159	1.08801	1.08439	1.08078	-0.805	-0.848	-0.890	-0.934
0.4250	1.14759	1.14415	1.14069	1.13724	-0.768	-0.813	-0.860	-0.909
0.5348	1.20262	1.19935	1.19607	1.19277	-0.640	-0.689	-0.738	-0.787
0.6634	1.25673	1.25360	1.25050	1.24733	-0.416	-0.462	-0.511	-0.556
0.8160	1.31071	1.30754	1.30442	1.30131	-0.162	-0.184	-0.208	-0.236
0.9035	1.33805	1.33487	1.33173	1.32862	-0.064	-0.072	-0.081	-0.096
1.0000	1.36575	1.36262	1.35953	1.35641	0.000	0.000	0.000	0.000

The standard uncertainties are $u(x) = 6 \times 10^{-3}$, $u(\rho) = 1 \times 10^{-3}$ g·cm^{-3}, $u(T) = 0.02$K, $u(P) = 1$ kPa and the combined expanded uncertainties Uc are Uc(V^E) = 0.005 cm^3·mol^{-1} (0.95 level of confidence).

Table 4
Speeds of sound (u), isentropic compressibilities (κ_S) and excess isentropic compressibilities (κ_S^E) for the binary mixtures of [emim][HSO$_4$] with DMSO, EtOH and n-PrOH as a function of mole fraction of [emim][HSO$_4$] (x_1), at T = (298.15 to 313.15)K and 0.1MPa pressure.

x_1	u /m·s^{-1}	κ_S/TPa^{-1}	κ_s^E/TPa^{-1}	x_1	u/m·s^{-1}	κ_S/TPa^{-1}	κ_s^E/TPa^{-1}
[emim][HSO$_4$] (1) + DMSO (2)							
T/K=298.15				T/K=308.15			
0.0000	1485.0	414.0	0.0	0.0000	1451.1	437.6	0.0
0.0494	1530.5	378.2	-15.0	0.0494	1495.9	399.2	-16.3
0.1349	1600.5	332.0	-29.3	0.1349	1564.8	350.0	-31.7
0.2377	1672.7	293.2	-35.2	0.2377	1635.9	308.6	-38.1
0.3638	1746.9	260.2	-34.3	0.3638	1709.3	273.5	-37.1
0.5219	1823.3	231.9	-27.6	0.5219	1784.9	243.3	-29.9
0.6517	1875.5	215.2	-20.4	0.6517	1836.6	225.6	-22.1
0.7261	1902.0	207.5	-16.0	0.7261	1862.8	217.3	-17.3
0.8081	1928.7	200.1	-11.1	0.8081	1889.3	209.5	-12.0
0.9182	1961.0	191.6	-4.6	0.9182	1921.5	200.5	-5.0
1.0000	1982.8	186.2	0.0	1.0000	1943.1	194.8	0.0
T/K=303.15				T/K=313.15			
0.0000	1468.3	425.4	0.0	0.0000	1434.2	450.0	0.0

30

0.0494	1513.4	388.4	-15.6	0.0494	1478.6	410.4	-17.0
0.1349	1582.9	340.7	-30.4	0.1349	1547.0	359.4	-33.0
0.2377	1654.4	300.7	-36.5	0.2377	1617.6	316.7	-39.7
0.3638	1728.2	266.7	-35.6	0.3638	1690.5	280.4	-38.7
0.5219	1804.2	237.5	-28.7	0.5219	1765.7	249.3	-31.2
0.6517	1856.1	220.3	-21.2	0.6517	1817.1	231.0	-23.0
0.7261	1882.4	212.3	-16.6	0.7261	1843.2	222.5	-18.1
0.8081	1909.0	204.7	-11.5	0.8081	1869.6	214.4	-12.6
0.9182	1941.2	196.0	-4.8	0.9182	1901.6	205.2	-5.3
1.0000	1962.9	190.5	0.0	1.0000	1923.2	199.3	0.0

[emim][HSO$_4$] (1) + EtOH (2)

		T/K=298.15				T/K=308.15	
0.0000	1142.7	975.3	0.0	0.0000	1108.8	1047.3	0.0
0.0281	1190.1	851.0	-73.3	0.0281	1152.1	917.3	-74.8
0.0878	1289.8	660.1	-167.8	0.0878	1245.3	714.3	-173.7
0.1779	1416.2	494.9	-211.3	0.1779	1370.9	532.1	-224.6
0.3378	1577.8	355.5	-185.9	0.3378	1538.6	376.1	-202.6
0.4731	1698.6	287.9	-148.7	0.4731	1653.0	305.6	-159.9
0.5770	1780.2	252.7	-118.3	0.5770	1731.4	268.5	-126.1
0.6689	1836.4	231.3	-89.9	0.6689	1796.0	243.1	-97.8
0.7759	1893.6	212.2	-58.8	0.7759	1850.2	223.3	-63.2
0.8797	1943.4	197.5	-31.3	0.8797	1900.8	207.4	-33.4
1.0000	1982.8	186.2	0.0	1.0000	1943.1	194.8	0.0
		T/K=303.15				T/K=313.15	
0.0000	1125.3	1011.2	0.0	0.0000	1091.5	1086.9	0.0
0.0281	1170.6	884.0	-74.1	0.0281	1132.9	953.7	-75.8
0.0878	1267.3	686.7	-171.1	0.0878	1222.8	744.2	-176.9
0.1779	1393.3	513.2	-218.1	0.1779	1348.0	552.5	-232.0
0.3378	1558.4	365.5	-194.5	0.3378	1516.6	388.3	-210.9
0.4731	1675.8	296.6	-154.3	0.4731	1630.3	315.1	-166.3
0.5770	1755.7	260.5	-122.2	0.5770	1707.9	276.7	-130.8
0.6689	1816.2	237.1	-93.8	0.6689	1773.8	249.8	-101.7
0.7759	1871.9	217.7	-61.0	0.7759	1828.5	229.2	-65.6
0.8797	1922.1	202.4	-32.4	0.8797	1879.5	212.7	-34.6
1.0000	1962.9	190.5	0.0	1.0000	1923.2	199.3	0.0

[emim][HSO$_4$] (1) + n-PrOH (2)

		T/K=298.15				T/K=308.15	
0.0000	1206.1	859.3	0.0	0.0000	1172.2	919.1	0.0
0.0519	1272.3	718.7	-77.8	0.0519	1237.1	767.3	-84.2
0.1097	1342.3	604.3	-128.5	0.1097	1305.9	643.8	-139.0
0.2473	1486.2	437.6	-164.6	0.2473	1448.3	464.1	-178.2
0.3301	1561.1	375.9	-159.4	0.3301	1522.1	398.0	-172.4
0.4250	1640.8	323.7	-143.8	0.4250	1601.4	341.8	-155.7

31

0.5348	1724.4	279.6	-119.1	0.5348	1684.2	294.8	-128.8
0.6634	1808.4	243.3	-85.6	0.6634	1767.3	256.0	-92.3
0.8160	1892.0	213.1	-44.9	0.8160	1850.6	223.9	-48.3
0.9035	1937.7	199.0	-23.2	0.9035	1898.1	208.4	-25.2
1.0000	1982.8	186.2	0.0	1.0000	1943.1	194.8	0.0
	T/K=303.15				*T*/K=313.15		
0.0000	1189.1	888.6	0.0	0.0000	1155.4	951.0	0.0
0.0519	1254.7	742.4	-80.9	0.0519	1219.7	793.0	-87.7
0.1097	1324.0	623.7	-133.4	0.1097	1288.1	664.5	-144.9
0.2473	1467.1	450.7	-171.0	0.2473	1429.1	478.4	-185.2
0.3301	1542.0	386.5	-165.8	0.3301	1502.6	409.8	-179.3
0.4250	1621.3	332.5	-149.5	0.4250	1581.7	351.5	-161.9
0.5348	1704.9	286.9	-123.8	0.5348	1664.9	302.5	-134.1
0.6634	1788.3	249.4	-88.9	0.6634	1747.8	262.4	-96.2
0.8160	1871.6	218.3	-46.6	0.8160	1830.1	229.4	-50.1
0.9035	1917.9	203.7	-24.2	0.9035	1878.1	213.4	-26.2
1.0000	1962.9	190.5	0.0	1.0000	1923.2	199.3	0.0

The standard uncertainties are $u(x) = 6 \times 10^{-3}$, $u(u) = 0.5$ m·s^{-1}, $u(T) = 0.02$ K, $u(P) = 1$ kPa and the combined expanded uncertainties Uc is Uc(κ_S^E) = 0.03 TPa^{-1} (0.95 level of confidence).

Table 5

Fitting parameters (A_i) for the Redlich–Kister equation (6) along with the corresponding standard deviations for excess functions $\sigma(Y^E)$ for the binary mixtures at 298.15 K $\leq T \leq$ 313.15 K and 0.1MPa pressure.

Temperature	A_0	A_1	A_2	A_3	A_4	$\sigma (Y^E)$
	[emim][HSO$_4$] (1) + DMSO (2)		V^E /cm^3·mol^{-1}			
298.15	-4.523	2.506	-1.194	1.152	-0.845	0.0014
303.15	-4.625	2.480	-1.289	1.314	-0.930	0.0012
308.15	-4.732	2.476	-1.466	1.514	-0.817	0.0013
313.15	-4.883	2.487	-1.344	1.593	-1.124	0.0022
	[emim][HSO$_4$] (1) + DMSO (2)		κ_s^E/TPa^{-1}			
298.15	-115.1	96.38	-60.52	58.15	-39.47	0.1438
303.15	-119.6	99.85	-62.79	61.01	-41.57	0.1493
308.15	-124.8	103.9	-66.55	64.12	-43.51	0.1683
313.15	-130.1	108.0	-67.57	67.12	-46.45	0.1748
	[emim][HSO$_4$] (1) + EtOH (2)		V^E /cm^3·mol^{-1}			
298.15	-4.143	1.463	-2.213	1.859	-1.430	0.0017
303.15	-4.370	1.574	-2.239	2.019	-1.445	0.0012
308.15	-4.597	1.684	-2.238	2.176	-1.498	0.0012

313.15	-4.822	1.793	-2.247	2.332	-1.544	0.0012

[emim][HSO₄] (1) + EtOH (2) κ_s^E/TPa^{-1}

298.15	-561.4	561.5	-520.2	773.6	-600.6	0.7327
303.15	-583.3	596.5	-565.8	753.0	-538.7	0.6006
308.15	-605.4	629.2	-597.3	730.6	-493.0	0.6624
313.15	-629.5	663.5	-631.3	711.4	-448.6	0.6567

[emim][HSO₄] (1) + n-PrOH (2) V^E /cm³·mol⁻¹

298.15	-2.760	2.624	0.380	0.175	-1.025	0.0025
303.15	-2.956	2.594	0.379	0.414	-1.008	0.0029
308.15	-3.149	2.541	0.283	0.729	-0.926	0.0022
313.15	-3.345	2.525	0.238	0.904	-0.993	0.0023

[emim][HSO₄] (1) + n-PrOH (2) κ_s^E/TPa^{-1}

298.15	-509.9	461.1	-319.8	343.3	-238.8	0.2461
303.15	-530.6	479.8	-324.7	354.9	-258.2	0.2640
308.15	-551.7	502.5	-340.9	365.4	-267.1	0.1886
313.15	-574.1	521.3	-352.8	384.0	-281.4	0.1361

Highlights:

- Densities and speeds of sound are measured for [emim][HSO$_4$] with ethanol, 1-propanol, and DMSO.
- Excess properties (V^E and κ_s^E) are derived for the studied binary systems.
- The experimental results are analyzed in terms of ion-dipole, H-bonding interactions and structural effects.
- Temperature dependence of the excess properties is discussed.
- Excess functions are correlated with Redlich–Kister equation.

Graphical Abstract:

Synthesis of Ca 2 SiO 4 :Dy 3+ phosphors from agricultural waste for solid state lighting applications

5 authors, including:

Lingam Lakshmi Devi
Sri Venkateswara University
8 PUBLICATIONS **116** CITATIONS

Ch. Basavapoornima
Sri Venkateswara University
47 PUBLICATIONS **979** CITATIONS

Vemula Venkatramu
Yogi Vemana University
94 PUBLICATIONS **2,357** CITATIONS

P. Babu
Government Degree College, Palamaner, India
92 PUBLICATIONS **3,701** CITATIONS
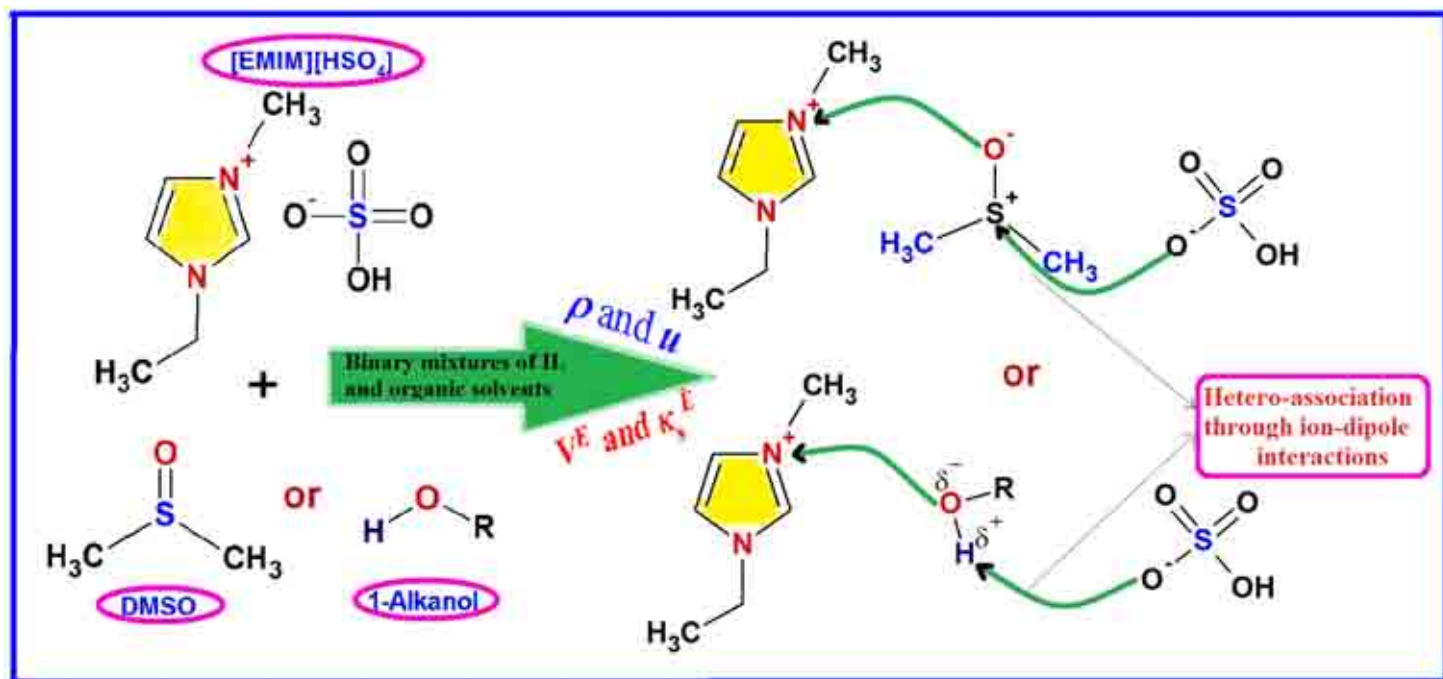
Some of the authors of this publication are also working on these related projects:

Nanophosphors View project

DST and DAE View project
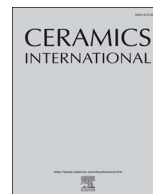
CERAMICS
INTERNATIONAL

CrossMark

Synthesis of Ca_2SiO_4:Dy^{3+} phosphors from agricultural waste for solid state lighting applications

L. Lakshmi Devi[a], Ch. Basavapoornima[a], V. Venkatramu[b], P. Babu[c], C.K. Jayasankar[a,*]

[a] Department of Physics, Sri Venkateswara University, Tirupati 517502, India
[b] Department of Physics, Yogi Vemana University, Kadapa 516003, India
[c] Department of Physics, SVCR Govt. Degree College, Palamaner 517408, India

ABSTRACT

Trivalent dysprosium (Dy^{3+}) ions -doped calcium silicate (Ca_2SiO_4) phosphors have been synthesized by utilizing agricultural waste of egg shell and rice husk through solid-state reaction method. The synthesized Ca_2SiO_4 powders thus obtained are crystallized in monoclinic structure with unit cell parameters of a = 5.53 Å; b = 6.67 Å; c = 9.13 Å; β = 87.43° and irregular shape morphology. Luminescent properties of Dy^{3+}:Ca_2SiO_4 phosphors were studied by varying active ion concentration. The phosphors emit characteristic blue and yellow emissions of Dy^{3+} ions corresponding to the $^4F_{9/2} \rightarrow {}^6H_{15/2}$ and $^4F_{9/2} \rightarrow {}^6H_{13/2}$ transitions, respectively. Color coordinates evaluated from emission spectra are found to fall in the white light region. Decay curves for the $^4F_{9/2}$ level of Dy^{3+} ions exhibit single exponential nature and turn into non-exponential with shortening of lifetime from 739 μs to 510 μs when Dy^{3+} ion concentration is increased from 0.001 to 0.5 mol%. All these results confirm that Ca_2SiO_4:Dy^{3+} phosphors are suitable for the use as low cost white light emitting phosphors.

1. Introduction

In recent years, the conversion of agricultural waste into low cost luminescent materials is a challenging task to reduce environmental pollution by converting waste into useful low cost materials [1–8]. The trivalent lanthanide (Ln^{3+}) ions-doped luminescent materials have attracted much attention due to their superb applications in the fields of lighting, display, optical sensors, solar energy harvesting, bio-imaging, and so on [9–14], in particular for the development of light emitting devices. Among all the light emitting devices (LEDs), the white light emitting devices (WLEDs) are deemed to become important sources because of their low power consumption, higher brightness, longer durability, fast response, environment benign, etc. [15–17]. The WLEDs are normally fabricated by the combination of a blue LED with a yellow emitting phosphor (YAG:Ce^{3+}). But the yellow phosphor show chemical instability, low absorption cross-section and moreover they are synthesized with commercial chemicals [18,19]. Hence, the quest to identify/develop new phosphors with low cost, chemically stable and high luminescence efficiency is a daunting task.

Hence, the present investigation is aimed at synthesis of low cost white light emitting phosphors by utilizing agricultural waste materials such as rice husk and egg shells. Nowadays recycling of agricultural residues such as rice husk and egg shells into luminescent materials is

attracting much attention as there is twofold advantage in it. One is prevention of environmental pollution and second one is development of luminescent materials at the low cost. Therefore, the main objective of the present study is not only to reduce environmental pollution but also to make use of them effectively for the development of phosphors with better luminescence properties by using agricultural waste materials (rice husk and egg shells). Rice husk is a renewable agricultural material and contains an active form of silica (SiO_2) of about 98%, substitute for commercial SiO_2. Another key waste material is egg shell (ES), which is comprised of calcium oxide (CaO) of about 96%, substitute for commercial CaO.

Among Ln^{3+} ions, Dy^{3+} ion is capable of emitting a white light since its emission spectrum consists of blue and yellow emissions [20–36]. The $^4F_{9/2} \rightarrow {}^6H_{13/2}$ transition is hypersensitive in nature and its emission intensity strongly depends on the local environment whereas the $^4F_{9/2} \rightarrow {}^6H_{15/2}$ transition is magnetic-dipole in nature and its intensity is almost independent of surrounding environment. Hence, Dy^{3+}-doped phosphors are capable of emitting white light by varying the chemical composition of the host.

In recent years, RE^{3+}-doped phosphors such as vanadates [20], molybdates [37], tungstates [38,39], silicates [40], and aluminates [41,42] besides RE^{3+}-doped glasses [21,35,43] have been investigated. Among these host materials, silicates are attractive class of inorganic

phosphors due to their higher physical and chemical stabilities, and wide transparency [44]. The main objective of the present investigation is synthesis of Dy^{3+}-doped Ca_2SiO_4 phosphors using the agricultural waste materials such as rice husk ash and egg shells and study their structural, morphological and luminescent properties for the development of low cost white light emitting phosphors.

2. Experimental procedure

Ca_2SiO_4:xDy^{3+} (x = 0.001, 0.005, 0.01, 0.05, 0.1, 0.2, 0.3, 0.4 and 0.5 mol%) phosphors were prepared by a conventional solid-state reaction method in three steps and the detailed procedure is shown in the following sections.

2.1. Synthesis of SiO_2 from rice husk

Rice husk (RH) was washed with normal tap water for removing soil and dust. After that RH was dried at normal room temperature for 24 h, and placed uniformly in aluminum rectangular tray with large surface area. Flat trays were chosen for uniform distribution of rice husk powder so as to have sufficient air circulation. The tray containing RH was placed in a furnace at 600 °C for 6 h and then 1000 °C for 8 h for sintering, finally white rice husk ash (RHA) was obtained which was grinded very well to obtain fine powder.

2.2. Synthesis of CaO from egg shells

White egg shells (ES) were washed with tap water to remove all adhering albumen, dried at room temperature for 12 h, after that the ES were crushed into small pieces. These crushed ES were placed uniformly in aluminum rectangular tray with large surface area for sufficient air circulation. The tray containing ES was placed in a furnace at 900 °C for 4 h for sintering and finally white ES powder was obtained and then well grinded to obtain fine powder.

2.3. Synthesis of Dy^{3+}- doped Ca_2SiO_4 phosphors

Calcium silicate (Ca_2SiO_4) phosphors doped with Dy_2O_3 ions was prepared with the following chemical equation:

$$8CaO + 4 SiO_2 + 2Dy_2O_3 \rightarrow 4 Ca_2SiO_4Dy + 3O_2 \uparrow$$
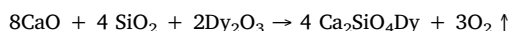
With the help of above chemical equation, the stoichiometric ratio of $Ca_{2(1-x)}SiO_4$: xDy^{3+} (where x = 0.001, 0.005, 0.01, 0.05, 0.1, 0.2, 0.3, 0.4 and 0.5 mol%) have been synthesized by using solid state reaction method.

The stoichiometric quantities of CaO from egg shells, SiO_2 from rice husk and Dy_2O_3 (99.99%) from Sigma-Aldrich were weighed and grinded using an agate mortar. The grinded powders were pre-sintered at 1250 °C for 8 h with several intermediate grindings and finally sintered at 1250 °C for 8 h. The structure of the prepared powders were characterized by using X-ray diffractometer (RIGAKU, Miniflex-600) using Cu k_α radiation (1.5406 Å). The morphology of these phosphors was studied by scanning electron microscope (SEM) and elemental analysis was carried out using energy dispersive spectroscopy (EDS), by using CARL ZEISS EVO MA15 SEM. The excitation and emission spectra and decay curves were recorded using Edinburgh UV–vis–NIR (FLS 980) spectrometer equipped with xenon arc lamp (450 W) as an excitation source.

3. Results and discussion

3.1. Structure and morphology

The XRD patterns have been measured for undoped and Dy^{3+}-doped Ca_2SiO_4 phosphors. These XRD patterns along with their planes ($h\ k\ l$) have been shown in Fig. 1 for undoped and 0.5 mol% Dy^{3+}-doped

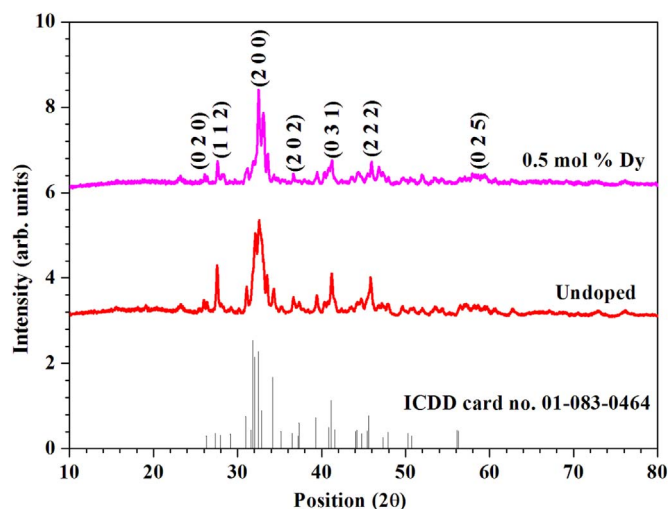**Fig. 1.** X-Ray diffraction patterns and their ($h\ k\ l$) planes for undoped Ca_2SiO_4 and 0.5 mol% Dy^{3+}-doped Ca_2SiO_4 phosphor powders.

Ca_2SiO_4 phosphors. These patterns matches well with the standard ICDD card no. 01-083-0464. This clearly indicates that Dy^{3+}-doped Ca_2SiO_4 phosphors are crystallized in monoclinic structure with unit cell parameters of a = 5.53 Å; b = 6.67 Å; c = 9.13 Å; β = 87.43°; and volume of 340 Å³. The particle size was calculated using the Scherrer's formula and is found to be 33 nm. The morphology of the 0.001–0.5 mol% Dy^{3+}-doped Ca_2SiO_4 phosphor has been characterized by SEM and is shown in Fig. 2 for 0.2 mol% Dy^{3+}-doped Ca_2SiO_4 phosphor. As can be seen from SEM images, particles of irregular in shape are distributed non-uniformly in synthesized phosphors. Further, elemental analysis has been carried out using EDS for all synthesized phosphors and is shown for 0.1 mol% Dy^{3+}-doped Ca_2SiO_4 phosphor (see Fig. 3). As can be seen from EDS spectrum, all the elements, i.e., calcium (Ca), dysprosium (Dy), silica (Si) and oxygen (O) have been identified in their respective proportions.

3.2. Luminescence spectra

The luminescence excitation spectra for the Dy^{3+}-doped Ca_2SiO_4 phosphors have been measured by monitoring the yellow emission at 573 nm. The excitation spectrum for 0.5 mol% Dy^{3+}-doped Ca_2SiO_4 phosphors are shown in Fig. 4 and exhibited three intense bands at 351 nm ($^6H_{15/2} \rightarrow ^6P_{7/2} + ^4M_{15/2}$), 366 nm ($^6H_{15/2} \rightarrow ^6P_{5/2}$) and 387 nm

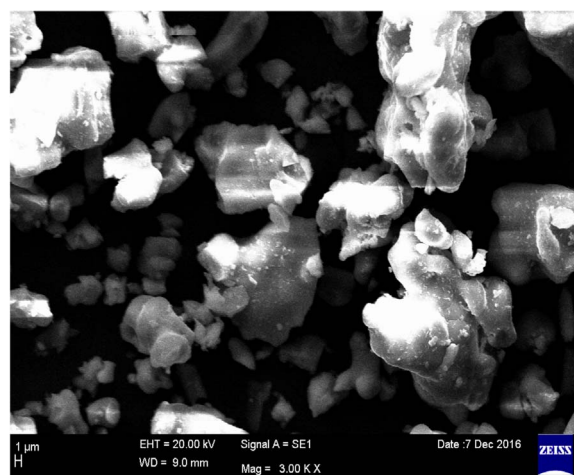**Fig. 2.** Scanning electron micrograph of 0.2 mol% Dy^{3+}-doped Ca_2SiO_4 phosphors.
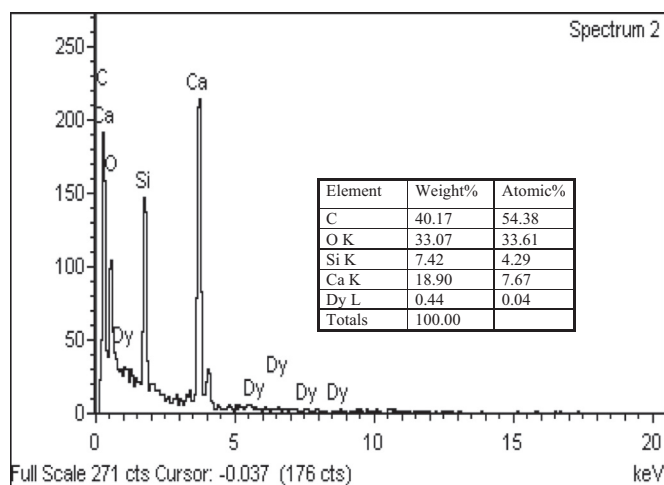
Fig. 3. Energy dispersive spectrum for 0.2 mol% Dy^{3+}-doped Ca_2SiO_4 phosphors.

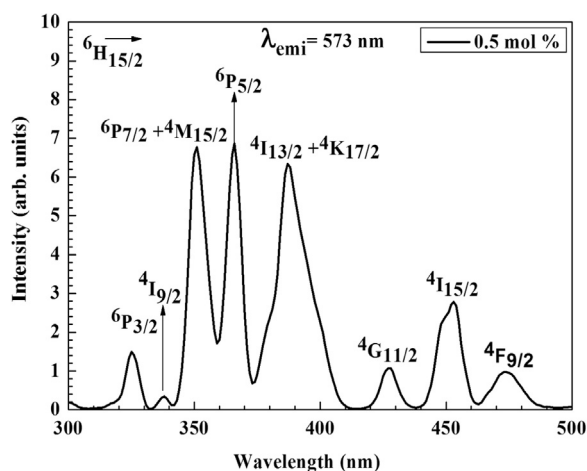**Fig. 4.** Excitation spectrum for 0.5 mol% Dy^{3+}-doped Ca_2SiO_4 phosphors.

($^6H_{15/2} \rightarrow {}^4I_{13/2} + {}^4K_{17/2}$) as well as two moderate bands at 325 nm ($^6H_{15/2} \rightarrow {}^6P_{3/2}$), 453 nm ($^6H_{15/2} \rightarrow {}^4I_{15/2}$) and three feeble bands at 337 nm ($^6H_{15/2} \rightarrow {}^4I_{9/2}$), 428 nm ($^6H_{15/2} \rightarrow {}^4G_{11/2}$) and 473 nm ($^6H_{15/2} \rightarrow {}^4F_{9/2}$). As can be seen from Fig. 4, high intensity bands are observed in the near UV and blue regions for $Ca_2SiO_4:Dy^{3+}$ phosphor, which is prerequisite for the development of white-light emitting devices using commercial blue InGaN/GaN LED chip.

The emission spectra for Dy^{3+}-doped Ca_2SiO_4 phosphors have been measured under 351 nm excitation. It consist of four emission peaks in blue (460–500 nm), yellow (555–600 nm), feeble red (650–685 nm) and deep red (740–780 nm) regions. These blue, yellow, feeble red and deep red emissions are assigned to the $^4F_{9/2} \rightarrow {}^6H_{15/2}$, $^4F_{9/2} \rightarrow {}^6H_{13/2}$, $^4F_{9/2} \rightarrow {}^6H_{11/2}$ and $^4F_{9/2} \rightarrow {}^6H_{9/2}$ transitions, respectively, as shown in Fig. 5. The blue emission corresponding to the $^4F_{9/2} \rightarrow {}^6H_{15/2}$ transition is magnetic-dipole in nature and its intensity is almost independent of local surroundings of the active ions. The yellow emission due to the $^4F_{9/2} \rightarrow {}^6H_{13/2}$ transition is hypersensitive and is allowed only at low symmetries with no inversion center. Therefore, in the present Ca_2SiO_4 phosphor, the Dy^{3+} ions are placed in such low symmetry sites of monoclinic and hence the $^4F_{9/2} \rightarrow {}^6H_{13/2}$ transition is prominent in their emission spectra. From the Fig. 5, it is found that the blue and yellow emission bands are splitted into two components due to the partial lifting of degeneracy by the crystal-field around the Dy^{3+} ion. With the increasing concentration, the crystal-field splitting increases due to the increase of surrounding Stark effect. As can be seen from the Fig. 5, it is observed that there is gradual increase in emission intensity with increase in Dy^{3+} ion concentration from 0.001 to 0.5 mol%
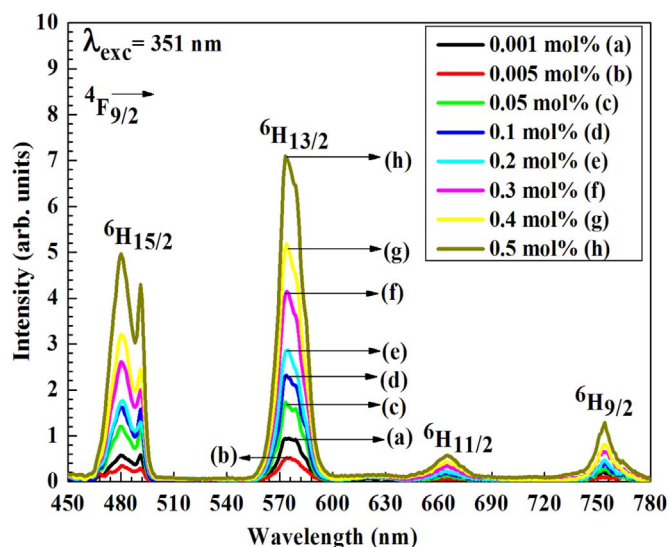

Fig. 5. Luminescence spectra for Dy^{3+}-doped Ca_2SiO_4 phosphors.

[23,45,46]. It clearly indicates that the Ca^{2+} (r = 240 pm) ions are replaced by Dy^{3+} (r = 235 pm) ions which are the luminescence centers.

The (Y/B) intensity ratios of luminescence spectra have been evaluated. It is possible to generate white light by tuning of these colors (yellow and blue) emitted from the Dy^{3+} ions. In general, the Y/B ratio is sensitive to the chemical composition of the host but little changes are observed with the variation of Dy^{3+} ions concentration in the present study (See Table 1). From the Y/B ratios of $Ca_2SiO_4:Dy^{3+}$ phosphors, the maximum value of 1.92 for 0.01 mol% and minimum value of 1.27 for 0.05 mol% of Dy^{3+} ions have been noticed. These small changes in Y/B ratios can be explained by the structural changes in the vicinity of Dy^{3+} ions [21,22,47,48]. The concentration dependent variations of Y/B ratios as well as excitation wavelength dependent variation of Y/B ratios are very small in the present $Ca_2SiO_4:Dy^{3+}$ phosphors and hence the later experimental results are not shown. These results indicate that the Dy^{3+} ions occupy lower symmetry of monoclinic structure in the Ca_2SiO_4 powders as evidenced from XRD results.

The evaluated Y/B ratios of $Ca_2SiO_4:Dy^{3+}$ phosphors are compared in Table 2 with those of other commercially available Dy^{3+}-doped luminescent materials [13,14,27–30,36,48–51]. As the Y/B ratios of the present $Ca_2SiO_4:Dy^{3+}$ phosphors are higher than those of Dy^{3+}-doped $Y_2CaZnO_5:Dy^{3+}$ (0.5 mol%) [14], $Ba_5CaAl_4O_{12}:Dy^{3+}$ (0.10 mol%) [27], $Sr_3Y(PO_4)_3:Dy^{3+}$ (4 mol%) [28], $Ca_3Si_2O_7:Dy^{3+}$ (0.1 mol%) [29], $Na_3SrB_5O_{10}:Dy^{3+}$ (7 mol%) [30], $KY_{(1-x)}BO_3:Dy^{3+}$ (0.3 mol%) [36], $NaLa(MoO_4)_2:Dy^{3+}$ (0.02 mol%) [49], $YAl_3(BO_3)_4:Dy^{3+}$ (0.5 mol%) [50] and $Ca_3Gd_7(PO_4)(SiO_4)_5O_2:Dy^{3+}$ (0.10 mol%) [51], whereas lower than those of $BYF_5:Dy^{3+}$ (1 mol%) [13] and $Lu_3Ga_5O_{12}:Dy^{3+}$ (2.0 mol%) [48].

Table 1
Y/B ratio, color coordinates (x, y) and lifetimes (τ, μs) for different concentrations (C, mol%) of Dy^{3+}-doped Ca_2SiO_4 phosphors for 351 nm excitation.

S. no.	C	Y/B ratio	(x, y)	τ
1	0.001	1.52	(0.284, 0.286)	711
2	0.005	1.34	(0.239, 0.258)	739
3	0.01	1.92	(0.286, 0.288)	713
4	0.05	1.27	(0.264, 0.272)	712
5	0.1	1.31	(0.276, 0.292)	660
6	0.2	1.47	(0.299, 0.324)	573
7	0.3	1.47	(0.313, 0.338)	541
8	0.4	1.49	(0.317, 0.342)	515
9	0.5	1.33	(0.320, 0.349)	510

Table 2
Comparison of Y/B ratio, color coordinates (x, y) and lifetimes (τ, μs) for Dy^{3+}: phosphors.

S. no.	Host	Y/B ratio	(x, y)	τ
1	Ca_2SiO_4:0.5 Dy^{3+} [Present work]	1.33	(0.320, 0.349)	510
2	BYF_5:1 Dy^{3+} [13]	1.98	(0.354, 0.402)	1300
3	Y_2CaZnO_5:0.5 Dy^{3+} [14]	1.12	(0.378, 0.438)	458
4	YVO_4:1 Dy^{3+} [24]	–	(0.39, 0.44)	290
5	$Ca_9La(PO_4)_5(SiO_4)Cl_2$:0.20 Dy^{3+} [25]	–	–	477
6	$Ba_{10}F_2(PO_4)_6$:0.40 Dy^{3+} [26]	–	(0.300, 0.357)	688
7	$Ba_5CaAl_4O_{12}$:0.10 Dy^{3+} [27]	1.09	(0.333, 0.361)	–
8	$Sr_3Y(PO_4)_3$:4 Dy^{3+} [28]	0.876	(0.330, 0.366)	–
9	$Ca_3Si_2O_7$:0.1 Dy^{3+} [29]	0.765	(0.33, 0.33)	–
10	$Na_3SrB_5O_{10}$:7 Dy^{3+} [30]	0.89	(0.305, 0.317)	570
11	$NaPbB_5O_9$:0.02 Dy^{3+} [31]	–	(0.33, 0.36)	349
12	Li_2SrSiO_4:0.5 Dy^{3+} [32]	–	(0.259, 0.289)	902
13	$Sr_3Bi(PO_4)_3$:0.07 Dy^{3+} [33]	–	(0.327, 0.353)	–
14	$KY_{(1-x)}BO_3$:0.3 Dy^{3+} [36]	1.20	(0.29, 0.32)	130
15	$Lu_3Ga_5O_{12}$:2.0 Dy^{3+} [48]	2.57	(0.386, 0.391)	1450
16	$NaLa(MoO_4)_2$:0.02 Dy^{3+} [49]	1.63	(0.336, 0.392)	–
17	$YAl_3(BO_3)_4$:0.5 Dy^{3+} [50]	0.9462	(0.2838, 0.3101)	565
18	$Ca_3Gd_7(PO_4)(SiO_4)_5O_2$:0.10 Dy^{3+} [51]	1.14	(0.328, 0.343)	–
19	Sr_2SiO_4:6 Dy^{3+} [53]	–	(0.351, 0.389)	59.3
20	$KLa(PO_3)_4$:0.5 Dy^{3+} [54]	–	(0.215, 0.221)	870
21	$Gd(BO_2)_3$:0.06 Dy^{3+} [55]	–	–	12
22	$Ca_9Y(VO_4)_7$:0.1 Dy^{3+} [56]	–	(0.339, 0.417)	226
23	$Sr_2MgSi_2O_7$:0.5 Dy^{3+} [58]	–	(0.310, 0.328)	–
24	$ZnWO_4$:0.5 Dy^{3+} [59]	–	(0.2681, 0.3091)	–
25	$Sr_3Gd(PO_4)_3$:0.08 Dy^{3+} [60]	–	(0.2461, 0.2784)	–
26	$LaBSiO_5$:0.008 Dy^{3+} [61]	–	(0.3145, 0.3943)	–

3.3. Color coordinates

The color coordinates are necessary to know the nature of color emitted by phosphors. The color coordinates have been determined using the emission spectra and are inturn used to calculate the correlated color temperatures (CCTs) [52]. The evaluated color coordinates for the Ca_2SiO_4:Dy^{3+} phosphors are shown in Fig. 6 and also presented in Table 1. From Fig. 6, it is observed that the color coordinates of present phosphors fall within the white light region and are close to the "ideal white light" (x = 0.33, y = 0.33) in the chromaticity diagram. The color coordinates for the present and reported systems are compared in Table 2. As can be seen, the color coordinates obtained for Ca_2SiO_4:Dy^{3+} are comparable to those of the reported systems [13,14,24,26–33,36,48–51,53,54,56,58–61]. The CCT values for Ca_2SiO_4:Dy^{3+} phosphors are found to vary from 4989 to 6369 K. From these observations, it is worth noting that the present phosphors made

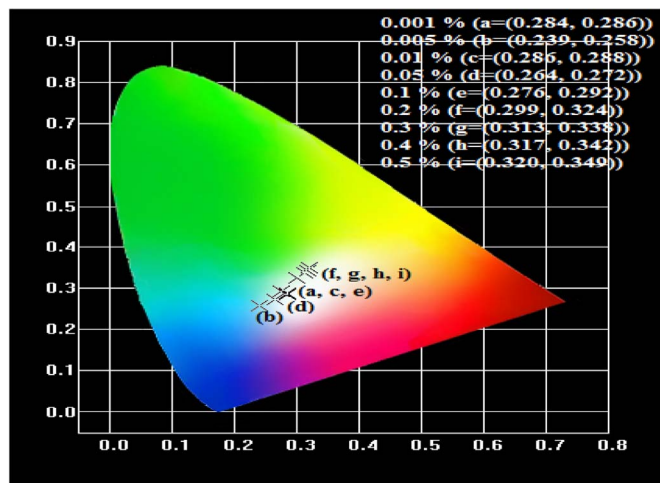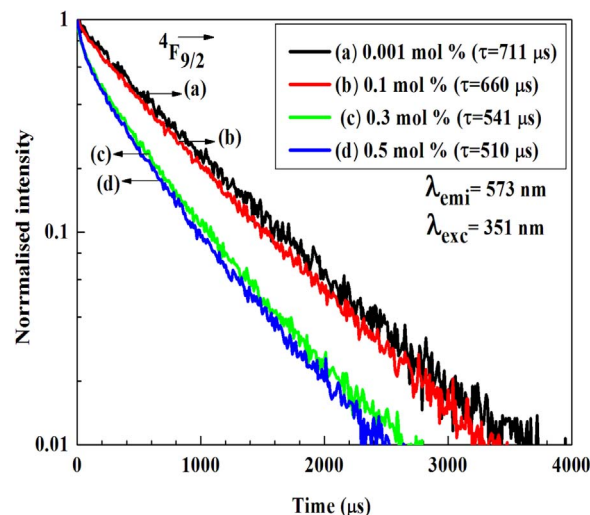**Fig. 6.** CIE chromaticity graph for Dy^{3+}-doped Ca_2SiO_4 phosphors.

Fig. 7. Decay curves for $^4F_{9/2}$ level of Dy^{3+} ions in Ca_2SiO_4 phosphors.

from the agriculture waste materials (rice husk and egg shells), exhibit white light luminescence [24,31,53] and are comparable to those of other reported phosphors [31,49,55]. Hence, the Ca_2SiO_4:Dy^{3+} phosphors synthesized from the utilization of agriculture waste could be useful for the fabrication of low cost white light-emitting devices.

3.4. Luminescent decay curves

The concentration dependent luminescent decay curves for the $^4F_{9/2}$ luminescent level of Dy^{3+} ions in Ca_2SiO_4 phosphors measured under 351 nm excitation by monitoring 573 nm emission, are presented in Fig. 7. For lower concentrations (0.001, 0.005, 0.01, 0.05 0.1 and 0.2 mol%), the decay curves are found to be nearly single exponential and as the concentration increases they turned to non-exponential nature (≥ 0.3 mol%). Hence, the effective lifetimes ($τ_{eff}$) for both the near single exponential and non-exponential decay curves have been evaluated using the expression,

$$\tau_{eff} = \frac{\int t I(t)dt}{\int I(t)dt} \tag{1}$$

The effective lifetimes for $^4F_{9/2}$ level of Dy^{3+} ions are found to be 711, 739, 713, 712, 660, 573, 541, 515 and 510 μs for 0.001, 0.005, 0.01, 0.05, 0.1, 0.2, 0.3, 0.4 and 0.5 mol% Dy^{3+}-doped Ca_2SiO_4 phosphors, respectively, and are shown in Table 1. It is found that the lifetime for the $^4F_{9/2}$ level increases upto 0.005 mol% Dy^{3+} concentration and then decreases. The increase in lifetime with increase in Dy^{3+} concentration from 0.001 to 0.005 mol% is due to the process of reabsorption. It is well known that for lower concentrations, the lifetime is higher and increases slightly with increase in concentration due to reabsoption of emitted photons. Beyond certain value, the lifetime starts to decrease with increase in concentration due to energy transfer between the luminescent ions. As can be seen from Table 1, in the present work also, lifetime increases with increase in concentration and then starts to decrease. The effective lifetimes are found to decrease with increase in Dy^{3+} concentration due to energy transfer between Dy^{3+} ions through cross-relaxation processes [13,48] and/or energy transfer to luminescence quenching centers (impurities). Similar decreasing trend with increase in Dy^{3+} concentration was reported for other Dy^{3+}: phosphors [25,26,30,31,55].

Lifetimes for the $^4F_{9/2}$ level of Dy^{3+} ions in different phosphors have been compared in Table 2. The effective lifetimes observed for the present Ca_2SiO_4:Dy^{3+} phosphors are found to be higher than those of BYF_5:Dy^{3+} (1 mol%) [13], $Ba_{10}F_2(PO_4)_6$:Dy^{3+} (0.40 mol%) [26], $Na_3SrB_5O_{10}$:Dy^{3+} (7 mol%) [30], Li_2SrSiO_4:Dy^{3+} (0.5 mol%) [32],
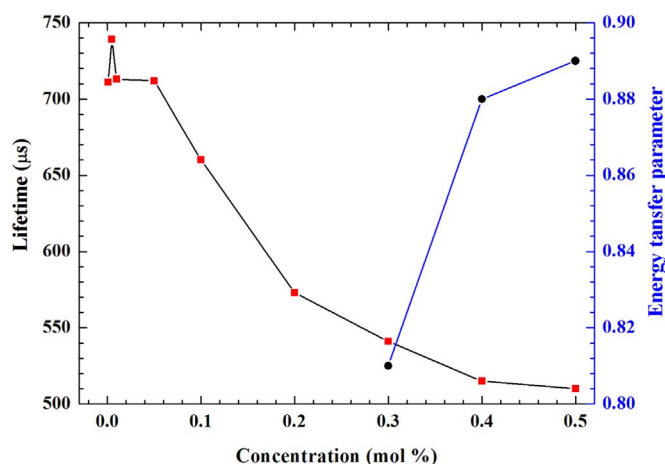
Fig. 8. The concentration dependent lifetime and energy transfer parameter for Dy^{3+}-doped Ca_2SiO_4 phosphors.

$Lu_3Ga_5O_{12}:Dy^{3+}$ (2.0 mol%) [48], $YAl_3(BO_3)_4:Dy^{3+}$ (0.5 mol%) [50], $KLa(PO_3)_4:Dy^{3+}$ (0.5 mol%) [54], whereas lower than those of $Y_2CaZnO_5:Dy^{3+}$ (0.5 mol%) [14], $YVO_4:Dy^{3+}$ (1 mol%) [24], $Ca_9La(PO_4)_5(SiO_4)Cl_2:Dy^{3+}$ (0.20 mol%) [25], $NaPbB_5O_9:Dy^{3+}$ (0.02 mol%) [31], $KY_{(1-x)}BO_3:Dy^{3+}$ (0.3 mol%) [36], $Sr_2SiO_4:Dy^{3+}$ (6 mol%) [53], $Gd(BO_2)_3:Dy^{3+}$ (0.06 mol%) [55], $Ca_9Y(VO_4):Dy^{3+}$ (0.1 mol%) [56].

The non-exponential decay curves of Dy^{3+}-doped Ca_2SiO_4 powders arises due to multipolar (dipole-dipole, dipole-quadrupole, quadrupole-quadrupole) interactions between active ions. To know the type of the multipolar interaction in our phosphors, Inokuti-Hirayama (IH) [57] model has been adopted. According to this model, the decay of luminescence intensity, I(t), is

$$I(t) = I_0 \exp\left\{ -\frac{t}{\tau_0} - Q\left(\frac{t}{\tau_0}\right)^{3/S} \right\} \qquad (2)$$

where 't' is the time after excitation, τ_0 is the intrinsic decay time of the donors in the absence of acceptors. Q is the energy transfer parameter, which depends on dipole-dipole ($S = 6$), dipole-quadrupole ($S = 8$) and quadrupole-quadrupole ($S = 10$) interactions. As can be seen from Fig. 7, the best fit has been obtained for $S = 6$, which indicates that the mechanism of energy transfer between Dy^{3+} ions is of dipole-dipole type. The energy transfer parameter (Q) increases with increase in concentration of Dy^{3+} ions. The lifetime values decreases with increase in Dy^{3+} ions concentrations (see Fig. 8).

4. Conclusions

A series of Dy^{3+}-doped Ca_2SiO_4 phosphors have been successfully synthesized from agricultural waste by the solid-state reaction method and investigated their structural, morphological, and luminescence properties. The synthesized Dy^{3+}-doped Ca_2SiO_4 phosphors are crystallized in monoclinic structure. The morphology of the Dy^{3+}-doped Ca_2SiO_4 phosphors are of irregular in shape with different sizes. The Y/B ratios are found to vary from 1.52 to 1.33 when Dy^{3+} concentrations vary from 0.001 mol% to 0.5 mol%. The color co-ordinates obtained from emission spectra are found to fall within the white light zone. The fluorescence decay curves are found to be nearly single exponential in nature for lower Dy^{3+} ions concentration and turns into non-exponential for higher concentrations ($\geq$ 0.3 mol%) due to energy transfer between Dy^{3+} ions through dipole-dipole interactions. The results obtained indicate that the $Ca_2SiO_4:Dy^{3+}$ phosphors are suitable for fabrication of low cost white light emitting devices.

References

[1] J. Kaewkhao, P. Limsuwan, Utilization of rice husk fly ash in the color glass production, Procedia Eng. 32 (2012) 670–675.
[2] T. Lee, R. Othman, F.Y. Yeoh, Development of photoluminescent glass derived from rice husk, Biomass. Bioenery 59 (2013) 380–392.
[3] S. Angkulsupakul, R. Buntem, W. Kungkapradit, Preparation of Chromium-doped Glass from Rice Husk Ash, Thailand-Japan Student Science Fair P_CHM36, 2015, pp. 1–3.
[4] S. Sinyoung, K. Kunchariyakun, S. Asavapisit, K.J.D. MacKenzie, Synthesis of belite cement from nano-silica extracted from two rice husk ashes, J. Environ. Manag. 190 (2017) 53–60.
[5] S. Li, R.A. Cooke, L. Wang, F. Ma, R. Bhattarai, Characterization of fly ash ceramic pellet for phosphorus removal, J. Environ. Manag. 189 (2017) 67–74.
[6] C.S. Prasad, K.N. Maiti, R. Venugopal, Effect of substitution of quartz by rice husk ash and silica fume on the properties of whiteware compositions, Ceram. Int. 29 (2003) 907–914.
[7] N.P. Stochero, E. Marangon, A.S. Nunes, M.D. Tier, Development of refractory ceramics from residual silica derived from rice husk ash and steel fibres, Ceram. Int. (2017), http://dx.doi.org/10.1016/j.ceramint.2017.07.111 (In Press).
[8] L. Song, Z. Li, P. Duan, M. Huang, X. Hao, Y. Yu, Novel low cost and durable rapid-repair material derived from industrial and agricultural by-products, Ceram. Int. (2017), http://dx.doi.org/10.1016/j.ceramint.2017.07.106 (In Press).
[9] X. Huang, S. Han, W. Huang, X. Liu, Enhancing solar cell efficiency: the search for luminescent materials as spectral converters, Chem. Soc. Rev. 42 (2013) 173–201.
[10] X. Liu, R. Deng, Y. Zhang, Y. Wang, H. Chang, L. Huang, X. Liu, Probing the nature of upconversion nanocrystals: instrumentation matters, Chem. Soc. Rev. 44 (2015) 1479–1508.
[11] F. Wang, X. Liu, Recent advances in the chemistry of lanthanide-doped upconversion nanocrystals, Chem. Soc. Rev. 38 (2009) 976–989.
[12] F. Auzel, Upconversion and anti-Stokes processes with f and d ions in solids, Chem. Rev. 104 (2004) 139–173.
[13] P. Haritha, I.R. Martín, C.S. Dwaraka Viswanath, N. Vijaya, K. Venkata Krishnaiah, C.K. Jayasankar, D. Haranath, V. Lavín, V. Venkatramu, Structure, morphology and optical characterization of Dy^{3+}-doped $BaYF_5$ nanocrystals for warm white light emitting devices, Opt. Mat. 70 (2017) 16–24.
[14] R. Rajeswari, C.K. Jayasankar, D. Ramachari, S. Surendra Babu, Synthesis, structural and luminescence properties of near white light emitting Dy^{3+}-doped Y_2CaZnO_5 nanophosphor for solid state lighting, Ceram. Int. 39 (2013) 7523–7529.
[15] Y. Shimizu, K. Sakano, Y. Noguchi, T. Moriguchi, Light Emitting Device Having a Nitride Compound Semiconductor and a Phosphor Containing a Garnet Fluorescent Material, U.S. Patent 59998925, 1999.
[16] Y. Hu, W. Zhuang, H. Ye, D. Wang, S. Zhang, X. Huang, A novel red phosphor for white light emitting diodes, J. Alloy. Compd. 390 (2005) 226–229.
[17] X. He, M. Guan, N. Lian, J. Sun, T. Shang, Synthesis and luminescence characteristics of $K_2Bi(PO_4)(MO_4):Eu^{3+}$ (M = Mo, W) red-emitting phosphor for white LEDs, J. Alloy. Compd. 492 (2010) 452–455.
[18] H.Y. Jiao, Y.H. Wang, Intense red phosphors for near-ultraviolet light-emitting diodes, Appl. Phys. B 98 (2010) 423–427.
[19] G. Blasse, B.C. Grabmaier, Luminescent Materials, Springer, Berlin, 1994.
[20] N.S. Singh, R.S. Ningthoujam, M.N. Luwang, S.D. Singh, R.K. Vatsa, Luminescence, lifetime and quantum yield studies of $YVO_4:Ln^{3+}$ ($Ln^{3+} = Dy^{3+}$, Eu^{3+}) nanoparticles: concentration and annealing effects, Chem. Phys. Lett. 480 (2009) 237–242.
[21] J. Pisarska, R. Lisiecki, W. Ryba-Romanowski, T. Goryczka, W.A. Pisarski, Unusual luminescence behavior of Dy^{3+}-doped lead borate glass after heat treatment, Chem. Phys. Lett. 489 (2010) 198–201.
[22] S. Ruengsri, S. Insiripong, N. Sangwaranatee, H.J. Kim, N. Wantana, A. Angnanon, J. Kaewkhao, Development of Dy^{3+}-doped $Gd_2MoB_2O_9$ phosphor and their luminescence behaviour, Integr. Ferroelectr. 177 (2017) 39–47.
[23] S.N. Ogugua, H.C. Swart, O.M. Ntwaeaborwa, White light emitting $LaGdSiO_5:Dy^{3+}$ nanophosphors for solid state lighting applications, Physica B 480 (2016) 131–136.
[24] K.E. Foka, B.F. Dejene, H.C. Swart, The effect of urea: nitrate ratio on the structure and luminescence properties of $YVO_4:Dy^{3+}$ phosphors, Physica B 480 (2016) 95–99.
[25] H. Liu, L. Liao, Q. Guo, D. Yang, L. Mei, $Ca_9La(PO_4)_5(SiO_4)Cl_2:Dy^{3+}$:a white-emitting apatite-type phosphor pumped for n-UV W- LEDs, J. Lumin. 181 (2017)

407–410.

[26] Z. Zhang, A. Song, Xihaishen, Q. Lian, X. Zheng, A novel white emission in $Ba_{10}F_2(PO_4)_6:Dy^{3+}$ single phase full-color phosphor, Mater. Chem. Phys. 151 (2015) 345–350.

[27] F. Yang, H. Ma, Y. Liu, B. Han, H. Feng, Q. Yu, Photoluminescence properties of novel Dy^{3+} doped $Ba_5CaAl_4O_{12}$ phosphors, Ceram. Int. 40 (2014) 10189–10192.

[28] J. Wang, J. Wang, P. Duan, Luminescent properties of Dy^{3+} doped $Sr_3Y(PO_4)_3$ for white LEDs, Mater. Lett. 107 (2013) 96–98.

[29] X. Zhang, Z. Lu, F. Meng, L. Hu, X. Xu, J. Lin, C. Tang, Luminescence properties of $Ca_3Si_2O_7:Dy^{3+}$ phosphor for white light-emitting diodes, Mater. Lett. 79 (2012) 292–295.

[30] G.R. Dillip, S.J. Dhoble, B. Deva Prasad Raju, Luminescence properties of $Na_3SrB_5O_{10}:Dy^{3+}$ plate-like microstructures for solid state lighting applications, Opt. Mater. 35 (2013) 2261–2266.

[31] D. Rajesh, M. Dhamodhara Naidu, Y.C. Ratnakaram, Synthesis and photoluminescence properties of $NaPbB_5O_9:Dy^{3+}$ phosphor materials for white light applications, J. Phys. Chem. Solids 75 (2014) 1210–1216.

[32] P. You, G. Yin, X. Chen, B. Yue, Z. Huang, X. Liao, Y. Yao, Luminescence properties of Dy^{3+}-doped Li_2SrSiO_4 for NUV-excited white LEDs, Opt. Mater. 33 (2011) 1808–1812.

[33] Z. Yang, Y. Liu, C. Liu, F. Yang, Q. Yu, X. Li, F. Lu, Multiwavelength excited white-emitting Dy^{3+} doped $Sr_3Bi(PO_4)_3$ phosphor, Ceram. Int. 39 (2013) 7279–7283.

[34] V. Venkatramu, M. Giarola, G. Mariotto, S. Enzo, S. Polizzi, C.K. Jayasankar, F. Piccinelli, M. Bettinelli, A. Speghini, Nanocrystalline lanthanide-doped $Lu_3Ga_5O_{12}$ garnets: interesting materials for light-emitting devices, Nanotechnology 21 (2010) 1–12 (175703).

[35] K. Venkata Krishnaiah, K. Upendra Kumar, C.K. Jayasankar, Spectroscopic properties of Dy^{3+}-doped oxyfluoride glasses for white light emitting diodes, Mater. Exp. 3 (1) (2013) 61–70.

[36] G. Sowjanya, L. Rama Moorthy, Ch Basavapoornima, C.K. Jayasankar, Structural and luminescent properties of $KY_{(1−x)}Dy_xBO_3$ phosphors, Spectrochim. Acta Part A: Mol. Biomol. Spectrosc. 170 (2017) 206–213.

[37] X. Yang, X. Yu, H. Yang, Y. Guo, Y. Zhou, The investigation of optical properties by doping halogen in the $BaMoO_4$: Pr^{3+} phosphor system, J. Alloy. Compd. 479 (2009) 307–309.

[38] J. Liao, B. Qiu, H. Lai, Synthesis and luminescence properties of $Tb^{3+}:NaGd(WO_4)_2$ novel green phosphors, J. Lumin. 129 (2009) 668–671.

[39] J. Liao, B. Qiu, H. Wen, J. Chen, W. You, Hydrothermal synthesis and photoluminescence of $SrWO_4:Tb^{3+}$ novel green phosphor, Mater. Res. Bull. 44 (2009) 1863–1866.

[40] J. Wen, Y.Y. Yeung, L. Ning, C.K. Duan, Y. Huang, J. Zhang, M. Yin, Effects of vacancies on valence stabilities of europium ions in β-Ca_2SiO_4: Eu phosphors, J. Lumin. 178 (2016) 121–127.

[41] H. Ryu, K.S. Bartwal, Exploration and optimization of Dy codoping in polycrystalline $CaAl_2O_4$: Eu, J. Alloy. Compd. 476 (2009) 379–382.

[42] C. Chang, W. Li, X. Huang, Z. Wang, X. Chen, X. Qian, R. Guo, Y. Ding, D. Mao, Photoluminescence and afterglow behavior of Eu^{2+}, Dy^{3+} and Eu^{3+} Dy^{3+} in $Sr_3Al_2O_6$ matrix, J. Lumin. 130 (2010) 347–350.

[43] V. Ravi kumar, G. Giridhar, N. Veeraiah, Influence of modifier oxide on emission

features of Dy^{3+} ion in Pb_3O_4-ZnO-P_2O_5 glasses, Opt. Mater. 60 (2016) 594–600.

[44] L. Lin, M. Yin, C.S. Shi, W.P. Zhang, Luminescence properties of a new red long-lasting phosphor:$Mg_2SiO_4:Dy^{3+}$, Mn^{2+}, J. Alloy. Compd. 455 (2008) 327–330.

[45] J.B. Gruber, B. Zandi, Uygun V. Valiev, Sh.A. Rakhimov, Energy level of Dy^{3+} ($4f^9$) in orthoaluminate crystals, J. Appl. Phys. 94 (2) (2003) 1030–1034.

[46] K.N. Shinde, S.J. Dhoble, A. Kumar, Synthesis of novel Dy^{3+} activated phosphate phosphors for NUV excited LED, J. Lumin. 131 (2011) 931–937.

[47] U. Fawad, Myeongjin Oh, H. Park, Sunghwan Kim, H.J. Kim, Luminescent investigations of $Li_6Lu(BO_3)_3:Tb^{3+}$, Dy^{3+} phosphors, J. Alloy. Compd. 610 (2014) 281–287.

[48] P. Haritha, I.R. Martín, K. Linganna, V. Monteseguro, P. Babu, S.F. León-Luis, C.K. Jayasankar, U.R. Rodríguez-Mendoza, V. Lavín, V. Venkatramu, Optimizing white light luminescence in Dy^{3+}-doped $Lu_3Ga_5O_{12}$ nano-garnets, J. Appl. Phys. 116 (2014) 1–7 (174308).

[49] L. Li, W. Zi, G. Li, S. Lan, G. Ji, S. Gan, H. Zou, X. Xu, Hydrothermal synthesis and luminescent properties of $NaLa(MoO_4)_2:Dy^{3+}$ phosphor, J. Solid State Chem. 191 (2012) 175–180.

[50] G.V. Lokeswara Reddy, L. Rama Moorthy, B.C. Jamalaiah, T. Sasikala, Preparation, structural and luminescent properties of $YAl_3(BO_3)_4:Dy^{3+}$ phosphor for white light emission under UV excitation, Ceram. Int. 39 (2013) 2675–2682.

[51] M. Tong, Y. Liang, G. Li, Z. Xia, M. Zhang, F. Yang, Q. wang, Luminescent properties of single Dy^{3+} ions activated $Ca_3Gd_7(PO_4)(SiO_4)_5O_2$ phosphor, Opt. Mater. 36 (2014) 1566–1570.

[52] C.S. McCamy, Correlated color temperature as an explicit function of chromaticity co-ordinates, Color Res. Appl. 17 (1992) 142–144.

[53] M.A. Tshabalala, F.B. Dejene, Shreyas S. Pitale, H.C. Swart, O.M. Ntwaeaborwa, Generation of white-light from Dy^{3+} doped Sr_2SiO_4 phosphor, Physica B 439 (2014) 126–129.

[54] S. Chemingui, M. Ferhi, K. Horchani-Naifer, M. Férid, Synthesis and luminescence characteristics of Dy^{3+} doped $KLa(PO_3)_4$, J. Lumin. 166 (2015) 82–87.

[55] X. Zhang, F. Meng, W. Li, S.I. Kim, Y.M. Yu, H.J. Seo, Investigation of energy transfer and concentration quenching of Dy^{3+} luminescence in $Gd(BO_2)_3$ by means of fluorescence dynamics, J. Alloy. Compd. 578 (2013) 72–76.

[56] L. Jing, X. Liu, Y. Li, Y. Wang, Synthesis and photoluminescence properties of $Ca_9Y(VO_4)_7:Dy$ phosphors for white light-emitting diodes, J. Lumin. 162 (2015) 185–190.

[57] M. Inokuti, F. Hirayama, Effect of energy transfer by the exchange mechanism on donor luminescence, J. Chem. Phys. 43 (1965) 1978–1989.

[58] R. Shrivastava, J. Kaur, M. Dash, Studies on white light emission of $Sr_2MgSi_2O_7$doped with Dy^{3+} phosphors, Superlattices Microstruct. 82 (2015) 262–268.

[59] Z. Yongqing, L. Xuan, L. Jia, J. Man, A novel white-emitting phosphor $ZnWO_4:Dy^{3+}$, J. Rare Earths 33 (2015) 350–354.

[60] Q. Xu, J. Sun, D. Cui, Q. Di, J. Zeng, Synthesis and luminescence properties of novel $Sr_3Gd(PO_4)_3:Dy^{3+}$ phosphor, J. Lumin. 158 (2015) 301–305.

[61] S. Liu, Y. Liang, M. Tong, D. Yu, Y. Zhu, X. Wu, C. Yan, Photoluminescence properties of novel white phosphor of Dy^{3+}-doped $LaBSiO_5$ glass, Mater. Sci. Semicond. Process. 38 (2015) 266–270.